Measles induces immune amnesia pp. 560 & 599

Russia debates a plan to make gene-edited babies p. 562

Finding a hidden black hole p. 637

Science

$15
1 NOVEMBER 2019
sciencemag.org

AAAS



GENE FLOW

Hybridization boosts butterfly genome complexity pp. 570 & 594

CONTENTS

1 NOVEMBER 2019 • VOLUME 366 • ISSUE 6465



562
Geneticist Denis Rebrikov is open about his plans to correct a deafness mutation in babies, using the genome editor CRISPR.

PHOTO: SERGEY PONOMAREV

NEWS

IN BRIEF

552 News at a glance

IN DEPTH

555 Genetics lab accused of misusing African DNA
Sanger institute's aborted effort to commercialize gene chip could hinder research in Africa *By E. Stokstad*

556 Mud in storied ice core hints at a thawed Greenland
Dirty base of Camp Century ice core warns of future ice sheet retreat
By P. Voosen

558 Alien comets may be common, analysis of 2I/Borisov suggests
A dozen interstellar objects may be passing near the Sun
By W. W. Gibbs

558 Gates and NIH join forces on HIV and sickle cell diseases
A unique marriage aims to speed development of simple DNA-based cures
By J. Cohen and J. Kaiser

559 DOE readies multibillion-dollar AI push
U.S. supercomputing leader is the latest big backer in a globally crowded field
By R. F. Service

560 How measles causes the body to 'forget' past infections
With cases rising around the world, studies underscore the importance of widespread vaccination *By E. Frederick*
RESEARCH ARTICLE P. 599; *SCI. IMMUNOL.* RESEARCH ARTICLE BY V. PETROVA *ET AL.* 10.1126/SCIIMMUNOL.AAY6125; PODCAST

561 After decades, progress against an 'undruggable' cancer target
New drugs appear to block KRAS tumor growth protein *By J. Kaiser*

FEATURES

562 Crossing the line
Inside Russia's debate about a scientist's plan to create gene-edited babies *By J. Cohen*

564 Parents weigh promise and risks of germline editing *By J. Cohen*

INSIGHTS

PERSPECTIVES

566 Pesticide impacts through aquatic food webs
Effects of neonicotinoid insecticides ricochet all the way to fisheries yields *By O. P. Jensen*
REPORT p. 620

568 A layered defense against plant pathogens
Microbial consortia may be key to robust protection of roots from disease *By S. G. Tringe*
RESEARCH ARTICLE p. 606

569 Toward synthetic cells
Frog egg cytoplasm self-organizes into cell-like units by microtubule aster assembly and partition *By T. J. Mitchison and C. M. Field*
REPORT p. 631

570 Mapping footprints of past genetic exchange
Widespread mating between species creates mosaic genomes in *Heliconius* butterflies
By L. H. Rieseberg
RESEARCH ARTICLE p. 594

572 Deep sleep drives brain fluid oscillations
Rhythmic fluid flows in deep sleep may allow communication and clearance of waste products *By S. Grubb and M. Lauritzen*
REPORT p. 628

573 Order emerging from disorder
Entropy stabilization provides a new direction for developing functional materials
By N. Dragoe and D. Bérardan

574 The immune system mimics a pathogen
A host metabolite binds a bacterial enzyme and traps its B_{12} cofactor in an inactive state
By A. K. Boal
RESEARCH ARTICLE p. 589

POLICY FORUM

576 To help aging populations, classify organismal senescence
Comprehensive disease classification and staging is required to address unmet needs of aging populations *By S. R. G. Calimport* et al.

Published by AAAS

BOOKS *ET AL.*

579 Masculinity molecule, debunked
Challenging stereotypes, two scholars unpack the social and cultural contexts of testosterone *By E. L. Milam*

580 What does it mean to be alive?
A winding romp through advances in cell biology pushes readers to ponder the boundaries of life *By M. A. Fisher*

LETTERS

581 Moon missions spark the human imagination
By D. K. Lahiri

581 Radiation is not a political tool
By M. Murakami et al.

582 Salmon in clear and present danger
By N. J. Muñoz et al.

RESEARCH

IN BRIEF

583 From *Science* and other journals

REVIEWS

586 Medicine
Clonal hematopoiesis in human aging and disease
S. Jaiswal and B. L. Ebert
REVIEW SUMMARY; FOR FULL TEXT: DX.DOI.ORG/10.1126/SCIENCE.AAN4673

587 Microbiology
Microbiota and the social brain
E. Sherwin et al.
REVIEW SUMMARY; FOR FULL TEXT: DX.DOI.ORG/10.1126/SCIENCE.AAR2016

RESEARCH ARTICLES

588 Combustion physics
A unified mechanism for unconfined deflagration-to-detonation transition in terrestrial chemical systems and type Ia supernovae *A. Y. Poludnenko* et al.
RESEARCH ARTICLE SUMMARY; FOR FULL TEXT: DX.DOI.ORG/10.1126/SCIENCE.AAU7365

589 Radical enzymes
Itaconyl-CoA forms a stable biradical in methylmalonyl-CoA mutase and derails its activity and repair
M. Ruetz et al.
PERSPECTIVE p. 574



PHOTO: 10'000 HOURS/GETTY IMAGES

594 Butterfly genomics
Genomic architecture and introgression shape a butterfly radiation *N. B. Edelman* et al.
PERSPECTIVE p. 570

599 Viral immunology
Measles virus infection diminishes preexisting antibodies that offer protection from other pathogens
M. J. Mina et al.
NEWS STORY p. 560; *SCI. IMMUNOL.* RESEARCH ARTICLE BY V. PETROVA *ET AL.* 10.1126/SCIIMMUNOL.AAY6125

606 Plant microbiota
Pathogen-induced activation of disease-suppressive functions in the endophytic root microbiome *V. J. Carrión* et al.
PERSPECTIVE p. 568

613 Isotopic separation
Barely porous organic cages for hydrogen isotope separation *M. Liu* et al.

REPORTS

620 Neonicotinoids
Neonicotinoids disrupt aquatic food webs and decrease fishery yields
M. Yamamuro et al.
PERSPECTIVE p. 566

623 Surface magnetism
Atomic-scale spin sensing with a single molecule at the apex of a scanning tunneling microscope *B. Verlhac* et al.

628 Neuroscience
Coupled electrophysiological, hemodynamic, and cerebrospinal fluid oscillations in human sleep *N. E. Fultz* et al.
PERSPECTIVE p. 572

631 Cell biology
Spontaneous emergence of cell-like organization in *Xenopus* egg extracts
X. Cheng and J. E. Ferrell Jr.
PERSPECTIVE p. 569

637 Black holes
A noninteracting low-mass black hole–giant star binary system
T. A. Thompson et al.
PODCAST

640 Structural virology
Architecture of African swine fever virus and implications for viral assembly *N. Wang* et al.

645 Batteries
Reversible epitaxial electrodeposition of metals in battery anodes *J. Zheng* et al.

DEPARTMENTS

551 Editorial
Equity and excellence in science
By H. Holden Thorp

654 Working Life
Finding community during coffee breaks
By Vivienne Tam

ON THE COVER



Heliconius melpomene (left) and *H. erato* (right) gained protection from predators by evolving similar warning colors, an example of Müllerian mimicry. These species are among 20 sequenced butterfly genomes that illustrate the importance of hybridization and gene flow in genomic evolution. See pages 570 and 594.
Photo: Andrew Neild

Science Staff 550
New Products 649
Science Careers 650

SCIENCE (ISSN 0036-8075) is published weekly on Friday, except last week in December, by the American Association for the Advancement of Science, 1200 New York Avenue, NW, Washington, DC 20005. Periodicals mail postage (publication No. 484460) paid at Washington, DC, and additional mailing offices. Copyright © 2019 by the American Association for the Advancement of Science. The title SCIENCE is a registered trademark of the AAAS. Domestic individual membership, including subscription (12 months): $165 ($74 allocated to subscription). Domestic institutional subscription (51 issues): $1971; Foreign postage extra: Mexico, Caribbean (surface mail) $55; other countries (air assist delivery): $98. First class, airmail, student, and emeritus rates on request. Canadian rates with GST available upon request, GST #125488122. Publications Mail Agreement Number 1069624. **Printed in the U.S.A.**
Change of address: Allow 4 weeks, giving old and new addresses and 8-digit account number. **Postmaster:** Send change of address to AAAS, P.O. Box 96178, Washington, DC 20090–6178. **Single-copy sales:** $15 each plus shipping and handling; bulk rate on request. **Authorization to reproduce** material for internal or personal use under circumstances not falling within the fair use provisions of the Copyright Act can be obtained through the Copyright Clearance Center (CCC), www.copyright.com. The identification code for *Science* is 0036-8075. *Science* is indexed in the *Reader's Guide to Periodical Literature* and in several specialized indexes.

Published by AAAS

Science AAAS

Editor-in-Chief Jeremy Berg, jberg@aaas.org

Executive Editor Monica M. Bradford

Editors, Research Valda Vinson, Jake S. Yeston **Editor, Insights** Lisa D. Chong

DEPUTY EDITORS Julia Fahrenkamp-Uppenbrink (UK), Stella M. Hurtley (UK), Phillip D. Szuromi, Sacha Vignieri **SR. EDITORIAL FELLOW** Andrew M. Sugden (UK) **SR. EDITORS** Gemma Alderton (UK), Caroline Ash (UK), Brent Grocholski, Pamela J. Hines, Paula A. Kiberstis, Marc S. Lavine (Canada), Steve Mao, Ian S. Osborne (UK), Beverly A. Purnell, L. Bryan Ray, H. Jesse Smith, Jelena Stajic, Peter Stern (UK), Valerie B. Thompson, Brad Wible, Laura M. Zahn **ASSOCIATE EDITORS** Michael A. Funk, Priscilla N. Kelly, Tage S. Rai, Seth Thomas Scanlon (UK), Keith T. Smith (UK), Yury V. Suleymanov **LETTERS EDITOR** Jennifer Sills **LEAD CONTENT PRODUCTION EDITORS** Harry Jach, Lauren Kmec **CONTENT PRODUCTION EDITORS** Amelia Beyna, Jeffrey E. Cook, Chris Filiatreau, Julia Katris, Nida Masiulis, Suzanne M. White **SR. EDITORIAL COORDINATORS** Carolyn Kyle, Beverly Shields **EDITORIAL COORDINATORS** Aneera Dobbins, Joi S. Granger, Jeffrey Hearn, Lisa Johnson, Maryrose Madrid, Ope Martins, Shannon McMahon, Jerry Richardson, Alana Warnke, Alice Whaley (UK), Anita Wynn **PUBLICATIONS ASSISTANTS** Jeremy Dow, Alexander Kief, Ronmel Navas, Hilary Stewart (UK), Brian White **EXECUTIVE ASSISTANT** Jessica Slater **ASI DIRECTOR, OPERATIONS** Janet Clements (UK) **ASI SR. OFFICE ADMINISTRATOR** Jessica Waldock (UK)

News Editor Tim Appenzeller

NEWS MANAGING EDITOR John Travis **INTERNATIONAL EDITOR** Martin Enserink **DEPUTY NEWS EDITORS** Elizabeth Culotta, Lila Guterman, David Grimm, Eric Hand (Europe), David Malakoff **SR. CORRESPONDENTS** Daniel Clery (UK), Jon Cohen, Jeffrey Mervis, Elizabeth Pennisi **ASSOCIATE EDITORS** Jeffrey Brainard, Catherine Matacic **NEWS REPORTERS** Adrian Cho, Jennifer Couzin-Frankel, Jocelyn Kaiser, Kelly Servick, Robert F. Service, Erik Stokstad (Cambridge, UK), Paul Voosen, Meredith Wadman **INTERN** Alex Fox **CONTRIBUTING CORRESPONDENTS** Warren Cornwall, Ann Gibbons, Mara Hvistendahl, Sam Kean, Eli Kintisch, Kai Kupferschmidt (Berlin), Andrew Lawler, Mitch Leslie, Eliot Marshall, Virginia Morell, Dennis Normile (Shanghai), Elisabeth Pain (Careers), Charles Piller, Michael Price, Tania Rabesandratana (Barcelona), Emily Underwood, Gretchen Vogel (Berlin), Lizzie Wade (Mexico City) **CAREERS** Donisha Adams, Rachel Bernstein (Editor), Katie Langin **COPY EDITORS** Julia Cole (Senior Copy Editor), Cyra Master (Copy Chief) **ADMINISTRATIVE SUPPORT** Meagan Weiland

Creative Director Beth Rakouskas

DESIGN MANAGING EDITOR Marcy Atarod **GRAPHICS MANAGING EDITOR** Alberto Cuadra **PHOTOGRAPHY MANAGING EDITOR** William Douthitt **WEB CONTENT STRATEGY MANAGER** Kara Estelle-Powers **SENIOR DESIGNER** Chrystal Smith **DESIGNER** Christina Aycock **GRAPHICS EDITOR** Nirja Desai **INTERACTIVE GRAPHICS EDITOR** Xing Liu **SENIOR SCIENTIFIC ILLUSTRATORS** Valerie Altounian, Chris Bickel **SCIENTIFIC ILLUSTRATOR** Alice Kitterman **SENIOR GRAPHICS SPECIALISTS** Holly Bishop, Nathalie Cary **SENIOR PHOTO EDITOR** Emily Petersen

Interim Chief Executive Officer and Executive Publisher Alan Leshner

Publisher, Science Family of Journals Bill Moran

DIRECTOR, BUSINESS SYSTEMS AND FINANCIAL ANALYSIS Randy Yi **DIRECTOR, BUSINESS OPERATIONS & ANALYSIS** Eric Knott **DIRECTOR OF ANALYTICS** Enrique Gonzales **MANAGER, BUSINESS OPERATIONS** Jessica Tierney **SENIOR BUSINESS ANALYST** Cory Lipman, Meron Kebede **FINANCIAL ANALYST** Alexander Lee **ADVERTISING SYSTEM ADMINISTRATOR** Tina Burks **SENIOR SALES COORDINATOR** Shirley Young **DIGITAL/PRINT STRATEGY MANAGER** Jason Hillman **QUALITY TECHNICAL MANAGER** Marcus Spiegler **ASSISTANT MANAGER DIGITAL/PRINT** Rebecca Doshi **SENIOR CONTENT SPECIALISTS** Steve Forrester, Jacob Hedrick, Antoinette Hodal, Lori Murphy **DIGITAL PRODUCTION MANAGER** Lisa Stanford **CONTENT SPECIALIST** Kimberley Oster **ADVERTISING PRODUCTION OPERATIONS MANAGER** Deborah Tompkins **DESIGNER, CUSTOM PUBLISHING** Jeremy Huntsinger **SR. TRAFFIC ASSOCIATE** Christine Hall **SPECIAL PROJECTS ASSOCIATE** Sarah Dhere

ASSOCIATE DIRECTOR, BUSINESS DEVELOPMENT Justin Sawyers **GLOBAL MARKETING MANAGER** Allison Pritchard **DIGITAL MARKETING MANAGER** Aimee Aponte **MARKETING MANAGER** Shawana Arnold **MARKETING ASSOCIATES** Tori Velasquez, Mike Romano, Ashley Hylton **DIGITAL MARKETING SPECIALIST** Asleigh Rojanavongse **SENIOR DESIGNER** Kim Huynh **TRADE SHOW AND MEETINGS ASSOCIATE** Andrew Clamp

DIRECTOR AND SENIOR EDITOR, CUSTOM PUBLISHING Sean Sanders **ASSISTANT EDITOR, CUSTOM PUBLISHING** Jackie Oberst

DIRECTOR, PRODUCT & PUBLISHING DEVELOPMENT Chris Reid **DIRECTOR, BUSINESS STRATEGY AND PORTFOLIO MANAGEMENT** Sarah Whalen **ASSOCIATE DIRECTOR, PRODUCT MANAGMENT** Kris Bishop **ASSOCIATE DIRECTOR, PRODUCT DEVELOPMENT AND SPJ** Hannah Heckner **SR. PRODUCT ASSOCIATE** Robert Koepke **DIGITAL PRODUCT STRATEGIST** Michael Hardesty **SPJ ASSOCIATE** Samantha Bruno Fuller

DIRECTOR, INSTITUTIONAL LICENSING Iquo Edim **ASSOCIATE DIRECTOR, RESEARCH & DEVELOPMENT** Elisabeth Leonard **MARKETING MANAGER** Kess Knight **SENIOR INSTITUTIONAL LICENSING MANAGER** Ryan Rexroth **INSTITUTIONAL LICENSING MANAGER** Marco Castellan **MANAGER, SYSTEMS AND OPERATIONS** Brian Holiahn **MANAGER, AGENT RELATIONS & CUSTOMER SUCCESS** Judy Lillibridge **SENIOR OPERATIONS ANALYST** Lana Guz **FULFILLMENT COORDINATOR** Melody Stringer

DIRECTOR, GLOBAL SALES Tracy Holmes **US EAST COAST AND MID WEST SALES** Stephanie O'Connor, Glen Cox **US WEST COAST SALES** Lynne Stickrod **US SALES MANAGER, SCIENCE CAREERS** Claudia Paulsen-Young **US SALES REP, SCIENCE CAREERS** Tracy Anderson **ASSOCIATE DIRECTOR, ROW** Roger Goncalves **SALES REP, ROW** Sarah Lelarge **SALES ADMIN ASSISTANT, ROW** Bryony Cousins **DIRECTOR OF GLOBAL COLLABORATION AND ACADEMIC PUBLISHING RELATIONS, ASIA** Xiaoying Chu **ASSOCIATE DIRECTOR, INTERNATIONAL COLLABORATION** Grace Yao **SALES MANAGER** Danny Zhao **PROJECT MANAGER** Kilo Lan **ASCA CORPORATION, JAPAN** Kaoru Sasaki (Tokyo), Miyuki Tani (Osaka) **COLLABORATION/CUSTOM PUBLICATIONS/JAPAN** Adarsh Sandhu

DIRECTOR, COPYRIGHT, LICENSING AND SPECIAL PROJECTS Emilie David **RIGHTS AND LICENSING COORDINATOR** Jessica Adams **RIGHTS AND PERMISSIONS ASSOCIATE** Elizabeth Sandler **CONTRACTS AND LICENSING ASSOCIATE** Lili Catlett

---

MAIN HEADQUARTERS
Science/AAAS
1200 New York Ave. NW
Washington, DC 20005

SCIENCE INTERNATIONAL
Clarendon House
Clarendon Road
Cambridge, CB2 8FH, UK

SCIENCE CHINA
Room 1004, Culture Square
No. 59 Zhongguancun St.
Haidian District, Beijing, 100872

SCIENCE JAPAN
ASCA Corporation
Sibaura TY Bldg. 4F, 1-14-5
Shibaura Minato-ku
Tokyo, 108-0073 Japan

EDITORIAL
science_editors@aaas.org

NEWS
science_news@aaas.org

INFORMATION FOR AUTHORS
sciencemag.org/authors/science-information-authors

REPRINTS AND PERMISSIONS
sciencemag.org/help/reprints-and-permissions

MEDIA CONTACTS
scipak@aaas.org

MULTIMEDIA CONTACTS
SciencePodcast@aaas.org
ScienceVideo@aaas.org

INSTITUTIONAL SALES AND SITE LICENSES
sciencemag.org/librarian

PRODUCT ADVERTISING & CUSTOM PUBLISHING
advertising.sciencemag.org/products-services
science_advertising@aaas.org

CLASSIFIED ADVERTISING
advertising.sciencemag.org/science-careers
advertise@sciencecareers.org

JOB POSTING CUSTOMER SERVICE
employers.sciencecareers.org
support@sciencecareers.org

MEMBERSHIP AND INDIVIDUAL SUBSCRIPTIONS
sciencemag.org/subscriptions

MEMBER BENEFITS
aaas.org/membercentral

AAAS BOARD OF DIRECTORS
CHAIR Margaret A. Hamburg
PRESIDENT Steven Chu
PRESIDENT-ELECT Claire M. Fraser
TREASURER Carolyn N. Ainslie
INTERIM CHIEF EXECUTIVE OFFICER Alan Leshner
BOARD Cynthia M. Beall, May R. Berenbaum, Rosina M. Bierbaum, Ann Bostrom, Stephen P. A. Fodor, S. James Gates, Jr., Laura H. Greene, Kaye Husbands Fealing, Maria Klawe, Robert B. Millard, William D. Provine

Science serves as a forum for discussion of important issues related to the advancement of science by publishing material on which a consensus has been reached as well as including the presentation of minority or conflicting points of view. Accordingly, all articles published in *Science*—including editorials, news and comment, and book reviews—are signed and reflect the individual views of the authors and not official points of view adopted by AAAS or the institutions with which the authors are affiliated.

BOARD OF REVIEWING EDITORS (Statistics board members indicated with **(S)**)

Adriano Aguzzi, *U. Hospital Zürich*
Takuzo Aida, *U. of Tokyo*
Leslie Aiello, *Wenner-Gren Foundation*
Judith Allen, *U. of Manchester*
Sebastian Amigorena, *Institut Curie*
James Analytis, *U. of California, Berkeley*
Paola Arlotta, *Harvard U.*
Johan Auwerx, *EPFL*
David Awschalom, *U. of Chicago*
Clare Baker, *U. of Cambridge*
Nenad Ban, *ETH Zürich*
Franz Bauer, *Pontificia Universidad Católica de Chile*
Ray H. Baughman, *U. of Texas at Dallas*
Peter Bearman, *Columbia U.*
Carlo Beenakker, *Leiden U.*
Yasmine Belkaid, *NIAID, NIH*
Philip Benfey, *Duke U.*
Gabriele Bergers, *VIB*
Bradley Bernstein, *Mass. General Hospital*
Alessandra Biffi, *Harvard Med. School*
Peer Bork, *EMBL*
Chris Bowler, *École Normale Supérieure*
Ian Boyd, *U. of St. Andrews*
Emily Brodsky, *U. of California, Santa Cruz*
Ron Brookmeyer, *U. of California, Los Angeles* **(S)**
Christian Büchel, *UKE Hamburg*
Dennis Burton, *Scripps Research*
Carter Tribley Butts, *U. of California, Irvine*
György Buzsáki, *New York U. School of Med.*
Blanche Capel, *Duke U.*
Annmarie Carlton, *U. of California, Irvine*
Lars-Erik Cederman, *ETH Zürich*
Nick Chater, *U. of Warwick*
Zhijian Chen, *UT Southwestern Med. Ctr.*
Ib Chorkendorff, *Denmark TU*
James J. Collins, *MIT*
Robert Cook-Deegan, *Arizona State U.*
Alan Cowman, *Walter & Eliza Hall Inst.*
Carolyn Coyne, *U. of Pittsburgh*
Roberta Croce, *VU Amsterdam*
Jeff L. Dangl, *U. of North Carolina*
Tom Daniel, *U. of Washington*
Chiara Daraio, *Caltech*
Nicolas Dauphas, *U. of Chicago*
Frans de Waal, *Emory U.*
Claude Desplan, *New York U.*
Sandra Díaz, *Universidad Nacional de Córdoba*
Hong Ding, *Inst. of Physics, CAS*
Jennifer Dionne, *Stanford U.*
Dennis Discher, *U. of Penn.*
Jennifer A. Doudna, *U. of California, Berkeley*
Bruce Dunn, *U. of California, Los Angeles*
William Dunphy, *Caltech*
Christopher Dye, *U. of Oxford*
Todd Ehlers, *U. of Tübingen*
Jennifer Elisseeff, *Johns Hopkins U.*
Tim Elston, *U. of North Carolina*
Andrea Encalada, *U. San Francisco de Quito*
Nader Engheta, *U. of Penn.*
Karen Ersche, *U. of Cambridge*
Barry Everitt, *U. of Cambridge*
Vanessa Ezenwa, *U. of Georgia*
Michael Feuer, *The George Washington U.*
Toren Finkel, *U. of Pittsburgh Med. Ctr.*
Gwenn Flowers, *Simon Fraser U.*
Peter Fratzl, *Max Planck Inst. Potsdam*
Elaine Fuchs, *Rockefeller U.*
Eileen Furlong, *EMBL*
Jay Gallagher, *U. of Wisconsin*
Susan Gelman, *U. of Michigan*
Daniel Geschwind, *U. of California, Los Angeles*
Karl-Heinz Glassmeier, *TU Braunschweig*
Ramon Gonzalez, *U. of South Florida*
Elizabeth Grove, *U. of Chicago*
Nicolas Gruber, *ETH Zürich*
Kip Guy, *U. of Kentucky College of Pharmacy*
Taekjip Ha, *Johns Hopkins U.*
Christian Haass, *Ludwig Maximilians U.*
Sharon Hammes-Schiffer, *Yale U.*
Wolf-Dietrich Hardt, *ETH Zürich*
Louise Harra, *U. College London*
Jian He, *Clemson U.*
Carl-Philipp Heisenberg, *IST Austria*
Ykä Helariutta, *U. of Cambridge*
Janet G. Hering, *Eawag*
Hans Hilgenkamp, *U. of Twente*
Kai-Uwe Hinrichs, *U. of Bremen*
David Hodell, *U. of Cambridge*
Lora Hooper, *UT Southwestern Med. Ctr.*
Fred Hughson, *Princeton U.*
Randall Hulet, *Rice U.*
Auke Ijspeert, *EPFL*
Akiko Iwasaki, *Yale U.*
Stephen Jackson, *USGS and U. of Arizona*
Kai Johnsson, *EPFL*
Peter Jonas, *IST Austria*
Matt Kaeberlein, *U. of Washington*
William Kaelin Jr., *Dana-Farber Cancer Inst.*
Daniel Kammen, *U. of California, Berkeley*
V. Narry Kim, *Seoul Nat. U.*
Robert Kingston, *Harvard Med. School*
Nancy Knowlton, *Smithsonian Institution*
Etienne Koechlin, *École Normale Supérieure*
Alexander Kolodkin, *Johns Hopkins U.*
Thomas Langer, *U. of Cologne*
Mitchell A. Lazar, *U. of Penn.*
Ottoline Leyser, *U. of Cambridge*
Wendell Lim, *U. of California, San Francisco*
Marcia C. Linn, *U. of California, Berkeley*
Jianguo Liu, *Michigan State U.*
Luis Liz-Marzán, *CIC biomaGUNE*
Jonathan Losos, *Washington U. in St. Louis*
Ke Lu, *Chinese Acad. of Sciences*
Christian Lüscher, *U. of Geneva*
Fabienne Mackay, *U. of Melbourne*
Anne Magurran, *U. of St. Andrews*
Oscar Marín, *King's College London*
Charles Marshall, *U. of California, Berkeley*
Christopher Marx, *U. of Idaho*
Geraldine Masson, *CNRS*
C. Robertson McClung, *Dartmouth College*
Rodrigo Medellín, *U. of Mexico*
Graham Medley, *London School of Hygiene & Tropical Med.*
Jane Memmott, *U. of Bristol*
Edward Miguel, *U. of California, Berkeley*
Tom Misteli, *NCI, NIH*
Yasushi Miyashita, *U. of Tokyo*
Alison Motsinger-Reif, *NC State U.* **(S)**
Daniel Nettle, *Newcastle U.*
Daniel Neumark, *U. of California, Berkeley*
Beatriz Noheda, *U. of Groningen*
Helga Nowotny, *Austrian Council*
Rachel O'Reilly, *U. of Warwick*
Harry Orr, *U. of Minnesota*
Pilar Ossorio, *U. of Wisconsin*
Andrew Oswald, *U. of Warwick*
Isabella Pagano, *Istituto Nazionale di Astrofisica*
Margaret Palmer, *U. of Maryland*
Elizabeth Levy Paluck, *Princeton U.*
Jane Parker, *Max Planck Inst. Cologne*
Giovanni Parmigiani, *Dana-Farber Cancer Inst.* **(S)**
Samuel Pfaff, *Salk Inst. for Biological Studies*
Julie Pfeiffer, *UT Southwestern Med. Ctr.*
Matthieu Piel, *Institut Curie*
Kathrin Plath, *U. of California, Los Angeles*
Martin Plenio, *Ulm U.*
Elvira Poloczanska, *Alfred-Wegener-Inst.*
Julia Pongratz, *Ludwig Maximilians U.*
Philippe Poulin, *CNRS*
Jonathan Pritchard, *Stanford U.*
David Randall, *Colorado State U.*
Félix A. Rey, *Institut Pasteur*
Trevor Robbins, *U. of Cambridge*
Amy Rosenzweig, *Northwestern U.*
Mike Ryan, *U. of Texas at Austin*
Mitinori Saitou, *Kyoto U.*
Shimon Sakaguchi, *Osaka U.*
Miquel Salmeron, *Lawrence Berkeley Nat. Lab*
Nitin Samarth, *Penn. State U.*
Jürgen Sandkühler, *Med. U. of Vienna*
Alexander Schier, *Harvard U.*
Wolfram Schlenker, *Columbia U.*
Susannah Scott, *U. of California, Santa Barbara*
Rebecca Sear, *London School of Hygiene & Tropical Med.*
Vladimir Shalaev, *Purdue U.*
Jie Shan, *Cornell U.*
Beth Shapiro, *U. of California, Santa Cruz*
Jay Shendure, *U. of Washington*
Brian Shoichet, *U. of California, San Francisco*
Robert Siliciano, *Johns Hopkins U. School of Med.*
Lucia Sivilotti, *U. College London*
Alison Smith, *John Innes Centre*
Richard Smith, *U. of North Carolina* **(S)**
Mark Smyth, *QIMR Berghofer*
Pam Soltis, *U. of Florida*
John Speakman, *U. of Aberdeen*
Tara Spires-Jones, *U. of Edinburgh*
Allan C. Spradling, *Carnegie Institution for Science*
V. S. Subrahmanian, *U. of Maryland*
Ira Tabas, *Columbia U.*
Sarah Teichmann, *U. of Cambridge*
Rocio Titiunik, *Princeton U.*
Shubha Tole, *Tata Inst. of Fundamental Research*
Wim van der Putten, *Netherlands Inst. of Ecology*
Reinhilde Veugelers, *KU Leuven*
Bert Vogelstein, *Johns Hopkins U.*
Kathleen Vohs, *U. of Minnesota*
David Wallach, *Weizmann Inst. of Science*
Jane-Ling Wang, *U. of California, Davis* **(S)**
David Waxman, *Fudan U.*
Jonathan Weissman, *U. of California, San Francisco*
Chris Wikle, *U. of Missouri* **(S)**
Terrie Williams, *U. of California, Santa Cruz*
Ian A. Wilson, *Scripps Research* **(S)**
Yu Xie, *Princeton U.*
Jan Zaanen, *Leiden U.*
Kenneth Zaret, *U. of Penn. School of Med.*
Jonathan Zehr, *U. of California, Santa Cruz*
Maria Zuber, *MIT*

EDITORIAL

Equity and excellence in science



H. Holden Thorp
Editor-in-Chief, *Science* journals.
hthorp@aaas.org;
@hholdenthorp

The long strange trip to where I am today—the new Editor-in-Chief of the *Science* family of journals—began in the theater. My mom started the community theater in my hometown and my experiences there taught me many things, but two stand out. First, I was a bad actor. My mom humored me for a while giving me parts, but she let out a huge sigh of relief when I decided I could contribute more with a wrench or a bass guitar in my hand than on the stage.

Moving off the stage got me focused on the sound, lights, and music of the theater. That's how I learned the second thing: that it was fun to tinker with things and learn the laws of disciplines like music, especially how creativity happens within those laws.

Science was a logical progression of being creative within laws. My research interests have gone from physical inorganic chemistry to drug development, with lots of stops in between. All of those stops were shaped and informed by the research, news, and commentaries of *Science*, so it is with profound gratitude and sense of responsibility that I assume the role.

When I first started reading *Science*'s editorials, they were written by Dan Koshland. He and all of the individuals who have served as Editor-in-Chief have brought great distinction to the position, and it is both daunting and inspiring to follow them. My immediate predecessors Jeremy Berg and Marcia McNutt independently described the role using the phrase "kid in a candy store" when talking about what it is like to see all the great research that flows through the journal.

Nonetheless, it's a very serious job. The quality and reproducibility of the science must remain at the highest possible level. Authors deserve to have their work reviewed objectively and as expeditiously as possible. And reviewers deserve recognition of the extraordinary service that they provide.

With the cynicism and outright attacks encountered by journalism around the world, the news section of *Science* remains one of the few places where in-depth reporting about science occurs. There is a proper firewall between my office and the news staff that protects its ability to report on things without interference, but I am here to defend and advocate for the great work that they do at a time when it has never been more needed or challenging.

Although opinion surveys globally still show scientists as some of the most respected folks in society, the political assault on science in the United States and around the world shows no signs of slowing down. The full-throated defense of science, especially around the international emergency of climate change, must come from all quarters: Evidence, inductive reasoning, and dispassionate analysis can't be celebrated enough.

> **"I will... do everything possible to promote the wonder and importance of science..."**

As Editor-in-Chief, Jeremy has done a fantastic job. Through his expert data analysis, he has opened our eyes to important trends in what and who succeeds in getting published in the journal. I'm deeply grateful for his leadership and fully embrace the goals that he has set out.

As for my own goals, I hope to continue the great work of my predecessors while taking a deep interest in the development and nurturing of the scientific workforce around the world. After 11 years as a university leader at the University of North Carolina and Washington University, I have seen time and again how much needs to be done to achieve equity and excellence in science.

Succeeding at all this requires a robust partnership with our readers. We want manuscripts, reviews, news tips and, most of all, feedback. I will respond to messages, show up to give talks, engage on social media, and do everything possible to promote the wonder and importance of science and the *Science* journals.

Thank you for all you do for the pursuit of truth and the sustenance of this treasured institution.

–H. Holden Thorp

PHOTO: STEVE EXUM

10.1126/science.aaz9585

Published by AAAS

> “Doctors … have an obligation to engage in all kinds of nonviolent social protests to address the climate emergency.”
>
> **Richard Horton**, editor-in-chief of the medical journal *The Lancet*, about reducing the health risks to patients of climate change.

IN BRIEF

Edited by **Jeffrey Brainard**



A child receives polio vaccine in Afghanistan, one of two countries to report new cases this year.

INFECTIOUS DISEASE

Another polio strain is wiped out

An independent commission certified to the World Health Organization last week that the second of three wild virus strains that cause polio no longer circulates in humans, bringing the global vaccination push to eradicate the crippling disease closer to its goal. The type 3 strain joins wild type 2, which was declared eradicated in 2015, in the history books. Meanwhile, there have been 94 cases of polio caused by type 1 wild poliovirus so far this year, according to the Global Polio Eradication Initiative, a public-private partnership based in Geneva, Switzerland. The most commonly used vaccine contains weakened strains of the wild virus that, on rare occasions, can mutate to become virulent again. A version of the vaccine that contains only types 1 and 3 went into wide use in 2016.

Some NIH chimps to stay put

ANIMAL RESEARCH | The U.S. National Institutes of Health (NIH) announced last week that it will not retire to a sanctuary all the research chimpanzees it owns or supports, as it pledged to do in 2015. NIH Director Francis Collins said 44 chimps at the Alamogordo Primate Facility in New Mexico are too sick and old to move to Chimp Haven, a federally funded chimpanzee sanctuary in Keithville, Louisiana, and that some of the additional 134 NIH-owned or -supported chimpanzees at two other biomedical facilities could remain in place as well. Approximately 190 more U.S. chimps live in private research facilities. Biomedical groups are applauding the move, saying the animals will be safer where they are, but animal welfare groups say every chimpanzee deserves to live out the rest of its life in a sanctuary.

Argentina elects science ally

POLITICS | Many Argentine scientists praised the election on 27 October of lawyer Alberto Fernández as the country’s president because of his support for reversing deep spending cuts to research. During his campaign, Fernández included scientists among his advisers and hosted meetings tailored to researchers. He also promised to restore the Ministry of Science, which the current president, Mauricio Macri, had downgraded to a subsection of the Ministry of Education. But Argentina’s economic crisis, featuring soaring inflation and a plunging peso, could make reversing cuts a challenge.

Quantum supremacy questioned

COMPUTING | IBM last week cast doubt on a claim by a group at Google that it had used a quantum computer to achieve a computing milestone known as “quantum supremacy.” In the 23 October issue of *Nature*, the Google researchers said their device performed an arcane calculation in 200 seconds that would take Summit, the world’s fastest conventional supercomputer, many centuries to complete—a feat the group said met computer science’s definition of “quantum supremacy.” But on 21

PHOTO: MAJID SAEEDI/GETTY IMAGES

Published by AAAS

October, IBM, which built Summit for the U.S. Department of Energy, said the machine could do the task in only 2.5 days, using a different approach. That would mean Google's machine had achieved an important milestone, IBM said, but not quantum supremacy. Designers of quantum computers seek a performance edge over classical ones by using strange aspects of quantum mechanics.

Ten schizophrenia genes bagged

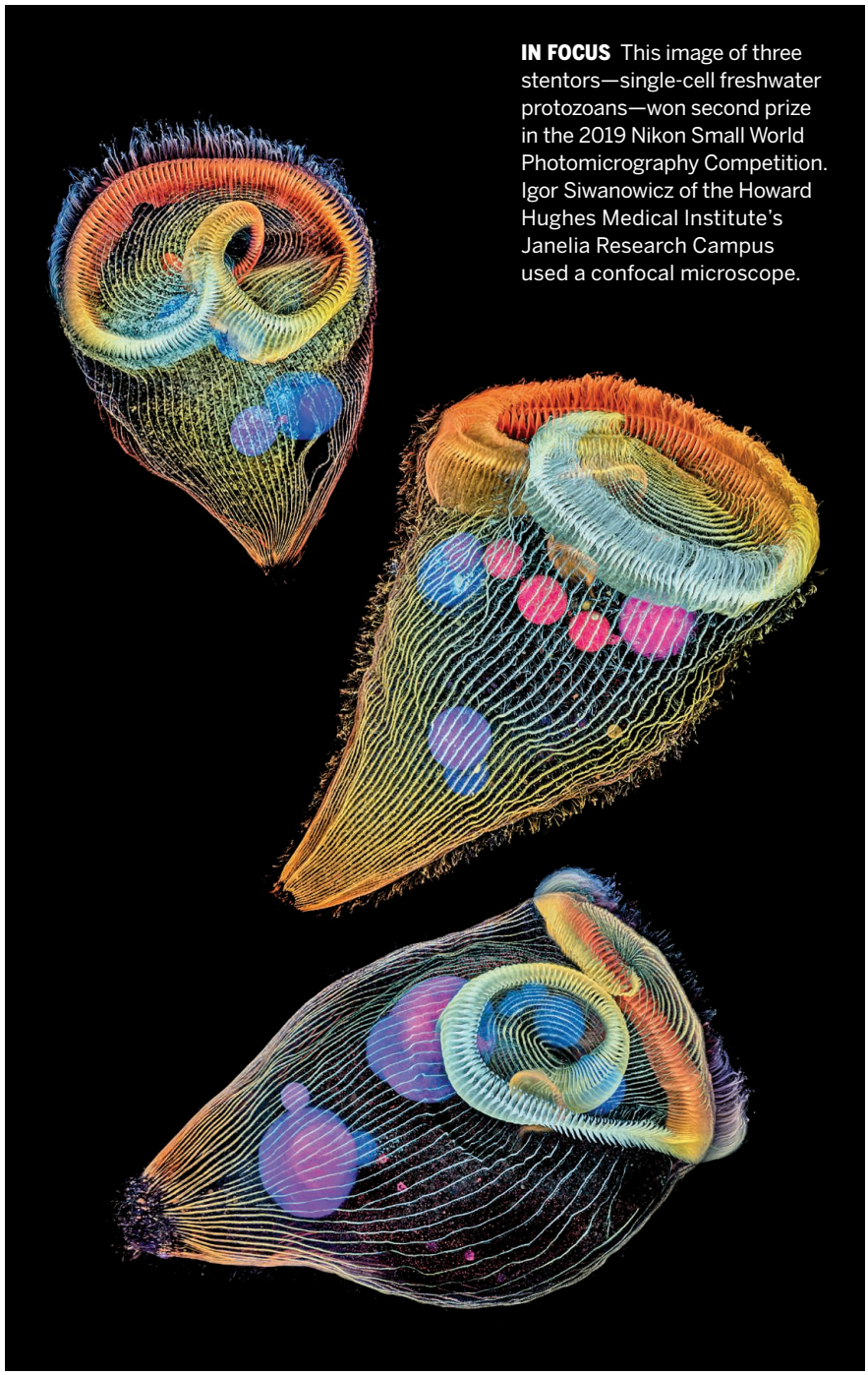
BIOMEDICINE | Geneticists have found a handful of rare genes that, when disabled, appear to directly contribute to schizophrenia. Although this severe psychiatric disease tends to run in families, a long-running search for causative genes has yielded mostly indirect clues, such as DNA markers that may be associated with those genes. But on 15 October, a global research consortium called Schizophrenia Exome Sequencing Meta-analysis reported at the American Society of Human Genetics annual meeting in Houston, Texas, that it may have cracked this puzzle. By comparing the exomes, or protein-coding DNA, of 24,000 schizophrenia patients with those of people without it, the consortium has identified 10 genes with variants that greatly increase the risk of schizophrenia. Two genes code for brain receptors for the neurotransmitter glutamate, supporting a long-standing hypothesis that the glutamate pathway is involved in the disease.

Rover to check Moon ice

PLANETARY SCIENCE | NASA will launch a robotic rover to the Moon's south pole in 2022 to hunt for ice, the agency's administrator, Jim Bridenstine, announced on 25 October. The $250 million Volatiles Investigating Polar Exploration Rover (VIPER), paid for by NASA's human spaceflight division, will operate for 100 days, looking for water ice in the shallow subsurface using a neutron detector and a drill. VIPER, the size of a golf cart, would validate signs of water ice detected remotely by orbiting spacecraft. Water could be used to support life or processed into rocket fuel. Its likely presence at the Moon's south pole is one reason NASA is planning to send astronauts there in 2024.

NSF tallies 16 #MeToo cases

HARASSMENT | The National Science Foundation has received 16 notifications of alleged sexual harassment at NSF-funded institutions since it implemented new reporting requirements 1 year ago. The tally, including three reports in October, far exceeds what NSF officials expected, given that universities need only report accusations involving researchers who received an award after 22 October 2018, and only when an institution takes an "administrative action" in response. Such actions could include anything from monitoring the accused's behavior to banning them from campus. Institutions must also notify the agency once they complete a harassment investigation involving an NSF grantee. Even as universities try to stamp out harassment, some administrators worry the NSF reporting rules could undermine their ability to protect the privacy of all parties involved in an investigation.



IN FOCUS This image of three stentors—single-cell freshwater protozoans—won second prize in the 2019 Nikon Small World Photomicrography Competition. Igor Siwanowicz of the Howard Hughes Medical Institute's Janelia Research Campus used a confocal microscope.

PHOTO: IGOR SIWANOWICZ/HHMI

Eagles' roaming bill soars

ANIMAL BEHAVIOR | After researchers tagged 13 eagles this summer to study their migration, they were surprised to receive a big telephone bill—for hundreds of dollars

Published by AAAS

of data roaming charges racked up by some birds who wandered through areas with sparse mobile coverage. Scientists at the Russian Raptor Research and Conservation Network equipped the raptors with tracking tags designed to send four SMS messages a day to indicate their locations as they migrated south from Russia and Kazakhstan. But after a few of the eagles flew out of contact with cell towers, all the messages stored during the summer were sent at once as the animals arrived in Iran, where message rates are more than three times those in Kazakhstan. Because the researchers lacked enough money to pay, the Russian telephone company Megafon instead lowered the bill via a cheaper data plan, bringing an easier landing.

Panel faults blood test claim

BIOMEDICINE | A commission at Heidelberg University in Germany announced last week it had found evidence of "extensive and severe scientific misconduct" by Christof Sohn, director of the women's clinic at the university's hospital and the lead researcher behind a highly publicized but questionable blood test designed to detect breast cancer. In a press release in February, Sohn touted the test, which looks for biomarkers of cancer-related genetic processes, as a "revolutionary" complement to mammograms. But that release ignored the test's high false positive rate. The university has suspended Sohn from teaching and research for 3 months and he faces a disciplinary inquiry.

Pandemic virus search ends

PUBLIC HEALTH | The U.S. government has decided to end a widely praised program for detecting animal viruses that might jump into humans and cause pandemics. The PREDICT program, funded by the U.S. Agency for International Development (USAID), began 10 years ago in the wake of mounting fears that novel bird flu viruses like H5N1 might spark a human pandemic. PREDICT, an alliance of several research institutions, sent teams into the field to sample animals in more than 30 countries and found more than 1000 new viruses, helping improve outbreak responses. The program also trained thousands of researchers in Africa and Asia. USAID, which spent about $200 million on PREDICT, did not explain the decision, reported last week by *The New York Times*.

Cystic fibrosis drug approved

DRUG DEVELOPMENT | The U.S. Food and Drug Administration approved on 21 October a triple-drug therapy for cystic fibrosis that targets its most common gene mutation in patients 12 years and older, increasing the number of patients for whom treatment can address the disease's underlying genetic cause. Research published this week shows that the drug, called Trikafta, boosts lung function and alleviates symptoms of lung disease in many patients. Made by Vertex Pharmaceuticals and priced at $311,000 per year, according to news reports, Trikafta adds a new drug to two existing ones. Together, they help correct effects of the gene mutation, found in about 90% of people with cystic fibrosis. In this week's issue of *The New England Journal of Medicine*, an international team of researchers funded by Vertex reports that 200 patients on Trikafta were able to exhale, on average, 14% more air (an indicator of lung health) than the 203 people who took a placebo.

AAAS names new head

SCIENTIFIC SOCIETIES | A health care management executive has been chosen as the next CEO of AAAS (which publishes *Science*). Sudip Parikh, 46, spent 8 years as a health and science specialist for the Senate appropriations committee before joining Battelle, where he rose to become vice president of health policy. He is currently a senior vice president at the Drug Information Association, a global membership organization based in Washington, D.C. Parikh will succeed Alan Leshner, who led AAAS from 2001 to 2015 before returning this summer on an interim basis to replace Rush Holt, who served for 4 years before retiring. Parikh, who grew up in North Carolina, earned a Ph.D. in biochemistry from the Scripps Research Institute in San Diego, California.



PHOTO: PURI LOPEZ

ECOLOGY

Rift Valley ponds reveal the limits of life

The region of Africa that may have given birth to humans also contains a place where no life seems to exist at all. Biologists at the French national research agency CNRS and the University of Paris-Sud used microscopy, cell sorting, genomics, and other techniques to look for microbes in geothermal ponds (above) and lakes in the Rift Valley near Ethiopia's northern border. These water bodies are saltier, hotter, and more acidic than most, if not all, other places on Earth. In ponds where salt concentrations top 50% and the salt contains magnesium and not sodium, biologist Purificación López-García and colleagues detected no signs of permanent life—suggesting those conditions are too harsh for even the toughest microbes, they report this week in *Nature Ecology & Evolution*. But large microbial communities dominated by archaea thrived in other ponds only slightly less extreme, less than 1 kilometer away. The findings "give us a lot more tools for exploring the potential of life existing elsewhere," says Nathan Smith, a paleontologist at the Natural History Museum of Los Angeles County in California.

S SCIENCEMAG.ORG/NEWS
Read more news from *Science* online.

Published by AAAS

Corrected 31 October 2019. See full text.



IN DEPTH

African people, including some with Khoisan ancestry, contributed DNA samples used to develop a gene chip.

PHOTO: CORY RICHARDS/NATIONAL GEOGRAPHIC CREATIVE

GENOMICS

Genetics lab accused of misusing African DNA

Sanger institute's aborted effort to commercialize gene chip could hinder research in Africa

By **Erik Stokstad**

Advocates for genomic research in Africa are worried about fallout from a dispute that has roiled the Wellcome Sanger Institute, a major genome research center in Hinxton, U.K. Last year, whistleblowers privately accused Sanger of commercializing a gene chip without proper legal agreements with partner institutions and the consent of the hundreds of African people whose donated DNA was used to develop the chip. "What happened at Sanger was clearly unethical. Full stop," says Jantina de Vries, a bioethicist at the University of Cape Town in South Africa, who has followed the dispute.

Sanger's troubles have mounted since the beginning of the dispute, which was first made public last month. The institute says it did not commercialize the chips or profit from them, but admits in a statement that its relationship with some African partners has been "disrupted." Stellenbosch University in South Africa has demanded that Sanger return samples. In addition, one whistleblower says she was fired because of the controversy, and a large research team has left the institute and ended a plan to study the genomes of 100,000 Africans.

More broadly, Sanger's mishandling of the matter could erode trust between researchers and African people, setting back genomic research that could benefit them, de Vries says. "The tragedy and the scandal is that the people who will pay the price are Africans."

Genome sequencing can reveal the genetic roots of diseases and offer clues for new drugs and personalized medicine. But whole genome sequencing costs $800 to $1200 per person. Researchers use gene chips as a cheaper shortcut to look at key spots in a person's genome where variation might be expected. The chips can lower the cost to less than $100 per sample, but first they need to be designed based on entire genomes from a given population.

> **"The tragedy and the scandal is that the people who will pay the price are Africans."**
> **Jantina de Vries**, University of Cape Town

In a $2.2 million deal inked in 2017, Thermo Fisher Scientific made 75,000 gene chips, or microarrays, for Sanger based on African genomic data gathered through several collaborations. Working with a unit of the Medical Research Council in Entebbe, Uganda, researchers at Sanger sequenced nearly 2100 genomes of Ugandan people. To capture more of the variation on the continent, they partnered with other institutions in Africa to sequence the genomes of about 400 more people.

Sanger planned to use the new chips to study the genomes of up to 100,000 Africans, looking for genetic insights into conditions such as heart disease, diabetes, and high blood pressure. The data could benefit Africans, and because populations in Africa are more diverse than other populations, they also might contain genetic variants—rare or missing elsewhere in the world—that could help researchers understand the mechanisms behind common diseases.

The problems started when some Sanger scientists questioned the financial arrangements with their partner institutions, according to a whistleblower who was involved in the project. Thermo Fisher planned to pay $384,000 cash back on Sanger's $2.2 million order, which would be distributed among the other partners. Sanger initially agreed not to take a share, according to internal emails seen by *Science*, as it was getting a discount on the chips. But the emails indicate that later in the process, administrators wanted Sanger to get a share of the payment. In early 2018, partners objected that they hadn't been fully consulted.

Four scientists made a formal complaint in April 2018 to the Wellcome Trust, which provides the bulk of Sanger's funding. They were also concerned that Sanger had developed the chips without the necessary legal agreements and consent. Some of the material transfer agreements (MTAs) Sanger had signed with African universi-

Published by AAAS

Corrected 31 October 2019. See full text.

ties did not allow for commercialization. Sanger administrators agreed they would need to gain permission from their partners, according to the emails. But these records also indicate that Sanger was eager to buy the arrays before Thermo Fisher's price guarantee expired at the end of 2018. In October 2017, Sanger and Thermo Fisher went ahead with a press release announcing the commercial launch of the gene chips, and Sanger ordered its chips in December 2017 without permission from all its partners. "The way it was done, we were in breach with ethics and many of these legal agreements," says one whistleblower, who wishes to remain anonymous for fear of retribution in her career. The institute planned to consult with partners and get the required permissions if Thermo Fisher were to publicly sell any of the chips, spokesperson Steve Palmer says.



The Wellcome Sanger Institute ordered 75,000 gene chips without the consent of all its partners.

In March of this year, Stellenbosch University demanded Sanger return about 100 samples donated by the Nama people, as its MTA did not permit commercialization. "This conduct of the Wellcome Sanger Institute raises serious legal and ethical consequences," wrote Vice-Rector Eugene Cloete. The University of KwaZulu-Natal in South Africa, which had gathered DNA from 100 people of Zulu descent, has also expressed concerns.

Ciara Staunton, an expert in the governance of genomic data at Middlesex University in London, says manufacturing and purchasing the chips, even for internal use, is commercial and should be consistent with MTAs and participant consent. "To do otherwise is hugely concerning, and legally and ethically questionable," she says.

Sanger disputes the whistleblower allegations, which were first reported by *The Times* on 14 October. The institute says intellectual property lawyers who reviewed the whistleblowers' complaint found no breach of contract or infringement of intellectual property. "There was no commercialization of the arrays," Palmer says, adding that the institute never sold the arrays and has not received any payments in connection with them. Ron O'Brien, a spokesperson for Thermo Fisher in Waltham, Massachusetts, also claims the company did not commercialize the array.

The Thermo Fisher chip would have been cheaper than another gene chip created for African populations in 2017 by Illumina, researchers say. Researchers involved in Human Heredity and Health in Africa (H3Africa), a collaboration funded since 2010 by the U.S. National Institutes of Health (NIH) and the Wellcome Trust, have already used the "H3A" chip to screen 60,000 Africans to find gene variants linked to disease. Ambroise Wonkam, a medical geneticist at the University of Cape Town, is using them to study 2000 people with sickle cell anemia to learn about genes that favor survival. "The H3A chip is already helping a lot," he says.

That chip was developed with a different set of African donor DNA. The donors' consent did not restrict commercial use, says de Vries, who chaired the H3Africa ethics committee. She and others worry the Sanger affair could jeopardize the trust the collaboration has built with African institutions and people. "I do not want the fallout to start to have effects on H3Africa," says Charles Rotimi, a member of the H3Africa steering committee and a genetic epidemiologist at NIH's National Human Genome Research Institute in Bethesda, Maryland. "We are just gaining traction with genomics on the African continent."

After the whistleblowers filed their complaint, the Wellcome Trust's subsidiary that oversees Sanger asked an external lawyer to investigate. A summary of the lawyer's report, which Sanger released in October 2018, addressed a separate complaint about alleged bullying by senior Sanger management, concluding that no wrongdoing took place. Regarding the gene chip work, it found there was "no wrongful exploitation of scientific work."

All four whistleblowers have since left Sanger. One says she was fired in June for bringing Sanger "into disrepute" for writing emails to colleagues about the issue. Sanger declined to comment on personnel. The 75,000 gene arrays, stored at Sanger, have not been used and will expire in December. ■

With additional reporting by Sarah Wild.

ANCIENT CLIMATE

Mud in storied ice core hints at a thawed Greenland

Dirty base of Camp Century ice core warns of future ice sheet retreat

By **Paul Voosen**, *in Burlington, Vermont*

In one of the Cold War's oddest experiments, the United States dug a 300-meter-long military base called Camp Century into the ice of northwest Greenland in the early 1960s, powered it with a nuclear reactor, and set out to test the feasibility of shuttling nuclear missiles beneath the ice. A constant struggle against intruding snow doomed the base, which was abandoned in 1966. But Camp Century has left a lasting, entirely nonmilitary legacy: a 1.3-kilometer-long ice core drilled at the site.

The core, extracted by a team that included glaciologist Chester Langway, yielded a record of past temperatures that helped kick off studies of Earth's ancient climate. And last week, dozens of scientists met here at the University of Vermont (UVM) to take stock of another gift from the core: mud from Greenland's ancient land surface, serendipitously discovered in archived samples. New analyses of the mud suggests Greenland's massive ice sheet was largely absent in a warm period during the past million years when global climate was much like today's. The samples likely have more stories to tell, UVM geophysicist Paul Bierman said at the gathering, which he organized to discuss recent results and plan further analyses. "There is a lot of new data, 90% of which seemed to be generated in the last 48 hours."

The Camp Century core was largely forgotten by the mid-1990s, and Langway was eager to retire from the University at Buffalo (UB), part of the State University of New York system. He contacted longtime colleagues in Denmark, asking them to take his ice. Either that, the story goes, or it was going to end up in Lake Erie. Soon enough, 20 crates and two shipping containers full of ice arrived in Copenhagen, says Jørgen Peder Steffensen, a glaciologist at the University of Copenhagen and the curator of

PHOTO: ROBERT EVANS/ALAMY STOCK PHOTO

Published by AAAS



A 9-meter rig in Camp Century's secret ice tunnel drilled a core that is still yielding discoveries.

its ice core repository. "We knew we should hang on to the ice because you never know when it becomes valuable." But at the time, the Danes were busy with their own drilling, and some of Langway's boxes were left unopened—and eventually forgotten.

That changed late last year. Steffensen and Dorthe Dahl-Jensen, a glaciologist at the University of Copenhagen who has led many large European drilling efforts in Greenland and Antarctica, unearthed 30 glass jars containing the Camp Century core's bottom 3 meters of sediment. This was a rare haul: Only a few drilling efforts have penetrated Greenland's ice to the land beneath. The Danes told two leading geochemist detectives about their find: Bierman and Joerg Schaefer at Columbia University.



Dirt from the core's base was once exposed at the surface.

Both are experts at analyzing the trace amounts of radioactive isotopes created when cosmic rays strike exposed rock and soil, which provide clues to when currently ice-covered terrain was last exposed. Several years ago, the two worked on dirt and rock recovered from the bottom of the GISP2 ice core from central Greenland, where drilling finished in 1993. Schaefer found that the existing ice sheet could not have covered the site at a time more than 1 million years ago. But that was one pinprick in a vast ice sheet. So, the researchers couldn't believe their luck when they visited Copenhagen this spring to see the Camp Century "cookie jars," as Steffensen calls them. What they held could double existing knowledge. "It would cost tens of millions of dollars to get a sample like this," Bierman says.

He and his colleagues set out to tease every bit of information they could from the recovered dirt. Some 800 grams of samples, representing the top and bottom of the muddy layer, arrived at Bierman's lab in the middle of July. Drew Christ, a geochemist in the lab who prepared the samples, says when the jars were opened, the room grew pungent with a smell from more than 60 years ago: the diesel fuel that was pumped into the hole to keep it open.

Christ sent thawed samples to the lab of Eric Steig, a glaciologist at the University of Washington in Seattle, who measured ratios of oxygen isotopes to tease out past temperature. He also sent pieces of frozen muck to Tammy Rittenour, a geologist at Utah State University in Logan who specializes in luminescence dating: blasting rocks with light to dislodge electrons that record when the rocks were last exposed to sunlight. The early results suggested the site may have been free of ice as recently as 400,000 years ago, she says, during a warm period between ice ages.

A day before last week's meeting, Bierman's group got results on cosmic ray isotopes that point to a similar conclusion. His group measures and compares two radioactive isotopes, aluminum-26 and beryllium-10. The aluminum isotope forms seven times as fast as the beryllium, and, once cut off from the surface by ice, decays twice as fast; the declining ratio between the two isotopes serves as clock.

Bierman expected Greenland's cold northern part—where Camp Century was located—would have been a stronghold of ice for millions of years, perhaps since the beginning of the Pleistocene 2.6 million years ago, when a gradually cooling Earth tipped into its current cycles of ice ages. Instead, the clock suggested ice has covered Camp Century for at most 1 million years—matching the GISP2 results. "It could be less, but a million years is the maximum," Bierman says. "So you can't argue for full Pleistocene stability at either site."

"Camp Century is sort of a litmus test," Steffensen adds. If you can say it was ice free, "that actually points at a severely reduced Greenland Ice Sheet." Sea level would have been many meters higher than today, even though the climate 1 million years ago was similar to today's greenhouse-warmed climate. "This stuff is really scary," Schaefer says.

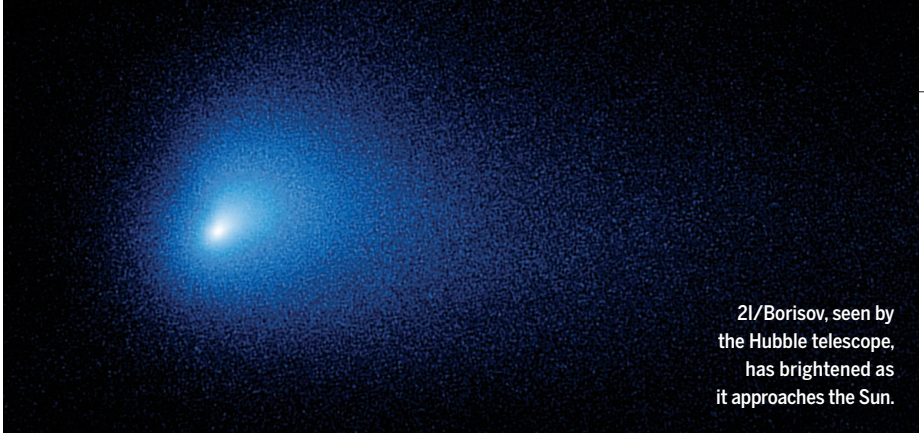
Bierman adds that it is also very preliminary. Evidence from marine cores and elsewhere also suggests a large fraction of the ice sheet disappeared 400,000 years ago. And DNA found at the bottom of several ice cores is from plants that would have thrived at summer temperatures of 10°C—although its age is uncertain. Yet in what may be a contradictory finding, ice at the bottom of a different ice core, called GRIP, has been dated at 1 million years old. "The old data and the new data seem to support each other in being difficult," Dahl-Jensen says.

There is one scenario that could match the conflicting evidence, says Jason Briner, a geologist at UB. "Maybe the Greenland Ice Sheet vanished and reformed many times until 1 million years ago."

The 28 cookie jars left from the Camp Century mud likely hold more secrets. Scientists are hunting through macrofossils, leaf wax, mineral types, noble gases, and much more to answer questions about what Greenland's ancient landscape looked like when it was last exposed. But they must choose their targets wisely, Bierman says. "There's less of this stuff than there is Moon rocks." ■

PHOTOS: (TOP TO BOTTOM) DAVID ATWOOD/U.S. ARMY ERDC-CRREL/AIP
EMILIO SEGRE VISUAL ARCHIVES; JEAN-LOUIS TISON/UNIVERSITÉ LIBRE DE BRUXELLES

Published by AAAS



2I/Borisov, seen by the Hubble telescope, has brightened as it approaches the Sun.

PLANETARY ASTRONOMY

Alien comets may be common, analysis of 2I/Borisov suggests

A dozen interstellar objects may be passing near the Sun

By **W. Wayt Gibbs**

The comet is an alien intruder from another star system. But 2I/Borisov, the second known interstellar visitor after far smaller 'Oumuamua, discovered in 2017, looks remarkably like a typical comet from our own Solar System: an object a few kilometers across spewing carbon monoxide gas, water vapor, and dust. Researchers who announced their analysis this week say the size of the two objects, along with the rate of their discovery and other factors, suggests that at any given moment, more than a dozen interstellar visitors at least as large as 'Oumuamua are passing through the Solar System.

"Our current telescopes are not powerful enough to detect all of these objects," says Bryce Bolin, an astronomer at the California Institute of Technology in Pasadena and lead author of the new study. But in the future, he says, large telescopes could catch these visitors more often, perhaps two or three times a year.

The study is the most comprehensive look yet at an object that captured astronomers' attention from the start. In the wee hours of 30 August, Gennady Borisov, an amateur astronomer in Crimea, was peering through a 65-centimeter telescope that he built himself when he spotted the first hints of what would become his namesake. Within weeks, astronomers found that Borisov was moving so fast, and on such an odd trajectory, that it must have originated from a distant star system.

Now, just 2 months later, a team of 43 astronomers from 26 institutions in eight countries has prepared a detailed study to submit to the American Astronomical Society for publication. Whereas cigar-shaped 'Oumuamua lacked a bright halo or tail and was discovered on its way out of the Solar System, Borisov is brighter and more active. The team says its nucleus is at most 2 to 3 kilometers across—an order of magnitude larger than 'Oumuamua. The new comet, still inbound, will continue to brighten until it gets closest to the Sun on 7 December.

Spectra of the comet at first suggested it had a reddish hue and was emitting cyanogen gas, which is also found in Solar System comets. The new study concludes Borisov is gray and is also releasing plumes of carbon monoxide and water vapor, which account for its brightening.

In that respect, Borisov looks "remarkably like a normal Solar System comet," says Colin Snodgrass, an astronomer at the University of Edinburgh who has seen the study. He's impressed by how active it was early on—and how detectable it was so far away. If that behavior is typical, he says, then the Large Synoptic Survey Telescope, a giant telescope set to begin to operate in 2022, may find such objects even earlier.

That excites Snodgrass, who is the deputy principal investigator for the European Space Agency's (ESA's) Comet Interceptor. After launch in 2028, it will "park" itself in solar orbit between Earth and Mars and wait for a comet to study. The ESA team plans to intercept one of the pristine Solar System comets that, every year, make their first pass into the inner Solar System. Now, it appears the mission could catch an alien comet as well, Snodgrass says. "This means that we may have a chance to actually see one up close." ■

W. Wayt Gibbs is a journalist based in Seattle, Washington, and editorial director at Intellectual Ventures.

PUBLIC HEALTH

Gates and NIH join forces on HIV and sickle cell diseases

A unique marriage aims to speed development of simple DNA-based cures

By **Jon Cohen** *and* **Jocelyn Kaiser**

An unusual collaboration between the U.S. National Institutes of Health (NIH) and the Bill & Melinda Gates Foundation aims to take on the breathtakingly complex challenge of bringing cutting-edge, gene-based cures for HIV and sickle cell disease to sub-Saharan Africa. Each partner will devote at least $100 million over the next 4 years to speeding the development of interventions that are already showing promise in clinical trials but will need to be retooled to be feasible in a region that still struggles to have access to basic medicines. "Yes, this is audacious," NIH Director Francis Collins said last week in announcing the partnership.

The goal is to steer clear of expensive, complex strategies that require stem cell transplantation, and instead develop affordable, easily administered therapies that would replace or edit genes in the body. Although NIH and the Gates Foundation have collaborated before, this partnership is fundamentally different. "This is the first time that it's more than just let's share the expenses," says Anthony Fauci, who heads NIH's National Institute of Allergy and Infectious Diseases in Bethesda, Maryland.

After decades of work and setbacks, the traditional gene therapy approach of delivering DNA to replace a defective gene is now a proven treatment for disorders including inherited blindness and neuromuscular disease. In sickle cell disease, which results from a defect in the oxygen-carrying hemoglobin protein in red blood cells, several ongoing gene therapy and gene-editing clinical trials are either adding a new hemoglobin gene to cells or turning on a gene for a fetal form of the protein that can substitute for the defective hemoglobin. In HIV, clinical trials have used CRISPR or other genome editors in stem cells to cripple a cell-surface

PHOTO: NASA/ESA/D. JEWITT (UCLA)

Published by AAAS

protein, CCR5, that gives the virus a toehold as it establishes an infection.

But those are complex and risky interventions. Doctors must remove stem cells from the body, add or modify their genes, and then reinfuse the cells back into the body after using chemotherapy to wipe out a patient's original stem cells. In sub-Saharan Africa, where medical infrastructure is limited, those procedures are largely out of reach. Yet the region is home to more than 12 million people with sickle cell disease and 25 million living with HIV—two-thirds of the world's total for both diseases.

The new collaboration will instead seek to put gene therapy or gene editing into a one-time infusion. The strategy would enlist a harmless virus or nanoparticles to ferry sophisticated molecular tools into the body. "The potential beauty of in vivo gene editing is that it might be given ultimately as a single shot, curing everyone in a scalable manner," says Steven Deeks, a leading HIV cure researcher at the University of California, San Francisco (UCSF).

Although several labs are working on such in vivo gene therapy or editing to modify blood stem cells in animals, "A major challenge is modifying enough cells," says Harvard University stem cell scientist Stuart Orkin. He estimates that at a minimum 20% of a patient's blood stem cells within the bone marrow would have to be modified to cure sickle cell, which would be "a real stretch."

Mike McCune, an immunologist who has long worked on HIV/AIDS at UCSF and recently joined the Gates Foundation, came up with the idea for the collaboration and approached NIH. McCune, who has worked with Deeks, says he realized existing strategies won't be enough to defeat HIV in Africa. "Antiretroviral treatment alone is not going to cut it," he says. The foundation was already talking about investing in in vivo gene editing for sickle cell. Merging the two disease efforts made sense, McCune says.

Collins met in December 2018 with Bill Gates, co-chair of the foundation, to hash out details. Each institution will fund its own grants, but they will share information about proposals each is considering so they can identify redundancies and gaps. The Gates Foundation can act more quickly and is freer to collaborate with industry if it wants. NIH, for its part, has a vast clinical trials network throughout sub-Saharan Africa, where the collaboration aims to launch trials in 7 to 10 years. "I don't think this is traditionally something the foundation or the NIH would do on its own," McCune says.

Hematologist Alexis Thompson of the Northwestern University Feinberg School of Medicine in Chicago, Illinois, who is working on sickle cell gene therapy trials, calls the NIH-Gates collaboration "phenomenal." But she says a low-tech need is more urgent: expanded screening of newborns in Africa for sickle cell so those afflicted can receive antibiotics. Many die before age 5 from bacterial infections because the sickled cells impair the spleen's immunological function. "It's almost being able to crawl or walk before you sprint," Thompson says. Gates and NIH say that outside the collaboration, they plan to support screening efforts.

The new effort also hopes to develop other genome-based strategies to cure these diseases, including cutting-edge approaches such as excising HIV from genomes. "This might be science fiction now, but one day may be a real possibility," Deeks says. ■



PHOTO: JUNIOR D. KANNAH/AFP/GETTY IMAGES

Some 12 million people in sub-Saharan Africa have sickle cell disease, and many die in childhood, from infections.

ARTIFICIAL INTELLIGENCE

DOE readies multibillion-dollar AI push

U.S. supercomputing leader is the latest big backer in a globally crowded field

By **Robert F. Service**, *in Washington, D.C.*

The U.S. Department of Energy (DOE) is planning a major initiative to use artificial intelligence (AI) to speed up scientific discoveries. At a meeting here last week, DOE officials said they will likely ask Congress for between $3 billion and $4 billion over 10 years, roughly the amount the agency is spending to build next-generation "exascale" supercomputers.

"That's a good starting point," says Earl Joseph, CEO of Hyperion Research, a high-performance computing analysis firm in St. Paul that tracks AI research funding. He notes, though, that DOE's planned spending is modest compared with the feverish investment in AI by China and industry.

But DOE has a big asset: torrents of data. The agency funds atom smashers, surveys of the universe, and the sequencing of thousands of genomes. "We generate almost unimaginable amounts of data, petabytes per day," Chris Fall, who directs DOE's Office of Science, said at the last of four town halls DOE has held here to build support for the AI initiative. Algorithms trained with these data could help discover new materials or spot signs of new physics. "It's going to impact everything we do," Fall says.

DOE is joining a global rush to fund AI. Worldwide corporate AI funding is expected to hit $35.8 billion this year, up 44% from 2018, according to IDC, a market analysis firm. Companies see commercial advantages in AI. It helps banks detect and prevent credit card fraud, and oil and gas companies use it to pinpoint productive drilling sites in mounds of geological data.

Governments are also jumping in, with goals as diverse as improving traffic flow and detecting early-stage cancers. In February, President Donald Trump signed an executive order launching the American AI Initiative, and the administration requested nearly $1 billion for AI and ma-

Published by AAAS

chine learning research in fiscal year 2020 across all civilian agencies, according to the U.S. Office of Science and Technology Policy. The U.S. Department of Defense is seeking a similar level of funding for unclassified military AI programs.

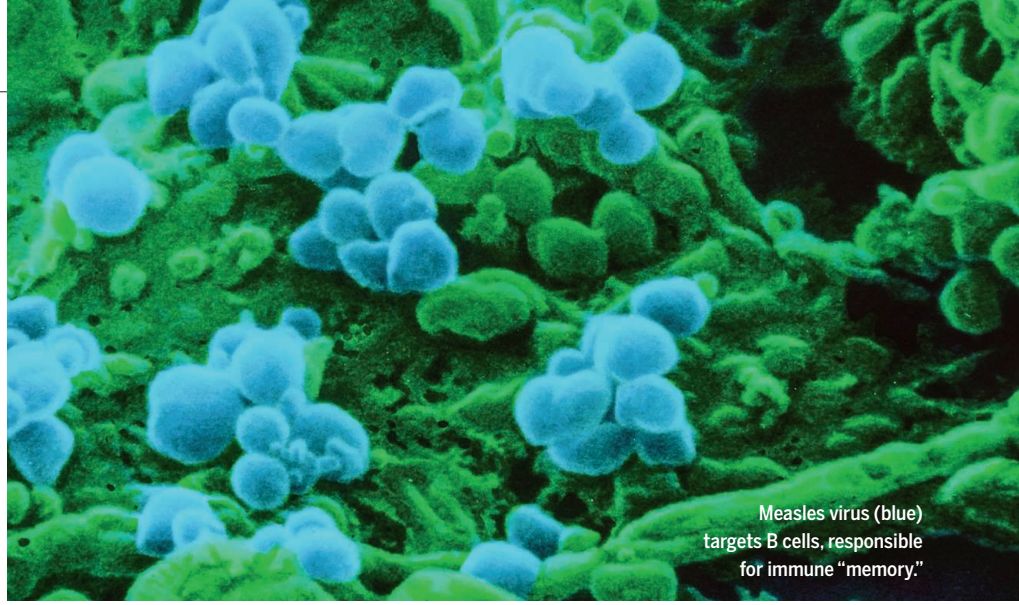
Definitive numbers are harder to come by for other countries. But in 2017, China announced a national AI plan that aims for global leadership, and a projected commercial AI market worth 1 trillion yuan ($140 billion) by 2030. And the European Union has committed to spending €20 billion through 2020. "Just as with the race to create the first exascale computer, the AI world is getting really competitive," Joseph says.

Just who is leading the race depends on what you measure. According to Hyperion Research, China accounted for 60% of all investments in AI from 2013 to 2018. U.S. investments were about 30% of the global total. China dominates the number of AI publications, whereas the European Union has the most AI researchers, Joseph says. But U.S. researchers in AI get the most citations per paper, he says, suggesting their research has the most impact.

DOE officials say the AI initiative will help keep U.S. researchers at the forefront. Though DOE has yet to detail its program, it's likely to include funding for national labs to optimize existing supercomputers for AI, and external funding for academic research into AI computer architectures, says Rick Stevens, associate laboratory director for computing, environment, and life sciences at Argonne National Laboratory in Lemont, Illinois.

Not only is the initiative likely to speed up data analysis, but it could also boost the pace of data collection, by using AI to come up with hypotheses and design new experiments. "AI won't replace scientists," says Jeff Nichols, associate laboratory director for computing and computational science at Oak Ridge National Laboratory in Tennessee. "But scientists who use AI will replace scientists who don't." Battery researchers, for example, could use these tools to test the properties of thousands of materials in days.

Nichols acknowledges that DOE's push for AI lags efforts at the U.S. National Science Foundation (NSF), which has spent roughly $4.5 billion over the past decade on research to improve AI algorithms and software. Nevertheless, Erwin Gianchandani, NSF's acting assistant director for computer and information science and engineering, says that given DOE's role in funding major user facilities such as supercomputers, the agency's AI push "would dovetail well" with NSF's programs. ■



Measles virus (blue) targets B cells, responsible for immune "memory."

IMAGE: NIBSC/SCIENCE SOURCE

IMMUNOLOGY

How measles causes the body to 'forget' past infections

With cases rising around the world, studies underscore the importance of widespread vaccination

By **Eva Frederick**

One of the most contagious human pathogens, the measles virus is dangerous enough by itself, with sometimes-fatal complications including pneumonia and brain inflammation. Two detailed studies of blood from unvaccinated Dutch children who contracted measles now reveal how such infections can also compromise the immune system for months or years afterward, causing the body to "forget" immunity it had developed to other pathogens in the past.

To what extent this "immune amnesia" increases illness and deaths from other infections isn't clear. But the results are another good reason to immunize children against the virus, the studies' authors and other infectious disease experts say. The findings are particularly sobering now that measles cases are increasing sharply—by more than 30% globally from 2017 to 2018—because of undervaccination and misguided vaccine safety concerns. "If we allow [measles] outbreaks to happen, we are knowingly creating pockets of people who are susceptible to other diseases as well," says Velislava Petrova at the Wellcome Sanger Institute in Hinxton, U.K., who led one study.

"These two studies provide further strong evidence for the highly immunosuppressive effects of measles infection and the power of measles vaccination to counter it," adds population biologist Bryan Grenfell of Princeton University, whose group in 2015 reported early evidence for the effect.

That finding was based on population data showing that mortality from other pathogens increases after a measles outbreak. Experiments in animals have also suggested the measles virus impairs immunity. So Petrova's group and another, headed by Stephen Elledge of Harvard University, decided to explore this phenomenon more closely in people. Both teams chose a well-known cohort of children from an Orthodox Protestant community in the Netherlands whose parents had opted out of all vaccines for their children for religious reasons.

Michael Mina, a Harvard virologist who also worked on the population study, teamed up with Elledge to analyze blood samples from 77 of the children before and after they became infected during a 2013 measles outbreak in the Netherlands. Tomasz Kula, a postdoc in Elledge's lab, had developed a technology called VirScan that enabled the team to test the antibodies in the infected children's blood against antibody targets representing most known human pathogenic viruses.

Before the children contracted measles, their blood contained antibodies to many common pathogens. "These were really healthy kids," Mina says. After the disease, the children lost, on average, about 20% of their antibody repertoire. Some fared much worse, losing more than 70% of their immunity to viral pathogens, the research-

Published by AAAS

ers report on p. 599. They did not see the effect in their controls: five unimmunized children who never contracted measles over the course of the study, as well as more than 100 other children and adults. They also saw no loss of antibodies in children after they received a vaccination against measles.

The diminished antibody shield means that after a case of measles, unvaccinated children become vulnerable again to viruses they had been exposed to in the past. For example, if a child had contracted mumps prior to having measles, they might be susceptible to mumps again. "It's like taking somebody's immune system and rewinding time, putting them at a more naïve state," Mina says.

To understand the effect, Petrova's group did a different analysis of blood from the Dutch children. The team went straight to the source of antibodies: B cells, which the measles virus is known to infect. They found that measles infection reduced the diversity of memory B cells, which "remember" past infections and are quick to fight any recurrence. The virus killed off B cells specific to other pathogens, allowing new, measles-specific memory B's to replace them.

Measles also decreased the diversity of another category of B cells: nonspecific naïve B cells in the bone marrow, which stand ready to fight unfamiliar infections. A measles infection left this cell repertoire "immature, similar to that of a fetus," says Petrova, whose study appeared this week in *Science Immunology*. Basically, the measles virus doesn't just delete immune memory—it makes it harder for the immune system to respond to new pathogens in the future.

"This [measles-induced immune amnesia] has never been characterized to the extent that they've done here," says Mark Slifka, an immunologist at Oregon Health & Science University in Portland. But its long-term significance is unclear, he says, noting that immunity naturally fades as the body destroys some antibodies to keep their numbers in check. "Hopefully these families will be willing to continue to be involved with the researchers," he says.

The only way to prevent measles from erasing immune memory, Mina says, is the obvious one: Prevent cases by vaccinating. In fact, Mina says, after a child has measles, physicians should consider revaccinating them against all common pathogens. "The Catch-22 is that [these children] are only getting measles because they're not vaccinated in the first place," he says.

On the other hand, says Jennifer Lighter, an infectious disease physician at New York University's Langone Health in New York City, "I think after you see your child that has measles, you wouldn't want your child to get other infections and to suffer needlessly." ■

DRUG DEVELOPMENT

After decades, progress against an 'undruggable' cancer target

New drugs appear to block KRAS tumor growth protein

By **Jocelyn Kaiser**

Cancer researchers are making progress toward a goal that has eluded them for more than 30 years: shrinking tumors by shutting off a protein called KRAS that drives growth in many cancer types. A new type of drug aimed at KRAS made tumors disappear in mice and shrank tumors in lung cancer patients, two companies report in papers published this week.

It's not yet clear whether the drugs will extend patients' lives, but the results are generating a wave of excitement. And one company, Amgen, reports an unexpected bonus: Its drug also appears to stimulate the immune system to attack tumors, suggesting it could be even more powerful if paired with widely available immunotherapy treatments. "This is a nice demonstration that [a combination of drugs] might actually work," says KRAS researcher Channing Der of the University of North Carolina in Chapel Hill.

> **"Having been in this field so long, a glimmer of hope is great."**
>
> **Channing Der**, University of North Carolina

KRAS is one of three genes in the *RAS* family that produce proteins controlling an on-off switch for cell growth; mutated forms of these genes are found in about 25% of all cancers. But RAS proteins have been considered "undruggable," in part because their smooth surfaces offer no obvious pockets to target with a drug. In 2013, however, chemical biologist Kevan Shokat's lab at the University of California, San Francisco, identified a small molecule that could slip into a groove on a KRAS mutant called G12C. The mutant is present in about 13% of the most common lung tumors, 3% of colorectal cancers, and 2% of other solid tumors. A company called Wellspring Biosciences later showed that when given to mice implanted with KRAS(G12C)-carrying human tumors, an improved version of Shokat's molecule shrank the growths.

Amgen's drug, AMG510, targets a second groove in the same KRAS protein. That appears to make it more potent and specific than Wellspring's compound, the company reports this week in *Nature*. After mice with several types of tumors with KRAS(G12C) were given sufficient doses of the drug alone or in combination with other drugs, most tumors shrank or even disappeared.

Amgen also describes early results from the first human trial of a KRAS inhibitor, finding its drug partially shrank tumors in two of four patients with advanced lung cancer. In meetings this year the company also reported that tumors regressed in about half of a larger group of 13 lung cancer patients. (Early results for colon cancer aren't as encouraging; only one of 12 patients has responded. But "that was expected," says Amgen director of research Jude Canon, because colon cancer is more biologically complex and may require drug combinations.)

A second company, Mirati, also reported promising human results this week at a meeting and in a paper in *Cancer Discovery*. Its KRAS(G12C) inhibitor shrank tumors in three of six lung cancer patients, as well as in one of four colon cancer patients.

Besides blocking the KRAS(G12C) protein, the Amgen drug stimulates immune cells called T cells to attack the tumor, the researchers report. When AMG510 was combined with a drug called a PD-1 inhibitor that removes a brake on T cells, tumors vanished for good in nine of 10 mice. PD-1 inhibitors alone can eliminate some cancers, but most patients don't respond. The results suggest "cures may be possible" if PD-1 drugs are given together with Amgen's KRAS drug, Canon says. (Amgen has already begun to test this drug combination in cancer patients.)

The new results are an "encouraging" step toward "a clinically effective [KRAS] inhibitor," says Harold Varmus of Weill Cornell Medicine in New York City, who launched the RAS Initiative, an effort to target those proteins, in 2013, when he was head of the National Cancer Institute.

Der, who consults for Mirati, cautions that because tumors will likely develop resistance to these KRAS inhibitors, patients will undoubtedly need drug combinations. Still, says Der, who was among those who discovered *RAS*'s role in cancer in 1982, "I'm excited about these inhibitors. Having been in this field so long, a glimmer of hope is great." ■

Published by AAAS



FEATURES

CROSSING THE LINE

Inside Russia's debate about a scientist's plan to create gene-edited babies

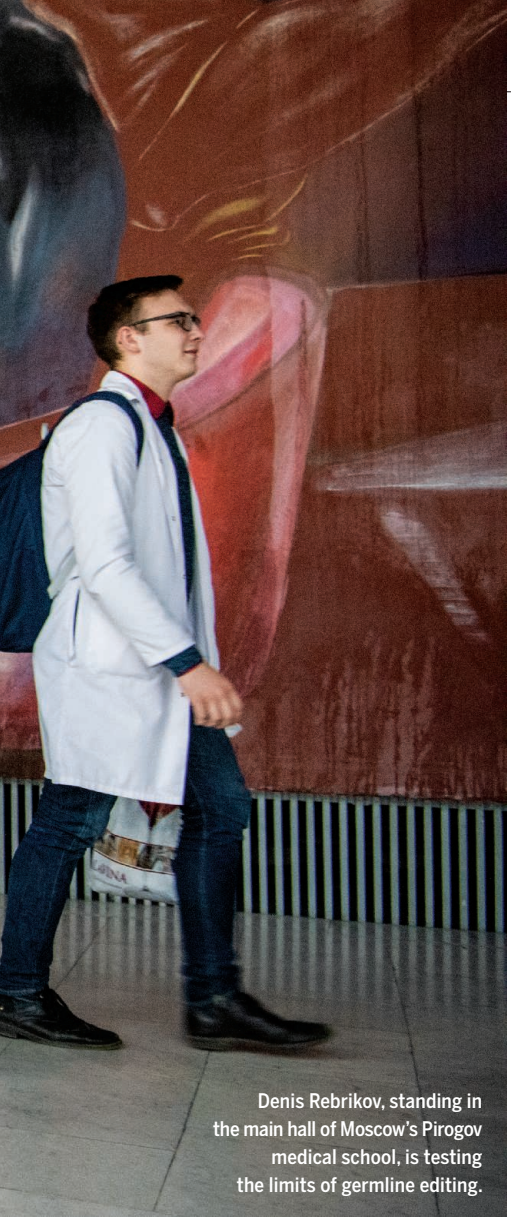
By **Jon Cohen**, *in Moscow and St. Petersburg, Russia; Photography by* **Sergey Ponomarev**

Early in October, Denis Rebrikov went to an old mansion in Moscow that now houses the Russian Academy of Sciences's (RAS's) Institute of Philosophy to confront his critics and set the record straight. Rebrikov was a well-regarded but little-known geneticist across town at the Pirogov Russian National Research Medical University when a June article in *Nature* reported his controversial plan to create genetically engineered babies by altering the DNA in human embryos with CRISPR, the powerful genome editor. He became the focus of worldwide attention—and widespread condemnation as a reckless self-promoter.

At the opening of the meeting, attended by bioethicists, geneticists, and clinicians, Rebrikov lamented that the group wanted to debate his proposed experiment before he had described it in detail. "People are discussing my thoughts and my intentions as if I'm not here," Rebrikov said. "In Russia, we have a saying, 'I have not read Pasternak, but I have my opinions about him,'" he added, referring to the author of *Doctor Zhivago*. "That's my case."

The fury Rebrikov has faced builds on the outrage surrounding He Jiankui, the

Published by AAAS



Denis Rebrikov, standing in the main hall of Moscow's Pirogov medical school, is testing the limits of germline editing.

Chinese scientist who had stealthily used CRISPR to edit human embryos in an attempt to make them resistant to HIV and then implanted them, leading to the birth of twin girls in October 2018. Not only had He proceeded with flimsy regulatory review, but the girls were not facing an immediate danger of infection that outweighed the potential risks of the procedure. He lost his university job and is subject to ongoing government investigations (*Science*, 2 August, p. 430). He's experiment also sparked new calls for a moratorium on subsequent attempts to do germline editing—making DNA changes that can be passed to future generations.

Unlike He, Rebrikov has been public about his intentions. He plans to seek rigorous ethical and regulatory review. He would use the technology to treat inherited deafness, addressing a medical need that is arguably more compelling than the theoretical one He chose. Rebrikov says he has a detailed research plan to assess the risks of altering embryos with CRISPR before any are implanted to develop into babies. And whereas He had no expertise in reproductive medicine, Rebrikov works as the chief geneticist at Russia's largest government-run in vitro fertilization (IVF) clinic.

Rebrikov's critics have suggested he has ulterior motives: winning personal fame or grants for his institution, gaining respect for Russian science, or prodding the country's strict regulators to loosen control. A stocky 43-year-old who is a former champion in sambo, a Russian martial art that combines judo and wrestling, Rebrikov deftly ducks and counterpunches, dismissing criticisms with a "ha ha" or a shrug. "People are usually very conservative, and that's normal," he says. He suspects some opposition comes from scientists who are religious. They have "cockroaches in their brains," he says—a Russian phrase meaning they are confused, if not delusional.

This story was supported by the Pulitzer Center.

Rebrikov stresses his belief that germline editing has great promise to help people. "When I see a new technology come forward, I want to see how it works and how I can improve it. I am doing research at the speed that natural biological factors allow."

Some highly respected scientists in Russia who know him well openly support his efforts. Sergey Lukyanov, a molecular biologist who heads the Pirogov medical school—and is Rebrikov's former Ph.D. adviser and frequent collaborator—agrees that germline editing is premature for now. But he supports Rebrikov's step-by-step approach. Rebrikov "is one of these people who takes action towards any imperfection of the universe that can, from his point of view, be corrected. For him, this is an opportunity to give happiness to parents to have healthy children."

Rebrikov's critics, even after learning the details of his plans at the meeting, think he is the one with cockroaches in his brain. "The clinical use for gene editing is like taking something out of the air, it's imagined," Sergey Kutsev, a clinician who heads Moscow's Research Centre for Medical Genetics and is the top genetic adviser to the Ministry of Health, told the gathering. "I'm absolutely sure the technology's not ready, the same as every other doctor."

Rebrikov acknowledges the scientific consensus that a bright red line now prohibits germline editing because the young CRISPR technology remains too error prone. Yet to the utter dismay of many colleagues, he has put his toes right on the line. And he is forcing Russia and the world at large to confront the key question: How, exactly, do you responsibly cross it?

REBRIKOV FIRST described editing embryos at a Russian conference nearly 1 month before the He story would explode. "I was really surprised that in the full auditorium of 500 people he was freely speaking about this issue," says Egor Prokhortchouk, a genomics specialist at RAS's Research Center of Biotechnology in Moscow. Even though Rebrikov's study didn't violate Russian regulations, Prokhortchouk still thought it was pushing the limits of what the strict science and health ministries would allow.

Working with nonviable embryos made at his IVF clinic, Rebrikov and his co-workers used CRISPR to introduce a deletion into a gene for a protein, CCR5, that studs the surface of white blood cells. People who naturally inherit a defective *CCR5* gene from both parents are highly resistant to HIV; this is the same gene that He tried to cripple in the twin girls. But Rebrikov's experiment simply explored the efficiency of CRISPR. At the conference, he did not discuss implanting edited embryos. "Nobody asked questions about ethical things," Prokhortchouk says.

In February, Prokhortchouk learned about Rebrikov's greater ambitions. Rebrikov and colleagues had described the *CCR5* embryo study in the *Bulletin of RSMU*, of which he is editor-in-chief, and Prokhortchouk invited him to a student journal club. "Rebrikov insisted that he wants to create *CCR5*-edited babies and that this will protect them from HIV infection from their mothers," says Prokhortchouk, who opposes such plans.

Rebrikov says his goal all along was to prove that germline editing, which he believes will one day be widely used, can safely help people. He wanted to build his case by finding people with rare medical situations that would warrant potential risks. He hoped to identify, for example, women who were living with HIV and wanted babies but were not responding to any antiretroviral drugs. Using IVF to create embryos homozygous for the *CCR5* mutant in theory could help prevent the women from infecting their babies.

Rebrikov's initial CRISPR embryo experiments aimed to better gauge the risks and challenges. Ideally, when CRISPR is introduced right after an egg is fertilized in an IVF clinic, it will make its desired edit at the one-cell zygote stage, so that as the embryo divides, every cell is corrected. But if CRISPR enters later, it may not correct all of an embryo's cells. This "mosaic" child could still be vulnerable to HIV. But out of eight embryos edited using CRISPR, Rebrikov's team found evidence of mosaicism in only three of them at the blastocyst stage, when they are 5 days old and have about 250 cells.

Published by AAAS

The study did not assess an equally concerning possibility: that the editing would create accidental, "off-target" mutations, which in theory could trigger a cancer or cause other health problems. Rebrikov's publication attracted little attention.

But the world reacted loudly when *Nature* said he hoped to implant an edited embryo within 6 months. Leading CRISPR scientists and bioethicists outside of Russia slammed the idea as "irresponsible," "unsettling," and "a slippery slope," charging that he was a "cowboy" who had "weak data" and was trying to "grab some attention." Rebrikov denies that he hyped his plans. "If somebody called me and asked, 'Would you answer my questions?' OK, well, why not?" he says, noting that he has stopped replying to most media requests.

The international hubbub led to a July meeting in Moscow, instigated by Prokhortchouk and hosted by Kutsev. Among the 10 attendees was Maria Vorontsova, a pediatric endocrinologist widely reported to be Russian President Vladimir Putin's daughter, although there is no confirmation of that. Her presence prompted a 29 September *Bloomberg* story, "Future of Genetically Modified Babies May Lie in Putin's Hands," that suggested the meeting was "secret" and, with little evidence, that Vorontsova would influence Russia's position on germline editing. "The meeting was not secret," retorts geneticist Igor Korobko, a Ministry of Health official who attended. "And we have rules and laws: It's not the president's decision."

REBRIKOV COULDN'T find the HIV-infected women he deemed appropriate for germline editing, so he recently began to seek hearing-impaired couples who are homozygous for a mutation known as 35delG in a gene, *GJB2*, that produces a protein in gap junctions, the channels that help move biochemicals between cells, including in the inner ear. The mutation is one of the most common genetic causes of hearing loss, and Rebrikov wants to use CRISPR to correct its single aberrant DNA base.

Rebrikov told *Science* that he plans to do extensive safety checks before seeking approval to implant an edited embryo. First, he wants to sequence the entire genomes of each prospective parent to get a baseline for assessing off-target mutations in their edited embryos. He then wants to stimulate the potential mother's ovaries, obtain about 20 eggs, fertilize them with her partner's sperm, and then add the mutation-fixing CRISPR and grow the embryos for 5 days, to the blastocyst stage. Finally, he will do repeated rounds of whole-genome sequencing of 10 blastocysts to identify all mutations that differ from the genomes of the parents.

If the number of new mutations is in the range seen normally in an unedited embryo—about 100—he will move to the next stage with the remaining edited embryos: He will remove five to seven cells and check them for many types of genetic defects and for mosaicism. He concedes that unaltered cells or off-target changes could go undetected. "We always will have some limits of the technology," Rebrikov says.

This summer, Rebrikov met with a husband and wife who he confirmed are homozygous for 35delG and certain to have a deaf child—and he has found four other couples he suspects face the same prospects. The couple he met with (see sidebar, below) has yet to decide whether they want to participate in his experiment.

Several clinicians and researchers who specialize in hearing loss contend that the couple should not risk editing their embryos. For one thing, 35delG homozygotes sometimes only have mild hearing impairment. And an alternative is available: a cochlear implant, an electronic device that stimulates auditory nerves. It can restore some hearing and is particularly successful when implanted in young children. People homozygous for 35delG mutations



Yevgenievna and her husband have a genetic form of deafness and do not want to pass on their mutations to a child.

PHOTO: SERGEY PONOMAREV

Parents weigh promise and risks of germline editing

On a lightly snowing Sunday evening in a suburban Moscow restaurant loud with live Georgian music, a woman in her late 20s joins me to discuss her potential participation in Denis Rebrikov's controversial plans to create gene-edited babies (see main story, p. 562). Yevgenievna—she does not want to be identified beyond her patronymic—has been deaf since birth and cannot hear the music. But she can hear some sounds with the help of a hearing aid and is adept at reading lips.

Yevgenievna and her husband, who is partially deaf, want to have a child who will not inherit hearing problems. Russia has no clear regulations prohibiting editing in vitro fertilization (IVF) embryos to create altered babies, but Yevgenievna is deeply ambivalent about the risks of the CRISPR genome editor. She is also uneasy about publicity. "We were told if we become the first couple to do this experiment we'll become famous, and HBO already tried to reach me."

She and her husband, who could hear until he was 15 years old, have a daughter—Yevgenievna asks me not to reveal her age—who failed a hearing test at birth. Doctors initially believed it was a temporary problem, but 1 month later, "We were told our daughter had zero hearing," Yevgenievna says. "I was shocked, and we cried."

Their daughter could have received a cochlear implant, which uses surgically inserted electrodes to stimulate the auditory nerve. People with such implants can understand speech, although they typically can't hear music. But she developed partial hearing and, like her father, does well with hearing aids. And friends in the Russian deaf community had bad experiences with implants—likely because they didn't receive the proper rehabilitation after the surgery.

Later, they learned their daughter had one of the most common genetic causes of hearing loss, a mutation called 35delG,

Published by AAAS

"do really well with cochlear implants," says Richard Smith, an otolaryngologist at the University of Iowa in Iowa City. Smith and others also question whether hearing loss warrants such an extreme measure. Smith says he would pick something more "lethal."

David Corey, a neurobiologist at Harvard Medical School in Boston, adds that several biotech companies are developing therapies to correct the mutation after birth. "If I were a parent, I'd wait for a gene therapy delivered only to the affected cells."

Rebrikov counters that potential parents, properly informed of the risks, should make the decision. "How do they estimate the quality of life of their babies?" he asks. "Yes, hearing is not a life-or-death issue, but parents can say, 'Well, we think that we very strongly want our child to have hearing.'"

Pavel Tishchenko, a bioethicist at the RAS Institute of Philosophy who organized the meeting there, challenged this idea. "Just agreement of some patients is not enough for many reasons," he said. "What will you tell the patients? The whole truth or just a part of it?" Will they know, Tishchenko asked Rebrikov, that germline editing has been declared premature by several expert panels? (Rebrikov says he will make his informed consent documents public.)

Tishchenko also worried that Rebrikov's proposal will not get close scrutiny from bioethicists. The Ministry of Health has a competent ethical committee, he told the gathering, but he has less faith in other Russian levels of review. "We have a lot of ethical committees who will say yes to any innovations."

And who is accountable if the child suffers a bad outcome? Rebrikov said if regulators OK an experiment and something goes wrong, the researcher should be absolved. But Tishchenko recalled the story of an ancient Greek who threw a lance at a sporting event and killed a spectator. "Who is responsible? The one who threw the lance or the organizer of the lance-throwing competition?" he asked. "The question is not answered until this day."

The ultimate scientific question is whether Rebrikov's proposed experiment will clarify the safety of germline editing. Several researchers who have expertise in DNA sequencing told *Science* they think his team would likely miss too many off-target mutations caused by CRISPR. Spotting these unintended edits "is not trivial," says Fyodor Urnov, scientific director of the Innovative Genomics Institute at the University of California, Berkeley, who opposes editing of human embryos even for research purposes. Even with state-of-the-art sequencing machines like the one Rebrikov says he will use, it would take sophisticated bioinformatics to detect the rare mutations in the 250 cells of a blastocyst. Urnov, a native of Russia, notes that other groups that have edited human embryos with CRISPR have found troubling levels of off-target mutations. If Rebrikov developed a convincing way to identify such mutations and found that they were few, would that alter Urnov's confidence in germline editing? "Yes it would," he says. "From its current state of zero confidence."

THE DAY BEFORE the group meeting with Rebrikov, the Russian Ministry of Health broke what many had seen as its curious silence about germline editing. "Issuing permission to edit the human genome in clinical practice would now be a premature and irresponsible measure," it said in a press statement, noting that this was in line with a World Health Organization (WHO) expert committee on human genome editing. Korobko, who heads the ministry's department of science, innovation, and biomedical health risks, says the statement came in response to yet another media account of Rebrikov's plans in an influential Russian newspaper.

Korobko says Rebrikov's work isn't prohibited under Russian law. Still, he doubts an ethics committee at the ministry would approve a clinical trial of germline editing. "The recommendation of the WHO means a lot to the Russian Federation."

Yet RAS, the country's main science organization, remains silent on the topic. One reason may be that many Russian scientists did not take Rebrikov seriously. "When I first heard about this proposal, I considered this a bad joke because our country overregulates research," says Raul Gainetdinov, a psychiatrist who heads the Institute of Translational Biomedicine at St. Petersburg State University.

Elena Grebenshchikova, a bioethicist at RAS's Institute of Scientific Information on Social Sciences, told the Moscow meeting attendees that she is glad Rebrikov pushed issues of germline editing into the public arena in Russia. "There's a lack of communication between scientists and the society," she said. "His openness to the subject is really a plus to shift the responsibility from a simple scientist or an institution to the shared responsibility where all of society is included."

Having opened the debate, Rebrikov declares he is weary of the frenzied media coverage. He no longer will say when he'll seek approval to implant an edited embryo. "That's a very strange question because now, we're not making babies. We're just proceeding in a scientific way." ■

in both copies of *GJB2*, a gene key to the function of ear cells. Neither parent had ever had their genes tested—or thought a child could inherit their hearing problems.

This summer, Yevgenievna decided that despite her reservations about cochlear implants, she wanted one for herself. Through the hearing specialist she found, she learned of a genetic study of deaf couples who wanted to have children. This led the couple to Rebrikov, who scanned their genomes. If either Yevgenievna or her husband had a normal copy of *GJB2*, a fertility clinic could have created embryos by IVF and tested a few cells in each one to select a heterozygote—which would have normal hearing. But they learned that like their daughter, they are both 35delG homozygous. "We were told the only option [to have a hearing child] would be to edit an IVF embryo," she says.

Yevgenievna says Rebrikov explained how CRISPR editing works and some of the risks. She understands an edit might fail to correct the deafness gene in all cells of an embryo and might create unwanted, dangerous mutations. Those discussions left her "both for and against the experiment," she says. "We were impressed by this wondrous possibility." But then she consulted hearing specialists. "Many told me that it's better to have a deaf child and an implant rather than a genetically modified baby."

Yevgenievna's husband is now willing to take the risk. "If I said yes today, he'd say, 'Yes, let's do it,'" she says, noting that "he greatly supports Rebrikov and his activities." But her husband is leaving the decision to Yevgenievna, who hasn't decided for sure she wants a second child, let alone one edited with CRISPR. "Which is better: to hear music or be suffering from cancer?"

Yevgenievna has not even agreed to the ovarian stimulation that would allow harvesting of multiple eggs, the first step in the protocol. This month, she had her own cochlear implant surgery, and emailed afterward that she and her husband often discuss "the opportunity."

"I believe one should come to this as confidently as I decided on a cochlear implant," she says. "It is worth noting that 2 years ago I was an ardent opponent of the cochlear implant, but when I learned more, I changed my mind, and I am happy that I decided to take this step. The same is true with Rebrikov's experiment. Time will tell." —*J.C.*

This story was supported by the Pulitzer Center.

Published by AAAS

The study did not assess an equally concerning possibility: that the editing would create accidental, "off-target" mutations, which in theory could trigger a cancer or cause other health problems. Rebrikov's publication attracted little attention.

But the world reacted loudly when *Nature* said he hoped to implant an edited embryo within 6 months. Leading CRISPR scientists and bioethicists outside of Russia slammed the idea as "irresponsible," "unsettling," and "a slippery slope," charging that he was a "cowboy" who had "weak data" and was trying to "grab some attention." Rebrikov denies that he hyped his plans. "If somebody called me and asked, 'Would you answer my questions?' OK, well, why not?" he says, noting that he has stopped replying to most media requests.

The international hubbub led to a July meeting in Moscow, instigated by Prokhortchouk and hosted by Kutsev. Among the 10 attendees was Maria Vorontsova, a pediatric endocrinologist widely reported to be Russian President Vladimir Putin's daughter, although there is no confirmation of that. Her presence prompted a 29 September *Bloomberg* story, "Future of Genetically Modified Babies May Lie in Putin's Hands," that suggested the meeting was "secret" and, with little evidence, that Vorontsova would influence Russia's position on germline editing. "The meeting was not secret," retorts geneticist Igor Korobko, a Ministry of Health official who attended. "And we have rules and laws: It's not the president's decision."

REBRIKOV COULDN'T find the HIV-infected women he deemed appropriate for germline editing, so he recently began to seek hearing-impaired couples who are homozygous for a mutation known as 35delG in a gene, *GJB2*, that produces a protein in gap junctions, the channels that help move biochemicals between cells, including in the inner ear. The mutation is one of the most common genetic causes of hearing loss, and Rebrikov wants to use CRISPR to correct its single aberrant DNA base.

Rebrikov told *Science* that he plans to do extensive safety checks before seeking approval to implant an edited embryo. First, he wants to sequence the entire genomes of each prospective parent to get a baseline for assessing off-target mutations in their edited embryos. He then wants to stimulate the potential mother's ovaries, obtain about 20 eggs, fertilize them with her partner's sperm, and then add the mutation-fixing CRISPR and grow the embryos for 5 days, to the blastocyst stage. Finally, he will do repeated rounds of whole-genome sequencing of 10 blastocysts to identify all mutations that differ from the genomes of the parents.

If the number of new mutations is in the range seen normally in an unedited embryo—about 100—he will move to the next stage with the remaining edited embryos: He will remove five to seven cells and check them for many types of genetic defects and for mosaicism. He concedes that unaltered cells or off-target changes could go undetected. "We always will have some limits of the technology," Rebrikov says.

This summer, Rebrikov met with a husband and wife who he confirmed are homozygous for 35delG and certain to have a deaf child—and he has found four other couples he suspects face the same prospects. The couple he met with (see sidebar, below) has yet to decide whether they want to participate in his experiment.

Several clinicians and researchers who specialize in hearing loss contend that the couple should not risk editing their embryos. For one thing, 35delG homozygotes sometimes only have mild hearing impairment. And an alternative is available: a cochlear implant, an electronic device that stimulates auditory nerves. It can restore some hearing and is particularly successful when implanted in young children. People homozygous for 35delG mutations



Yevgenievna and her husband have a genetic form of deafness and do not want to pass on their mutations to a child.

PHOTO: SERGEY PONOMAREV

Parents weigh promise and risks of germline editing

On a lightly snowing Sunday evening in a suburban Moscow restaurant loud with live Georgian music, a woman in her late 20s joins me to discuss her potential participation in Denis Rebrikov's controversial plans to create gene-edited babies (see main story, p. 562). Yevgenievna—she does not want to be identified beyond her patronymic—has been deaf since birth and cannot hear the music. But she can hear some sounds with the help of a hearing aid and is adept at reading lips.

Yevgenievna and her husband, who is partially deaf, want to have a child who will not inherit hearing problems. Russia has no clear regulations prohibiting editing in vitro fertilization (IVF) embryos to create altered babies, but Yevgenievna is deeply ambivalent about the risks of the CRISPR genome editor. She is also uneasy about publicity. "We were told if we become the first couple to do this experiment we'll become famous, and HBO already tried to reach me."

She and her husband, who could hear until he was 15 years old, have a daughter—Yevgenievna asks me not to reveal her age—who failed a hearing test at birth. Doctors initially believed it was a temporary problem, but 1 month later, "We were told our daughter had zero hearing," Yevgenievna says. "I was shocked, and we cried."

Their daughter could have received a cochlear implant, which uses surgically inserted electrodes to stimulate the auditory nerve. People with such implants can understand speech, although they typically can't hear music. But she developed partial hearing and, like her father, does well with hearing aids. And friends in the Russian deaf community had bad experiences with implants—likely because they didn't receive the proper rehabilitation after the surgery.

Later, they learned their daughter had one of the most common genetic causes of hearing loss, a mutation called 35delG,

Published by AAAS

"do really well with cochlear implants," says Richard Smith, an otolaryngologist at the University of Iowa in Iowa City. Smith and others also question whether hearing loss warrants such an extreme measure. Smith says he would pick something more "lethal."

David Corey, a neurobiologist at Harvard Medical School in Boston, adds that several biotech companies are developing therapies to correct the mutation after birth. "If I were a parent, I'd wait for a gene therapy delivered only to the affected cells."

Rebrikov counters that potential parents, properly informed of the risks, should make the decision. "How do they estimate the quality of life of their babies?" he asks. "Yes, hearing is not a life-or-death issue, but parents can say, 'Well, we think that we very strongly want our child to have hearing.'"

Pavel Tishchenko, a bioethicist at the RAS Institute of Philosophy who organized the meeting there, challenged this idea. "Just agreement of some patients is not enough for many reasons," he said. "What will you tell the patients? The whole truth or just a part of it?" Will they know, Tishchenko asked Rebrikov, that germline editing has been declared premature by several expert panels? (Rebrikov says he will make his informed consent documents public.)

Tishchenko also worried that Rebrikov's proposal will not get close scrutiny from bioethicists. The Ministry of Health has a competent ethical committee, he told the gathering, but he has less faith in other Russian levels of review. "We have a lot of ethical committees who will say yes to any innovations."

And who is accountable if the child suffers a bad outcome? Rebrikov said if regulators OK an experiment and something goes wrong, the researcher should be absolved. But Tishchenko recalled the story of an ancient Greek who threw a lance at a sporting event and killed a spectator. "Who is responsible? The one who threw the lance or the organizer of the lance-throwing competition?" he asked. "The question is not answered until this day."

The ultimate scientific question is whether Rebrikov's proposed experiment will clarify the safety of germline editing. Several researchers who have expertise in DNA sequencing told *Science* they think his team would likely miss too many off-target mutations caused by CRISPR. Spotting these unintended edits "is not trivial," says Fyodor Urnov, scientific director of the Innovative Genomics Institute at the University of California, Berkeley, who opposes editing of human embryos even for research purposes. Even with state-of-the-art sequencing machines like the one Rebrikov says he will use, it would take sophisticated bioinformatics to detect the rare mutations in the 250 cells of a blastocyst. Urnov, a native of Russia, notes that other groups that have edited human embryos with CRISPR have found troubling levels of off-target mutations. If Rebrikov developed a convincing way to identify such mutations and found that they were few, would that alter Urnov's confidence in germline editing? "Yes it would," he says. "From its current state of zero confidence."

THE DAY BEFORE the group meeting with Rebrikov, the Russian Ministry of Health broke what many had seen as its curious silence about germline editing. "Issuing permission to edit the human genome in clinical practice would now be a premature and irresponsible measure," it said in a press statement, noting that this was in line with a World Health Organization (WHO) expert committee on human genome editing. Korobko, who heads the ministry's department of science, innovation, and biomedical health risks, says the statement came in response to yet another media account of Rebrikov's plans in an influential Russian newspaper.

Korobko says Rebrikov's work isn't prohibited under Russian law. Still, he doubts an ethics committee at the ministry would approve a clinical trial of germline editing. "The recommendation of the WHO means a lot to the Russian Federation."

Yet RAS, the country's main science organization, remains silent on the topic. One reason may be that many Russian scientists did not take Rebrikov seriously. "When I first heard about this proposal, I considered this a bad joke because our country overregulates research," says Raul Gainetdinov, a psychiatrist who heads the Institute of Translational Biomedicine at St. Petersburg State University.

Elena Grebenshchikova, a bioethicist at RAS's Institute of Scientific Information on Social Sciences, told the Moscow meeting attendees that she is glad Rebrikov pushed issues of germline editing into the public arena in Russia. "There's a lack of communication between scientists and the society," she said. "His openness to the subject is really a plus to shift the responsibility from a simple scientist or an institution to the shared responsibility where all of society is included."

Having opened the debate, Rebrikov declares he is weary of the frenzied media coverage. He no longer will say when he'll seek approval to implant an edited embryo. "That's a very strange question because now, we're not making babies. We're just proceeding in a scientific way." ■

in both copies of *GJB2*, a gene key to the function of ear cells. Neither parent had ever had their genes tested—or thought a child could inherit their hearing problems.

This summer, Yevgenievna decided that despite her reservations about cochlear implants, she wanted one for herself. Through the hearing specialist she found, she learned of a genetic study of deaf couples who wanted to have children. This led the couple to Rebrikov, who scanned their genomes. If either Yevgenievna or her husband had a normal copy of *GJB2*, a fertility clinic could have created embryos by IVF and tested a few cells in each one to select a heterozygote—which would have normal hearing. But they learned that like their daughter, they are both 35delG homozygous. "We were told the only option [to have a hearing child] would be to edit an IVF embryo," she says.

Yevgenievna says Rebrikov explained how CRISPR editing works and some of the risks. She understands an edit might fail to correct the deafness gene in all cells of an embryo and might create unwanted, dangerous mutations. Those discussions left her "both for and against the experiment," she says. "We were impressed by this wondrous possibility." But then she consulted hearing specialists. "Many told me that it's better to have a deaf child and an implant rather than a genetically modified baby."

Yevgenievna's husband is now willing to take the risk. "If I said yes today, he'd say, 'Yes, let's do it,'" she says, noting that "he greatly supports Rebrikov and his activities." But her husband is leaving the decision to Yevgenievna, who hasn't decided for sure she wants a second child, let alone one edited with CRISPR. "Which is better: to hear music or be suffering from cancer?"

Yevgenievna has not even agreed to the ovarian stimulation that would allow harvesting of multiple eggs, the first step in the protocol. This month, she had her own cochlear implant surgery, and emailed afterward that she and her husband often discuss "the opportunity."

"I believe one should come to this as confidently as I decided on a cochlear implant," she says. "It is worth noting that 2 years ago I was an ardent opponent of the cochlear implant, but when I learned more, I changed my mind, and I am happy that I decided to take this step. The same is true with Rebrikov's experiment. Time will tell." —*J.C.*

This story was supported by the Pulitzer Center.

Published by AAAS



AQUATIC ECOSYSTEMS

Pesticide impacts through aquatic food webs

Effects of neonicotinoid insecticides ricochet all the way to fisheries yields

By **Olaf P. Jensen**

Testing chemicals for toxicity is straightforward, but detecting their effects at the population, community, or ecosystem level is exceedingly difficult. As one moves to higher levels of ecological organization, the number of confounding factors and compensatory mechanisms increases (*1*). Standardized, laboratory studies of pesticides, required by regulatory agencies, typically focus on the short-term effects of acute exposure to individual model organisms with the results scaled up mathematically to estimate long-term and indirect effects. However, long-term and ecosystem-scale ecological studies frequently show surprises and emergent phenomena that couldn't be predicted by extrapolating from results at smaller temporal, spatial, and organizational scales (*2*). To understand the long-term ecosystem impacts of contaminants, one must study entire ecosystems for a long time. On page 620 of this issue, Yamamuro *et al.* (*3*) have done just this, demonstrating that neonicotinoid pesticides can affect entire food webs.

Much of what we know about indirect food web impacts of contaminants comes from studies of oil spills. However, even oil spills that release millions of barrels of crude oil can have weak or undetectable effects at the population or community level. The Deepwater Horizon spill—the largest in United States history—is a good example. Extensive studies of nearshore fish populations following the spill have found little evidence of declines (*1*, *4*), despite known toxicity and exposure (*5*). Pesticides present a challenge similar to that of oil spills, but a different kind of exposure: a continued "press" disturbance as they are

PHOTO: JTB PHOTO/UIG UNIVERSAL IMAGES GROUP/NEWSCOM

Published by AAAS



Insecticides from rice paddies may make their way to lakes and alter aquatic food webs. Rice paddies in Unnan, Japan are located near Lake Shinji.

repeatedly added to the environment rather than the discrete "pulse" disturbance of a major oil spill.

Using more than 20 years of data on the chemistry, biology, and fishery harvests of Lake Shinji, Japan, Yamamuro *et al.* track the impacts of pesticides up the food chain from arthropods such as aquatic insect larvae and crustacean zooplankton to the commercial harvest of smelt and eel. Neonicotinoid pesticides were first used in the rice paddies surrounding Lake Shinji in 1993. Arthropod populations in the lake collapsed that same year, followed shortly thereafter by a complete collapse of the fisheries for fish species that feed on these arthropods. Changes in fish catch are not a perfect reflection of changes in the fish populations themselves—fishers often give up when fish become rare, causing catch to decline more rapidly than abundance—but this is a large and astoundingly fast response to a food web perturbation.

This study by Yamamuro *et al.*, although observational, presents compelling evidence from more than a decade of data both before and after neonicotinoid insecticides were introduced to this region. In courtroom dramas, a conviction requires evidence of means, opportunity, and motive. A convincing case for impacts at the ecosystem scale likewise requires a means (plausible pathway for impacts to occur), an opportunity (toxic concentrations measured in the relevant environment), and if not a motive, then the elimination of other plausible suspects. In this case, the means are clear: Arthropods, including midges and, to a lesser extent, crustacean zooplankton, are exceptionally sensitive to neonicotinoids (*6*). This is no surprise—killing insects is what insecticides are designed to do. The means for such impacts on arthropods to then propagate to other species in the food web are also evident. Although the specific trophic pathways fueling aquatic food webs depend heavily on the size of the lake or river (*7*), most links between primary production and fish are through arthropods. Neonicotinoid concentrations in Lake Shinji suggest plenty of opportunity. Observations immediately following the first use of these insecticides in the region are missing, but measurements in 2018 show concentrations well above the lethal amounts for many arthropods. Several alternative explanations for the collapse in aquatic arthropods and fisheries were evaluated and rejected: Invasive species, hypoxia, or changes in fish stocking cannot plausibly explain the observations. Further implicating the collapse of arthropods in the decline of fisheries, the commercial harvest of a third fish species, less reliant on arthropod prey, did not decline.

If neonicotinoids are toxic enough to have caused the rapid decline of arthropod and fish populations in Lake Shinji, then why aren't there reports of widespread effects on aquatic ecosystems? After all, neonicotinoids are the most widely used insecticides in the world. One explanation is that the use of neonicotinoids on rice involves the direct application of insecticide or insecticide-treated seeds to an aquatic environment, the rice paddy. Although this may be a worst-case scenario, it is not an unusual one; rice is one of the three largest cereal crops in the world (*8*). Rice seeds coated with neonicotinoids are widely used, and more than 90% of this coating ends up in soil or water (*9*). Also, there is the issue of not seeing a problem if we don't look for it. Long-term monitoring of zooplankton is rare, geographically unrepresentative, and often confounded by impacts from multiple stressors (*10*). Freshwater fisheries and fish populations are also notoriously data deficient (*11*). Despite such data limitations, Yamamuro *et al.* are not alone in finding indirect food web effects of neonicotinoids. A study in the Netherlands (*12*) showed an association between neonicotinoid use and population declines in birds. The more we look for population- or ecosystem-level impacts of neonicotinoids, the more we are likely to find them.

Proponents of industrial agriculture and its heavy reliance on new chemicals argue that, although it would be ideal to reduce the use of pesticides, there are many mouths to feed. Yamamura *et al.* show that the trade-off is also between one type of food production (agriculture) and another (fisheries). A fishery that was sustainable for decades collapsed within a year after farmers began using neonicotinoids. This is hardly the only pronounced impact of agriculture on fisheries. Runoff from "America's breadbasket" creates a recurring dead zone in the Gulf of Mexico roughly the size of Israel (*13*) with serious economic losses for fishermen (*14*). A more comprehensive comparison of the environmental impacts of the world's food systems is urgently needed (*15*) and must include the indirect impacts that propagate through food webs. ■

Department of Marine and Coastal Sciences, Rutgers University, New Brunswick, NJ 08901, USA.
Email: ojensen@rutgers.edu

REFERENCES AND NOTES

1. F. J. Fodrie *et al.*, *Bioscience* **64**, 778 (2014).
2. S. R. Carpenter, *Ecology* **77**, 677 (1996).
3. M. Yamamuro *et al.*, *Science* **366**, 620 (2019).
4. E. J. Ward *et al.*, *Environ. Monit. Assess.* **190**, 530 (2018).
5. A. Whitehead *et al.*, *Proc. Natl. Acad. Sci. U.S.A.* **109**, 20298 (2012).
6. C. A. Morrissey *et al.*, *Environ. Int.* **74**, 291 (2015).
7. Y. Vadeboncoeur, G. Peterson, M. J. Vander Zanden, J. Kalff, *Ecology* **89**, 2542 (2008).
8. U.N. Food and Agriculture Organization (2019), FAOSTAT 2019: FAO Statistical Databases; www.fao.org/faostat/en/#home, Rome.
9. R. Sur, A. Stork, *Bull. Insectol.* **56**, 35 (2003).
10. E. Jeppesen *et al.*, *Hydrobiologia* **676**, 279 (2011).
11. D. M. Bartley, G. J. De Graaf, J. Valbo-Jørgensen, G. Marmulla, *Fish. Manag. Ecol.* **22**, 71 (2015).
12. C. A. Hallmann, R. P. B. Foppen, C. A. M. van Turnhout, H. de Kroon, E. Jongejans, *Nature* **511**, 341 (2014).
13. N. N. Rabalais *et al.*, *Estuaries Coasts* **30**, 753 (2007).
14. M. D. Smith *et al.*, *Proc. Natl. Acad. Sci. U.S.A.* **114**, 1512 (2017).
15. B. S. Halpern *et al.*, *Proc. Natl. Acad. Sci. U.S.A.* **116**, 18152 (2019).

ACKNOWLEDGMENTS

I thank N. McAuliffe, Malin Pinsky, N. Rabalais, C. Rowe, E. Turner, and R. Winfree for comments on this manuscript. This work was supported by a grant from the Gulf of Mexico Research Initiative to the Coastal Waters Consortium. The funders had no role in the design, execution, or analyses of this project.

10.1126/science.aaz6436

Published by AAAS

PLANT BIOLOGY

A layered defense against plant pathogens

Microbial consortia may be key to robust protection of roots from disease

By **Susannah G. Tringe**

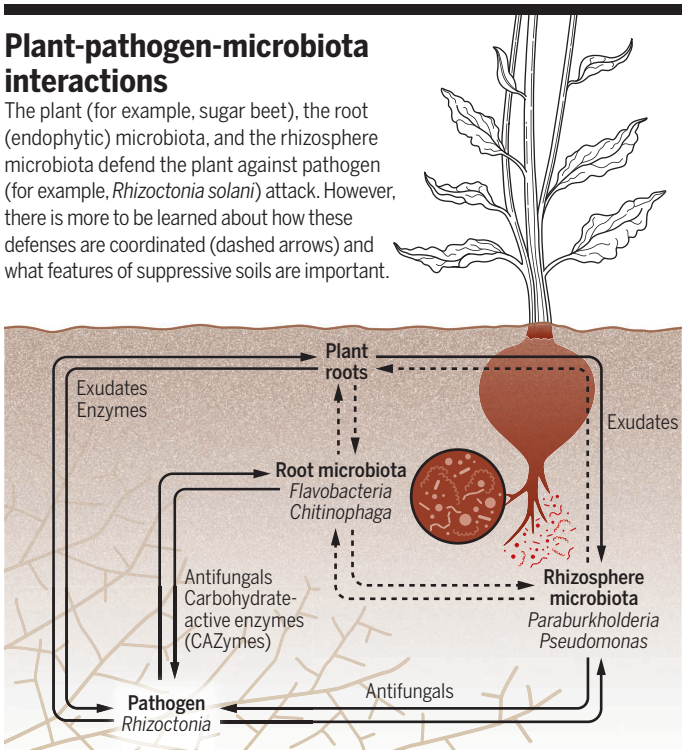
Diseases affecting crops take a toll on agricultural yields worldwide. Strategies to eradicate or mitigate these pathogens include breeding resistant genotypes, crop rotation, and chemical or biological treatments. A phenomenon called "suppressive soils" has attracted considerable interest because such soils can reduce disease incidence despite pathogen presence, a susceptible host, and favorable conditions for infection. If the secrets of suppressive soils could be unlocked, it might be possible to confer suppressiveness to other soils without the risks and losses associated with repeated cropping on disease-affected fields. Suppressive soils have long been suspected to be mediated by microbiota, particularly because suppressiveness is lost upon sterilization and can be transferred from one soil to another through mixing. On page 606 of this issue, Carrión *et al.* (*1*) demonstrate that they can confer disease suppressiveness when specific bacteria are added as a consortium to a conducive soil.

Suppressive soils can exhibit both general suppression, in which disease incidence of a range of pathogens is reduced, or specific suppression, in which a particular pathogen's impact is dampened. These have been compared to innate and adaptive immune responses, respectively (*2*). General suppression is typically attributed to competitive exclusion of pathogens by an active microbiota and appears inherent to the soil. Specific suppression typically arises after multiple seasons of growing a susceptible crop in the presence of a pathogen, during which an initial high disease incidence drops with each successive growth season. This suppressive activity remains as long as the susceptible crop is grown in the soil but can quickly dissipate if another crop is grown or new pathogens are introduced. However, which soils are likely to develop suppressive activity in subsequent growth seasons after a disease outbreak is unknown and challenging to test.

Careful microbiological work has identified a handful of microorganisms that contribute to suppression of specific pathogens (*3*, *4*). Over the past decade, molecular methods have accelerated these studies and started to reveal a complex interplay of organisms, genes, and biochemical factors that contributes to this intriguing process. Carrión *et al.* identified and cultivated several bacteria whose abundance inside plant roots was increased upon inoculation of a plant with the fungal pathogen *Rhizoctonia solani* in suppressive soil. Notably, the ability of these organisms to penetrate the plant roots indicates that their interactions with the plant host may be equally critical to suppression as direct interactions with the pathogen. Moreover, the increased effectiveness of the consortium compared with individual isolates implies that they may interact with each other as well (see the figure).

Plant-pathogen-microbiota interactions

The plant (for example, sugar beet), the root (endophytic) microbiota, and the rhizosphere microbiota defend the plant against pathogen (for example, *Rhizoctonia solani*) attack. However, there is more to be learned about how these defenses are coordinated (dashed arrows) and what features of suppressive soils are important.



Carrión *et al.* also identified key bacterial genes that increased in expression upon plant infection in suppressive soil—hinting at the mechanisms of pathogen suppression and pointing toward the development of robust consortia that confer the suppressive phenotype. These genes include carbohydrate-active enzymes (CAZymes, which degrade carbohydrates), especially those potentially active against fungal cell walls, and biosynthetic gene clusters (BGCs) for specialized metabolite production. Most notably, one of the BGCs in the disease-suppressing *Flavobacterium* isolate was demonstrated to be critical for full disease suppression through site-directed mutagenesis.

The study of Carrión *et al.* focuses on *Rhizoctonia*, a genus of fungi encompassing pathogens of diverse crops that cause considerable global yield losses, including the causative agents of bare patch and root rot of wheat, rice sheath blight, and root and crown rot of sugar beet. Soils suppressive to *Rhizoctonia* pathogens have been observed in various fields across the globe, including the Dutch site examined by Carrión *et al.* Previous work from this group has demonstrated that certain species of *Paraburkholderia*, *Pseudomonas*, and *Streptomyces* are increased in abundance near the roots (rhizosphere) of plants grown in these *R. solani*–suppressive soils and that some isolates of these genera can confer suppressive activity (*5*, *6*). This activity has been linked to production of a chlorinated lipopeptide (thanamycin) by *Pseudomonas* and of sulfurous volatile compounds by *Paraburkholderia* (see the figure). As suggested by Carrión *et al.*, these rhizosphere inhabitants may form the first line of defense against soilborne *Rhizoctonia*; subsequent attack and colonization of plant roots by the pathogen prompts the plant to mobilize a second line of defense by bacteria inside the root. Not all isolates with disease-suppressive activity in plants also

CREDIT: A. KITTERMAN/*SCIENCE*

U.S. Department of Energy (DOE) Joint Genome Institute, Walnut Creek, CA 94598, USA. Email: sgtringe@lbl.gov

Published by AAAS

exhibit antifungal activity in vitro, implying that additional signals or factors are required for disease suppression (*6*).

Studies of *R. solani*–suppressive soils at other locations have identified other bacterial strains and genes involved in suppression, implying that there are many paths to success and, therefore, many promising avenues to pursue in developing agricultural products or practices to build suppressive activity (*4*). The bacterial strains and consortia tested by Carrión *et al.* have only been demonstrated to confer suppressive activity on nearby conducive soils with similar biogeochemistry and microbiology. Individual microbes often fail to establish and confer disease suppression when seeded into new environments; it is hoped that synthetic consortia will prove more successful at displacing indigenous microbiota in addition to working synergistically to inhibit pathogens (*2*), but evidence for this is anecdotal so far. Moreover, there may be additional physical, chemical, and microbiological features that enable suppression at particular locations but not others that have yet to be characterized.

Demonstrating disease suppression by a microbial isolate or consortium in a variety of conducive soils, particularly in a field setting, would be a major advance. If, as seems likely, suppressive activity is dependent on the soil background, controlled experiments on sterile growth substrates could help eliminate the "unknowns" associated with growth in soil, including the presence of other pathogenic or beneficial microbes (*7*). Inoculation into sterilized soils that have lost suppressive activity, particularly cross-inoculations with other suppressive soils, could also help distinguish physical and chemical factors from biological ones, establishing, for example, requirements for specific nutrient levels for suppression to be effective. Ultimately, such studies could build a "recipe" for reliable disease suppression that is robust to field variability. ■

REFERENCES AND NOTES

1. V. J. Carrión *et al.*, *Science* **366**, 606 (2019).
2. J. M. Raaijmakers, M. Mazzola, *Science* **352**, 1392 (2016).
3. D. M. Weller, J. M. Raaijmakers, B. B. Gardener, L. S. Thomashow, *Annu. Rev. Phytopathol.* **40**, 309 (2002).
4. D. Schlatter, L. Kinkel, L. Thomashow, D. Weller, T. Paulitz, *Phytopathology* **107**, 1284 (2017).
5. R. Mendes *et al.*, *Science* **332**, 1097 (2011).
6. V. J. Carrión *et al.*, *ISME J.* **12**, 2307 (2018).
7. S. L. Lebeis *et al.*, *Science* **349**, 860 (2015).

ACKNOWLEDGMENTS

Thanks to L. Kinkel and K. Hartman for helpful comments. The work conducted by the U.S. Department of Energy (DOE) Joint Genome Institute, a DOE Office of Science User Facility, is supported by the DOE under contract no. DE-AC02-05CH11231.

10.1126/science.aaz5619

SYNTHETIC BIOLOGY

Toward synthetic cells

Frog egg cytoplasm self-organizes into cell-like units by microtubule aster assembly and partition

By **Timothy J. Mitchison**[1,2] *and* **Christine M. Field**[1,2]

An aspirational goal in cell biology is de novo synthesis of whole cells, with the expectation that this will reveal principles of spatiotemporal organization. Natural cells are defined by their boundaries, usually lipid bilayer plasma membranes stabilized by external cell walls or cytoskeletal cortices comprising actin. Typically, researchers approach cell synthesis by preparing protein mixtures in bulk, then partitioning them into cell-sized containers using water-in-oil emulsions, giant unilamellar vesicles, or microfabricated chambers. On page 631 of this issue, Cheng and Ferrell (*1*) describe an alternative approach to cell synthesis, whereby a bulk preparation of concentrated extract from frog eggs self-organizes into regularly spaced, cell-like units.

The resulting preparations resemble natural syncytia, which are large cells in which many nuclei share a common cytoplasm. Like natural syncytia, they are organized by microtubule asters, which are cytoskeletal structures that usually emanate from a centrosome (see the figure). Partitioning of frog egg cytoplasm into cell-like units by microtubule asters was reported previously (*2*, *3*). However, Cheng and Ferrell found that self-organization can occur in the absence of centrosomes and that mitotic division of units can happen when they contain DNA and centrosomes.

Syncytial organization is characteristic of certain protist and fungal species (*4*). It has been most studied in early fruit fly (*Drosophila melanogaster*) embryos, for which the first 13 divisions are syncytial. The cell-like units in syncytial *D. melanogaster* embryos are composed of a nucleus with an associated centrosome, microtubule aster, and organelles. They are called energids and behave in many ways like membrane-delimited cells (*5*, *6*). How energids self-organize, divide, and space out, all while sharing a common cytoplasm, remains unclear.

Cheng and Ferrell reported mitotic division of their cell-like units when nuclei and centrosomes were present, in resemblance to natural syncytia. Similar syncytial divisions were reported in droplets extracted from syncytial *D. melanogaster* embryos with a micropipette (*7*), but the frog extract system can be biochemically manipulated. Frog egg extracts have long been used to study cell cycle oscillations driven by cyclin B synthesis and destruction (*8*). Cycles can continue for many hours if oxygen and carbon dioxide exchange are facilitated by partitioning the extract into cell-like droplets (*9*). It is exciting to now see this biochemical oscillator drive syncytial mitosis. In fertilized frog eggs, each cell cycle is accompanied by cell division. However, syncytial division can occur when cell division (specifically cytokinesis, when duplicated cells are separated) is blocked (*10*), so the mechanisms that organize normal cleavage divisions can also generate syncytia, as seen in Cheng and Ferrell's extract system.

"Frog egg extract provides a versatile system for cell synthesis..."

What molecular mechanisms are likely to organize and partition asters in synthetic syncytia and their natural counterparts? In physical systems, assembly of discrete particles or droplets out of a bulk phase can be driven by a simple condensation or aggregation process. It is possible that the syncytial organization observed by Cheng and Ferrell is also driven by some bulk condensation or aggregation process. Egg extract contains high concentrations of endoplasmic reticulum, mitochondria, ribosomes, and glycogen, any of which might spontaneously aggregate. Using chemical inhibitors, Cheng and Ferrell found that emergence of syncytium-like organization depended on microtubules and the minus-end–directed motor protein dynein, pointing to a role of microtubule-based mechanisms rather than bulk aggregation.

Cheng and Ferrell observed microtubule aster formation with or without centrosomes. In frog eggs, asters are nucleated by centrosomes, and their growth to hundreds of microns is further facilitated by microtubule-stimulated nucleation distant from the

[1]Harvard Medical School, Boston, MA, USA.
[2]Marine Biological Laboratory, Woods Hole, MA, USA.
Email: timothy_mitchison@hms.harvard.edu; christine_field@hms.harvard.edu

Published by AAAS

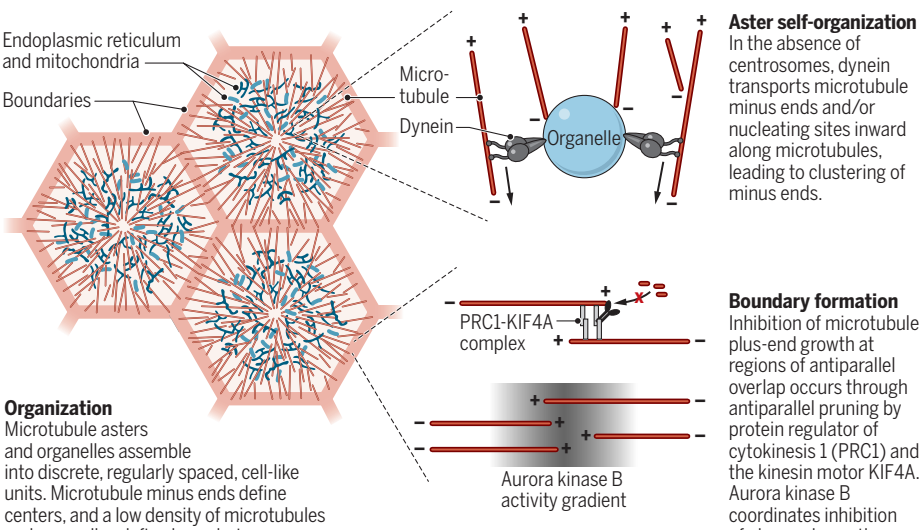
centrosome (*11*). Radial asters can also self-assemble by dynein-dependent mechanisms in the absence of centrosomes. These partially understood mechanisms are thought to involve inward transport of microtubule minus ends, and/or microtubule nucleating complexes, by dynein that can be part of a multiprotein complex (*12*) or attached to vesicles (*13*).

Syncytia also require boundaries to delimit asters and space them out. These boundary-formation mechanisms need only operate directly on microtubules, because organelles are entrained to microtubules by dynein-mediated transport. One known boundary-forming mechanism involves pruning of antiparallel microtubules by the combined action of a microtubule cross-linker [protein regulator of cytokinesis 1 (PRC1)] and a kinesin motor that caps plus ends, KIF4A (*14*). Another involves inhibition of plus-end growth by aurora kinase B (*3*), which is transported to aster boundaries by kinesins as part of the chromosomal passenger complex (*2*). These mechanisms cooperate to partition the microtubule cytoskeleton during cytokinesis and may be involved in the mitotic division of cell-like units observed by Cheng and Ferrell.

Synthetic approaches test hypotheses for cell organization in a manner that is orthogonal to genetic perturbation. Frog egg extract provides a versatile system for cell synthesis, whether in bulk to form syncytia (*1*, *3*) or in droplets to mimic individual cells (*9*). Individual proteins can be removed or added, and knowledge of the quantitative proteome facilitates systems-level analysis (*15*). One important caveat is that the frog egg is not an ordinary cell, especially in its huge spatial dimension, and egg organization mechanisms may differ in interesting ways from those in small cells. Cell biologists are urged to consider syncytia in research as well as physically discrete cells. Understanding how energids, microtubule asters, or equivalent organization units assemble, divide, and space out in a shared cytoplasm is likely to reveal organization principles that are relevant to all cells. ■

Model of assembly and partitioning of cell-like units

Cheng and Ferrell observed syncitium-like organization of frog egg extract, potentially providing an alternative method of cell synthesis.



Organization
Microtubule asters and organelles assemble into discrete, regularly spaced, cell-like units. Microtubule minus ends define centers, and a low density of microtubules and organelles define boundaries.

Aster self-organization
In the absence of centrosomes, dynein transports microtubule minus ends and/or nucleating sites inward along microtubules, leading to clustering of minus ends.

Boundary formation
Inhibition of microtubule plus-end growth at regions of antiparallel overlap occurs through antiparallel pruning by protein regulator of cytokinesis 1 (PRC1) and the kinesin motor KIF4A. Aurora kinase B coordinates inhibition of plus-end growth.

REFERENCES AND NOTES

1. X. Cheng, J. E. Ferrell, *Science* **366**, 631 (2019).
2. P. A. Nguyen *et al.*, *Science* **346**, 244 (2014).
3. C. M. Field, J. F. Pelletier, T. J. Mitchison, *Curr. Biol.* **29**, 1999 (2019).
4. S. E. Roberts, A. S. Gladfelter, *Curr. Opin. Microbiol.* **28**, 60 (2015).
5. V. E. Foe, B. M. Alberts, *J. Cell Sci.* **61**, 31 (1983).
6. M. Mavrakis, R. Rikhy, J. Lippincott-Schwartz, *Commun. Integr. Biol.* **2**, 313 (2009).
7. I. A. Telley, I. Gáspár, A. Ephrussi, T. Surrey, *J. Cell Biol.* **197**, 887 (2012).
8. A. W. Murray, M. J. Solomon, M. W. Kirschner, *Nature* **339**, 280 (1989).
9. Y. Guan *et al.*, *eLife* **7**, e33549 (2018).
10. C. M. Beal, K. E. Dixon, *J. Exp. Zool.* **192**, 277 (1975).
11. K. Ishihara, P. A. Nguyen, A. C. Groen, C. M. Field, T. J. Mitchison, *Proc. Natl. Acad. Sci. U.S.A.* **111**, 17715 (2014).
12. F. Verde *et al.*, *J. Cell Biol.* **112**, 1177 (1991).
13. V. I. Rodionov, G. G. Borisy, *Nature* **386**, 170 (1997).
14. P. A. Nguyen, C. M. Field, T. J. Mitchison, *Mol. Biol. Cell* **29**, 304 (2018).
15. M. Wühr *et al.*, *Curr. Biol.* **24**, 1467 (2014).

ACKNOWLEDGMENTS

T.J.M. and C.M.F. are supported by National Institutes of Health grant GM131753.

10.1126/science.aaz5635

EVOLUTION

Mapping footprints of past genetic exchange

Widespread mating between species creates mosaic genomes in *Heliconius* butterflies

By **Loren H. Rieseberg**

Controversies in evolutionary biology can linger for centuries. This is not because evolutionary biologists are unusually contentious, but rather because evolution is a challenging science that involves the reconstruction of events tracing back more than 3.7 billion years. Also, evolutionary processes common to one organismal group may be absent in another. Thus, generalizations about evolution must be built on studies of many taxa, with the recognition that exceptions to every rule are likely. Given these challenges, celebrations should be had when major controversies are put to rest. On page 594 of this issue, Edelman *et al.* (*1*) help bring one such controversy to a close by demonstrating the importance of hybridization (interbreeding between species) in the diversification of *Heliconius* butterflies. They also develop a new technique to disentangle genomic patterns caused by hybridization from those caused by stochastic processes within species.

The controversy about the role of hybridization in evolution began almost 300 years ago when the Swedish botanist Carl Linnaeus posited that new forms of plants could arise by hybridization (*2*). This suggestion was criticized by members of the clergy because it challenged the immutability of species. Darwin (*3*) also expressed skepticism about the importance of hybridization, albeit for scientific reasons. In the 20th century, the prevailing view among evolutionary biologists aligned closely with Darwin's, holding that hybridization was rare, and when it did occur, it was likely

Department of Botany, The University of British Columbia, Vancouver, BC V6T 1Z4, Canada. Email: lriesebe@mail.ubc.ca

GRAPHIC: K. HOLOSKI/*SCIENCE*

Published by AAAS

to be maladaptive and transitory, leading either to the completion of speciation or to the merging of hybridizing entities (*4*, *5*). The alternative view held that hybridization was more common than generally appreciated, but even when rare, it could provide useful genetic variation that could be exploited through natural selection (*6*).

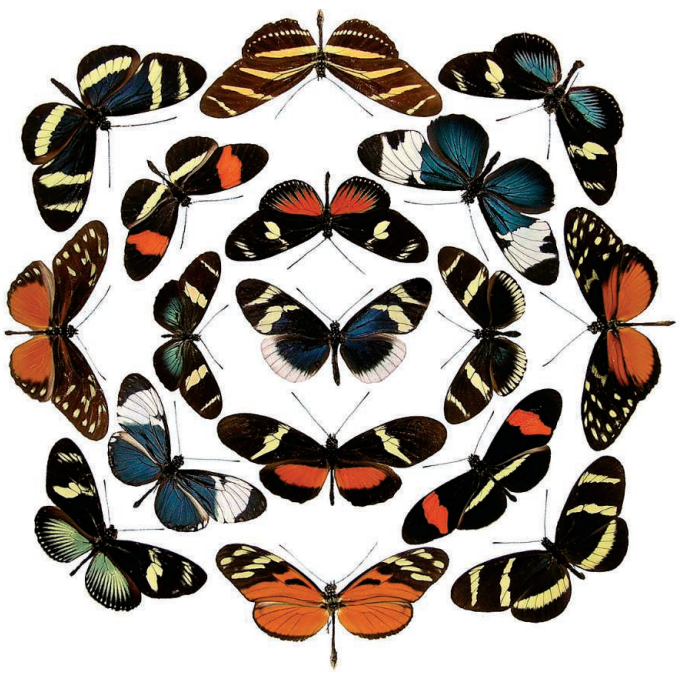
With fully sequenced genomes now available for many organisms, as well as methods for detecting the genomic signatures of past hybridization events (*7*), it is now possible to assess both the presence and genomic extent of admixture (the presence of DNA in an individual that derives from distantly related lineages, often due to hybridization). Admixture has been detected in numerous genomes across the domains of life, including more than 70 cases where it is known to be adaptive (enhance evolutionary fitness) (*8*). The extent of genetic exchange is such that some biologists have argued that the use of trees for depictions of the history of life should be abandoned in favor of networks, which can depict both branching and reticulate evolutionary histories (*9*).

Heliconius butterflies are endemic to tropical America and comprise ~40 species, which are known for the spectacular diversity (and beauty) of their wing patterns (see the photo). The colorful wing patterns not only warn predators of a butterfly's distastefulness, they also offer cues for mate recognition, which contributes to speciation by promoting breeding within species. Hybridization underlies the origin and exchange of wing patterns, aiding the establishment of new hybrid species (*10*), as well as the evolution of Müllerian mimics (*11*), in which different unpalatable species share similar warning wing patterns. However, these inferences have been questioned (*12*), partly because of technical difficulties in distinguishing between admixture (hybridization) and the stochastic sorting of ancestral polymorphisms, called incomplete lineage sorting (ILS). The latter occurs when there is not enough time for genetic drift to resolve polymorphic loci (that is, the extinction of all but one allele at a locus) prior to the next speciation event. Consequently, genealogies frequently differ from the species phylogeny, imitating phylogenomic patterns caused by hybridization.

To estimate the importance of hybridization and introgression (interspecific genetic exchange by hybridization) in *Heliconius*, Edelman *et al.* generated 20 new genome assemblies for *Heliconius* species and related genera. The authors then determined the genealogies of loci from across the *Heliconius* genome. Most genealogies were incongruent: They differed from each other and from a consensus "species" phylogeny for the group, suggesting that ILS and/or admixture were common.

To distinguish between these possibilities, Edelman *et al.* developed a new method called "quantifying introgression via branch lengths" (QuIBL). The method takes advantage of the observation that the internal branch lengths in a genealogy are expected to be longer on average if incongruence is due to introgression rather than ILS. Extensive simulations over a wide range of demographic conditions indicate that this method is more accurate than previous approaches. When applied to small genomic regions across 13 *Heliconius* genomes, ~20% of genomic windows were estimated to have a history of introgression, and ~70% of incongruent genealogies were due to introgression compared with 30% from ILS. This implies that even when speciation events occur close together in time, such as in rapidly diversifying groups, hybridization rather than ILS is the dominant cause of genealogical incongruence.

So, is the observed extensive introgression of evolutionary importance? Analyses of the genomic distribution of introgressions indicate that they are associated with high recombination rates. This distribution implies that most introgressions probably are maladaptive (*13*). Recombination can remove harmful alleles from introgressions (leaving neutral fragments behind) before they are eliminated from the genome by natural selection. The authors also report a new chromosomal inversion that likely represents an example of adaptive introgression. Inversions typically suppress recombination in heterozygotes and can aid adaptive divergence and speciation by preventing combinations of adaptive alleles from being broken up by recombination. This particular inversion includes the *cortex* locus, which underlies the evolution of wing coloration patterns and mimicry in another *Heliconius* species (*14*). Thus, introgression likely has had both harmful and beneficial consequences in *Heliconius*.



Variation in wing patterns in *Heliconius* butterflies defines different species, which often have admixed genomes.

PHOTO: MARCUS KRONFORST/HARVARD UNIVERSITY

The study of Edelman *et al.* adds to a growing literature indicating that the footprints of hybridization are a common feature of plant and animal genomes and that hybridization can provide the fuel for adaptive diversification. However, this does not necessarily mean that hybridization is common at the population level. For example, a single successful hybridization event early in the divergence of a lineage could leave traces in all descendants. Thus, an important next step is to estimate the number and diversity of hybridization events required to account for observed patterns of genomic admixture. ■

REFERENCES AND NOTES

1. N. B. Edelman *et al.*, *Science* **366**, 594 (2019).
2. C. Linné, Disquisitio de sexu plantarum, ab Academia Imperiali Scientiarum Petropolitana praemio ornata. *Amoenitates Academicae* **10**, 100 (1760).
3. C. Darwin, in *On the Origin of Species by Means of Natural Selection, or the Preservation of Favoured Races in the Struggle for Life* (John Murray, 1859), p. 43.
4. T. Dobzhansky, *Genetics and the Origin of Species* (Columbia Univ. Press, 1937).
5. W. H. Wagner Jr., *Taxon* **19**, 146 (1970).
6. E. Anderson, *Introgressive Hybridization* (Wiley, 1949).
7. B. A. Payseur, L. H. Rieseberg, *Mol. Ecol.* **25**, 2337 (2016).
8. E. Bapteste *et al.*, *Trends Genet.* **29**, 439 (2013).
9. M. L. Arnold, K. Kunte, *Trends Ecol. Evol.* **32**, 601 (2017).
10. J. Mavárez *et al.*, *Nature* **441**, 868 (2006).
11. The *Heliconius* Genome Consortium, *Nature* **487**, 94 (2012).
12. A. V. Z. Brower, I. J. Garzón-Orduña, *Cladistics* **34**, 151 (2017).
13. M. Schumer *et al.*, *Science* **360**, 656 (2018).
14. N. J. Nadeau *et al.*, *Nature* **534**, 106 (2016).

10.1126/science.aaz1576

Published by AAAS

NEUROSCIENCE

Deep sleep drives brain fluid oscillations

Rhythmic fluid flows in deep sleep may allow communication and clearance of waste products

By **Søren Grubb**[1] *and* **Martin Lauritzen**[1,2]

Getting enough quality sleep at the right times helps protect physical and mental health. Slow-wave sleep (SWS) represents high-intensity sleep and predominates in the first part of the night. Rapid eye movement (REM) sleep accompanies dreaming and is not influenced by prior sleep or waking and shows a rhythmicity with the body clock (circadian rhythm) (*1*): Sleep starts with a light form of SWS, progresses to deeper SWS and then shallow SWS, and concludes with REM sleep before beginning a new cycle (*2*). During SWS, the cerebral blood flow is reduced by 25%, which lowers cerebral blood volume (CBV) by ~10% (*3*). On page 628 of this issue, Fultz *et al.* (*4*) show that this reduction in CBV in the human brain allows inflow of cerebrospinal fluid (CSF) to the third and fourth ventricles—fluid-filled cavities in the central brain—which may facilitate communication between fluid compartments and clearance of waste products.

"Slow waves" refer to electrical signatures, which are distinct from the fast activities that dominate the awake state and REM sleep. Highly organized rhythmic activities, such as in SWS, enable neurons to form coherent assemblies that can propagate meaningful information to other networks (*5*) and contribute to the long-term consolidation of new memories. The neocortex is active during SWS, the intracortical dialogue is maintained (*6*), and the responsiveness of cortical neurons to callosal volleys—signaling between the two hemispheres—is increased (*7*). At the same time, the cerebral cortex is shut off from the environment because the nuclei that normally relay information to the cortex become unresponsive to external inputs (*8*). Despite this high level of activity, energy turnover in the brain is reduced, and consequently, so is the cerebral metabolism of oxygen (*3*, *9*).

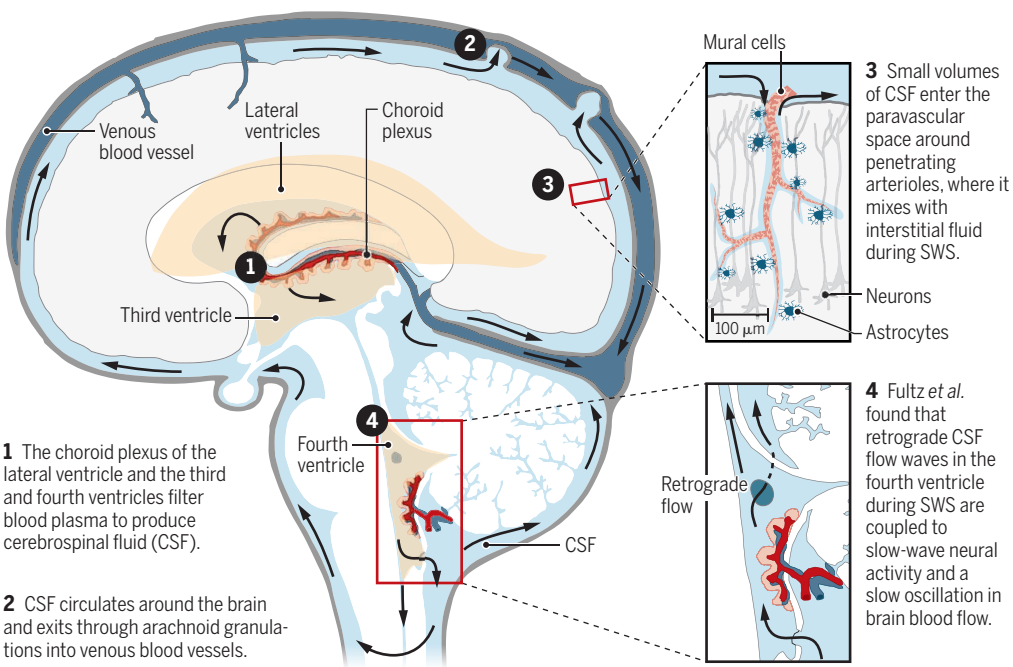
CSF is produced by the choroid plexuses and flows from the lateral ventricles into the third ventricle and then to the fourth (see the figure). CSF then passes into the subarachnoid space surrounding the brain and spinal cord; there, it normally moves along the brain convexity to the top of the brain, where it is absorbed in the arachnoid granulations of the dural venous sinuses. Fultz *et al.* describe reversal of the direction of CSF flow during SWS. Most likely, CSF flows from the subarachnoid space to the fourth and third ventricle (*4*). The waves of CSF inflow were generated by the slow electrical brain oscillations and the corresponding fluctuations in blood flow and CBV.

CSF flow mediates mixing of brain fluids, facilitates signaling through volume transmission of neuromodulators, and increases the disposal of potentially harmful substances. There is substantial variation in brain volume, but an estimate of 1260 ml is reasonable for an average adult human brain, and the global reduction in cerebral blood flow during SWS gives rise to an overall reduction in CBV of 1.26 ml (*10*), which corresponds to ~1% of the CSF present at any one time. Thus, the CSF volume available for fluid oscillations is small, but the data presented by Fultz *et al.* suggest that the fluctuations occur in structures that are crucial for CSF exchange between the central cavities and the convexity. The CSF oscillations in human sleep described by Fultz *et al.* may contribute to the disposal of waste products, such as toxic brain proteins that cause neurodegeneration.

CSF also drains along the perivascular pathways, which likewise direct the flow of interstitial fluid (ISF) along cerebral blood vessels (*11*) to cervical lymph nodes (*12*), but drainage of CSF and ISF along glymphatic pathways from periarteriolar to perivenous sites has been suggested to contribute as well (*13*). The glymphatic theory suggests that during SWS, convection of ISF removes toxic proteins from the brain extracellular

Brain fluid flow switches direction in deep sleep

Fultz *et al.* show that retrograde brain fluid waves follow the fluctuations in neural activity and brain blood volume in slow-wave sleep (SWS).



GRAPHIC: N. DESAI/*SCIENCE* FROM S. GRUBB AND M. LAURITZEN

[1]Department of Neuroscience, Faculty of Health Sciences, University of Copenhagen, DK-2200 Copenhagen N, Denmark. [2]Department of Clinical Neurophysiology, Rigshospitalet, DK-2600 Glostrup, Denmark.
Email: mlauritz@sund.ku.dk

Published by AAAS

environment (*13*). However, the existence of a glymphatic system is much debated because of the lack of evidence for the ability of the ISF to transport solutes (*14*) and the evidence in favor of diffusion of small and large molecules without ISF flow (*15*). However, the brainwide pulsations in CBV that cause CSF inflow to brain ventricles every 20 s during SWS as shown by Fultz *et al*. suggest that CSF and ISF do mix during deep sleep and that SWS has important homeostatic functions (*13*).

The identified reversal of CSF flow during SWS by Fultz *et al*. facilitates the mixing of subarachnoid and ventricular fluids and may serve as a communication pathway between fluid compartments. The bidirectional CSF flow may also serve to keep the small apertures that link the ventricles and the subarachnoid space open to maintain free CSF flow from the choroid plexus to the subarachnoid space. This will prevent accumulation of CSF and waste products within the brain and preserve low intracranial pressure, which is essential for brain survival. Disturbances of SWS commonly accompany aging, major depressive disorders, and dementia (*2*). It will be interesting to assess whether the CSF dynamics linked to SWS can be used as a biomarker for disease states and whether strategies that restore SWS can rescue brain function in neurodegeneration. ■

"The [cerebrospinal fluid] oscillations in human sleep... may contribute to the disposal of waste products..."

REFERENCES AND NOTES

1. A. A. Borbély, *Hum. Neurobiol.* **1**, 195 (1982).
2. B. O. Watson, G. Buzsáki, *Daedalus* **144**, 67 (2015).
3. P. L. Madsen *et al*., *J. Appl. Physiol.* **70**, 2597 (1991).
4. N. E. B. Fultz *et al*., *Science* **366**, 628 (2019).
5. B. O. Watson, D. Levenstein, J. P. Greene, J. N. Gelinas, G. Buzsáki, *Neuron* **90**, 839 (2016).
6. I. Timofeev, D. Contreras, M. Steriade, *J. Physiol.* **494**, 265 (1996).
7. M. Steriade, *Neuroscience* **137**, 1087 (2006).
8. R. R. Llinás, M. Steriade, *J. Neurophysiol.* **95**, 3297 (2006).
9. R. Mangold *et al*., *J. Clin. Invest.* **34**, 1092 (1955).
10. R. L. Grubb Jr., M. E. Raichle, J. O. Eichling, M. M. Ter-Pogossian, *Stroke* **5**, 630 (1974).
11. H. Mestre *et al*., *Nat. Commun.* **9**, 4878 (2018).
12. E. N. Bakker *et al*., *Cell. Mol. Neurobiol.* **36**, 181 (2016).
13. L. Xie *et al*., *Science* **342**, 373 (2013).
14. N. J. Abbott, M. E. Pizzo, J. E. Preston, D. Janigro, R. G. Thorne, *Acta Neuropathol.* **135**, 387 (2018).
15. E. Syková, C. Nicholson, *Physiol. Rev.* **88**, 1277 (2008).

ACKNOWLEDGMENTS

The authors are supported by the Lundbeck Foundation and the Independent Research Fund Denmark.

10.1126/science.aaz5191

MATERIALS SCIENCE

Order emerging from disorder

Entropy stabilization provides a new direction for developing functional materials

By **Nita Dragoe** *and* **David Bérardan**

Twenty-six metals are usually found in alloys. Combining five of those metals and varying the composition in 1% increments leads to 2,822,599,802,880 different possible compounds. For six metals, the number of possible combinations is 902,943,619,878,430. Not all of these combinations are stable, but adding more elements counterintuitively stabilizes simpler structures by increasing entropy, a measure of disorder. Creating new materials by using entropy as a driving force is an emerging topic in materials science. Initially, this concept was used to obtain high-entropy alloys (HEA), which typically consisted of five elements. These alloys exhibit intriguing structural properties (*1*, *2*). Recently, the strategy of using the entropy of mixing to stabilize a new phase has been extended outside metallic alloys and into functional materials.

By analogy to HEAs, single-phase samples of entropy-stabilized functional materials (ESFMs) have been loosely named as high-entropy materials. More accurately, a new phase formed because of the configuration entropy should be called "entropy stabilized." By contrast, multicomponent conventional solid solutions have a high entropy of configuration but are generally not entropy stabilized. The key distinction is the presence of a phase transition at a critical temperature for the entropic phase. Therefore, all reported entropy-stabilized materials are also high-entropy materials, but the opposite is not true.

Synthesizing ESFMs requires heating a multicomponent mixture at high temperature followed by quenching, when the system has a small positive enthalpy. The configuration entropy (S) is equal to $S = -R\Sigma x_i \ln(x_i)$, where x_i is the fraction of each component. Entropy is equal to $1.61R$ for five equimolar elements, neglecting other entropic contributions (such as vibrational or magnetic). Thus, at high temperature the entropy becomes the main component of the total Gibbs free energy $\Delta G = \Delta H - T\Delta S$. For example, a reaction temperature of 1000 K compensates for a 13.37 kJ/mol heat of formation. A high-entropy phase will be thermodynamically favored, and the elements will be distributed over the available crystallographic sites. The existence of disorder favors the formation of a new simple phase.

This entropy-stabilized high-temperature phase can be frozen at room temperature through quenching. It is important to note that the resulting materials are not simple "conventional" solid solutions but metastable, entropy-stabilized solid solutions, with properties that are difficult to predict. As such, not only are these new materials, they represent a new paradigm in the design of functional materials, having a stability driven by the entropy of configuration.

One of the first entropy-stabilized oxides, (Mg,Co,Ni,Cu,Zn)O, was reported in 2015 (*3*). Heating the mixture of five oxides above 1150 K and quenching resulted in material with a simple rock salt structure (see the figure). This structure was not expected because some of the binary oxides do not crystallize in the rock salt structure and do not form a solid solution. The material is metastable because it will separate into several constituents when heated below 1150 K, but the structure is preserved at 300 K. In other words, (Mg,Co,Ni,Cu,Zn)O is kinetically stable at room temperature.

The formation of this type of new material is governed by entropy, which forces the cations to occupy randomly cationic sites. All five cations of (Mg,Co,Ni,Cu,Zn)O occupy similar octahedral sites at high temperature. This allows placement of cations in uncommon configurations or geometries that may result in new and unexpected properties.

Other ESFM structures have been claimed since 2015 with different classes of oxides, including perovskites (*4*), fluorite (*5*), spinels (*6*), as well as carbides (*7*), silicides (*8*), and borides (*9*). Some of these compounds still need to be tested in order to verify whether they are complex solid solutions or entropy-stabilized compounds.

Although cations have been used for entropic stabilization up to now, we have no reason to rule out anionic stabilization, and we can imagine this leading to increased structural complexity. Moreover, several cationic sites can be present. The perovskite

Institut de Chimie Moléculaire et des Matériaux d'Orsay, Université Paris-Saclay, Université Paris-Sud, UMR 8182 CNRS, 91405 Orsay, France. Email: nita.dragoe@u-psud.fr

Published by AAAS

(ABO_3) structure, for example, presents three different possible entropy-stabilized structures with a distribution of cations on the crystallographic A site, on the B site, or on both sites.

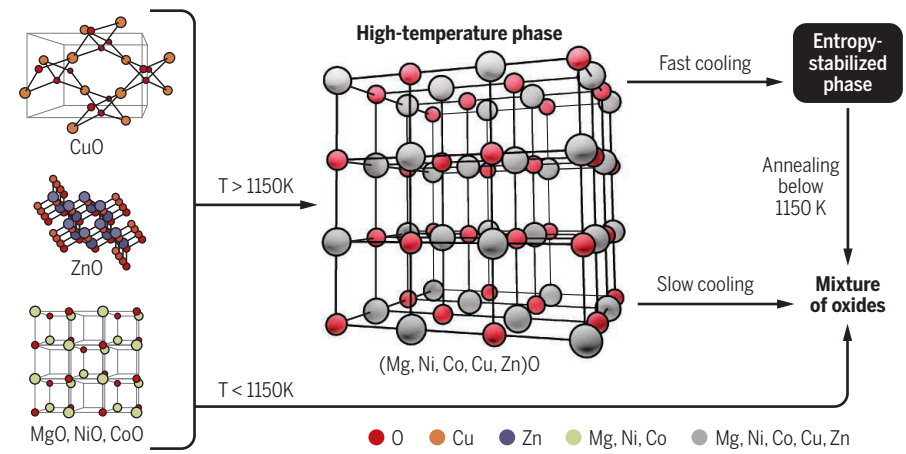
Although more materials are being added to the list of ESFMs, their properties have just begun to be investigated. The huge complexity of the systems and the dominant role of the entropy in their stabilization make the properties unpredictable. For example, doping (Mg,Co,Ni,Cu,Zn)O with alkali ions resulted in compounds with a colossal dielectric constant (*10*) and superionic conductivity (*11*). As a consequence, the system may be important for energy storage applications (*12*). In general, doping allows fine-tuning of the composition and increases the already huge compositional space.

not limited to 3d electron–based systems because 4d and 5d transition-metal oxides also provide distinct properties owing to the interplay between electron correlation and spin-orbit coupling. Applying entropy-stabilization to more-complex oxides could give rise to intriguing physical properties, including thermoelectric materials, thermal barrier coatings, catalysis, or multifunctional properties.

Until now, such disordered systems have been almost completely overlooked in the search for new materials properties in solid-state physics. We believe that entropy-stabilized materials can provide a new impetus for the exploration of exotic properties and functions. However, one important challenge is deciding which of the staggering number of compounds to focus on. ■

Entropy-stabilized oxides

Oxides with different crystal structures may not easily combine together. Increasing the disorder, otherwise known as entropy, by increasing the number of elements can stabilize simple crystal structures at high temperatures. Keeping these materials stable at lower temperatures requires fast cooling.



The random cationic distribution of ESFMs suggests the potential for glass-like physical properties. For example, low electrical mobility, glass-like thermal transport, diamagnetism, or paramagnetism may stem from the disorder. (Mg,Co,Ni,Cu,Zn)O has a very low thermal conductivity (*13*) and is electrically insulating (*10*). However, this compound has peculiar magnetic properties, such as giant enhancement of exchange coupling in heterostructures (*14*) and long-range magnetic order (*15*). The long-range magnetic order is surprising in a chemically disordered system. The type of neighboring magnetic ion can change the magnitude or even the sign of the interaction. As a result, magnetic interactions might vary throughout the crystal structure. These types of systems are promising for studying the emergence of exotic magnetism. The electronic properties are

REFERENCES AND NOTES

1. E. P. George, D. Raabe, R. O. Ritchie, *Nat. Rev. Mater.* **4**, 515 (2019).
2. M. C. Gao *et al.*, *J. Mater. Res.* **33**, 3138 (2018).
3. C. M. Rost *et al.*, *Nat. Commun.* **6**, 8485 (2015).
4. R. Witte *et al.*, *Phys. Rev. Mater.* **3**, 034406 (2019).
5. J. Gild *et al.*, *J. Eur. Ceram. Soc.* **38**, 3578 (2018).
6. J. Dąbrowa *et al.*, *Mater. Lett.* **216**, 32 (2018).
7. X. Yan *et al.*, *J. Am. Ceram. Soc.* **101**, 4486 (2018).
8. Y. Qin *et al.*, *J. Adv. Ceram.* **8**, 148 (2019).
9. J. Gild *et al.*, *Sci. Rep.* **6**, 37946 (2016).
10. D. Bérardan, S. Franger, D. Dragoe, A. K. Meena, N. Dragoe, *Phys. Status Solidi Rapid Res. Lett.* **10**, 328 (2016).
11. D. Bérardan, S. Franger, A. K. Meena, N. Dragoe, *J. Mater. Chem. A Mater. Energy Sustain.* **4**, 9536 (2016).
12. A. Sarkar *et al.*, *Nat. Commun.* **9**, 3400 (2018).
13. J. L. Braun *et al.*, *Adv. Mater.* **30**, 1805004 (2018).
14. P. B. Meisenheimer, T. J. Kratofil, J. T. Heron, *Sci. Rep.* **7**, 13344 (2017).
15. J. J. Zhang *et al.*, *Chem. Mater.* **31**, 3705 (2019).

ACKNOWLEDGMENTS

We acknowledge support on this topic from Labex CHARM3AT, Université Paris-Saclay.

10.1126/science aaz1598

ENZYMOLOGY

The immune system mimics a pathogen

A host metabolite binds a bacterial enzyme and traps its B_{12} cofactor in an inactive state

By **Amie K. Boal**

Microbes evolve diverse chemical strategies to survive in restrictive environments. *Mycobacterium tuberculosis* (*Mtb*) infection is a notable example of microbial persistence in a harsh milieu. *Mtb* causes tuberculosis (TB), a disease that kills more than 1.3 million people annually (*1*). On page 589 of this issue (*2*), Ruetz *et al.* describe how the immune system fights back against *Mtb* by stealing a page from the bacterial chemical warfare playbook.

When attacked by macrophages—immune cells that kill bacteria by engulfing them in an acidic intracellular compartment—*Mtb* undergoes metabolic changes that allow it to subsist in severely nutrient-limited conditions (*3*). The creative strategies that *Mtb* uses to hide in this persistent state are still being discovered. For example, recent analysis of lipid profiles in patient-derived *Mtb* strains revealed that the pathogen coats itself with a lipid- and nucleotide-derived antacid molecule (*4*), which serves as chemical body armor for the macrophage-entrenched bacterium.

Mtb-infected immune cells respond by diverting a common aerobic metabolite, *cis*-aconitate, to large-scale production of the host immunomodulator itaconate (*5*). Although the antibacterial properties of itaconate have been known for more than 30 years, the recent discovery that it accumulates to millimolar concentrations in activated macrophages sparked renewed interest in its molecular mechanism. Itaconate can be appended to the key metabolic cofactor coenzyme A (CoA) to yield itaconyl-CoA (I-CoA). Itaconate and I-CoA resemble intermediates in bacterial pathways for lipid

Department of Chemistry and Department of Biochemistry and Molecular Biology, The Pennsylvania State University, PA 16802, USA. Email: akb20@psu.edu

GRAPHIC: A KITTERMAN/*SCIENCE*

Published by AAAS

and amino acid catabolism, and their ability to inhibit metabolic enzymes in other bacteria suggested a possible route to itaconate-mediated growth inhibition in pathogens (*5*). However, the precise target(s) of itaconate and modes of inhibition in *Mtb* were unknown.

Ruetz *et al.* now address both questions by showing that I-CoA strongly inhibits *Mtb* methylmalonyl-CoA mutase (MCM) by undergoing covalent attachment to the enzyme's vitamin B_{12}–derived cobalamin (Cbl) cofactor. MCM promotes the carbon-skeleton rearrangement that converts its namesake substrate to succinyl-CoA. The reaction transforms a compound produced by breakdown of amino acids and lipids into an intermediate that feeds directly into the tricarboxylic acid cycle (*6*). MCM uses adenosylcobalamin (AdoCbl) to generate a reactive 5′-deoxyadenosyl radical (5′-dA•) intermediate (see the figure). In the native transformation, the enzyme carefully controls the radical, using it catalytically to abstract hydrogen (H•) from a substrate methyl group. Formation of the radical enables rearrangement of the carbon skeleton, and H• is returned by the 5′-dAH to allow the AdoCbl cofactor to be regenerated. This intricate choreography depends, in part, on the enzyme's long access tunnel, which accommodates and recognizes the CoA appendage. Only when the substrate is bound does the enzyme promote 5′-dA• formation.

Ruetz *et al.* show that the immunometabolite I-CoA disguises itself in the active site of *Mtb* MCM and turns the enzyme's potent chemistry against itself, leading to an irrevocable attack on the AdoCbl cofactor. I-CoA and the native MCM substrate have nearly identical shapes. When I-CoA is bound to MCM, this similarity tricks the enzyme into forming its 5′-dA• intermediate. However, I-CoA directs its terminal olefin (rather than the sp^3-hybridized carbon that, in methylmalonyl-CoA, donates H•) toward 5-dA•. The authors demonstrated that this feature of the *Mtb* I-CoA complex with MCM results in radical addition to the cofactor, forming a new covalent C–C bond in the active site. This permanently traps the cofactor in an inactive state. The inhibition strategy, called mechanism-based suicide inactivation, is also the basis for some of our most potent pharmaceuticals, because it minimizes off-target effects and cells can recover the affected pathway only through new enzyme synthesis.

Most organisms that require vitamin B_{12} use dedicated pathways to repair their cobalamin enzyme cofactors, which are difficult to synthesize and acquire (*7*). Ruetz *et al.* examined whether I-CoA–inhibited MCM can be targeted by vitamin B_{12} repair machinery, which transfers the inactivated cofactor to a second protein for replacement of the deoxyadenosyl ligand and cofactor reactivation. The authors showed that I-CoA–bound MCM is recognized by B_{12} repair machinery, but the inhibited enzyme does not exchange its inactivated AdoCbl for a new cofactor. Failure to deliver new cofactors to MCM can cause the repair system to break apart AdoCbl waiting to be loaded onto enzymes (*8*), suggesting that itaconate could ultimately induce B_{12} deficiency in *Mtb* (*9*).

MCM is one of two vitamin B_{12} enzymes in humans, where it is used to prevent accumulation of toxic lipid and protein catabolites. Ruetz *et al.* show that human MCM is also susceptible to irreversible inactivation by itaconate, raising questions about how human cells protect themselves from the immunometabolite during *Mtb* infection. Recent work suggests that the human immune system takes additional inspiration from bacteria to shield its own B_{12} enzymes from itaconate attack. Microbes that synthesize and excrete toxic chemicals to kill neighboring cells typically produce their own internal resistance proteins. A 2017 study (*9*) identified a human itaconate breakdown pathway involving an orphan enzyme, citramalyl-CoA lyase (CLYBL), in detoxification of I-CoA before it can inhibit human B_{12} enzymes. Loss of CLYBL leads to B_{12} deficiency, which is now linked by the new study to I-CoA suicide inhibition of human MCM and inactivation of human cobalamin repair pathways. *Mtb* and other pathogens have analogous itaconate resistance pathways (*10*).

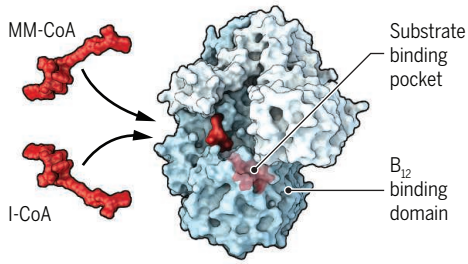
How *Mtb* acquires vitamin B_{12} during infection is unknown, but the pathogen might rely on host B_{12} for survival. Itaconate could affect TB disease progression through nutritional immunity, a phenomenon in which the immune system limits access to necessary transition metals for intracellular pathogens (*11*). Certain human populations have a high incidence (3 to 6%) of biallelic mutations in the *CLYBL* gene. In these individuals, loss of the human itaconate detoxification pathway and subsequent B_{12} deficiency in macrophages could further enhance the ability of the immune system to fight TB through cobalt cofactor deprivation (*9*).

Whereas Cbl enzymes are rare, radical chemistry is common in microbes. Radical S-adenosyl-methionine (SAM) enzymes use an iron-sulfur cluster and SAM instead of AdoCbl to generate 5′-dA• for aliphatic H• abstraction. Although they rely on a simpler cofactor, these more widespread bacterial proteins might be similarly vulnerable to mechanism-based 5′-dA• capture by host or microbe-derived small molecules. ■

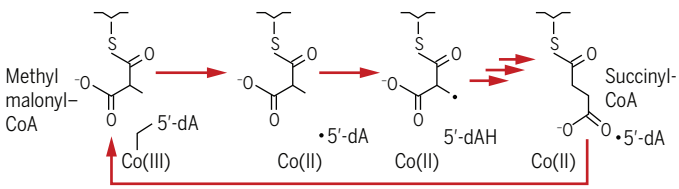
Itaconate blocks a bacterial B_{12} enzyme

Mycobacterium tuberculosis (*Mtb*) methylmalonyl–coenzyme A (MM-CoA) mutase uses a long tunnel to bind and orient its native substrate MM-CoA or the irreversible inactivator itaconyl-CoA (I-CoA) near a vitamin B_{12}–derived cofactor. MM-CoA and I-CoA each trigger formation of a 5′-deoxyadenosyl (5′-dA•) intermediate.

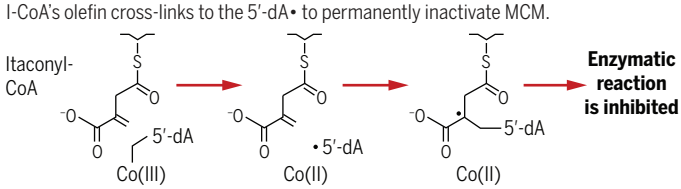
Structure of *Mtb* MM-CoA mutase
MM-CoA and I-CoA have similar shapes. The buried active site of MM-CoA mutase can accommodate either molecule to initiate a B_{12}-dependent radical reaction.



Catalytic MM-CoA reaction
5′-dA• is regenerated after substrate H-atom abstraction and rearrangement.



Inhibitory itaconyl-CoA reaction
I-CoA's olefin cross-links to the 5′-dA• to permanently inactivate MCM.



GRAPHIC: C. BICKEL/*SCIENCE*

REFERENCES AND NOTES

1. World Health Organization, Global Tuberculosis Report (2018).
2. M. Ruetz *et al.*, *Science* **366**, 589 (2019).
3. J. D. McKinney *et al.*, *Nature* **406**, 735 (2000).
4. J. Buter *et al.*, *Nat. Chem. Biol.* **15**, 889 (2019).
5. L. A. J. O'Neill, M. N. Artyomov, *Nat. Rev. Immunol.* **19**, 273 (2019).
6. R. Banerjee, *Chem. Rev.* **103**, 2083 (2003).
7. C. Gherasim, M. Lofgren, R. Banerjee, *J. Biol. Chem.* **288**, 13186 (2013).
8. G. C. Campanello *et al.*, *J. Am. Chem. Soc.* **140**, 13205 (2018).
9. H. Shen *et al.*, *Cell* **171**, 771 (2017).
10. H. Wang *et al.*, *Proc. Natl. Acad. Sci. U.S.A.* **116**, 15907 (2019).
11. E. M. Zygiel, E. M. Nolan, *Annu. Rev. Biochem.* **87**, 621 (2018).

10.1126/science.aaz4540

Published by AAAS

POLICY FORUM

AGING

To help aging populations, classify organismal senescence

Comprehensive disease classification and staging is required to address unmet needs of aging populations

By **Stuart R. G. Calimport, Barry L. Bentley, Claire E. Stewart, Graham Pawelec, Angelo Scuteri, Manlio Vinciguerra, Cathy Slack, Danica Chen, Lorna W. Harries, Gary Marchant, G. Alexander Fleming, Michael Conboy, Adam Antebi, Gary W. Small, Jesus Gil, Edward G. Lakatta, Arlan Richardson, Clifford Rosen, Karoly Nikolich, Tony Wyss-Coray, Lawrence Steinman, Thomas Montine, João Pedro de Magalhães, Judith Campisi, George Church**

Globally, citizens exist for sustained periods in states of aging-related disease and multimorbidity. Given the urgent and unmet clinical, health care, workforce, and economic needs of aging populations, we need interventions and programs that regenerate tissues and organs and prevent and reverse aging-related damage, disease, and frailty (*1*). In response to these challenges, the World Health Organization (WHO) has called for a comprehensive public-health response within an international legal framework based on human rights law (*1*). Yet for a clinical trial to be conducted, a disease to be diagnosed, intervention prescribed, and treatment administered; a corresponding disease classification code is needed, adopted nationally from the WHO International Classification of Diseases (ICD). Such classifications and staging are fundamental for health care governance among governments and intergovernmental bodies. We describe a systematic and comprehensive approach to the classification and staging of organismal senescence and aging-related diseases at the organ and tissue levels in order to guide policy and practice and enable appropriate interventions and clinical guidance, systems, resources, and infrastructure.

Through the ICD, the WHO oversees the international approval of disease classifications and staging that are subsequently adopted by governmental and regulatory bodies at the national level for use in epidemiological, clinical, and management contexts. Classification submission information is structured to describe the temporality, severity, and pathology of a disease, covering components such as etiology, manifestation, function, treatment, and diagnosis.

Organ and tissue senescence and age-related damage, disease, and frailty are currently classified and staged within the ICD, but in a nonsystematic and noncomprehensive manner, including by means of classification codes for skin aging, geriatric, time in life and senility, and the old age code, in addition to aging-related diseases such as cancers, cardiovascular diseases, and dementias. Within this system, a patient may have a disease classified in one organ that exists unclassified in another organ, with the possibility of nonrecorded drug effects in distal organs. Because of the lack of classifications and staging, developing pathology may not be registered or treated. Drugs that prevent or reverse this pathology may be left sitting on the shelf.

Current practices include incomplete and imprecise approaches and categorization of patients as "at risk of disease" and through predisease and advanced pathology classifications. Our aim is to augment and, where appropriate, replace these approaches. To not classify diseases and stages comprehensively is arbitrary, which may give legal justification for action. Governments and the WHO may have a duty to ensure that the classification systems are systematic and comprehensive.

SYSTEMATIC AND COMPREHENSIVE

In our view, the systematic and comprehensive classification and staging of organismal senescence and aging-related diseases at the system, organ, tissue, and metabolic level is readily achievable through synthesis of the existing knowledge base (*2*–*10*). Tissue and organ senescence are defined similarly to organismal senescence at the tissue and organ level and involve pathologic and pathogenic hallmarks of organismal and cellular senescence, including reduced organ function, cell loss, stem cell dysfunction and niche decline, telomere shortening, senescence-associated secretory phenotype–related pathology, inflammation, nuclear and mitochondrial mutation burden, matrix composition dysregulation, protein aggregation, reduced genomic stability, epigenetic dysregulation, extracellular cross-links, steatosis, and polyploidization (*2*–*10*).

Organismal senescence at the tissue and organ level, which may involve replicative cellular senescence, has pathologic and pathogenic characteristics (*2*–*10*). Although replicative cellular senescence may have a protective effect in relation to oncogenesis, we submit that replicative cellular senescence may be pathogenic (*2*–*4*, *8*, *9*), which may be targeted, in specific tissues, and removed in relation to pathologic and pathogenic disease states of tissue and organ senescence, treatment of comorbid conditions, and any preventative and regenerative approaches. Circulating DNA can be traced to tissue of origin (*11*), which may enable organ- and tissue-specific biomarkers for aging-related diseases and syndromes by severity stage. Senescent cell burden and senescence-associated secretory factors have also been assessed from plasma protein (*9*), in addition to studies in humans, with the removal of senescence cells demonstrating an alleviation of physical dysfunction (*10*). Comparative biology demonstrates that cellular and organismal senescence vary across cell types and species, with some cell types being biologically immortal and some organisms being negligibly senescent, retaining their regenerative capabilities and being cancer resistant (*12*, *13*).

Potential benefits of such a staging and classification system include improvements in (i) understanding of tissue and organ biology and pathology—including accelerated organ and tissue senescence from progeroid disorders, metabolic diseases, and exogenous causes such as chemotherapy and radiotherapy—through the meeting of clinical diagnostic criteria development requirements and enhancement of diagnostic criteria, and with clinical studies; (ii) drug development and repurposing through more accurately described diseases and stages, including increased accuracy and comprehensiveness of indications, staging, and the increased availability and comprehensiveness of functional end points; (iii) drug development through regulatory pathway development; (iv) preclinical trial models corresponding to the proposed classifications and staging; (v) clinical trials with patient stratification and selection related to indications, multi-indications, multistaged indications, combination drug

The list of author affiliations is available in the supplementary materials.
Email: stuart.calimport07@alumni.imperial.ac.uk

Published by AAAS

regimens, multimodal therapies, enhanced end points, and differential responses; (vi) personalized medicine strategies; (vii) early diagnosis and early prevention, rehabilitation, and regeneration; (viii) diagnoses in general; (ix) medical records and digital twins; (x) intervention capability in complex late-stage indications and multimorbidities; (xi) mitigation of age-related risk factors in prescribing and surgery; (xii) preventative, regenerative, and rehabilitative approaches and treatment planning; (xiii) patient outcomes; and (xiv) public health statistics, policy, and resourcing.



ILLUSTRATION: ZOE VAN DIJK

PROPOSED SYSTEMS

We propose that organ and tissue senescence and related disease classification and staging systems be instantiated as WHO ICD disease codes with appropriate corresponding general extension codes because they relate to senescing, atrophic, pathologically remodeled, calcified, and otherwise metabolically dysfunctional tissue. This should include subclassifications for each tissue and disease subtype and associated extension codes for staging and severity from effectively zero tissue senescence, atrophy, pathologic remodeling, calcification, and metabolic dysfunction. Codes should be classified under etiology and pathology, with tissue and cellular subclassifications to account for differences in rates of aging at the tissue, organ, and organism level; the existence of aging damage during development and across life; and for the development of a chronologic-age–agnostic organ and tissue pathology framework with associated phenotypes and biomarkers. A comprehensive set of classifications—ICD–Aging-related (ICD-A), or otherwise ICD-Senescent (ICD-S)—should be used for senescing, atrophic, remodeled, calcified, and metabolically dysfunctional tissue for each organ and gland.

Similar to codes relating to cancer classifications, we propose "Senescent," "Senescent Secretory," "Atrophic," "Calcified," and "Uncertain whether Senescent or Effectively Zero Senescence." We envisage that organ-by-organ, tissue-by-tissue, senescing, atrophic, pathologic remodeling, calcification, and metabolic dysfunction codes, with cell-specific subclassifications comparable with ICD-O (oncology) classifications, would work in concert with existing age-related disease codes such as dementias, cancers, and cardiovascular disease and other systemic, metabolic, and infectious disease codes to provide a comprehensive and systematic disease classification framework. Hyperactive and hyperproliferative tissues should be appropriately coded within such a framework. Any such classifications relating to aging tissue that have been developed on an ad hoc basis, such as skin aging, should be formatted and combined with the proposed comprehensive and systematic classification and staging and structure outlined here, including classification of the "aging-related" extension code as an etiology and causality code (*14*) (WHO ICD classification submissions by S.R.G.C. and B.L.B. are provided in the supplementary materials).

A 0-V staging system for senescing tissue and a 0-X severity scale for atrophy, remodeling, calcification, and aging-related metabolic dysfunction classifications are appropriate, with "0" indicating effectively zero tissue senescence and zero pathologic atrophy, remodeling, calcification, or metabolic dysfunction. A staging system for senescent tissue comparable with the TNM Classification of Malignant Tumors (TNM) may be useful for the inflammatory and pathologic secretory phenotype of senescing tissue. We propose that a Senescing, Secretory, and pathologic Atrophy, Remodeling, and Calcification (SSeARC) Classification of Senescing Tissue system be developed.

The rationale for proposing a staging severity scale and a pathogenic stage system for organ and tissue senescence has its basis in oncology classifications, in which cells that escape the pathologic phenotype of cellular senescence become cancerous with progressive and distal tissue effects. These cells have both the TNM and the Stage 0 to IV systems.

Specific markers are envisaged to differ per tissue, organ, and location within the body and by the corresponding staging and severity scales. The staging system would classify senescing tissue from effectively zero presence of organ and tissue senescence pathology and any appearance, features, and diagnostic criteria. Stage I may include cells nearing senescence with minimal pathological effect; stage II may include senescent cell presence with minimal pathological effect; stage III may include senescent cell presence and extracellular cross-linking with emerging pathological effect; stage IV may include senescent cell and extracellular cross-linking with onset of age-related disease; and stage V may include hallmarks of organ, tissue, and replicative senescence able to cause fatality.

Characterization of atrophic tissue pathology and pathologic remodeling and the related staging thresholds may include histopathologic and functional studies in combination with population-based epidemiologic and personalized medicine metrics, with tissue- and organ-specific disease classifications, including relevant structural, functional, and clinical criteria.

We envisage aging-related atrophic, pathologic remodeling, calcification, systemic, and metabolic dysfunction disease classifications to be classified and staged in a similar manner. Diagnostic criteria may involve a range of noninvasive and minimally invasive tests and

Published by AAAS

include functional imaging; fluid-, needle-, or tissue-based biopsy tests; biomarker; and biomarker panels with histopathology and tissue -omics as required (*7*, *9*, *10*, *15*).

Classification pathology, appearance, features, and diagnostic criteria would include similarities between organs and tissues relating to fundamental processes of tissue senescence and commonalities in organ and tissue damage and organ- and tissue-specific criteria. Clinical biomarkers should be developed to classify tissue senescence to the quality of classification and staging appropriate for clinical practice.

To illustrate the proposed classification and staging system, a 55-year-old Caucasian male patient at a general medical checkup may present a range of multimorbidities, including stage III aging-related muscle atrophy and stage II muscle senescence; stage IV vascular senescence with risk of rupture, thresholded with arterial stiffness measured from pulse wave velocity; and atherosclerosis type III, diagnosed with magnetic resonance imaging and blood test. The clinical response includes the following: treatment recommendations with one or more senolytic interventions that act on vascular or muscle senescence and the atherosclerotic plaque, which takes into account organ-specific disease staging differentials, and an exercise regimen aimed at reversal of aging-related muscle atrophy and atherosclerosis while also preventing senescence stage progression.

Sarcopenia should be included in a systematic and comprehensive manner alongside the senescence, atrophy, remodeling, and calcification of each and every tissue, gland, and organ. We submit that tissue atrophy and remodeling has pathological effects, such as can be seen in the pineal gland, heart muscle atrophy, and thymic involution and remodeling. We propose that a systematic and comprehensive framework cover all tissues, organs, and glands across all functional scales, including the heart and vasculature, neural lobes and architecture, glia, the pineal gland, and the blood-brain barrier. Senescence, atrophy, remodeling, and calcification should be looked to in relation to glands, lymph nodes, and bone marrow in addition to any corresponding blood cell populations relating to immunosenescence and tissues that function as barriers or are associated with filtration and microbial burden.

Metabolic diseases should be appropriately classified toward trials and treatment, including diseases that accelerate organ and tissue senescence, and for patients with both senescent tissues and organs and co-morbid metabolic and infectious diseases that affect multiple tissues and organs in combination. "At Risk of Age-Related Disease" should be considered in relation to each and all aging-related indications in relation to items here and otherwise to enhance approaches to the treatment of those at risk of disease and with predisease conditions.

An overall scoring system should be developed for each organ and for patients that combines organ and tissue senescence, pathologic remodeling, metabolic damage, atrophy, and aging-related disease classifications and stages for aggregate scoring of organ damage and integrity and patient status.

There are challenges to be surmounted for the comprehensive characterization of disease, including subtypes, stages, molecular mechanisms, and biomarkers. However, diseases such as tumors were classified as neoplasms and staged as benign or malignant before any genetic characterization. Skin aging is already classified in the ICD and staged in the absence of a complete mechanistic understanding and molecular characterization of organ and tissue senescence. Limitations before a comprehensive molecular characterization of a disease may be present in relation to (i) the molecular metabolic disease classifications, (ii) disease severity staging solely on the basis of molecular mechanisms and biomarkers, and (iii) molecular biomarker development in relation to WHO ICD classifications and diagnostic criteria.

IMPLEMENTATION

The United Nations and WHO should support classification and staging efforts as part of the WHO policy focus on Healthy Aging and Life Course. The WHO, the International Agency for Research on Cancer (IARC), and relevant other groups should develop such classifications and staging systems, including the underlying pathology, appearance, features, and diagnostic criteria toward improving health globally in relation to organismal senescence. Given the global importance of an aging society, governments and intergovernmental bodies should engage in the development of, and support for, appropriate classifications and staging with aligned health care policy and resourcing. Governments should consider bringing such a motion before the World Health Assembly for ratification to replicate the successes of ICD-O and the IARC for organ and tissue senescence. We submit that a WHO body commensurate to the IARC should be established for aging and for the development of aging classifications and staging, or otherwise the IARC remit be expanded to include organ and tissue senescence and related diseases in addition to cancer. Policy and resourcing requirements for organ and tissue senescence and aging-related organ and tissue damage and frailty involve similar considerations as those of oncology classifications and staging.

As a counterpart to WHO ICD classifications and staging systems, corresponding preclinical models should be developed, including the development of organism-, organ-, and tissue-specific counterparts to the WHO ICD classifications and stages for disease pathology characterization and drug development, with aligned government resourcing and policy. Comprehensive and systematic classification and staging of organ and tissue senescence, pathologic remodeling, atrophy, calcification, and aging-related metabolic disease is an urgent and unmet need.

The classification and staging frameworks proposed are intended to be used independently or in combination with existing classification codes in a complementary manner, across disease diagnosis, prevention, management, and reversal. The proposed approach will complement existing codes for diseases and syndromes already recognized to improve patient outcomes and will add value to overall patient care by addressing gaps in international health care governance.

We invite governments and the World Health Organization to act on the items discussed here and welcome members of the scientific, medical, and patient advocacy communities to contribute to this effort, including through feedback, consensus development, and the development and use of the proposed classification, staging, and disease criteria frameworks. ■

REFERENCES AND NOTES

1. WHO, *World Report on Ageing and Health* (WHO, 2015); https://who.int/iris/handle/10665/186463.
2. A. Hernandez-Segura, J. Nehme, M. Demaria, *Trends Cell Biol.* **28(6)**, 436 (2018).
3. J. P. Coppé *et al.*, *PLOS Biol.* **6**, e301 (2008).
4. J. L. Kirkland, *Pub. Pol. Aging Rep.* **23**, 12 (2013).
5. C. López-Otín, M. A. Blasco, L. Partridge, M. Serrano, G. Kroemer, *Cell* **153**, 1194 (2013).
6. A. J. Freemont, J. A. Hoyland, *J. Pathol.* **211**, 252 (2007).
7. A. Bürkle *et al.*, *Mech. Ageing Dev.* **151**, 2 (2015).
8. D. Muñoz-Espín, M. Serrano, *Nat. Rev. Mol. Cell Biol.* **15**, 482 (2014).
9. T. Tanaka *et al.*, *Aging Cell.* **17, 5** e12799 (2018).
10. J. N. Justice *et al.*, *EBioMedicine* **40**, 554 (2019).
11. M. W. Snyder, M. Kircher, A. J. Hill, R. M. Daza, J. Shendure, *Cell* **164**, 57 (2016).
12. S. Piraino, F. Boero, B. Aeschbach, V. Schmid, *Biol. Bull.* **190**, 302 (1996).
13. R. J. Buffenstein, *Comp. Physiol. B* **178**, 439 (2008).
14. S. R. G. Calimport, B. L. Bentley, *Rejuv. Res.* **22**, 281 (2019).
15. Unity Biotechnology, "An exploratory clinical study to investigate biomarkers of senescence in patients with osteoarthritis of the knee," identification no. NCT03100799 (2017); https://clinicaltrials.gov/ct2/show/NCT03100799.

ACKNOWLEDGMENTS

Acknowledgments and disclosures are provided in the supplementary materials.

SUPPLEMENTARY MATERIALS

science.sciencemag.org/content/366/6465/576/suppl/DC1

10.1126/science.aay7319

Published by AAAS



BOOKS *et al.*

The idea that parenting and masculinity are opposing forces is reinforced by some notions of testosterone.

PHOTO: 10'000 HOURS/GETTY IMAGES

ENDOCRINOLOGY

Masculinity molecule, debunked

Challenging stereotypes, two scholars unpack the social and cultural contexts of testosterone

By **Erika Lorraine Milam**

Sexual desire, intelligence, strength, power, and speed. Popular culture would have us believe that these traits and more are enhanced by testosterone. For Rebecca Jordan-Young and Katrina Karkazis, such claims have transformed masculinity into the property of young, white, successful men and made this seem the natural result of a small steroidal hormone.

Jordan-Young and Karkazis style their book as a daring push from outside the world of testosterone science, challenging long-held assumptions about the hormone. Although they have only recently turned their keen analytical gaze to testosterone, both authors have previously engaged with scientific debates that blend social and biological causation, from the neurobiological basis of sex differences to intersexuality. At the heart of their book is a hope of replacing readers' beliefs that testosterone is merely biological with a nuanced understanding of how both social interactions and internal physiology affect levels of testosterone and its effects.



Testosterone: An Unauthorized Biography
Rebecca M. Jordan-Young and Katrina Karkazis
Harvard University Press, 2019. 288 pp.

Each of the book's chapters disposes of zombie facts and "undead ideas" about testosterone that have lingered in popular culture despite repeated attempts to vanquish them. The authors label their exploration of testosterone's influence "unauthorized," which allows them to explore those narrative threads they find the most interesting—the confounding intellectual spaces rather than the tidy ones.

Testosterone is not just a male hormone. It appears to play a crucial role in ovulation and also emerged as a dramatic actor in Amy Cuddy's contested research on "power poses." Cuddy's initial publications [summarized in (*1*)] and a TED talk that has been viewed more than 54 million times suggested that the key to female success in business could lie in harnessing the power of testosterone. By physically enacting a series of "power poses"—picture Wonder Woman, arms akimbo, legs apart, standing tall—Cuddy argued that women could raise their testosterone levels and become more effective in their public negotiations. That women felt more confident after these rituals turned out to be consistent with later attempts to replicate her research, but the changing testosterone levels were not.

What the authors find fascinating about this debate has little to do with the replication crisis in biomedical sciences. Instead, they ask why readers and viewers found Cuddy's claims to be so powerful. They posit that her research promised a personal mechanism for overcoming structural inequality in social hierarchies of power. In short, people hoped to be able to mobilize testosterone like a personalized precision drug. Reality proved more complicated. As Jordan-Young and Karkazis make clear, the entanglements of biology and culture matter.

These mutual entanglements are at the core of their analysis throughout the book. Risk-taking behavior, for example, has been associated with elevated testosterone in stock brokers, and Jordan-Young and Karkazis query what these results mean when some men, such as coal miners, often take risks out of financial necessity and restricted job opportunities. Risk-taking, they note, is rather less risky for those with high social status.

Research also indicates that testosterone levels in men drop when they become parents. This might mean that men have evolved a physiological adaptation that shifts their behavior from mate seeking to involved parenting, but Jordan-Young and Karkazis point out that even this claim reinforces stereotypes that fatherhood and other masculine traits function as trade-offs. For athletes, testosterone may help build muscle mass but only in combination with rigorous workouts; the hormone alone has almost no effect.

In broad prospect, Jordan-Young and Karkazis warn against investing too much in debates over the details of testosterone's role in determining gender, risk-taking, parenting behavior, and fairness in athletics. They demonstrate in each case that concentrating on testosterone as a molecule draws our attention away from important social and economic sources of systemic inequality. "T talk," as they define it, therefore serves to maintain the status quo as natural. All claims about testosterone, they argue, are power moves in a competitive intellectual landscape.

This is equally true of their book. One way of reading *Testosterone* is as an act of debunking; here, the authors see their goal as seeking "less false" science rather than supplying the last word. They also provide a vision for better understanding socially and biologically entwined entities: Scientists and science studies scholars should work together, from the beginning. In their hands, testosterone provides fruitful ground for understanding what it means to be human, not as isolated physical bodies but as dynamic social beings. ■

The reviewer is at the Department of History, Princeton University, Princeton, NJ 08544, USA. Email: emilam@princeton.edu

REFERENCES AND NOTES

1. A. Cuddy, *Presence: Bringing Your Boldest Self to Your Biggest Challenges* (Little, Brown, 2015).

10.1126/science.aaz1788

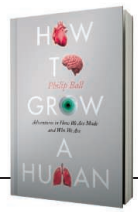
Published by AAAS

CELL BIOLOGY

What does it mean to be alive?

A winding romp through advances in cell biology pushes readers to ponder the boundaries of life

How to Grow a Human: Adventures in How We Are Made and Who We Are
Philip Ball
University of Chicago Press, 2019. 384 pp.



By **Michael A. Fisher**

A small bundle of human nerve cells are being cultured in a petri dish. The cells divide. They differentiate into cell types found in the brain. The cell network grows dense and develops brain-like structures—layers and folds. The cells begin to signal. The brain cell cluster has been derived from skin cells harvested from science writer Philip Ball's shoulder.

The scientists who created Ball's skin-turned-brain organoid study brain development and want to understand the basis of neurodegeneration. But what exactly goes on inside these cell aggregates, and could we reach a point at which they are more "brain" than "brain-like"?

Biologists can also build embryo-like structures (embryoids) from human stem cells, which can be used to study early prenatal development. However, synthetic embryos can develop certain features—such as the primitive streak, a structure that establishes bilateral symmetry in an organism—that mark, for some, the transition from embryo to individual human being.



All living things come from an egg, argued William Harvey (incorrectly) in 1651.

Ball's experience grappling with how to think about these living structures, as documented in his new book, *How to Grow a Human*, is part of a larger question with which humanity has wrestled for centuries: What is life, and how might our understanding of it change with our ever-increasing capability to manipulate it?

The book offers a provocative, meandering take on the progression of groundbreaking biotechnological capabilities. For example, in chapter 3, Ball explores the dawn of tissue culture at the turn of the 20th century and the motivations of the scientists who conducted the research. Ross Harrison sought to settle a debate between Camillo Golgi and Santiago Ramón y Cajal over the makeup of nervous systems; the former argued that nervous systems were one uninterrupted structure, whereas the latter believed there to be distinct nerve cells. Along the way to showing that nerve fibers lengthen through nerve cell proliferation, confirming Ramón y Cajal's hypothesis, Harrison was the first to develop a technique to keep tissues alive with active cell growth in vitro, sustaining amphibian embryonic tissue in jars.

Alexis Carrel, on the other hand, was a white supremacist striving to preserve "a 'superior stock' of humankind." Carrel and his team iterated on and applied Harrison's method to many different tissues, including those of birds, embryonic chickens, and, of course, humans. Here, Ball also works in how science fiction writing was influenced by early advances in cell biology, describing Julian Huxley's "The Tissue-Culture King," which centers on a biologist who redesigns members of a remote tribe and builds living objects of worship from the flesh of the tribe's king. Although interesting, asides such as this disrupt the narrative's continuity.

Ball's writing is most absorbing when he reflects on boundary-pushing research, such as advances toward converting human skin cells to eggs or sperm or the promise of approaches for fabricating human organs to help people who need transplants. In chapter 5, for example, he describes experiments in which rat cells formed pancreases in mice, and others in which human cells survived in pig and cattle embryos, and then considers how governments and the public might approach the prospect of harvesting human organs grown in other animals.

Discussing how and where we have drawn ethical and legal lines for procedures such as in vitro fertilization and preimplantation genetic diagnosis (PGD) of embryos, Ball contemplates what historical precedent may mean for the governance of emerging biotechnological capabilities. Unlike in the United Kingdom, where PGD is permitted only to avoid implanting an embryo with a serious heritable disease, the United States does not regulate PGD-enabled embryo selection at the federal level, meaning PGD can be used to select for offspring of a particular gender or to rule out embryos that have an elevated risk of intellectual disability. (As Ball points out, it may be possible to adapt this testing to screen for embryos that are predicted to have exceptional cognitive ability.)

At the center of an adjacent debate are germline genome-editing technologies. As exemplified by the so-called "CRISPR-baby" controversy and expounded upon by Ball, access to, and affordability of, new biotechnologies may serve some segments of society while underserving others. Ball appeals to the democratic process to determine the balance between personal liberty and state-dictated equity, acknowledging that everyone has a stake in and therefore the right to be heard on this important issue.

Because of the immense power of emerging biotechnologies, those of us who are intimately involved with these advances must make a concerted effort to equip both policy-makers and the public with the knowledge and tools needed to navigate this evolving landscape. Ambitious and expansive, *How to Grow a Human* could be one piece of this effort—Ball's look at the state of human-facing cutting-edge bioscience is a thought-provoking read. ■

10.1126/science.aay3861

The reviewer co-leads the Congressional Science Policy Initiative at the Federation of American Scientists, Washington, DC 20036, USA. Email: mfisher@fas.org

ILLUSTRATION: W. HARVEY/WELLCOME COLLECTION/CC BY

Published by AAAS



LETTERS

Astronaut Buzz Aldrin walks on the surface of the Moon in 1969.

PHOTO: NASA

Edited by **Jennifer Sills**

Moon missions spark the human imagination

J. Berg's Editorial "A child of Apollo" (19 July, p. 203) is spot on. Fifty years ago, my older brother and I watched the Apollo 11 mission from India, sharing a worldwide sense of pride. The legacy of Apollo continues, with technological and medical benefits (*1*). It has inspired a new generation to think big and take great risks. Fifty years later, I watched Chandrayaan-2, India's lunar exploration mission, from the United States, connected to my brother by the internet though thousands of miles apart. The latest Moon mission provides a cause for celebration.

The public's exposure to advances in science, medicine, and engineering continues on many fronts. Fifty years ago, it was a luxury for a country to perform space exploration; now a private Moon lander is the buzz (*2*). A society may survive on its earthly activities, but it thrives on the human imagination that has given us rockets, satellites, and a continued search for knowledge. The Chandrayaan-2 mission drives a change in India that was initiated by the Apollo mission so many years ago.

Space exploration spurs global creativity, including China's successful Chang'E-4 landing on the far side of Moon (*3*) and the bold attempt of the Israeli spacecraft Beresheet (*4*). Science can transcend time and distance to unite people and nurture their imaginations. If agencies like the Indian Space Research Organisation and the National Aeronautics and Space Administration worked together, along with China and private companies, another Moon journey would be possible. This is the time for the next generation to pursue their dreams.

Debomoy K. Lahiri
Department of Psychiatry and Department of Medical and Molecular Genetics, Stark Neuroscience Research Institute, Indiana University School of Medicine, Indianapolis, IN 46202, USA. Email: dlahiri@iupui.edu

REFERENCES AND NOTES

1. K. Fong, *Lancet* **394**, 205 (2019).
2. E. Gibney, *Nature* **566**, 434 (2019).
3. C. Li *et al.*, *Nature* **569**, 378 (2019).
4. E. Gibney, *Nature* **568**, 286 (2019).

10.1126/science.aaz6067

Radiation is not a political tool

With the recent tensions between Japan, Korea, and surrounding countries, Korea has begun to raise questions about the safety of radiation doses in foods and at Olympic venues in Fukushima (*1*). However, these allegations are not based on scientific evidence; the international scientific community has already resolved that radiation doses from the Fukushima nuclear accident in 2011 are limited (*2*, *3*). The current doses in Fukushima residents from external exposures are comparable to or lower than exposures in other countries (*4*), and additional doses from internal exposures are also negligible (<0.01 mSv/y) (*5*). This concern about radiation exposure is not a problem of radiation safety but a matter of the trust and social norms that govern radiation risk perception and generate radiation anxiety (*6*, *7*).

Public trust has still not fully recovered, even in Japan (*8*), where about 50% of the population still perceives a likelihood that the health of the next generation has been adversely affected (*9*), despite the current scientific consensus (*2*, *3*). Radiation anxiety is a root cause of social division and can create stigma, discrimination, and conflicts in society (*10*). This type of social division can also be accelerated in conjunction with emotion-based information spread by social media (*11*).

Radiation issues must not be used as a political tool. Politicizing radiation issues divides the public into factions and unnecessarily increases the public perception of radiation risks among individuals and the public, ultimately worsening social misery. Sharing scientific findings and engaging in calm discussions will reassure people in relevant countries and across the globe.

Michio Murakami[1]*, Atsushi Kumagai[1], Aleksandr N. Stojarov[2], Masaharu Tsubokura[1,3]
[1]Fukushima Medical University School of Medicine, Fukushima, Fukushima, 960–1295, Japan. [2]Belarussian State Medical University, Minsk, 220116, Belarus. [3]Minamisoma Municipal General Hospital, Minamisoma, Fukushima, 975-0033, Japan.
*Corresponding author. Email: michio@fmu.ac.jp

REFERENCES AND NOTES

1. S. Denyer, "Radioactive sushi: Japan-South Korea spat extends to Olympic cuisine," *The Washington Post* (2019); www.washingtonpost.com/world/asia_pacific/radioactive-sushi-japan-south-korea-spat-extends-to-olympic-cuisine/2019/08/23/3b4882d0-c483-11e9-8bf7-cde2d9e09055_story.html.
2. United Nations Scientific Committee on the Effects of Atomic Radiation, "Developments since the 2013 UNSCEAR report on the levels and effects of radiation exposure due to the nuclear accident following The Great East-Japan Earthquake and Tsunami: A 2017 white paper to guide the scientific committee's future programme of work" (New York, 2017).
3. International Atomic Energy Agency, "The Fukushima Daiichi accident" (Vienna, 2015).
4. N. Adachi *et al.*, *J. Radiol. Prot.* **36**, 49 (2016).
5. K. Iwaoka, *Health Phys.* **111**, 471 (2016).
6. R. Morioka, *Soc. Sci. Med.* **107**, 105 (2014).
7. M. Murakami, J. Nakatani, T. Oki, *PLOS One* **11**, e0165594 (2016).
8. S. Denyer, "Eight years after Fukushima's meltdown, the land is recovering, but public trust is not," *The Washington Post* (2019); www.washingtonpost.com/world/asia_pacific/eight-years-after-fukushimas-meltdown-the-land-is-recovering-but-public-trust-has-not/2019/02/19/0bb29756-255d-11e9-b5b4-1d18dfb7b084_story.html.

Published by AAAS

9. K. Shirai, N. Yoshizawa, Y. Takebayashi, M. Murakami, *PLOS One* **14**, e0221561 (2019).
10. T. Sawano, Y. Nishikawa, A. Ozaki, C. Leppold, M. Tsubokura, *J. Rad. Res.* **59**, 381 (2018).
11. M. Tsubokura *et al.*, *PLOS One* **13**, e0203594 (2018).

10.1126/science.aaz3408

Salmon in clear and present danger

During the summer of 2019, record heat events caused thousands of adult Pacific salmon to die of heat stress while migrating to their spawning grounds throughout Alaska (*1*). These die-offs come as many rivers in western North America have started transitioning to a regime of lower summer flows and higher temperatures during the salmon migration and spawning season (*2*). This transition, driven by warmer air temperatures and reduced snow and ice, will increase in severity and pervasiveness during the next few decades (*3*). Marine heat waves are also increasing in frequency (*4*), causing poor marine survival of many salmon populations (*5*). The threat of climate change is here and demands action now.

Curtailing the rise of global air temperatures by reducing carbon emissions is vital for salmon conservation. Aside from emission reductions, we urge federal governments to prioritize climate change resilience in fisheries and environmental policy. This means protecting evolutionarily unique populations of salmon as well as diverse landscapes that naturally vary in hydrology (*6*, *7*). It also means that the remaining hotspots of salmon productivity must be safeguarded against degradation.



Record heat has caused salmon to die from heat stress, putting populations at risk.

PHOTO: RALPH LEE HOPKINS/GETTY IMAGES

One such region is the watersheds of Bristol Bay, Alaska, where the controversial Pebble Mine has been proposed (*8*). Bristol Bay supports the most abundant sockeye salmon populations in the world, with a wild salmon fishery that provides 12,000 jobs and generates $1.5 billion annually (*9*) while providing food security for rural Alaskans. However, the U.S. Environmental Protection Agency recently overturned its previous conclusion that the mine would cause irreparable harm to this ecosystem (*10*); barring congressional intervention, the final permitting decision is expected from the U.S. Army Corps of Engineers in early 2020.

Habitat destruction has driven the collapse of wild salmon fisheries from California to Washington, where 93% of wild salmon abundance has been lost (*11*). Intact habitat confers resilience to environmental change; the Pebble Mine would erode resilience when it is needed most. The warming caused by global carbon emissions will continue to kill salmon (*12*) and will kill the jobs and food security that salmon provide if our governments do not give them a fighting chance.

Nicolas J. Muñoz[1]*, John D. Reynolds[1], Jonathan W. Moore[1], Bryan D. Neff[2]
[1]Earth to Ocean Research Group, Simon Fraser University, Burnaby, BC, Canada. [2]Department of Biology, Western University, London, ON, Canada.
*Corresponding author.
Email: nmunoz445@gmail.com

REFERENCES AND NOTES

1. M. C. Martin, "Warm waters across Alaska cause salmon die-offs" *Juneau Empire* (2019); www.juneauempire.com/news/warm-waters-across-alaska-cause-salmon-die-offs/.
2. P. W. Mote, A. F. Hamlet, M. P. Clark, D. P. Lettenmaier, *Bull. Amer. Meteor. Soc.* **86**, 39 (2005).
3. S. U. Islam, S. J. Déry, A. T. Werner, *J. Hydrometeorol.* **18**, 473 (2017).
4. T. L. Frölicher, C. Laufkötter, *Nat. Commun.* **9**, 650 (2018).
5. S. T. Lindley *et al.*, "What caused the Sacramento River fall Chinook stock collapse?" (Tech. Memo NMFS-SWFSC-447, National Oceanic and Atmospheric Administration, 2009).
6. K. I. Ashley, in *Salmon 2100: The Future of Wild Pacific Salmon*, R. T. Lackey, D. H. Lach, S. L. Duncan, Eds. (AFS, 2006), chap. 4.
7. D. E. Schindler *et al.*, *Fisheries* **33**, 502 (2008).
8. U.S. Army Corps of Engineers (USACE), "Pebble Project EIS" (USACE, 2019); www.pebbleprojecteis.com/.
9. G. Knapp, M. Guettabi, S. Goldsmith, "The economic importance of the Bristol Bay salmon industry" (Institute of Social and Economic Research, 2013; https://iseralaska.org/publications/?id=1410).
10. S. Bronstein, C. Devine, D. Griffin, A. Hackett, "EPA dropped salmon protection after Trump met with Alaska governor" *CNN* (2019); www.cnn.com/2019/08/09/us/epa-alaska-pebble-mine-salmon-invs/index.html.
11. T. Gresh, J. Lichatowish, P. Schoonmaker, *Fisheries* **25**, 15 (2000).
12. N. J. Muñoz, A. P. Farrell, J. W. Heath, B. D. Neff, *Nat. Clim. Change* **5**, 163 (2015).

10.1126/science.aaz3914

Published by AAAS

RESEARCH

IN *SCIENCE* JOURNALS

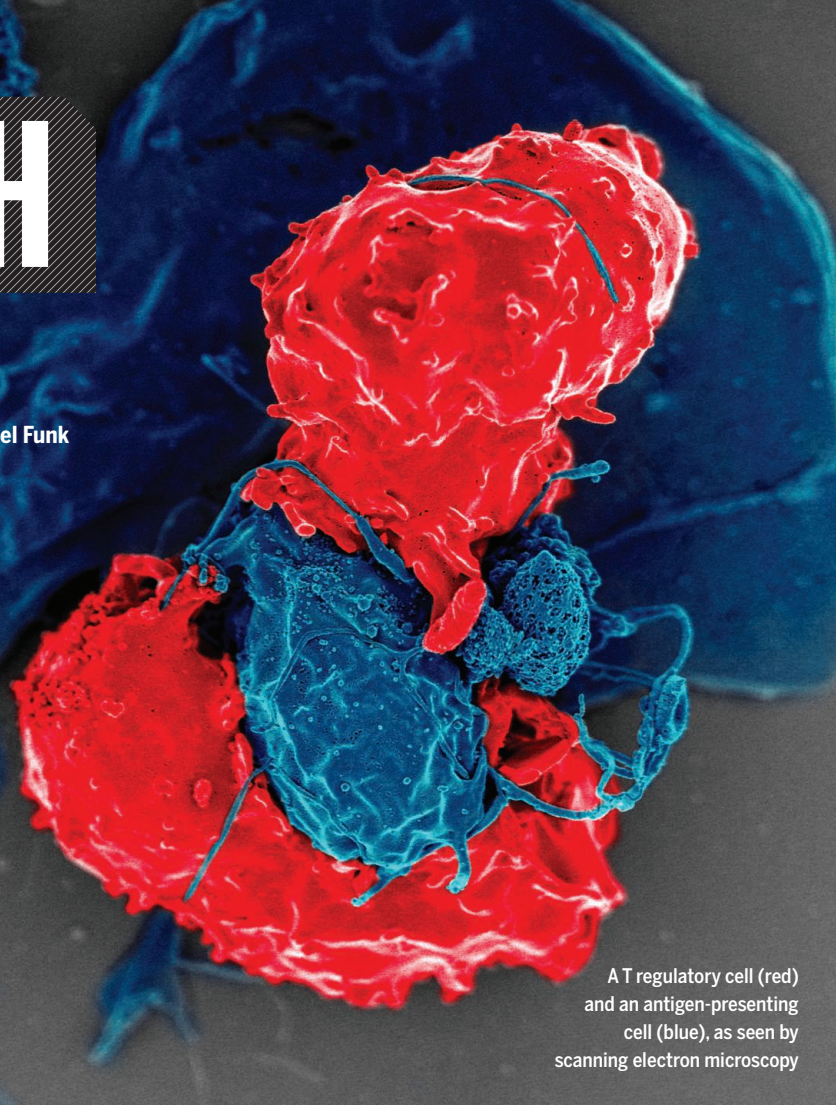
Edited by **Michael Funk**

IMMUNE REGULATION

Pharmacological retraining for T cells

Regulatory T cells (T_{regs}) expressing the Foxp3 transcription factor play a critical role in dampening overactive immune responses, including autoimmune diseases. Akamatsu *et al.* screened a library of small molecules and identified a compound that promotes T_{reg} differentiation by inhibiting the cyclin-dependent kinases CDK8 and CDK19. The T_{reg}-promoting activity of the CDK8/19 inhibitor reduced disease activity in mouse models of autoimmune diabetes and encephalomyelitis. CDK8/19 inhibitors are thus a new class of immunomodulatory drugs capable of generating T_{regs} with potential clinical applications in promoting tolerance and reducing autoimmunity. —IRW

Sci. Immunol. **4**, eaaw2707 (2019).



A T regulatory cell (red) and an antigen-presenting cell (blue), as seen by scanning electron microscopy

PHOTO: SCIENCE SOURCE

VIRAL IMMUNOLOGY

The toll of measles on the immune system

Many of the deaths attributable to measles virus are caused by secondary infections because the virus infects and functionally impairs immune cells. Whether measles infection causes long-term damage to immune memory has been unclear. This question has become increasingly important given the resurgence in measles epidemics worldwide. Using a blood test called VirScan, Mina *et al.* comprehensively analyzed the antibody repertoire in children before and after natural infection with measles virus as well as in children before and after measles vaccination. They found that measles infection can greatly diminish previously acquired immune memory, potentially leaving individuals at risk for infection by other pathogens. These adverse effects on the immune system were not seen in vaccinated children. —PAK

Science, this issue p. 599

CELL BIOLOGY

Order in the cytoplasm

Extracts of the very large eggs of the African clawed frog, *Xenopus laevis*, have proven a valuable model system for the study of cell division. Cheng and Ferrell found that after homogenization, such cytoplasm can reorganize back into cell-like structures and undergo multiple rounds of division (see the Perspective by Mitchison and Field). This reorganization apparently occurs without the usual factors that are known to lead to such structural changes during cell division, such as F-actin, myosin II, various individual kinesins, aurora kinase A, or DNA. What is required is energy from adenosine triphosphate, microtubule polymerization, cytoplasmic dynein activity, and a specific kinase-involved cell cycle progression. Nongenetic information in the cytoplasm is apparently sufficient for basic spatial organization of the cell. —LBR

Science, this issue p. 631; see also p. 569

STRUCTURAL VIROLOGY

Unveiling African swine fever virus

African swine fever virus (ASFV) is highly contagious and often lethal. With no vaccine or effective treatment, infections often require large-scale culling of pigs. Wang *et al*. apply cutting-edge cryo–electron microscopy techniques to determine the structure of this very large DNA virus. An 8.8-angstrom-resolution reconstruction shows the five layers of the virus, and the fourth capsid layer could be reconstructed at 4.8-angstrom resolution. The structure reveals epitopes in the major capsid protein that distinguish ASFV from other nucleocytoplasmic large DNA viruses and shows how the minor capsid proteins stabilize the capsid. —VV

Science, this issue p. 640

ISOTOPIC SEPARATION

Quantum sieves for hydrogen isotopes

One method for improving the efficiency of separation of hydrogen from deuterium (D) is to exploit kinetic quantum sieving with nanoporous solids. This method requires ultrafine pore apertures (around 3 angstroms), which usually leads to low pore

Published by AAAS

volumes and low D_2 adsorption capacities. Liu *et al*. used organic synthesis to tune the pore size of the internal cavities of organic cage molecules. A hybrid cocrystal contained both a small-pore cage that imparted high selectivity and a larger-pore cage that enabled high D_2 uptake. —PDS

Science, this issue p. 613

ANTHROPOLOGY

Symbolic behavior in Neanderthals

A new discovery provides rare evidence of symbolic behavior in Neanderthal communities and extends the record further geographically and temporally across Europe. Rodríguez-Hidalgo *et al*. analyzed recently unearthed Spanish imperial eagle phalanges, which were found along the Iberian Peninsula, and inferred that Neanderthal communities used these talons for symbolic purposes. Neanderthals most likely cut the eagle phalanges to extract the talon, presumably for use as pendants. These findings address questions around the recurrent appearance of large raptor talons throughout the Middle Paleolithic time frame. —AC

Sci. Adv. 10.1126/sciadv.aax1984 (2019).



Bones from an eagle talon with parallel cut marks

BLACK HOLES

A black hole hiding in a binary star

As material falls toward a black hole, it heats up and emits x-rays. Almost all black holes are discovered by this x-ray emission. Thompson *et al*. observed light from a giant star that is Doppler shifted, indicating an orbit around a binary companion. The companion object must weigh more than 2.6 solar masses, but it emits no light, including x-rays. This indicates the presence of a black hole that is not currently consuming any material. There may be a population of similarly hidden black holes that have been missed by x-ray observations. —KTS

Science, this issue p. 637

BATTERIES

Controlling electrode growth

Batteries with metal anodes can grow dendrites during cycling, which can cause short circuits in a battery or subsequently reduce the charge capacity. Zheng *et al*. developed a process to electrodeposit zinc on a graphene-coated stainless-steel electrode, such that the zinc forms plates with preferential orientation parallel to the electrode. This is achieved by depositing a graphene layer on stainless steel designed to epitaxially match the basal (002) plane of metallic zinc, minimizing lattice strain. During cycling, the zinc will redeposit in plate form rather than as a dendrite such that the batteries show excellent reversibility over thousands of cycles. —MSL

Science, this issue p. 645

IN OTHER JOURNALS

Edited by **Caroline Ash** *and* **Jesse Smith**



ECOLOGY

Nocturnal migration of night hunters

Bird migration is a vast global biannual phenomenon requiring food as fuel on a similar scale. Superimposed on these twice-yearly events are other regular occurrences, including tightly predictable lunar cycles. Norevik *et al*. wondered how the moon might influence migration of birds that hunt at night, such as the European nightjar *Caprimulgus europaeus*. These birds hunt insect prey by sight and are more active during moonlit nights, giving a monthly boost to their food intake. Using GPS-linked data loggers, the authors found that migration activity in these birds en route tends to peak after a full-moon feeding binge. The lunar cycle strongly synchronizes migration responses among individuals, which means a large proportion of a population migrates simultaneously. Such synchronized responses may make them vulnerable to climate change–related or other adverse events along their migration route. —CA

PLOS Biol. 10.1371/journal.pbio.3000456 (2019).

CANCER

The ABCs of brain tumor prognosis

Meningiomas are brain tumors that are typically benign and curable by surgery. In about 20% of cases, however, the tumors recur, and then patient prognosis is poor. Tumor histopathology is currently used to predict which patients might benefit from more aggressive treatment, but this method can be inaccurate. Patel *et al*. used clinical, gene expression, and sequencing data to classify meningiomas from 140 patients. Their analysis identified three distinct groups of tumors (A, B, and C), with type C being the most likely to recur. Type C tumors were characterized by altered activity of a protein complex that controls cell cycle progression. Importantly, this molecular classification system was a better predictor of prognosis than the method currently used in clinics. —PAK

Proc. Natl. Acad. Sci. U.S.A. **116**, 21715 (2019).

MOLECULAR BIOLOGY

Stepping on the condensation

Condensin complexes are molecular motors that extrude DNA loops in a highly conserved and adenosine triphosphate–dependent manner, essential for eukaryotic chromosome condensation during mitosis. Elbatsh *et al*. mutated condensin at two motor sites (AS1 and AS2). They found that mutating AS1 impairs the initiation of loop formation leading to hypocondensation, and mutating AS2 speeds up contraction of DNA and diminishes the formation of high-order, stable

PHOTOS: (FROM LEFT) ANTONIO RODRÍGUEZ-HIDALGO; JAMES WARWICK/GETTY IMAGES

Published by AAAS



European nightjar (*Caprimulgus europaeus*) in flight at dusk

loop structures. AS1 and AS2 thus serve as the accelerator and brake of the condensin machine. Regulating these two opposite adenosine triphosphatase activities is important for controlling chromatin structure. —SYM

Mol. Cell 10.1016/j.molcel.2019.09.020 (2019).

ATOMIC PHYSICS

Dynamics in a box

Cold atomic gases provide a versatile setting for the study of many-body dynamics. When interactions between atoms are strong, transport coefficients in these systems become universal functions of density and temperature. To measure the sheer viscosity of an atomic gas, experimentalists rely on studying the expansion of the gas as it is released from a trap; however, in such experiments, the hydrodynamic description breaks down at cloud edges. To avoid this complication, Baird *et al*. trapped a gas of lithium-6 atoms in a uniform "box" potential and studied its response to a periodic perturbation. The researchers found that, unlike in expansion experiments, the response depended on thermal conductivity. The extracted value of thermal conductivity was in agreement with theoretical calculations. —JS

Phys. Rev. Lett. **123**, 160402 (2019).

STEM WORKFORCE

Quantifying gender bias

Gender biases persist in academia, but no tool that quantifies the extent of these biases currently exists. Tran *et al*. developed and validated the Perceived Subtle Gender Bias Index (PSGBI), designed to quantify women's perceptions of subtle biases within academia. The PSGBI contains four subscales: perceived gender inequity, collegiality, mentorship, and institutional support. The PSGBI was able to differentiate the higher perceptions of subtle gender biases by academic rank, tenured women, and women in men-dominated contexts, that is, associate and full professors perceived more inequality and biases relative to assistant professors. Moving forward, the PSGBI can provide women academics and their allies with data for further discussing gender bias as well as a set of events and experiences to understand where and when biases may be experienced. —MMc

Psychol. Women Q. 10.1177/0361684319877199 (2019).

CELL BIOLOGY

Parasite actin in action

In apicomplexan parasites, such as *Plasmodium* or *Toxoplasma* species, the major function of parasite filamentous actin (F-actin) was thought to be limited to gliding motility and host cell invasion. Using live-cell imaging, Periz *et al*. studied transgenic parasites labeled with anti-actin camel antibodies fused to fluorescent markers. They found that *Toxoplasma* parasites within host cell vacuoles formed an F-actin network that connected individual parasites and was required for recycling of maternal organelles. Using similar technologies, Del Rosario *et al*. investigated the F-actin dynamics of apicomplexan parasites during host cell invasion. Superresolution microscopy revealed that invading parasites have perinuclear F-actin that eases passage of the parasite nucleus into the host cell. Thus, apicomplexan F-actin can form highly dynamic filaments in vivo that fulfill multiple functions during parasite development and invasion. —SMH

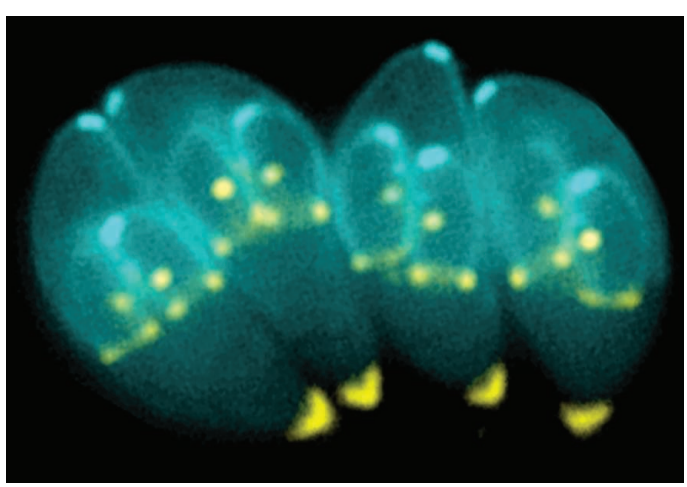
Nat. Commun. **10**, 4183 (2019); *EMBO Rep.* **2019**, e48896 (2019).

ORGANIC CHEMISTRY

Oxygen caught amid three carbons

Oxygen rarely forms more than two bonds to carbon centers. Surrounding one oxygen with three alkyl groups produces an oxonium ion that tends to be highly reactive. In this vein, a tricyclic oxonium motif has been invoked in the biosynthetic pathways postulated for certain natural products associated with the *Laurencia* genus of red algae. Chan *et al*. prepared several of these posited intermediates by halide abstraction and characterized them directly by nuclear magnetic resonance spectroscopy at –78°C. Displacement reactions with a range of nucleophiles gave rise to 10 related natural products. —JSY

J. Am. Chem. Soc. **141**, 15951 (2019).



Fluorescence microscopy image of a cluster of *Toxoplasma gondii* parasites

IMAGE: KE HU AND JOHN M. MURRAY (CC BY 4.0)

Published by AAAS

ALSO IN *SCIENCE* JOURNALS

Edited by **Michael Funk**

MEDICINE

Cryptic signs of aging in our blood

Time is not a friend to our DNA. Aging is associated with an accumulation of somatic mutations in normal dividing cells, including the hematopoietic stem cells (HSCs) that give rise to all blood cells. Certain mutations in HSCs confer a fitness advantage that results in clonal expansions of mutant blood cells that sometimes—but not always—forecast the development of cancer and other age-related diseases. Jaiswal and Ebert review this process of "clonal hematopoiesis," including the mechanisms by which it arises and the current state of knowledge regarding its effects on human health. —PAK

Science, this issue p. 586

MICROBIOLOGY

Animal sociability through microbes

Accumulating evidence suggests that the microbiota living in and on animals has important functions in the social architecture of those animals. Sherwin *et al*. review how the microbiota might facilitate neurodevelopment, help program social behaviors, and facilitate communication in various animal species, including humans. Understanding the complex relationship between microbiota and animal sociability may also identify avenues for treating social disorders in humans. —GKA

Science, this issue p. 587

COMBUSTION PHYSICS

Achieving unconfined supersonic explosions

In some forms of supernovae and chemical explosions, a flame moving at subsonic speeds (deflagration) spontaneously evolves into one driven by a supersonic shock (detonation), vastly increasing the power output. The mechanism of this deflagration-to-detonation transition (DDT) is poorly understood. Poludnenko *et al*. developed an analytical model to describe DDTs, then tested it with lab experiments and numerical simulations. Their model successfully reproduced the DDT seen in the experiments and predicted a DDT in type Ia supernovae, which is consistent with observational constraints. The same mechanism may apply to DDTs in any unconfined explosion. —KTS

Science, this issue p. 588

BUTTERFLY GENOMICS

Following gene flow in butterfly genomes

The role of hybridization in evolution and species radiations has long been debated. In *Heliconius* butterflies, introgression was a major factor in their radiation, and the genetic variation it imparted into species is variable across the genome. Edelman *et al*. developed a new sequencing strategy and produced 20 *Heliconius* genomes (see the Perspective by Rieseberg). They also developed a means by which to identify genetic variation that originates from incomplete lineage sorting versus hybridization. Applying this model to their newly developed genomes, they investigated the evolutionary history of the genus and, in particular, the impact of introgression. —LMZ

Science, this issue p. 594; see also p. 570

RADICAL ENZYMES

Itaconate brings metalloenzyme to a halt

Controlled radicals enable unusual enzymatic transformations, but radical generation and management require dedicated systems. Ruetz *et al*. investigated how the immunometabolite itaconate might undermine these intricate systems to inhibit propionate metabolism, a crucial metabolic pathway in pathogenic *Mycobacterium tuberculosis* (Mtb) (see the Perspective by Boal). They found that the coenzyme A (CoA) derivative of itaconate can irreversibly inhibit the enzyme methylmalonyl-CoA mutase (MCM), which uses the radical-generating cofactor adenosylcobalamin, or coenzyme B_{12}. Itaconyl-CoA derails the normal radical reaction catalyzed by MCM, forming a long-lived, biradical species, which is incapable of completing the catalytic cycle and cannot be recycled by the endogenous coenzyme B_{12} regeneration machinery. Itaconate blocks Mtb growth on propionate, and this inhibition mechanism may be relevant to how macrophages resist Mtb infection. —MAF

Science, this issue p. 589; see also p. 574

PLANT MICROBIOTA

Protecting plants from the inside out

Some soils show a remarkable ability to suppress disease caused by plant pathogens, an ability that is attributed to plant-associated microbiota. Carrión *et al*. investigated the role of endophytes, the intimate microbial community found within roots, in fungal disease suppression (see the Perspective by Tringe). The wilt fungus *Rhizoctonia solani* infects sugar beets, whereupon transcriptional analysis shows that several bacterial endophyte species activate biosynthetic gene clusters to cause disease suppression. These organisms produce antifungal effectors, including enzymes that can digest fungal cell walls, and secondary metabolites, including phenazines, polyketides, and siderophores, which may contribute to the antifungal phenotype. —CA

Science, this issue p. 606; see also p. 568

NEUROSCIENCE

Fluid dynamics during sleep

During non–rapid eye movement sleep, low-frequency oscillations in neural activity support memory consolidation and neuronal computation. Sleep is also associated with increased interstitial fluid volume and clearance of metabolic waste products. It is unknown why these processes co-occur and how they are related. Fultz *et al*. simultaneously measured electrophysiological, hemodynamic, and flow signals in the human brain (see the Perspective by Grubb and Lauritzen). Large oscillations of fluid inflow to the brain appeared during sleep and were tightly coupled to functional magnetic resonance imaging signals and entrained to electroencephalogram slow waves. Slow oscillatory neuronal activity thus leads to oscillations in blood volume, drawing cerebrospinal fluid into and out of the brain. —PRS

Science, this issue p. 628; see also p. 572

NEONICOTINOIDS

Cascading effects of pesticide use

It is now well known that neonicotinoids negatively affect pollinators. As research has expanded, it has become clear that these globally used insecticides directly affect other ecosystem components, including vertebrates. Yamamuro *et al*. now show that these compounds are indirectly affecting species through trophic cascades (see the Perspective by Jensen). Since the application of neonicotinoids to agricultural fields began in the 1990s, zooplankton biomass has plummeted in a Japanese lake surrounded by these fields. This decline has led to shifts in food web structure and a collapse of two commercially harvested freshwater fish

Published by AAAS

species. The authors argue that such dynamics are likely occurring widely. —SNV

Science, this issue p. 620; see also p. 566

SURFACE MAGNETISM

Single molecules sense spin

Imaging surface magnetism, and, in particular, spin excitations of adsorbed molecules or films, is challenging. Verlhac *et al*. demonstrate spin-sensing capability by using the magnetic exchange interaction between a surface sample and the spin-excited states of a nickelocene molecule attached to a scanning tunneling microscope tip. The spatial dependence of the exchange field at the atomic scale enabled imaging of magnetic corrugation with atomic-scale lateral resolution for iron atoms and small islands of cobalt atoms absorbed on nonmagnetic copper surfaces. —PDS

Science, this issue p. 623

REGENERATIVE MEDICINE

Secreting healing factors

One of the main complications associated with the use of nonsteroidal anti-inflammatory drugs (NSAIDs) is the development of gastric ulcers. Proton-pump inhibitors are used to alleviate this condition; however, they are also associated with serious adverse events. Xia *et al*. developed a porcine model of NSAID-induced gastric ulcers and showed that intragastric administration of adipose tissue–derived mesenchymal stem cells rapidly promoted healing and reduced gastric inflammation. The therapeutic effect was mediated by activation of signaling pathways in ulcer tissue induced by stem cell–secreted factors. Mesenchymal stem cells or their secretome could be useful in treating NSAID-induced gastric ulcers. —MM

Sci. Transl. Med. **11**, eaat7455 (2019).

FIBROSIS

Protecting against liver fibrosis

Chronic liver disease stimulates hepatic stellate cells and ultimately leads to fibrosis. Sundaram *et al*. found that mice lacking the pseudoprotease iRhom2, which activates the metalloprotease ADAM17, showed increased stellate cell activation and susceptibility to liver fibrosis induced by bile duct ligation (see the Focus by Badenes and Adrain). iRhom2-activated ADAM17 promoted the shedding of tumor necrosis factor (TNF) receptors from stellate cells. Treating iRhom2-deficient mice with the TNF-α inhibitor etanercept reduced liver fibrosis induced by bile duct ligation. —AMV

Sci. Signal. **12**, eaax1194, eaaz0444 (2019).

Published by AAAS

REVIEW SUMMARY

MEDICINE

Clonal hematopoiesis in human aging and disease

Siddhartha Jaiswal* and Benjamin L. Ebert*

BACKGROUND: Somatic mutations accumulate in normal tissues as a function of time. The great majority of these mutations have no effect on fitness, so selection does not act upon them. Rarely, a mutation will arise that confers a selective growth advantage to the cell in which it occurs. Such a mutation would allow that cell and its progeny, referred to as a "clone," to progressively expand over time. This is now appreciated to occur in a number of tissues, particularly in aged individuals. When this happens in a hematopoietic stem cell (HSC), "clonal hematopoiesis" may result if the mutated clone contributes to the production of a substantial proportion of mature blood cells.

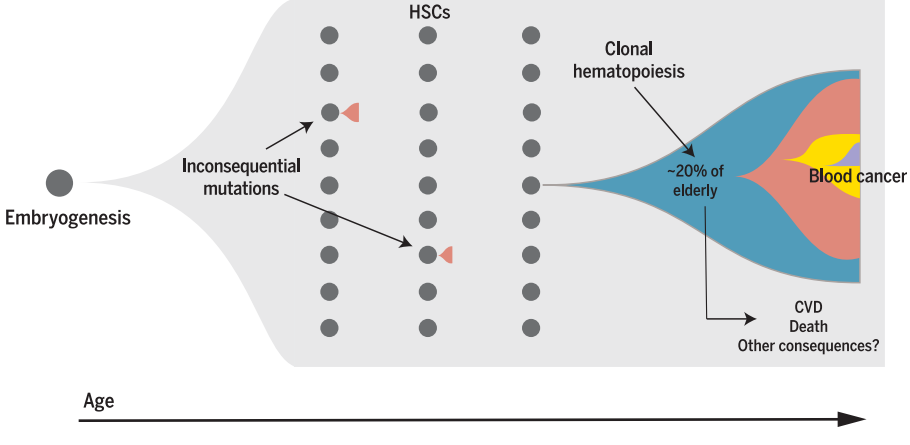
Mutations in genes involved in epigenetic regulation (*DNMT3A*, *TET2*, *ASXL1*) account for the majority of mutation-driven clonal hematopoiesis in humans. These mutations are rare in the young but highly prevalent in the elderly, with between 10 and 20% of those older than age 70 harboring a clone of appreciable size. These individuals usually have only a single driver gene mutated, in contrast to individuals with frank malignancy, where there might be several such mutations. Clonal hematopoiesis of indeterminate potential (CHIP) is a clinical entity defined by the presence of a cancer-associated clonal mutation in at least 4% of nucleated blood cells of individuals without frank neoplasia.

ADVANCES: Large-scale genetic studies have revealed the prevalence and clinical associations of somatic, clonal mutations in blood cells of individuals without hematologic malignancies. One expected consequence of harboring a cancer-associated mutation in blood is an increased risk of developing an overt hematologic malignancy, as the initiating mutation may progress to cancer if additional cooperating mutations are acquired. Indeed, recent studies have demonstrated that CHIP is associated with an increased risk of developing blood cancers, confirming that it is a bona fide premalignant state. Individuals with CHIP progress to malignancy at a rate of about 0.5 to 1% per year. Factors that influence the likelihood of progression to malignancy include the size of the clone, the number of mutations, and the specific gene or genes that are mutated.

The process of precancerous clonal expansion likely occurs in all mitotically active tissues, as has recently been shown in studies of human skin and esophagus. Clonal hematopoiesis may also be relevant to phenotypes apart from malignancy. The blood stem cells that harbor the mutations give rise to immune cells such as granulocytes, monocytes, macrophages, and lymphocytes. As these cells reside in nearly all tissues, mutations that alter their function could have a variety of phenotypic consequences. For example, recent studies have suggested that CHIP is associated with an increased risk of all-cause mortality and an increased risk of cardiovascular diseases such as myocardial infarction, stroke, and venous thrombosis. The risk appears to be substantial, as the hazard ratio associated with CHIP is as great as or greater than many commonly assessed risk factors for cardiovascular disease, such as smoking, cholesterol levels, and high blood pressure. Mouse models that carry some of the common CHIP mutations display enhanced atherosclerosis, consistent with a causal relationship between the mutations and the disease. At a mechanistic level, the mutations may amplify the inflammatory response by the innate immune system, a known contributing factor in the development of atherosclerosis. CHIP may be a general factor underlying age-related inflammation and could potentially influence several diseases of aging.

ON OUR WEBSITE

Read the full article at http://dx.doi.org/10.1126/science.aan4673



Somatic mutations, clonal hematopoiesis, and aging. Somatic mutations are acquired by all cells throughout life. Most are inconsequential, but rare mutations will lead to clonal expansion of hematopoietic stem cells (HSCs). If additional mutations are acquired, blood cancers may result. Emerging data also associate the presence of such clones with increased risk of cardiovascular disease (CVD) and death. Clonal hematopoiesis provides a glimpse into the process of mutation and selection that likely occurs in all somatic tissues.

OUTLOOK: Although the past few years have seen an explosion of research on clonal hematopoiesis, many mysteries remain. The exact mechanisms by which CHIP-associated mutations cause clonal expansion remain unknown, as does a role for environmental or heritable factors in this process. Nor is it understood why some people develop rapid clonal expansion and progression to malignancy, whereas others have clones that lay dormant for many years. It is likely that the presence of CHIP influences several other diseases of aging, in addition to cancer and cardiovascular disease, but this has not yet been studied systematically. In addition to addressing questions directed at the basic science underlying clonal hematopoiesis, we need to develop strategies aimed at mitigating the adverse consequences of CHIP, such as lifestyle modifications or drugs that lower the risk of hematologic cancer and heart disease.

The process of mutation and clonal selection is likely to be universal across all organs and tissues. Understanding the causes and consequences of clonal hematopoiesis may provide a framework to understand this process, and aging, more broadly. ■

The list of author affiliations is available in the full article online.
*Corresponding author. Email: sjaiswal@stanford.edu (S.J.); benjamin_ebert@dfci.harvard.edu (B.L.E.)
Cite this article as S. Jaiswal and B. L. Ebert, *Science* **366**, eaan4673 (2019). DOI: 10.1126/science.aan4673

REVIEW

MEDICINE

Clonal hematopoiesis in human aging and disease

Siddhartha Jaiswal[1]* and Benjamin L. Ebert[2,3]*

As people age, their tissues accumulate an increasing number of somatic mutations. Although most of these mutations are of little or no functional consequence, a mutation may arise that confers a fitness advantage on a cell. When this process happens in the hematopoietic system, a substantial proportion of circulating blood cells may derive from a single mutated stem cell. This outgrowth, called "clonal hematopoiesis," is highly prevalent in the elderly population. Here we discuss recent advances in our knowledge of clonal hematopoiesis, its relationship to malignancies, its link to nonmalignant diseases of aging, and its potential impact on immune function. Clonal hematopoiesis provides a glimpse into the process of mutation and selection that likely occurs in all somatic tissues.

Aging is associated with a steady increase in the number of somatic mutations in nearly all tissues (*1*–*5*). These age-associated mutations fall into several classes. The most frequent class arises from the spontaneous deamination of 5-methylcytosine to thymine and primarily occurs at CpG dinucleotides, which are often in the methylated state (*6*). If a cell has not repaired this error before replication, one daughter cell will have a thymine:adenine pairing of DNA bases instead of the parental cytosine:guanine. This process occurs at a linear rate with respect to time and is therefore considered a signature of aging (*7*). A second class of mutation is small insertions and deletions (indels), which commonly arise from errors introduced during nonhomologous end joining of DNA double-strand breaks and can result in frameshift mutations if the breaks occur in protein-coding portions of the genome (*8*). Evidence from model organisms suggests that double-strand breaks may become more common as cells age (*9*). A third mechanism of mutation is replication error by DNA polymerase, which also typically results in base substitutions or small indels. The error rate of eukaryotic DNA replication tends to be very low, except in the case where DNA mismatch repair function is compromised (*10*, *11*) The number of replication cycles that a cell has undergone typically increases with age; therefore the number of polymerase errors also cumulatively increases (*12*). The fourth type of age-associated mutation is large structural variation, such as insertions, deletions, loss of heterozygosity, or rearrangements spanning several kilobases or more, although these occur somewhat less commonly than base substitutions and small indels (*13*).

In combination, these mutational processes create a broad array of genetically distinct tissue stem cells. Through Darwinian selection, some of these stem cells gain a competitive advantage, a phenomenon that has been most extensively studied in the human hematopoietic system. It is estimated that humans have 50,000 to 200,000 hematopoietic stem cells (HSCs) (*14*). As each HSC acquires about one exonic mutation per decade of life (*3*), by the age of 70 an average person would be expected to harbor up to 1.4 million protein-coding variants, corresponding to an average of 70 mutations per gene, in at least one HSC (Fig. 1). If just one of these mutations is capable of imparting a fitness advantage to the cell in which it arose, expansions of mutated HSCs, termed "clones," should be common in aging humans. Indeed, numerous studies have now shown that such outgrowths of mutated blood cells, termed "clonal hematopoiesis," are highly prevalent in the elderly. An equivalent state is also pervasive in the epithelium of skin (*15*) and esophagus (*16*, *17*), suggesting that somatic mutation–driven clonal expansions may be a characteristic of aging in several tissues. Here, we review recent developments in our understanding of clonal hematopoiesis and its implications for human health.

A brief history of clonal hematopoiesis

Clonal hematopoiesis is characterized by the overrepresentation of blood cells derived from a single clone. Blood cancers such as chronic myeloid leukemia were first demonstrated to be clonal from karyotypic analysis and are the prototypical example of clonal hematopoiesis (*18*). But in the 1990s, studies of nonrandom X-chromosome inactivation (XCI) in women led to the discovery that clonal hematopoiesis also occurs in individuals without cancer (*19*). One X chromosome is randomly inactivated in each cell during female embryonic development, which means that each of the two X chromosomes is inactive in ~50% of cells. The chromosome that is inactivated remains constant across cell divisions; therefore, the demonstration of nonrandom XCI in a population of cells is evidence of a clonal process. Notably, nonrandom XCI in blood cells was observed to increase in frequency with age, although the underlying mechanism was unclear (*20*). A more complete catalog of the genetic framework of blood cancers allowed investigators to look for cancer-associated somatic mutations in these cases. In 2012, mutations in *TET2* (a gene coding for an enzyme that oxidizes methylated DNA) were found in ~5% of elderly women with nonrandom XCI. This was the first demonstration that mutation-driven clonal hematopoiesis occurs in healthy persons (*21*).

A second line of evidence that supported the existence of premalignant clonal expansions in healthy individuals came from studies of patients who were in remission after being treated for acute myeloid leukemia (AML). Like most cancers, AML generally results from several driver mutations that occur sequentially in the same clone over time (*3*). If the first mutation to be acquired leads to clonal expansion without malignant transformation, it should be possible to identify a premalignant stage in which only the initiating lesion is present (*22*). This was first demonstrated in a case study of a patient with AML in which the driver mutation of the leukemia, an *AML1/ETO* translocation, could be detected in a fraction of phenotypically normal HSCs and mature hematopoietic cells in remission samples (*23*). In later studies, DNA sequencing of HSCs from AML patients in remission revealed that stem cells with only a single driver mutation were often present, suggesting that premalignant clonal hematopoiesis was a generalizable finding in AML (*24*–*26*). However, the extent of mutation-driven clonal hematopoiesis in the healthy population, its full genetic spectrum, and its natural history remained unknown.

Clonal hematopoiesis in the genome sequencing era

In 2014, three groups examined exome sequencing data from studies that together comprised more than 30,000 persons for the presence of mutations associated with hematological cancers (*27*–*29*). Some of these individuals had diabetes, schizophrenia, or solid cancers, but they were unselected for hematological phenotypes. Notably, the source of DNA was peripheral blood cells, thus permitting the study of mutation-driven clonal hematopoiesis on a larger scale than was previously possible. These studies can be thought of as a natural experiment of saturation mutagenesis in

[1]Department of Pathology, Stanford University School of Medicine, Stanford, CA 94305, USA. [2]Department of Medical Oncology, Howard Hughes Medical Institute, Boston, MA. [3]Broad Institute of MIT and Harvard, Cambridge, MA 02142, USA.
*Corresponding author. Email: sjaiswal@stanford.edu (S.J.); benjamin_ebert@dfci.harvard.edu (B.L.E.)

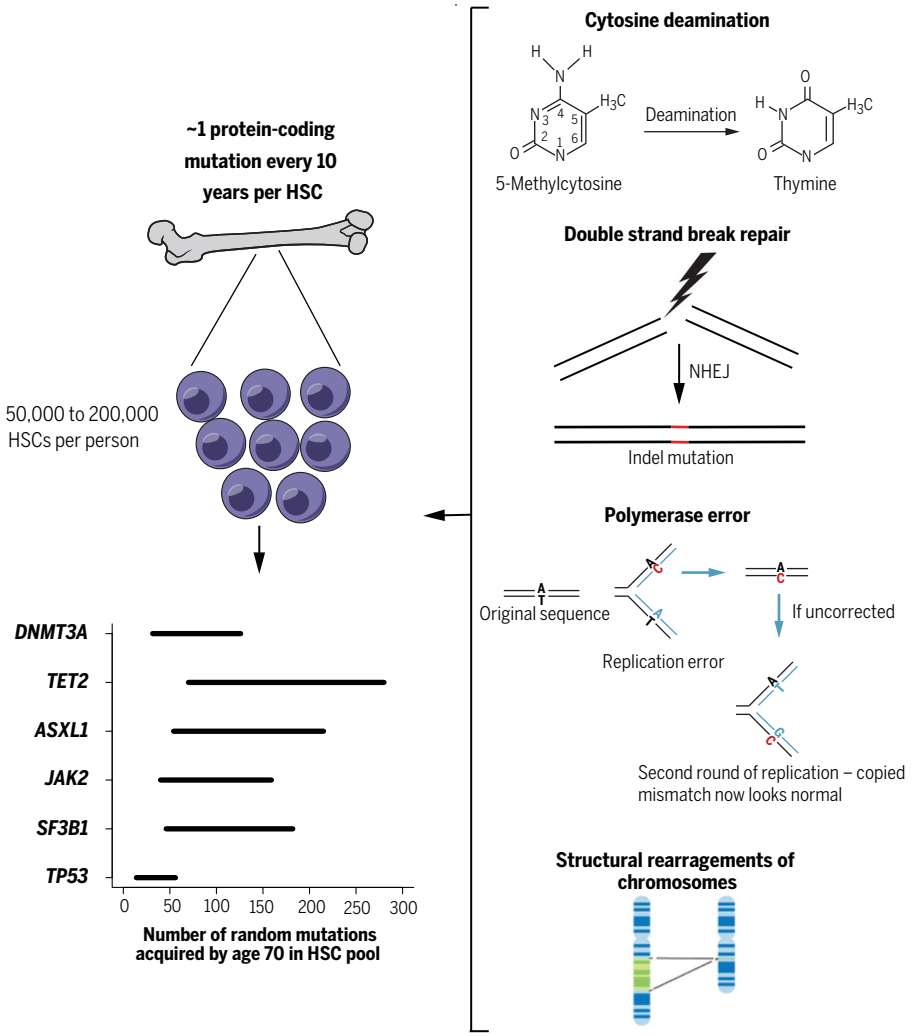


Fig. 1. Mutational processes in aging. A single hematopoietic stem cell (HSC) in a healthy person acquires approximately one protein-coding mutation per decade of life (*3*). Four mutational processes contribute to the bulk of these age-associated mutations (right): spontaneous deamination of 5-methylcytosine to thymine, insertions and deletions (indels) caused by nonhomologous end-joining (NHEJ) of DNA double-strand breaks, errors in replication by DNA polymerase, and structural rearrangements of chromosomes, such as large insertions, deletions, and translocations. Assuming there are 50,000 to 200,000 HSCs in an average person (*14*), we estimate that by age 70, an average person without a hematological cancer will harbor 350,000 to 1.4 million protein coding mutations in his or her HSC pool. Shown at the bottom left is the expected number of random mutations (expressed as a range) in HSCs in the exons of *DNMT3A*, *TET2*, *ASXL1*, *JAK2*, *SF3B1*, and *TP53* by age 70 per person. A subset of these mutations may lead to clonal expansions.

humans and can be summarized in a simple postulate—given a sufficiently large population, every possible mutation that can occur will occur in some HSCs. Those cells carrying mutations that are neutral or deleterious will not expand and therefore will not be detectable from blood DNA. Those mutations that are detectable are the ones that cause clonal expansion, and these will point to biological pathways that increase the fitness of HSCs.

The surprising result of this experiment of nature was that clonal hematopoiesis largely results from mutations in a very restricted set of genes. Mutations in classical oncogenes and tumor suppressors, such as those involved in cellular growth signaling (*JAK2*, *GNAS*, *GNB1*, *CBL*) and the DNA damage response (*TP53*, *PPM1D*), were seen but were not the most common. Instead, nearly two-thirds of clonal hematopoiesis could be accounted for by loss-of-function mutations in just two enzymes involved in DNA methylation: *DNMT3A* and *TET2*. The third most commonly mutated gene was *ASXL1*, a chromatin regulator, and mutations in splicing factors (*SF3B1*, *SRSF2*, *PRPF8*, *U2AF1*) were also frequent. Why these mutations cause clonal expansion remains an intense area of investigation (see "Mechanisms of clonal expansion" below).

A second observation that emerged from these studies was that clonal hematopoiesis is an age-related phenomenon. Somatic clones were detectable in less than 1% of individuals under age 40, but they increased in frequency with each decade of life. By contrast, 10 to 20% of individuals age 70 or older harbored a detectable clone. The size of these mutant clones was massive; in one study, a median of ~18% of blood cells carried the mutations (*29*). For comparison, previously described mutations in the blood of persons without cancer, such as *BCR-ABL* or *BCL2* translocations, were usually present in less than 0.01% of cells and were often transient (*30*, *31*). One important consideration is that the prevalence of clonal hematopoiesis is highly dependent on the sensitivity of the method used to detect it (Fig. 2). These initial studies used whole-exome sequencing, which is relatively insensitive to smaller clones. Subsequent studies using more sensitive approaches have found the prevalence of clonal hematopoiesis to be much higher, although the biological importance of the smaller clones is unknown (*32*–*34*).

Thus far, our discussion of clonal hematopoiesis has focused on mutational changes that are limited to small stretches of DNA, such as base substitutions and small indels. But large structural variation, such as gains or losses of large segments of chromosomes, also increases with age and has clinically meaningful associations (*35*–*37*). Although the accumulation of both small and large somatic variants is linked to aging, the underlying biology of the two is generally nonoverlapping. For example, copy-number gains or losses of *DNMT3A*, *TET2*, and *ASXL1* are rarely found in surveys of somatic large structural variation (*36*). Instead, changes associated with chronic lymphocytic leukemia (CLL) and losses of sex chromosomes are the most common variants that accumulate in aging (*37*). Mechanistic understanding of why these variants are positively selected during aging is lacking in most cases. Further complicating the picture, clonal hematopoiesis has been observed in the absence of any known driver mutation (*28*, *38*). What causes apparent clonal expansion in these cases is unknown, but clonal expansion could be due to mutations in genes not previously queried in surveys of clonal hematopoiesis, mutations in the noncoding genome, or even genetic drift due to age-related constriction of the stem cell pool (*38*).

Clonal hematopoiesis of indeterminate potential (CHIP)

Clonal hematopoiesis generally refers to any clonal outgrowth of hematopoietic cells, regardless of cause or disease state. Thus, someone with a frank malignancy like AML would be considered to have clonal hematopoiesis. Stochastic processes such as constriction of

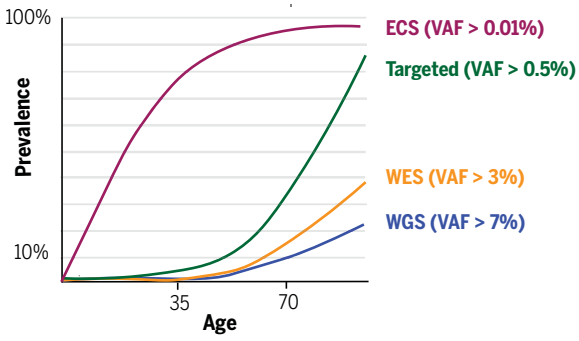


Fig. 2. Prevalence of CHIP. The estimated prevalence of clonal hematopoiesis as a function of age varies according to the sequencing method used. Methods that are more sensitive, such as deep sequencing of select genes (*34*, *72*, *73*), will detect clonal hematopoiesis in more people than methods such as exome (*28*, *29*) or genome sequencing (*38*), which typically have a much lower depth of coverage. The clinical consequences of clonal hematopoiesis are best understood for larger clones (>2% VAF). VAF, variant allele fraction; ECS, error corrected sequencing; WES, whole-exome sequencing; WGS, whole-genome sequencing.

the stem cell pool with aging may also lead to clonal hematopoiesis in the absence of a known driver mutation. The term "clonal hematopoiesis of indeterminate potential" (CHIP) was introduced to distinguish nonmalignant clonal hematopoiesis that is clearly linked to cancer-associated mutations from other forms of clonal hematopoiesis (*39*). CHIP refers to the presence of a cancer-associated variant in the blood cells of a person without a frank malignancy or another recognized clonal entity, such as monoclonal B-lymphocytosis (MBL) or paroxysmal nocturnal hemoglobinuria (*40*). The term "indeterminate potential" is intended to invoke the medical uncertainty associated with such a state. By this definition, cancer-free persons with somatic mutations in genes such as *TET2* or *TP53* would be considered to have CHIP. This term would not apply to persons with copy-number abnormalities associated with MBL and CLL or clonal expansion in the absence of a known driver mutation. To meet the definition of CHIP, the clones must also meet a certain size threshold. If sequenced deeply enough, a cancer-associated mutation may be detectable in most people over the age of 50 (*34*), but only clones that reach a certain size are likely to be clinically meaningful. The threshold for CHIP was set at a variant allele fraction (VAF) of 2% (meaning 2% of the sequenced alleles contained the mutation, or roughly 4% of cells, assuming the mutation is heterozygous), but may be revised if it is demonstrated that there is prognostic relevance for clones below this size.

Mechanisms of clonal expansion

The role of CHIP-associated genes in hematopoiesis has been extensively reviewed elsewhere (*41*, *42*). For some of these genes, clear mechanisms for clonal expansion have been found. HSCs from mice with mutations in either *Tp53* (*43*) or *Ppm1d*, a gene encoding a regulator of p53 and other members of the DNA damage response pathway (*44*, *45*), can enter the cell cycle despite the presence of DNA damage, leading to a stem cell advantage in the setting of cytotoxic drugs. Activating mutations in *JAK2* allow constitutive signaling though growth factor receptors, thus leading to clonal expansion by enhanced proliferation of cells that carry this mutation (*46*).

Less clear is why mutations in *TET2* or *DNMT3A* lead to clonal expansion. Especially perplexing is that these two genes have ostensibly opposite biochemical functions. DNMT3A is one of the two enzymes responsible for de novo methylation of the fifth position in cytosine bases of DNA, a mark that is thought to influence gene expression (*47*, *48*). TET2 is one of three enzymes responsible for catalyzing the oxidation of 5-methylcytosine to 5-hydroxymethylcytosine and further intermediates, which can eventually lead to demethylation (*49*, *50*). Mouse models carrying loss-of-function mutations in either of these genes clearly show an HSC competitive advantage in vivo as well as a propensity for leukemia when cooperating mutations are present (*51*–*54*). Stem cells from these mice can grow colonies in vitro for several passages, whereas wild-type stem cells quickly lose this capacity, suggestive of enhanced self-renewal capacity in the mutant stem cells (*55*, *56*). However, it is unknown why loss of cytosine methylation or hydroxymethylation, broadly or at specific genomic loci, leads to changes in self-renewal ability.

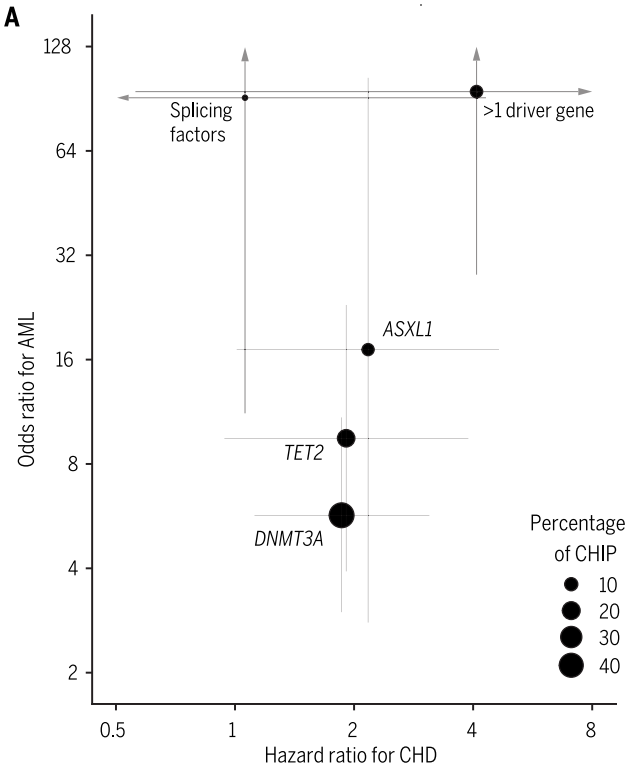
Mutations in genes encoding core members of the spliceosome are also found in CHIP, though less commonly than mutations in *TET2* and *DNMT3A*. HSCs from mice mutant for these genes, *Sf3b1* (*57*), *Srsf2* (*58*), and *U2af1* (*59*), have a competitive disadvantage in vivo, unlike the clonal expansion observed in humans with these mutations. The reason for the disparity of phenotypes in humans and mice is unclear. Partly because of the inability to model clonal hematopoiesis in these mice, the exact mechanisms whereby these mutations lead to clonal expansion remains unknown.

Clonal hematopoiesis is also commonly found in aplastic anemia, a disorder caused by an autoimmune attack on bone marrow progenitor cells that results in severely depressed blood counts (*60*). In contrast to the mutations associated with CHIP, the mutations most commonly seen in aplastic anemia affect the genes *PIGA*, *BCOR*, and *BCORL1*. The *PIGA* gene is required for the synthesis of glycophosphatidylinositol (GPI), and its loss results in down-regulation of several cell surface proteins that are GPI anchored (*61*). Loss of some of these proteins may allow for immune escape, thus explaining selection for *PIGA*-mutated clones. The mechanism of selection for *BCOR* and *BCORL1* mutations in this setting is unknown.

The risk of developing clonal hematopoiesis is largely related to the stochastic acquisition of somatic mutations in HSCs during aging. However, some epidemiological studies have implicated environmental and heritable components as well. For example, CHIP has been reported to be more common in older men (*29*) and smokers (*28*) and less common in Hispanics (*29*), although these associations are all relatively modest. Recent studies have implicated genetic predispositions (*38*, *62*) as well as the microbiome (*63*) in the etiology and progression of clonal hematopoiesis. More insights into the factors that influence clonal expansions are expected to emerge from genetic sequencing of large population cohorts with richly annotated clinical phenotypes.

CHIP and hematological malignancy

CHIP itself does not denote a malignancy, nor is it associated with clinically significant alterations in blood counts (*29*, *64*). But many of the most commonly seen mutations in CHIP are also recurrent drivers of AML (*65*), myelodysplastic syndrome (MDS) (*66*–*68*), myeloproliferative neoplasms (*69*), and certain lymphomas (*70*, *71*). Thus, one might predict that individuals with CHIP would develop hematological malignancies at a rate above background because they have the "first hit" needed for malignant transformation. Indeed, in population-based cohorts that underwent exome sequencing, the presence of CHIP was associated with an ~10-fold increased relative risk of these malignancies over several years of follow-up (*28*, *29*). In one study, 4% of CHIP carriers developed a blood cancer over the subsequent 8 years, corresponding to ~0.5% of CHIP cases converting to malignancy per year (*29*). Notably, the risk of malignancy in the carriers of CHIP was associated with the size of the mutant clone, as those who went on to develop malignancy had substantially



B

	HR (95% CI)
Age 50-59	**2.2** (1.3-3.7)
Age 60-69	**2.4** (1.4-4.0)
Age ≥70	**6.3** (3.8-10.4)
Female	**0.7** (0.5-0.9)
Has T2D	**2.2** (1.6-3.0)
Former or current smoker	**1.4** (1.0-1.9)
Hypertension stage II-IV	**1.4** (1.0-1.9)
TC >200 mg/dL	**1.4** (1.0-1.9)
HDL<35 mg/dL	**1.4** (1.0-2.2)
HDL>60 mg/dL	**0.8** (0.5-1.1)
CHIP present	**1.8** (1.1-2.9)

Fig. 3. CHIP is associated with increased risk of acute myeloid leukemia and coronary heart disease. (**A**) Forest plots for risk of developing acute myeloid leukemia (AML) (*72*) and coronary heart disease (CHD) (*80*) in individuals with mutations in the genes listed. Only those mutations meeting the definition of CHIP were included. Individuals with mutations in more than one driver mutation are shown in the figure as a separate category (>1 driver gene). Lines represent the 95% confidence interval for odds or hazard ratios, and the sizes of the dots reflect the percentage of total CHIP mutations that are accounted for by each gene. (**B**) Hazard ratio (HR) and 95% confidence interval (CI) for developing CHD based on Framingham risk factors plus presence of CHIP mutations. Data are taken from population-based cohorts unselected for CHD status (*29*).

larger clone sizes than those who did not. Myeloid malignancies were most common, although some people with CHIP did develop lymphoid cancers (*28*, *29*).

To refine risk estimates for developing AML associated with clonal hematopoiesis, two groups performed nested case-control studies within large population-based cohorts that had several years of follow-up (*72*, *73*). Both groups found that individuals with antecedent clonal hematopoiesis were at about three- to fivefold increased risk for developing AML in the subsequent years (Fig. 3A). The risk was lower than the ~10-fold increase seen in previous studies because clonal hematopoiesis was identified using methods that were more sensitive than exome sequencing, which resulted in the detection of more clones of smaller size, including clones below the size threshold for CHIP. Similar to previous studies, the risk of AML positively correlated with the size of the mutant clone. An intriguing finding from these studies was that mutations in *TP53*, *JAK2*, *SF3B1*, *SRSF2*, and *U2AF1* were linked to a particularly high risk of developing AML; however, many of these individuals had multiple driver gene mutations, making the assessment of risk for singleton mutations challenging. Nonetheless, such studies could provide a rationale for population-wide screening for those at especially high risk for transformation, though it remains to be seen what interventions would be beneficial in these individuals.

A feared complication in patients who have been treated with cytotoxic drugs for solid cancers is therapy-related development of secondary AML and MDS. Several studies have found that patients with CHIP and solid tumors or lymphoma have an increased risk of these therapy-related myeloid neoplasms after treatment for the primary disease (*74*–*76*). It is hypothesized that preexisting mutant HSC clones selectively expand under the pressure of cytotoxic therapy and can cause cancer several years later with the acquisition of subsequent mutations (*77*). One study of a patient population treated for solid cancers found that CHIP mutations were more prevalent in this group than in populations not selected for cancer (*78*). Furthermore, the mutational spectrum in patients with nonhematologic cancers was altered, as mutations in DNA damage response genes such as *TP53* and *PPM1D* were far more prevalent in this setting, likely due to strong selective pressure from exposure to cytotoxic therapies. Patients with CHIP also had increased mortality, most often due to progression of their primary malignancy. These studies indicate that CHIP in the setting of other cancers is likely to be especially pervasive and portends a poor prognosis.

CHIP and nonmalignant disease

Most clonal expansion states are expected to increase the risk of neoplasia in the tissues in which they arise. But might there be consequences of the mutant clones apart from cancer? Although it will be fascinating to determine these consequences in all tissues, some characteristics of the hematopoietic system make it particularly noteworthy as a potential cause of nonmalignant disease. First, tissue architecture constrains the extent of clonal expansion within tissues such as gut or skin epithelium to patches that are rarely larger than a few square millimeters (*16*), but there is no such spatial restriction on HSCs, which freely admix throughout the bone marrow and body (*79*). Indeed, some individuals with clonal hematopoiesis have nearly all of their blood cells arising from a single mutated HSC (*29*). Second, alterations in hematopoietic cells have the potential to affect a

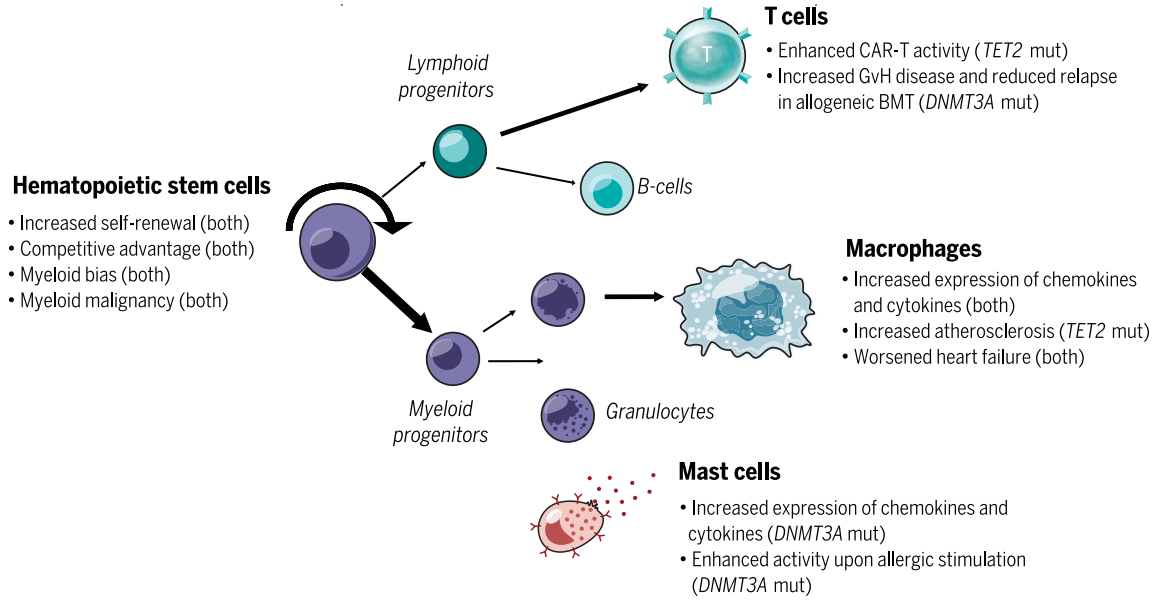


Fig. 4. Phenotypic changes in HSCs and immune cells with TET2 or DNMT3A mutations. HSCs that lack *TET2* or *DNMT3A* display several convergent phenotypes in model systems, such as competitive advantage, enhanced self-renewal, myeloid bias in differentiation, and propensity for transformation to myeloid malignancies (*51*–*56*). The mature immune effector cells that derive from these mutated HSCs are increasingly appreciated to be functionally altered as well. Recent work has found that loss of *TET2* or *DNMT3A* increases inflammatory responses in macrophages (*80*, *87*, *88*, *93*) and mast cells (*95*). Emerging work also suggests an effect of these mutations on T cell function, which may influence immune response to tumors (*96*, *97*). CAR-T, chimeric antigen receptor T cell; GvH, graft-versus-host; BMT, bone marrow transplant.

wide range of disease states. In contrast to tissue-specific cells or epithelia, immune cells such as lymphocytes, granulocytes, and monocytes can migrate to and influence nearly every organ. These immune effector cells are derived from HSCs, so any mutations that occur in HSCs can also potentially alter the immune response or baseline inflammatory state.

These observations have prompted an examination of the effects of mutation-driven clonal hematopoiesis on human health and disease beyond blood cancer. Several studies have found that CHIP is associated with a 30 to 40% increased mortality risk (*28*, *29*, *38*). In an initial study, this risk could not be explained by cancer deaths but was instead related to increased cardiovascular mortality (*29*). Further analysis revealed that the risk of future ischemic stroke and coronary heart disease was more than doubled in carriers of CHIP (*29*) (Fig. 3A). In this study of primarily middle-aged individuals, the risk of coronary heart disease and ischemic stroke associated with CHIP was as great as or greater than that conferred by well-known risk factors for cardiovascular disease, such as circulating low-density lipoprotein (LDL)–cholesterol levels, smoking, and blood pressure (Fig. 3B). Replication studies in additional cohorts confirmed and extended the early work. In studies of middle-aged and older individuals, the risk for coronary heart disease was nearly twice as high for individuals with CHIP compared to individuals without CHIP (*80*). The risk for early-onset myocardial infarction (MI), defined as heart attack before age 40 in men or age 50 in women, was four times higher in those with CHIP compared to those without CHIP. The relative risk for coronary heart disease in individuals bearing mutations in *DNMT3A*, *TET2*, or *ASXL1* was roughly doubled compared to those without CHIP; in individuals bearing *JAK2* mutations, the relative risk was ~12-fold higher compared to those without CHIP. In addition, individuals with larger mutant clones had the greatest risk of cardiovascular disease, mirroring the situation for malignancy risk. Just as CHIP is associated with an increased risk of cardiovascular disease, lower-risk subtypes of MDS are also associated with a doubling of the risk of dying from cardiovascular causes (*81*).

The link between CHIP and cardiovascular outcomes is not limited to atherosclerotic disease. Recent evidence suggests that individuals with post-MI–related congestive heart failure who carry CHIP-associated *DNMT3A* or *TET2* mutations have worse survival outcomes than individuals without CHIP (*82*). In a separate study (*83*), individuals with CHIP-associated *JAK2* mutations were reported to have a ~12 times greater risk of developing venous thrombosis than those without CHIP, whereas individuals with mutations in other CHIP-associated genes had a doubling of the risk (*83*). Thus, CHIP is likely to be an indicator of poor prognosis for several distinct cardiovascular disorders.

Although it is clear that CHIP-associated mutations play a causal role in the development of blood cancer, it is less clear, a priori, whether their role in nonmalignant diseases is causal or merely correlative. Like several other well-described markers in blood cells, such as red cell distribution width (*84*), DNA methylation clocks (*85*), and loss of Y chromosome (*86*), CHIP is associated with multiple adverse outcomes in epidemiological studies. One potential explanation is that all of these biomarkers are measures of some aspect of biological aging but are themselves not directly causal for health outcomes. What distinguishes CHIP from these other measures is the ability to manipulate model organisms experimentally to test causality.

In 2017, two research groups used mouse models to establish a causal role for CHIP in atherosclerosis. Both groups found that loss of *Tet2* in bone marrow cells led to an increase in the size of atherosclerotic lesions in hyperlipidemic mice, an effect that could not be explained by quantitative changes in blood cell parameters of the mutant mice (*80*, *87*). Rather, the mutant bone marrow–derived macrophages up-regulated many proinflammatory molecules, suggesting a potential mechanism for the increase in atherosclerosis. In support of this hypothesis, loss of *Tet2* in myeloid cells was sufficient to confer enhanced atherosclerosis. In addition, blockade of the proinflammatory cytokine interleukin-1β (IL-1β) reversed the accelerated atherosclerosis seen in *Tet2* mutant mice (*87*).

Subsequent studies showed that loss of *Tet2* or *Dnmt3a* led to worsening heart function in a mouse model of congestive heart failure, corroborating the human genetic association (*88*, *89*). Heart function in these studies was also improved with blockade of IL-1β, suggesting that this may be a common pathway for reversing the effects of CHIP in the heart. There is also evidence that *Jak2* mutations in bone marrow enhance atherosclerosis in mouse models by altering macrophage function (*90*). Mutations in *JAK2* have a well-described role in activating signal transducer and activator of transcription (STAT) transcription factors, which are central to immune response in several cell types involved in atherosclerosis. Furthermore, *JAK2* mutations prime neutrophils to form neutrophil extracellular traps, leading to thrombosis, which may also contribute to poor cardiovascular outcomes (*83*). Together, these studies provide strong evidence that somatic mutation–driven clonal hematopoiesis has a causal role in cardiovascular disease.

To date, few studies have demonstrated an unequivocal link between CHIP and other diseases of aging. CHIP has been found to be associated with a 30% increase in the likelihood of having type 2 diabetes (*29*). However, causality could not be established, and this could represent a case of reverse causation, as hyperglycemia might influence the development or expansion of clones by interfering with TET2 function (*91*). Other studies have found links between CHIP and chronic obstructive pulmonary disease (*38*, *64*). However, CHIP was also strongly linked to smoking in these studies, so the result could be confounded by this association.

Immune function and CHIP

As many of the genes associated with CHIP are involved in transcriptional regulation, one might expect mutations in these genes to have broad effects on immune function. Several recent studies have examined the role of *TET2* and *DNMT3A* in immunity (Fig. 4). One group found that mice deficient in *Tet2* developed more severe inflammation in several tissues upon challenge with bacterial endotoxin, and this was partially explained by increased expression of the proinflammatory cytokine *Il6* in dendritic cells and macrophages (*92*). Unexpectedly, this effect on *Il6* expression was independent of the catalytic function of Tet2 and was instead reported to be related to a direct interaction between Tet2 and histone deacetylases, resulting in transcriptional repression. Subsequent studies have confirmed the overexpression of *Il6* and also found that *Il1b*, IL8 family chemokines, and other inflammatory mediators show increased expression in *Tet2*-deficient macrophages challenged with LDL or endotoxin (*80*, *87*, *93*). Humans with mutations in *TET2* are also reported to have increased concentrations of circulating IL-8 protein (*80*). The changes in expression are relatively modest for each gene (about two- to threefold increase) but appear to be biologically important given the number of genes that are dysregulated and the breadth of phenotypes seen in *Tet2* knockout mice. These molecules are thought to enhance inflammation locally within atherosclerotic plaques by increasing chemotaxis of leukocytes to arterial intima, which potentially explains the accelerated atherosclerosis seen with loss of *Tet2* (*94*).

Less is known about the role of *DNMT3A* in innate immune function, but most studies to date have found evidence of enhanced inflammation when its function is perturbed. For example, one study found that mast cells from mice that lacked *Dnmt3a* produced higher amounts of IL-6, tumor necrosis factor–α, and IL-13 in response to stimulation with immunoglobulin E in vitro, and enhanced mast cell activity was also seen in a mouse model of allergy (*95*). Another study used CRISPR to mutate *Dnmt3a* in mouse RAW 264.7 macrophages and observed increased expression of *Cxcl1*, *Cxcl2*, and *Il6* in response to endotoxin (*88*). Mechanistically, very little is known about why these specific gene expression changes are seen with loss of *Dnmt3a*.

CHIP may be relevant in the adaptive immune response as well. Bone marrow transplant recipients with hematological malignancies who received donor marrow from carriers of CHIP had higher rates of graft-versus-host disease and reduced relapse rates (*96*). One possible explanation for this finding is that the donor cells harboring the mutations were capable of mounting stronger immune responses against both normal host tissues and the tumor. There is also a report of an exceptional response in a patient with CLL treated by infusion of chimeric antigen receptor (CAR)–T cells in which the CAR construct disrupted one copy of *TET2*, while the other copy had been previously mutated somatically (*97*). The authors speculate that the resulting *TET2*-deficient CAR-T clone was more effective at eliminating the tumor cells because of an expanded central memory $CD8^+$ T cell population, reduced T cell exhaustion in response to stimulus, and enhanced cytokine production in T cells.

Growing evidence thus supports a role for the commonly mutated CHIP genes in immune function, and CHIP may underlie some part of the phenomenon termed "inflammaging," the age-associated increase in systemic inflammation (*98*).

Future outlook

Clonal hematopoiesis provides a fascinating glimpse into the end result of decades of mutation and natural selection within a tissue. The potential health implications of CHIP are broad. It is associated with blood cancers, cardiovascular disease, and overall mortality. Although our knowledge of this condition has increased exponentially over the past several years, this research has also highlighted fundamental biological questions and opened new pathways for translational discovery.

A major area of uncertainty is the range of disease states associated with CHIP. As CHIP is linked to enhanced inflammation, it is possible that links between CHIP and several diseases of aging will be found. Does CHIP influence the risk of Alzheimer's disease, autoimmunity, liver disease, or others? As ever larger genetic cohorts with rich phenotypic information are assembled, these links may be systematically discovered.

Although CHIP at the population level is clearly linked to cancer, cardiovascular disease, and death, the degree of risk for these outcomes for any given individual with CHIP may be substantially higher or lower than the group average. For example, individuals with mutations in splicing factors, or mutations in multiple genes, are much more likely to develop AML than those with singleton mutations in *TET2* or *DNMT3A* (*72*). Furthermore, the interaction of CHIP with other risk factors, such as having type 2 diabetes or elevated serum concentrations of C-reactive protein, may be synergistic for adverse outcomes. To have power to detect such associations, very large population-based cohorts are needed. Additional biomarkers such as plasma proteins, metabolites, and DNA methylation may prove useful for risk stratification as well. Studies of serial samples have shown that the trajectory of a clone can vary among people. Some people have clones that remain stagnant in size for many years, whereas other people have clones that show steady growth (*29*, *34*). Because clone size is associated with the risk of leukemia and other adverse outcomes, it is imperative to understand this situation. It is likely that cell-extrinsic factors, such as the bone marrow microenvironment, the microbiome, or diet, will play a role.

The mechanisms by which the CHIP-associated mutations cause clonal expansion and enhanced inflammation are also a central unanswered question. It is notable that the two most commonly mutated genes in CHIP, *DNMT3A* and *TET2*, are opposing enzymes in DNA methylation, yet both lead to convergent phenotypes in stem cell biology and immunity. It is also uncertain why some people have apparent clonal hematopoiesis in the absence of a known driver mutation. This may be due to mutations in genes that are currently unknown, but could some of these clonal expansions result purely from selection for epigenetic fitness in the absence of alterations to DNA sequence?

We especially need to find ways to reverse the pathogenic effects of CHIP. Blockade of downstream inflammatory molecules may be one way to treat CHIP-associated atherosclerosis. But ideally, drugs will be found that can suppress the mutant clones directly, which could potentially mitigate the risk of both cancer and cardiovascular disease. The positive effects of CHIP on antitumor immunity may also one day be harnessed for therapy.

The process of mutation and clonal selection is likely to be universal across all organs and tissues. Understanding the causes and consequences of clonal hematopoiesis may provide a framework to understand this process, and aging, more broadly.

REFERENCES AND NOTES

1. F. Blokzijl *et al*., Tissue-specific mutation accumulation in human adult stem cells during life. *Nature* **538**, 260–264 (2016). doi: 10.1038/nature19768; pmid: 27698416
2. M. L. Hoang *et al*., Genome-wide quantification of rare somatic mutations in normal human tissues using massively parallel sequencing. *Proc. Natl. Acad. Sci. U.S.A.* **113**, 9846–9851 (2016). doi: 10.1073/pnas.1607794113; pmid: 27528664
3. J. S. Welch *et al*., The origin and evolution of mutations in acute myeloid leukemia. *Cell* **150**, 264–278 (2012). doi: 10.1016/j.cell.2012.06.023; pmid: 22817890
4. I. Martincorena, P. J. Campbell, Somatic mutation in cancer and normal cells. *Science* **349**, 1483–1489 (2015). doi: 10.1126/science.aab4082; pmid: 26404825
5. K. Yizhak *et al*., RNA sequence analysis reveals macroscopic somatic clonal expansion across normal tissues. *Science* **364**, eaaw0726 (2019). doi: 10.1126/science.aaw0726; pmid: 31171663
6. B. K. Duncan, J. H. Miller, Mutagenic deamination of cytosine residues in DNA. *Nature* **287**, 560–561 (1980). doi: 10.1038/287560a0; pmid: 6999365
7. L. B. Alexandrov *et al*., Signatures of mutational processes in human cancer. *Nature* **500**, 415–421 (2013). doi: 10.1038/nature12477; pmid: 23945592
8. K. Rodgers, M. McVey, Error-Prone Repair of DNA Double-Strand Breaks. *J. Cell. Physiol.* **231**, 15–24 (2016). doi: 10.1002/jcp.25053; pmid: 26033759
9. I. Beerman, J. Seita, M. A. Inlay, I. L. Weissman, D. J. Rossi, Quiescent hematopoietic stem cells accumulate DNA damage during aging that is repaired upon entry into cell cycle. *Cell Stem Cell* **15**, 37–50 (2014). doi: 10.1016/j.stem.2014.04.016; pmid: 24813857
10. T. A. Kunkel, DNA replication fidelity. *J. Biol. Chem.* **279**, 16895–16898 (2004). doi: 10.1074/jbc.R400006200; pmid: 14988392
11. M. A. Sanders *et al*., MBD4 guards against methylation damage and germ line deficiency predisposes to clonal hematopoiesis and early-onset AML. *Blood* **132**, 1526–1534 (2018). doi: 10.1182/blood-2018-05-852566; pmid: 30049810
12. C. Tomasetti, B. Vogelstein, Variation in cancer risk among tissues can be explained by the number of stem cell divisions. *Science* **347**, 78–81 (2015). doi: 10.1126/science.1260825; pmid: 25554788
13. C. C. Laurie *et al*., Detectable clonal mosaicism from birth to old age and its relationship to cancer. *Nat. Genet.* **44**, 642–650 (2012). doi: 10.1038/ng.2271; pmid: 22561516
14. H. Lee-Six *et al*., Population dynamics of normal human blood inferred from somatic mutations. *Nature* **561**, 473–478 (2018). doi: 10.1038/s41586-018-0497-0; pmid: 30185910
15. I. Martincorena *et al*., High burden and pervasive positive selection of somatic mutations in normal human skin. *Science* **348**, 880–886 (2015). doi: 10.1126/science.aaa6806; pmid: 25999502
16. I. Martincorena *et al*., Somatic mutant clones colonize the human esophagus with age. *Science* **362**, 911–917 (2018). doi: 10.1126/science.aau3879; pmid: 30337457
17. A. Yokoyama *et al*., Age-related remodelling of oesophageal epithelia by mutated cancer drivers. *Nature* **565**, 312–317 (2019). doi: 10.1038/s41586-018-0811-x; pmid: 30602793
18. J. D. Rowley, Letter: A new consistent chromosomal abnormality in chronic myelogenous leukaemia identified by quinacrine fluorescence and Giemsa staining. *Nature* **243**, 290–293 (1973). doi: 10.1038/243290a0; pmid: 4126434
19. M. F. Fey *et al*., Clonality and X-inactivation patterns in hematopoietic cell populations detected by the highly informative M27 beta DNA probe. *Blood* **83**, 931–938 (1994). pmid: 8111064
20. K. M. Champion, J. G. Gilbert, F. A. Asimakopoulos, S. Hinshelwood, A. R. Green, Clonal haemopoiesis in normal elderly women: Implications for the myeloproliferative disorders and myelodysplastic syndromes. *Br. J. Haematol.* **97**, 920–926 (1997). doi: 10.1046/j.1365-2141.1997.1933010.x; pmid: 9217198
21. L. Busque *et al*., Recurrent somatic TET2 mutations in normal elderly individuals with clonal hematopoiesis. *Nat. Genet.* **44**, 1179–1181 (2012). doi: 10.1038/ng.2413; pmid: 23001125
22. T. Reya, S. J. Morrison, M. F. Clarke, I. L. Weissman, Stem cells, cancer, and cancer stem cells. *Nature* **414**, 105–111 (2001). doi: 10.1038/35102167; pmid: 11689955
23. T. Miyamoto, I. L. Weissman, K. Akashi, AML1/ETO-expressing nonleukemic stem cells in acute myelogenous leukemia with 8;21 chromosomal translocation. *Proc. Natl. Acad. Sci. U.S.A.* **97**, 7521–7526 (2000). doi: 10.1073/pnas.97.13.7521; pmid: 10861016
24. M. Jan *et al*., Clonal evolution of preleukemic hematopoietic stem cells precedes human acute myeloid leukemia. *Sci. Transl. Med.* **4**, 149ra118 (2012). doi: 10.1126/scitranslmed.3004315; pmid: 22932223
25. L. I. Shlush *et al*., Identification of pre-leukaemic haematopoietic stem cells in acute leukaemia. *Nature* **506**, 328–333 (2014). doi: 10.1038/nature13038; pmid: 24522528
26. M. R. Corces-Zimmerman, W. J. Hong, I. L. Weissman, B. C. Medeiros, R. Majeti, Preleukemic mutations in human acute myeloid leukemia affect epigenetic regulators and persist in remission. *Proc. Natl. Acad. Sci. U.S.A.* **111**, 2548–2553 (2014). doi: 10.1073/pnas.1324297111; pmid: 24550281
27. M. Xie *et al*., Age-related mutations associated with clonal hematopoietic expansion and malignancies. *Nat. Med.* **20**, 1472–1478 (2014). doi: 10.1038/nm.3733; pmid: 25326804
28. G. Genovese *et al*., Clonal hematopoiesis and blood-cancer risk inferred from blood DNA sequence. *N. Engl. J. Med.* **371**, 2477–2487 (2014). doi: 10.1056/NEJMoa1409405; pmid: 25426838
29. S. Jaiswal *et al*., Age-related clonal hematopoiesis associated with adverse outcomes. *N. Engl. J. Med.* **371**, 2488–2498 (2014). doi: 10.1056/NEJMoa1408617; pmid: 25426837
30. C. Biernaux, M. Loos, A. Sels, G. Huez, P. Stryckmans, Detection of major bcr-abl gene expression at a very low level in blood cells of some healthy individuals. *Blood* **86**, 3118–3122 (1995). pmid: 7579406
31. Y. Liu, A. M. Hernandez, D. Shibata, G. A. Cortopassi, BCL2 translocation frequency rises with age in humans. *Proc. Natl. Acad. Sci. U.S.A.* **91**, 8910–8914 (1994). doi: 10.1073/pnas.91.19.8910; pmid: 8090743
32. T. McKerrell *et al*., Leukemia-associated somatic mutations drive distinct patterns of age-related clonal hemopoiesis. *Cell Reports* **10**, 1239–1245 (2015). doi: 10.1016/j.celrep.2015.02.005; pmid: 25732814
33. R. Acuna-Hidalgo *et al*., Ultra-sensitive Sequencing Identifies High Prevalence of Clonal Hematopoiesis-Associated Mutations throughout Adult Life. *Am. J. Hum. Genet.* **101**, 50–64 (2017). doi: 10.1016/j.ajhg.2017.05.013; pmid: 28669404
34. A. L. Young, G. A. Challen, B. M. Birmann, T. E. Druley, Clonal haematopoiesis harbouring AML-associated mutations is ubiquitous in healthy adults. *Nat. Commun.* **7**, 12484 (2016). doi: 10.1038/ncomms12484; pmid: 27546487
35. A. Bonnefond *et al*., Association between large detectable clonal mosaicism and type 2 diabetes with vascular complications. *Nat. Genet.* **45**, 1040–1043 (2013). doi: 10.1038/ng.2700; pmid: 23852171
36. K. B. Jacobs *et al*., Detectable clonal mosaicism and its relationship to aging and cancer. *Nat. Genet.* **44**, 651–658 (2012). doi: 10.1038/ng.2270; pmid: 22561519
37. P. R. Loh *et al*., Insights into clonal haematopoiesis from 8,342 mosaic chromosomal alterations. *Nature* **559**, 350–355 (2018). doi: 10.1038/s41586-018-0321-x; pmid: 29995854
38. F. Zink *et al*., Clonal hematopoiesis, with and without candidate driver mutations, is common in the elderly. *Blood* **130**, 742–752 (2017). doi: 10.1182/blood-2017-02-769869; pmid: 28483762
39. A. J. Silver, S. Jaiswal, Clonal hematopoiesis: Pre-cancer PLUS. *Adv. Cancer Res.* **141**, 85–128 (2019). doi: 10.1016/bs.acr.2018.12.003; pmid: 30691686
40. D. P. Steensma *et al*., Clonal hematopoiesis of indeterminate potential and its distinction from myelodysplastic syndromes. *Blood* **126**, 9–16 (2015). doi: 10.1182/blood-2015-03-631747; pmid: 25931582
41. A. S. Sperling, C. J. Gibson, B. L. Ebert, The genetics of myelodysplastic syndrome: From clonal haematopoiesis to secondary leukaemia. *Nat. Rev. Cancer* **17**, 5–19 (2017). doi: 10.1038/nrc.2016.112; pmid: 27834397
42. R. L. Bowman, L. Busque, R. L. Levine, Clonal Hematopoiesis and Evolution to Hematopoietic Malignancies. *Cell Stem Cell* **22**, 157–170 (2018). doi: 10.1016/j.stem.2018.01.011; pmid: 29395053
43. T. Bondar, R. Medzhitov, p53-mediated hematopoietic stem and progenitor cell competition. *Cell Stem Cell* **6**, 309–322 (2010). doi: 10.1016/j.stem.2010.03.002; pmid: 20362536
44. J. D. Kahn *et al*., *PPM1D*-truncating mutations confer resistance to chemotherapy and sensitivity to PPM1D inhibition in hematopoietic cells. *Blood* **132**, 1095–1105 (2018). doi: 10.1182/blood-2018-05-850339; pmid: 29954749
45. J. I. Hsu *et al*., PPM1D Mutations Drive Clonal Hematopoiesis in Response to Cytotoxic Chemotherapy. *Cell Stem Cell* **23**, 700–713.e6 (2018). doi: 10.1016/j.stem.2018.10.004; pmid: 30388424
46. R. Kralovics *et al*., A gain-of-function mutation of JAK2 in myeloproliferative disorders. *N. Engl. J. Med.* **352**, 1779–1790 (2005). doi: 10.1056/NEJMoa051113; pmid: 15858187
47. M. Okano, S. Xie, E. Li, Cloning and characterization of a family of novel mammalian DNA (cytosine-5) methyltransferases. *Nat. Genet.* **19**, 219–220 (1998). doi: 10.1038/890; pmid: 9662389
48. D. Schübeler, Function and information content of DNA methylation. *Nature* **517**, 321–326 (2015). doi: 10.1038/nature14192; pmid: 25592537
49. Y. F. He *et al*., Tet-mediated formation of 5-carboxylcytosine and its excision by TDG in mammalian DNA. *Science* **333**, 1303–1307 (2011). doi: 10.1126/science.1210944; pmid: 21817016
50. S. Ito *et al*., Tet proteins can convert 5-methylcytosine to 5-formylcytosine and 5-carboxylcytosine. *Science* **333**, 1300–1303 (2011). doi: 10.1126/science.1210597; pmid: 21778364
51. M. Ko *et al*., Ten-Eleven-Translocation 2 (TET2) negatively regulates homeostasis and differentiation of hematopoietic stem cells in mice. *Proc. Natl. Acad. Sci. U.S.A.* **108**, 14566–14571 (2011). doi: 10.1073/pnas.1112317108; pmid: 21873190
52. G. A. Challen *et al*., Dnmt3a is essential for hematopoietic stem cell differentiation. *Nat. Genet.* **44**, 23–31 (2012). doi: 10.1038/ng.1009; pmid: 22138693
53. O. A. Guryanova *et al*., DNMT3A mutations promote anthracycline resistance in acute myeloid leukemia via impaired nucleosome remodeling. *Nat. Med.* **22**, 1488–1495 (2016). doi: 10.1038/nm.4210; pmid: 27841873
54. C. B. Cole *et al*., Haploinsufficiency for DNA methyltransferase 3A predisposes hematopoietic cells to myeloid malignancies. *J. Clin. Invest.* **127**, 3657–3674 (2017). doi: 10.1172/JCI93041; pmid: 28872462
55. K. Moran-Crusio *et al*., Tet2 loss leads to increased hematopoietic stem cell self-renewal and myeloid transformation. *Cancer Cell* **20**, 11–24 (2011). doi: 10.1016/j.ccr.2011.06.001; pmid: 21723200
56. H. Celik *et al*., Enforced differentiation of Dnmt3a-null bone marrow leads to failure with c-Kit mutations driving leukemic transformation. *Blood* **125**, 619–628 (2015). doi: 10.1182/blood-2014-08-594564; pmid: 25416276
57. E. A. Obeng *et al*., Physiologic Expression of Sf3b1(K700E) Causes Impaired Erythropoiesis, Aberrant Splicing, and Sensitivity to Therapeutic Spliceosome Modulation. *Cancer Cell* **30**, 404–417 (2016). doi: 10.1016/j.ccell.2016.08.006; pmid: 27622333
58. E. Kim *et al*., SRSF2 Mutations Contribute to Myelodysplasia by Mutant-Specific Effects on Exon Recognition. *Cancer Cell* **27**, 617–630 (2015). doi: 10.1016/j.ccell.2015.04.006; pmid: 25965569
59. C. L. Shirai *et al*., Mutant U2AF1 Expression Alters Hematopoiesis and Pre-mRNA Splicing In Vivo. *Cancer Cell* **27**, 631–643 (2015). doi: 10.1016/j.ccell.2015.04.008; pmid: 25965570
60. T. Yoshizato *et al*., Somatic Mutations and Clonal Hematopoiesis in Aplastic Anemia. *N. Engl. J. Med.* **373**, 35–47 (2015). doi: 10.1056/NEJMoa1414799; pmid: 26132940
61. R. A. Brodsky, Paroxysmal nocturnal hemoglobinuria. *Blood* **124**, 2804–2811 (2014). doi: 10.1182/blood-2014-02-522128; pmid: 25237200

62. D. A. Hinds *et al*., Germ line variants predispose to both JAK2 V617F clonal hematopoiesis and myeloproliferative neoplasms. *Blood* **128**, 1121–1128 (2016). doi: 10.1182/blood-2015-06-652941; pmid: 27365426
63. M. Meisel *et al*., Microbial signals drive pre-leukaemic myeloproliferation in a Tet2-deficient host. *Nature* **557**, 580–584 (2018). doi: 10.1038/s41586-018-0125-z; pmid: 29769727
64. M. Buscarlet *et al*., *DNMT3A* and *TET2* dominate clonal hematopoiesis and demonstrate benign phenotypes and different genetic predispositions. *Blood* **130**, 753–762 (2017). doi: 10.1182/blood-2017-04-777029; pmid: 28655780
65. T. J. Ley *et al*., Genomic and epigenomic landscapes of adult de novo acute myeloid leukemia. *N. Engl. J. Med.* **368**, 2059–2074 (2013). doi: 10.1056/NEJMoa1301689; pmid: 23634996
66. R. Bejar *et al*., Clinical effect of point mutations in myelodysplastic syndromes. *N. Engl. J. Med.* **364**, 2496–2506 (2011). doi: 10.1056/NEJMoa1013343; pmid: 21714648
67. E. Papaemmanuil *et al*., Clinical and biological implications of driver mutations in myelodysplastic syndromes. *Blood* **122**, 3616–3627, quiz 3699 (2013). doi: 10.1182/blood-2013-08-518886; pmid: 24030381
68. R. C. Lindsley *et al*., Prognostic Mutations in Myelodysplastic Syndrome after Stem-Cell Transplantation. *N. Engl. J. Med.* **376**, 536–547 (2017). doi: 10.1056/NEJMoa1611604; pmid: 28177873
69. J. Nangalia *et al*., Somatic CALR mutations in myeloproliferative neoplasms with nonmutated JAK2. *N. Engl. J. Med.* **369**, 2391–2405 (2013). doi: 10.1056/NEJMoa1312542; pmid: 24325359
70. L. Couronné, C. Bastard, O. A. Bernard, TET2 and DNMT3A mutations in human T-cell lymphoma. *N. Engl. J. Med.* **366**, 95–96 (2012). doi: 10.1056/NEJMc1111708; pmid: 22216861
71. A. Reddy *et al*., Genetic and Functional Drivers of Diffuse Large B Cell Lymphoma. *Cell* **171**, 481–494.e15 (2017). doi: 10.1016/j.cell.2017.09.027; pmid: 28985567
72. S. Abelson *et al*., Prediction of acute myeloid leukaemia risk in healthy individuals. *Nature* **559**, 400–404 (2018). doi: 10.1038/s41586-018-0317-6; pmid: 29988082
73. P. Desai *et al*., Somatic mutations precede acute myeloid leukemia years before diagnosis. *Nat. Med.* **24**, 1015–1023 (2018). doi: 10.1038/s41591-018-0081-z; pmid: 29988143
74. C. J. Gibson *et al*., Clonal Hematopoiesis Associated With Adverse Outcomes After Autologous Stem-Cell Transplantation for Lymphoma. *J. Clin. Oncol.* **35**, 1598–1605 (2017). doi: 10.1200/JCO.2016.71.6712; pmid: 28068180
75. N. K. Gillis *et al*., Clonal haemopoiesis and therapy-related myeloid malignancies in elderly patients: A proof-of-concept, case-control study. *Lancet Oncol.* **18**, 112–121 (2017). doi: 10.1016/S1470-2045(16)30627-1; pmid: 27927582
76. K. Takahashi *et al*., Preleukaemic clonal haemopoiesis and risk of therapy-related myeloid neoplasms: A case-control study. *Lancet Oncol.* **18**, 100–111 (2017). doi: 10.1016/S1470-2045(16)30626-X; pmid: 27923552
77. T. N. Wong *et al*., Role of TP53 mutations in the origin and evolution of therapy-related acute myeloid leukaemia. *Nature* **518**, 552–555 (2015). doi: 10.1038/nature13968; pmid: 25487151
78. C. C. Coombs *et al*., Therapy-related clonal hematopoiesis in patients with non-hematologic cancers is common and associated with adverse clinical outcomes. *Cell Stem Cell* **21**, 374–382.e4 (2017). doi: 10.1016/j.stem.2017.07.010; pmid: 28803919
79. D. E. Wright, A. J. Wagers, A. P. Gulati, F. L. Johnson, I. L. Weissman, Physiological migration of hematopoietic stem and progenitor cells. *Science* **294**, 1933–1936 (2001). doi: 10.1126/science.1064081; pmid: 11729320
80. S. Jaiswal *et al*., Clonal Hematopoiesis and Risk of Atherosclerotic Cardiovascular Disease. *N. Engl. J. Med.* **377**, 111–121 (2017). doi: 10.1056/NEJMoa1701719; pmid: 28636844
81. A. M. Brunner *et al*., Risk and timing of cardiovascular death among patients with myelodysplastic syndromes. *Blood Adv* **1**, 2032–2040 (2017). doi: 10.1182/bloodadvances.2017010165; pmid: 29296849
82. L. Dorsheimer *et al*., Association of Mutations Contributing to Clonal Hematopoiesis With Prognosis in Chronic Ischemic Heart Failure. *JAMA Cardiol.* **4**, 25–33 (2019). doi: 10.1001/jamacardio.2018.3965; pmid: 30566180
83. O. Wolach *et al*., Increased neutrophil extracellular trap formation promotes thrombosis in myeloproliferative neoplasms. *Sci. Transl. Med.* **10**, eaan8292 (2018). doi: 10.1126/scitranslmed.aan8292; pmid: 29643232
84. K. V. Patel, L. Ferrucci, W. B. Ershler, D. L. Longo, J. M. Guralnik, Red blood cell distribution width and the risk of death in middle-aged and older adults. *Arch. Intern. Med.* **169**, 515–523 (2009). doi: 10.1001/archinternmed.2009.11; pmid: 19273783
85. S. Horvath, K. Raj, DNA methylation-based biomarkers and the epigenetic clock theory of ageing. *Nat. Rev. Genet.* **19**, 371–384 (2018). doi: 10.1038/s41576-018-0004-3; pmid: 29643443
86. S. Haitjema *et al*., Loss of Y Chromosome in Blood Is Associated With Major Cardiovascular Events During Follow-Up in Men After Carotid Endarterectomy. *Circ Cardiovasc Genet* **10**, e001544 (2017). doi: 10.1161/CIRCGENETICS.116.001544; pmid: 28768751
87. J. J. Fuster *et al*., Clonal hematopoiesis associated with TET2 deficiency accelerates atherosclerosis development in mice. *Science* **355**, 842–847 (2017). doi: 10.1126/science.aag1381; pmid: 28104796
88. S. Sano *et al*., CRISPR-Mediated Gene Editing to Assess the Roles of Tet2 and Dnmt3a in Clonal Hematopoiesis and Cardiovascular Disease. *Circ. Res.* **123**, 335–341 (2018). doi: 10.1161/CIRCRESAHA.118.313225; pmid: 29728415
89. S. Sano *et al*., Tet2-Mediated Clonal Hematopoiesis Accelerates Heart Failure Through a Mechanism Involving the IL-1β/NLRP3 Inflammasome. *J. Am. Coll. Cardiol.* **71**, 875–886 (2018). doi: 10.1016/j.jacc.2017.12.037; pmid: 29471939
90. W. Wang *et al*., Macrophage Inflammation, Erythrophagocytosis, and Accelerated Atherosclerosis in Jak2 ^{V617F} Mice. *Circ. Res.* **123**, e35–e47 (2018). doi: 10.1161/CIRCRESAHA.118.313283; pmid: 30571460
91. D. Wu *et al*., Glucose-regulated phosphorylation of TET2 by AMPK reveals a pathway linking diabetes to cancer. *Nature* **559**, 637–641 (2018). doi: 10.1038/s41586-018-0350-5; pmid: 30022161
92. Q. Zhang *et al*., Tet2 is required to resolve inflammation by recruiting Hdac2 to specifically repress IL-6. *Nature* **525**, 389–393 (2015). doi: 10.1038/nature15252; pmid: 26287468
93. A. H. Cull, B. Snetsinger, R. Buckstein, R. A. Wells, M. J. Rauh, Tet2 restrains inflammatory gene expression in macrophages. *Exp. Hematol.* **55**, 56–70.e13 (2017). doi: 10.1016/j.exphem.2017.08.001; pmid: 28826859
94. P. Natarajan, S. Jaiswal, S. Kathiresan, Clonal Hematopoiesis: Somatic Mutations in Blood Cells and Atherosclerosis. *Circ Genom Precis Med* **11**, e001926 (2018). doi: 10.1161/CIRCGEN.118.001926; pmid: 29987111
95. C. Leoni *et al*., *Dnmt3a* restrains mast cell inflammatory responses. *Proc. Natl. Acad. Sci. U.S.A.* **114**, E1490–E1499 (2017). doi: 10.1073/pnas.1616420114; pmid: 28167789
96. M. Frick *et al*., Role of donor clonal hematopoiesis in allogeneic hematopoietic stem-cell transplantation. *J. Clin. Oncol.* **37**, 375–385 (2019). doi: 10.1200/JCO.2018.79.2184; pmid: 30403573
97. J. A. Fraietta *et al*., Disruption of TET2 promotes the therapeutic efficacy of CD19-targeted T cells. *Nature* **558**, 307–312 (2018). doi: 10.1038/s41586-018-0178-z; pmid: 29849141
98. C. Franceschi, J. Campisi, Chronic inflammation (inflammaging) and its potential contribution to age-associated diseases. *J. Gerontol. A Biol. Sci. Med. Sci.* **69** (suppl. 1), S4–S9 (2014). doi: 10.1093/gerona/glu057; pmid: 24833586

ACKNOWLEDGMENTS

Funding: S.J. is supported by the Burroughs Wellcome Fund, Evans Foundation, Ludwig Center for Cancer Stem Cell Research, and Leducq Foundation. B.L.E. is an investigator of the Howard Hughes Medical Institute and received funding from the NIH (P01CA066996, P50CA206963, and R01HL082945). B.L.E. has also received research funding from the biopharmaceutical company Celgene and from the DEERFIELD Foundation.
Competing interests: S.J. and B.L.E. have received consulting fees from GRAIL, a company developing methods for early detection of cancer. S.J. and B.L.E. are inventors on patent applications filed by Partners Healthcare that are related to risk assessment of cardiovascular disease and therapeutic interventions in individuals with clonal hematopoiesis.

10.1126/science.aan4673

REVIEW SUMMARY

MICROBIOLOGY

Microbiota and the social brain

Eoin Sherwin, Seth R. Bordenstein, John L. Quinn, Timothy G. Dinan, John F. Cryan*

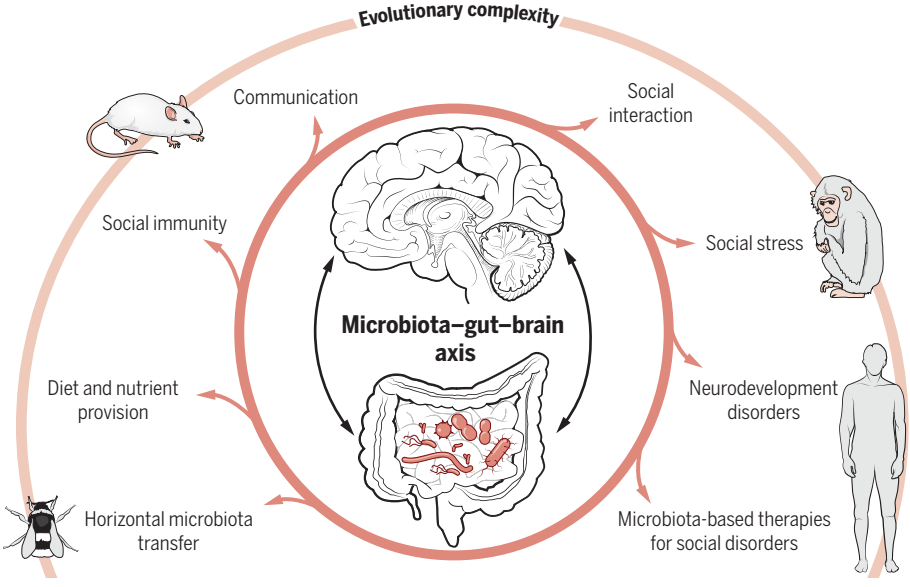
BACKGROUND: Increasingly, it is recognized that the microbes resident in the gastrointestinal tract can influence brain physiology and behavior. Research has shown that the gastrointestinal microbiota can signal to the brain via a diverse set of pathways, including immune activation, production of microbial metabolites and peptides, activation of the vagus nerve, and production of various neurotransmitters and neuromodulators in the gut itself. Collectively, this bidirectional pathway is known as the microbiota-gut-brain axis. In the absence of a microbiota, germ-free and antibiotic-treated mice exhibit alterations to several central physiological processes such as neurotransmitter turnover, neuroinflammation, neurogenesis, and neuronal morphology. Perhaps as a result of these neurological alterations, the behavior of rodents lacking a microbiota—especially social behavior—is remarkably different from that of rodents colonized with bacteria. Conversely, supplementation of animals with certain beneficial live bacteria (e.g., *Bifidobacterium* and *Lactobacillus*) can lead to notable improvements in social behavior both in early life and in adulthood. Collectively, these results suggest that microbial signals are important for healthy neurodevelopment and programming of social behaviors in the brain. Although research on the functional and ecological implications of the gut microbiota in natural populations is growing, from an evolutionary perspective it remains unclear why and when relationships between microbes and the social brain arose. We propose that a trans-species analysis may aid in our understanding of human sociability.

ADVANCES: Sociability comprises a complex range of interactive behaviors that can be cooperative, neutral, or antagonistic. Across the animal kingdom, the level of sociability an animal displays is variable; some are highly social (e.g., primates, termites, and honey bees), living within cooperative communities, whereas others have a mostly solitary existence (e.g., bears). Consequently, although studies on germ-free and antibiotic-treated animals have yielded insights into how the microbiota may influence social behaviors, they are perhaps too reductionist to fully appreciate the complex relationship between symbiotic bacteria in the gastrointestinal tract and host sociability when considering a broader zoological perspective. Some social interactions have evolved to facilitate horizontal transmission of microbiota. Observations across both invertebrate and vertebrate species suggest that factors such as diet and immunity generate selection pressures that drive the relationship between microbiota and social behavior. Although microbiota may influence behaviors endogenously through regulation of the gut-brain axis, some animal species may have evolved to use symbiotic bacteria exogenously to mediate communication between members of the same species. Hyenas, for example, produce an odorous paste from their scent glands that contains fermentative bacteria that is suggested to facilitate social cohesion among conspecifics. This complex relationship between animals and microbiota raises the hypothesis that microbes may have influenced the evolution of the social brain and behavior as a means to propagate their own genetic material.

ON OUR WEBSITE

Read the full article at http://dx.doi.org/10.1126/science.aar2016

OUTLOOK: Understanding the factors that affect the development and programming of social behaviors across the animal kingdom is important not only in terms of rethinking the evolution of brain physiology and behavior, but also in terms of providing greater insight into disorders of the social brain in humans [including autism spectrum disorders (ASDs), social phobia, and schizophrenia]. Evidence for a link between the microbiota and these conditions is growing, and preclinical and emerging clinical data raise the hypothesis that targeting the microbiota through dietary or live biotherapeutic interventions can improve the associated behavioral symptoms in such neurodevelopmental disorders. Larger clinical trials are required to confirm the efficacy of such interventions before they are recognized as a first-line treatment for neurodevelopmental disorders. Although such connections between gut bacteria and neurodevelopmental disorders are currently an intriguing area of research, any role for the microbiota in the evolution of social behaviors in animals does not supersede other contributing factors. Rather, it adds an additional perspective on how these complex behaviors arose. ■



The relationship between the microbiota-gut-brain axis and social behavior. The bidirectional pathway between the gut microbiota and the central nervous system, the microbiota-gut-brain axis, influences various complex aspects of social behavior across the animal kingdom. Some animals have evolved their own unique relationship with their gut microbiota that may assist them in interacting with conspecifics. The relationship between the gut microbiota and social behavior may help to explain social deficits observed in conditions such as autism spectrum disorders (ASDs) and could potentially lead to the development of new therapies for such conditions.

The list of author affiliations is available in the full article online.
*Corresponding author. Email: j.cryan@ucc.ie
Cite this article as E. Sherwin *et al.*, *Science* **366**, eaar2016 (2019). DOI: 10.1126/science.aar2016

REVIEW

MICROBIOLOGY

Microbiota and the social brain

Eoin Sherwin[1], Seth R. Bordenstein[2], John L. Quinn[3], Timothy G. Dinan[1,4], John F. Cryan[1,5]*

Sociability can facilitate mutually beneficial outcomes such as division of labor, cooperative care, and increased immunity, but sociability can also promote negative outcomes, including aggression and coercion. Accumulating evidence suggests that symbiotic microorganisms, specifically the microbiota that reside within the gastrointestinal system, may influence neurodevelopment and programming of social behaviors across diverse animal species. This relationship between host and microbes hints that host-microbiota interactions may have influenced the evolution of social behaviors. Indeed, the gastrointestinal microbiota is used by certain species as a means to facilitate communication among conspecifics. Further understanding of how microbiota influence the brain in nature may be helpful for elucidating the causal mechanisms underlying sociability and for generating new therapeutic strategies for social disorders in humans, such as autism spectrum disorders (ASDs).

In 1973, Konrad Lorenz, Niko Tinbergen, and Karl von Frisch won the Nobel Prize for their groundbreaking research concerning the genetic origin, development, and elicitation of social behavior patterns in mammals. Their work provided a foundation for assessing the various intrinsic and extrinsic factors that affect social behavior. Enormous advances in understanding behavior have since been made, and social behavior in particular has grown to be one of the most intriguing and complex fields in organismal biology research (Fig. 1).

Social behavior can be defined as a behavior that is observed only when animals occur in a group. Some of these behaviors, such as cooperation, shared risk, empathy, and interdependence, are beneficial; others, such as conflict, dominance, and coercion, are costly (*1*). An understanding of the intrinsic and extrinsic factors that regulate social interactions is important for unraveling how individuals and populations thrive, for determining why some species of animals have evolved to be more sociable than others, and for elucidating the underlying etiology of social behavior disorders (*2*).

A new appreciation of host-microbe interactions has led to unprecedented focus on the microbial world in animals, both invertebrates (e.g., termites, honey bees, wasps) and vertebrates (birds, hyenas, humans). Pioneering research has identified influences of the gastrointestinal microbiota on health, including immunity, metabolism, cardiovascular function, hormonal production and secretion, reproduction, and longevity (*3*–*5*). The microbiota also seems to play a role in neurodevelopment from early life to adulthood and influences neurological processes such as neurotransmission, neuroinflammation, and behavior throughout an animal's lifespan (*6*–*9*). Microbe-derived signals may directly or indirectly alter brain function (*10*), and because animals evolved in a microbial world, these signals may have influenced animal brains throughout evolution.

Emerging research is now conceptualizing animals as "holobionts": dynamic ecosystems, comprising a host and its associated microorganisms, that can vary with time, localization, and function (*11*–*13*). Collectively, the host and microbial genomes of a holobiont are termed a hologenome, and variation in the hologenome caused by changes in the host and/or microbes may affect phenotypes that may be subject to natural selection (*11*). In some instances, this conceptualization may offer an integrative paradigm for explaining the evolution of social behaviors. Microbes influence host nervous systems (*8*) and are implicated in determining social cues in animals such as hyenas, mice, and fruitflies (*14*–*16*). Indeed, microbe-induced increases in social interactions can in principle facilitate the spread of microbes between hosts (*17*). Reciprocally, social organization and behavior may influence the microbiota composition within a group of animals (*18*). Therefore, the microbiota and social behavior are intertwined across the animal kingdom, and this has implications for how host-microbiota relationships may have evolved (*12*) as well as for the pathogenesis of human disorders of social behavior. In this review, we summarize the proposed mechanisms underlying links between the gut microbiota and the social brain, and describe the diversity of such connections across the animal kingdom. These links may help to explain why the microbiota is implicated in social disorders and how it can be targeted to influence brain health.

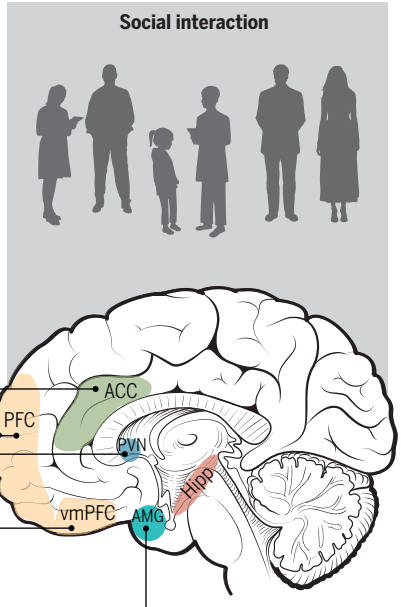
Mechanisms of microbiota-gut-brain communication

The concept that gut bacteria may influence brain physiology and behavior has existed for a long time. In 1910, the English physician George Porter Phillips proposed that major depression could be treated by the administration of a gelatin-whey formulation containing lactic acid bacteria (*19*). Currently evidence is accumulating that many behavioral responses observed across the animal kingdom might be regulated by the gut microbiota at various stages of an animal's life (Box 1). Within this paradigm, there is a growing emphasis on elucidating the mechanisms by which enteric bacteria communicate with the brain (Fig. 2). Such efforts are still in their infancy and are heavily focused on laboratory rodents. Nonetheless, a number of pathways of communication are particularly relevant to microbial influences on social behavior. These include activation of the vagus nerve, the production of microbial metabolites such as short-chain fatty acids (SCFAs) and neurotransmitters, the immune system, and sensory pathways such as the olfactory system (*8*).

Vagus nerve

The vagus nerve represents the main neural pathway connecting the gastrointestinal tract to the nucleus of the solitary tract (a cluster of afferent nerve fibers from the periphery that projects to regions of the neocortex such as the hypothalamus) in the brainstem in mammals (*20*). The nerve does not directly interact with the gut microbiota, although it may sense microbial signals through the release of various bacterial metabolites or through microbiota-mediated modulation of enteroendocrine cells in the gut epithelium (*21*). Indeed, vagal afferents have recently been shown to form synaptic connections with enteroendocrine cells in the gut, which facilitates the communication of nutritional signals to the brain via glutamatergic neurotransmission (*22*). Vagal nerve fibers are enriched with receptors such as 5-HT3, Toll-like receptor 4 (TLR4), free fatty acid receptors (FFARs), and gut peptide receptors; thus, they are ideally placed to transmit signals from the gut lumen to the brain (*21*). There is even preclinical evidence that the vagus nerve is capable of transporting proteins from the gut to the brain. For instance, in rats (*Rattus norvegicus*), α-synuclein, which forms aggregates in the brain in Parkinson's disease, was localized within the gastrointestinal system and transported from the gut to the brain via axonal transport by neurons contained

[1]APC Microbiome Ireland, University College Cork, Cork, Ireland. [2]Department of Biological Sciences, Vanderbilt Microbiome Initiative, Vanderbilt University, Nashville, TN, USA. [3]School of Biological, Earth and Environmental Sciences, University College Cork, Cork, Ireland. [4]Department of Psychiatry and Neurobehavioral Sciences, University College Cork, Cork, Ireland. [5]Department of Anatomy and Neuroscience, University College Cork, Cork, Ireland.
*Corresponding author. Email: j.cryan@ucc.ie



Anterior cingulate cortex (ACC)
This brain region functions in the detection and valuation of social processes such as interactions with dominant males and females in primates, and decision-making games in humans.

Prefrontal cortex (PFC)
In humans, this brain region is activated in response to various social cognitive tasks such as empathy, moral decision making, and judging the mental states of others. In rodents, stimulation of excitatory neurons abolishes social exploration and preference.

Paraventricular nucleus of the hypothalamus (PVN)
Magnocellular neurons of the PVN produce the neuropeptide oxytocin. Oxytocin is secreted to brain regions involved in sociability and social cognition, such as the ventral tegmental area and PFC. Reduced levels of oxytocin are documented in autism.

Ventromedial prefrontal cortex (vmPFC)
Lesions to this part of PFC result in social isolation and apathy in humans. The vmPFC is also important in the learning of cues that predict social reward. Children with ASD display reduced vmPFC activation in response to social reward.

Amygdala (AMG)
Amygdalar volume correlates with the size and complexity of social networks in humans. This brain region functions in the analysis of social situations. Individuals with autism demonstrate reduced activation of this brain region in response to social judgment tasks.

Fig. 1. Social behavior is governed by multiple interconnected limbic brain regions. Preclinical and clinical imaging studies have helped delineate the neurocircuitry underlying social behavior in humans and other mammals. Social interaction is governed by several subcortical forebrain structures such as the prefrontal cortex (PFC), anterior cingulate cortex (ACC), amygdala (AMG), hippocampus (Hipp), and hypothalamus (paraventricular nucleus, PVN), which form part of an integral interconnected network to facilitate this complex behavior. Damage or dysfunction to any one of these brain regions can give rise to perturbations in social behavior. Indeed, the neurobiology of regions such as the AMG and PFC have been shown to be altered in disorders of the social brain such as autism spectrum disorders (ASDs).

within the vagus nerve (*23*). Whether this influences the pathology and neuroinflammation observed in Parkinson's disease is unknown. However, there is a growing body of observational data in humans, from Danish and Swedish healthcare registries, that demonstrates an association between vagotomy (the surgical denervation of the vagus nerve) and a reduced risk for the development of Parkinson's disease (*24*).

Perhaps the most striking observation regarding the role of the vagus nerve in the microbiota-gut-brain axis comes from vagotomy studies in mice (*Mus musculus*). For instance, the ability of the bacterium *Lactobacillus rhamnosus* JB-1 to modulate anxiety-like behavior and γ-aminobutyric acid (GABA)–mediated neurotransmission in mice was lost after vagotomy (*25*). Similarly, the anxiolytic-like effects of the bacterium *Bifidobacterium longum* NCC3001 were absent in mice that underwent vagotomy (*26*). Moreover, *Lactobacillus reuteri*, a probiotic (live bacteria that when consumed confer health benefits to the host), increased the central expression and secretion of oxytocin (a hormone that functions in mammalian pair-bonding and is implicated in the neurobiological alterations reported to occur in ASDs) in mice, which was abrogated after vagotomy (*17*, *27*). However, not all microbial signals to the brain are mediated by the vagus nerve. Anxiety-like behavior in mice induced by a mild gastrointestinal infection was evident after vagotomy, which indicates that other biological pathways (some of which are known to be influenced by the microbiota) can mediate the anxiogenic effects of gastrointestinal infection (*28*).

Microbial metabolites

Gut microbiota are capable of producing a plethora of metabolites such as volatile carboxylic acids, esters, neurotransmitters (e.g., serotonin), and various fatty acids, some of which are implicated in influencing brain physiology and behavior. In vitro studies demonstrated that certain bacteria are capable of producing neurotransmitters such as noradrenaline, dopamine, and GABA (*29*–*31*). However, whether these gut-derived neurotransmitters are capable of reaching the central nervous system (CNS) to elicit an effect on their cognate receptors is unknown and unlikely considering their short half-lives and inability to cross the blood-brain barrier. The gut microbiota has indirectly been shown to influence serotonergic neurotransmission by regulating the availability of its precursor, tryptophan. Circulating tryptophan concentrations were found to be higher in male germ-free mice compared to controls with an intestinal microbiota (*32*). This corresponded with an increase in hippocampal serotonin and its metabolite, 5-hydroxy-indole acetic acid (*32*). Whether this has any bearing on the social deficits observed in these animals is unknown and requires further investigation.

Gut bacteria produce various SCFA metabolites such as butyrate, propionate, acetate, and valerate. These small molecules can regulate various physiological functions through their cognate FFARs. However, they may also mediate epigenetic modification through their histone deacetylase properties. FFARs are expressed on the vagus nerve, which partially mediates the effects of SCFAs. SCFAs have also been shown to influence certain central physiological processes. For instance, administration of a mixture of acetate, propionate, and butyrate was capable of restoring the morphological deficits of microglia (CNS-resident immune cells) that are observed in germ-free mice (*33*) and reversed the behavioral and physiological effects of chronic stress in mice (*34*). Moreover, SCFAs may influence the production of neurotransmitters in the brain through regulating the expression of enzymes involved in their biosynthesis. Administration of propionate and butyrate to PC12 cells (rat neuroblasts that differentiate into neuron-like cells) in vitro increased the expression of tyrosine hydroxylase, the rate-limiting enzyme in noradrenaline and dopamine synthesis (*35*). However, it is not clear whether these microbial metabolites are capable of regulating neurotransmission in vivo. Indeed, more evidence is needed to determine the extent to which physiologically relevant concentrations of SCFAs produced by the gut microbiota are capable of reaching the brain because they have short half-lives (25 min to 3 hours). To date, many studies investigating the effect of exogenous SCFA administration on brain physiology and behavior typically use concentrations that far exceed what is microbially derived (*36*).

Immune mechanisms

The immune system, by protecting the host against invading pathogens and internal damage, is fundamental for the survival of all species. Immunity also serves a critical role in mediating communication between the gut microbiota and the brain. The gut microbiota may influence the immune system locally at sites such as Peyer's patches (lymphatic nodules

Box 1. Modeling behavior and microbiota dysregulation.

Germ-free mice are completely devoid of microorganisms in and around their body and are raised in sterile isolator units to prevent their exposure to various bacteria, viruses, and fungi. In the absence of a microbiota, germ-free mice displayed deficits in social recognition and social cognition (*17*, *108*, *130*). Post-weaning reconstitution with gut microbiota restored the preference to interact with a conspecific mouse over an object or an empty chamber, but not the ability to discriminate between an unknown and a familiar mouse (*130*). These observations suggest that some facets of social behavior are amenable to manipulation by the microbiota, whereas others are not. However, in a separate study in germ-free mice, an increase in sociability and social cognition was observed in the absence of a gastrointestinal microbiota, contradicting other reports of decreased social behavior (*17*, *130*, *131*). Given that the strain of mouse and the animal supplier were the same between the studies observing a decrease (*130*) and an increase (*131*) in the sociability of germ-free mice, it is difficult to identify any discernible cause for the contrasting behaviors.

Despite these discrepancies, studies in germ-free mice have yielded insights into how gut bacteria influence brain physiology and behavior, with the amygdala being a brain region that is sensitive to microbiota manipulation (*8*, *25*, *132*, *133*). Transcriptional pathways linked to neuronal activation in the amygdala were increased in germ-free mice, indicating that the functionality of this brain region is altered in the absence of a microbiota (*133*). Furthermore, the expression of microRNAs linked to anxiety, stress, and the regulation of neurotrophins in the amygdala was affected in these animals and was somewhat restored after reconstitution with microbiota (*133*). In addition, the morphology of neurons within the amygdala of germ-free mice was altered, with an increase observed in the overall size of the various amygdalar subnuclei (*133*).

The use of antibiotics to deplete the microbiota has also been a successful strategy in unraveling the role of the microbiota in social behavior, with deficits observed in rodents after antibiotic administration from the adolescent period through to adulthood (*134*). Social recognition and cognition in mice were also affected after antibiotic administration (*135*). This effect of antibiotics on social behavior is not specific to rodents; a mixture of antibiotics also reduced social cohesion in zebrafish (*Danio rerio*) (*136*). Although studies using antibiotics have been beneficial in demonstrating a potential role for the gut microbiota in regulating social behavior, there are instances when this class of drug can facilitate sociability. The mechanism by which antibiotic administration modulates social behavior may be dependent on several variables such as preexisting gastrointestinal inflammation, baseline microbiota composition, diet, and stress perception. In invertebrate species, antibiotics can also affect cooperative behaviors. For example, diet-dependent mating of fruitflies (*Drosophila melanogaster*) was ablated after antibiotic administration but was subsequently reversed after supplementation with the gut bacterium *Lactobacillus plantarum* (*137*, *138*).

present in the small intestine that monitor gastrointestinal bacterial populations) or mesenteric lymph nodes. However, bacteria can also release various immune agonists such as lipopolysaccharide (LPS) and peptidoglycan (PGN) into blood circulation, where they might gain access to the brain. For example, neurons in the developing mouse brain express receptors that sense bacterial PGN (*37*). Germ-free and antibiotic-treated mice both display a reduction in the expression of several of the receptors that detect PGN in the striatum, which suggests that gene expression in the brain might be sensitive to microbiota manipulation. Moreover, knockdown of one of these PGN-sensing receptors, PGLYRP2 (PGN recognition protein 2), resulted in an increase in sociability in both male and female mice, indicating that loss of the ability to sense PGN results in behavioral changes to the host (*37*).

There is some preclinical evidence to suggest that the gut microbiota may influence development of the immune system, even in the CNS. For example, microglia isolated from the brains of germ-free mice display an immature phenotype compared with microglia from controls (*33*). Germ-free mouse–derived microglia demonstrated reduced activation in response to stimulation with bacterial LPS, with a concomitant reduction in the level of pro-inflammatory cytokine production (*33*). This observation was replicated after administration of antibiotics to mice and microglial functionality was restored in both scenarios after supplementation with SCFAs, which further corroborates a role for the gut microbiota in influencing the development of the immune system (*33*). The precise role that microglia play in social behavior is not completely understood. However, interference with microglial-neuronal communication (*38*) and depletion of microglia in early life (*39*) have both been shown to impair social behavior in both mice and rats.

Olfactory mechanisms

Olfaction, the ability to perceive odors, is fundamental to all animal life on Earth. It allows species to detect food and to sense potential toxins in the environment, and it also assists in social interaction. There is growing appreciation for an association between the gut microbiota and the brain through olfaction across the animal kingdom, with species such as hyenas, birds, mongooses, and locusts using gut microbial by-products such as volatile fatty acids and esters to mediate communication (see below). Preliminary evidence suggests that both enteric and environmental bacteria can influence olfaction. For example, when the gut microbiota of *Drosophila melanogaster* was manipulated early in life to contain *Lactobacillus* species, the fruitflies displayed an increased olfactory-guided preference toward *Lactobacillus*-enriched medium. Similarly, *D. melanogaster* in which *Acetobacter* dominated the gut microbiota displayed a preference toward *Acetobacter*-enriched medium (*40*). Such results suggest that the composition of the microbiota can influence olfactory-directed behavior in some animals.

Perhaps the most striking observations regarding a role for the gut microbiota in olfaction have arisen in germ-free mice. The olfactory epithelium of germ-free mice displays a thinning of the layer of ciliated epithelium relative to control animals (*41*). Moreover, expression of genes linked to olfactory receptor transduction and xenobiotic metabolism were all found to be reduced in the absence of microbiota. These transcriptional changes in olfactory transduction and metabolism corresponded with alterations in olfactory detection, with a greater activation of olfactory sensory neurons of germ-free mice in response to various odorants (*41*). Given that mice rely on olfaction to facilitate social interaction, alterations to the olfactory system in the absence of a gastrointestinal microbiota may contribute toward the behavioral deficits observed in germ-free mice.

Microbiota and social behavior

Sociability varies markedly among animal taxa and associates with different lifestyle behaviors (*42*) (Table 1). Sociability can also vary over time and within species. For example, most bears (Ursidae) are largely nonsocial for the majority of their life but highly social during breeding season. Whether the gut microbiota influences this spectrum of sociability in bears, and indeed in most species, and how this might act alongside other causal factors (such as genetics, development, and environmental factors) (Fig. 3) in the wild, remains very poorly understood. Nonetheless, evidence suggests that selection pressures over the course of evolutionary history may have influenced an association between gut bacteria and social behavior. Although some studies suggest that the gut microbiota can influence social behavior, other evidence suggests that social behavior allows horizontal transmission of microbes between conspecifics (transfer of

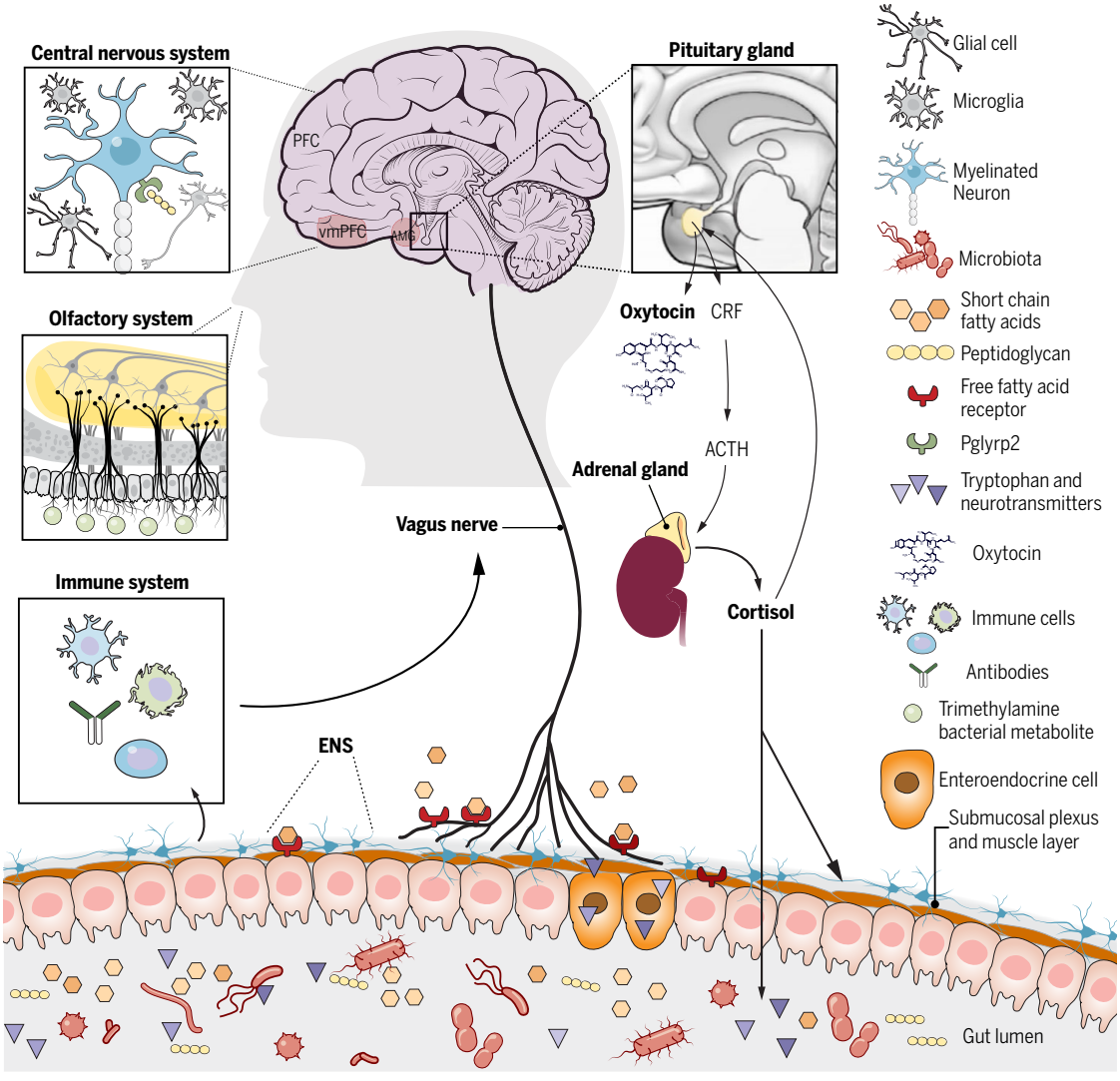


Fig. 2. Biological pathways underlying the regulation of social behavior by gut microbiota. There are numerous pathways through which the gut microbiota may influence behavioral processes such as sociability. Although additional unidentified metabolites and pathways connecting gut microbiota and the brain may exist, much focus has been on the bidirectional communication mediated via neural immune and metabolic routes. Bacterial fermentation and metabolism in the gastrointestinal tract lead to the production of metabolites such as neurotransmitters and short-chain fatty acids (SCFAs). SCFAs may be indirectly capable of influencing brain physiology and behavior through binding to and activating free fatty acid receptors (FFARs) expressed on the vagus nerve. Additionally, their ability to inhibit histone deacetylases locally within the gastrointestinal system may indirectly influence signaling of various mediators to the brain. Vagotomy studies have provided empirical evidence that the vagus nerve is an additional route through which the microbiota can communicate with the brain. The association between the gut microbiota and the immune system is another highly explored pathway through which commensal bacteria can exert their influence on brain physiology and behavior. Bacterial peptidoglycan expressed on the cell wall of Gram-negative and Gram-positive bacteria is capable of influencing the development of social behavior through the activation of specific pathogen recognition receptors, such as PGLYRP2, expressed in the brain (central nervous system inset). The microbiota can also influence social interaction through the excretion of metabolites that act as olfactory pheromones. Trimethylamine secreted in mouse urine can facilitate social cohesion of mouse conspecifics through the activation of olfactory receptors (olfactory system inset). Through these various pathways, the gut microbiota has been shown to modulate multiple central physiological processes such as neuroinflammation, serotonin turnover, myelination, and the secretion of the prosocial hormone oxytocin, thereby providing mechanistic insights into how gut bacteria influence social behavior. After exposure to a stressor, adrenocorticotropic hormone (ACTH) is released from the anterior pituitary gland (pituitary gland inset) and stimulates the release of stress hormone glucocorticoids (cortisol in humans, bears, ruminants, fish, and some rodents; corticosterone in rats, mice, birds, and reptiles). Glucocorticoids influence metabolism and mediate immune activation, among other systemwide effects. Exposure of commensal bacteria to glucocorticoids has been shown to decrease their relative abundance. Moreover, under conditions of chronic stress, increased release of glucocorticoids is associated with a reduction in gut microbiota diversity and richness.

microbiota across members of the same species that are not parent-child pairs), which may be evolutionarily beneficial for the microbiota. Thus, there appears to be a bidirectional relationship between the microbiota and social behaviors.

In addition to taking care when interpreting the direction of causality in correlational studies from the wild, caution is also advised when studying wild animals under captive conditions. Moving animals from the wild to captivity can cause substantial shifts in the composition of the gut microbiota in many animals, including bears (*43*), primates (*44*, *45*), horses (*46*), birds (*47*), and reptiles (*48*). This is to be expected, not just because the diets of wild animals are more diverse and can be difficult to acquire, but also because they are likely exposed to a more diverse environmental microbiota than captive animals. What this means for our ability to extrapolate findings from laboratory studies to animals in the wild, and especially to humans, remains to be clarified.

Sociability

Social interaction can influence the transmission of microbiota among conspecifics for many invertebrate species. For example, transmission of microbiota among termite (Blattodea) conspecifics can occur through social events such as coprophagia (consumption of feces) and proctodeal trophallaxis

Table 1. The relationship between microbiota and social behavior across the animal kingdom. Examining the microbiota composition of social and nonsocial species reveals that the same bacterial phyla are present in many animal species. However, different species use their associated microbiota in various ways to facilitate various forms of social interaction. For each animal, gut bacterial phyla are ranked in terms of the most to least abundant. For each study cited, the microbiota analysis was performed on fecal samples with the exception of the termite and honey bee studies, in which proctodeal segments were analyzed.

Species	Behavior	Ranking of dominant phyla in the microbiota	Relationship between social behavior and microbiota	Reference
Honey bee (*Apis mellifera*)	This eusocial invertebrate species exists within colonies consisting of a queen bee along with worker and soldier bees. Worker and soldier bees interact in a cooperative manner to ensure maintenance and survival of the colony.	1. Firmicutes 2. Actinobacteria 3. Proteobacteria	Social interaction facilitates horizontal transmission of microbiota that confers immune resistance against pathogens.	(*51*)
Desert locust (*Schistocerca gregaria*)	Desert locusts can shift from solitary to gregarious behavior depending on the environment and other factors. During the gregarious phase, locusts exist in large swarms, which aids in protecting them from predators.	Proteobacteria	Volatile fatty acids produced by the proteobacterium *Pantoea agglomerans* facilitate social cohesion of locust swarms.	(*66*, *140*)
Firebrat (*Thermobia domestica*)	Although they lack any known form of long-distance communication, firebrats gather around conspecific feces and former firebrat shelters. Moreover, these insects are capable of locating mates in their environment, presumably through odor detection.	1. Proteobacteria 2. Firmicutes	The bacterium *Enterobacter cloacae* present in the feces of firebrats mediates aggregation of conspecifics. The aggregation leads to the horizontal transmission of microbiota.	(*67*, *68*)
Termite (*Mastotermes darwiniensis*)	Termites are an eusocial insect species existing within a colony of multiple queens along with soldier and worker termites. Worker termites undertake the most work in the colony, cooperating in food storage as well as brood and nest maintenance.	1. Spirochaetes 2. Bacteroidetes 3. Firmicutes	Social interaction facilitates the horizontal transmission of microbiota that aids in food digestion.	(*62*, *63*)
Zebrafish (*Danio rerio*)	This species of fish aggregates into large groups, known as shoals. They can also exhibit aggression toward conspecifics, which typically arises as a result of territoriality. These fish can exhibit anxiety-like behavior when under threat from other animals.	1. Fusobacteria 2. Proteobacteria 3. Firmicutes	Modulation of the microbiota has been shown to influence shoaling behavior of zebrafish. Antibiotic treatment reduces shoaling behavior. Conversely, probiotic supplementation can increase shoaling behavior.	(*136*, *141*)
Zebra finch (*Taeniopygia guttata*)	The zebra finch is a social species that typically forms monogamous pair bonds during mating season. These birds tend to forage in groups for food rather than individually.	1. Firmicutes 2. Proteobacteria	Zebra finches have been shown to transmit bacteria through allogrooming that results in colonization of the gastrointestinal tract.	(*142*, *143*)

continued on next page

Species	Behavior	Ranking of dominant phyla in the microbiota	Relationship between social behavior and microbiota	Reference
Mouse (*Mus musculus*)	Rodents such as mice are social animals that prefer to exist within groups. Mice react aversely to social isolation, which is considered a stressor on the animal. Mice participate in cooperative behaviors such as grooming and play.	1. Firmicutes 2. Bacteroidetes 3. Proteobacteria 4. Actinobacteria	1. The microbial metabolite trimethylamine is excreted in the urine of mice and acts as a chemoattractant toward mouse conspecifics and a repellent of predators such as rats. 2. Mouse models of autism display microbiota alterations in addition to deficits in social behavior. 3. Germ-free and antibiotic-treated mice display deficits in social behavior that can be partly restored after reconstitution with microbiota.	(*15*, *17*, *109*, *130*, *134*)
Hyena (*Hyaena hyaena*)	Hyenas live in large social communities called clans. Females are typically the dominant sex in these communities and can dominate males and subordinate females. Social cognition is quite developed in hyenas, with animals capable of recognizing individual conspecifics and even distant relatives.	1. Firmicutes 2. Actinobacteria 3. Bacteroidetes 4. Fusobacteria	Fermentative bacteria in the scent glands produce volatile fatty acids that facilitate specific odors for social recognition among hyena conspecifics.	(*14*)
Meerkats (*Suricata suricatta*)	Meerkats are social animals existing within groups of up to 30 conspecifics. They engage in cooperative behaviors such as grooming and teaching of young to forage for food; females protect offspring of the dominant members of the group.	1. Firmicutes 2. Bacteroidetes 3. Proteobacteria 4. Actinobacteria 5. Fusobacteria	The anal gland of the meerkat contains volatile chemicals that correlate with the presence of various bacterial species. Genes related to lipid metabolism are expressed at higher amounts in the anal pouch of dominant males compared to subordinates, which may enhance communication.	(*71*)
Koala (*Phascolarctos cinereus*)	Koalas are typically asocial, with females and males existing in separate territories until breeding season. Although koalas tend to avoid aggressive interactions, antagonistic behaviors can occur, especially when one male occupies the territory of another male.	1. Bacteroidetes 2. Firmicutes	At weaning, the mother produces a liquid form of feces, called pap, which the offspring (joey) ingests. This pap contains a microbiota that aids in the digestion of eucalyptus, the primary food of the koala.	(*144*)
Gorilla (*Gorilla gorilla*)	This great ape species exists within communities typically comprising an alpha male, several females, and offspring. Multiple-male troops also exist. Gorillas engage in social behaviors such as grooming and playing.	1. Firmicutes 2. Proteobacteria 3. Bacteroidetes	Less social gorillas have a reduced risk of contracting the Ebola-Zaire virus. The composition of the gorilla gut microbiota can be influenced by interactions with gorilla conspecifics and sympatry with other ape species.	(*61*, *145*)

continued on next page

Species	Behavior	Ranking of dominant phyla in the microbiota	Relationship between social behavior and microbiota	Reference
Chimpanzee (*Pan troglodytes*)	Primates exhibit highly social behavior within large communities. Chimpanzees participate in cooperative behaviors such as grooming and play.	1. Proteobacteria 2. Firmicutes 3. Bacteroidetes	Social interaction among conspecifics results in the horizontal transmission of microbiota, resulting in the preservation of microbial diversity across generations.	(*61*, *146*)
Humans (*Homo sapiens*)	Humans are highly social animals existing within large and complex social communities. Social interaction in humans consists of a wide variety of intricate languages, values, rituals, and cultures. Humans interact on a daily basis to facilitate work, education, and rearing of offspring.	1. Firmicutes 2. Bacteroidetes 3. Actinobacteria 4. Proteobacteria	1. Humans occupying the same environment share similar gut microbiota characteristics relative to those who do not. 2. Kissing can facilitate the horizontal transmission of microbiota from one individual to another. 3. Alterations to the composition of the gut microbiota have been documented in individuals with deficits in sociability such as autism spectrum disorder.	(*53*, *100*, *147*)

(transfer of food, fluid, or nutrients from the rectum of one animal to the mouth of another) (*49*). Similarly, honey bees (*Apis mellifera*) acquire gut microbiota after adult emergence from the pupa via social interaction with worker bees (*50*). Social interaction also facilitated the acquisition of a homogeneous gut microbiota phylotype among various species of honey bees, in contrast to solitary bees that harbor a more diverse microbiota containing bacteria associated with the environment as well as potentially pathogenic genera (such as *Wolbachia*) (*51*). The presence of bacterial genera such as *Bifidobacterium* and *Lactobacillus* in the gut microbiota of social bees can promote the production of SCFAs, which may serve important biological roles in nutritional provision during periods when food is scarce (*51*). Indeed, supplementation of honey bees with a combination of *Bifidobacterium* and *Lactobacillus* increased eusocial cooperative behaviors observed as enhanced hive work output (*52*).

Most studies of invertebrate and vertebrate microbiota to date have used low-resolution 16*S* DNA sequencing. Therefore, it is premature to identify any association between microbiota composition in an animal and its social proclivities at a strain or functional level. In the future, higher sequencing resolution and functional output provided by a shotgun metagenomic approach may allow the field to address such associations in greater detail by identifying bacterial strains and their predicted metabolic by-products influenced by social interactions.

Social interaction can shape the microbiota of many primate species via the horizontal transfer of bacteria. For instance, kissing in humans (*Homo sapiens*) facilitates the transfer of oral microbiota (*53*). Indeed, married couples have greater gut microbial diversity and species richness than individuals living alone, which may aid in understanding the health benefits of marriage compared to solitary living (*54*, *55*). Long-term cohabitation results in the convergence of human gut microbiota that is evident even at a strain level. However, the directionality and routes of transmission of microbiota are largely unknown because of the difficulty in providing evidence for such factors in a species with complex social intricacies (*55*). Intriguingly, female humans exhibit increased microbiome similarity with members of their households and spouses compared with males who live in the same household, which suggests that sex may be an important determinant in the transmission of gut microbiota in humans (*55*).

In primates, the weaning of infant rhesus monkeys (*Macaca mulatta*) into social groups leads to a convergence of gut microbial community structure, with changes observed in *Prevotella*, *Blautia*, and *Ruminococcus* taxa (*56*). Among baboon (*Simia hamadryas*) conspecifics, social behaviors such as grooming result in the convergence of core gut microbial taxa (*57*). Moreover, it appears that position within a social network, and not just social behavior itself, is an important correlate in shared gut microbial composition for some species, such as the red-bellied lemur (*Eulemur rubriventer*) (*58*). In a separate study on lemurs, the density of grooming networks was shown to correlate with microbiota homogeneity, with more gregarious members of a social group harboring a more diverse microbiota presumably through increased grooming behavior and scent marking (*59*). Social interaction may also influence gut bacterial diversity and species richness within and across generations of chimpanzees (*60*).

Although sociability can lead to microbiota transmission between animals of the same species, some evidence suggests that transmission between different species can also occur. For example, primate species in the same geographic area share more similar gut microbiota than the same species living in geographic isolation. This highlights the potential impact of the environment on horizontal microbial transmission and differentiation of gut microbiota between species (*61*). Consequently, social interaction may enable the preservation of gut microbial diversity across large periods of time, which may have important implications for the evolution and ecology of a particular species' microbiota.

Although variation in gut microbiota seems to covary with sociability across some species, this is not always the case. For example, both honey bees and termites are colonial and highly social, but they have markedly different microbiotas. Honey bees harbor a rather simple microbiota consisting of six to nine bacterial phylotypes, with *Bifidobacterium* (Actinobacteria) and *Lactobacillus* (Firmicutes) as the predominant genera (*49*, *51*). By contrast, the termite microbiota consists of hundreds of bacterial species, predominantly characterized by the Spirochaetes phylum, with the Firmicutes and Bacteroidetes phyla also present (*62*, *63*). Indeed, many of the bacterial species identified in the gut microbiota of the termite are endemic to the host species, with diet likely to be

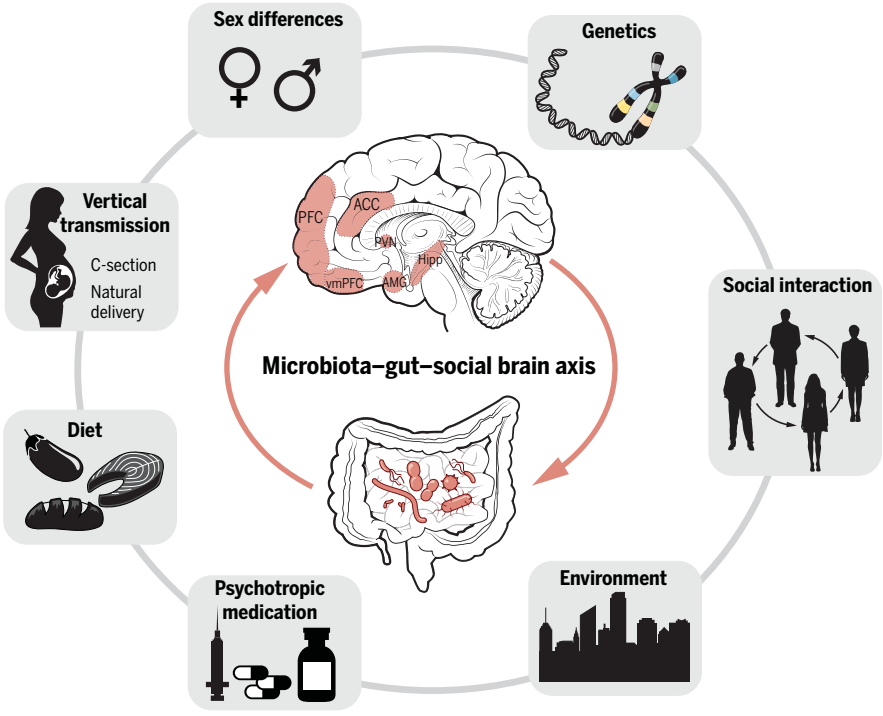


Fig. 3. The social brain is influenced by multiple biological and environmental factors. Social behavior is governed by multiple interconnected brain regions such as the hypothalamus, amygdala, cingulate cortex, and prefrontal cortex that are influenced by multiple extrinsic and intrinsic factors such as sex, genetic and epigenetic mechanisms, and the environment. Each of these factors may influence social behavior directly. However, they may also act in combination with one another to shape such behaviors. For instance, host genetics can influence the composition of the host gastrointestinal microbiota, thereby influencing the relative contribution of enteric bacteria toward social behavior. Moreover, extrinsic factors such as diet, psychotropic medication and environment can also affect the composition of the microbiota to indirectly modify behavior (*17*, *116*, *132*, *139*, *148*, *149*). PFC, prefrontal cortex; vmPFC, ventromedial prefrontal cortex; ACC, anterior cingulate cortex; AMG, amygdala; PVN, paraventricular nucleus of the hypothalamus.

an influential factor in shaping differences in microbiota composition (*62*, *64*, *65*). Thus, divergent evolutionary processes caused by distinct selective pressures could be at play, pointing to the need for considering phylogenetic influences when searching for microbial signatures of sociability.

Communication

For some invertebrate species, the gut microbiota can facilitate communication between conspecifics. In the gut of the desert locust (*Schistocerca gregaria*), the bacterium *Pantoea agglomerans* is responsible for the production of guaiacol, a volatile organic compound that serves as one of the main constituents in the locust swarming pheromone (*66*). Firebrats (*Thermobia domestica*; wingless hexapod insects) are known to aggregate with conspecifics in response to the presence of the bacterium *Enterobacter cloacae* found in their feces (*67*). Moreover, the aggregation of firebrats by this species of *Enterobacter* facilitates the horizontal transmission of this symbiont among conspecifics, thereby ensuring its survival and propagation in the host population (*68*). Volatile carboxylic acids produced by the gut microbiota of the cockroach species *Blattella germanica* mediate the aggregation of conspecifics (*69*). This was demonstrated through the inoculation of germ-free cockroaches with a cocktail of commensal bacterial species (*Enterococcus avium*, *Weissella cibaria*, *Pseudomonas japonica*, *Pseudomonas monteilii*, *Acinetobacter pittii*, *Acinetobacter* sp.), which resulted in the attraction of nymphs to their feces (*69*). The roles of the microbiota in mediating social communication in invertebrates is not limited to enteric bacteria; for example, certain gut fungi species in the bark beetle *Dendroctonus ponderosae* can also produce cohesion pheromones (*70*).

The microbiota may also assist in facilitating communication for some vertebrate species. For example, the microbial metabolite trimethylamine, a waste by-product of dietary choline metabolism by gut commensal bacteria, is expelled in the urine of numerous species. Remarkably, trimethylamine excreted in the urine of laboratory-raised male mice acts as a chemoattractant for other conspecifics (*15*). Moreover, the bacterial metabolite acts as a chemorepellent to rats, which are a natural predator to mice (*15*). Knockdown of TAAR5 (trace amine associated receptor 5) in mice abolished the prosocial properties of trimethylamine, thereby supporting a causal link between the gut microbiota and social interaction.

There is also emerging evidence of this phenomenon occurring in wild animals, although the inability to control for various confounding variables makes causality difficult to ascertain. For example, hyenas (from the family Hyaenidae) produce a paste from their scent glands that contains fermentative bacteria such as *Clostridium*, which synthesize volatile fatty acids (*14*). The strong odor associated with these volatile fatty acids supports the premise that hyena paste is used as a marker of territory or even social cohesion (*14*). Interestingly, comparisons between the volatile fatty acid profiles from the spotted hyena (*Crocuta crocuta*) and striped hyena (*Hyaena hyaena*) reveals marked differences, with a greater degree of variation in the highly social spotted hyena's paste compared to that of the less social striped hyena (*14*). Thus, the more diverse microbial-produced fatty acid profile produced by the spotted hyena may facilitate more complex interactions. Similar to the observations in hyenas, the anal pouch of wild meerkats (*Suricata suricatta*) contains bacterial genera such as *Corynebacterium*, *Anaerococcus*, and *Porphyromonas* (*71*). Bacterial genes encoding for lipid biogenesis were more prevalent in the anal pouch of dominant males compared with females and subordinates (*71*), pointing to the possibility that volatile lipids of microbial origin play a role in the olfactory communication of status within meerkat groups.

The microbiota of some species may function in the discrimination of conspecifics. For example, the uropygial gland of birds, which functions primarily to provide an oily substance for waterproofing feathers, is also considered to be the main odor source in this taxa; this oil harbors a unique microbiota containing fermentative bacteria that produce a wide array of volatile fatty acids, hydrocarbons, and esters (*47*, *72*). Although for a long time it was thought that most species of birds rely primarily on vocal communication, smell is increasingly realized to play a role. The mixture of volatile fatty acids and other chemicals allows birds such as starlings (*Sturnus unicolor*) to discriminate between the sexes. In addition, horses (*Equus ferus caballus*) are capable of distinguishing between conspecifics according to the smell of their feces, which is microbial in origin (*46*). Moreover, the anal gland of the Indian mongoose (*Herpestes auropunctatus*) produces volatile chemicals as a by-product of bacterial metabolism that facilitates conspecific recognition (*73*). Consequently, the microbiota may be an important mechanism of social recognition for many animals.

Table 2. Clinical and preclinical studies of microbiota-based interventions for the treatment of social behavior deficits. ASD, autism spectrum disorder; ATEC, Autism Treatment Evaluation Checklist; CFU, colony-forming units; PBS, phosphate-buffered saline; FOS, fructo-oligosaccharide; GABA, γ-aminobutyric acid; GOS, galacto-oligosaccharide; poly(I:C), polyinosinic:polycytidylic acid; Shank3, SH3 and multiple ankyrin repeat domains 3.

Subjects	Intervention	Behavioral outcomes	Biological outcomes	Reference
Clinical studies				
17 ASD subjects (4 to 16 years of age)	Daily oral *Lactobacillus plantarum* WCFS1 (4×10^{10} CFU per capsule) administration for 12 weeks	Anxiety and antisocial measures improved after probiotic supplementation, as assessed by the standardized developmental behavioral checklist	Increased relative abundance of *Lactobacillus* species and a decrease in *Clostridium* cluster XIVa in fecal samples	(*113*)
30 ASD subjects (19 boys and 11 girls; 5 to 9 years of age); 30 age- and gender-matched controls from ASD participants' families	Daily oral *L. rhamnosus*, *L. acidophilus*, and *Bifidobacterium longum* (500×10^6 CFU per sachet) for 3 months	Sociability, speech and language communication, and sensory awareness improved after treatment, as assessed by the ATEC checklist	Probiotic treatment improved gastrointestinal symptoms (abdominal pain, flatulence, constipation, etc.)	(*114*)
18 ASD subjects (7 to 17 years of age); 20 age- and gender-matched neurotypical controls	Oral dose of standard human microbiota cocktail (2.5×10^{12} CFU for 2 days followed by 2.5×10^9 CFU maintenance dose for 8 weeks)	Sociability, communication, and hyperactivity scores improved after treatment, as assessed by the Childhood Autism Rating Scale and Parent Global Impressions III scale	Gastrointestinal symptoms (i.e., constipation, abdominal pain, etc.) improved by 80% according to the Gastrointestinal Symptom Rating Scale	(*115*)
26 ASD subjects (4 to 11 years of age)	Oral dose of 1.8 g of Bimuno-GOS (B-GOS) or maltodextrin for 6 weeks combined with a gluten and casein exclusion diet	Antisocial behavior improved after treatment, as assessed by the ATEC checklist and the Autism Spectrum Quotient	Exclusionary diet improved gastrointestinal symptoms (i.e., abdominal pain); B-GOS consumption increased the relative abundance of *B. longum* in fecal samples and reduced urinary arachidonic acid	(*128*)
13 male ASD subjects (10 to 12 years of age)	Oral dose of 1.5 g of omega-3 fatty acids (eicosapentanoic acid and docosahexanoic acid) per day for 6 weeks	Hyperactive behavior improved after treatment, as assessed by the Aberrant Behavior Checklist	No measurements included in study	(*124*)
24 ASD subjects (3 to 8 years of age)	Oral dose of 1.3 g of omega-3 fatty acids (eicosapentanoic acid and docosahexanoic acid) for 12 weeks	Nonsignificant improvement in hyperactive behavior, as assessed by the Aberrant Behavior Checklist	Decreases in percentages of monosaturated and omega-9 fatty acids in blood plasma after treatment	(*125*)
Preclinical studies				
Male C57BL/6N mice from mothers administered either saline vehicle or poly(I:C) 20 mg/kg (induces in utero inflammation; environmental model of ASD) via the intraperitoneal cavity on gestational day 12.5; aged 6 weeks at the beginning of behavioral testing	1×10^{10} CFU of *Bacteroides fragilis* NCTC 9343 or vehicle was administered in sugar-free applesauce over standard rodent chow	Improvement in anxiety-like and stereotyped behaviors after probiotic treatment; treatment also improved ultrasonic vocalizations; sociability was unaffected by treatment	Treatment with *B. fragilis* ameliorated heightened intestinal permeability, intestinal inflammation, and alterations to the intestinal microbiota	(*109*)
Male C57BL6/J mice from mothers fed a high-fat diet (60% fat consistency; environmental model of ASD) before and during pregnancy until weaning of offspring were used for experimentation; mice were aged 7 to 12 weeks at the beginning of behavioral testing	1×10^8 CFU of *L. reuteri* MM4-1A or a PBS vehicle was administered in drinking water and changed daily	Treatment with *L. reuteri* improved deficits in social behavior; anxiety or stereotyped behaviors were unaffected by treatment	Treatment with *L. reuteri* increased hypothalamic oxytocin expression	(*17*)

continued on next page

Subjects	Intervention	Behavioral outcomes	Biological outcomes	Reference
Male C57BL/6J mice aged 7 weeks at the beginning of behavioral testing	FOS and GOS were administered separately or in combination in drinking water at a dose of 0.3 to 0.4 g per mouse per day	A combination of GOS and FOS reversed chronic social stress–induced deficits in social interaction, anxiety, and cognition	A combination of GOS and FOS protected gut microbiota composition against exposure to chronic stress; the combination of both prebiotics reduced circulating corticosterone and attenuated stress-induced pro-inflammatory cytokine production	(*88*)
Male and female *Shank3* (ASD risk gene; genetic model of ASD) knockout and wild-type mice aged 8 to 11 weeks at the beginning of behavioral testing	1×10^9 CFU of *L. reuteri* MM4-1A or a PBS vehicle was administered via oral gavage twice a week for 3 weeks	Treatment with *L. reuteri* improved deficits in social behavior in male but not female *Shank3* knockout mice; *L. reuteri* also reduced stereotyped behaviors	Treatment with *L. reuteri* increased the expression of $GABA_A$ receptor subunits in the prefrontal cortex and hippocampus in both male and female Shank3 mice; oxytocin expression in the hypothalamus was also increased after treatment	(*107*)
Male *Shank3* knockout (genetic model of ASD), oxytocin receptor knockout, germ-free, BTBR, and C57BL/6J mice exposed to in utero valproic acid (teratogenic drug; environmental model of ASD) on gestational day 12.5	1×10^8 CFU of *L. reuteri* MM4-1A or a PBS vehicle was administered in drinking water and changed daily	Treatment with *L. reuteri* improved deficits in social behavior in all animal models of ASD tested	Treatment with *L. reuteri* increased hypothalamic expression of oxytocin in all animal models tested	(*108*)

Social immunity

Group living offers a wide range of potential benefits, but it also comes with many costs, including increased exposure to infectious agents. Social gorillas, for example, are thought to be more susceptible to acquiring the Ebola-Zaire virus than solitary ones (*74*). Moreover, blood parasite levels increase with sociability among bird species (*75*). This increased threat of exposure to infectious agents with sociability is counterbalanced by increased microbiota diversity (*18*, *54*). This allows the immune system to function in cooperation with the microbiota to protect against harmful microorganisms (*76*, *77*). Immunity and host response to invading pathogens may also have an impact on the microbial underpinnings of social behavior, given that the immune system serves as a conduit between enteric commensal bacteria and the CNS through a variety of immune signaling mechanisms [reviewed in (*78*)]. For example, many species of birds invest considerable periods of time in cooperative maintenance behaviors, such as allogrooming (social grooming between members of the same species) (*79*), thus increasing the endoparasitic load within the gastrointestinal system (*80*). Intriguingly, colonization of the gut of some species of animals with helminths (parasitic worms) can confer increased microbial diversity while also beneficially modulating host immunity through their anti-inflammatory properties (*81*, *82*). In such instances, social behaviors (e.g., allogrooming) may be beneficial to the host and the intestinal microbiota because they improve microbial diversity and prevent the growth of pathogenic bacteria, potentially leading to improved overall fitness.

Similar to that observed in vertebrates, the host immune response of some invertebrates also appears to be an important selection pressure in promoting social behavior. For example, the acquisition of microbiota through social interaction is vital in protecting bumble bees (*Bombus terrestris*) against the highly virulent parasite *Crithidia bombi* (*83*). Moreover, antimicrobial compounds produced by eusocial bees (those that live in colonies), such as *Trigona carbonaria*, are orders of magnitude more effective than those produced by the asocial bee species *Amegilla asserta* (*84*). As bee colony size increases, so does genetic relatedness and antimicrobial strength among eusocial species. With increases in group sizes and genetic relatedness, increased prevalence and susceptibility to microbial pathogens likely acted as a selection pressure to drive the evolution of stronger antimicrobial activity in bees (*84*). Additionally, social immunity among ant species is an important defensive behavior that ensures the survival of individual members within the insect society. Garden ants (*Lasius neglectus*) have been shown to selectively groom broods that were infected with the fungus *Metarhizium brunneum* while also producing a formic acid–based chemical disinfectant that inhibits the growth of fungal spores on the broods (*85*). A carbohydrate-rich diet increased social immunity among garden ants while also reducing worker ant mortality rates when the colony was infected with *Metarhizium*, indicating that modulation of microbiota through diet can further improve this behavior (*86*).

Diet and stress

The positive effects of sociability on animal behavior are typically accompanied by a wide range of negative effects, including stress. Stress is an evolutionary adaption to protect animals in danger by mediating a fight-or-flight response. In the short term, stress responses are beneficial because they aid the survival of the animal. However, long-term exposure to stress can be detrimental to both physiological and behavioral health. The perception of stress is instigated not only in response to dangers in the environment but also after certain social interactions. By elevating glucocorticoid hormones, social stress can even affect the gut microbiota, observed as a reduction in the diversity of enteric bacteria, in addition to the many other physiological effects of stress (*87*, *88*). In the North American barn swallow (*Hirundo rustica erythrogaster*), for example, increased social interaction between the sexes during the mating season is associated with higher corticosterone levels and reduced gut microbial diversity (*89*). Moreover,

chronic exposure to social stress in mice also leads to a reduction in gut microbiota diversity (*88*). With decreases in the availability of salmon, densities of the normally asocial black bear (*Ursus americanus*) increase, which correlates with an elevation in circulating cortisol. An increase in social stress among black bears is likely to have deleterious effects on their microbiota through a reduction in nutritional intake, thereby affecting gut microbial diversity. Social stress–induced reductions in nutritional intake may have detrimental effects on bears during hibernation periods, for which the microbiota plays an important role in regulating lipid, bile acid, and glucose metabolism (*90*).

Social stress can lead to a decline in health and fertility and increase susceptibility to disease, thereby compromising the overall fitness of a species (*91*). In the case of carnivorous animals such as bears, solitary behavior may be beneficial to the gut microbiota because it promotes sufficient nutritional intake while minimizing cortisol levels, which has been shown to reduce gut bacterial diversity in other species (*88*). Although social interactions may be harmful to the gut microbiota through increased exposure to stress, they can also be beneficial. The balance between the beneficial and detrimental effects of social interaction on the gut microbiota appears to be largely relationship-dependent. However, environmental factors (i.e., availability of food) may also play a critical role.

Herbivorous or carnivorous diets and their subsequent effect on the composition of the gut microbiota may also have influenced the evolution of social behaviors in some species. In herbivores, the presence of microbes is vital for the digestion of plant-derived dietary components such as cellulose and hemicellulose (*92*). Such a diverse diet could have hypothetically driven the evolution of social interactions to facilitate the horizontal transfer of specialized microbiota among conspecifics to aid digestion (*92*, *93*). Although such a hypothesis may be difficult to assess in higher animals such as mammals, and is probably modest given the importance of other better-known selection pressures (such as predation, immune response to pathogens, or sexual competition), there is some evidence in invertebrate species to suggest that diet may have facilitated the acquisition of social behavior.

The cockroach (*Periplaneta americana*) harbors intracellular symbionts in addition to a gut microbial community, whereas the closely related but more social termite species contains only gastrointestinal microbiota (*94*). One particular nongastrointestinal bacterial symbiont, *Blattabacterium*, serves an important role in nutrient provision for the cockroach by synthesizing vitamins and amino acids through nitrogen fixation (*95*). Interestingly, this species of bacteria is either completely absent or has undergone genome shrinkage in termites (*94*), the functional loss of which is thought to be compensated for by having a diverse hindgut microbiota facilitated by the evolution of social behavior and greater transmission of microbiota among conspecifics (*95*). In support of this idea, the absence of *Blattabacterium* may have led to the evolution of social behaviors in termites to facilitate the reliable transmission of microbiota among conspecifics to enable the digestion of a complex lignocellulose diet (*95*). In support of this idea, limited transmission of microbiota has been observed among cockroach conspecifics, which harbor a gut microbiota community dominated by *Bacteroides*, *Paludibacter*, and *Parabacteroides* species (*49*, *95*). Conversely, the microbiota of the more social *Mastotermes darwiniensis* and *Heterotermes aureus* termite species is characterized by a high degree of homogeneity among conspecifics, suggesting horizontal transmission, with bacterial genera including *Tannerella*, *Clostridium*, *Treponema*, and Rikenellaceae being most abundant (*49*, *95*). Consequently, in some instances, selection of a social phenotype may allow for the preservation of certain host-environmental interactions (i.e., nutrient provision via microbiota) not only across conspecifics but across generations.

Social disorders

Given the complex, sometimes bidirectional effects of the microbiota and the social brain across the animal kingdom, it is perhaps not surprising that evidence for an important role of the microbiota in disorders of sociability in humans is accumulating. Deficits in social behavior manifest in several neuropsychiatric conditions such as ASDs, schizophrenia, social anxiety, and depression, with patients either incapable of interacting with others or withdrawing from social interaction (*8*). Because social interaction can be such a vital component of human mental health, altered behavior may have deleterious effects on overall fitness and mortality (*96*). Interestingly, several preclinical and clinical studies documented perturbations in the gastrointestinal microbiota (including reductions in bacterial diversity and reduced abundance of beneficial bacteria) among individuals with these neuropsychiatric disorders, and dysregulation may be linked with the behavioral symptoms observed (*17*, *88*, *97*–*99*). Analysis of the fecal microbiota of children with ASDs, for example, reveals profound alterations in microbial diversity, with losses in key bacterial taxa (such as *Bifidobacterium*) along with the presence of harmful strains within genera frequently associated with pathology, such as *Clostridium* and *Desulfovibrio* (*100*–*102*).

Clostridium perfringens strains isolated from the microbiota of children with ASDs were found to express the gene encoding β2 toxin, *cpb2*, to a greater extent than the same strain isolated from the microbiota of neurotypical children (*102*). This toxin is associated with various gastrointestinal diseases, which may help to explain the comorbid gastrointestinal symptoms (such as bloating, constipation, acid reflux, and diarrhea) that are frequently observed in ASD individuals. However, the etiology of this perturbed microbiota in ASDs is currently unknown and most likely reflects several biological, genetic, and environmental factors (*100*, *103*). For example, the mode of childbirth (vaginally or Caesarean section) and its influence on the vertical transmission of microbiota from mother to offspring may affect neurodevelopment. However, epidemiology studies vary, with some studies showing a modest relationship between mode of delivery and incidence of ASDs, psychosis, and attention deficit–hyperactivity disorder (ADHD) and others finding no relationship. In a study of ~2.7 million individuals, birth via Caesarean section was associated with a modest ~20% increase in the relative risk of an ASD diagnosis. However, this effect was not evident when a sub-analysis of sibling controls was added, implying that underlying familial factors such as genetics may be contributing (*104*). Nonetheless, more work is needed to understand whether there are long-term consequences of early-life microbiota disturbances for the social brain.

Diet confounds the interpretation of microbiota data from children with ASDs because many of them exhibit a stereotyped (persistent, repetitive, and inflexible) behavior pattern in their dietary intake and may avoid certain food types that benefit the microbiota. For example, prebiotics, such as inulin-rich foods, are indigestible dietary components metabolized by the gut microbiota that promote the growth of beneficial bacteria including the genera *Bifidobacterium* and *Lactobacillus*. Indeed, one clinical study observed that a large increase in the abundance of the genus *Cyanobacterium* in the fecal microbiota of several children with ASDs was anecdotally predicted by their dietary intake of chia seeds (*100*). Thus, the reported alterations to the composition of the microbiota of autistic individuals may simply be due to the absence of sufficient nutrient intake. Moreover, some psychotropic medications (such as the antipsychotic drug olanzapine) can negatively alter the microbiota composition, which represents an additional consideration when investigating links to microbiota in certain psychiatric conditions (*105*). Consequently, there is variable evidence of alterations to the microbiota in individuals with ASDs, with no consistent microbial signature that is representative of the

neurodevelopmental disorder. Despite this limitation, the clinical findings currently demonstrate that the microbiota is affected in conditions such as ASDs, and future studies with more patients (for statistical power) and appropriate controls may provide greater insights into any causative role for gut microbiota in such disorders.

Targeting the microbiota

Associations between microbiota and social disorders suggest that targeting the microbiota could ameliorate deficits in social behavior. Microbiota-based strategies have demonstrated the potential to alter social behavior in various preclinical models, with some preliminary evidence suggesting effects in humans (Table 2). Such strategies may have broad implications not only for the treatment of social brain disorders in humans, but also for the rest of the animal kingdom in terms of potentially reducing stress while in captivity, aiding in mating programs, and enhancing survival in the wild.

Probiotics

Although perturbations to the microbiota often negatively influence social behavior, modulation of gut bacteria through probiotic administration can have a beneficial effect. For example, mice derived from mothers on a high-fat diet have an altered microbiota composition (with notable reductions in several *Lactobacillus* species) and display a reduced ability to discriminate between a conspecific and an empty chamber, as well as a reduced ability to discriminate between a familiar and an unknown conspecific. These social deficits can be reversed after treatment with *Lactobacillus reuteri* (*17*), an effect that is linked to increased CNS expression of the prosocial hormone oxytocin, in the paraventricular nucleus of the hypothalamus and its secretion into blood circulation (*17*, *106*). Adult administration of *Lactobacillus reuteri* has been shown to improve social behavioral deficits in an oxytocin-dependent manner in multiple animal models of ASD [including in utero valproic acid exposure, the BTBR mouse model of ASD, oxytocin receptor knockout mouse, and genetic knockdown of the autism candidate gene *Shank3* (SH3 and multiple ankyrin repeat domains 3) in mice], further validating its preclinical efficacy and potential mechanism of action (*17*, *107*, *108*).

Other bacterial strains, such as *Bacteroides fragilis*, have efficacy in improving certain ASD-associated behaviors in the maternal immune activation mouse model of ASD (*109*). Interestingly, *Bacteroides fragilis* had little impact on social recognition or social cognitive processes in mice, demonstrating that the impact of microbiota on specific social behaviors may be strain-specific. Although *Bacteroides fragilis* is a commensal gut bacterium and influences human health through modulation of host immune responses and gastrointestinal development (from infancy to adulthood), it is also an opportunistic pathogen and is associated with an increased risk for gastrointestinal cancer and inflammatory bowel disease (*110*, *111*). Consequently, despite its efficacy in improving ASD-associated behavior in mice, the status of *Bacteroides fragilis* as a probiotic is hindered by its potential pathogenic effects.

Taken together, these preclinical observations must be interpreted with caution. *Lactobacillus* species have previously been effective in improving behavior preclinically in mice while having no observable effect when tested in healthy humans (*25*, *112*), possibly because the microbiota of a mouse differs considerably from that of a human. Consequently, the efficacy of probiotics to modify behavior established in preclinical studies of mice may not always align with clinical observations. Moreover, although there has been considerable development in assessing the efficacy of probiotics to ameliorate ASD-related behavior in preclinical models, clinical data are currently limited. In a small double-blind, randomized, placebo-controlled trial, the probiotic *Lactobacillus plantarum* WCSF1 was found to improve antisocial and anxiety behavior in children with ASDs, as assessed by parental rating of the standardized developmental behavioral checklist (*113*). However, the dropout rates from this study were quite high, which likely affected the statistical power of the results (*113*). In an open-label study, ASD behavior, as assessed by the autism treatment evaluation checklist, was improved in 30 children with ASDs after treatment with a probiotic cocktail comprising *Bifidobacterium longum*, *Lactobacillus acidophilus*, and *Lactobacillus rhamnosus* for 3 months (*114*). In a separate open-label study, children with ASDs treated with a standardized human microbiota cocktail displayed improvement in some of the associated behavioral and gastrointestinal symptoms (*115*). Although these clinical observations are promising, they must be interpreted with caution, especially considering that open-label investigations have a high risk of both selection and performance bias.

Diet and prebiotics

Dietary composition may also influence social behaviors through modulating the gut microbiota (*116*). Diets rich in sources of omega-3 polyunsaturated fatty acids (e.g., certain species of fish, walnuts, and soybeans) beneficially modulated gut microbial composition by increasing the relative abundance of beneficial bacteria such as *Bifidobacterium* and *Lactobacillus* species while also improving social interaction in rats, mice, and guinea pigs (*Cavia porcellus*) (*117*–*120*). Conversely, early-life dietary deficiency of omega-3 fatty acids led to deficits in social recognition in mice, highlighting the importance of diet in facilitating normal brain neurodevelopment and behavior (*120*). The mechanism by which omega-3 fatty acids modulate social behaviors has not been fully elucidated, and the relative contribution of their effects on microbiota versus host cellular oxidative stress and inflammation remain unclear (*121*–*123*). Moreover, it is unknown whether any of the potential beneficial effects of omega-3 fatty acids reported in small open-label clinical trials are due to their effects on the microbiota (*124*, *125*).

Diets can affect other aspects of social behavior. For example, a diet rich in fat and low in carbohydrates decreased aggression and promoted non-agonistic interactions in pigs (from the family *Suidae*) and nonhuman primates (*126*, *127*). Prebiotics also promote social behavior in some instances. The prebiotics galacto-oligosaccharide (GOS) and fructo-oligosaccharide (FOS) increased social interaction in chronically stressed mice, which was associated with alterations in gut microbiota composition and metabolite production (*88*). Specifically, ingestion of a FOS and GOS combination increased the relative abundance of the key bacterial genera *Akkermansia* and *Bacteroides* while also reducing the presence of potentially pathogenic genera such as *Desulfovibrio* (*88*). These changes were also associated with alterations in microbial metabolism, with increased cecal concentrations of acetate and propionate, a concomitant reduction in butyrate levels, and a reduction in circulating tryptophan concentrations (*88*). More recently, a combination of a gluten- and casein-free diet with the prebiotic Bimuno-GOS (B-GOS) resulted in an improvement in gastrointestinal and social behavior symptoms in a pilot study of children with ASDs, which was associated with an increase in the abundance of *Bifidobacterium longum* in fecal samples (*128*). However, the study did not investigate whether the increase in the abundance of this strain had any bearing on the behavioral changes observed. Although these small-scale clinical studies are certainly promising, interpreting their clinical importance is limited by their small sample size and experimental design. Appropriate statistically powered and double-blinded clinical studies are required to fully elucidate the clinical efficacy of any potential intervention for treating disorders of the social brain.

Conclusions and future perspectives

Many theories have been proposed to account for how behaviors such as sociability evolved and why animals exhibit these behaviors along a spectrum. For instance, the social brain theory posits that some animals, such as primates, evolved larger brains due to the cognitive

demands of social behavior (*129*). However, researchers of the social brain and other hypotheses rarely consider that microbial input may have facilitated, at least in some lineages, the evolution of sociability. Social behavior is a possible means to ensure the transmission of microbial symbionts from one animal to another, both within generations (horizontal transfer) and across generations (vertical transfer), to the benefit of the host animal and the microbes. This holobiont-level hypothesis is substantiated by evidence documenting how changes in gut microbiota composition can affect social behavior in laboratory animals and in some cases wild animals. Additionally, sociability can affect the microbiota both positively and negatively. Consequently, the impact of the microbiota on sociability and its neurobiological underpinnings has potentially enormous implications for ecology, evolution, and human biology. This association between microbiota and the CNS provides a biological framework to elucidate how complex behavioral patterns ranging from eusociability to asocial behaviors may have evolved across the animal kingdom. Moreover, it raises important considerations about the impact of certain lifestyle choices [such as diet, medication use (e.g., antibiotics), and relationships] on human health, while also helping to provide a greater understanding of the neurobiology underlying certain neuropsychiatric conditions and the potential development of future therapies. Although most attention has focused on the role of the gut microbiota, other host-microbiota interactions in different tissues (such as oral, skin, birth canal, etc.) may also contribute to social behaviors, and so it is important to examine the entire holobiont.

Expanding microbiome-sequencing analyses across the animal kingdom remains a major challenge but will allow for greater insight into how social behavior interacts with microbial symbionts within and across diverse ecosystems. It will also be important to identify commonalities in the mechanisms through which microbiota are transferred from one animal to another, so as to provide an evolutionary hologenomic framework explaining how symbiotic bacteria contribute to the spectrum of social behaviors observed throughout nature. Moreover, a greater emphasis is needed to establish causation through elucidating the functional pathways by which bacteria affect behaviors. To date, there has been an over-reliance on correlative associations between gut bacteria and behavior. If we are to ascertain how gut bacteria influence behaviors such as sociability, we must approach future studies with causal functionality as the primary objective. Finally, there is ample evidence that social behavior affects the composition of the microbiota, but the functional consequences of this on the social brain have yet to be elucidated. Such findings will provide insights into the evolution of social behavior and will also expand our understanding of disorders of the social brain.

REFERENCES AND NOTES

1. P. Mason, H. Shan, A valence-free definition of sociality as any violation of inter-individual independence. *Proc. R. Soc. B* **284**, 284 (2017). doi: 10.1098/rspb.2017.0948; pmid: 29118128
2. G. A. Matthews, K. M. Tye, Neural mechanisms of social homeostasis. *Ann. N.Y. Acad. Sci.* nyas.14016 (2019). doi: 10.1111/nyas.14016; pmid: 30875095
3. J. M. Brown, S. L. Hazen, Microbial modulation of cardiovascular disease. *Nat. Rev. Microbiol.* **16**, 171–181 (2018). doi: 10.1038/nrmicro.2017.149; pmid: 29307889
4. B. Han *et al*., Microbial Genetic Composition Tunes Host Longevity. *Cell* **169**, 1249–1262.e13 (2017). doi: 10.1016/j.cell.2017.05.036; pmid: 28622510
5. E. Patterson *et al*., Gut microbiota, obesity and diabetes. *Postgrad. Med. J.* **92**, 286–300 (2016). doi: 10.1136/postgradmedj-2015-133285; pmid: 26912499
6. J. A. Foster, K. A. McVey Neufeld, Gut-brain axis: How the microbiome influences anxiety and depression. *Trends Neurosci.* **36**, 305–312 (2013). doi: 10.1016/j.tins.2013.01.005; pmid: 23384445
7. M. Lyte, Microbial endocrinology: Host-microbiota neuroendocrine interactions influencing brain and behavior. *Gut Microbes* **5**, 381–389 (2014). doi: 10.4161/gmic.28682; pmid: 24690573
8. E. Sherwin, K. V. Sandhu, T. G. Dinan, J. F. Cryan, May the Force Be With You: The Light and Dark Sides of the Microbiota-Gut-Brain Axis in Neuropsychiatry. *CNS Drugs* **30**, 1019–1041 (2016). doi: 10.1007/s40263-016-0370-3; pmid: 27417321
9. G. L. Davidson, A. C. Cooke, C. N. Johnson, J. L. Quinn, The gut microbiome as a driver of individual variation in cognition and functional behaviour. *Philos. Trans. R. Soc. London Ser. B* **373**, 373 (2018). pmid: 30104431
10. R. M. Stilling, S. R. Bordenstein, T. G. Dinan, J. F. Cryan, Friends with social benefits: Host-microbe interactions as a driver of brain evolution and development? *Front. Cell. Infect. Microbiol.* **4**, 147 (2014). doi: 10.3389/fcimb.2014.00147; pmid: 25401092
11. I. Zilber-Rosenberg, E. Rosenberg, Role of microorganisms in the evolution of animals and plants: The hologenome theory of evolution. *FEMS Microbiol. Rev.* **32**, 723–735 (2008). doi: 10.1111/j.1574-6976.2008.00123.x; pmid: 18549407
12. J. D. Shropshire, S. R. Bordenstein, Speciation by Symbiosis: The Microbiome and Behavior. *mBio* **7**, e01785-15 (2016). doi: 10.1128/mBio.01785-15; pmid: 27034284
13. S. R. Bordenstein, K. R. Theis, Host Biology in Light of the Microbiome: Ten Principles of Holobionts and Hologenomes. *PLOS Biol.* **13**, e1002226 (2015). doi: 10.1371/journal.pbio.1002226; pmid: 26284777
14. K. R. Theis *et al*., Symbiotic bacteria appear to mediate hyena social odors. *Proc. Natl. Acad. Sci. U.S.A.* **110**, 19832–19837 (2013). doi: 10.1073/pnas.1306477110; pmid: 24218592
15. Q. Li *et al*., Synchronous evolution of an odor biosynthesis pathway and behavioral response. *Curr. Biol.* **23**, 11–20 (2013). doi: 10.1016/j.cub.2012.10.047; pmid: 23177478
16. M. E. Chafee *et al*., Decoupling of host-symbiont-phage coadaptations following transfer between insect species. *Genetics* **187**, 203–215 (2011). doi: 10.1534/genetics.110.120675; pmid: 20944019
17. S. A. Buffington *et al*., Microbial Reconstitution Reverses Maternal Diet-Induced Social and Synaptic Deficits in Offspring. *Cell* **165**, 1762–1775 (2016). doi: 10.1016/j.cell.2016.06.001; pmid: 27315483
18. J. Tung *et al*., Social networks predict gut microbiome composition in wild baboons. *eLife* **4**, e05224 (2015). doi: 10.7554/eLife.05224
19. J. G. P. Phillips, The Treatment of Melancholia by the Lactic Acid Bacillus. *J. Ment. Sci.* **56**, 422–430 (1910). doi: 10.1192/bjp.56.234.422
20. W. Han *et al*., A Neural Circuit for Gut-Induced Reward. *Cell* **175**, 665–678.e23 (2018). doi: 10.1016/j.cell.2018.08.049; pmid: 30245012
21. B. Bonaz, T. Bazin, S. Pellissier, The Vagus Nerve at the Interface of the Microbiota-Gut-Brain Axis. *Front. Neurosci.* **12**, 49 (2018). doi: 10.3389/fnins.2018.00049; pmid: 29467611
22. M. M. Kaelberer *et al*., A gut-brain neural circuit for nutrient sensory transduction. *Science* **361**, eaat5236 (2018). doi: 10.1126/science.aat5236; pmid: 30237325
23. S. Holmqvist *et al*., Direct evidence of Parkinson pathology spread from the gastrointestinal tract to the brain in rats. *Acta Neuropathol.* **128**, 805–820 (2014). doi: 10.1007/s00401-014-1343-6; pmid: 25296989
24. E. Svensson *et al*., Vagotomy and subsequent risk of Parkinson's disease. *Ann. Neurol.* **78**, 522–529 (2015). doi: 10.1002/ana.24448; pmid: 26031848
25. J. A. Bravo *et al*., Ingestion of Lactobacillus strain regulates emotional behavior and central GABA receptor expression in a mouse via the vagus nerve. *Proc. Natl. Acad. Sci. U.S.A.* **108**, 16050–16055 (2011). doi: 10.1073/pnas.1102999108; pmid: 21876150
26. P. Bercik *et al*., The anxiolytic effect of Bifidobacterium longum NCC3001 involves vagal pathways for gut-brain communication. *Neurogastroenterol. Motil.* **23**, 1132–1139 (2011). doi: 10.1111/j.1365-2982.2011.01796.x; pmid: 21988661
27. T. Poutahidis *et al*., Microbial symbionts accelerate wound healing via the neuropeptide hormone oxytocin. *PLOS ONE* **8**, e78898 (2013). doi: 10.1371/journal.pone.0078898; pmid: 24205344
28. P. Bercik *et al*., Chronic gastrointestinal inflammation induces anxiety-like behavior and alters central nervous system biochemistry in mice. *Gastroenterology* **139**, 2102–2112.e1 (2010). doi: 10.1053/j.gastro.2010.06.063; pmid: 20600016
29. A. Taj, N. Jamil, Bioconversion of Tyrosine and Tryptophan Derived Biogenic Amines by Neuropathogenic Bacteria. *Biomolecules* **8**, 10 (2018). doi: 10.3390/biom8010010; pmid: 29438351
30. V. V. Roshchina, New Trends and Perspectives in the Evolution of Neurotransmitters in Microbial, Plant, and Animal Cells. *Adv. Exp. Med. Biol.* **874**, 25–77 (2016). doi: 10.1007/978-3-319-20215-0_2; pmid: 26589213
31. T. M. Marques *et al*., Influence of GABA and GABA-producing Lactobacillus brevis DPC 6108 on the development of diabetes in a streptozotocin rat model. *Benef. Microbes* **7**, 409–420 (2016). doi: 10.3920/BM2015.0154; pmid: 27013462
32. G. Clarke *et al*., The microbiome-gut-brain axis during early life regulates the hippocampal serotonergic system in a sex-dependent manner. *Mol. Psychiatry* **18**, 666–673 (2013). doi: 10.1038/mp.2012.77; pmid: 22688187
33. D. Erny *et al*., Host microbiota constantly control maturation and function of microglia in the CNS. *Nat. Neurosci.* **18**, 965–977 (2015). doi: 10.1038/nn.4030; pmid: 26030851
34. M. van de Wouw *et al*., Short-chain fatty acids: Microbial metabolites that alleviate stress-induced brain-gut axis alterations. *J. Physiol.* **596**, 4923–4944 (2018). doi: 10.1113/JP276431; pmid: 30066368
35. B. B. Nankova, R. Agarwal, D. F. MacFabe, E. F. La Gamma, Enteric bacterial metabolites propionic and butyric acid modulate gene expression, including CREB-dependent catecholaminergic neurotransmission, in PC12 cells—Possible relevance to autism spectrum disorders. *PLOS ONE* **9**, e103740 (2014). doi: 10.1371/journal.pone.0103740; pmid: 25170769
36. D. F. MacFabe, N. E. Cain, F. Boon, K. P. Ossenkopp, D. P. Cain, Effects of the enteric bacterial metabolic product propionic acid on object-directed behavior, social behavior, cognition, and neuroinflammation in adolescent rats: Relevance to autism spectrum disorder. *Behav. Brain Res.* **217**, 47–54 (2011). doi: 10.1016/j.bbr.2010.10.005; pmid: 20937326
37. T. Arentsen *et al*., The bacterial peptidoglycan-sensing molecule Pglyrp2 modulates brain development and behavior. *Mol. Psychiatry* **22**, 257–266 (2017). doi: 10.1038/mp.2016.182; pmid: 27843150
38. Y. Zhan *et al*., Deficient neuron-microglia signaling results in impaired functional brain connectivity and social behavior. *Nat. Neurosci.* **17**, 400–406 (2014). doi: 10.1038/nn.3641; pmid: 24487234
39. L. H. Nelson, K. M. Lenz, Microglia depletion in early life programs persistent changes in social, mood-related, and locomotor behavior in male and female rats. *Behav. Brain Res.* **316**, 279–293 (2017). doi: 10.1016/j.bbr.2016.09.006; pmid: 27613230
40. A. C. Wong *et al*., Gut Microbiota Modifies Olfactory-Guided Microbial Preferences and Foraging Decisions in Drosophila.

Curr. Biol. **27**, 2397–2404.e4 (2017). doi: 10.1016/j.cub.2017.07.022; pmid: 28756953
41. A. François *et al.*, Olfactory epithelium changes in germfree mice. *Sci. Rep.* **6**, 24687 (2016). doi: 10.1038/srep24687; pmid: 27089944
42. B. J. Ashton, A. R. Ridley, E. K. Edwards, A. Thornton, Cognitive performance is linked to group size and affects fitness in Australian magpies. *Nature* **554**, 364–367 (2018). doi: 10.1038/nature25503; pmid: 29414945
43. A. Borbón-García, A. Reyes, M. Vives-Flórez, S. Caballero, Captivity Shapes the Gut Microbiota of Andean Bears: Insights into Health Surveillance. *Front. Microbiol.* **8**, 1316 (2017). doi: 10.3389/fmicb.2017.01316; pmid: 28751883
44. J. B. Clayton *et al.*, Captivity humanizes the primate microbiome. *Proc. Natl. Acad. Sci. U.S.A.* **113**, 10376–10381 (2016). doi: 10.1073/pnas.1521835113; pmid: 27573830
45. R. Nomoto *et al.*, Isolation and identification of *Bifidobacterium* species from feces of captive chimpanzees. *Biosci. Microbiota Food Health* **36**, 91–99 (2017). doi: 10.12938/bmfh.16-027; pmid: 28748130
46. J. L. Metcalf *et al.*, Evaluating the impact of domestication and captivity on the horse gut microbiome. *Sci. Rep.* **7**, 15497 (2017). doi: 10.1038/s41598-017-15375-9; pmid: 29138485
47. S. M. Rodríguez-Ruano *et al.*, The Hoopoe's Uropygial Gland Hosts a Bacterial Community Influenced by the Living Conditions of the Bird. *PLOS ONE* **10**, e0139734 (2015). doi: 10.1371/journal.pone.0139734; pmid: 26445111
48. H. Y. Jiang *et al.*, Diets Alter the Gut Microbiome of Crocodile Lizards. *Front. Microbiol.* **8**, 2073 (2017). doi: 10.3389/fmicb.2017.02073; pmid: 29118742
49. P. Engel, N. A. Moran, The gut microbiota of insects - diversity in structure and function. *FEMS Microbiol. Rev.* **37**, 699–735 (2013). doi: 10.1111/1574-6976.12025; pmid: 23692388
50. V. G. Martinson, J. Moy, N. A. Moran, Establishment of characteristic gut bacteria during development of the honeybee worker. *Appl. Environ. Microbiol.* **78**, 2830–2840 (2012). doi: 10.1128/AEM.07810-11; pmid: 22307297
51. V. G. Martinson *et al.*, A simple and distinctive microbiota associated with honey bees and bumble bees. *Mol. Ecol.* **20**, 619–628 (2011). doi: 10.1111/j.1365-294X.2010.04959.x; pmid: 21175905
52. D. Alberoni *et al.*, Impact of beneficial bacteria supplementation on the gut microbiota, colony development and productivity of Apis mellifera L. *Benef. Microbes* **9**, 269–278 (2018). pmid: 29380644
53. R. Kort *et al.*, Shaping the oral microbiota through intimate kissing. *Microbiome* **2**, 41 (2014). pmid: 25408893
54. K. A. Dill-McFarland *et al.*, Close social relationships correlate with human gut microbiota composition. *Sci. Rep.* **9**, 703 (2019). doi: 10.1038/s41598-018-37298-9; pmid: 30679677
55. I. L. Brito *et al.*, Transmission of human-associated microbiota along family and social networks. *Nat. Microbiol.* **4**, 964–971 (2019). doi: 10.1038/s41564-019-0409-6; pmid: 30911128
56. W. Z. Amaral *et al.*, Social Influences on Prevotella and the Gut Microbiome of Young Monkeys. *Psychosom. Med.* **79**, 888–897 (2017). doi: 10.1097/PSY.0000000000000454; pmid: 28178033
57. L. E. Grieneisen, J. Livermore, S. Alberts, J. Tung, E. A. Archie, Group Living and Male Dispersal Predict the Core Gut Microbiome in Wild Baboons. *Integr. Comp. Biol.* **57**, 770–785 (2017). doi: 10.1093/icb/icx046; pmid: 29048537
58. A. Raulo *et al.*, Social behaviour and gut microbiota in red-bellied lemurs (Eulemur rubriventer): In search of the role of immunity in the evolution of sociality. *J. Anim. Ecol.* **87**, 388–399 (2018). doi: 10.1111/1365-2656.12781; pmid: 29205327
59. A. C. Perofsky, R. J. Lewis, L. A. Abondano, A. Di Fiore, L. A. Meyers, Hierarchical social networks shape gut microbial composition in wild Verreaux's sifaka. *Proc. R. Soc. B* **284**, 284 (2017). doi: 10.1098/rspb.2017.2274; pmid: 29212730
60. A. H. Moeller *et al.*, Social behavior shapes the chimpanzee pan-microbiome. *Sci. Adv.* **2**, e1500997 (2016). doi: 10.1128/AEM.07810-11 pmid: 26824072
61. A. H. Moeller *et al.*, Sympatric chimpanzees and gorillas harbor convergent gut microbial communities. *Genome Res.* **23**, 1715–1720 (2013). doi: 10.1101/gr.154773.113; pmid: 23804402
62. A. Brune, C. Dietrich, The Gut Microbiota of Termites: Digesting the Diversity in the Light of Ecology and Evolution. *Annu. Rev. Microbiol.* **69**, 145–166 (2015). doi: 10.1146/annurev-micro-092412-155715; pmid: 26195303
63. F. Warnecke *et al.*, Metagenomic and functional analysis of hindgut microbiota of a wood-feeding higher termite. *Nature* **450**, 560–565 (2007). doi: 10.1038/nature06269; pmid: 18033299
64. A. Mikaelyan *et al.*, Diet is the primary determinant of bacterial community structure in the guts of higher termites. *Mol. Ecol.* **24**, 5284–5295 (2015). doi: 10.1111/mec.13376; pmid: 26348261
65. Y. Hongoh, Diversity and genomes of uncultured microbial symbionts in the termite gut. *Biosci. Biotechnol. Biochem.* **74**, 1145–1151 (2010). doi: 10.1271/bbb.100094; pmid: 20530908
66. R. J. Dillon, C. T. Vennard, A. K. A. Charnley, Gut bacteria produce components of a locust cohesion pheromone. *J. Appl. Microbiol.* **92**, 759–763 (2002). pmid: 11966918
67. N. Woodbury, G. Gries, Firebrats, *Thermobia domestica*, aggregate in response to the microbes *Enterobacter cloacae* and *Mycotypha microspora*. *Entomol. Exp. Appl.* **147**, 154–159 (2013). doi: 10.1111/eea.12054
68. N. Woodbury, M. Moore, G. Gries, Horizontal transmission of the microbial symbionts *Enterobacter cloacae* and *Mycotypha microspora* to their firebrat host. *Entomol. Exp. Appl.* **147**, 160–166 (2013). doi: 10.1111/eea.12057
69. A. Wada-Katsumata *et al.*, Gut bacteria mediate aggregation in the German cockroach. *Proc. Natl. Acad. Sci. U.S.A.* **112**, 15678–15683 (2015). pmid: 26644557
70. L. Xu, Q. Lou, C. Cheng, M. Lu, J. Sun, Gut-Associated Bacteria of Dendroctonus valens and their Involvement in Verbenone Production. *Microb. Ecol.* **70**, 1012–1023 (2015). doi: 10.1007/s00248-015-0625-4; pmid: 25985770
71. S. Leclaire, S. Jacob, L. K. Greene, G. R. Dubay, C. M. Drea, Social odours covary with bacterial community in the anal secretions of wild meerkats. *Sci. Rep.* **7**, 3240 (2017). doi: 10.1038/s41598-017-03356-x; pmid: 28607369
72. L. Amo *et al.*, Sex recognition by odour and variation in the uropygial gland secretion in starlings. *J. Anim. Ecol.* **81**, 605–613 (2012). doi: 10.1111/j.1365-2656.2011.01940.x; pmid: 22220811
73. V. O. Ezenwa, A. E. Williams, Microbes and animal olfactory communication: Where do we go from here? *BioEssays* **36**, 847–854 (2014). doi: 10.1002/bies.201400016; pmid: 24986361
74. D. Caillaud *et al.*, Gorilla susceptibility to Ebola virus: The cost of sociality. *Curr. Biol.* **16**, R489–R491 (2006). doi: 10.1016/j.cub.2006.06.017; pmid: 16824905
75. J. L. Tella, The evolutionary transition to coloniality promotes higher blood parasitism. *J. Evol. Biol.* **15**, 32–41 (2002). doi: 10.1046/j.1420-9101.2002.00375.x
76. L. Chiu *et al.*, Protective Microbiota: From Localized to Long-Reaching Co-Immunity. *Front. Immunol.* **8**, 1678 (2017). doi: 10.3389/fimmu.2017.01678; pmid: 29270167
77. G. Eberl, T. Pradeu, Towards a General Theory of Immunity? *Trends Immunol.* **39**, 261–263 (2018). pmid: 29229264
78. S. El Aidy, T. G. Dinan, J. F. Cryan, Gut Microbiota: The Conductor in the Orchestra of Immune-Neuroendocrine Communication. *Clin. Ther.* **37**, 954–967 (2015). doi: 10.1016/j.clinthera.2015.03.002; pmid: 25846319
79. P. Cotgreave, D. H. Clayton, *Comparative Analysis of Time Spent Grooming by Birds in Relation to Parasite Load* (Brill, 1994). doi: 10.1163/156853994X00424
80. L. K. Newbold *et al.*, Helminth burden and ecological factors associated with alterations in wild host gastrointestinal microbiota. *ISME J.* **11**, 663–675 (2017). doi: 10.1038/ismej.2016.153; pmid: 27983724
81. S. C. Lee *et al.*, Helminth colonization is associated with increased diversity of the gut microbiota. *PLOS Negl. Trop. Dis.* **8**, e2880 (2014). doi: 10.1371/journal.pntd.0002880; pmid: 24851867
82. L. A. Reynolds, B. B. Finlay, Worming Their Way into the Picture: Microbiota Help Helminths Modulate Host Immunity. *Immunity* **43**, 840–842 (2015). doi: 10.1016/j.immuni.2015.10.025; pmid: 26588776
83. H. Koch, P. Schmid-Hempel, Socially transmitted gut microbiota protect bumble bees against an intestinal parasite. *Proc. Natl. Acad. Sci. U.S.A.* **108**, 19288–19292 (2011). doi: 10.1073/pnas.1110474108; pmid: 22084077
84. A. Stow *et al.*, Antimicrobial defences increase with sociality in bees. *Biol. Lett.* **3**, 422–424 (2007). doi: 10.1098/rsbl.2007.0178; pmid: 17504731
85. S. Tragust *et al.*, Ants disinfect fungus-exposed brood by oral uptake and spread of their poison. *Curr. Biol.* **23**, 76–82 (2013). doi: 10.1016/j.cub.2012.11.034; pmid: 23246409
86. A. D. Kay *et al.*, A carbohydrate-rich diet increases social immunity in ants. *Proc. R. Soc. B* **281**, 20132374 (2014). doi: 10.1098/rspb.2013.2374; pmid: 24430844
87. M. T. Bailey *et al.*, Exposure to a social stressor alters the structure of the intestinal microbiota: Implications for stressor-induced immunomodulation. *Brain Behav. Immun.* **25**, 397–407 (2011). doi: 10.1016/j.bbi.2010.10.023; pmid: 21040780
88. A. Burokas *et al.*, Targeting the Microbiota-Gut-Brain Axis: Prebiotics Have Anxiolytic and Antidepressant-like Effects and Reverse the Impact of Chronic Stress in Mice. *Biol. Psychiatry* **82**, 472–487 (2017). doi: 10.1016/j.biopsych.2016.12.031; pmid: 28242013
89. I. I. Levin *et al.*, Stress response, gut microbial diversity and sexual signals correlate with social interactions. *Biol. Lett.* **12**, 20160352 (2016). pmid: 27354713
90. F. Sommer *et al.*, The Gut Microbiota Modulates Energy Metabolism in the Hibernating Brown Bear Ursus arctos. *Cell Rep.* **14**, 1655–1661 (2016). doi: 10.1016/j.celrep.2016.01.026; pmid: 26854221
91. R. M. Sapolsky, Social Status and Health in Humans and Other Animals. *Annu. Rev. Anthropol.* **33**, 393–418 (2004). doi: 10.1146/annurev.anthro.33.070203.144000
92. M. Romano, Gut Microbiota as a Trigger of Accelerated Directional Adaptive Evolution: Acquisition of Herbivory in the Context of Extracellular Vesicles, MicroRNAs and Inter-Kingdom Crosstalk. *Front. Microbiol.* **8**, 721 (2017). doi: 10.3389/fmicb.2017.00721; pmid: 28473829
93. M. P. Lombardo, Access to mutualistic endosymbiotic microbes: An underappreciated benefit of group living. *Behav. Ecol. Sociobiol.* **62**, 479–497 (2007). doi: 10.1007/s00265-007-0428-9
94. Z. L. Sabree, N. A. Moran, Host-specific assemblages typify gut microbial communities of related insect species. *Springerplus* **3**, 138 (2014). doi: 10.1186/2193-1801-3-138; pmid: 24741474
95. Z. L. Sabree *et al.*, Genome shrinkage and loss of nutrient-providing potential in the obligate symbiont of the primitive termite Mastotermes darwiniensis. *Appl. Environ. Microbiol.* **78**, 204–210 (2012). doi: 10.1128/AEM.06540-11; pmid: 22020505
96. J. Holt-Lunstad, T. B. Smith, M. Baker, T. Harris, D. Stephenson, Loneliness and social isolation as risk factors for mortality: A meta-analytic review. *Perspect. Psychol. Sci.* **10**, 227–237 (2015). doi: 10.1177/1745691614568352; pmid: 25910392
97. J. R. Kelly *et al.*, Transferring the blues: Depression-associated gut microbiota induces neurobehavioural changes in the rat. *J. Psychiatr. Res.* **82**, 109–118 (2016). doi: 10.1016/j.jpsychires.2016.07.019; pmid: 27491067
98. A. V. Golubeva *et al.*, Microbiota-related Changes in Bile Acid & Tryptophan Metabolism are Associated with Gastrointestinal Dysfunction in a Mouse Model of Autism. *EBioMedicine* **24**, 166–178 (2017). doi: 10.1016/j.ebiom.2017.09.020; pmid: 28965876
99. K. A. Neufeld, N. Kang, J. Bienenstock, J. A. Foster, Effects of intestinal microbiota on anxiety-like behavior. *Commun. Integr. Biol.* **4**, 492–494 (2011). doi: 10.4161/cib.15702; pmid: 21966581
100. J. S. Son *et al.*, Comparison of Fecal Microbiota in Children with Autism Spectrum Disorders and Neurotypical Siblings in the Simons Simplex Collection. *PLOS ONE* **10**, e0137725 (2015). doi: 10.1371/journal.pone.0137725; pmid: 26427004
101. S. M. Finegold, Desulfovibrio species are potentially important in regressive autism. *Med. Hypotheses* **77**, 270–274 (2011). doi: 10.1016/j.mehy.2011.04.032; pmid: 21592674
102. B. Góra *et al.*, Toxin profile of fecal Clostridium perfringens strains isolated from children with autism spectrum disorders. *Anaerobe* **51**, 73–77 (2018). doi: 10.1016/j.anaerobe.2018.03.005; pmid: 29526827
103. E. A. Mayer, D. Padua, K. Tillisch, Altered brain-gut axis in autism: Comorbidity or causative mechanisms? *BioEssays* **36**, 933–939 (2014). doi: 10.1002/bies.201400075; pmid: 25145752
104. E. A. Curran *et al.*, Association Between Obstetric Mode of Delivery and Autism Spectrum Disorder: A Population-Based Sibling Design Study. *JAMA Psychiatry* **72**, 935–942 (2015). doi: 10.1001/jamapsychiatry.2015.0846; pmid: 26107922
105. K. J. Davey *et al.*, Gender-dependent consequences of chronic olanzapine in the rat: Effects on body weight, inflammatory, metabolic and microbiota parameters.

Psychopharmacology **221**, 155–169 (2012). doi: 10.1007/s00213-011-2555-2; pmid: 22234378
106. B. J. Varian *et al*., Microbial lysate upregulates host oxytocin. *Brain Behav. Immun.* **61**, 36–49 (2017). doi: 10.1016/j.bbi.2016.11.002; pmid: 27825953
107. L. Tabouy *et al*., Dysbiosis of microbiome and probiotic treatment in a genetic model of autism spectrum disorders. *Brain Behav. Immun.* **73**, 310–319 (2018). doi: 10.1016/j.bbi.2018.05.015; pmid: 29787855
108. M. Sgritta *et al*., Mechanisms Underlying Microbial-Mediated Changes in Social Behavior in Mouse Models of Autism Spectrum Disorder. *Neuron* **101**, 246–259.e6 (2019). doi: 10.1016/j.neuron.2018.11.018; pmid: 30522820
109. E. Y. Hsiao *et al*., Microbiota modulate behavioral and physiological abnormalities associated with neurodevelopmental disorders. *Cell* **155**, 1451–1463 (2013). doi: 10.1016/j.cell.2013.11.024; pmid: 24315484
110. H. M. Wexler, Bacteroides: The good, the bad, and the nitty-gritty. *Clin. Microbiol. Rev.* **20**, 593–621 (2007). doi: 10.1128/CMR.00008-07; pmid: 17934076
111. C. L. Sears, Enterotoxigenic Bacteroides fragilis: A rogue among symbiotes. *Clin. Microbiol. Rev.* **22**, 349–369 (2009). doi: 10.1128/CMR.00053-08; pmid: 19366918
112. J. R. Kelly *et al*., Lost in translation? The potential psychobiotic Lactobacillus rhamnosus (JB-1) fails to modulate stress or cognitive performance in healthy male subjects. *Brain Behav. Immun.* **61**, 50–59 (2017). doi: 10.1016/j.bbi.2016.11.018; pmid: 27865949
113. H. M. R. T. Parracho *et al*., A double-blind, placebo-controlled, crossover-designed probiotic feeding study in children diagnosed with autistic spectrum disorders. *Int. J. Probiotics Prebiotics* **5**, 69–74 (2010).
114. S. Y. Shaaban *et al*., The role of probiotics in children with autism spectrum disorder: A prospective, open-label study. *Nutr. Neurosci.* **21**, 676–681 (2018). doi: 10.1080/1028415X.2017.1347746; pmid: 28686541
115. D. W. Kang *et al*., Microbiota Transfer Therapy alters gut ecosystem and improves gastrointestinal and autism symptoms: An open-label study. *Microbiome* **5**, 10 (2017). doi: 10.1186/s40168-016-0225-7; pmid: 28122648
116. K. V. Sandhu *et al*., Feeding the microbiota-gut-brain axis: Diet, microbiome, and neuropsychiatry. *Transl. Res.* **179**, 223–244 (2017). doi: 10.1016/j.trsl.2016.10.002; pmid: 27832936
117. C. G. de Theije *et al*., Dietary long chain n-3 polyunsaturated fatty acids prevent impaired social behaviour and normalize brain dopamine levels in food allergic mice. *Neuropharmacology* **90**, 15–22 (2015). doi: 10.1016/j.neuropharm.2014.11.001; pmid: 25445491
118. M. M. Pusceddu *et al*., N-3 Polyunsaturated Fatty Acids (PUFAs) Reverse the Impact of Early-Life Stress on the Gut Microbiota. *PLOS ONE* **10**, e0139721 (2015). doi: 10.1371/journal.pone.0139721; pmid: 26426902
119. M. Nemeth *et al*., Sex-specific effects of dietary fatty acids on saliva cortisol and social behavior in guinea pigs under different social environmental conditions. *Biol. Sex Differ.* **7**, 51 (2016). doi: 10.1186/s13293-016-0107-5; pmid: 27688870
120. R. C. Robertson *et al*., Omega-3 polyunsaturated fatty acids critically regulate behaviour and gut microbiota development in adolescence and adulthood. *Brain Behav. Immun.* **59**, 21–37 (2017). doi: 10.1016/j.bbi.2016.07.145; pmid: 27423492
121. C. Lin *et al*., Omega-3 fatty acids regulate NLRP3 inflammasome activation and prevent behavior deficits after traumatic brain injury. *Exp. Neurol.* **290**, 115–122 (2017). doi: 10.1016/j.expneurol.2017.01.005; pmid: 28077335
122. C. S. Model *et al*., Omega-3 fatty acids alter behavioral and oxidative stress parameters in animals subjected to fenproporex administration. *Metab. Brain Dis.* **29**, 185–192 (2014). doi: 10.1007/s11011-013-9473-4; pmid: 24385143
123. C. O. Bondi *et al*., Adolescent behavior and dopamine availability are uniquely sensitive to dietary omega-3 fatty acid deficiency. *Biol. Psychiatry* **75**, 38–46 (2014). doi: 10.1016/j.biopsych.2013.06.007; pmid: 23890734
124. G. P. Amminger *et al*., Omega-3 fatty acids supplementation in children with autism: A double-blind randomized, placebo-controlled pilot study. *Biol. Psychiatry* **61**, 551–553 (2007). doi: 10.1016/j.biopsych.2006.05.007; pmid: 16920077
125. S. Bent, K. Bertoglio, P. Ashwood, A. Bostrom, R. L. Hendren, A pilot randomized controlled trial of omega-3 fatty acids for autism spectrum disorder. *J. Autism Dev. Disord.* **41**, 545–554 (2011). doi: 10.1007/s10803-010-1078-8; pmid: 20683766
126. A. M. Haagensen *et al*., High fat, low carbohydrate diet limit fear and aggression in Göttingen minipigs. *PLOS ONE* **9**, e93821 (2014). doi: 10.1371/journal.pone.0093821 pmid: 24740321
127. J. R. Kaplan *et al*., Demonstration of an association among dietary cholesterol, central serotonergic activity, and social behavior in monkeys. *Psychosom. Med.* **56**, 479–484 (1994). doi: 10.1097/00006842-199411000-00001; pmid: 7532867
128. R. Grimaldi *et al*., A prebiotic intervention study in children with autism spectrum disorders (ASDs). *Microbiome* **6**, 133 (2018). doi: 10.1186/s40168-018-0523-3; pmid: 30071894
129. R. I. Dunbar, The social brain hypothesis and its implications for social evolution. *Ann. Hum. Biol.* **36**, 562–572 (2009). doi: 10.1080/03014460902960289; pmid: 19575315
130. L. Desbonnet, G. Clarke, F. Shanahan, T. G. Dinan, J. F. Cryan, Microbiota is essential for social development in the mouse. *Mol. Psychiatry* **19**, 146–148 (2014). doi: 10.1038/mp.2013.65; pmid: 23689536
131. T. Arentsen, H. Raith, Y. Qian, H. Forssberg, R. Diaz Heijtz, Host microbiota modulates development of social preference in mice. *Microb. Ecol. Health Dis.* **26**, 29719 (2015). pmid: 26679775
132. C. D'Mello *et al*., Probiotics Improve Inflammation-Associated Sickness Behavior by Altering Communication between the Peripheral Immune System and the Brain. *J. Neurosci.* **35**, 10821–10830 (2015). doi: 10.1523/JNEUROSCI.0575-15.2015; pmid: 26224864
133. C. S. M. Cowan *et al*., Gutsy Moves: The Amygdala as a Critical Node in Microbiota to Brain Signaling. *BioEssays* **40**, 10.1002/bies.201700172 (2018). doi: 10.1002/bies.201700172; pmid: 29148060
134. L. Desbonnet *et al*., Gut microbiota depletion from early adolescence in mice: Implications for brain and behaviour. *Brain Behav. Immun.* **48**, 165–173 (2015). doi: 10.1016/j.bbi.2015.04.004; pmid: 25866195
135. F. Guida *et al*., Antibiotic-induced microbiota perturbation causes gut endocannabinoidome changes, hippocampal neuroglial reorganization and depression in mice. *Brain Behav. Immun.* **67**, 230–245 (2018). doi: 10.1016/j.bbi.2017.09.001; pmid: 28890155
136. X. Wang *et al*., Effects of β-diketone antibiotic mixtures on behavior of zebrafish (Danio rerio). *Chemosphere* **144**, 2195–2205 (2016). doi: 10.1016/j.chemosphere.2015.10.120; pmid: 26595314
137. G. Sharon *et al*., Commensal bacteria play a role in mating preference of Drosophila melanogaster. *Proc. Natl. Acad. Sci. U.S.A.* **107**, 20051–20056 (2010). pmid: 21041648
138. M. A. Najarro, M. Sumethasorn, A. Lamoureux, T. L. Turner, Choosing mates based on the diet of your ancestors: Replication of non-genetic assortative mating in Drosophila melanogaster. *PeerJ* **3**, e1173 (2015). doi: 10.7717/peerj.1173; pmid: 26339551
139. A. S. Brown, The environment and susceptibility to schizophrenia. *Prog. Neurobiol.* **93**, 23–58 (2011). doi: 10.1016/j.pneurobio.2010.09.003; pmid: 20955757
140. R. J. Dillon, V. M. Dillon, The gut bacteria of insects: Nonpathogenic interactions. *Annu. Rev. Entomol.* **49**, 71–92 (2004). doi: 10.1146/annurev.ento.49.061802.123416; pmid: 14651457
141. L. Borrelli *et al*., Probiotic modulation of the microbiota-gut-brain axis and behaviour in zebrafish. *Sci. Rep.* **6**, 30046 (2016). doi: 10.1038/srep30046; pmid: 27416816
142. S. Kulkarni, P. Heeb, Social and sexual behaviours aid transmission of bacteria in birds. *Behav. Processes* **74**, 88–92 (2007). doi: 10.1016/j.beproc.2006.10.005; pmid: 17118574
143. C. M. Benskin, G. Rhodes, R. W. Pickup, K. Wilson, I. R. Hartley, Diversity and temporal stability of bacterial communities in a model passerine bird, the zebra finch. *Mol. Ecol.* **19**, 5531–5544 (2010). doi: 10.1111/j.1365-294X.2010.04892.x; pmid: 21054607
144. R. Osawa, W. Blanshard, P. O'Callaghan, Microbiological Studies of the Intestinal Microflora of the Koala, Phascolarctos-Cinereus. 2. Pap, a Special Maternal Feces Consumed by Juvenile Koalas. *Aust. J. Zool.* **41**, 611–620 (1993). doi: 10.1071/ZO9930611
145. E. A. McKenney, M. Ashwell, J. E. Lambert, V. Fellner, Fecal microbial diversity and putative function in captive western lowland gorillas (Gorilla gorilla), common chimpanzees (Pan troglodytes), Hamadryas baboons (Papio hamadryas) and binturongs (Arctictis binturong). *Integr. Zool.* **9**, 557–569 (2014). doi: 10.1111/1749-4877.12112; pmid: 25236539
146. E. A. McKenney, A. Rodrigo, A. D. Yoder, Patterns of gut bacterial colonization in three primate species. *PLOS ONE* **10**, e0124618 (2015). doi: 10.1371/journal.pone.0124618; pmid: 25970595
147. D. Rothschild *et al*., Environment dominates over host genetics in shaping human gut microbiota. *Nature* **555**, 210–215 (2018). doi: 10.1038/nature25973; pmid: 29489753
148. S. Cussotto *et al*., Psychotropics and the Microbiome: A Chamber of Secrets. *Psychopharmacology* **236**, 1411–1432 (2019). doi: 10.1007/s00213-019-5185-8
149. J. F. Cryan *et al*., The Microbiota-Gut-Brain Axis. *Physiol. Rev.* **99**, 1877–2013 (2019). doi: 10.1152/physrev.00018.2018

ACKNOWLEDGMENTS

We thank R. Stilling, G. Moloney, A. P. Ventura Da Silva, D. Slattery, and G. Davidson for helpful comments. **Funding:** Supported by a Science Foundation Ireland (SFI) grant to APC Microbiome Ireland through the Irish Government's National Development Plan (grant SFI/12/RC/2273_P2), the Irish Health Research Board, Enterprise Ireland, and the Department of Agriculture, Food and the Marine (T.G.D. and J.F.C.); European Research Council Consolidator grant 617509 (J.L.Q.); and NIH grants R21 AI133522 and RO1 AI132581, NSF grant 1456778, and the Vanderbilt Microbiome Initiative (S.R.B.). **Competing interests:** T.G.D. and J.F.C. receive research funding from 4D-Pharma, Mead Johnson, Suntory Wellness, Nutricia, Cremo, and DuPont. T.G.D. has been an invited speaker at conferences organized by Servier, Lundbeck, Janssen, and AstraZeneca. J.F.C. has been an invited speaker at conferences organized by Mead Johnson, Nutricia, Alkermes, and Janssen. E.S., S.R.B., and J.L.Q. declare no competing interests.

10.1126/science.aar2016

RESEARCH ARTICLE SUMMARY

COMBUSTION PHYSICS

A unified mechanism for unconfined deflagration-to-detonation transition in terrestrial chemical systems and type Ia supernovae

Alexei Y. Poludnenko*, Jessica Chambers, Kareem Ahmed, Vadim N. Gamezo, Brian D. Taylor

INTRODUCTION: The nature of type Ia supernovae (SNIa)—thermonuclear explosions of white dwarf (WD) stars—is an open question in astrophysics. There is a general consensus that SNIa explosions are driven by fast thermonuclear burning in $^{12}C/^{16}O$ WD stars with a mass close to, or below, the Chandrasekhar-mass limit of 1.4 solar masses. Beyond this general statement, however, the exact mechanisms of SNIa remain unclear, with a number of possible scenarios.

Virtually all existing theoretical models of normal, bright SNIa—including the classical, single-degenerate Chandrasekhar-mass and sub-Chandrasekhar-mass scenarios, along with the double-degenerate merger model—require formation of a supersonic detonation wave. This wave consumes all of the stellar material as a WD begins to expand during the explosion. Detonation initiation in unconfined systems, such as the interior of a WD, remains poorly understood and is particularly difficult to achieve in the absence of the confining effect of walls and obstacles or preexisting or externally introduced strong shocks. Numerical models of SNIa are unable to capture detonation formation from first principles because of the extreme range of scales involved. Instead, they are forced to make two crucial assumptions: (i) that detonation ignition always occurs during an explosion and (ii) the time and location of the detonation formation. As a result, detonation initiation conditions are free parameters present in most existing SNIa models, which limits their predictive power.

RATIONALE: Thermonuclear combustion waves in SNIa are qualitatively similar to chemical combustion waves on Earth because they are controlled by the same physical mechanisms. This similarity allows us to seek insights into the fundamental aspects of the physical processes that control SNIa explosions by using theoretical, numerical, and experimental results obtained for terrestrial chemical systems. This includes detonation initiation phenomena that are also relevant to terrestrial applications that range from detonation-based propulsion and power-generation systems to the explosion safety of industrial facilities related to coal mining, fuel storage, chemical processing, and nuclear power generation.

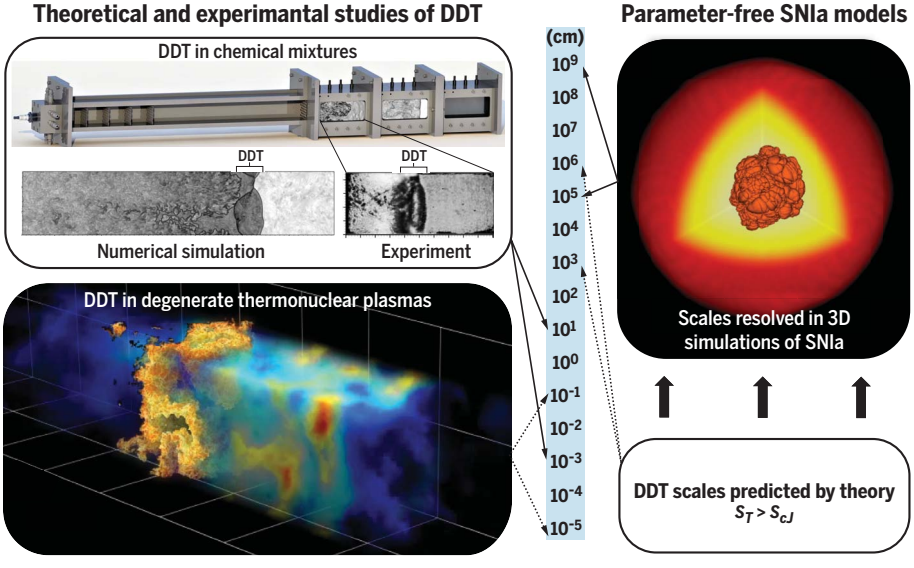
ON OUR WEBSITE

Read the full article at http://dx.doi.org/10.1126/science.aau7365

Prior direct numerical simulations (DNS) have shown that chemical flames interacting with high-intensity turbulence can spontaneously accelerate and produce strong shocks or detonations. Such turbulence-driven deflagration-to-detonation transition (tDDT) can occur in essentially unconfined settings.

RESULTS: We present a general analytical theory of tDDT in unconfined systems. The theory explains the behavior of fast turbulent flames that become unstable, produce shocks, and can transition to detonations. This occurs when the turbulent burning speed exceeds the Chapman-Jouguet deflagration velocity, which is the maximum possible speed of a steady-state reaction wave without a shock. We describe an experimental confirmation of this process in terrestrial H_2-air flames. Next, we used numerical simulations of a fully resolved turbulent thermonuclear flame in a degenerate ^{12}C stellar plasma to show that under conditions representative of those in a SNIa explosion, this mechanism can also result in the spontaneous formation of strong shocks. We show that these shocks can rapidly amplify by interacting with surrounding turbulent flames and ultimately trigger a detonation. Last, we used the developed theory to determine the criteria for detonation initiation in the classical single-degenerate Chandrasekhar-mass model of SNIa. We found that DDT is almost inevitable at densities in the range of 10^7 to 10^8 g cm^{-3}, with the maximum probability at 3×10^7 g cm^{-3}.

CONCLUSION: We developed a theory of turbulence-induced DDT and validated it by using experiments on chemical flames and numerical simulations of thermonuclear deflagrations. Our results describe a unified mechanism of unconfined DDT both in chemical and thermonuclear reacting flows. This theory is parameter free and can be used to predict self-consistently the conditions for detonation initiation in SNIa explosions. ■



Understanding the mechanism of the unconfined DDT in SNIa. The DDT in SNIa is predicted to occur on scales of ~10^3 to 10^6 cm, which is well below the characteristic scale of a WD star (10^9 cm) and mostly below the smallest scales resolvable in three-dimensional simulations, ~10^5 cm. To demonstrate the turbulence-driven, unconfined DDT in experiments and DNS, we considered turbulence-flame interaction on small scales of ~10^{-5} to 10 cm. The synergy between the experiments and DNS of chemical and thermonuclear flames led to our unified theory of DDT.

The list of author affiliations is available in the full article online.
*Corresponding author. Email: alexei.poludnenko@uconn.edu
Cite this article as A. Poludnenko *et al.*, *Science* **366**, eaau7365 (2019). DOI: 10.1126/science.aau7365

RESEARCH ARTICLE

COMBUSTION PHYSICS

A unified mechanism for unconfined deflagration-to-detonation transition in terrestrial chemical systems and type Ia supernovae

Alexei Y. Poludnenko[1,2]*, Jessica Chambers[3], Kareem Ahmed[3], Vadim N. Gamezo[4], Brian D. Taylor[5]

The nature of type Ia supernovae (SNIa)—thermonuclear explosions of white dwarf stars—is an open question in astrophysics. Virtually all existing theoretical models of normal, bright SNIa require the explosion to produce a detonation in order to consume all of stellar material, but the mechanism for the deflagration-to-detonation transition (DDT) remains unclear. We present a unified theory of turbulence-induced DDT that describes the mechanism and conditions for initiating detonation both in unconfined chemical and thermonuclear explosions. The model is validated by using experiments with chemical flames and numerical simulations of thermonuclear flames. We use the developed theory to determine criteria for detonation initiation in the single-degenerate Chandrasekhar-mass SNIa model and show that DDT is almost inevitable at densities of 10^7 to 10^8 grams per cubic centimeter.

Type Ia supernovae (SNIa) are a critical tool for measuring cosmological distances. Techniques used to calibrate SNIa for this purpose rely on empirical correlations (*1*–*3*) because of incomplete theoretical understanding of the mechanisms responsible for SNIa. Theoretical models of SNIa have remained limited because of uncertainties in the explosion mechanisms.

Explosions can involve two distinct types of combustion waves that differ by the propagation mechanism: deflagrations and detonations. Deflagrations, or flames, are relatively slow and propagate subsonically through heat conduction, diffusion, and advection. Detonations move supersonically because of ignition through shock compression and therefore always involve strong shocks and propagate at the shock speed.

SNIa explosions are driven by fast thermonuclear burning in $^{12}C/^{16}O$ white dwarf (WD) stars with a mass close to, or below, the Chandrasekhar mass limit of ≈1.4 solar masses ($M_\odot$) (*4*)—the maximum possible mass of a WD supported against gravitational collapse by electron degeneracy pressure. Beyond this general statement, however, the exact mechanisms of SNIa remain unclear (*5*–*8*), with a number of possible scenarios. These include the classical Chandrasekhar-mass (M_{ch}) model (*9*–*12*), sub-Chandrasekhar-mass (sub-M_{ch}) models (*13*–*16*), double-degenerate (DD) models that include mergers or collisions of two WDs (*17*–*20*), and gravitationally confined detonations (*21*, *22*).

All SNIa explosion scenarios share a common characteristic: To produce a normal, bright SNIa, detonation must be triggered in the stellar interior at some stage of the explosion. Such supersonic combustion is required to consume the entire WD, including its outer layers, which expand supersonically as the material becomes gravitationally unbound. Observations place tight upper limits on the amount of unburned ^{12}C in the resulting SNIa ejecta, indicating nearly complete combustion of the stellar material in the explosion (*23*, *24*). By contrast, pure deflagration M_{ch} explosion scenarios have been previously suggested as the mechanism that forms subluminous classes of supernovae, such as Type Iax (*25*).

Generally, igniting a detonation is more difficult than igniting a flame in a chemically or thermonuclearly explosive mixture. Detonation can typically form in one of three ways: (i) strong ignition, in which a detonation is directly initiated by a preexisting, or externally introduced, strong shock (*26*); (ii) weak ignition, in which a detonation develops by means of a spontaneous reaction wave propagating through a gradient of temperature or composition (*27*, *28*) created by weaker shocks or other processes (gradient mechanism); and (iii) deflagration-to-detonation transition (DDT), during which shocks are produced by fast flames, and the detonation may sometimes form at the final stages through the gradient mechanism (*29*).

Although strong ignition may be realized in the gravitationally confined model (*21*, *22*) or in the case of WD collisions (*20*, *30*), more widely accepted models such as the M_{ch} and sub-M_{ch} scenarios, as well as the DD mergers, generally do not have any natural mechanism to form preexisting shocks of sufficient strength to directly ignite a detonation. For example, in the classical M_{ch} scenario, detonation formation requires a DDT because burning must initially propagate as subsonic flames to pre-expand a star and produce intermediate-mass elements (*9*, *31*, *32*). In the sub-M_{ch} model, both the gradient and the DDT mechanisms of detonation formation cannot be ruled out. Material compression produced by accretion in the surface layers leads to ignition, which could produce either localized hotspots, directly triggering a detonation through the gradient mechanism, or a flame, which could subsequently trigger a DDT. We focused on the DDT in degenerate stellar matter as the potential mechanism of detonation ignition in the two leading SNIa scenarios, namely M_{ch} and sub-M_{ch}. Although DDT is generally not considered in the context of the DD models, the detailed ignition process in that scenario remains unclear.

Thermonuclear combustion waves are qualitatively similar to chemical combustion waves on Earth because they are controlled by the same physical mechanisms. This similarity allows us to seek insights into the fundamental aspects of the physical processes that control SNIa explosions using theoretical, numerical, and experimental results obtained for terrestrial chemical systems. DDT is also relevant to terrestrial applications that range from detonation-based propulsion and power-generation systems, such as detonation engines (*33*–*37*), to the industrial safety of mining operations (*38*), fuel-storage, chemical processing (*39*, *40*), and nuclear power–generation facilities (*41*). Large-scale industrial accidents in Buncefield, United Kingdom (fuel-storage facility, 2005) (*42*, *43*), Sago Mine, United States (coal mine, 2006) (*44*), Jaipur, India (chemical processing plant, 2009) (*45*), and Fukushima, Japan (nuclear power plant, 2011) (*46*) may all have involved a DDT.

The DDT process in SNIa occurs in essentially unconfined conditions, in the sense that there are no walls or obstructions that are usually present in terrestrial settings. The mechanism of such unconfined DDT is not understood in chemical systems on Earth. Direct numerical simulations (DNS) have shown that chemical flames interacting with high-intensity turbulence can spontaneously accelerate and produce strong shocks or detonations in a completely unconfined setting (*47*). We present an experimental confirmation of this shock generation and DDT mechanism in terrestrial systems and apply it to SNIa.

Theory of turbulence-induced DDT

DNS of chemical flames in high-intensity turbulent flows have shown that turbulent flames with burning speeds S_T above the speed of a

[1]Department of Aerospace Engineering, Texas A&M University, College Station, TX 77843, USA. [2]Department of Mechanical Engineering, University of Connecticut, Storrs, CT 06269, USA. [3]Department of Mechanical and Aerospace Engineering, University of Central Florida, Orlando, FL 32816, USA. [4]Laboratories for Computational Physics and Fluid Dynamics, Naval Research Laboratory, Washington, DC 20375, USA. [5]Munitions Directorate, Air Force Research Laboratory, Eglin, FL 32542, USA.
*Corresponding author. Email: alexei.poludnenko@uconn.edu

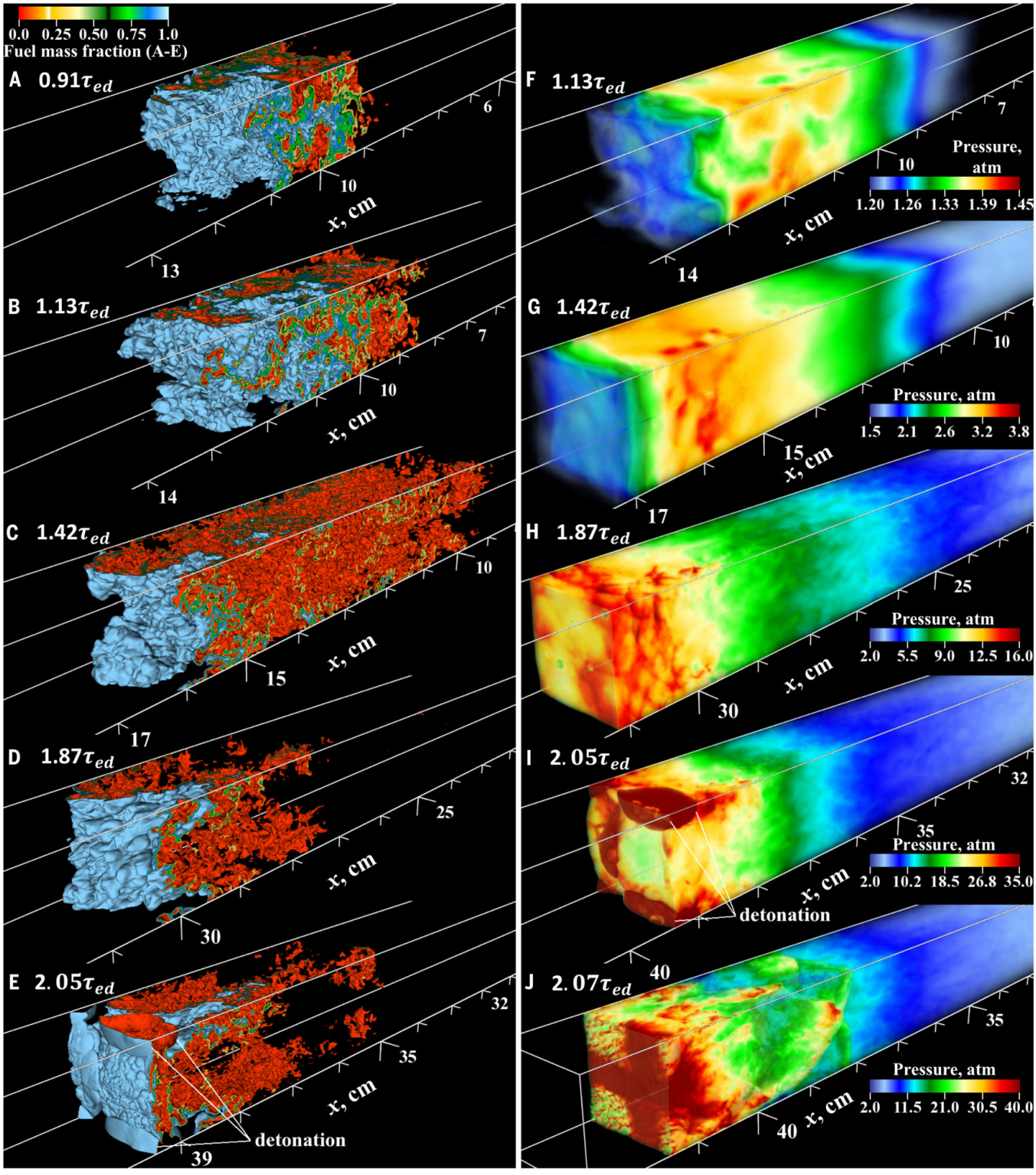


Fig. 1. Evolution of a turbulent flame and transition to a detonation in a stoichiometric methane-air mixture. This simulation was previously reported as case 11 in (47). (**A** to **E**) Structure of a turbulent flame propagating to the left. Shown is the isovolume bounded by the two isosurfaces of the fuel mass fraction Y = 0.05 and Y = 0.95. Colors indicate the value of Y. (**F** to **J**) Corresponding pressure fields. Color scales in (F) to (J) show pressure normalized by the upstream pressure in the domain, P_0 = 1 atm, and the color scale changes across (F) to (J) as the maximum pressure increases. Time for each frame is given in units of the eddy turnover time τ_{ed} = 0.367 ms. Corresponding turbulent flame speed and maximum pressures in the domain are shown in Fig. 2C. An animation of this simulation is provided in movie S1.

Chapman-Jouguet (CJ) deflagration, S_{CJ}, are intrinsically unstable and can transition to detonations (*47*). The S_{CJ} is defined as the flame speed, at which the flow on the product side of the flame becomes sonic in the reference frame comoving with the flame. Consequently, the condition for the turbulence-driven spontaneous DDT (tDDT) can be written as

$$S_T > S_{CJ} = c_s/\alpha \quad (1)$$

where c_s is the sound speed in hot products and $\alpha = \rho_f/\rho_p$ is the ratio of the densities of fuel ρ_f and combustion products ρ_p (*47*).

Once the flame speed exceeds S_{CJ}, transition to a detonation occurs as a catastrophic runaway process, which results in a rapid pressure buildup and creates strong shocks inside the turbulent flame. The evolution of a chemical turbulent flame in this process and its ultimate transition to a detonation are shown in Fig. 1 and movie S1 [this simulation was previously reported elsewhere (*47*)]. The corresponding histories of the turbulent flame speed and maximum pressures in the domain are shown in Fig. 2C.

This condition stems from S_{CJ} being the maximum possible speed of a steady-state deflagration, which satisfies conservation laws (*48*). The actual flame speed S_T depends on the turbulent intensity and the turbulent-flame structure and can exceed S_{CJ}. Because conservation laws prohibit a steady-state deflagration wave for $S_T > S_{CJ}$, the flow would evolve, producing shocks and accelerating, potentially reaching a new steady state permitted by the conservation laws. As a result, the flame could either become pulsatingly unstable (*49*), periodically oscillating between the speed above and below S_{CJ} and producing shocks, or it could transition to a CJ detonation, which can also be viewed as a CJ deflagration coupled to a shock.

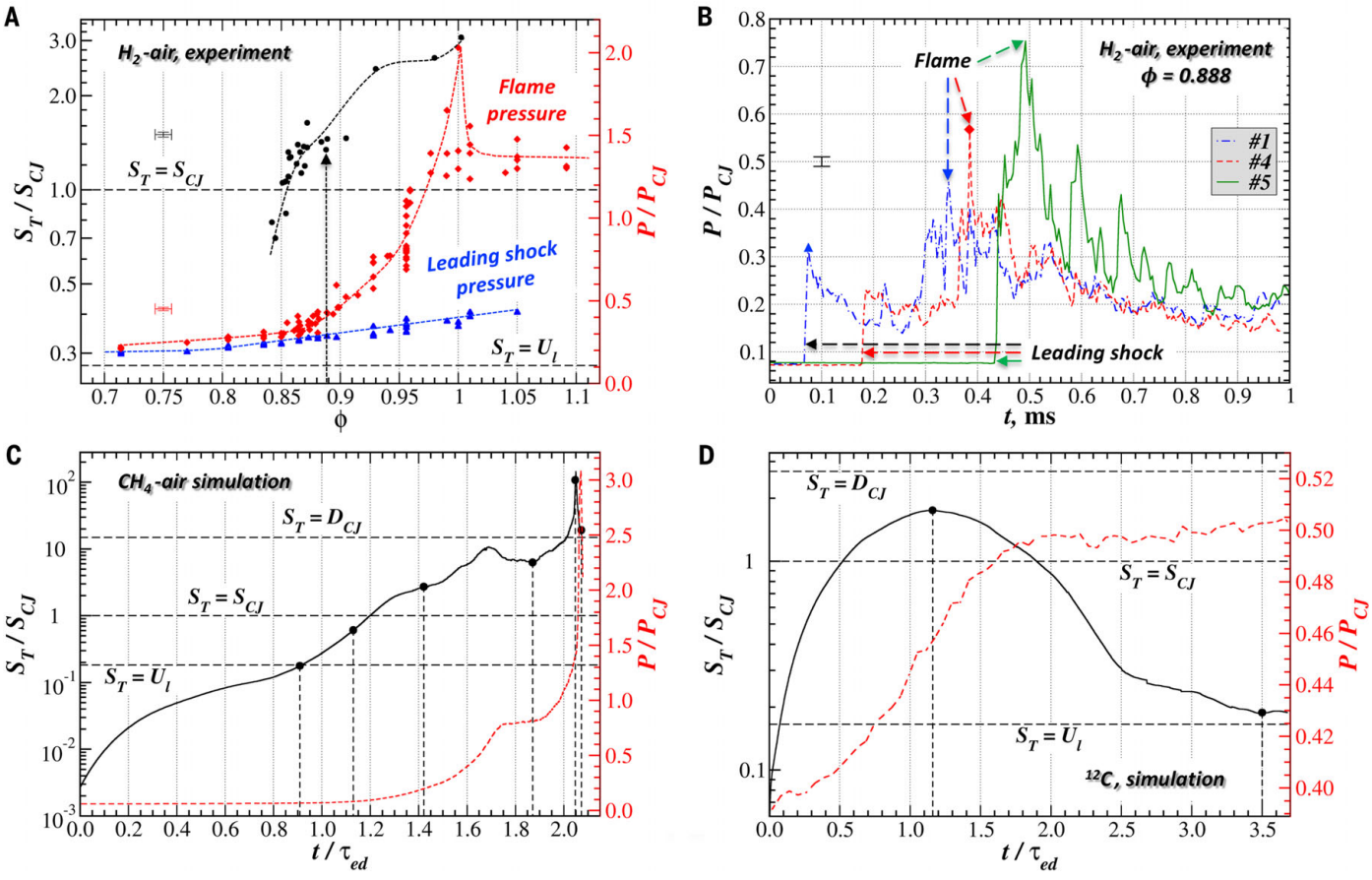


Fig. 2. Pressures, P, and turbulent flame speeds, S_T, observed in experiments and simulations for chemical and thermonuclear flames. (**A**) Summary of all experiments in hydrogen-air mixtures as a function of the equivalence ratio. Black circles indicate S_T measured at the beginning of the first test section (Fig. 3). Values of S_T are scaled by the CJ deflagration velocity S_{CJ}, which depends on ϕ and varies between 192 and 292 m s^{-1}. Blue triangles indicate peak pressures of the leading shock. Red diamonds indicate maximum pressures generated by the turbulent flame in the first test section. All pressures are scaled by the CJ detonation pressure P_{CJ}, which depends on ϕ and varies between 14.0 and 15.8 atm. Blue triangles and red diamonds in (A) correspond to pressure peaks indicated by a blue triangle and a red diamond in (B), respectively. The black dotted arrow marks the experiment shown in Fig. 4, F to H, and the black circle immediately to the right marks the experiment shown in Fig. 4, I and J. (**B**) Pressure histories recorded in the experiment with ϕ = 0.888 by three pressure transducers indicated in Fig. 3. Pressure is scaled by P_{CJ} = 15.06 atm. The first peak in each curve corresponds to the leading shock. The second pressure maximum is associated with the compressed region ahead of the flame (Fig. 4). (**C**) S_T and maximum instantaneous P in the computational domain as functions of time in the same simulation as that in Fig. 1. Initial pressure P_0 = 1 atm. S_T is scaled by S_{CJ} = 121.73 m s^{-1}, P is scaled by P_{CJ} = 17.12 atm, and time is scaled by the eddy turnover time τ_{ed} = 0.367 ms. Vertical dashed lines indicate times corresponding to frames shown in Fig. 1. (**D**) S_T and maximum instantaneous P in the computational domain in the simulation of a thermonuclear turbulent flame in pure ^{12}C at initial density $\rho_0 = 4 \times 10^8$ g cm^{-3}. S_T is scaled by $S_{CJ} = 4.8 \times 10^8$ cm s^{-1}, P is scaled by $P_{CJ} = 3.64 \times 10^{26}$ ergs cm^{-3}, and time is scaled by the integral-scale eddy turnover time $\tau_{ed} = 5.76 \times 10^{-11}$ s. Vertical dashed lines indicate times corresponding to frames shown in Fig. 5. Experimental uncertainties in quantities shown in (A) and (B) are indicated with error bars (*63*).

Equation 1 is equivalent to

$$\dot{e} \gtrsim e/t_s \quad (2)$$

where e is the internal (thermal) energy, $\dot{e}$ is the energy release rate in a flame, and $t_s = \delta_T/c_s$ is the sound-crossing time of a turbulent flame with width δ_T (*47*). Equation 2 essentially provides the physical meaning for Eq. 1: When the flame speed exceeds the CJ threshold, burning releases within a sound-crossing time the amount of energy close to, or greater than, the internal energy stored in the flame volume. This results in a buildup of pressure and ultimately causes the formation of strong shocks.

The criterion defined by Eq. 1 does not predict the onset of tDDT in a given turbulent reactive flow. Instead, we need to determine the corresponding critical turbulent conditions, at which the turbulent flame speed can reach S_{CJ} and thus allow the turbulence-induced pressure runaway to occur.

The tDDT process can occur while the flame remains in the flamelet regime, which is defined as the combustion regime in which the turbulent flame can be viewed as a folded laminar flame sheet with the internal structure minimally affected by turbulence (*47*). Other theoretical models (*50*–*53*) have suggested that turbulence-driven DDT requires formation of distributed flames and thus necessitates higher turbulent intensities capable of disrupting the internal flame structure. However, the tDDT mechanism, which triggers the pressure runaway and ultimately DDT, is not dependent on the structure of a turbulent flame or the particular combustion regime as long as Eq. 1 is satisfied. This process can be observed even in idealized one-dimensional (1D) flames by artificially increasing the flame speed (*54*). Therefore, a similar set of critical turbulent conditions can be obtained also for distributed flames. We focused on the derivation of the critical turbulent conditions in the flamelet regime.

In the flamelet regime, the turbulent flame speed S_T is

$$S_T = I_M S_L \frac{A_T}{L^2} \quad (3)$$

where A_T is the surface area of the flame sheet folded in a volume of size L, S_L is the laminar flame speed, and the coefficient I_M accounts for the effects of turbulent stretch (*55*). For thermonuclear flames, I_M is of order unity (*56*).

In the volume L^3, turbulence would fold the flame on all scales greater than some small scale λ_f, on which the turbulent intensity $U_\lambda \equiv U(\lambda)$ can be estimated (*57*) as

$$U_\lambda = \alpha I_M S_L \quad (4)$$

As a result of such packing, the flame surface density in a unit volume is equal to the inverse of the average flame-sheet separation, which is effectively the scale of the smallest flame folds λ_f

$$\frac{A_T}{L^3} = \frac{1}{\lambda_f} \quad (5)$$

On the basis of the criterion in Eq. 1, at the onset of the runaway, $S_T = c_s/\alpha$. Substituting this along with Eq. 5 into Eq. 3, we can find the characteristic flame volume L_{CJ}, in which the flame can achieve the CJ deflagration conditions

$$L_{CJ} = \lambda_f \frac{c_s}{\alpha I_M S_L} \quad (6)$$

In particular, the smallest possible size of the flame region in which tDDT can occur, L_{CJ}^{min},

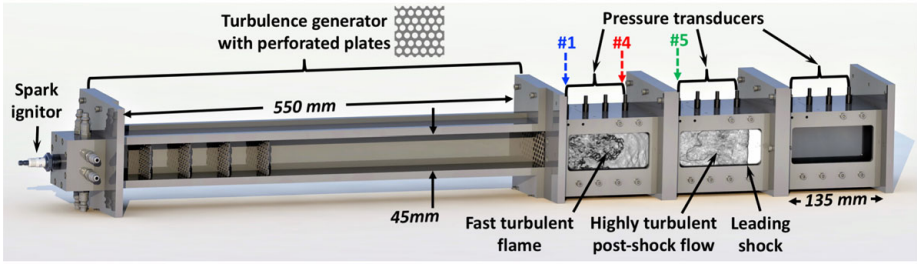


Fig. 3. Experimental TST facility. The section with perforated plates on the left is used to generate a fast turbulent flame, which propagates to the right. Test section is located past the last perforated plate at the distance of 550 mm from the ignition point. Blue, red, and green dashed arrows indicate the transducers 1, 4, and 5, respectively, that produced pressure signals shown in Fig. 2B.

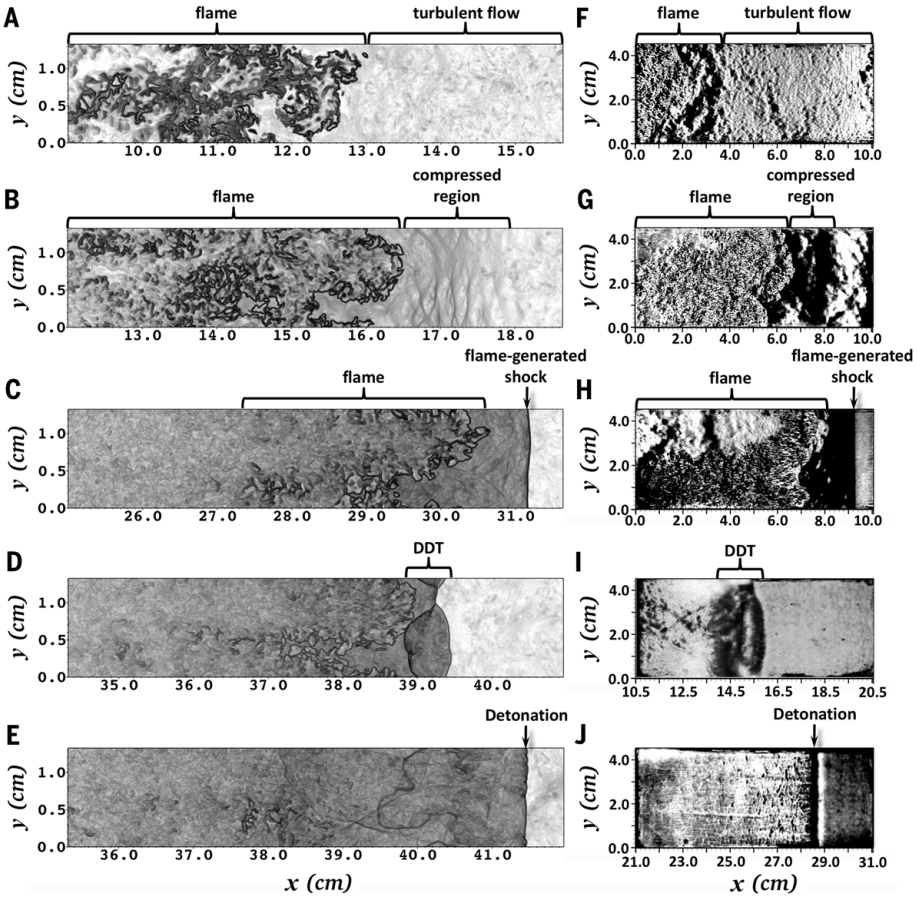


Fig. 4. Simulated and experimental schlieren images of the turbulent flame during the pressure runaway and subsequent detonation formation. (**A** to **E**) Simulated schlieren images. (**F** to **J**) Experimental schlieren images. The experiment in (F) to (H) was carried out at $\phi = 0.888$ (Fig. 2B), and the experiment in (I) and (J) was carried out at $\phi = 0.905$. Simulated schlieren images shown in (A) to (E) are from the same simulation as that in Fig. 1.

corresponds to the maximally tight flame packing, in which the average separation of flame-sheets, λ_f, is close to the laminar flame thickness, δ_L

$$L_{CJ}^{min} = \delta_L \frac{c_s}{\alpha I_M S_L} \quad (7)$$

We assume that turbulent properties of the reacting flow field can be effectively represented by homogeneous isotropic Kolmogorov-type turbulence. In reality, the presence of exothermic reactions can change the turbulence structure inside the flame (*58*–*60*). These changes are primarily driven by the fluid expansion as well as the increase of the temperature-dependent viscosity, and such effects can be pronounced in chemical flames. By contrast, in thermonuclear flames, their impact is minimal owing to very low density ratios across the flame $\alpha \lesssim 2$ and extremely small ratios of viscosity to thermal conduction in degenerate plasmas defined by the Prandtl number $Pr \sim 10^{-5}$ (*61*).

Using Kolmogorov scaling and the turbulent intensity at the scale $\lambda = \delta_L$ defined by Eq. 4, we can find turbulent intensity U_l^{max} at a characteristic integral scale, l, which would produce such maximally tight flame packing corresponding to Eq. 7

$$U_l^{max} = \alpha I_M S_L \left(\frac{l}{\delta_L}\right)^{1/3} \quad (8)$$

This integral turbulent velocity would provide the maximum burning rate per unit volume because it would create the most tightly packed flame configuration. Therefore, it would create conditions for the onset of tDDT in the smallest possible volume.

At the same time, CJ conditions can also be realized at lower turbulent intensities $U_l < U_l^{max}$. In this case, the smallest flame folds will occur on scales $\lambda_f > \delta_L$, and the resulting critical flame volume L_{CJ} required to achieve the CJ burning speed (Eq. 6) would be larger than L_{CJ}^{min}. In particular, turbulent intensity U_{CJ} at the scale L_{CJ}, which would provide sufficient flame packing on that scale to achieve $S_T = S_{CJ}$, can be found as

$$U_{CJ} = U_\lambda \left(\frac{L_{CJ}}{\lambda_f}\right)^{1/3} \quad (9)$$

Using Eqs. 4 and 6, this gives

$$U_{CJ} = (\alpha I_M S_L)^{2/3} c_s^{1/3} \quad (10)$$

This turbulent intensity is independent of scale and only depends on the properties of the reactive mixture. Therefore, we can use Eq. 10 and the Kolmogorov scaling to express L_{CJ} in terms of the characteristic turbulent integral scale, l, and velocity, U_l, in a given system

$$L_{CJ} = (\alpha I_M S_L)^2 c_s \frac{l}{U_l^3} \quad (11)$$

The critical flame speed $S_T = S_{CJ}$ at the scale L_{CJ} can be, and typically is, higher than the turbulent velocity $U_l = U_{CJ}$ at that scale (Fig. 2). Thus, such S_T does not represent the burning speed of a flame in equilibrium with the ambient turbulent flow field. For $S_T > U_l$, the upstream turbulence cannot supply fresh fuel to the turbulent flame sufficiently fast to sustain such high burning rates, and faster burning can be supported only by the fuel already contained within the flame. Such unsteady configurations can form either when a flame enters the region of sufficiently fast turbulence or when turbulent intensity gradually increases above the critical values given by U_{CJ} or U_l^{max}. Ultimately, this unsteady burning continues as a runaway process either until a detonation is formed or the fuel in the flame burns out, which can lead to the pulsating instability of turbulent flames associated with the periodic formation of shocks (*49*).

The criteria for the onset of the pressure runaway, at which $S_T = S_{CJ}$, are provided in Eqs. 7, 8, 10, and 11. In this sense, the criteria represent only the necessary conditions for the detonation initiation. The sufficiency condition, which defines whether a shock or a detonation form as a result of the pressure runaway, depends on the duration of this process. If the fuel in the turbulent flame burns out within a sound-crossing time of the flame, the result is equivalent to a constant-volume explosion, which generates pressures insufficient for a detonation initiation (both in chemical and thermonuclear mixtures). However, if the burnout lasts for several sound-crossing times, pressure will build up on the upstream side of the turbulent flame because of the gradient of the sound speed in the flame. Such gradual pressure accumulation will ultimately produce shocks of sufficient strength to ignite a detonation.

For packed flame configurations, the ratio of the burnout time $t_B = \lambda_f/(I_M S_L)$ of the flame to

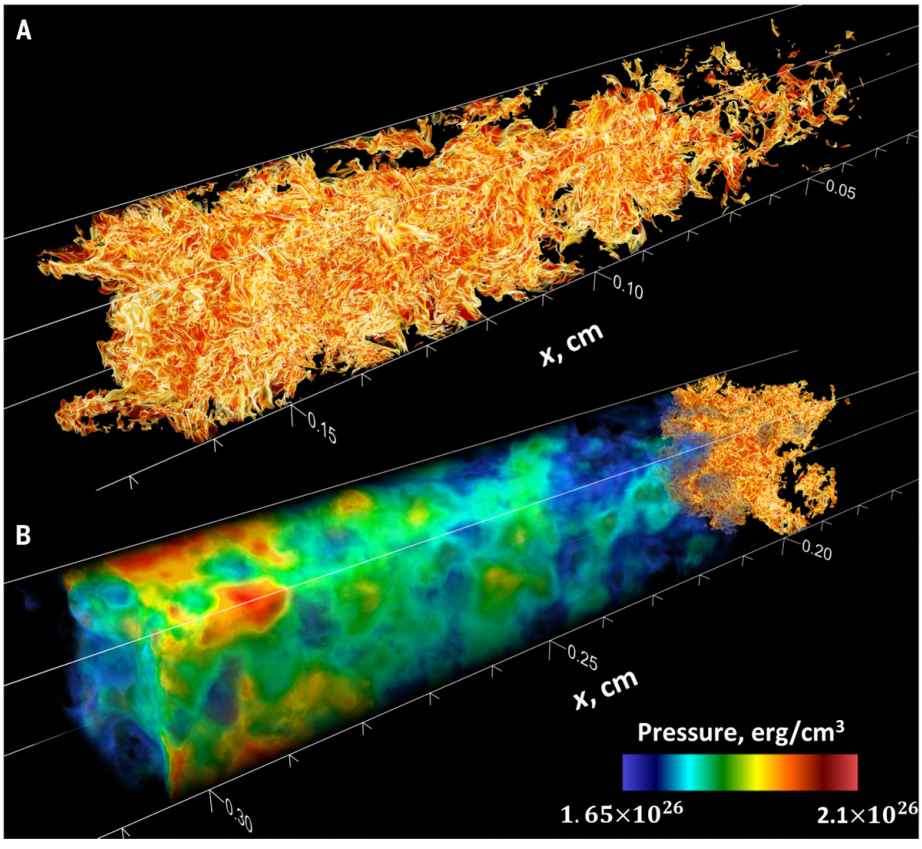


Fig. 5. Turbulence-driven spontaneous shock formation in a turbulent thermonuclear flame. (**A**) Flame structure at the time of maximum turbulent burning velocity, S_T. (**B**) Resulting flame-generated pressure field and the equilibrium structure of a turbulent flame at the end of the burnout phase. The flame propagates to the left and is shown as a semitransparent flame surface with varying opacity by using a ray-tracing visualization technique. Colors correspond to the light intensity, which increases from red to yellow to white. Corresponding turbulent flame speeds and maximum pressures are shown in Fig. 2D. This simulation is shown in movie S2.

the sound-crossing time $t_s = L_{CJ}/c_s$ is equal only to the flame density ratio

$$\frac{t_B}{t_s} = \alpha \qquad (12)$$

which follows from Eq. 6. Packed configurations formed by terrestrial chemical flames with $\alpha \sim 3$ to 10 (*48*) burn out during several sound-crossing times. This allows for the pressure accumulation on the upstream side of the flame and creates conditions for shock amplification, capable of producing DDT (Fig. 1, F, G, and H). For thermonuclear flames in degenerate plasmas, however, $\alpha = 1.2$ to 2.0 (*61*), and the burnout occurs during only one or two sound-crossing times. The resulting shocks are similar to those produced in a constant-volume explosion and are of insufficient strength to ignite detonations directly. These shocks, however, can further amplify by propagating in the density gradient of a star (*62*) or by interacting with surrounding turbulent flames on larger scales. We thus consider Eq. 1 as the criterion for DDT in SNIa, although the DDT mechanism in SNIa requires an additional step for shock amplification to DDT strengths.

These analytical results are consistent with the DNS of chemical flames (*47*). L_{CJ}^{min} is very close to the domain size in calculations in which pressure runaway was observed (*47*). Those DNS relied on a simplified physical model involving an ideal-gas equation of state and a single-step, first-order Arrhenius chemical kinetics representing H_2-air– and CH_4-air–like mixtures. Thus, comparison with those DNS does not determine whether this mechanism of tDDT would also be present in realistic chemical mixtures. In order to address this issue, we next present results of an experimental study that demonstrate the tDDT process in turbulent H_2-air flames propagating with super-CJ speeds.

Experimental study

During a SNIa explosion, DDT would occur in unconfined conditions, i.e., in the absence of walls or obstructions that could confine pressure, thus creating conditions for its buildup. It is difficult to create a similar experimental setting, in which the evolution of a perfectly unconfined flame can be observed from ignition to the onset of a detonation. However, even in a confined experimental configuration, it is possible to isolate the turbulence-flame coupling, which could lead to a pressure runaway and a DDT, from other phenomena related to the interactions of high-speed flows with obstructions or turbulent boundary layers. We designed an experiment to test this.

A schematic diagram of the Turbulent Shock Tube (TST) facility and the resulting flow structure are shown in Figs. 3 and 4. This facility is intended to create high-speed turbulent conditions, which can lead to the spontaneous flame acceleration and tDDT that were previously modeled in DNS (*47*, *49*). The TST consists of a 1.5-m-long channel with one open and one closed end, with a square cross section of 45 by 45 mm^2. A spark plug is mounted at the center axis of the channel at the closed end and used to ignite the flame. Each of the test sections is 152 mm long with optical access on three sides, which creates a visibility domain of approximately 135 by 45 mm for advanced flame and flow-field diagnostics (*63*). The diagnostic section windows are composed of 25-mm-thick fused silica designed to sustain high pressures associated with detonation waves. Premixed hydrogen-air mixtures with varying composition are used.

Upon ignition, the flame kernel initially expands to fill the entire cross-sectional area of the channel. Once the flame front has developed, it begins to propagate toward the open end of the channel. A series of five perforated plates are

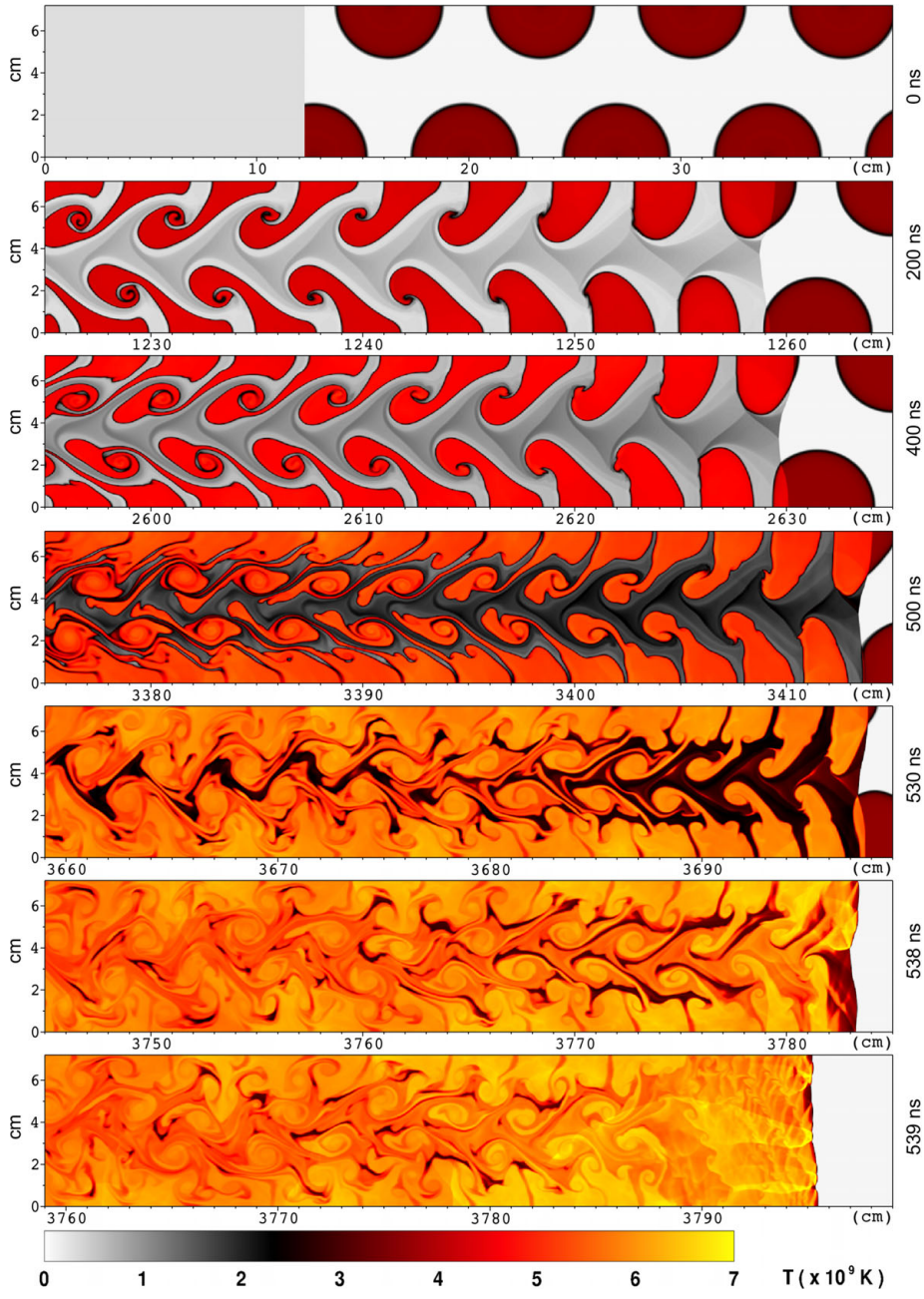


Fig. 6. Shock interaction with an idealized turbulent thermonuclear flame and the resulting DDT. Shown is the temperature distribution in a 2D calculation carried out at $\rho = 3 \times 10^7$ g cm^{-3} in a 50/50 $^{12}C/^{16}O$ mixture. Initial shock Mach number is 1.28, corresponding to a constant-volume explosion. Time since the start of the simulation is indicated to the right of each frame. Detonation ignition occurs at $t = 5.38 \times 10^{-7}$ s at $x \approx 3782$ cm.

positioned inside the facility close to the point of ignition to generate turbulence in the flow passing through them and thus to produce rapid flame acceleration. As a result, a leading shock wave with Mach ~2 to 3 is formed ahead of the flame. After this shock passes through the last perforated plate immediately before the diagnostic section, the post-shock flow creates multiple high-speed jets that produce high levels of turbulence within the reactants. The turbulent intensity is controlled by the equivalence ratio, ϕ, of the initial mixture. Higher values of ϕ result in faster laminar flame speeds and more rapid initial flame acceleration, which translates into larger leading shock velocities and higher turbulence levels. The geometric configuration used allows us to survey the flame regimes of interest and focus on the conditions for tDDT. Extensive experimental testing of the design and arrangement of perforated plates has been performed to ensure that desired turbulence conditions are achieved, specifically in terms of the amplitude of turbulent velocity fluctuations (*64*–*66*).

After the flame passes the last perforated plate and emerges in the diagnostic section, it starts to interact with the high-speed turbulence in this section. Subsequent flame evolution depends on the flame initial burning velocity, S_T, which is controlled by the level of turbulent fluctuations. Depending on the value of S_T relative to the CJ deflagration speed, the flame may or may not produce strong shocks and undergo the tDDT. In this setup, varying mixture composition over a very narrow range of ϕ allows us to probe the flame dynamics, as well as the details of the tDDT process, as S_T is increased from below to above the CJ threshold.

The turbulent flame evolution in the experiments is shown in Fig. 4, F to J, in a sequence of schlieren images, representing flow density gradients manifested by the gradients of the refractive index. Two experiments are shown with mixture equivalence ratios of ϕ = 0.888 (Fig. 4, F to H) and ϕ = 0.905 (Fig. 4, I and J) to highlight different stages of tDDT. Also shown in Fig. 4, A to E, are synthetic schlieren images obtained from the DNS (Fig. 1) (*47*) at the similar stages of the flame evolution. Synthetic schlieren images represent $\log(\nabla\rho)$ computed in a 3D volume and projected onto a 2D plane. Although an H_2-air mixture was used in the experiments, the DNS shown in Figs. 1 and 4 used a CH_4-air mixture, which demonstrates the independence of the results on the choice of a reactive mixture. The laminar flame speed in CH_4-air is almost an order of magnitude lower than in H_2-air (38 versus 302 cm s^{-1}, respectively). Calculations using H_2-air mixture have been discussed elsewhere (*47*). At the time shown in Fig. 4, F to J, extended boundary layers have not developed, and so their influence on the observed flame acceleration is negligible.

Simulated and experimental schlieren images in Fig. 4 show similar dynamics. Pressure waves generated within the turbulent flame propagate into the unburned material and form a compressed region ahead of the flame (Fig. 4, B and G). As the runaway process develops, multiple pressure waves coalesce into a flame-generated shock, the strength of which grows with time (Fig. 4, C and H). This shock forms between the flame and the leading shock that was transmitted through the last perforated plate. Eventually, the shock approaches the von Neumann (post-shock) pressure of a CJ detonation (Fig. 2A), at which point it triggers a DDT (Fig. 4, D and I) and forms a detonation (Fig. 4, E and J). The case with ϕ = 0.905 (Fig. 4, I and J) results in a detonation, but the corresponding peak pressure shown in Fig. 2A is lower than P_{CJ}. This is because pressures reported in Fig. 2A were measured in the first diagnostic window, whereas DDT occurred in the second window.

Peak pressures in the leading shock and those produced by the flame are shown in Fig. 2A, along with the corresponding turbulent flame speeds, as a function of the equivalence ratio in multiple experiments. The evolution of the pressure buildup inside the turbulent flame and the emergence of a flame-generated shock for a specific experiment with ϕ = 0.888 are demonstrated in Fig. 2B. It provides pressure histories recorded with several pressure transducers shown in Fig. 3.

The flame starts to generate strong pressure waves when its burning velocity S_T exceeds the S_{CJ} threshold—that is, when Eq. 1 is satisfied (Fig. 2A). This results in the formation of a compressed region of high pressure immediately ahead of the flame (Fig. 4, F to H). Pressure growth is associated with the turbulent flame and not supported by the closed end of the channel (Fig. 2B). Pressure in the vicinity of the flame as recorded with transducers increases by ≈70%. This occurs as the flame propagates down the length of the channel and passes transducers located progressively further downstream (Fig. 3). The pressure recorded by

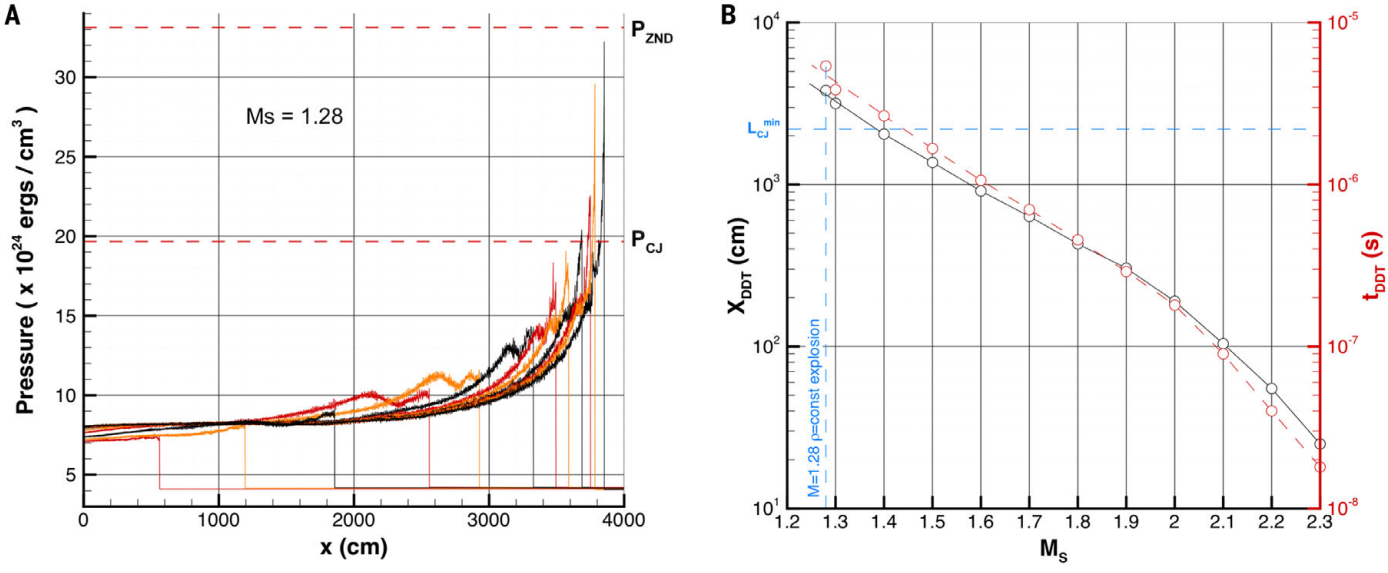


Fig. 7. DDT driven by shock-flame interaction. (**A**) Pressure evolution in the calculation shown in Fig. 6. Shown is the *y*-averaged distribution of pressure in the domain for several time instances. Several colors are used to separate overlapping curves. (**B**) Distance (left axis) and time (right axis) to DDT (Fig. 6) as a function of the shock Mach number.

transducer 1 at later times drops and eventually plateaus at a level well below the peak pressures recorded in the flame region. The pressure recorded at later times by transducer 4, which is located further ahead of transducer 1 (Fig. 2), exhibits the same decreasing trend and reaches values very close to those recorded with transducer 1. This shows that pressure upstream of the flame front close to the last perforated plate does not change with time, which would be the case if the observed increase in pressure in the flame region was the result of pressurization of the entire flow from the flame to the closed end of the channel.

The turbulent flame speed in the experiments shown in Fig. 4 satisfies Eq. 1 (Fig. 2A). We next considered whether turbulent conditions in these experiments are in agreement with the theory presented above. In particular, at ϕ = 0.888, turbulent integral velocity, U_l, ahead of the flame at the beginning of the diagnostic section—at the start of the runaway process, resulting in the pressure buildup—had an average value of 68.85 m s^{-1}, with the maximum and minimum values of 238.56 and 9.70 m s^{-1}, respectively, and a standard deviation of 37.68 m s^{-1} . Values of the turbulent integral scale, l, were 1.45 cm (average), 3.17 cm (maximum), 0.19 cm (minimum), and 0.45 cm (standard deviation). Procedures for determining these turbulent characteristics in the TST facility have been described elsewhere (*66*). The pressure and temperature of the reacting mixture in the compressed region ahead of the flame are 6.92 atm and 627 K, respectively. These allowed us to determine the corresponding laminar flame properties and S_{CJ}. The critical turbulent integral velocity U_l^{max} defined in Eq. 8 and corresponding to the average integral scale in the flow is 166.76 m s^{-1}. This turbulent velocity would be required to provide maximally tight flame packing. It is, however, larger than the average U_l = 68.85 m s^{-1} in the flow, which implies that flame would be folded on scales larger than δ_L. As a result, the flame volume required to reach the CJ conditions would be larger than L_{CJ}^{min} (Eq. 7) and instead would be defined by Eq. 6, namely L_{CJ} = 2.6 cm, which is within the range of values of l = 0.19 to 3.17 cm observed in the experiment and 80% larger than the average l = 1.45 cm. The corresponding U_{CJ} = 83.64 m s^{-1} (Eq. 10) is within 20%, and less than σ, of the average U_l = 68.85 m s^{-1} in the experiment. Therefore, theoretically predicted turbulent conditions for the onset of the pressure runaway are within the range of values observed in the experiment.

Similar analysis can be carried out for the DNS shown in Fig. 4. Turbulent integral velocity and scale in the calculation are U_l = 22.37 m s^{-1} and l = 0.31 cm, respectively. Despite the large turbulent intensities in this calculation, only the preheat zone of the flame,

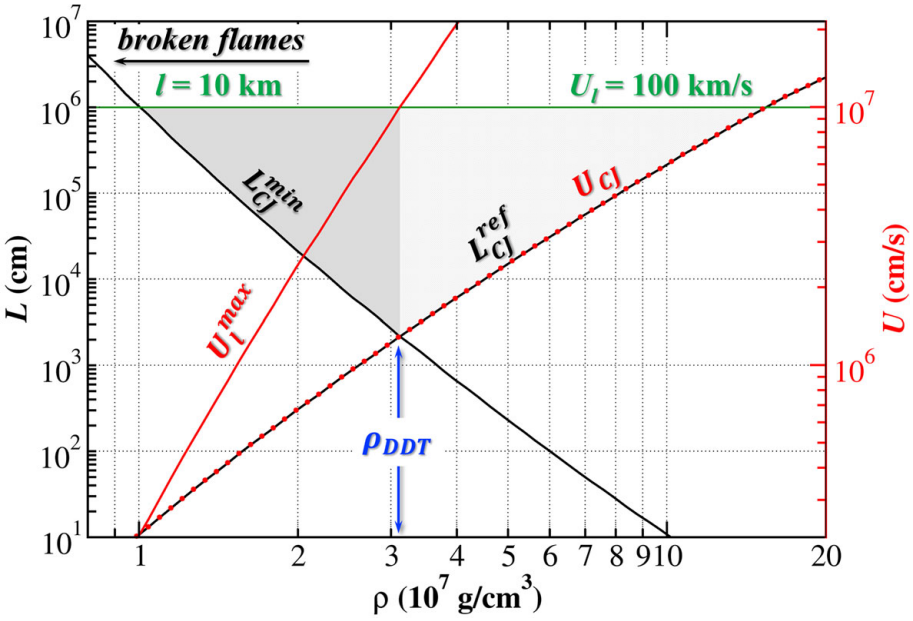


Fig. 8. Critical conditions for tDDT in the Chandrasekhar-mass explosion scenario. Quantities shown are L_{CJ}^{min} (Eq. 7), U_l^{max} (Eq. 8), L_{CJ}^{ref} (Eq. 11), and U_{CJ} (Eq. 10). $U\ell_{max}$ and L_{CJ}^{ref} were calculated assuming the reference turbulent conditions ℓ = 10 km and U_ℓ = 100 km/s (*51*, *52*, *76*). Gray areas show the range of parameters for which tDDT is possible, with the highest probability corresponding to ρ_{DDT}.

where the heat and products diffuse into the cold reactants, is broadened (*58*). Thus, overall, combustion proceeds in the flamelet regime, which is consistent with the theory developed above. Using the laminar-flame properties for the single-step CH_4-air reaction model (*67*), the corresponding U_{CJ} = 19.25 m s^{-1} and L_{CJ} = 0.2 cm, which are just below U_l and l in the calculation. Therefore, turbulent conditions in this calculation are also in agreement with the theoretical predictions for the onset of the pressure runaway.

Numerical modeling in thermonuclear systems

The equation of state, transport properties, and chemical kinetics that characterize degenerate thermonuclear plasma in a WD interior during a SNIa explosion differ in several aspects from those representative of chemical reactive systems. Thermonuclear deflagrations are characterized by very low density ratios, $\alpha \sim 1.2$ to 2 (*61*), in contrast with chemical flames, in which $\alpha \sim 3$ to 10 (*48*). Because the formation of a sonic point in a subsonic CJ deflagration is determined by the fluid expansion in a flame, lower density ratios in thermonuclear plasmas could affect the overall dynamics of turbulent super-CJ deflagrations. Therefore, we next tested our theoretical model under appropriate conditions of burning thermonuclear plasmas.

Numerical simulations allow only a limited range of scales to be modeled in a typical calculation of turbulent flames. To capture the tDDT process in a simulation, L_{CJ}^{min} for a given reactive mixture must be sufficiently small to be accommodated in a limited computational domain.

We considered a variety of mixture compositions, from pure ^{4}He and ^{4}He/^{12}C mixtures, which would represent sub-M_{ch} and DD models, to ^{12}C/^{16}O mixtures relevant to the M_{ch} scenario. We found that L_{CJ}^{min} becomes sufficiently small to be simulated—namely, $L_{CJ}^{min}/\delta_L \lesssim 100$—only for pure ^{12}C mixtures at high densities $\rho \gtrsim 2 \times 10^8$ g cm^{-3} (*63*). Although DDT would not be expected to occur at such densities in a SNIa, this nevertheless allowed us to simulate tDDT in a degenerate plasma undergoing thermonuclear burning.

We modeled thermonuclear flame dynamics using compressible reactive-flow equations solved with a finite-volume code Athena-RFX (*68*, *69*). Further details of the modeling approach are given in (*63*).

For the thermonuclear-flame simulation, we used a flame-in-a-box computational setup similar to the previous chemical-flame DNS (*47*) shown in Fig. 1, which has also been used in prior simulations of thermonuclear flames (*70*–*73*). Such calculations based on first principles represent a small region of the flow inside a WD, allowing us to fully resolve the flame and its evolution in the turbulent flow. The flame interacts with a homogeneous, isotropic upstream turbulence steadily driven at the scale of the domain width by using a spectral method, which introduces divergence-free velocity fluctuations into the flow, with a prescribed energy injection spectrum and rate (*69*). This approach ensures that the turbulent integral velocity, U_l, and scale, l, in the upstream flow are nearly constant both in space and time with a standard deviation of $\lesssim$2% and $\lesssim$5%,

respectively. An analysis of the resulting turbulence, both reacting and nonreacting, including comparison with prior experimental and DNS results, has been presented elsewhere (*58*, *59*).

The domain size and turbulent intensity were set according to the criteria given in Eqs. 7 to 10 (table S1). The calculation uses a rectangular domain with width equal to the minimal CJ system size $L_{CJ}^{min} = 0.02$ cm (Eq. 7) for the fuel density $\rho = 4 \times 10^8$ g cm^{-3}. At this density, the laminar flame speed $S_L = 1.35 \times 10^7$ cm s^{-1}, and the CJ speed $S_{CJ} = 4.8 \times 10^8$ cm s^{-1}, or respectively ≈2% and ≈70% of the sound speed in fuel. The calculation was performed on a uniform Cartesian mesh with a cell size $dx = 3.91 \times 10^{-5}$ cm, which corresponds to $\delta_L/dx = 4.68$. This resolution is sufficient to capture the laminar flame properties and is similar to that used in prior studies of fully resolved thermonuclear deflagrations (*72*, *73*). Initially, turbulence is allowed to evolve for $\approx 5.2\tau_{ed}$ in order to reach an equilibrium steady state, where $\tau_{ed} = l/U_l$ is the integral-scale eddy turnover time. The resulting turbulence is characterized by the integral velocity $U_l = 8 \times 10^7$ cm s^{-1} ≈ $1.84U_{CJ}$ (Eq. 10) or ≈12% of the sound speed in fuel, so $U_l < S_{CJ}$. The corresponding turbulent integral scale $l \approx L_{CJ}^{min}/4$. At the time $t = 5.2\tau_{ed}$, the thermodynamic state in the domain is reinitialized with the exact laminar flame solution corresponding to the initial fuel temperature 10^8 K. Boundary conditions are periodic in the spanwise direction (transverse to the direction of flame propagation) and zero-order extrapolation (outflow) along the flame-propagation direction, which allows products to flow out from the back of the domain and does not create a confining effect capable of promoting pressure buildup. Despite the substantial level of turbulent intensity, turbulent energy dissipation has a negligible effect on the system dynamics. By the end of the calculation, fuel temperature increases to $\approx 8.5 \times 10^8$ K from an initial 1.0×10^8 K. As a result, the laminar flame speed increases by ≲8%.

The evolution of S_T and maximum pressure in the domain in this calculation are shown in Fig. 2D. The burning speed increases, rapidly exceeding S_{CJ} and approaching the detonation speed D_{CJ}. Once S_T exceeds U_l, however, the flame decouples from the upstream turbulence. It rapidly consumes the fuel ingested into the flame during the early stages of the evolution, completing the burnout within approximately one sound-crossing time, which is in agreement with Eq. 12. Pressure growth accelerates once S_T crosses the S_{CJ} threshold, similar to the behavior observed in chemical mixtures (Fig. 2, A to C). Eventually, a strong shock forms, exits the flame, and propagates into the fuel upstream. Shown in Fig. 5 are the corresponding flame structure at the time of maximum S_T (Fig. 5A) and after the completion of the flame burnout (Fig. 5B), as well as the structure of the resulting shock wave (Fig. 5B; also see movie S2). The resulting shock has local peak pressures $\approx 2 \times 10^{26}$ erg cm^{-3} (Fig. 5B) and the spanwise-averaged peak pressures $\approx 1.85 \times 10^{26}$ erg cm^{-3} (Fig. 2D). The corresponding shock Mach number $M_s \approx 1.15$. This shock is stronger than the one produced in a constant-volume explosion at these plasma conditions, for which the peak pressure $P_{CV} = 1.73 \times 10^{26}$ erg cm^{-3} and Mach number $M_{CV} = 1.09$ (*63*).

Thus, similar to chemical mixtures, the interaction of a highly subsonic thermonuclear flame with a highly subsonic turbulence can produce strong shocks in unconfined degenerate plasmas. A rapid runaway process resulting in pressure buildup occurs once the flame speed exceeds the critical CJ deflagration threshold, in agreement with Eq. 1. The turbulent conditions derived above—namely, L_{CJ}^{min} (Eq. 7) and U_{CJ} (Eq. 10)—also match the onset of the runaway in degenerate plasmas. This suggests that the overall mechanism is applicable to both chemical and thermonuclear mixtures.

We next investigated whether shocks, which are produced in the process described above, can ultimately trigger a detonation. Such shocks can further amplify by propagating in the density gradient of a star (*62*) or by interacting with surrounding turbulent flames; we focused on the latter mechanism.

Although the strength of the shock observed in the DNS was larger than in a constant-volume explosion, we assumed conservatively that shocks produced by super-CJ flames in thermonuclear plasmas are close to those in constant-volume explosions. Propagating such a shock through a 3D turbulent flame until detonation ignites is computationally expensive. Therefore, we demonstrate this process in a 2D calculation, in which a turbulent flame is represented by a series of spherical flames. An additional benefit of considering this problem in two dimensions is that we can model this process at a density $\rho = 3 \times 10^7$ g cm^{-3} and in a realistic 50/50 ^{12}C/^{16}O composition, which are closer to the DDT conditions expected in SNIa. We considered the propagation of a constant-volume explosion shock with Mach number $M_s = 1.28$ and $P_{CV} = 7.1 \times 10^{24}$ erg cm^{-3} through a series of spherical flames with diameter $10\delta_L$ and separation between sphere centers $30\delta_L$. Such a configuration represents a loosely packed flame. We performed the calculation on a uniform grid with resolution $\Delta x = 0.0257$ cm, or 4.4 cells per half-^{12}C -reaction zone length of a CJ detonation, which is defined as the distance from the shock to the point at which the mass fraction of ^{12}C reaches half its maximum value. Similar resolution was used in prior detonation studies, in which it was shown to reproduce the detonation velocity and resolve the characteristic multidimensional cellular structure of unstable thermonuclear detonations (*74*). The size of such detonation cells is ≈3 cm (*74*), resulting in ≈2.4 detonation cells in the 7.2-cm-wide channel. The corresponding resolution of a laminar flame is 9.3 computational cells per δ_L. The initial flame configuration is shown in Fig. 6, top.

As the shock begins to propagate through the turbulent flame, it compresses the flame and generates more flame surface. Both processes accelerate burning, which ultimately results in a pressure increase that couples to the shock and amplifies it. This process is illustrated by the time sequence of frames in Fig. 6. The pressure distribution through the domain at several times is shown in Fig. 7A. As the shock accelerates, the pressure rapidly approaches the von Neumann value, at which point the detonation is ignited. The resulting detonation speed is 1.16×10^9 cm s^{-1}, which is equal to the ideal speed of a freely propagating CJ detonation.

The results of several 2D simulations performed for the same flame configuration but different initial shock numbers M_s are shown in Fig. 7B. These show the dependence of the distance and time to DDT on the initial shock strength. Both quantities decrease rapidly with increasing M_s; however, even in the case of the weakest constant-volume explosion shock, the distance to DDT is close to L_{CJ}^{min}. Therefore, L_{CJ}^{min} can be used to estimate the minimal flame region required for the tDDT process.

Transition density in the M_{ch} SNIa model

We used the theory developed and validated above to estimate conditions at which the tDDT can occur in SNIa. We restricted our analysis to the classical M_{ch} model.

In the M_{ch} scenario, the explosion starts when a thermonuclear flame is ignited near the WD center and propagates in the gravitational field of a WD (*31*, *32*, *75*). This flame is subject to the Rayleigh-Taylor (RT) instability, which generates convective flows and turbulence on multiple scales. The turbulent energy is transferred from larger to smaller scales through a turbulent cascade. The resulting turbulent flame propagates at subsonic speeds, thus allowing the WD to expand. The density of the burning material changes both with the distance from the WD center and because of the WD expansion.

Previous large-scale 3D simulations of SNIa explosions resolve scales from the WD size ~1000 km down to ~10 km using a computational mesh size ≲1 km (*32*, *75*). These scales are larger than the characteristic scales of thermonuclear flames, which are between ~10^{-4} and ~10 cm for ^{12}C burning (*61*). Therefore, large-scale simulations rely on subgrid models that describe the physics of flames on unresolved scales and provide the flame

speed for scales close to the computational mesh size. These simulations do not produce shocks unless detonations are artificially triggered at some point and do not resolve any shock-generation phenomena on scales ≲10 km. Fully resolving these scales in a 3D simulation of an exploding WD remains computationally prohibitive.

Using known properties of laminar thermonuclear flames in the 50/50 $^{12}C/^{16}O$ mixture, which represents a typical WD composition, we computed L_{CJ}^{min}, L_{CJ}, U_l^{max}, and U_{CJ} using Eqs. 7, 11, 8, and 10, respectively. These are shown in Fig. 8 as functions of density. Both L_{CJ}^{min} and U_{CJ} depend only on the mixture properties, which vary with local density. L_{CJ} and U_l^{max} also depend on the turbulent integral scale l and velocity U_l. They were calculated assuming l = 10 km and U_l = 100 km s^{-1}, values found in large-scale calculations of the M_{ch} explosions (*51*, *52*, *76*). The lack of fully developed turbulence on scales >10 km greatly reduces flame packing on these scales.

L_{CJ}^{min} decreases below l = 10 km at densities >10^7 g cm^{-3}, thus allowing the CJ conditions to arise in the flow (Fig. 8) (*77*). As the density increases, the minimum size of the critical flame region decreases rapidly. At ρ ≈ 3 × 10^7 g cm^{-3}, turbulent integral velocity U_l^{max} at the scale of 10 km required to produce tight flame packing associated with L_{CJ}^{min} becomes larger than the reference U_l = 100 km s^{-1}. Therefore, at higher densities, high turbulent intensities not observed in full-star SNIa simulations (*51*, *52*, *76*) would be required to pack the flame sufficiently tightly to achieve L_{CJ}^{min}. CJ conditions can be created by the turbulent intensity of 100 km s^{-1}, although they would correspond to a less tightly packed flame and a larger critical flame volume L_{CJ}. Corresponding values of L_{CJ} for the reference U_l = 100 km s^{-1}, that we denote L_{CJ}^{ref}, as well as the turbulent velocity U_{CJ} at that scale are also shown in Fig. 8. After the critical flame volume reaches a minimum value at ρ ≈ 3 × 10^7 g cm^{-3}, it starts growing again, becoming larger than 10 km at ρ ≈ 1.5 × 10^8 g cm^{-3}.

This shows that tDDT cannot occur for densities below ≈10^7 g cm^{-3} and above ≈10^8 g cm^{-3} because it would require critical flame volumes that we do not expect to be produced by the turbulence present during a SNIa explosion. A critical flame volume smaller than the integral scale does not mean that tDDT will occur, given the stochastic nature of the process. As the ratio L_{CJ}/l becomes smaller, the probability of the formation of CJ conditions within the turbulent flame increases because a smaller size of the critical region allows for many more possible realizations in a given flow volume of size l. Therefore, the maximum probability of detonation formation is at the density corresponding to the smallest value of L_{CJ} ≈ 2 × 10^3 cm, or l/L_{CJ} ≈ 500, at ρ_{DDT} ≈ 3 × 10^7 g cm^{-3}. At that density, the number of possible realizations of the CJ conditions in a volume of size l, which could form over one integral-scale eddy turnover time, τ_l, is

$$N_{DDT} \sim \left(\frac{l}{L_{CJ}^{min}}\right)^3 \left(\frac{\tau_l}{\tau_{L_{CJ}}}\right) = \left(\frac{l}{L_{CJ}^{min}}\right)^{11/3} \sim 10^{10} \quad (13)$$

Here, $\tau_{L_{CJ}}$ is the eddy turnover time on scale L_{CJ}. In other words, the probability of the formation of a flame configuration satisfying CJ conditions would have to be less than 10^{-10} to prevent the onset of the pressure runaway at this density in a given region of size l. Because l is approximately two orders of magnitude smaller than the size of the WD ~1000 km, a large number of such regions would exist during the explosion inside the WD at the relevant densities. This further increases the probability of the onset of the runaway, thus making tDDT in the M_{ch} model almost inevitable.

Discussion and conclusions

We presented a self-consistent theory of turbulence-induced shock generation and DDT and showed that it is in agreement with experiments involving chemical flames and direct numerical simulations of thermonuclear deflagrations in degenerate plasmas at conditions present in the stellar interior during a SNIa explosion. The overall process, which triggers pressure runaway and results in the formation of a strong shock, qualitatively is not sensitive to the details of the equation of state, microphysical transport, or reaction kinetics. Such runaway process will occur once the flame speed exceeds the speed of a CJ deflagration. This theory showed that in a $^{12}C/^{16}O$ WD in the classical M_{ch} explosion scenario, tDDT has a high probability of occurrence at densities in the range 10^7 to 10^8 g cm^{-3}, with the maximum probability at ρ_{DDT} ≈ 3 × 10^7 g cm^{-3}. This value is similar to the transition densities 1.3 × 10^7 to 2.4 × 10^7 g cm^{-3} adopted in subgrid-scale models used in prior large-scale calculations of the M_{ch} explosion scenario (*32*), which are consistent with observations.

This analysis assumed turbulent conditions previously observed in large-scale calculations of SNIa, namely integral velocity U_l = 100 km s^{-1} at the scale of l = 10 km. This is in contrast with prior theoretical models (*50*–*52*, *78*, *79*), which inherently required the formation of distributed flames to create conditions for the spontaneous reaction wave mechanism of DDT and thus necessitated higher turbulent intensities typically above ~1000 km s^{-1}, which we regard as implausible.

The multiple proposed explosion scenarios for normal, bright SNIa share a common aspect: detonation formation at some point in the explosion. In particular, in the context of the M_{ch} scenario, our analysis suggests that DDT is almost inevitable. The high probability of DDT given by Eq. 13, however, makes it difficult for the M_{ch} model to explain the class of subluminous SNIa, which were previously suggested to arise from purely deflagration-driven explosions (*25*). Furthermore, the validity of the M_{ch} model has been questioned because of the lack of identified nondegenerate companion stars surviving the explosion (*80*) or ejecta interaction with the companions stars (*81*) in some SNIa (*82*), although observational evidence of such interaction has been found in other events (*83*). If M_{ch} is not the dominant channel for normal bright SNIa, then it becomes unclear whether WDs can grow to the Chandrasekhar mass because once this mass limit is reached, then both core ignition and subsequent DDT would be almost unavoidable.

Our derived DDT conditions, L_{CJ}^{min} and U_{CJ} (Eqs. 7 and 10), depend only on the laminar flame properties, which in turn depend on the composition of stellar material in the interior of a WD at different radii. This suggests that the transition density ρ_{DDT} could vary substantially between 50/50 $^{12}C/^{16}O$ mixtures and more ^{12}C-poor compositions. Because the change in ρ_{DDT} would result in a different total ^{56}Ni yield and thus luminosity, we predict a connection in the M_{ch} scenario between the WD age and metallicity, which determine the interior composition, and the resulting SNIa light curve and spectral properties. This is potentially testable with observations. There may exist a minimal ^{12}C mass fraction, below which the onset of DDT would become unlikely because of either the high transition density, which would result in SNIa properties in disagreement with observations, or turbulent conditions required to produce super-CJ turbulent flames, which are not observed in full-star SNIa simulations. Studies on the effect of mixture composition and metallicity on a SNIa explosion (*52*, *84*, *85*) have suggested the dependence of ρ_{DDT} on the ^{12}C mass fraction (*52*). However, those results were obtained for a fundamentally different DDT mechanism, which relies on the formation of spontaneous reaction waves in a reactivity gradient produced in a distributed flame and an ad hoc prescription of ρ_{DDT} (*52*, *84*, *85*).

REFERENCES AND NOTES

1. M. M. Phillips, The absolute magnitudes of type Ia supernovae. *Astrophys. J.* **413**, L105 (1993). doi: 10.1086/186970
2. A. G. Riess, W. H. Press, R. P. Kirshner, Using type Ia supernova light curve shapes to measure the Hubble constant. *Astrophys. J.* **438**, L17 (1995). doi: 10.1086/187704
3. S. Jha, A. G. Riess, R. P. Kirshner, Improved distances to type Ia supernovae with multicolor light-curve shapes: MLCS2k2. *Astrophys. J.* **659**, 122–148 (2007). doi: 10.1086/512054
4. F. Hoyle, W. A. Fowler, Nucleosynthesis in supernovae. *Astrophys. J. Lett.* **132**, 565–590 (1960).
5. B. Wang, Z. Han, Progenitors of type Ia supernovae. *New Astron. Rev.* **56**, 122–141 (2012). doi: 10.1016/j.newar.2012.04.001

6. W. Hillebrandt, M. Kromer, F. K. Röpke, A. J. Ruiter, Towards an understanding of Type Ia supernovae from a synthesis of theory and observations. *Front. Phys.* **8**, 116–143 (2013). doi: 10.1007/s11467-013-0303-2
7. D. Maoz, F. Mannucci, G. Nelemans, Observational clues to the progenitors of type Ia supernovae. *Annu. Rev. Astron. Astrophys.* **52**, 107–170 (2014). doi: 10.1146/annurev-astro-082812-141031
8. F. K. Röpke, S. A. Sim, Models for type Ia supernovae and related astrophysical transients. *Space Sci. Rev.* **214**, 72 (2018). doi: 10.1007/s11214-018-0503-8
9. A. M. Khokhlov, Delayed detonation model for type Ia supernovae. *Astron. Astrophys.* **245**, 114–128 (1991).
10. P. A. Hoflich, A. M. Khokhlov, J. C. Wheeler, Delayed detonation models for normal and subluminous type Ia supernovae: Absolute brightness, light curves, and molecule formation. *Astrophys. J.* **444**, 831–847 (1995). doi: 10.1086/175656
11. V. N. Gamezo, A. M. Khokhlov, E. S. Oran, A. Y. Chtchelkanova, R. O. Rosenberg, Thermonuclear supernovae: Simulations of the deflagration stage and their implications. *Science* **299**, 77–81 (2003). doi: 10.1126/science.1078129; pmid: 12446871
12. I. R. Seitenzahl *et al.*, Three-dimensional delayed-detonation models with nucleosynthesis for Type Ia supernovae. *Mon. Not. R. Astron. Soc.* **429**, 1156–1172 (2013). doi: 10.1093/mnras/sts402
13. S. E. Woosley, T. A. Weaver, Sub-Chandrasekhar mass models for type Ia supernovae. *Astrophys. J.* **423**, 371–379 (1994). doi: 10.1086/173813
14. P. A. Hoeflich, A. M. Khokhlov, Explosion models for type Ia supernovae: A comparison with observed light curves, distances H_0q_0. *Astrophys. J.* **457**, 500–528 (1996). doi: 10.1086/176748
15. A. J. Ruiter *et al.*, Delay times and rates for type Ia supernovae and thermonuclear explosions from double-detonation sub-Chandrasekhar mass models. *Mon. Not. R. Astron. Soc.* **417**, 408–419 (2011). doi: 10.1111/j.1365-2966.2011.19276.x
16. D. A. Goldstein, D. Kasen, Evidence for sub-Chandrasekhar mass type Ia supernovae from an extensive survey of radiative transfer models. *Astrophys. J.* **852**, L33 (2018). doi: 10.3847/2041-8213/aaa409
17. R. Mochkovitch, M. Livio, The coalescence of white dwarfs and type Ia supernovae. *Astron. Astrophys.* **209**, 111–118 (1989).
18. M. Dan, S. Rosswog, J. Guillochon, E. Ramirez-Ruiz, Prelude to a double degenerate merger: The onset of mass transfer and its impact on gravitational waves and surface detonations. *Astrophys. J.* **737**, 89 (2010). doi: 10.1088/0004-637X/737/2/89
19. R. Pakmor *et al.*, Sub-luminous type Ia supernovae from the mergers of equal-mass white dwarfs with mass approximately ~0.9$M_\odot$. *Nature* **463**, 61–64 (2010). doi: 10.1038/nature08642; pmid: 20054390
20. O. Papish, H. B. Perets, Supernovae from direct collisions of white dwarfs and the role of helium shell ignition. *Astrophys. J.* **822**, 19 (2016). doi: 10.3847/0004-637X/822/1/19
21. T. Plewa, A. C. Calder, D. Q. Lamb, Type Ia supernova explosion: Gravitationally confined detonation. *Astrophys. J.* **612**, L37–L40 (2004). doi: 10.1086/424036
22. I. R. Seitenzahl *et al.*, Three-dimensional simulations of gravitationally confined detonations compared to observations of SN 1991T. *Astron. Astrophys.* **592**, A57 (2016). doi: 10.1051/0004-6361/201527251
23. G. H. Marion *et al.*, A catalog of near-infrared spectra from Type Ia supernovae. *Astron. J.* **138**, 727–757 (2009). doi: 10.1088/0004-6256/138/3/727
24. J. Parrent, B. Friesen, M. Parthasarathy, A review of type Ia supernova spectra. *Astrophys. Space Sci.* **351**, 1–52 (2014). doi: 10.1007/s10509-014-1830-1
25. M. Fink *et al.*, Three-dimensional pure deflagration models with nucleosynthesis and synthetic observables for Type Ia supernovae. *Mon. Not. R. Astron. Soc.* **438**, 1762–1783 (2014). doi: 10.1093/mnras/stt2315
26. J. W. Meyer, A. K. Oppenheim, On the shock-induced ignition of explosive gases. *Proc. Combust. Inst.* **13**, 1153–1164 (1971). doi: 10.1016/S0082-0784(71)80112-1
27. Ya. B. Zeldovich, V. B. Librovich, G. M. Makhviladze, G. I. Sivashinsky, Development of detonation in a nonuniformly preheated gas. *Astronaut. Acta* **15**, 313–321 (1970).
28. J. H. S. Lee, R. Knystautas, N. Yoshikawa, Photochemical initiation of gaseous detonations. *Astronaut. Acta* **5**, 971–982 (1978). doi: 10.1016/0094-5765(78)90003-6
29. E. S. Oran, V. N. Gamezo, Origins of the deflagration-to-detonation transition in gas-phase combustion. *Combust. Flame* **148**, 4–47 (2007). doi: 10.1016/j.combustflame.2006.07.010
30. C. Raskin *et al.*, 56Ni production in double-degenerate white dwarf collisions. *Astrophys. J.* **724**, 111–125 (2010). doi: 10.1088/0004-637X/724/1/111
31. V. N. Gamezo, A. M. Khokhlov, E. S. Oran, Three-dimensional delayed-detonation model of type Ia supernova. *Astrophys. J.* **623**, 337–346 (2005). doi: 10.1086/428767
32. F. K. Röpke, J. C. Niemeyer, Delayed detonations in full-star models of type Ia supernova explosions. *Astron. Astrophys.* **464**, 683–686 (2007). doi: 10.1051/0004-6361:20066585
33. K. Kailasanath, Review of propulsion applications of detonation waves. *Am. Inst. Aeronaut. Astronaut. J.* **38**, 1698–1708 (2000). doi: 10.2514/2.1156
34. K. Kailasanath, Recent developments in the research on pulse detonation engines. *Am. Inst. Aeronaut. Astronaut. J.* **41**, 145–159 (2003). doi: 10.2514/2.1933
35. P. Wolański, Detonative propulsion. *Proc. Combust. Inst.* **34**, 125–158 (2013). doi: 10.1016/j.proci.2012.10.005
36. F. K. Lu, E. M. Braun, Rotating detonation wave propulsion: Experimental challenges, modeling, and engine concepts. *J. Propuls. Power* **30**, 1125–1142 (2014). doi: 10.2514/1.B34802
37. B. A. Rankin *et al.*, Overview of performance, application, and analysis of rotating detonation engine technologies. *J. Propuls. Power* **33**, 131–143 (2017). doi: 10.2514/1.B36303
38. R. K. Zipf Jr., V. N. Gamezo, K. M. Mohamed, E. S. Oran, D. A. Kessler, Deflagration-to-detonation transition in natural gas-air mixtures. *Combust. Flame* **161**, 2165–2176 (2014). doi: 10.1016/j.combustflame.2014.02.002
39. V. H. Y. Tam, D. M. Johnson, Detonation: Should it be included in hazard and risk assessment? *Chem. Eng. Trans.* **48**, 451–456 (2016).
40. D. M. Johnson, V. H. Y. Tam, Why DDT is the only way to explain some vapor cloud explosions? *Process Saf. Prog.* **36**, 292–300 (2017). doi: 10.1002/prs.11874
41. W. Luangdilok, The probability of DDT during severe accidents. Technical Bulletin N-16-01 (Fauske, 2017).
42. V. H. Y. Tam, The Buncefield accident—Why was the explosion so severe? *Loss Prev. Bull.* **222**, 2–8 (2011).
43. J. Taveau, The Buncefield explosion: Were the resulting overpressures really unforeseeable? *Process Saf. Prog.* **31**, 55–71 (2012). doi: 10.1002/prs.10468
44. G. W. McMahon, J. R. Britt, J. L. O'Daniel, L. K. Davis, R. E. Walker, "CFD study and structural analysis of the Sago mine accident," ERDC/GSL TR-06-X (U.S. Army Corps of Engineers, Engineer Research and Development Center, Geotechnical and Structures Laboratory, 2007).
45. D. M. Johnson, Characteristics of the vapour cloud explosion incident at the IOC terminal in Jaipur, 29 October 2009. 8th Global Congress on Process Safety, Houston, TX, 2012.
46. Report of the Japanese government to the IAEA ministerial conference on nuclear safety—The accident at TEPCO's Fukushima nuclear power station, Nuclear Emergency Response Headquarters, Government of Japan (2011); https://japan.kantei.go.jp/kan/topics/201106/iaea_houkokusho_e.html.
47. A. Y. Poludnenko, T. A. Gardiner, E. S. Oran, Spontaneous transition of turbulent flames to detonations in unconfined media. *Phys. Rev. Lett.* **107**, 054501 (2011). doi: 10.1103/PhysRevLett.107.054501; pmid: 21867073
48. F. A. Williams, *Combustion Theory* (Benjamin/Cummings, ed. 2, 1985).
49. A. Y. Poludnenko, Pulsating instability and self-acceleration of fast turbulent flames. *Phys. Fluids* **27**, 014106 (2015). doi: 10.1063/1.4905298
50. A. M. Khokhlov, E. S. Oran, J. C. Wheeler, Deflagration-to-detonation transition in thermonuclear supernovae. *Astrophys. J.* **478**, 678–688 (1997). doi: 10.1086/303815
51. J. C. Niemeyer, S. E. Woosley, The thermonuclear explosion of Chandrasekhar mass white dwarfs. *Astrophys. J.* **475**, 740–753 (1997). doi: 10.1086/303544
52. S. E. Woosley, Type Ia supernovae: Burning and detonation in the distributed regime. *Astrophys. J.* **668**, 1109–1117 (2007). doi: 10.1086/520835
53. F. Ciaraldi-Schoolmann, I. R. Seitenzahl, F. K. Röpke, A subgrid-scale model for deflagration-to-detonation transitions in Type Ia supernova explosion simulations. *Astron. Astrophys.* **559**, A117 (2013). doi: 10.1051/0004-6361/201321480
54. V. N. Gamezo, A. Y. Poludnenko, E. S. Oran, "One-dimensional evolution of fast flames." Proceedings of the 23rd International Colloquium on the Dynamics of Explosions and Reactive Systems, Irvine, CA, 25 July 2011, paper 330.
55. J. F. Driscoll, Turbulent premixed combustion: Flamelet structure and its effect on turbulent burning velocities. *Prog. Energy Combust. Sci.* **34**, 91–134 (2008). doi: 10.1016/j.pecs.2007.04.002
56. L. J. Dursi *et al.*, The response of model and astrophysical thermonuclear flames to curvature and stretch. *Astrophys. J.* **595**, 955–979 (2003). doi: 10.1086/377433
57. A. Y. Poludnenko, E. S. Oran, The interaction of high-speed turbulence with flames: Turbulent flame speed. *Combust. Flame* **158**, 301–326 (2011). doi: 10.1016/j.combustflame.2010.09.002
58. P. E. Hamlington, A. Y. Poludnenko, E. S. Oran, Interactions between turbulence and flames in premixed reacting flows. *Phys. Fluids* **23**, 125111 (2011). doi: 10.1063/1.3671736
59. P. E. Hamlington, A. Y. Poludnenko, E. S. Oran, Intermittency in premixed turbulent reacting flows. *Phys. Fluids* **24**, 075111 (2012). doi: 10.1063/1.4729615
60. C. A. Z. Towery *et al.*, Spectral kinetic energy transfer in turbulent premixed reacting flows. *Phys. Rev. E* **93**, 053115 (2016). doi: 10.1103/PhysRevE.93.053115; pmid: 27300986
61. F. X. Timmes, S. E. Woosley, The conductive propagation of nuclear flames. I - Degenerate C + O and O + NE + MG white dwarfs. *Astrophys. J.* **396**, 649 (1992). doi: 10.1086/171746
62. C. Charignon, J.-P. Chiéze, Deflagration-to-detonation transition by amplification of acoustic waves in type Ia supernovae. *Astron. Astrophys.* **550**, A105 (2013). doi: 10.1051/0004-6361/201220483
63. Materials and methods are available as supplementary materials.
64. J. P. McGarry, K. A. Ahmed, Flame-turbulence interaction of laminar premixed deflagrated flames. *Combust. Flame* **176**, 439–450 (2017). doi: 10.1016/j.combustflame.2016.11.002
65. J. Chambers, K. Ahmed, Turbulent flame augmentation using a fluidic jet for deflagration-to-detonation. *Fuel* **199**, 616–626 (2017). doi: 10.1016/j.fuel.2017.03.023
66. J. Sosa, J. Chambers, K. A. Ahmed, A. Poludnenko, V. N. Gamezo, Compressible turbulent flame speeds of highly turbulent standing flames. *Proc. Combust. Inst.* **37**, 3495–3502 (2019). doi: 10.1016/j.proci.2018.07.039
67. D. A. Kessler, V. N. Gamezo, E. S. Oran, Simulations of flame acceleration and deflagration-to-detonation transitions in methane–air systems. *Combust. Flame* **157**, 2063–2077 (2010). doi: 10.1016/j.combustflame.2010.04.011
68. J. M. Stone, T. A. Gardiner, P. Teuben, J. F. Hawley, J. B. Simon, Athena: A new code for astrophysical MHD. *Astrophys. J.* **178**, 137–177 (2008). doi: 10.1086/588755
69. A. Y. Poludnenko, E. S. Oran, The interaction of high-speed turbulence with flames: Global properties and internal flame structure. *Combust. Flame* **157**, 995–1011 (2010). doi: 10.1016/j.combustflame.2009.11.018
70. A. J. Aspden, J. B. Bell, M. S. Day, S. E. Woosley, M. Zingale, Turbulence-flame interactions in Type Ia supernovae. *Astrophys. J.* **689**, 1173–1185 (2008). doi: 10.1086/592726
71. A. J. Aspden, J. B. Bell, S. E. Woosley, Distributed flames in type Ia supernovae. *Astrophys. J.* **710**, 1654–1663 (2010). doi: 10.1088/0004-637X/710/2/1654
72. J. B. Bell, M. S. Day, C. A. Rendleman, S. E. Woosley, M. Zingale, Direct numerical simulations of type Ia supernovae flames. I. The Landau-Darrieus instability. *Astrophys. J.* **606**, 1029–1038 (2004). doi: 10.1086/383023
73. J. B. Bell, M. S. Day, C. A. Rendleman, S. E. Woosley, M. Zingale, Direct numerical simulations of type Ia supernovae flames. II. The Rayleigh-Taylor instability. *Astrophys. J.* **608**, 883–906 (2004). doi: 10.1086/420841
74. V. N. Gamezo, J. C. Wheeler, A. M. Khokhlov, E. S. Oran, Multilevel structure of cellular detonations in Type Ia supernovae. *Astrophys. J.* **512**, 827–842 (1999). doi: 10.1086/306784
75. H. Ma, S. E. Woosley, C. M. Malone, A. Almgren, J. Bell, Carbon deflagration in type Ia supernova. I. Centrally ignited models. *Astrophys. J.* **771**, 58 (2013). doi: 10.1088/0004-637X/771/1/58
76. F. K. Röpke, Flame-driven deflagration-to-detonation transitions in type Ia supernovae? *Astrophys. J.* **668**, 1103–1108 (2007). doi: 10.1086/520830
77. At low densities $\rho \lesssim 10^7$ g cm^{-3}, turbulence would break the flame, causing it to enter the distributed burning regime (*69*, *70*). The formation of a distributed flame does not preclude the possibility of tDDT with our tDDT mechanism, provided that the burning speed of a distributed flame satisfies Eq. 1. However, the expressions for critical turbulent conditions we derive are not applicable in that regime.

78. A. M. Khokhlov, E. S. Oran, J. C. Wheeler, A theory of deflagration-to-detonation transition in unconfined flames. *Combust. Flame* **108**, 503–517 (1997). doi: 10.1016/S0010-2180(96)00105-8
79. S. E. Woosley, A. R. Kerstein, V. Sankaran, A. J. Aspden, F. K. Röpke, Type Ia supernovae: Calculations of turbulent flames using the linear eddy model. *Astrophys. J.* **704**, 255–273 (2009). doi: 10.1088/0004-637X/704/1/255
80. B. E. Schaefer, A. Pagnotta, An absence of ex-companion stars in the type Ia supernova remnant SNR 0509-67.5. *Nature* **481**, 164–166 (2012). doi: 10.1038/nature10692; pmid: 22237107
81. R. P. Olling *et al*., No signature of ejecta interaction with a stellar companion in three type Ia supernovae. *Nature* **521**, 332–335 (2015). doi: 10.1038/nature14455; pmid: 25993963
82. B. J. Shappee *et al*., Strong evidence against a non-degenerate companion in SN 2012cg. *Astrophys. J.* **855**, 6 (2018). doi: 10.3847/1538-4357/aaa1e9
83. Y. Cao *et al*., A strong ultraviolet pulse from a newborn type Ia supernova. *Nature* **521**, 328–331 (2015). doi: 10.1038/nature14440; pmid: 25993962
84. A. P. Jackson *et al*., Evaluating systematic dependencies of type Ia supernovae: The influence of deflagration to detonation density. *Astrophys. J.* **720**, 99–113 (2010). doi: 10.1088/0004-637X/720/1/99
85. A. C. Calder, B. K. Krueger, A. P. Jackson, D. M. Townsley, The influence of chemical composition on models of Type Ia supernovae. *Front. Phys.* **8**, 168–188 (2013). doi: 10.1007/s11467-013-0301-4

ACKNOWLEDGMENTS

We thank the late A. M. Khokhlov (University of Chicago) for inspiring the work on this problem. A.Y.P. and V.N.G. also thank J. C. Wheeler (University of Texas, Austin) for valuable discussions. Rendering of Fig. 5 and movies S1 and S2 was carried out by the U.S. Department of Defense (DOD) High Performance Computing Modernization Program (HPCMP) Data Analysis and Assessment Center (DAAC). **Funding:** A.Y.P. and B.D.T. were supported by the National Aeronautics and Space Administration (NASA) award NNH12AT33I. A.Y.P. was also supported by the Air Force Office of Scientific Research (AFOSR) award F4FGA06055G001. J.C. and K.A. were supported by the AFOSR award FA95501610403. V.N.G. was supported by the Alpha Foundation for the Improvement of Mine Safety and Health through grant AFC215FO-73. Computing resources were provided by the DOD HPCMP under the Frontier project award and by the Naval Research Laboratory. **Author contributions:** A.Y.P. conceived and oversaw the project, developed the theory and the code Athena-RFX, carried out DNS calculations and their analysis, applied the theory to SNIa, and led the writing of the manuscript. J.C. and K.A. developed the experimental facility and carried out experiments. V.N.G. developed the concept of shock amplification to a detonation through shock-flame interactions, contributed to the development of the overall theory and analysis of the DNS data and application of the theory to SNIa, and carried out simulations of shock-flame interactions. V.N.G. and K.A. contributed to the manuscript writing. B.D.T. implemented thermonuclear reaction kinetics and transport in Athena-RFX. **Competing interests:** The authors have no competing interests. **Data and materials availability:** Experimental data for Figs. 2, A and B, and 4, F to J are available in data file S1. Distribution of the Athena-RFX software falls under legal restrictions of the U.S. government's International Traffic in Arms Regulation (ITAR) and Export Administration Regulation (EAR). Access to the code may require an export license from the Directorate of Defense Trade Controls, U.S. Department of State. Subject to that provision, readers may obtain a copy of the software by contacting A.Y.P. Output data for all the simulations, totaling 35 terabytes, is permanently archived at the DOD Supercomputing Resource Center (DSRC) at the Engineer Research and Development Center (ERDC) in Vicksburg, Mississippi. Transfer of this large data volume can be arranged by contacting A.Y.P.

SUPPLEMENTARY MATERIALS

science.sciencemag.org/content/366/6465/eaau7365/suppl/DC1
Materials and Methods
Figs. S1 and S2
Table S1
Movies S1 and S2
Data File S1
References (*86*–*96*)

16 July 2018; accepted 20 September 2019
10.1126/science.aau7365

RESEARCH ARTICLE

RADICAL ENZYMES

Itaconyl-CoA forms a stable biradical in methylmalonyl-CoA mutase and derails its activity and repair

Markus Ruetz[1], Gregory C. Campanello[1]*, Meredith Purchal[2], Hongying Shen[3,4], Liam McDevitt[1], Harsha Gouda[1], Shoko Wakabayashi[5], Junhao Zhu[5], Eric J. Rubin[5], Kurt Warncke[6], Vamsi K. Mootha[3,4], Markos Koutmos[2,7], Ruma Banerjee[1]†

Itaconate is an immunometabolite with both anti-inflammatory and bactericidal effects. Its coenzyme A (CoA) derivative, itaconyl-CoA, inhibits B_{12}-dependent methylmalonyl-CoA mutase (MCM) by an unknown mechanism. We demonstrate that itaconyl-CoA is a suicide inactivator of human and *Mycobacterium tuberculosis* MCM, which forms a markedly air-stable biradical adduct with the 5′-deoxyadenosyl moiety of the B_{12} coenzyme. Termination of the catalytic cycle in this way impairs communication between MCM and its auxiliary repair proteins. Crystallography and spectroscopy of the inhibited enzyme are consistent with a metal-centered cobalt radical ~6 angstroms away from the tertiary carbon-centered radical and suggest a means of controlling radical trajectories during MCM catalysis. Mycobacterial MCM thus joins enzymes in the glyoxylate shunt and the methylcitrate cycle as targets of itaconate in pathogen propionate metabolism.

The immunomodulatory and antimicrobial effects of itaconate are evincing newfound interest in a compound historically used as a precursor in polymer synthesis. Upon activation, immune cells stimulate itaconate synthesis ~10-fold via aconitate decarboxylase (Irg1)–catalyzed decarboxylation of *cis*-aconitate, a tricarboxylic acid cycle intermediate (*1*). Itaconate activates Nrf2, inhibits succinate dehydrogenase, and blocks the transcription factor Iκβζ, leading to a switch from a pro- to an anti-inflammatory state (*2*). The antimicrobial activity of itaconate is purportedly due to its inhibition of two microbe-specific targets: isocitrate lyase in the glyoxylate shunt and methylcitrate lyase in the methylcitrate cycle, two enzymes that are needed for pathogen survival on acetate or propionate, respectively, as the sole carbon source (Fig. 1A) (*3*). Propionyl-coenzyme A (CoA) is derived from cholesterol catabolism and is used by pathogens like *Mycobacterium tuberculosis* (Mtb) for biomass production in the glucose-limiting conditions found in phagosomes (*4*).

An unexpected intersection between itaconate and B_{12}-dependent propionate metabolism was revealed recently by the demonstration that itaconyl-CoA (I-CoA) is a potent inhibitor of human 5′-deoxyadenosylcobalamin (AdoCbl)–dependent methylmalonyl-CoA mutase (*h*MCM) (*5*). Itaconate can be cleared by a C_5-dicarboxylate pathway (*6*) via acylation to I-CoA, hydration to citramalyl-CoA, and cleavage to acetyl-CoA and pyruvate, a reaction catalyzed by citramalyl-CoA lyase, which is encoded by the recently deorphaned *citrate lyase beta-like* (*CLYBL*) gene (*5*) (Fig. 1A). I-CoA (or methylenesuccinyl-CoA) is an analog of succinyl-CoA, which is interconverted to methylmalonyl-CoA (M-CoA) by the isomerase MCM. A metabolic connection between CLYBL and B_{12} was initially revealed in a genome-wide association study (*7*) that showed a correlation between the biallelic loss of *CLYBL*, which has an ~3 to 6% prevalence in certain populations (*8*), and B_{12} deficiency. Although I-CoA inhibition of MCM provides a molecular link between mitochondrial B_{12} and C_5-dicarboxylate metabolism, it does not explain why inhibited MCM cannot be repaired by the auxiliary protein system that is dedicated for this function (*9*). Given the homology between bacterial and human MCM, host-derived itaconate could also potentially target MCM in pathogenic bacteria, in which it is required for lipid breakdown.

Itaconate induces electrophilic stress and modifies small molecules and protein targets by alkylating cysteine residues (*10*, *11*). Here, we report a radical suicide inactivation mechanism in which addition of the elusive 5′-deoxyadenosyl radical (dAdo•) to I-CoA in MCM leads to an air-stable biradical comprising a tertiary carbon radical coupled to the metal-centered cob

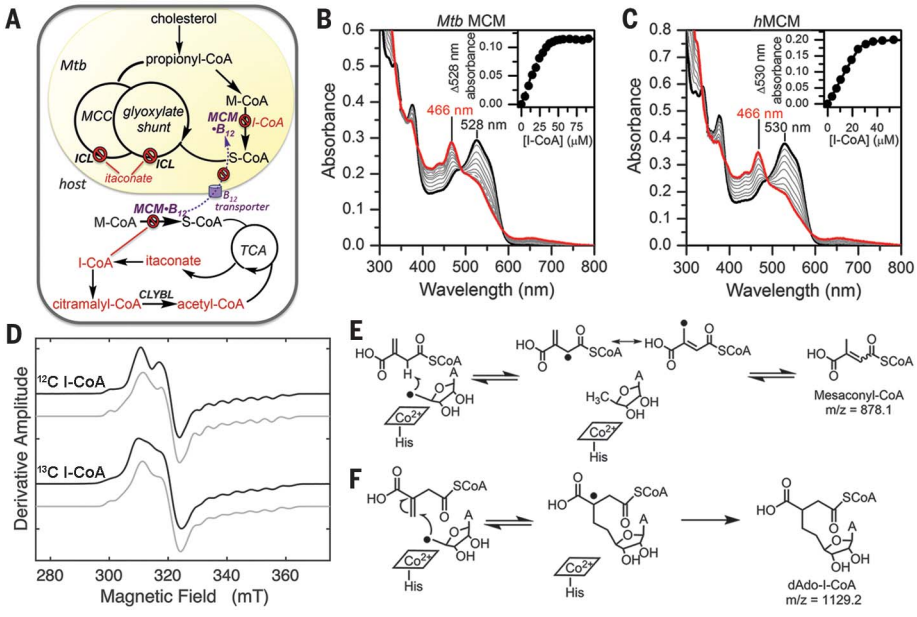


Fig. 1. I-CoA inhibits human and Mtb MCM by forming an air-stable biradical. (**A**) Mtb pathways targeted by I-CoA. MCC, methylcitrate cycle; ICL, isocitrate lyase; S-CoA, succinyl-CoA; TCA, tricarboxylic acid cycle. (**B** and **C**) Titration of holo-Mtb MCM (B) with 30 μM bound AdoCbl or holo-*h*MCM (C) with 40 μM bound AdoCbl (black traces) with increasing concentrations of I-CoA. The intermediate spectra (gray) were recorded after 5 min of equilibration. (Insets) Representative plots of Δ528 or Δ530 nm versus I-CoA indicated stoichiometric binding [n = 2 (Mtb MCM); n = 3 (*h*MCM)]. (**D**) EPR spectra of the 1 mM I-CoA-induced biradical on *h*MCM (375 μM) in the presence of natural abundance (top) or [^{13}C]I-CoA (bottom). The experimental and simulated spectra are in black and gray, respectively. (**E** and **F**) Possible fates of dAdo• when I-CoA behaves as substrate (E), not observed, or inhibitor (F).

[1]Department of Biological Chemistry, University of Michigan, Ann Arbor, MI 48109, USA. [2]Department of Chemistry, University of Michigan, Ann Arbor, MI 48109, USA. [3]Howard Hughes Medical Institute and Department of Molecular Biology, Massachusetts General Hospital, Boston, MA 02114, USA. [4]Broad Institute, Cambridge, MA 02142, USA. [5]Department of Immunology and Infectious Diseases, Harvard T. H. Chan School of Public Health, Cambridge, MA 02115, USA. [6]Department of Physics, Emory University, Atlanta, GA 30322, USA. [7]Program in Biophysics, University of Michigan, Ann Arbor, MI 48109, USA.
*Present address: Merck & Co., Inc., Kenilworth, NJ, USA.
†Corresponding author. Email: rbanerje@umich.edu

(II)alamin radical. We visualized Mtb MCM bound to a dAdo adduct of I-CoA at 2.0-Å resolution by x-ray crystallography. In addition to identifying MCM as an antimicrobial target of itaconate and demonstrating its importance for Mtb growth on propionate, our study provides molecular insights into how MCM controls radical trajectories during catalysis with its normal substrates to promote the desired chemistry and suppress unwanted side reactions.

I-CoA inactivates Mtb MCM by forming an air-stable biradical

MCM catalyzes the reversible isomerization of M-CoA to succinyl-CoA via an AdoCbl-dependent radical mechanism. To test our hypothesis that bacterial MCM is also a target of the antimicrobial effect of itaconate, we cloned and expressed Mtb MCM and the two auxiliary proteins that load and repair AdoCbl (fig. S1A). The kinetic parameters of Mtb MCM are comparable to those of the human homolog (fig. S1, B and C). Addition of I-CoA to Mtb MCM-AdoCbl led to a rapid shift in the absorption maximum (λ_{max}), from 528 nm to 466 nm (Fig. 1B), indicating stoichiometric binding (Fig. 1B, inset), as was also seen with *h*MCM (Fig. 1C) (*5*). Homolysis of the cobalt-carbon bond in AdoCbl, the first step in the MCM-catalyzed reaction, leads to formation of the radical pair dAdo• and cob(II)alamin, albeit with a different λ_{max} (474 nm). We therefore used electron paramagnetic resonance (EPR) spectroscopy to identify the 466-nm–absorbing products of I-CoA–inactivated MCM.

The EPR spectrum of MCM-bound cob(II)alamin displays the typical eight-line hyperfine splitting of the unpaired electron with the $I = {}^{7}/_{2}$ cobalt nucleus that is resolved in the high-field region of the spectrum (fig. S2, A and B). Additional superhyperfine splitting due to the coordinating $I = 1$ lower axial nitrogen from a histidine ligand is also observed. Notably, addition of I-CoA to human or Mtb MCM led to distinct spectra (Fig. 1D, top, and fig. S2C) that had the hallmarks of a hybrid triplet system. The spectra were reminiscent of the EPR spectrum of a transient catalytic intermediate trapped during MCM turnover, exhibiting strong electron-electron spin-coupling between the product succinyl-CoA radical and the low-spin cob(II)alamin (*12*). Similar biradical intermediates have also been trapped in the AdoCbl-dependent enzymes glutamate mutase (*13*) and 2-methyleneglutarate mutase (*14*). The hyperfine multiplicity and the substantial *g* anisotropy identified the cobalamin component in the triplet spin system.

The identity of the organic radical component was further assessed with [^{13}C]I-CoA (uniformly labeled in the itaconate carbons) or [^{13}C]AdoCbl (uniformly labeled in the adenosyl moiety). Whereas ^{13}C-labeled AdoCbl had no effect on the EPR spectrum, [^{13}C]I-CoA led to inhomogeneous broadening throughout the line shape, which is consistent with appreciable mixing of cob(II)alamin and organic radical quantum states in the strong electron-electron coupling regime (Fig. 1D, bottom). These results indicate an absence of marked unpaired electron spin density on the dAdo moiety, which is in accord with the near-unit spin density inferred for the electron-^{13}C interaction in the radical pair formed from [^{13}C]I-CoA. Spectral simulations predict an interspin distance of 5 to 6 Å, while the Euler angles position the organic radical at an angle of 43° relative to the principal axis of the d_z^2 orbital on cobalt. In other AdoCbl-dependent isomerases, the distance between the substrate and cobalamin radicals range between 5 to 6 Å and 8 to 12 Å, respectively, necessitating small or large movements of the initially formed dAdo• to reach the substrate hydrogen atom (H-atom) destined for abstraction (*15*).

The I-CoA–induced biradical was air stable for over 1 hour (figs. S3 and S4), unlike the transient biradical formed during catalytic turnover with M-CoA that was trapped by freeze-quenching (*12*). To understand the chemical basis of its unusual stability, we further investigated the identity of the organic radical.

The adenosyl radical is stabilized by addition to itaconyl-CoA

Following generation of the dAdo•-cob(II)alamin radical pair on MCM, the isomerization reaction

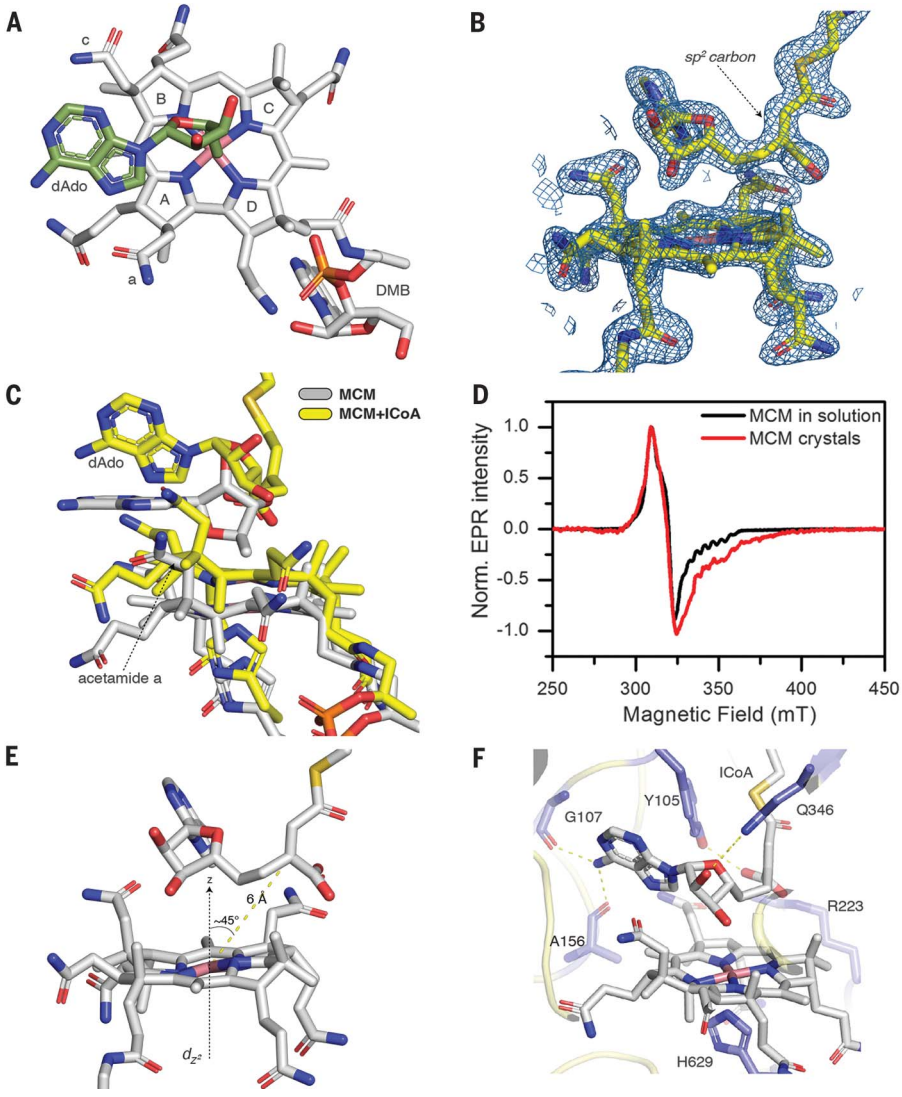


Fig. 2. Crystallographic capture of a biradical in I-CoA-inactivated Mtb MCM. (**A**) Orientation of dAdo (green) in relation to the corrin ring (gray; pyrrole rings A to D and acetamides a and c are shown) in native Mtb MCM. (**B**) 2Fo-Fc omit maps (blue) around B_{12} and I-CoA contoured at 1.5σ. (**C**) Shift in B_{12} and rotation of the adenine ring from the coplanar (gray) to perpendicular (yellow) position relative to the corrin ring. (**D**) EPR spectra of Mtb MCM + I-CoA. (**E**) Geometry of B_{12} and the I-CoA–dAdo adduct in crystal. (**F**) Hydrogen bonding interactions in the MCM–I-CoA structure.

is initiated by H-atom abstraction from M-CoA by dAdo•, forming a substrate-centered radical that undergoes rearrangement. The dAdo• is a primary and highly reactive alkyl radical that has eluded direct detection in all AdoCbl-dependent isomerases but recently was trapped in a radical *S*-adenosylmethionine enzyme (*16*). In principle, two potential reactions between dAdo• and I-CoA can be considered (Fig. 1, E and F). To distinguish between these mechanistic possibilities, the reaction products from Mtb and *h*MCM inactivated by I-CoA under single-turnover and aerobic conditions were separated by high-performance liquid chromatography (fig. S5). Two major product peaks with retention times of 22.9 and 27.0 min (peaks 2 and 5) were identified; Mtb MCM showed an additional peak at 23.5 min (peak 2b).

Matrix-assisted laser desorption/ionization–mass spectrometry (MS) analysis confirmed the second reaction pathway leading to an addition product between dAdo and I-CoA (Fig. 1G), indicating that dAdo• adds to the double bond in I-CoA, yielding a tertiary carbon radical additionally stabilized by delocalization onto the π-system of the adjacent carboxylate. MS analysis revealed that peaks 2a and 2b are isomers with the same mass/charge ratio (*m*/*z*) of 1145.4 (fig. S6), which is 16 mass units higher than the expected mass of the addition product (*m*/*z* 1129), indicating incorporation of an oxygen atom. We assign peak 2 as the hydroxyl derivative of the addition product and peak 5 (*m*/*z* 1099.3), which is 30 Da lighter, indicating the formal loss of formaldehyde to the oxidative decarboxylation product of peak 2 (fig. S7A). MS analysis of the *h*MCM samples yielded similar results (fig. S6, D and E).

Under anaerobic conditions, additional hydrophobic products were observed (fig. S8). Peak 6 with an *m*/*z* of 1129.4 represents the expected radical addition product, while peak 5 and the minor peaks 7 and 8, with *m*/*z* values that are two mass units lower (fig. S9), were assigned to intramolecular cyclization and/or elimination products (fig. S7, B and C). Ado• cyclization products have been reported during anaerobic photolysis of AdoCbl (*17*) and during the reaction of hydroxyl radicals with dAdo or deoxyguanosine (*18*), resulting in 5′,8-cyclopurine nucleosides.

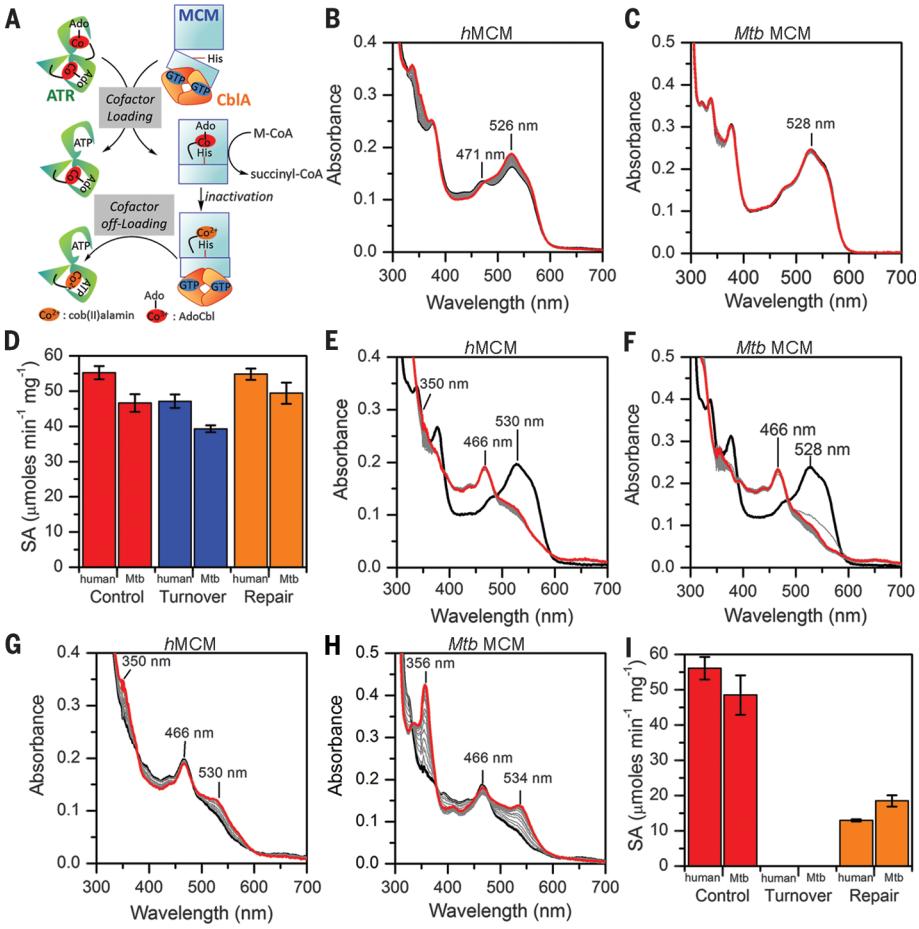


Fig. 3. I-CoA inactivation impairs MCM repair. (**A**) Scheme showing the role of the auxiliary proteins in cofactor loading/off-loading to/from MCM. (**B** and **C**) Enzyme-monitored turnover by human (B) and Mtb (C) MCM (black spectra) in the presence of M-CoA and human or Mtb CblA-GTP. Intermediate spectra (gray) were recorded every 2 min. Final spectra (red) were recorded at 1 hour. (**D**) Specific activity (SA) of human and Mtb MCM after 1-hour preincubation without or with M-CoA (red versus blue) and subsequent addition of the repair system (orange). (**E** and **F**) Addition of I-CoA to *h*MCM-AdoCbl [black, (E)] or Mtb MCM-AdoCbl [black, (F)] results in inactive enzyme (gray). Further incubation over 1 hour causes only modest spectral changes (red). (**G** and **H**) At the end of the experiments in (E) and (F), the repair system was added for 20 min to human (G) and Mtb (H) MCM. The increase in absorbance at 350 to 356 nm is indicative of OH_2Cbl formation (red). (**I**) Same as in (D) but with I-CoA; in both panels, data represent means ± SD (*n* = 3).

Crystallographic capture of the biradical on MCM

Given the protracted air stability of the biradical, we attempted to visualize the inhibited form by soaking AdoCbl-reconstituted Mtb MCM crystals with I-CoA. We determined structures of the unsoaked and I-CoA–soaked enzyme at 1.9-Å and 2.0-Å resolution, respectively (table S1). Mtb MCM, like the *Propionibacterium shermanii* protein (*19*), is a heterodimer comprising an α subunit that binds B_{12} and a β subunit that is inactive (fig. S10A). In the native structure, AdoCbl is bound with its endogenous dimethylbenzimidazole tail inserted in a side pocket while His-629 serves as the lower axial ligand (Fig. 2A). On the opposite face, the 5′-carbon of the upper axial dAdo ligand is 2.5 Å away from the cobalt atom, while the adenine group is coplanar with the corrin ring and oriented above pyrrole rings A and B.

I-CoA binding induces a large conformational change in the AdoCbl-binding α subunit [Cα root mean square deviation (RMSD), 1.47 Å], whereas the small subunit is almost unchanged (Cα RMSD, 0.26 Å) (fig. S10A). Soaking in I-CoA did not affect crystal stability, as there are no crystal contacts in the region affected by its binding. The α subunit collapses around the I-CoA binding pocket, with the motion being largest at the periphery and smallest where the α and β subunits are proximal. The crystal structure of *h*MCM, which is a homodimer with two B_{12} binding subunits, similarly closes in on its substrate, M-CoA (*20*).

We assigned the electron density in the active site to the adduct between I-CoA and the 5′-carbon of dAdo (Fig. 2B and fig. S10B). The 5′-carbon of the dAdo moiety is rotated almost 180° away from the cobalt, and the distance to the cobalt atom increases to 4.3 Å. The rotation places the 5′-carbon of dAdo 1.5 Å away from the methylene group of I-CoA, indicating the presence of a covalent bond between them. The geometry of the tertiary carbon

of I-CoA is planar, as expected for an sp^2 carbon (Fig. 2B and fig. S10, C and D). dAdo and corrin are shifted by 2.1 Å relative to the corrin ring in the structure without I-CoA. The acetamide group *a* on ring A is pushed up and in toward the adenine ring (Fig. 2C), which causes the adenine to move from a parallel to an almost perpendicular position relative to the corrin plane (fig. S10E), as predicted computationally (*21*). A strong biradical EPR signal associated with Mtb MCM crystals soaked with I-CoA confirmed that the spin-coupled carbon- and metal-centered radical pair can form in crystals (Fig. 2D). In the structure with the adduct, the tertiary carbon is 6 Å from the cobalt and at an ~45° angle from the principal d_z^2 orbital axis (Fig. 2E), in excellent agreement with EPR simulations. To our knowledge, the only other enzyme-bound, carbon-centered radical that has been crystallized is the acetyl-thiazolium cation radical in pyruvate:ferredoxin oxidoreductase, which is formed via a one-electron transfer to an iron-sulfur cluster (*22*).

In the resting state, the C2′-OH in dAdo is engaged in a hydrogen-bonding interaction between Gln^{346} and a water-mediated hydrogen bond network to His^{260} and Arg^{223} (fig. S10F). In the I-CoA–inactivated structure, the C2′-OH maintains a hydrogen bond with only Gln^{346}, and the adenine NH_2 group forms hydrogen bonds to the backbone carbonyls of Gly^{107} and Ala^{156} (Fig. 2F). These interactions likely orient dAdo• for H-atom abstraction in the catalytic cycle when M-CoA is present; however, when I-CoA is present, it places dAdo• in close proximity to the double bond, setting up the radical addition reaction. Tyr^{105} forms a hydrogen bond with the terminal carboxylate of I-CoA and also flanks the dAdo moiety. In the resting enzyme, Tyr^{105} points in the opposite direction, i.e., away from the substrate. Arg^{223} also engages via electrostatic interactions with the terminal carboxylate of I-CoA and the acetamide side group *c* in the corrin ring. The structure has implications for how MCM controls the dAdo• radical trajectory to promote H-atom abstraction from M-CoA and concomitantly suppresses unwanted side reactions that could lead to radical extinction. As first predicted in computational studies (*21*), rotation and upward movement of the adenine ring (Fig. 2C) position the C5′-carbon radical for H-atom abstraction from substrate. In contrast to MCM, glutamate mutase (*23*) and diol dehydratase (*24*) use ribose pseudorotation and N-glycosidic bond rotation, respectively, to bring the C5′-carbon of dAdo• to within van der Waal's distance of the respective substrates.

I-CoA inhibits MCM repair

While cob(II)alamin is an intermediate in the MCM-catalyzed reaction, it also represents the inactive form of the enzyme when it becomes decoupled from the dAdo moiety, and thus it fails to re-form AdoCbl at the end of the catalytic cycle (*9*). Under these conditions, the auxiliary proteins CblA and ATR engage with MCM to off-load cob(II)alamin onto ATR for repair (Fig. 3A). ATR catalyzes the adenosylation of cob(I)alamin to form AdoCbl and then transfers the cofactor to MCM to reconstitute the holoenzyme (*25*, *26*). Cofactor transfer in either direction between ATR and MCM requires the heterotrimeric guanine nucleotide–binding protein chaperone CblA and is fueled by its guanosine triphosphatase (GTPase) activity (*27*). Because I-CoA leads to rapid inactivation of MCM and formation of cob(II)alamin, which cannot re-form AdoCbl, we assessed whether the enzyme can be repaired by the ATR-CblA system.

Addition of M-CoA, to initiate catalytic turnover by MCM in the presence of CblA-GDP (guanosine diphosphate), led to small (*h*MCM) or no (Mtb MCM) changes in the absorption spectra, indicating that these enzymes are resistant to oxidative inactivation (Fig. 3, B and C). Consistent with this finding, the specific activities of both enzymes were reduced only ~15% after 1 hour of preincubation with M-CoA (Fig. 3D). By contrast, the *P. shermanni* and *M. extorquens* MCM are much more prone to inactivation and accumulate aquocobalamin (OH_2Cbl) during turnover (*28*). Addition of the repair system (ATR, ATP, and GTP) led to complete recovery of MCM activity (Fig. 3D), consistent with successful off-loading of inactive cob(II)alamin from MCM followed by reloading of AdoCbl from the assay mixture. In contrast to M-CoA, which supported catalytic turnover of MCM with minimal spectral changes, incubation of either human (Fig. 3E) or Mtb (Fig. 3F) MCM with I-CoA led to an immediate increase in absorption at 466 nm that did not change significantly over 1 hour and was correlated with complete loss of activity (Fig. 3I). Addition of the respective human and Mtb repair proteins led to an increase in absorbance at 350 to 356 nm and 530 to 534 nm, signaling oxidation of cob(II)alamin to OH_2Cbl (Fig. 3, G and H). By contrast, addition of the repair systems to the same enzymes incubated with M-CoA did not induce cofactor oxidation (fig. S11). Following repair, only 23% (human) and 38% (Mtb) of the initial MCM activity was recovered (Fig. 3I).

To gain insights into why the repair process is impeded by I-CoA but not M-CoA, we used *h*MCM, which forms a stable complex with CblA when it is in need of repair but is free in the active AdoCbl-bound state (fig. S12A) (*27*). In size exclusion chromatography profiles, *h*MCM is a stand-alone dimer (173 kDa) in the presence of M-CoA and the repair mixture (fig. S12B). However, in the presence of I-CoA, the MCM peak broadens and shifts to 211 kDa (fig. S12C), indicating the presence of a 1:1 *h*MCM:CblA

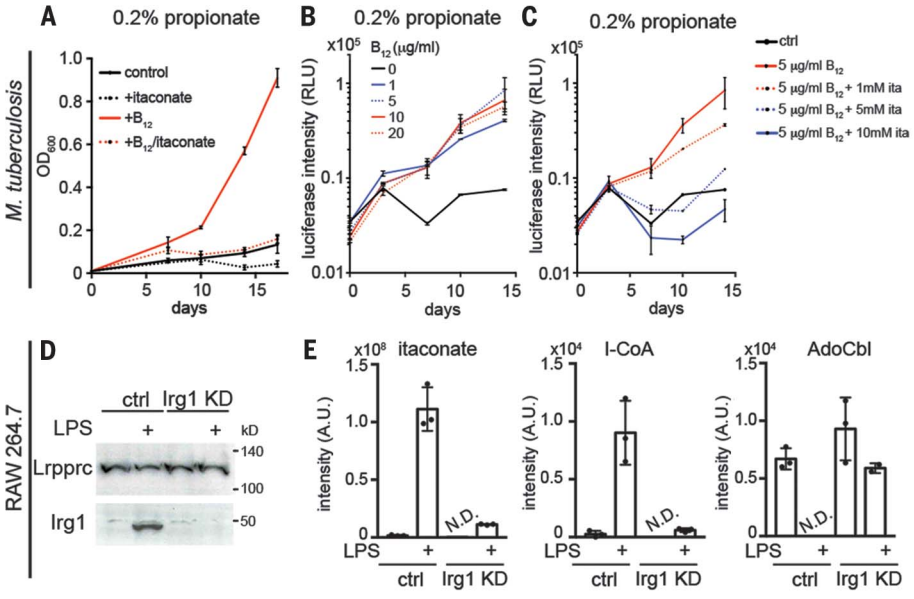


Fig. 4. Itaconate inhibits B_{12}-dependent Mtb and macrophage metabolism. (**A**) Vitamin B_{12} (10 μg/ml) stimulates growth of wild-type Mtb strain H37Rv on 0.2% propionate as the carbon source. OD, optical density. (**B** and **C**) B_{12} concentration dependence of Mtb growth and its inhibition by itaconate. (**D**) Western blot of Irg1 in *Irg*1 CRISPR knockdown (KD) RAW264.7 cells with or without LPS (10 ng/ml) stimulation for 6 hours. Lrpprc, a mitochondrial protein, was used as the loading control. (**E**) Liquid chromatography–MS of itaconate, I-CoA, and AdoCbl in control and *Irg*1 KD RAW264.7 cells with or without LPS stimulation for 6 hours. Data represent means ± SD of three independent experiments. N.D., not detected.

complex (mass of 237 kDa) and free MCM. The 173- and 211-kDa fractions have spectra corresponding to AdoCbl and the biradical, respectively (fig. S12, D and F). The 82-kDa ATR fractions show that with M-CoA, very little cofactor is transferred to ATR (fig. S12E), because very little inactive MCM forms. By contrast, whereas I-CoA completely inactivates MCM, very little cofactor is off-loaded to ATR (fig. S12G), indicating that the sustained presence of the dAdo-I-CoA adduct on MCM impedes cofactor repair.

Hobbling of the repair system helps explain why CLYBL deficiency is correlated with B_{12} deficiency. In the absence of available MCM active sites to off-load AdoCbl, ATR catalyzes an unusual sacrificial homolysis of the cobalt-carbon bond and sequesters cob(II)alamin, to which it binds more tightly than AdoCbl (*25*). We propose that CLYBL deficiency increases the propensity of I-CoA–dependent MCM inactivation and thereby leads to AdoCbl depletion (*5*). How a change in the mitochondrial B_{12} pool (AdoCbl) is signaled to the cytoplasm and affects B_{12} levels systemically is, however, not known.

Itaconate inhibits vitamin B_{12}-stimulated Mtb growth on propionate

To corroborate the in vitro evidence that itaconate inhibits Mtb MCM, we directly tested whether exogenous itaconate can blunt B_{12}-stimulated Mtb growth on propionate as the sole carbon source. As reported previously, vitamin B_{12} supplementation at concentrations as low as 1 μg/ml stimulate growth of Mtb H37Rv on propionate (Fig. 4, A and B), which has been attributed to the MCM-dependent pathway for propionate utilization (*29*). Growth stimulation was reduced in the presence of 1 mM itaconate and was completely inhibited at ≥5 mM itaconate (Fig. 4C). Millimolar concentrations of itaconate are endogenously produced in activated macrophages (*1*), and Irg1-deficient mice, unlike controls, succumb early to Mtb infection (*30*), suggesting that such an inhibitory mechanism could be physiologically relevant.

MCM inhibition and AdoCbl depletion in macrophages require endogenous I-CoA synthesis

Mtb infection in mice elevates itaconate production in lungs (*31*), presumably through Irg1 induction. To recapitulate the metabolic consequence of endogenous itaconate production, we stimulated RAW264.7 cells with lipopolysaccharide (LPS), a potent activator of *Irg*1 transcription and itaconate production (*1*). We previously found that LPS stimulation depletes AdoCbl in macrophages (*5*). Using a CRISPR knockdown of Irg1 in RAW264.7 cells (Fig. 4D), we observed that AdoCbl depletion is dependent on Irg1, which is transcriptionally upregulated in LPS-stimulated macrophages (*1*, *32*). Treatment with LPS induced an increase in itaconate and I-CoA levels, which was significantly attenuated in Irg1 knockdown cells (Fig. 4E). Although LPS stimulation reduced AdoCbl to undetectable levels in control cells, it was not significantly changed in the Irg1 knockdown cells (Fig. 4E). Together, these data suggest that AdoCbl depletion and MCM inhibition in macrophages is caused by endogenous itaconate produced by Irg1 and induced during LPS stimulation.

Conclusions

AdoCbl is a radical initiator that generates the "working" dAdo• and "spectator" cob(II)alamin radical by homolytic cleavage of its cobalt-carbon bond. We found that I-CoA triggers homolytic cleavage of the cobalt-carbon bond in AdoCbl as in the normal MCM catalytic cycle, but proximity effects promote suicidal addition of dAdo• into its double bond. A chemically akin, albeit nonspecific, Michael addition mechanism has been invoked to explain itaconate-induced electrophilic stress (*10*, *11*). The combined action of itaconate and I-CoA on Mtb propionate metabolism would be predicted to result in increased levels of toxic propionate/propionyl-CoA derived from cholesterol-dependent growth of this pathogen in host phagosomes (*29*). Although the conditions are not known under which the Mtb pathway for de novo B_{12} biosynthesis might be operative (*33*), Mtb can scavenge B_{12} from its host (*34*). Itaconate-induced B_{12} deficiency in host macrophages thus might be a strategy for restricting pathogen growth, in addition to targeting pathogen enzymes involved in propionate metabolism (Fig. 1A); the relative importance of each inhibitory arm is unknown, however. We speculate that the *CLYBL* null background could boost the efficacy of this pathogen containment strategy, explaining the prevalence of the null genotype in human populations (*5*). In this context, it is noteworthy that the incidence of active tuberculosis is reported to be markedly lower in patients with B_{12} deficiency due to pernicious anemia (*35*).

REFERENCES AND NOTES

1. A. Michelucci *et al.*, *Proc. Natl. Acad. Sci. U.S.A.* **110**, 7820–7825 (2013).
2. L. A. J. O'Neill, M. N. Artyomov, *Nat. Rev. Immunol.* **19**, 273–281 (2019).
3. R. Kumar, *Int. J. Integr. Biol.* **7**, 69–72 (2009).
4. J. D. McKinney *et al.*, *Nature* **406**, 735–738 (2000).
5. H. Shen *et al.*, *Cell* **171**, 771–782.e11 (2017).
6. J. Sasikaran, M. Ziemski, P. K. Zadora, A. Fleig, I. A. Berg, *Nat. Chem. Biol.* **10**, 371–377 (2014).
7. N. Grarup *et al.*, *PLOS Genet.* **9**, e1003530 (2013).
8. M. Lek *et al.*, *Nature* **536**, 285–291 (2016).
9. D. Padovani, R. Banerjee, *Proc. Natl. Acad. Sci. U.S.A.* **106**, 21567–21572 (2009).
10. E. L. Mills *et al.*, *Nature* **556**, 113–117 (2018).
11. M. Bambouskova *et al.*, *Nature* **556**, 501–504 (2018).
12. S. O. Mansoorabadi *et al.*, *Biochemistry* **44**, 3153–3158 (2005).
13. H. Bothe *et al.*, *Biochemistry* **37**, 4105–4113 (1998).
14. W. Buckel *et al.*, *Eur. J. Inorg. Chem.* **2006**, 3622–3626 (2006).
15. R. Banerjee, *Biochemistry* **40**, 6191–6198 (2001).
16. H. Yang *et al.*, *J. Am. Chem. Soc.* **141**, 12139–12146 (2019).
17. H. P. C. Hogenkamp, *J. Biol. Chem.* **238**, 477–480 (1963).
18. P. Jaruga, M. Dizdaroglu, *DNA Repair* **7**, 1413–1425 (2008).
19. F. Mancia *et al.*, *Structure* **4**, 339–350 (1996).
20. D. S. Froese *et al.*, *J. Biol. Chem.* **285**, 38204–38213 (2010).
21. R. A. Kwiecien *et al.*, *J. Am. Chem. Soc.* **128**, 1287–1292 (2006).
22. E. Chabrière *et al.*, *Science* **294**, 2559–2563 (2001).
23. K. Gruber, R. Reitzer, C. Kratky, *Angew. Chem. Int. Ed.* **40**, 3377–3380 (2001).
24. J. Masuda, N. Shibata, Y. Morimoto, T. Toraya, N. Yasuoka, *Structure* **8**, 775–788 (2000).
25. G. C. Campanello *et al.*, *J. Am. Chem. Soc.* **140**, 13205–13208 (2018).
26. D. Padovani, T. Labunska, B. A. Palfey, D. P. Ballou, R. Banerjee, *Nat. Chem. Biol.* **4**, 194–196 (2008).
27. M. Ruetz *et al.*, *Cell Chem. Biol.* **26**, 960–969.e4 (2019).
28. D. Padovani, R. Banerjee, *Biochemistry* **45**, 9300–9306 (2006).
29. S. Savvi *et al.*, *J. Bacteriol.* **190**, 3886–3895 (2008).
30. S. Nair *et al.*, *J. Exp. Med.* **215**, 1035–1045 (2018).
31. J. H. Shin *et al.*, *J. Proteome Res.* **10**, 2238–2247 (2011).
32. A. K. Jha *et al.*, *Immunity* **42**, 419–430 (2015).
33. K. Gopinath, A. Moosa, V. Mizrahi, D. F. Warner, *Future Microbiol.* **8**, 1405–1418 (2013).
34. K. Gopinath *et al.*, *Open Biol.* **3**, 120175 (2013).
35. M. Barron, *JAMA* **100**, 1590–1592 (1933).

ACKNOWLEDGMENTS

We acknowledge H. Sharma (University of Michigan) for his assistance with crystallization and the GM/CA CAT at the Advanced Light Source for beam time. We also acknowledge the NIH Common Fund Metabolite Standards Synthesis Core (NHLBI contract no. HHSN268201300022C) for providing [^{13}C]itaconate. **Funding:** This work was supported in part by grants from the National Institutes of Health (RO1-DK45776 to R.B., 5 F32 GM113405 to G.C.C., K99-GM124296 to H.S., R35GM122455 to V.K.M., R01-DK054514 to K.W., and U19AI107774 to E.J.R.) and start-up funds from the University of Michigan (to M.K.). V.K.M. is an Investigator of the Howard Hughes Medical Institute. **Author contributions:** M.R. and G.C.C. performed the majority of the biochemical studies, H.G. did the kinetic analysis of *h*MCM, and L.M. and M.R. cloned and expressed the Mtb genes used in this study. M.P. and M.K. were responsible for the crystallographic analyses, and K.W. was responsible for the EPR spectroscopic analysis. H.S. performed the macrophage experiments, and J.Z. and S.W. performed the Mtb growth experiments. M.R., G.C.C., and R.B. wrote the manuscript. All authors were involved with data analysis of experiments performed by them or in their laboratories and edited the manuscript. **Competing interests:** V.K.M. is a paid advisor to Janssen Pharmaceuticals and 5AM Ventures and owns equity in Raze Therapeutics. **Data and materials availability:** All data are available in the manuscript or supplementary materials. The structure factors and coordinates for Mtb MCM (6OXC) and Mtb MCM + I-CoA (6OXD) have been deposited in the Protein Data Bank.

SUPPLEMENTARY MATERIALS

science.sciencemag.org/content/366/6465/589/suppl/DC1
Materials and Methods
Figs. S1 to S12
Table S1
References (*36*–*59*)

View/request a protocol for this paper from *Bio-protocol*.

19 May 2019; accepted 3 September 2019
10.1126/science.aay0934

BUTTERFLY GENOMICS

Genomic architecture and introgression shape a butterfly radiation

Nathaniel B. Edelman[1]*, Paul B. Frandsen[2,3], Michael Miyagi[1], Bernardo Clavijo[4], John Davey[5,20], Rebecca B. Dikow[3], Gonzalo García-Accinelli[4], Steven M. Van Belleghem[6], Nick Patterson[7,8], Daniel E. Neafsey[8,9], Richard Challis[10], Sujai Kumar[11], Gilson R. P. Moreira[12], Camilo Salazar[13], Mathieu Chouteau[14], Brian A. Counterman[15], Riccardo Papa[6,16], Mark Blaxter[10], Robert D. Reed[17], Kanchon K. Dasmahapatra[5], Marcus Kronforst[18], Mathieu Joron[19], Chris D. Jiggins[20], W. Owen McMillan[21], Federica Di Palma[4], Andrew J. Blumberg[22], John Wakeley[1], David Jaffe[8,23], James Mallet[1]*

We used 20 de novo genome assemblies to probe the speciation history and architecture of gene flow in rapidly radiating *Heliconius* butterflies. Our tests to distinguish incomplete lineage sorting from introgression indicate that gene flow has obscured several ancient phylogenetic relationships in this group over large swathes of the genome. Introgressed loci are underrepresented in low-recombination and gene-rich regions, consistent with the purging of foreign alleles more tightly linked to incompatibility loci. Here, we identify a hitherto unknown inversion that traps a color pattern switch locus. We infer that this inversion was transferred between lineages by introgression and is convergent with a similar rearrangement in another part of the genus. These multiple de novo genome sequences enable improved understanding of the importance of introgression and selective processes in adaptive radiation.

Adaptive radiations play a fundamental role in generating biodiversity. Initiated by key innovations and ecological opportunity, radiation is fueled by niche competition that promotes rapid diversification of species (*1*). Reticulate evolution may enhance radiation by introducing genetic variation, enabling rapidly emerging populations to take advantage of new ecological opportunities (*2*, *3*). Diverging from its sister genus *Eueides* ~12 million years (My) ago, *Heliconius* radiated in a burst of speciation in the last ~5 My (*4*). Introgression is well known in *Heliconius*, with widespread reticulate evolution across the genus (*5*), although this has been disputed (*6*). Nonetheless, how introgression varies across the genome is known only in one pair of sister lineages (*7*, *8*). Here, we use multiple de novo whole-genome assemblies to improve the resolution of introgression, incomplete lineage sorting (ILS), and genome architecture in deeper branches of the *Heliconius* phylogeny.

Phylogenetic analysis

We generated 20 de novo genome assemblies for species in both major *Heliconius* subclades and three additional genera of Heliconiini. We then aligned the 16 highest-quality Heliconiini assemblies to two *Heliconius* reference genomes and seven other Lepidoptera genomes, resulting in an alignment of 25 taxa (*9*). De novo assembly provides superior sequence information for low-complexity regions, allows for discovery of structural rearrangements, and improves alignment of evolutionarily distant clades (*10*). Other studies in *Heliconius* have shown a high level of phylogenetic discordance, arguably a result of rampant introgression (*4*, *5*). We attempted to reconstruct a bifurcating species tree by estimating relationships using protein-coding genes, conserved coding regions, and conserved noncoding regions. We generated phylogenies with coalescent-based and concatenation approaches using both the full Lepidoptera alignment and a restricted, Heliconiini-only subalignment. These topologies were largely congruent among analytical approaches, but weakly supported nodes were resolved inconsistently. These approaches therefore failed to resolve the phylogeny of *Heliconius* as a simple bifurcating tree (Fig. 1A and fig. S20).

To determine whether hybridization was a cause of the species tree uncertainty, we calculated Patterson's *D* statistics (*11*) for every triplet of the 13 *Heliconius* species using a member of the sister genus, *Eueides tales*, as the outgroup. In 201 of 286 triplets, we observed values significantly different from zero based on block-jackknifing, demonstrating strong evidence for introgression (fig. S53). However, these tests alone yield little quantitative information about admixture. We therefore used phyloNet (*12*) to infer reticulate phylogenetic networks of these species based on random samples of 100 10-kb windows across the alignment. For each sample, we coestimated all 100 regional gene trees and the overall species network in parallel (*12*). To improve alignments, we analyzed the *melpomene*-silvaniform group with respect to the *Heliconius melpomene* Hmel2.5 assembly (*13*) and the *erato-sara* group with respect to the *H. erato demophoon* v1 assembly (*9*, *14*). Most species exhibited an admixture event at some point in their history using this method; we confirmed extensive reticulation among silvaniform species and discovered major gene-flow events in the *erato-sara* clade. On the basis of these results, we propose the reticulate phylogenies shown in Fig. 1, B to C.

Correlation of local ancestry with genome architecture

We next analyzed the distribution of tree topologies across the genome, again treating each major clade separately and using its respective reference genome. The *melpomene*-silvaniform group lacked topological consensus, unsurprisingly because introgression, especially of key mimicry loci, is well known in this clade (*15*). The most common tree topology was found in only 4.3% of windows, with an additional 14 topologies appearing in 1.0 to 3.4% of windows (fig. S19 to S21). By contrast, we here focus on the *erato-sara* group, in which two topologies dominate (Fig. 2). One (Fig. 2B, Tree 2) matched our bifurcating consensus topology (Fig. 1A) and a recently published tree (*4*), whereas the other (Tree 1) differs in that it places *H. hecalesia* and *H. telesiphe* as sisters.

Regions with local topologies discordant from the species tree may have arisen through introgression or ILS. To make within-topology

[1]Department of Organismic and Evolutionary Biology, Harvard University, Cambridge, MA 02138, USA. [2]Department of Plant and Wildlife Sciences, Brigham Young University, Provo, UT 84602, USA. [3]Data Science Lab, Office of the Chief Information Officer, Smithsonian Institution, Washington, DC 20560, USA. [4]Earlham Institute, Norwich Research Park, Norwich NR4 7UZ, UK. [5]Bioscience Technology Facility, Department of Biology, University of York, York YO10 5DD, UK. [6]Department of Biology, University of Puerto Rico, Río Piedras Campus, San Juan, PR 00931-3360, Puerto Rico. [7]Department of Human Evolutionary Biology, Harvard University, Cambridge, MA 02138, USA. [8]Broad Institute of MIT and Harvard, Cambridge, MA, 02142 USA. [9]Harvard TH Chan School of Public Health, Boston, MA 02115, USA. [10]Wellcome Sanger Institute, Wellcome Genome Campus, Cambridge CB10 1SA, UK. [11]Institute of Evolutionary Biology, University of Edinburgh, Edinburgh EH9 3JT, UK. [12]Departamento de Zoologia, Universidade Federal do Rio Grande do Sul, Porto Alegre, 91501-970 Brasil. [13]Biology Program, Faculty of Natural Sciences and Mathematics, Universidad del Rosario, Carrera 24, No. 63C-69, Bogotá D.C. 111221, Colombia. [14]Laboratoire Ecologie, Evolution, Interactions des Systèmes Amazoniens (LEEISA), USR 3456, Université De Guyane, CNRS Guyane, 275 Route de Montabo, 97334 Cayenne, French Guiana. [15]Department of Biological Sciences, Mississippi State University, Starkville, MS 39762, USA. [16]Molecular Sciences and Research Center, University of Puerto Rico, San Juan, PR 00931-3360, Puerto Rico. [17]Department of Ecology and Evolutionary Biology, Cornell University, Ithaca, NY 14853, USA. [18]Department of Ecology and Evolution, University of Chicago, Chicago, IL 60637, USA. [19]CEFE, CNRS, Université de Montpellier, Université Paul Valéry Montpellier 3, EPHE, IRD, 34090 Montpellier, France. [20]Department of Zoology, University of Cambridge, Cambridge CB2 3EJ, UK. [21]Smithsonian Tropical Research Institute, Apartado 0843-03092 Panamá, Panama. [22]Department of Mathematics, University of Texas, Austin, TX 78712, USA. [23]10x Genomics, Pleasanton, CA 94566, USA.
*Corresponding author. Email: nedelman@g.harvard.edu (N.B.E.); jmallet@oeb.harvard.edu (J.M.)

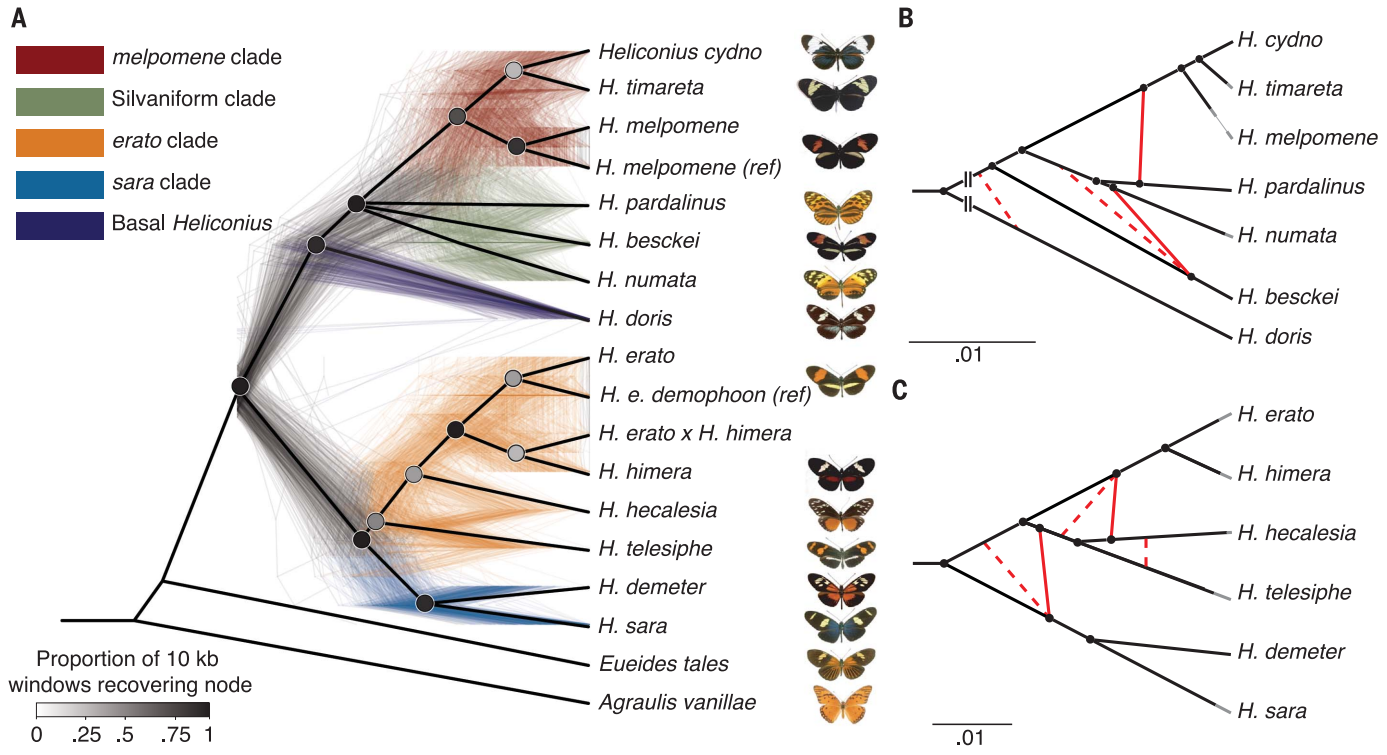


Fig. 1. Phylogeny and phylogenetic networks of *Heliconius* do not support a bifurcating tree. (**A**) All nodes resolved in a majority of species trees are shown in this cladogram (heavy black lines), whereas the poorly resolved silvaniform clade is collapsed as a polytomy (fig. S20). The 500 colored trees were sampled from 10-kb nonoverlapping windows and constructed with maximum likelihood. (**B** and **C**) High-confidence tree structure (black) and introgression events (red) are shown as solid lines. Dashed red lines indicate weakly supported introgression events. Gray branch ends are cosmetic. The *melpomene*-silvaniform clade is shown in (B) and the *erato-sara* clade in (C). Euclidean lengths of solid black lines are proportional to genetic distance along the branches. Scale bars are in units of substitutions per site. Breaks at the base in (B) indicate that the branch leading to *H. doris* has been shortened for display.

locus-by-locus inferences, we developed a statistical test to distinguish between ILS and introgression based on the distribution of internal branch lengths among windows for a given three-taxon subtree, conditional on its topology. We call this method "quantifying introgression via branch lengths" (QuIBL). In the absence of introgression, we expect internal branch lengths of triplet topologies discordant with the species tree (due to ILS) to be exponentially distributed. However, if introgression has occurred, then their distribution should have that same exponential component but also include an additional component with a nonzero mode corresponding to the time between the introgression event and the most recent common ancestor of all three species (*9*). Like other tree-based methods, QuIBL is potentially sensitive to the assumption that each tree is inferred from loci with limited internal recombination (fig. S75). We therefore chose small (5-kb) windows to reduce the probability of intralocus recombination breakpoints.

For every triplet in the *erato-sara* clade, we calculated the likelihood that the distribution of internal branch lengths is consistent with introgression or with ILS only. We formally distinguished between these two models using a Bayesian information criterion (BIC) test with a strict cutoff of $\Delta BIC > 10$. Consistent with our results from *D* statistics, we found that 13 of 20 triplets have evidence for introgression (table S13). For example, using QuIBL on the triplet *H. erato*–*H. hecalesia*–*H. telesiphe*, we infer that 76% of discordant loci, or 38% of all loci genome-wide, are introgressed. Averaging over all triplets, we infer that 71% (67% with BIC filtering) of loci with discordant gene trees have a history of introgression, or 20% (19% with BIC filtering) of all triplet loci, indicating a broad signal of introgression throughout the clade [Eq. 7.7, table S13; see (*9*) for additional discussion].

In hybrid populations, individuals have genomic regions that originate from different species and may be incompatible with the recipient genome or with their environment (*16*). Linked selection causes harmless or even beneficial introgressed loci to be removed along with these deleterious loci if they are tightly linked; this effect depends on the strength of selection and the local recombination rate (*17*, *18*). We therefore expect introgressed loci to be enriched in regions where selection is likely to be weak, such as gene deserts or regions of high recombination, where harmless introgressed loci more readily recombine away from linked incompatibility loci.

In *Heliconius*, even distant species such as *H. erato* and *H. melpomene* have the same number of broadly collinear chromosomes (*13*), facilitating direct comparisons among species. Furthermore, each chromosome in *Heliconius* has approximately one crossover per meiosis in males (there is no crossing over in female *Heliconius*) (*14*, *19*). Chromosomes vary in length, and chromosome size is inversely proportional to recombination rate per base pair (*8*, *13*). We found a strong correlation between the fraction of windows in each chromosome that show a given topology and physical chromosome length (Fig. 3A). Such relationships exist for all eight trees in Fig. 2B (*9*), but we focus here on the two most common trees: Tree 1 has a strongly negative correlation with chromosome size ($r^2 = 0.883$, $t = 11.7$, 18 df, $p < 0.0001$), whereas Tree 2 (concordant with our inferred species tree) has a positive correlation ($r^2 = 0.726$, $t = 6.9$, 18 df, $p < 0.0001$). Results from QuIBL indicate that 94% of windows that recover a Tree 1 triplet topology are consistent with introgression (fig. S70 and table S13). The Z (sex) chromosome 21 is strongly

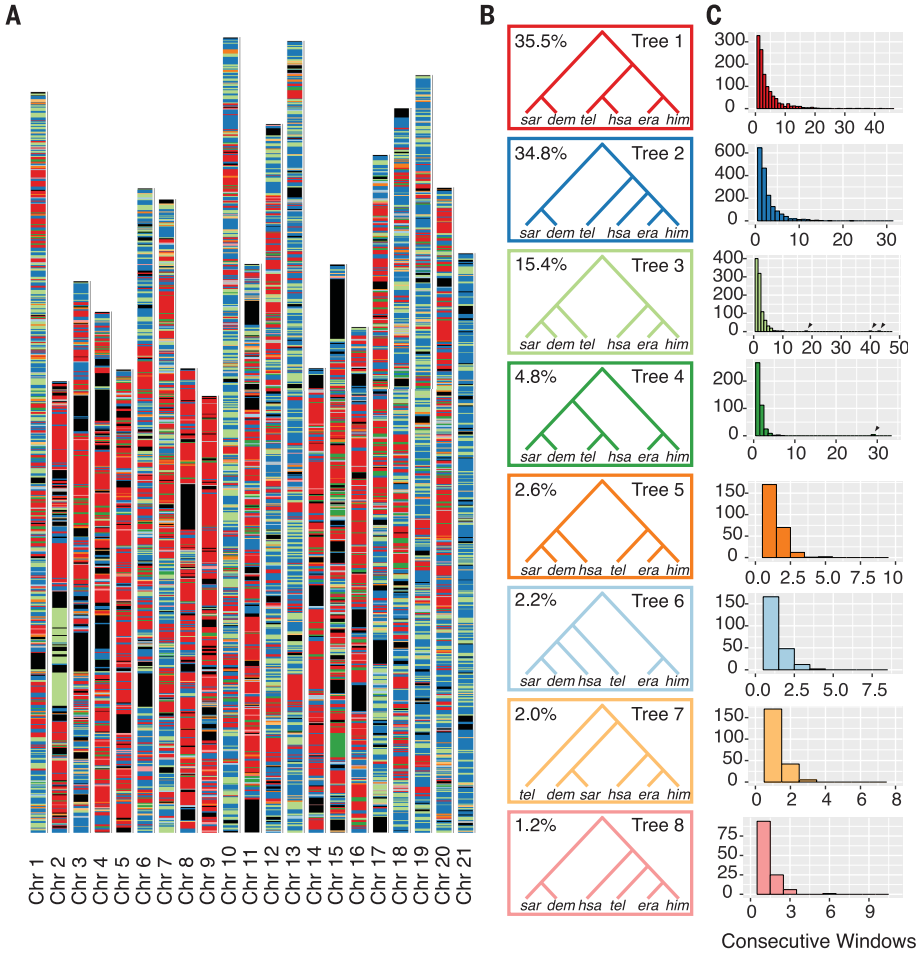


Fig. 2. Local evolutionary history in the erato-sara clade is heterogeneous across the genome. (**A**) Each bar represents a chromosome, in terms of the *H. erato* reference (*14*). Colored bands represent tree topologies of each 50-kb window; colors correspond to the topologies in (B), with black regions showing missing data. (**B**) The eight most common trees. The value in the top left corner is the percentage of all 50-kb windows that recover that topology. (**C**) Each histogram corresponds to the topology of the same color in (B) and shows the distribution of the number of consecutive 50-kb windows with that topology. Arrows indicate long blocks in inversions.

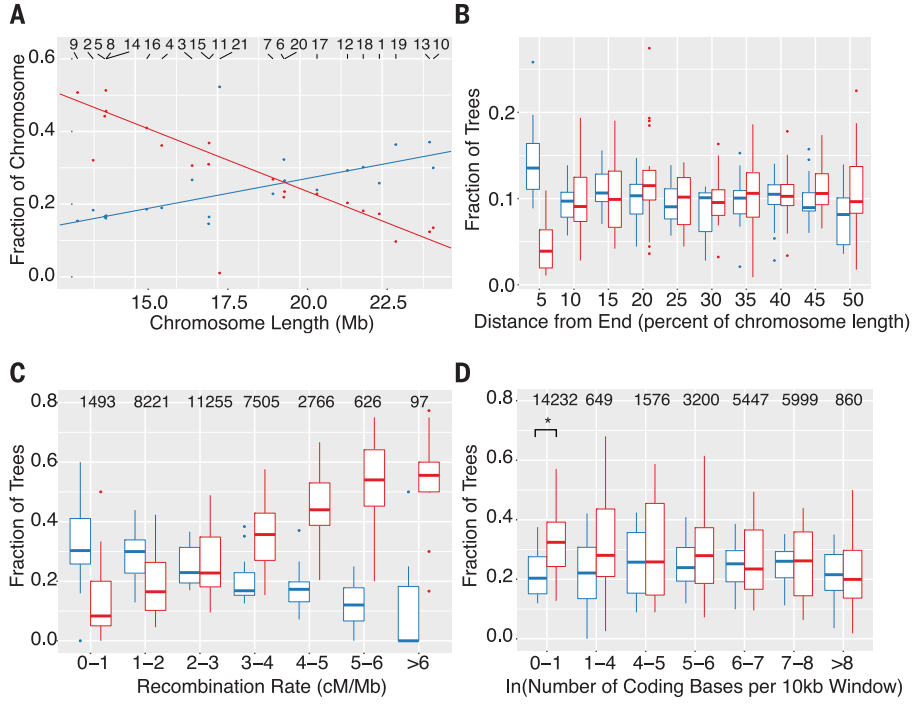


Fig. 3. Chromosomal architecture is strongly correlated with local topology. Tree 1 is shown in red and Tree 2 is shown in blue, as in Fig. 2. (**A**) Tree 1 shows a negative relationship with chromosome size, whereas Tree 2 shows a positive relationship. Lines are linear regressions with chromosome 21 excluded. Numbers along the top indicate chromosome number. (**B**) Each chromosome was divided into 10 equally sized bins, and the occupancy of each topology in each bin was calculated as the number of windows that recovered the topology in the bin divided by the number of windows that recovered the topology in the chromosome. (**C**) Windows are binned by recombination rate, and boxes show the fraction of each tree in each bin for each chromosome separately. Numbers above boxes are the numbers of windows in each bin. (**D**) Boxes showing the relationship of tree topology with coding density. Asterisk denotes significance at the 5% level (paired *t* test, $p < 0.025$). In all boxplots, the central line is the median, box edges are first and third quartile, and whiskers extend to the largest value no farther than 1.5 × (interquartile range).

enriched for Tree 2, suggesting that it may harbor more incompatibility loci than autosomes. Interspecific hybrid females in *Heliconius* are often sterile, conforming to Haldane's rule, and sex chromosomes have been implicated as being particularly important in generating incompatibilities (*8*, *20*–*24*).

To test whether the pattern that we observed among chromosomes is related to differences in recombination, we investigated the relationship between recombination rate and tree topology within chromosomes. The recombination rate declines at the ends of chromosomes (fig. S85), and the species tree (Tree 2) is more abundant in those regions

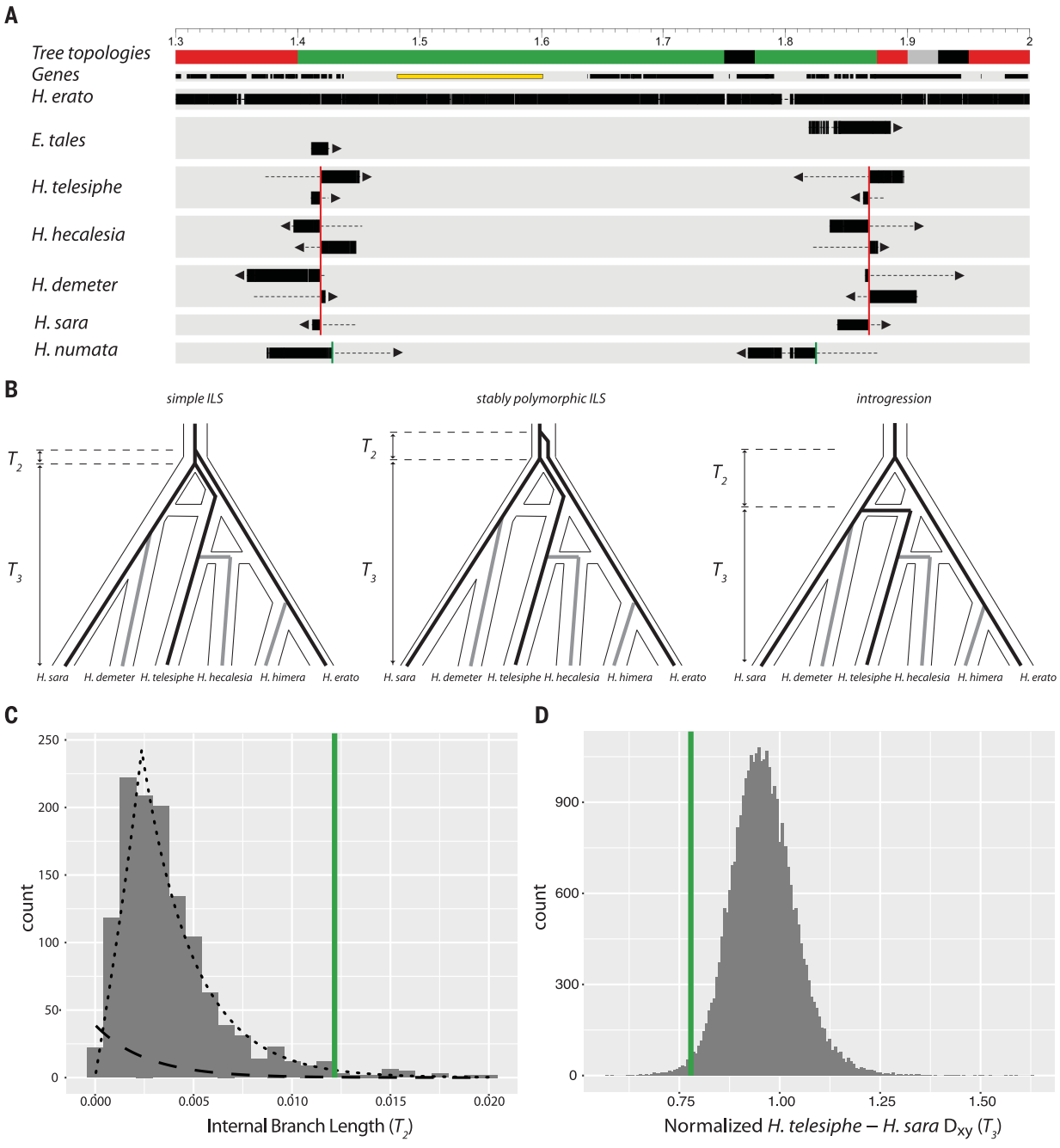


Fig. 4. Parallel evolution of a major inversion at the cortex supergene locus. (**A**) Map of 1.7-Mb region on chromosome 15. Coordinates are in terms of Hmel 2.5 and ticks are in Mb. Tree topology colors correspond to those in Fig. 2. Genes are shown as black rectangles; *cortex* is highlighted in yellow. Each line shows the mapping of a single contig. Aligned sections of each contig are shown as thick bars, whereas unaligned sections are shown as dotted lines. Arrows indicate the strand of the alignment. The *H. erato* group breakpoints are shown with red vertical lines and the *H. numata* breakpoints are shown with green vertical lines. (**B**) Evolutionary hypotheses consistent with the topology observed in this inversion in the context of the previously estimated phylogenetic network. The three species used in the triplet gene tree method, *H. erato*, *H. telesiphe*, and *H. sara*, are shown as black lines; lineages not included are shown as gray lines. (**C**) Histogram of internal branch lengths (T_2) in windows with the topology *H. erato* (*H. telesiphe*, *H. sara*). The inferred ILS distribution is shown as a dashed line, and the inferred introgression distribution is shown as a dotted line. The average internal branch length in the inversion is shown as a green vertical line. (**D**) Histogram of normalized D_{XY} (T_3) between *H. telesiphe* and *H. sara*. Mean normalized D_{XY} in the inversion is shown as a green vertical line.

(Fig. 3B). In addition, when windows were grouped by local recombination rate calculated from population genetic data (*9*, *14*), we observed a strong relationship with the recovered topology (Fig. 3C). Finally, we observed a minor enrichment of Tree 1 in regions of very low gene density, but this effect was weak (Fig. 3D) compared with that of recombination. Taken together, these results show that tighter linkage on longer chromosomes and in lower recombination regions within chromosomes leads to removal of more introgressed variation in those regions. This very strong correlation is consistent with a highly polygenic architecture of incompatibilities between species.

Introgression of a convergent inversion

The topology block size distribution in the *erato* clade generally decayed exponentially (Fig. 2C), but two unusually long blocks contained minor topologies: one on chromosome 2 (Tree 3, composed of three sub-blocks) and the other on chromosome 15 (Tree 4). Our study of the ~3-Mb topology block on chromosome 2 confirms an earlier finding of an inversion in *H. erato* (*13*), and we show here that its rare topology is most likely explained by ILS, including a long period of ancestral polymorphism (fig. S95).

The topology block on chromosome 15 is of particular interest because it spans *cortex*, a genetic hotspot of wing color pattern diversity in Lepidoptera (*25*, *26*). We hypothesized that this block could be an inversion, as in *H. numata*, where the P_1 "supergene" inversion polymorphism around *cortex* controls color pattern switching among mimicry morphs (*27*). This block recovers *H. telesiphe* and *H. hecalesia* as a monophyletic subclade, which together are sisters to the *sara* clade (Fig. 2B, Tree 4). We searched our de novo assemblies for contigs that mapped across topology transitions. Taking *H. melpomene* as the standard arrangement, we found clear inversion breakpoints in *H. telesiphe*, *H. hecalesia*, *H. sara*, and *H. demeter*. Conversely, *H. erato*, *H. himera*, and *E. tales* all contain contigs that map in their entirety across the breakpoints (Fig. 4A), implying that they have the ancestral *H. melpomene* arrangement.

This chromosome 15 inversion covers almost exactly the same region as the 400-kb P_1 inversion in *H. numata* (*25*, *27*, *28*). However, de novo contigs from our *H. numata* assembly show that the breakpoints of P_1 are close to but not identical to those of the inversion in the *erato* clade (Fig. 4A). Furthermore, in topologies for *H. numata*, *H. telesiphe*, *H. erato*, and *E. tales* across chromosome 15, not a single window recovered *H. numata* and *H. telesiphe* as a monophyletic subclade, as would be expected if the *erato* group inversion were homologous to P_1 in *H. numata*.

We used QuIBL with the triplet *H. erato*–*H. telesiphe*–*H. sara* to elucidate the evolutionary history of this inversion. A small internal branch would suggest ILS, whereas a large internal branch would be more consistent with introgression (Fig. 4B). The average internal branch length in the inversion was much longer than the genome-wide average, corresponding to a 79% probability of introgression (Fig. 4C). If the inversion were polymorphic in the ancestral population for some time, then we could also recover a similarly long internal branch (Fig. 4B, center). We distinguished between this longer-term polymorphic scenario and introgression by comparing the genetic distance (D_{XY}) between *H. telesiphe* and *H. sara*, represented by T_3 in Fig. 4B. Normalized D_{XY} (as in fig. S95) within the inversion is ~25% less than in the rest of the genome. Given that this is a large genomic block, introgression is therefore the most parsimonious explanation for the evolutionary history of the inversion (Fig. 4D) (*29*).

Discussion

Species involved in rapid radiations are prone to hybridization because of frequent geographical overlap with closely related taxa. In both the *melpomene* and *erato* clades of *Heliconius*, introgression has overwritten the original bifurcation history of several species across large swathes of the genome, a pattern also observed in *Anopheles* mosquitos (*30*). This observation is also consistent with genomic analysis of other rapid radiations characterized by widespread hybridization and introgression, including Darwin's finches (*2*) and African cichlids (*31*). In other radiations, the role of introgression is less clear: in *Tamias* chipmunks, widespread introgression of mitochondrial DNA was identified, in contrast to an absence of evidence for nuclear gene flow (*32*). With few genomic comparisons available to date, it is perhaps too early to say whether introgression is a major feature of adaptive radiations in general, but evidence thus far suggests this to be the case.

Our results raise the question of why some genomic regions cross species boundaries and others do not. In the *erato* clade, we found a strong correlation between recombination rate and introgression probability. Similar associations with topology also exist between sister species in the *melpomene* clade (*8*). Associations between recombination and introgression in hybridizing populations of fishes and monkey flowers (*Mimulus* spp.) support the role of linked selection on a highly polygenic landscape of interspecific incompatibilities (*18*, *33*, *34*). Our results establish that this relationship persists and may indeed be strengthened with time since introgression. While hybridization is ongoing, many introgressed blocks are constantly reintroduced into the population. If linked to weakly deleterious alleles, introgressed loci will finally be purged by linked selection only long after introgression ceases.

Recombination rate alone cannot account for differential introgression, so we must delve into specific regions to elucidate their function and relevance to speciation. It is critical, therefore, to have tools that can confidently identify introgressed loci, and much effort has gone into developing such methods (*11*, *35*). Our test using internal branch lengths in triplet gene trees is based in coalescent theory and takes advantage of the discriminatory power of a property of gene trees not explicitly accounted for by other methods. QuIBL allows us to assess probability of introgression for each locus in each species triplet (*9*). Here, we used this method to identify the evolutionary origin of a convergent inversion that has undergone multiple independent introgression events and to show that genomic regions with discordant topologies arose mostly through hybridization. Just as sex aids adaptation within species, occasional introgression and recombination among species can have major long-term effects on the genome, contributing variation that could fuel rapid adaptive divergence and radiation.

REFERENCES AND NOTES

1. D. Schluter, *The Ecology of Adaptive Radiation* (Oxford Univ. Press, 2000).
2. S. Lamichhaney *et al.*, *Nature* **518**, 371–375 (2015).
3. J. B. Pease, D. C. Haak, M. W. Hahn, L. C. Moyle, *PLOS Biol.* **14**, e1002379 (2016).
4. K. M. Kozak *et al.*, *Syst. Biol.* **64**, 505–524 (2015).
5. K. M. Kozak, O. McMillan, M. Joron, C. D. Jiggins, Genome-wide admixture is common across the Heliconius radiation. bioRxiv 414201 [Preprint]. 11 September 2018.
6. A. V. Z. Brower, I. J. G. Orduña, *Cladistics* **34**, 151–166 (2018).
7. S. H. Martin *et al.*, *Genome Res.* **23**, 1817–1828 (2013).
8. S. H. Martin, J. W. Davey, C. Salazar, C. D. Jiggins, *PLOS Biol.* **17**, e2006288 (2019).
9. Materials and methods are available as supplementary materials.
10. A. G. Clark *et al.*, *Nature* **450**, 203–218 (2007).
11. N. Patterson *et al.*, *Genetics* **192**, 1065–1093 (2012).
12. D. Wen, L. Nakhleh, *Syst. Biol.* **61**, 439–457 (2017).
13. J. W. Davey *et al.*, *Evol. Lett.* **1**, 138–154 (2017).
14. S. M. Van Belleghem *et al.*, *Nat. Ecol. Evol.* **1**, 52 (2017).
15. C. D. Jiggins, *The Ecology and Evolution of Heliconius Butterflies* (Oxford Univ. Press, 2017).
16. J. A. Coyne, H. A. Orr, *Speciation* (Sinauer, 2004).
17. D. J. Begun, C. F. Aquadro, *Nature* **356**, 519–520 (1992).
18. M. Schumer *et al.*, *Science* **360**, 656–660 (2018).
19. J. W. Davey *et al.*, *G3: Genes Genomes Genetics* **6**, 695–708 (2016).
20. T. Dobzhansky, *Genetics and the Origin of Species* (Columbia Univ. Press, 1937).
21. H. A. Orr, M. Turelli, *Genetics* **143**, 613–616 (1996).
22. C. D. Jiggins *et al.*, *Evolution* **55**, 1631–1638 (2001).
23. R. E. Naisbit, C. D. Jiggins, M. Linares, C. Salazar, J. Mallet, *Genetics* **161**, 1517–1526 (2002).
24. S. M. Van Belleghem *et al.*, *Mol. Ecol.* **27**, 3852–3872 (2018).
25. M. Joron *et al.*, *PLOS Biol.* **4**, e303–e310 (2006).
26. N. J. Nadeau *et al.*, *Nature* **534**, 106–110 (2016).
27. P. Jay *et al.*, *Curr. Biol.* **28**, 1839–1845.e3 (2018).
28. M. Joron *et al.*, *Nature* **477**, 203–206 (2011).
29. F. Roda, F. K. Mendes, M. W. Hahn, R. Hopkins, *Mol. Ecol.* **26**, 2317–2330 (2017).
30. M. C. Fontaine *et al.*, *Science* **347**, 1258524 (2015).
31. J. I. Meier *et al.*, *Nat. Commun.* **8**, 14363 (2017).
32. J. M. Good, D. Vanderpool, S. Keeble, K. Bi, *Evolution* **69**, 1961–1972 (2015).
33. Y. Brandvain, A. M. Kenney, L. Flagel, G. Coop, A. L. Sweigart, *PLOS Genet.* **10**, e1004410 (2014).

34. H. F. Gante *et al*., . *Mol. Ecol.* **25**, 6143–6161 (2016).
35. S. H. Martin, J. W. Davey, C. D. Jiggins, *Mol. Biol. Evol.* **32**, 244–257 (2015).
36. N. B. Edelman, P. B. Frandsen, M. Miyagi, B. Clavijo, J. Davey, R. B. Dikow, G. García-Accinelli, S. M. Van Belleghem, N. Patterson, D. E. Neafsey, R. Challis, S. Kumar, G. R. P. Moreira, C. Salazar, M. Chouteau, B. A. Counterman, R. Papa, M. Blaxter, R. D. Reed, K. K. Dasmahapatra, M. Kronforst, M. Joron, C. D. Jiggins, W. O. McMillan, F. Di Palma, A. J. Blumberg, J. Wakeley, D. Jaffe, J. Mallet, Multispecies, whole-genome alignment and subalignment data for: Genomic architecture and introgression shape a butterfly radiation, Dryad (2019); https://doi.org/10.5061/dryad.b7bj832.
37. N. B. Edelman, P. B. Frandsen, M. Miyagi, B. Clavijo, J. Davey, R. B. Dikow, G. García-Accinelli, S. M. Van Belleghem, N. Patterson, D. E. Neafsey, R. Challis, S. Kumar, G. R. P. Moreira, C. Salazar, M. Chouteau, B. A. Counterman, R. Papa, M. Blaxter, R. D. Reed, K. K. Dasmahapatra, M. Kronforst, M. Joron, C. D. Jiggins, W. O. McMillan, F. Di Palma, A. J. Blumberg, J. Wakeley, D. Jaffe, J. Mallet, Code used in data analysis for: Genomic architecture and introgression shape a butterfly radiation, Zenodo (2019); https://doi.org/10.5281/zenodo.3401692.
38. N. B. Edelman, P. B. Frandsen, M. Miyagi, B. Clavijo, J. Davey, R. B. Dikow, G. García-Accinelli, S. M. Van Belleghem, N. Patterson, D. E. Neafsey, R. Challis, S. Kumar, G. R. P. Moreira, C. Salazar, M. Chouteau, B. A. Counterman, R. Papa, M. Blaxter, R. D. Reed, K. K. Dasmahapatra, M. Kronforst, M. Joron, C. D. Jiggins, W. O. McMillan, F. Di Palma, A. J. Blumberg, J. Wakeley, D. Jaffe, J. Mallet, Code used in data analysis for: Genomic architecture and introgression shape a butterfly radiation, Zenodo (2019); https://doi.org/10.5281/zenodo.3401698.

ACKNOWLEDGMENTS

We thank the Harvard FAS Research Computing team, the BYU Fulton Supercomputing Lab, and the Smithsonian Institution High Performance Cluster (SI/HPC) for their support. Conversations with S. Martin were instrumental in developing our thinking around recombination rate. We also thank J. Edelman for assistance with the Scaffolding with DISCOVAR pipeline and J. Zhu and L. Nakhleh for their guidance with the PhyloNet toolkit. We thank C. Frandsen for assistance with figure design, E. Harney for assistance with qpGraph, as well as N. Rosser, F. Seixas, T. Xiong, P. Muralidhar, and C. Veller for illuminating discussions. **Funding:** This project was funded by a SPARC Grant from the Broad Institute of Harvard and MIT and startup and studentship funds from Harvard University to J.M. and N.B.E. Additional funding was received through NSF grant DGE1745303 to M.M.; BBSRC Core Strategic Programme Grant BB/CSP17270/1 at the Earlham Institute to B.C., G.G.-A., and F.D.P.; a Herchel Smith Postdoctoral Research Fellowship and a Smithsonian Tropical Research Institute Fellowship to J.D.; NSF grant OIA 1736026 to B.C. and R.P.; Brazilian National Council for Scientific and Technological Development" (CNPq) grant 309853/2014-1 to G.R.P.M.; Fondos Concursables Universidad del Rosario 2016-PIN-2017-001 to C.S.; Marie Sklodowska-Curie fellowship (FITINV, N 655857) and NSERC fellowship to M.C.; NERC award UKSBS PR18037 to M.B.; NSF grant IOS-1656514 to R.D.R.; NSF grant IOS-1656389 to R.P.; NERC NE/K012886/1 to K.K.D.; and NSF grant IOS-1452648 and NIH grant GM108626 to M.K. M.J. was supported by French National Research Agency: ANR-12-JSV7-0005-HybEvol and ANR-18-CE02-0019-Supergene. A.J.B. was supported by NIH grants 5U54CA193313 and GG010211-R01-HIV and AFOSR grant FA9550-18-1-0415. D.E.N. was supported in part by federal funds from the National Institute of Allergy and Infectious Diseases, National Institutes of Health, Department of Health and Human Services, under grant U19AI110818 to the Broad Institute. D.J.'s work on DISCOVAR de novo was funded in part with federal funds from the National Human Genome Research Institute, U.S. National Institutes of Health, U.S. Department of Health and Human Services, under grants R01HG003474 and U54HG003067. LepBase development was supported by BBSRC grants BB/K020161/1 and BB/R015325/1. The Smithsonian Tropical Research Institute provided funding for W.O.M. R.P. and S.M.V.B. were additionally supported by the University of Puerto Rico (Puerto Rico INBRE grant P20 GM103475 from the National Institute for General Medical Sciences). **Author contributions:** N.B.E., N.P., D.E.N., R.C., S.K., M.B., R.D.R., K.K.D., M.K., M.J., C.D.J., W.O.M., D.J., and J.M. conceived the project; N.B.E., P.B.F., M.M., B.C., D.J., and J.M. designed experiments; J.D., G.R.P.M., C.S., M.C., B.A.C., R.D.R., K.K.D., M.J., C.D.J., W.O.M., and J.M. supplied specimens and extracted DNA; D.J., B.C., G.G.-A., and F.D.P. assembled genomes; P.B.F. inferred species trees; N.B.E. performed reference gap filling, phylogenetic network, local gene tree, recombination rate, and genome structure analyses; J.D. and S.M.V.B. generated linkage maps; M.M., J.W., and A.J.B. developed the branch length test; and N.B.E. and J.M. wrote and edited the manuscript with input from all authors. **Competing interests:** The authors declare no competing interests. **Data and materials availability:** Reads generated are available in the SRA, BioProject PRJNA531399. Genome assemblies are available on LepBase (http://lepbase.org). The full multispecies, whole-genome alignment, as well as subalignments for windows and their respective inferred phylogenies, are available on Dryad (*36*). Also on Dryad are configuration files for progressiveCactus, the inferred LD recombination map for *H. erato*, loci used for phyloNet, and repeatMasker output for all assemblies. All code used to analyze data is available on Zenodo (*37*, *38*).

SUPPLEMENTARY MATERIALS

science.sciencemag.org/content/366/6465/594/suppl/DC1
Materials and Methods
Figs. S1 to S95
Tables S1 to S14
References (*39*–*91*)

View/request a protocol for this paper from *Bio-protocol*.

11 December 2018; accepted 16 September 2019
10.1126/science.aaw2090

VIRAL IMMUNOLOGY

Measles virus infection diminishes preexisting antibodies that offer protection from other pathogens

Michael J. Mina[1,2,3]*†, Tomasz Kula[1,2], Yumei Leng[1], Mamie Li[2], Rory D. de Vries[4], Mikael Knip[5,6], Heli Siljander[5,6], Marian Rewers[7], David F. Choy[8], Mark S. Wilson[8], H. Benjamin Larman[9], Ashley N. Nelson[10]‡, Diane E. Griffin[10], Rik L. de Swart[4], Stephen J. Elledge[1,2,11]†

Measles virus is directly responsible for more than 100,000 deaths yearly. Epidemiological studies have associated measles with increased morbidity and mortality for years after infection, but the reasons why are poorly understood. Measles virus infects immune cells, causing acute immune suppression. To identify and quantify long-term effects of measles on the immune system, we used VirScan, an assay that tracks antibodies to thousands of pathogen epitopes in blood. We studied 77 unvaccinated children before and 2 months after natural measles virus infection. Measles caused elimination of 11 to 73% of the antibody repertoire across individuals. Recovery of antibodies was detected after natural reexposure to pathogens. Notably, these immune system effects were not observed in infants vaccinated against MMR (measles, mumps, and rubella), but were confirmed in measles-infected macaques. The reduction in humoral immune memory after measles infection generates potential vulnerability to future infections, underscoring the need for widespread vaccination.

In the time before vaccination, nearly every child experienced measles, which resulted in millions of deaths. Global measles vaccination efforts have led to logarithmic reductions in the incidence of measles virus (MV) infections and measles-related mortality. However, measles remains endemic in much of the world, affecting >7 million people annually and causing >100,000 deaths (*1*–*3*). After decades of decline, the number of worldwide cases of measles has increased by nearly 300% since 2018 as a result of reduced vaccination (*2*). This increase is likely to be accompanied by substantial mortality risks (*3*). The resurgence of measles underscores the importance of understanding the full consequences of MV infection and accurately estimating the value of measles vaccination (*4*).

Immunosuppression was first documented when children with measles showed negative cutaneous tuberculin reactions after previously testing positive (*5*). Subsequent studies have shown decreased interferon signaling, skewed cytokine responses, lymphopenia, and suppression of lymphocyte proliferation shortly after infection (*6*). The MV receptor CD150/SLAMF1 (signaling lymphocytic activation molecule family member 1) is highly expressed on memory T, B, and plasma cells, resulting in their infection and depletion without an effect on total immunoglobulin G (IgG) levels (*7*–*12*). Recovery of the functional immune response, including resolution of lymphopenia, occurs 2 to 4 weeks after viral clearance (*6*, *10*, *13*, *14*). However, MV replication in immune cells has been hypothesized to impair immune memory, potentially causing "immunological amnesia" (*10*, *15*, *16*).

Most bona fide immune memory cells reside in the lymphoid tissues and bone marrow (*17*–*20*). Peripheral blood mononuclear cells are often used for evaluating immunological memory repertoires. However, these cells are in relative flux owing to recent infections, which limits their utility for measuring long-term immune memory. Antibodies are thought to better represent long-lived humoral memory (*18*, *20*). Most antibodies in the peripheral blood are produced by bone marrow long-lived plasma cells (LLPCs) and are impervious to disruptions in peripheral memory cells (*17*–*22*). Changes in pathogen-specific antibodies measured in the peripheral blood reflect changes in the long-lived permanent memory repertoire.

Epidemiological evidence has associated MV infections with increases in morbidity and mortality for as long as 5 years (*15*, *23*) and suggests that in the pre-vaccine era, MV may have been associated with up to 50% of all childhood deaths from infectious diseases, mostly from non-MV infections (*15*). This phenomenon might be explained by immune amnesia. However, to date, no study has successfully resolved whether measles-induced immune amnesia—a reduction in the diversity of the immune memory repertoire after measles infections—indeed exists. To address this issue, we have studied paired blood samples collected before and after MV infection using a seroprofiling tool that allows the detection of thousands of pathogen-specific antibodies.

Measuring the consequences of measles on immune memory

During a recent measles outbreak in the Netherlands, families in communities with low vaccination rates consented to provide blood samples. Plasma was collected before and after laboratory-confirmed MV infection from 77 unimmunized children with a mean age of 9 (SD ± 2) years, plus five unimmunized children who remained uninfected during the study (*24*). Of the 77 children, 34 were reported to have mild measles and 43 to have severe measles [detailed in (*24*)]. The mean time between sample collections was 10 weeks, and mean time of collection after MV infection was 7 weeks (table S1).

To measure the diversity and magnitude of the epitope-specific antibody repertoires in these children and controls, we used VirScan (*25*), a phage-display immunoprecipitation and sequencing (PhIP-Seq) technology (*26*) developed for virome-wide detection of antibodies against viral epitopes. VirScan primarily detects antibodies to short contiguous epitopes as opposed to conformational epitopes. The cells producing antibodies to all epitopes are phenotypically similar, aside from their antibody product. Thus, changes in the antibody repertoire detected by VirScan represent changes across the spectrum of antibodies, and these include neutralizing and non-neutralizing antibodies. For this study, we generated an expanded VirScan library that encodes the full proteomes of most known human pathogenic viruses (~400 species and strains) plus many bacterial proteins. For each sample, we obtained a comprehensive measure of the individual's antipathogen antibody repertoire diversity (i.e., the total epitope hits across all pathogen peptides). We also derived an antibody epitope binding signal (EBS), which is

[1]Division of Genetics, Brigham and Women's Hospital, Howard Hughes Medical Institute, Boston, MA 02115, USA. [2]Department of Genetics, Harvard Medical School, Boston, MA 02115, USA. [3]Department of Pathology, Brigham and Women's Hospital, Harvard Medical School, Boston, MA 02115, USA. [4]Department of Viroscience, Postgraduate School of Molecular Medicine, Erasmus MC, University Medical Centre Rotterdam, 3015 CN, Rotterdam, Netherlands. [5]Children's Hospital, University of Helsinki and Helsinki University Hospital, 00290 Helsinki, Finland. [6]Research Program for Clinical and Molecular Metabolism, University of Helsinki, 00014 Helsinki, Finland. [7]Barbara Davis Center for Diabetes, University of Colorado School of Medicine, Denver, CO 80045, USA. [8]Genentech Inc., South San Francisco, CA 94080, USA. [9]Department of Pathology, Johns Hopkins University School of Medicine, Baltimore, MD 21287, USA. [10]W. Harry Feinstone Department of Molecular Microbiology and Immunology, Johns Hopkins Bloomberg School of Public Health, Baltimore, MD 21205, USA. [11]Program in Virology, Harvard Medical School, Boston, MA 02115, USA.
*Present address: Center for Communicable Disease Dynamics, Department of Epidemiology and Department of Immunology and Infectious Diseases, Harvard School of Public Health, Boston, MA 02115, USA.
†Corresponding author. Email: selledge@genetics.med.harvard.edu (S.J.E.); mmina@hsph.harvard.edu (M.J.M.) ‡Present address: Human Vaccine Institute, Duke University Medical Center, Durham, NC 27710, USA.

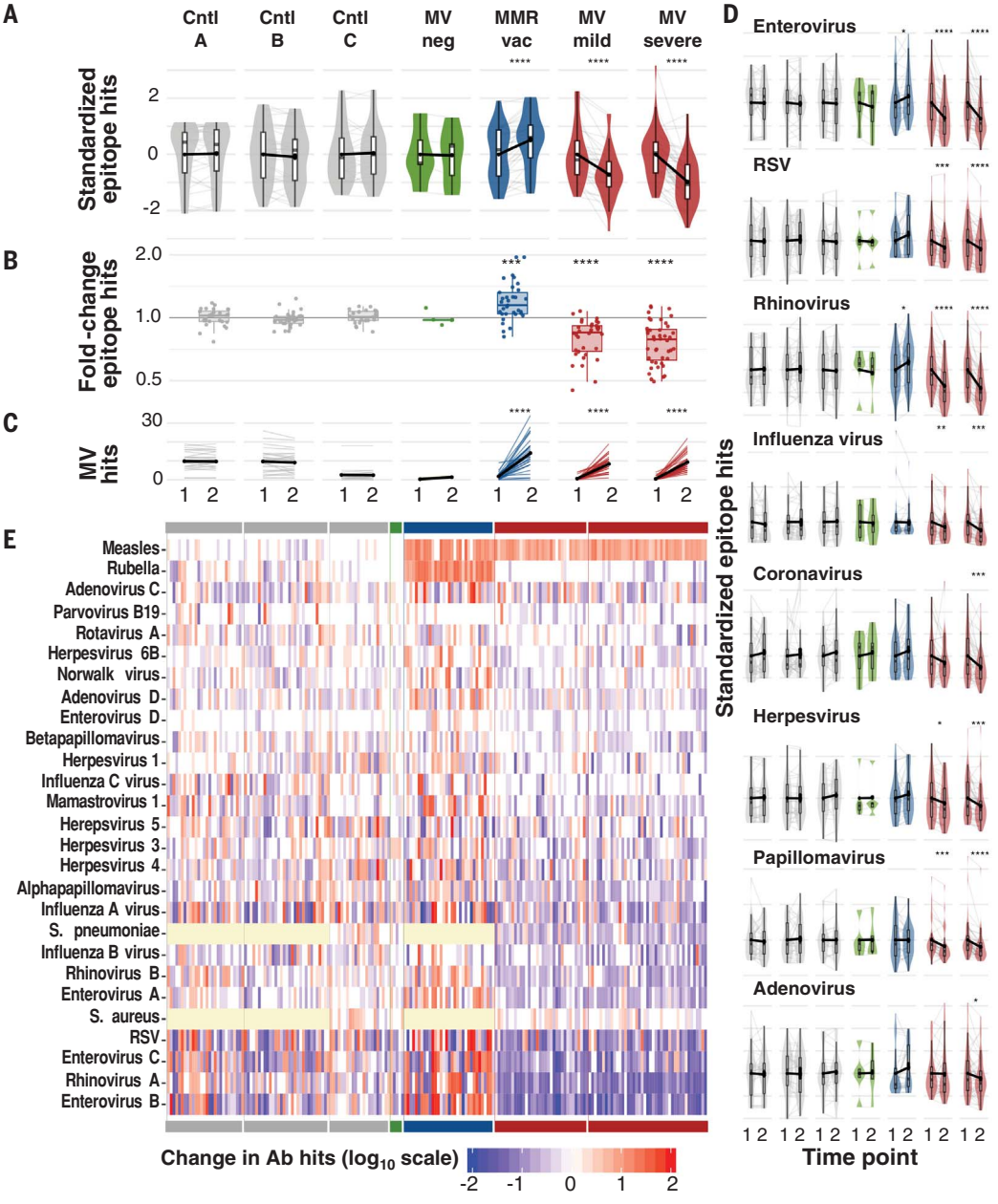


Fig. 1. Measles virus infections reduce antibody diversity. (**A**) Total epitopes recognized at time 1, left, and time 2, right, per cohort. For comparison across cohorts, values are standardized across all samples per cohort to a mean of 0 and standard deviation of 1. Each gray line indicates a paired sample from an individual, and black connecting lines indicate mean change from zero. Boxplots indicate interquartile range and median. Asterisks indicate paired *t* test *P* values. (**B**) Fold change of total antibody diversity (i.e., number of total epitope hits) at time 2 versus time 1. Each point represents one paired sample from an individual. Boxplots indicate interquartile range and median. Asterisks indicate significant differences relative to control A (Cntl A), based on student's *t* test *P* values. (**C**) Number of measles epitope hits per sample at time 1 and time 2. Thin lines indicate paired samples. Black lines indicate cohort averages. (**D**) As in (A), but for individual viruses. Bonferroni-corrected *P* values in (A to D): $*P < 0.05$, $**P < 0.001$, $***P < 0.001$, $****P < 0.0001$. (**E**) Heatmap indicating the change in the total number of epitope hits per species between time 1 and time 2. Each column represents an individual paired sample and each row a pathogen. Cohorts are indicated by the solid bars at top and bottom and are in the same order (left to right) as in (A). Yellow cells indicate that pathogen was not assayed in those samples. Ab, antibody.

a relative measure of antibody titer for each epitope.

We used VirScan to profile the immune memory antibody repertoires before (time 1) and after (time 2) MV infection. Paired samples were also obtained from four control cohorts (n = 119 paired specimens; table S1). These samples were derived from: (i) approximately age-matched controls sampled at similar intervals (~3 months) as the measles cohorts (control A; n = 28 paired specimens); (ii) age-matched controls with samples collected ~1 year apart (control B; n = 31); (iii) adult controls with collection intervals similar to the measles-infected individuals (control C; n = 22); (iv) young children before and after their first measles-mumps-rubella (MMR) vaccination (MMR vaccinated; n = 33); and (v) unvaccinated children from the same community as the MV cases but who remained seronegative for MV (MV negative; n = 5). Control cohorts A, B, and C were individuals with no known exposure to MV.

Measles modulates the diversity of the antibody repertoire and causes loss of preexisting antibodies

We assessed changes in antibody repertoire diversity (measured as the total number of unique pathogen epitopes recognized, or epitope hits) before and after measles relative to those observed in controls, standardizing the total number of epitope hits per individual by cohort for comparison (Fig. 1A). We detected substantial reductions in the number of pathogen epitopes recognized after measles but limited changes in the absence of measles. MV infections were associated with a mean reduction of ~20% in the overall diversity or size of the antibody repertoire measured by VirScan (Fig. 1B), and this was consistent across individual pathogens (Fig. 1, D and E, and fig. S1). However, effect sizes varied. Notably, 12 of the 77 children (16%) lost >40% of their overall antibody repertoire diversity. We detected increases in MV-specific epitopes in children after measles infection or MMR vaccination (Fig. 1C). No changes in the total IgG, IgA, or IgM levels were detected, as determined by quantitative ELISA (enzyme-linked immunosorbent assay) (fig. S2). These results suggest

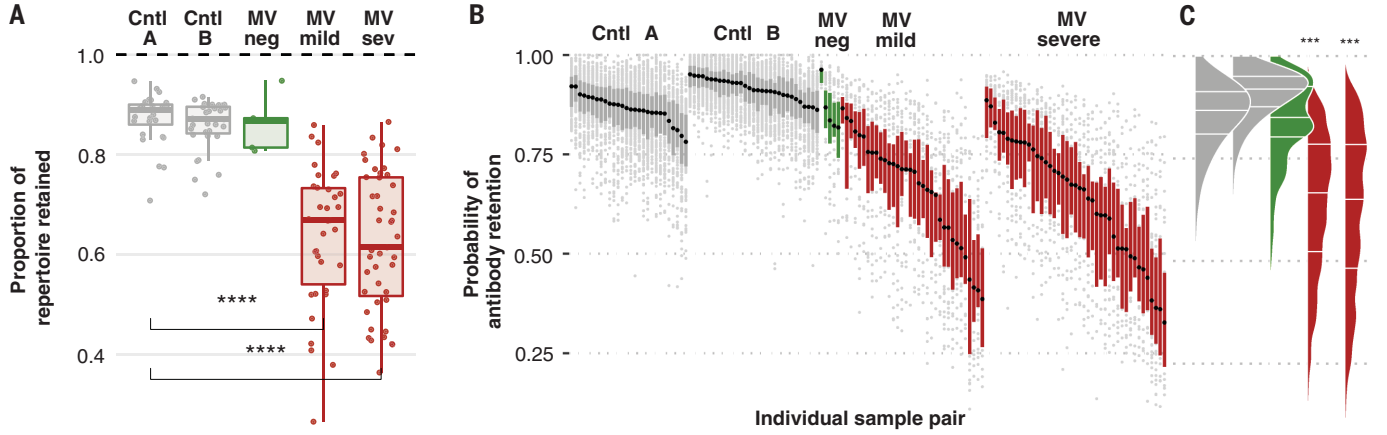


Fig. 2. Measles eliminates preexisting immune memory. (**A**) The proportion of total epitopes detected at time 1 that were retained at time 2. One point represents one child. Bonferroni-adjusted student's *t* test *P* values for significant differences relative to control A are shown (****$P < 0.0001$). (**B**) Probability of retaining initial antibodies at time 2 for individual pathogens per child. Each point represents a single pathogen per child. Probabilities are obtained by fitting a binomial random effects model controlling for interval duration (materials and methods). Each boxplot represents the interquartile range and median retention probabilities calculated across pathogens for a single child. Points indicate pathogen-specific retentions that are outside of the interquartile range per child. Children are rank ordered along the *x* axis by the median (black dot per boxplot) retention probabilities. (**C**) Density distribution of probabilities shown in (B), derived by collapsing all points in (B) by cohort. Bonferroni-adjusted Wilcoxon signed rank test *P* values for differences relative to control A are shown (***$P < 0.001$).

that, rather than a simple loss of total IgG, there is a restructuring of the antibody repertoire after measles.

To measure the full effect of measles on the pre-measles repertoire and to circumvent interference from new exposures during follow-up, we next restricted analysis to epitopes detected at the first time point and quantified retention or loss of epitope recognition. After severe or mild measles, children lost a median of 40% (range: 11 to 62%) or 33% (range: 12 to 73%), respectively, of their total preexisting pathogen-specific antibody repertoires (Fig. 2A and fig. S3). In contrast, controls retained ~90% of their repertoires over similar or longer durations.

Controlling for interval duration in a binomial random effects model (see materials and methods), we estimated the per-pathogen probability of antibody retention for each child (Fig. 2, B and C). Loss of antibodies after MV infection varied widely for specific pathogens and between children. A small fraction of MV-infected individuals retained antibodies similar to the bottom quartile of the controls. However, the most-affected 20% of children lost >50% of the pathogen-specific antibodies for most pathogens. In some of these children, up to 70% loss was detected for specific pathogens.

Antibody repertoire retention (~90%) was similar in control cohorts A and B despite the longer sampling interval in B compared with A (1 year versus 3 months). The retained antibody repertoire could represent a core stable LLPC repertoire (~90%), and the 10% that was lost could represent a transient repertoire derived from IgG-secreting B cells and plasmablasts. This result is consistent with previous studies that showed no effect of immunosuppressive therapy, such as B cell–depleting anti-CD19 or anti-CD20 treatment, on retention of the majority of the antibody repertoire (*17*, *19*, *21*, *22*). Therefore, measles is associated with greater loss of antibody-mediated epitope recognition than can be explained by ablation of B cells, suggesting a direct effect on the LLPC compartment.

Measles decreases the strength of epitope recognition

Simply counting epitope numbers recognized before and after measles underestimates immune memory impairment because epitope recognition can be detected even when a large fraction of cellular clones producing the relevant antibody are eliminated. To quantify the relative abundance of particular antibodies, we generated an EBS metric, which is a *z*-score that measures the relative enrichment of an epitope in a VirScan immunoprecipitation (see materials and methods). Thus, EBS represents a VirScan analog of relative antibody titers and can be measured over time to detect changes in epitope recognition. Significant increases in EBS for a given epitope usually indicate a new exposure during the follow-up interval. In controls, significant reductions are normally detected when a recent exposure has occurred before the first time point, resulting in a peak around time 1 followed by an expected rapid decay of the antibody signal that is detected at time 2.

To evaluate changes in EBS for each pathogen species in each child, EBS signals were clustered by pathogen species and child (EBS_{PC}) and a paired *t* test (paired per epitope) was used to test for significant differences at time 2 versus time 1. False discovery rate (fdr)–adjusted *P* values, sample size, and effect size (calculated as the fold change of the geometric mean at time 2 versus time 1) are shown for each EBS_{PC} cluster (Fig. 3A and fig. S4).

Significant changes in EBS_{PC} were detected in children in each cohort. Among controls, these changes were distributed equally, below and above a fold change of 1, indicating recent pathogen exposures before time 1 or during the follow-up interval, respectively. Unlike the controls, after measles, the significant changes in pathogen-specific EBS_{PC} were both more frequent and nearly uniformly negative with median fold changes (0.58 and 0.62), indicating ~40% reductions in EBSs (Fig. 3A). The effect was stronger after severe versus mild MV infections ($P < 0.001$). We confirmed these results by comparing the fold changes in EBS_{PC} to quantitative ELISA assays for adenovirus, enterovirus, and respiratory syncytial virus (RSV) in a selection of children who had decreased or increased EBS, and found good correlation (correlation coefficient $r = 0.73$; $P < 0.001$) (fig. S5, A and B).

To further clarify cohort-level changes, we combined the epitopes from all individuals and evaluated changes on a per-pathogen-species basis across each cohort (fig. S6). Among MV-infected individuals, the median fold change in EBS measured across all species was a strongly negative effect (median fold change: 0.69 or −31%; $P < 0.0001$). In contrast, among controls, the antibody EBS

was significantly changed only for relatively few pathogen species, and these were roughly balanced between positive and negative effects.

Measles disrupts recognition of pathogen epitopes across the cohort

At the cellular level, MV would not be expected to preferentially infect particular antibody-secreting cells on the basis of their pathogen targets or the type of antibodies produced (i.e., neutralizing or not). We therefore tested for cohort-wide differences in EBSs on a per-epitope basis. Across approximately 1100 epitopes each from the control A and B cohorts, none significantly changed (Fig. 3, B and C, and fig. S7), indicating that antibody epitope recognition across a group of individuals is remarkably stable, even when changes are detected at the pathogen species level, as in fig. S6. In contrast, EBS was substantially reduced in 12% of the 855 epitopes evaluated after mild MV infections and in 39% of the 1079 epitopes evaluated after severe MV infections ($P < 0.0001$) (Fig. 3, B and C). Only one epitope in mild measles and three in severe measles showed a significant increase, <0.2% overall.

VirScan detects neutralizing antibodies when those antibodies target short contiguous epitopes encoded in the phage display. A well-characterized neutralizing short contiguous epitope is the 24-amino-acid target of the anti-RSV monoclonal antibody therapies palivizumab and motavizumab. Among 22 MV-infected children with antibodies against this neutralizing epitope and without evidence of new RSV exposure, we detected a fold change in EBS of 0.59 (SD ± 0.18; $P < 0.001$) (fig. S8), in line with the observations above and indicating that the effects of MV are the same for the neutralizing and non-neutralizing antibody repertoires.

The MMR vaccine does not impair the immune repertoire

A marked increase in the overall antibody repertoire diversity was noted in MMR-vaccinated controls (Fig. 1), indicating that a similar loss of antibodies does not appear to accompany receipt of MMR vaccines compared with MV infections. However, in infants and young children, such as the MMR-vaccinated cohort in this study, the antibody repertoire continues to add antibody diversity over time (fig. S9). This is particularly true during the second year of life, following depletion of maternal antibodies, when measles vaccines are first given. These overall increases in antibody diversity over time could be obscuring potential minor impairments from measles vaccine, especially given the relatively long sampling interval for the vaccinated controls. To determine whether viral responses before or after MMR vaccination might be impaired, we analyzed EBS for antibodies detected surrounding MMR vaccine. We found no overall change in EBS after MMR vaccination (fig. S10), which is consistent with observations that the MV vaccine strains are not associated with widespread infection of $CD150^+$ lymphocytes (*27*, *28*). Thus, this higher-resolution analysis failed to detect immune impairment at the epitope level. Combined with increased epitope diversity after MMR vaccination (Fig. 1A), this analysis supports decades of observations that MMR vaccines do not increase susceptibility to subsequent infections (*29*, *30*).

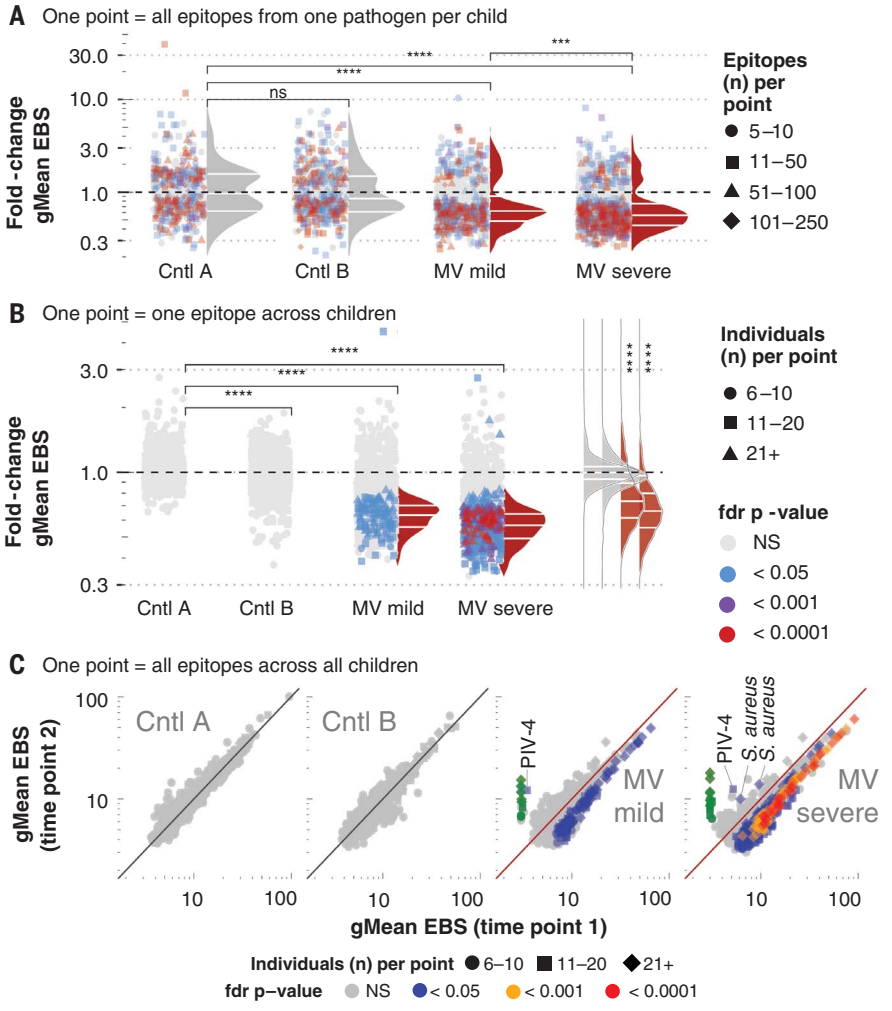


Fig. 3. Measles virus infections are associated with diminished epitope binding signal. Epitope binding signal (EBS) was measured for each epitope. (**A**) Each point represents one pathogen species per sample pair. Changes in EBS for all epitopes recognized per pathogen per sample pair were compared using a Wilcoxon matched-pairs signed rank test. Fdr-adjusted *P* values (adjusted for a fdr of 5%) are indicated by color of each symbol. The total number of epitopes included in each paired test (i.e., the number of epitopes recognized for each species per paired sample) are indicated by the symbol shape. For each pathogen, the geometric mean (gMean) EBS was calculated at each time and the fold change at time 2 versus time 1 was calculated and indicated by the position of each point along the *y* axis. Density distributions adjacent to the points reflect the distribution of points that were significantly changed on the basis of a fdr *P* value < 0.05. Only pathogens with antibodies targeting ≥5 epitopes were included. (**B**) Change in gMean EBS per epitope, across all paired samples per cohort. Format as in (A), except here each point represents a single epitope, and the gMean EBS is calculated across all paired samples with the epitope detected. The color of each point represents the fdr-adjusted Wilcoxon matched-pairs signed rank test *P* value, and shapes indicate the number of paired samples per cohort with antibodies against the particular epitope). Only epitopes recognized in >6 paired samples were included. (**C**) Scatter plot showing each epitope (point) shown in (B), but instead of plotting the fold change, the gMean EBS at time 1 (*x* axis) versus time 2 (*y* axis) is plotted. The *P* values (colors) and samples sizes (shapes) are indicated. MV-specific epitopes were included and highlighted in green. Epitopes significantly changed in a positive direction are labeled with pathogen species name. NS, not significant; PIV-4, parainfluenza virus-4.

Nevertheless, because of the naturally rapidly increasing antibody diversity in this young cohort at the time of MMR receipt, we cannot definitively rule out the potential for minor reductions of antibody-producing cells with measles vaccination.

Reconstruction of the antibody repertoire with high-transmission pathogens is spatially clustered

Although antibody diversity and abundance were negatively affected for almost all pathogens, a subset of children had increased EBS and/or epitope hits for particular pathogens after measles (Figs. 1, D and E, and 3A; and figs. S4, S8, and S11), suggestive of potential restoration of immune memory after the initial immune depletion.

Across all of the pathogen-child combinations with significantly increased EBS after measles, 80% were attributable to only six pathogens: adenovirus C, influenza A virus, respiratory syncytial virus, human herpesvirus 4 (Epstein-Barr virus; HHV-4), *Streptococcus pneumoniae* and *Staphylococcus aureus*. In these children, the probability of retaining preexisting antibodies for these pathogens was relatively high (fig. S12).

If reconstruction of the antibody repertoire requires new exposures, children experiencing repertoire reconstruction for transmissible pathogens should cluster spatially. Using postal codes and household identifiers, we observed clustering of pathogen-specific repertoire reconstruction at both the postal code or school level and the household level (Fig. 4). Among 19 children with increased adenovirus C antibody EBS, eight (42%) came from a single postal code (number 7) that included only 12 (16%) of the 77 measles cases (Fig. 4A). Thus, children in this postal code had significantly increased odds [odds ratio (OR) 9.4; Fisher's exact test, $P < 0.001$] of recovering their adenovirus C repertoire versus other postal codes, suggesting recovery is associated with pathogen transmission. Moreover, six of these children (75%) shared a household with another child with increased adenovirus C EBS. We found similar clustering effects for other respiratory pathogens: influenza A virus [of eight children with increased influenza A EBS, five (63%) were from a single postal code representing only 26% of the measles cases (OR 5.8; $P < 0.05$) and two were from the same household; Fig. 4B]; RSV [of nine with increased EBS, five (56%) were from the same postal code (OR 4.5; $P < 0.05$) and four of them (44%) shared a house; Fig. 4C]; rhinovirus [of 12 with increased EBS, eight (67%) shared a household with at least one other child with increased rhinovirus EBS]; and *S. pneumoniae* [of 13, seven (54%) came from a single postal code (OR 4.5; $P < 0.05$) and two shared a household]. Combined, these indicate local pathogen transmission and suggest that reconstruction of the antibody repertoire occurs on a per-pathogen basis and is associated with new exposures.

In contrast to the highly transmissible respiratory pathogens above, where mean EBS was increased after measles infection, we found that for chronic viruses [i.e., HHV-4 and human herpesvirus 5 (cytomegalovirus; HHV-5)], there was no evidence of spatial clustering. Further, only 6 out of 12 individuals (50%) with increased HHV-4 antibody EBS also developed antibodies against new HHV-4 epitopes. HHV-5 behaved similarly, with only 33% of individuals with increased HHV-5 antibody EBS also developing new antibodies to previously untargeted HHV-5 epitopes. The lack of development of antibodies targeting new epitopes, despite increases in EBS of existing antibodies for these two pathogens, is different from what we observed for the more-transmissible viruses noted above, in which 90% of pathogen-specific increases in EBS at time 2 were associated with development of new antibodies against previously unrecognized pathogen-specific epitopes. An increase in EBS without addition of new epitope recognition points toward reinfection with or reactivation of the same virus.

Two additional notable pathogens for which positive changes in EBS were often detected after measles were the bacteria *S. pneumoniae*

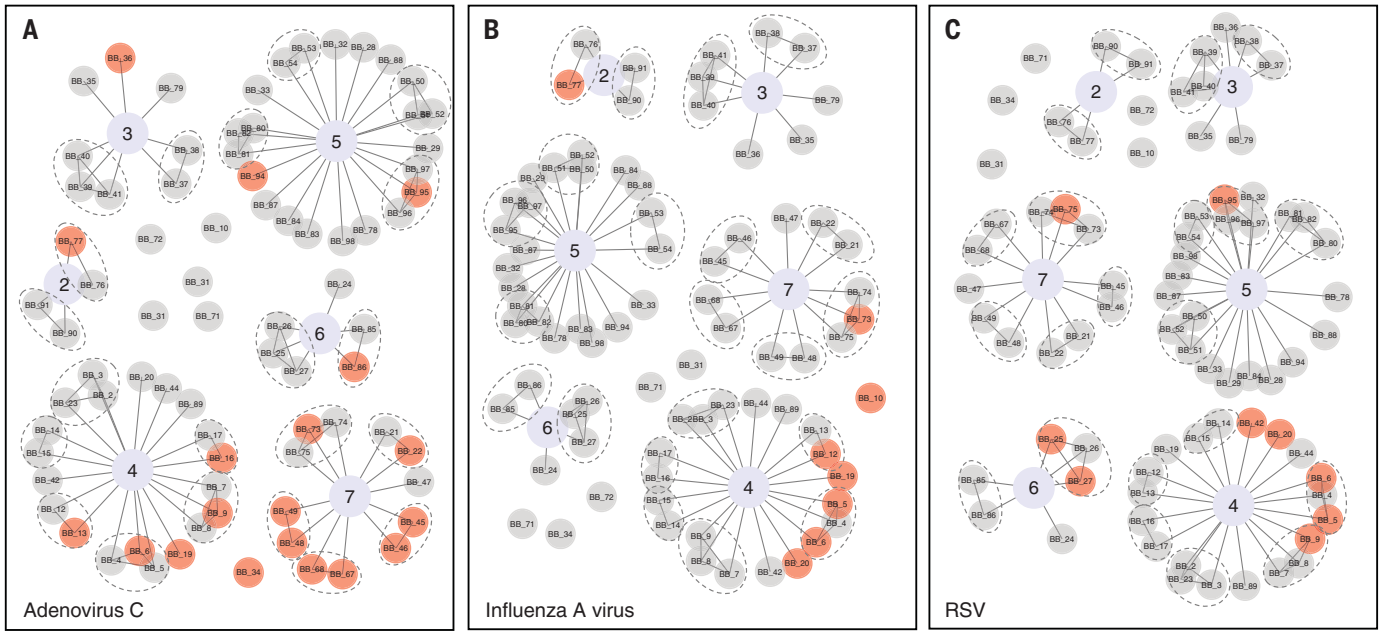


Fig. 4. Increases in antibody epitope binding signal cluster within households and in postal units. We tested whether individuals with increased EBS indicate new exposures due to pathogen transmission by looking for evidence of spatial clustering among children with increases in EBS. In (**A** to **C**), each child (node) is connected by an edge to their postal code (indicated by a central node with an assigned value, 2 through 7). Children shown as single nodes were the only children studied from their postal code. Children from the same household are connected by an edge and encircled by dashed gray ovals. Each of the three viruses where increases in EBS were most common are shown: (A) adenovirus C, (B) influenza A virus, and (C) respiratory syncytial virus. Children with significantly increased EBS for the pathogen (indicating exposure during the interval) are highlighted with red circles and those with decreased or unchanged EBS with gray circles.

and *S. aureus*. Acute viral respiratory infections, including measles, increase susceptibility to respiratory bacterial infections (*6*, *31*–*33*). After measles, new acquisitions of bacteria or increased replication of already colonizing bacteria could elicit antibody responses and reinstate antibody diversity and protection against these pathogens. In line with this, we observed net increases in antibody diversity, including development of antibodies against new epitopes, and increases in EBS for *S. aureus* [the only pathogen for which a net positive change in antibody diversity or EBS was detected after measles; 45 of 77 children (58%) had increased EBS] (Fig. 1 and fig. S11). Increases were also observed for *S. pneumoniae*, although the overall cohort-level effect remained negative.

Reconstruction of the antibody repertoire through reexposure after measles carries risks

Despite the potential benefits of reinstating the antibody repertoire, exposure to pathogens after measles—especially when in the presence of diminished preexisting immune memory—can carry risks. Ten of 43 children (23%) with severe measles were diagnosed with acute otitis media (AOM; most commonly pneumococcal), which was associated with a threefold increase in odds of carrying greater pneumococcal antibody diversity after measles compared with children without an AOM diagnosis. In addition, two children with mild measles and AOM and one with a diagnosis of bacterial pneumonia had increased pneumococcal antibody diversity at follow-up. Combined, these effects suggest that the antibody repertoire begins rebuilding soon after measles, through pathogen exposures, and that pathogen exposure after measles, while serving to reinstate immune memory, may pose excess risk.

Experimental MV infection confirms a decrease in previously acquired immune memory

To confirm the findings above using a controlled experimental setting with longer follow-up, we used VirScan to profile the antibody repertoire in plasma collected before and 5 months after experimental MV infection of four rhesus macaques (*34*). The overall diversity of the antibody repertoire was decreased an average of 26% (range: 21 to 35%), and reductions were distributed across pathogens (Fig. 5A). Notable exceptions were observed for simian foamy virus and Epstein-Barr virus, both of which can reactivate during immune dysregulation and thus may be early contributors to repertoire reconstruction. As expected, we detected increases in recognition of MV epitopes (Fig. 5B). Out of 21 MV epitopes recognized after measles, only one (phosphoprotein/V protein 29) was recognized before infection and was reduced by 40%. This likely represented a cross-reactive epitope that was diminished along with the rest of the repertoire.

Each monkey lost, on average, 40 to 60% of its preexisting antibody repertoire (Fig. 5C), and this loss persisted for at least 5 months after MV infection. In each monkey, the fractions lost were distributed across the pathogens, which is expected for a virus that indiscriminately infects antibody-secreting cells.

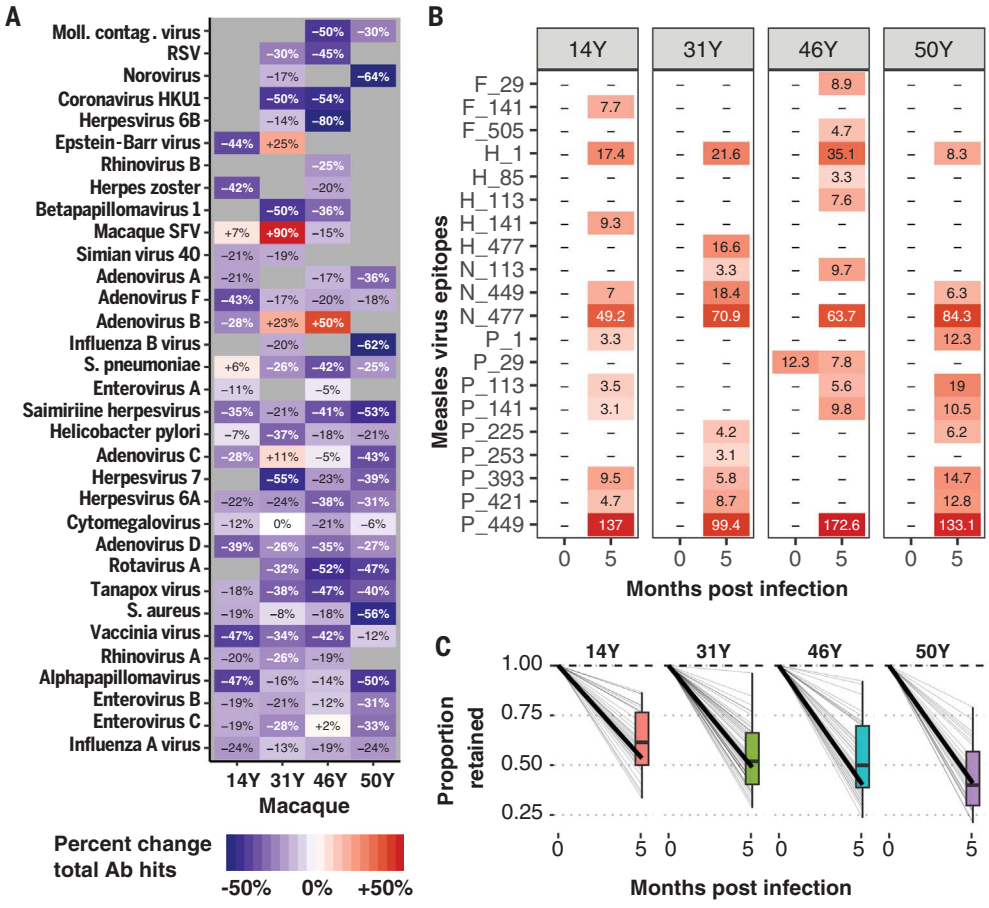


Fig. 5. Measles virus infection in macaques deletes preexisting immune memory. Four rhesus macaques (14Y, 31Y, 46Y, and 50Y) were infected with the Bilthoven strain of wild-type MV [detailed in (*34*)], and plasma samples were collected before and 5.1 months after infection. (**A**) Heatmap showing the percentage change in total epitopes recognized per pathogen in each monkey from time 1 to time 2. Pathogens with >10 unique epitopes recognized at either time point per macaque are shown. The color and text indicate percent change in total epitopes recognized per pathogen species before versus after infection. (**B**) Heatmap showing the signal strength of anti-measles antibodies (EBS) for each epitope for which at least one monkey developed an antibody. Colors and text of each cell represent the respective EBS values.Letters indicate the MV protein (F, fusion protein; H, hemagglutinin; N, nucleoprotein; and P, phosphoprotein), and the numbers indicate the position along the protein of the first amino acid of the 56-amino-acid peptide. (**C**) The fractions of epitopes recognized before MV infection that remained 5 months after are shown (0 months after infection is baseline and thus set to 1 for all pathogens). Each gray line indicates a different pathogen, and the dark black line indicates the average across the pathogens. The boxplot summarizes the interquartile range and median fraction retained across the pathogens.

Cumulative evidence supports the establishment of an immune amnesia state after measles

Using VirScan, we quantified the effects of measles on antipathogen antibody repertoires in plasma obtained before and after natural and experimental MV infections. We found that measles is associated with large reductions in both the diversity of the antibody repertoire and magnitude of the binding signal, likely reflecting reduced antibody titers resulting from diminished numbers of cells producing the respective antibody. The reduction of diversity may be greater than we report because even if particular antibody-producing cells have been eliminated, an antibody half-life of ~3 weeks (*35*) means that residual antibodies were still detectable at the time of sampling. Our findings show that after recovery from MV infections, individuals enter a state in which immune functionality is restored, but memory cell elimination induced by measles may alter previously acquired memory.

MV can infect 20 to 70% of memory cells, including B cells, T cells, and plasma cells in the lymphoid tissue and peripheral blood during the first 3 to 10 days after infection (*7*, *10*, *24*). Clinical trials of systemic administration of engineered MV for oncolytic therapy of multiple myeloma also demonstrated efficient entry of MV into the bone marrow and plasma cell infection (*36*). In wild-type MV infections, lymphocytes undergo rapid proliferation during immune activation (*37*), and lymphocyte counts (and other immunological markers) return to normal levels within weeks of infection. Thus, the immunological toll of measles is often considered limited to that period. After experimental MV infection in monkeys, we found that we could no longer detect up to 60% of the antibody repertoire, and this persisted for at least 5 months. This loss could be permanent, owing to elimination of B cells as well as LLPCs (*11*), although we cannot rule out possible involvement of additional unknown pleiotropic effects that may also cause antibody-secreting cells to down-regulate antibody production. Furthermore, because T cells also express SLAM and are infected by MV, T cell immunity may be diminished through similar mechanisms, and this could explain the loss of cutaneous tuberculin reactions after measles (*5*). Lasting remissions of autoimmune-related disorders after measles have been detected by researchers since the 1940s (*38*), supporting the potential persistence of immune suppression and pointing to persistent long-term effects. Because LLPCs are terminally differentiated and do not replicate (*39*), the rebuilding of immune memory after measles-induced LLPC elimination would likely require reexposures, either through natural infection or vaccination; thus it could potentially take months or years to return the immune repertoire back to baseline for all relevant pathogens. During the rebuilding process, individuals would potentially be at increased risk for other infectious diseases. Revaccination with routine childhood vaccines after measles could help to mitigate long-term suffering that might stem from immune amnesia and subsequent increased susceptibility to other infections.

We previously reported evidence that measles epidemics link to population mortality 2 to 3 years later (*15*, *40*). We hypothesized that the observed dynamics could potentially be explained by an immunomodulatory effect of measles, similar to what we show here. We found no such debilitative effects for the live MMR vaccine (*15*). Furthermore, because, in the prevaccine era, MV infected nearly all children within the first decade of life, the vaccine may have contributed to considerably greater benefits by preventing measles and immune amnesia. By preserving immunity, measles vaccines may have reset overall baseline morbidity and mortality rates to lower levels (*15*).

Given the variation in the degree of immune repertoire modulation we observed, we anticipate that future risk of morbidity and mortality after measles would not be homogeneous but would be skewed toward individuals with the most severe elimination of immunological memory. These findings underscore the crucial need for continued widespread vaccination. More than 7 million people are estimated to have been infected with measles in 2018 (*1*–*3*). Comprehensive coverage with MV vaccine would not only help prevent the >120,000 deaths that will be directly attributed to measles this year, but, by preventing MV immune amnesia and thus preserving immunity, MV vaccines could also avert potentially hundreds of thousands of additional deaths attributable to the lasting damage to the immune system. The WHO recently reported that between 2000 and 2017, MV vaccines have prevented more than 21 million deaths directly attributable to measles (*41*). These findings suggest that the number of deaths averted might be much greater, and they attest to the immense public health value of the measles vaccine.

REFERENCES AND NOTES

1. A. Dabbagh *et al.*, *MMWR Morb. Mortal. Wkly. Rep.* **67**, 1323–1329 (2018).
2. World Health Organization, New measles surveillance data for 2019 (2019); www.who.int/immunization/newsroom/measles-data-2019/en/.
3. A. Portnoy *et al.*, *Lancet Glob. Health* **7**, e472–e481 (2019).
4. H. S. Goodridge *et al.*, *Nat. Rev. Immunol.* **16**, 392–400 (2016).
5. C. Pirquet, *Dtsch. Med. Wochenschr.* **34**, 1297–1300 (1908).
6. D. E. Griffin, *Immunol. Rev.* **236**, 176–189 (2010).
7. R. L. de Swart *et al.*, *PLOS Pathog.* **3**, e178 (2007).
8. H. Tatsuo, N. Ono, K. Tanaka, Y. Yanagi, *Nature* **406**, 893–897 (2000).
9. B. Hahm, N. Arbour, M. B. Oldstone, *Virology* **323**, 292–302 (2004).
10. R. D. de Vries *et al.*, *PLOS Pathog.* **8**, e1002885 (2012).
11. J. De Salort, J. Sintes, L. Llinàs, J. Matesanz-Isabel, P. Engel, *Immunol. Lett.* **134**, 129–136 (2011).
12. B. M. Laksono *et al.*, *J. Virol.* **92**, e00131-18 (2018).
13. J. J. Ryon, W. J. Moss, M. Monze, D. E. Griffin, *Clin. Diagn. Lab. Immunol.* **9**, 994–1003 (2002).
14. V. G. Tamashiro, H. H. Perez, D. E. Griffin, *Pediatr. Infect. Dis. J.* **6**, 451–453 (1987).
15. M. J. Mina, C. J. E. Metcalf, R. L. de Swart, A. D. M. E. Osterhaus, B. T. Grenfell, *Science* **348**, 694–699 (2015).
16. R. D. de Vries, R. L. de Swart, *PLOS Pathog.* **10**, e1004482 (2014).
17. P. Isnard *et al.*, *Proc. Natl. Acad. Sci. U.S.A.* **116**, 10899–10904 (2019).
18. J. L. Halliley *et al.*, *Immunity* **43**, 132–145 (2015).
19. E. Hammarlund *et al.*, *Nat. Commun.* **8**, 1781 (2017).
20. I. J. Amanna, N. E. Carlson, M. K. Slifka, *N. Engl. J. Med.* **357**, 1903–1915 (2007).
21. M. D. Pescovitz *et al.*, *J. Allergy Clin. Immunol.* **128**, 1295–1302.e5 (2011).
22. J. Hill *et al.*, *Blood Adv.* 10.1182/bloodadvances.2019000717 (2019).
23. K. Gadroen *et al.*, *BMJ Open* **8**, e021465 (2018).
24. B. M. Laksono *et al.*, *Nat. Commun.* **9**, 4944 (2018).
25. G. J. Xu *et al.*, *Science* **348**, aaa0698 (2015).
26. H. B. Larman *et al.*, *Nat. Biotechnol.* **29**, 535–541 (2011).
27. R. S. van Binnendijk, R. W. van der Heijden, G. van Amerongen, F. G. UytdeHaag, A. D. Osterhaus, *J. Infect. Dis.* **170**, 443–448 (1994).
28. R. L. de Swart *et al.*, *NPJ Vaccines* **2**, 22 (2017).
29. M. M. Coughlin, A. S. Beck, B. Bankamp, P. A. Rota, *Viruses* **9**, 11 (2017).
30. W. J. Moss, D. E. Griffin, *Nat. Rev. Microbiol.* **4**, 900–908 (2006).
31. M. J. Mina, J. A. McCullers, K. P. Klugman, *mBio* **5**, e01040-13 (2014).
32. M. J. Mina, K. P. Klugman, *Lancet Respir. Med.* **2**, 750–763 (2014).
33. R. Cole, *J. Am. Med. Assoc.* **70**, 1147–1153 (1918).
34. A. N. Nelson *et al.*, *Sci. Rep.* **7**, 11474 (2017).
35. P. R. Hinton *et al.*, *J. Immunol.* **176**, 346–356 (2006).
36. A. Dispenzieri *et al.*, *Leukemia* **31**, 2791–2798 (2017).
37. D. E. Griffin, B. J. Ward, E. Jauregui, R. T. Johnson, A. Vaisberg, *N. Engl. J. Med.* **320**, 1667–1672 (1989).
38. R. W. Blumberg, H. A. Cassady, *Am. J. Dis. Child.* **73**, 151–166 (1947).
39. M. K. Slifka, R. Antia, J. K. Whitmire, R. Ahmed, *Immunity* **8**, 363–372 (1998).
40. M. J. Mina, B. T. Grenfell, C. J. E. Metcalf, *Science* **365**, eaax6498 (2019).
41. World Health Organization, Measles fact sheet (2019); www.who.int/news-room/fact-sheets/detail/measles.
42. M. J. Mina, S. J. Elledge, Measles Immune Amnesia: Data and Code for Mina *et al. Science* 2019, Dryad (2019); https://doi.org/10.5061/dryad.5tb2rbp0j.

ACKNOWLEDGMENTS

We express our gratitude to the participants, including children, parents, school staff, and other volunteers, who provided time and samples for this work. We also thank B. T. Grenfell and C. J. E. Metcalf for their early insights into this work and E. Shrock for assistance with assays. **Funding:** This work was supported by a grant from the Value of Vaccine Research Network to S.J.E. and M.J.M.; a grant from the Gates Foundation to S.J.E.; an NIH/NIAID U24 grant to H.B.L. and S.J.E.; a grant from the European Union Seventh Framework Program (grant 202063) and a grant from the Academy of Finland (Centre of Excellence in Molecular Systems Immunology and Physiology; grant 250114) to M.K.; NIH R01 DK032493 to M.R.; NIH R21 AI095981 and R01 AI131228 to D.E.G.; and a grant from PREPARE Europe (EU FP7 grant 602525) to R.L.d.S. S.J.E. is an Investigator with the Howard Hughes Medical Institute. **Author contributions:** Conceptualization: M.J.M., T.K., R.L.d.S., and S.J.E.; Investigation: M.J.M., T.K., Y.L., and M.L.; Reagents and samples: H.S., M.K., D.F.C., M.R., M.S.W., D.E.G., A.N.N., H.B.L., R.D.d.V., and R.L.d.S.; Writing: M.J.M., T.K., and S.J.E.; Supervision: S.J.E. **Competing interests:** M.S.W. and D.F.C. are employees of Genentech. S.J.E. is a founder of TSCAN Therapeutics, MAZE Therapeutics, and Mirimus. S.J.E. serves on the scientific advisory boards of CRISPR Therapeutics, Homology Medicines, TSCAN Therapeutics, and XChem and is

an adviser for MPM Capital, none of which affect this work. M.J.M. has served as a member of Sanofi advisory board for RSV therapeutics. D.E.G. is a member of the GlaxoSmithKline Vaccine Research and Development Advisory Board. S.J.E., T.K., and H.B.L. are inventors on a patent application filed by The Brigham and Women's Hospital (US20160320406A) that covers the use of the VirScan library to identify pathogen antibodies in blood. All other authors declare no competing interests. **Data and materials availability:** The VirScan library is available under a material transfer agreement. Data are available in the main text, the supplementary materials, or on Dryad (*42*).

SUPPLEMENTARY MATERIALS

science.sciencemag.org/content/366/6465/599/suppl/DC1
Materials and Methods
Figs. S1 to S12
Table S1
References (*43*–*45*)

View/request a protocol for this paper from *Bio-protocol*.

9 July 2019; accepted 30 September 2019
10.1126/science.aay6485

PLANT MICROBIOTA

Pathogen-induced activation of disease-suppressive functions in the endophytic root microbiome

Víctor J. Carrión[1,2], Juan Perez-Jaramillo[1,3]*, Viviane Cordovez[1,2]*, Vittorio Tracanna[4]*, Mattias de Hollander[1], Daniel Ruiz-Buck[1], Lucas W. Mendes[5], Wilfred F.J. van Ijcken[6], Ruth Gomez-Exposito[1,7], Somayah S. Elsayed[2], Prarthana Mohanraju[7], Adini Arifah[7], John van der Oost[7], Joseph N. Paulson[8], Rodrigo Mendes[9], Gilles P. van Wezel[1,2], Marnix H. Medema[4]†, Jos M. Raaijmakers[1,2]†

Microorganisms living inside plants can promote plant growth and health, but their genomic and functional diversity remain largely elusive. Here, metagenomics and network inference show that fungal infection of plant roots enriched for Chitinophagaceae and Flavobacteriaceae in the root endosphere and for chitinase genes and various unknown biosynthetic gene clusters encoding the production of nonribosomal peptide synthetases (NRPSs) and polyketide synthases (PKSs). After strain-level genome reconstruction, a consortium of *Chitinophaga* and *Flavobacterium* was designed that consistently suppressed fungal root disease. Site-directed mutagenesis then revealed that a previously unidentified NRPS-PKS gene cluster from *Flavobacterium* was essential for disease suppression by the endophytic consortium. Our results highlight that endophytic root microbiomes harbor a wealth of as yet unknown functional traits that, in concert, can protect the plant inside out.

Past and present plant microbiome studies have generated a large amount of sequence data and a wealth of (mostly) descriptive information on the diversity and relative abundance of different taxonomic groups in the rhizosphere, phyllosphere, spermosphere, and endosphere of a multitude of plant species (*1*, *2*). To date, however, relatively few studies have demonstrated the functional importance of microbiomes for specific plant phenotypes, that is, plant growth, development, and health (*3*–*9*). Furthermore, the molecular and chemical basis of the causal relationships between these plant phenotypes and microbiome structure and functions are, in most cases, still unknown. The aim of this study was to investigate the genomic diversity and functional potential of the endophytic root microbiome in the protection of plants against fungal infections. To this end, we integrated multiple approaches, including network inference and metagenomics, to identify root endophytic bacterial consortia and functional gene clusters associated with a soil that is suppressive to disease caused by *Rhizoctonia solani*, a fungal root pathogen of several plant species, including rice, wheat, and sugar beet.

Disease-suppressive soils are exceptional ecosystems in which plants are protected from root pathogens as a result of antagonistic activities of the root-associated microbiome. Suppressive soils have been described for various soil-borne pathogens, including fungi, bacteria, oomycetes, and nematodes (*3*, *5*, *10*–*15*). Disease suppression can be eliminated by selective heat treatment and can be transplanted to nonsuppressive (conducive) soils, analogous to fecal transplants in humans (*5*, *16*). Specific suppression of soils to fungal root pathogens, such as *R. solani*, is induced in field soils by a disease outbreak during continuous cultivation of a susceptible host plant (*17*). Once established, the suppression can dissipate if nonhost plants are grown but is regained in the presence of the host plant and the specific fungal pathogen. Therefore, the three-way interactions between the fungal pathogen, the host plant, and its root microbiome are key elements of the onset and persistence of specific disease suppression. We previously showed that in a soil suppressive to the fungal root pathogen *R. solani*, several bacterial genera inhabiting the rhizosphere of sugar beet, in particular *Paraburkholderia*, *Pseudomonas*, and *Streptomyces* (*5*, *18*, *19*), act as a first line of defense. To understand what role microorganisms that live within plant root tissues (endophytes) play in disease suppression, we conducted a metagenomic analysis of the endosphere of sugar beet seedlings grown in field soil suppressive to *R. solani* and identified the microorganisms associated with disease suppression, distinguished which biosynthetic gene clusters (BGCs) were up-regulated during infection, reconstructed synthetic endosphere consortia, and finally made site-directed mutations to test the role of specific BGCs in disease suppression.

Taxonomic diversity and network inference of the endophytic microbiome

Sugar beet plants were grown in disease-conducive (C) and disease-suppressive (S) soils inoculated (or not) with the root pathogen *R. solani* (fig. S1). Disease incidence in the pathogen-inoculated suppressive soil (S+R) was 15 to 30%, whereas disease incidence in the pathogen-inoculated conducive soil (C+R) exceeded 80% (fig. S1A), typical of our previous studies (*5*, *16*). Given the high disease incidence in C+R, there was not enough root material left for in-depth microbiome analysis of this condition. The taxonomic diversity and functional potential of the root endophytic microbiome of plants grown in the remaining three soil conditions (C, S, and S+R) was investigated after 4 weeks of plant growth. After metagenome sequencing and bioinformatic analyses (fig. S2 and tables S1 and S2), taxonomic assignment of the microbial cell fraction from the sugar beet endosphere showed that 76.1, 10.5, and 0.0065% of the sequence reads corresponded to the domains Bacteria, Eukarya, and Archaea, respectively (fig. S3, A and B). For the eukaryotic reads, constrained analysis of principal coordinates showed significant differences [permutational multivariate analysis of variance (PERMANOVA), $P < 0.05$] between the endophytic fungal community composition in C, S, and S+R (fig. S4A). This was largely due to a statistically significant increase in *Rhizoctonia*-related sequence reads in the suppressive soil inoculated with *R. solani* (S+R) (fig. S4, B and C). Most of the other sequence reads could not be reliably assigned to specific fungal taxa. Collectively, these results indicate that after inoculation into the disease-suppressive soil, *R. solani* colonized and penetrated the plant roots but caused little disease.

16*S* ribosomal RNA (rRNA) data from the metagenome sequences (fig. S2) showed that Proteobacteria and Bacteroidetes dominated the endophytic bacterial community, with 10 operational taxonomic units spanning Pseudomonadaceae (two), Xanthomonadaceae (four), Chitinophagaceae (one), Flavobacteriaceae (two), and Veillonellaceae (one) (fig. S5), all of which became enriched in the S+R condition compared with the S condition (Fig. 1A). Co-occurrence network analysis revealed increased complexity in the S+R condition (fig. S6, A to C, and table S3) compared with C and S conditions (table S3). Highly connected

[1]Department of Microbial Ecology, Netherlands Institute of Ecology (NIOO-KNAW), Droevendaalsesteeg 10, 6708 PB Wageningen, Netherlands. [2]Institute of Biology, Leiden University, Sylviusweg 72, 2333 BE Leiden, Netherlands. [3]PECET, University of Antioquia, Medellín, Antioquia 050010, Colombia. [4]Bioinformatics Group, Wageningen University, Droevendaalsesteeg 1, 6708 PB Wageningen, Netherlands. [5]Cell and Molecular Biology Laboratory, Center for Nuclear Energy in Agriculture (CENA), University of Sao Paulo (USP), Piracicaba, Brazil. [6]Erasmus MC, University Medical Center Rotterdam, Department of Cell Biology, Center for Biomics, 3025 CN Rotterdam, Netherlands. [7]Laboratory of Microbiology, Wageningen University and Research, Stippeneng 4, 6708 WE Wageningen, Netherlands. [8]Department of Biostatistics, Product Development, Genentech Inc., South San Francisco, CA 94080, USA. [9]Laboratory of Environmental Microbiology, Brazilian Agricultural Research Corporation, Embrapa Environment, Rodovia SP 340, Km 127.5, 13820-000 Jaguariúna, Brazil.
*These authors contributed equally to this work.
†Corresponding author. Email: j.raaijmakers@nioo.knaw.nl (J.M.R.); marnix.medema@wur.nl (M.H.M.)

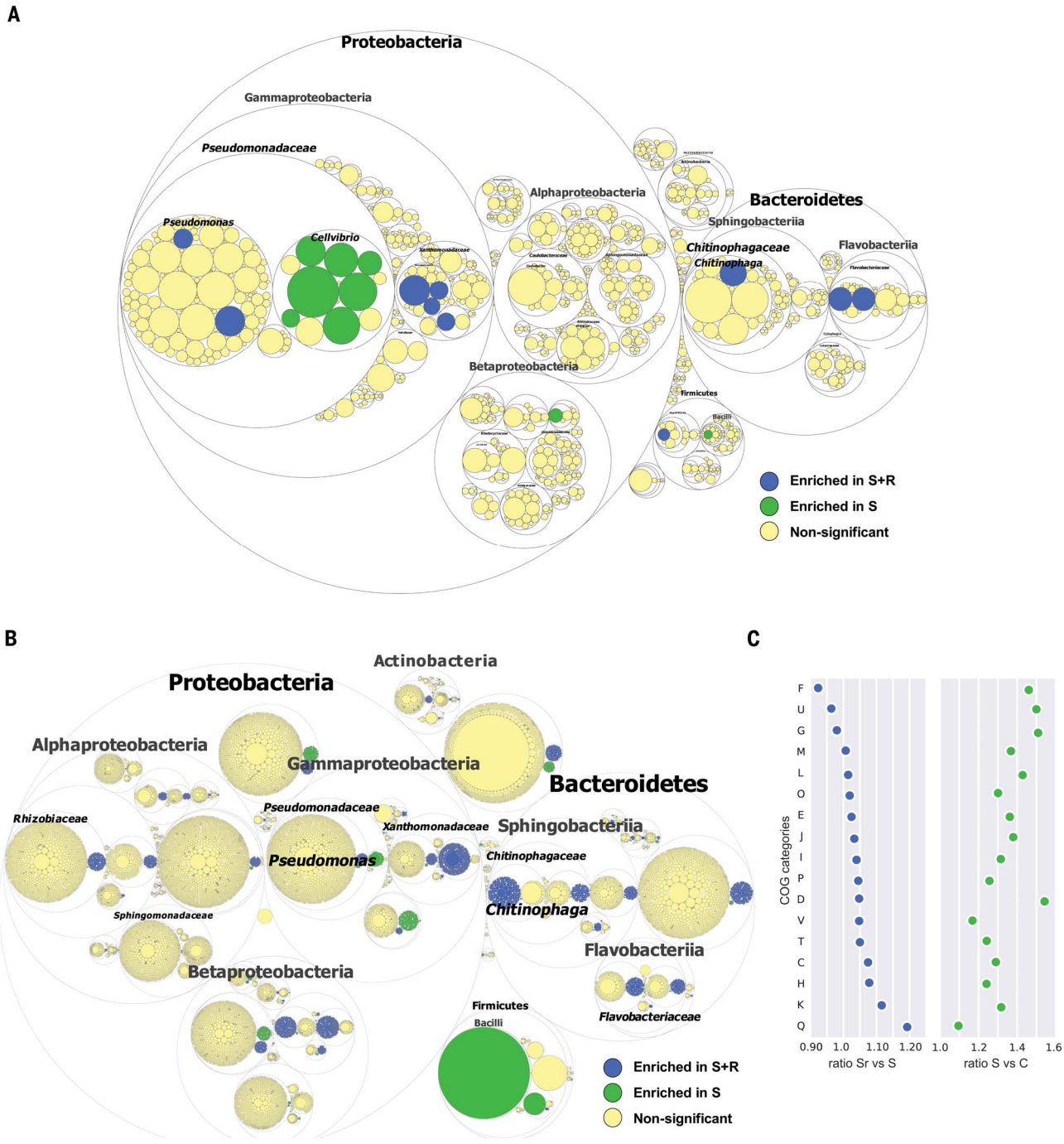


Fig. 1. Pathogen-induced changes in endophytic microbiome diversity and functions. Differential abundance of endophytic bacterial communities from plants grown in S or S+R soils. (**A**) Taxonomic differences are based on 16S rRNA sequences extracted from the metagenome. The largest circles represent phylum level, and the inner circles represent class, family, and genus. (**B**) Functional differences are based on the metagenome sequence data and assigned to taxonomic groups. The smallest circles represent the COG categories groups. The circle sizes represent the mean read relative abundance of the differentially abundant taxa and functions. Bacterial taxa or functions that are significantly enriched (FDR < 0.1) in the comparison between S and S+R are indicated in green for S and in blue for S+R; nonsignificant taxa and functions are indicated in yellow. (**C**) Strip plot depicting the average abundance ratios of all genes from Bacteroidetes belonging to core COG functional categories that contain significantly enriched genes in S+R (Sr) compared with S and in S compared with C. Categories are sorted from top to bottom by S+R/S ratio. Each COG type is abbreviated as follows: C, energy production and conversion; D, cell cycle control, cell division, and chromosome partitioning; E, amino acid transport and metabolism; F, nucleotide transport and metabolism; G, carbohydrate transport and metabolism; H, coenzyme transport and metabolism; I, lipid transport and metabolism; J, translation, ribosomal structure, and biogenesis; K, transcription; L, replication, recombination, and repair; M, cell wall, cell membrane, and cell envelope biogenesis; O, posttranslational modification, protein turnover, and chaperones; P, inorganic ion transport and metabolism; Q, secondary metabolites biosynthesis, transport, and catabolism; T, signal transduction mechanisms; U, intracellular trafficking, secretion, and vesicular transport; and V, defense mechanisms.

networks, like those in the S+R samples, can occur when microbiota face environmental perturbation, such as pathogen invasion (*20*). Interestingly, 80% of the interacting nodes in the S+R network belonged to *Chitinophaga*, *Flavobacterium*, and *Pseudomonas* species (table S4). When sequence reads from the Bacteroidetes were removed from the datasets, the endophytic signals from the C and S soils were indistinguishable (fig. S7, A and B), once again indicating an association of the Bacteroidetes genera *Chitinophaga* and *Flavobacterium* with the disease-suppressive phenotype.

Functional diversity of the endophytic microbiome

Of the genes retrieved from the metagenome data, 50 to 70% were assigned to a known function (fig. S3, C to E). For the other genes, grouping annotations indicated 56,175 taxa-associated functions, of which 402 functions were significantly enriched in the endophytic bacterial community of plants grown in the S soil compared with that of plants grown in the C soil [false discovery rate (FDR) < 0.1; fig. S8, B and C]. In the S+R condition, this proportion of functional enrichment increased more than 10-fold (4443) (FDR < 0.1; Fig. 1B). These genes belonged mainly to pathways classified as "carbohydrate transport and metabolism" and "signal transduction mechanisms." Several endophytic bacterial families—including Chitinophagaceae and Flavobacteriaceae (Bacteroidetes); Pseudomonadaceae and Xanthomonadaceae (Gammaproteobacteria); Hyphomicrobiaceae and Rhizobiaceae (Alphaproteobacteria); and Burkholderiaceae (Betaproteobacteria)—were specifically associated with the functional enrichment we observed (Fig. 1, B and C, and fig. S9A). The majority of the overrepresented genes in S+R (3138 genes of 4443) were associated with Chitinophagaceae and Flavobacteriaceae (Fig. 1B and fig. S9A). When we used a more stringent significance level of $P < 0.05$, 2063 of 56,175 taxa-associated functions were overrepresented, with 461 functions associated mainly with Chitinophagaceae and Flavobacteriaceae. Cumulative differential abundance analyses of all Bacteroidetes' genes between samples highlighted that genes from cluster of orthologous groups (COG) category Q (secondary metabolites biosynthesis, transport, and catabolism) were among the most differentially abundant between S+R and S, whereas genes from category G (carbohydrate transport and metabolism) were among the most differentially abundant between S and C (Fig. 1C).

For more detailed resolution of the specific functions associated with COGs G and Q, we searched for carbohydrate-active enzymes (CAZymes) and secondary metabolite biosynthetic gene clusters within the metagenome sequences using dbCAN (*21*, *22*) and antiSMASH (*23*), respectively. Using dbCAN, we were able to annotate 1822 genes in the endophytic metagenome with glycoside hydrolase, glycosyltransferase, polysaccharide lyase, and carbohydrate esterase domains, as well as noncatalytic carbohydrate-binding modules. Because many of these domains are evolutionary related and have related functionalities, we mapped the domain diversity in a protein family similarity network constructed using the hhsearch algorithm (*24*). Glycoside hydrolases and glycosyltransferases were more abundant in the S+R endophytic microbiome

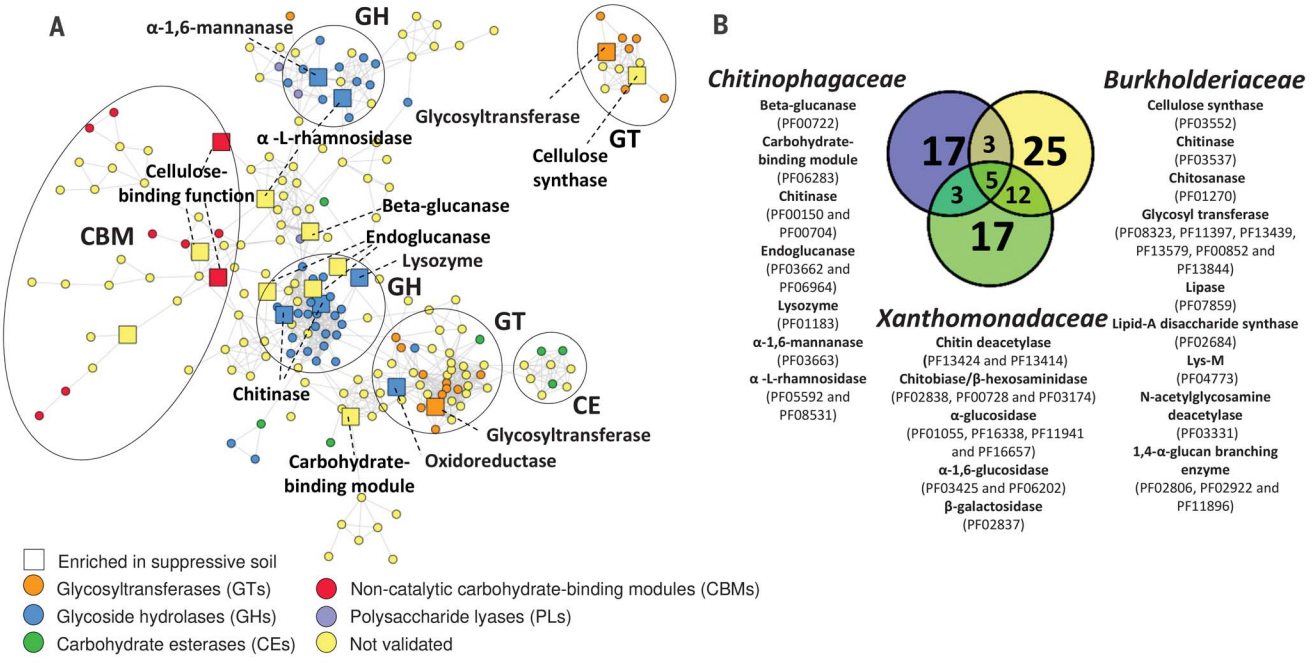


Fig. 2. Diversity and distribution of carbohydrate-active enzymes in the endophytic microbiome. (**A**) Similarity network of known and putative protein domains of enzymes involved in carbohydrate metabolism (CAZymes). From the endophytic metagenome of plants grown in suppressive soil (S) or in suppressive soil inoculated with the fungal root pathogen *R. solani* (S+R), a total of 1822 genes were annotated as CAZymes. Domain-domain distances and their relatedness are shown in the network. Nodes were grouped into five functional classes: glycoside hydrolases (GH, blue), glycosyltransferases (GT, orange), polysaccharide lyases (PL, purple), carbohydrate esterases (CE, green), and the noncatalytic carbohydrate-binding modules (CBM, red). Unknown domains or domains for which the function has not been experimentally validated are shown in yellow. Squared nodes represent enzymes that are significantly overrepresented (FDR < 0.1) in S+R compared with S and taxonomically assigned to the Chitinophagaceae. Enzymes significantly overrepresented in S+R and taxonomically classified as Burkholderiaceae and Xanthomonadaceae are shown in fig. S9, B and C, respectively. (**B**) Venn diagram with different CAZymes annotated for three endophytic bacterial families enriched in S+R, that is, Burkholderiaceae (yellow), Chitinophagaceae (blue), and Xanthomonadaceae (green). For each of the CAZymes, the Pfam number is shown in parentheses. The Venn diagram shows the number of domains detected exclusively for each bacterial family and the domains shared by these endophytic bacterial families.

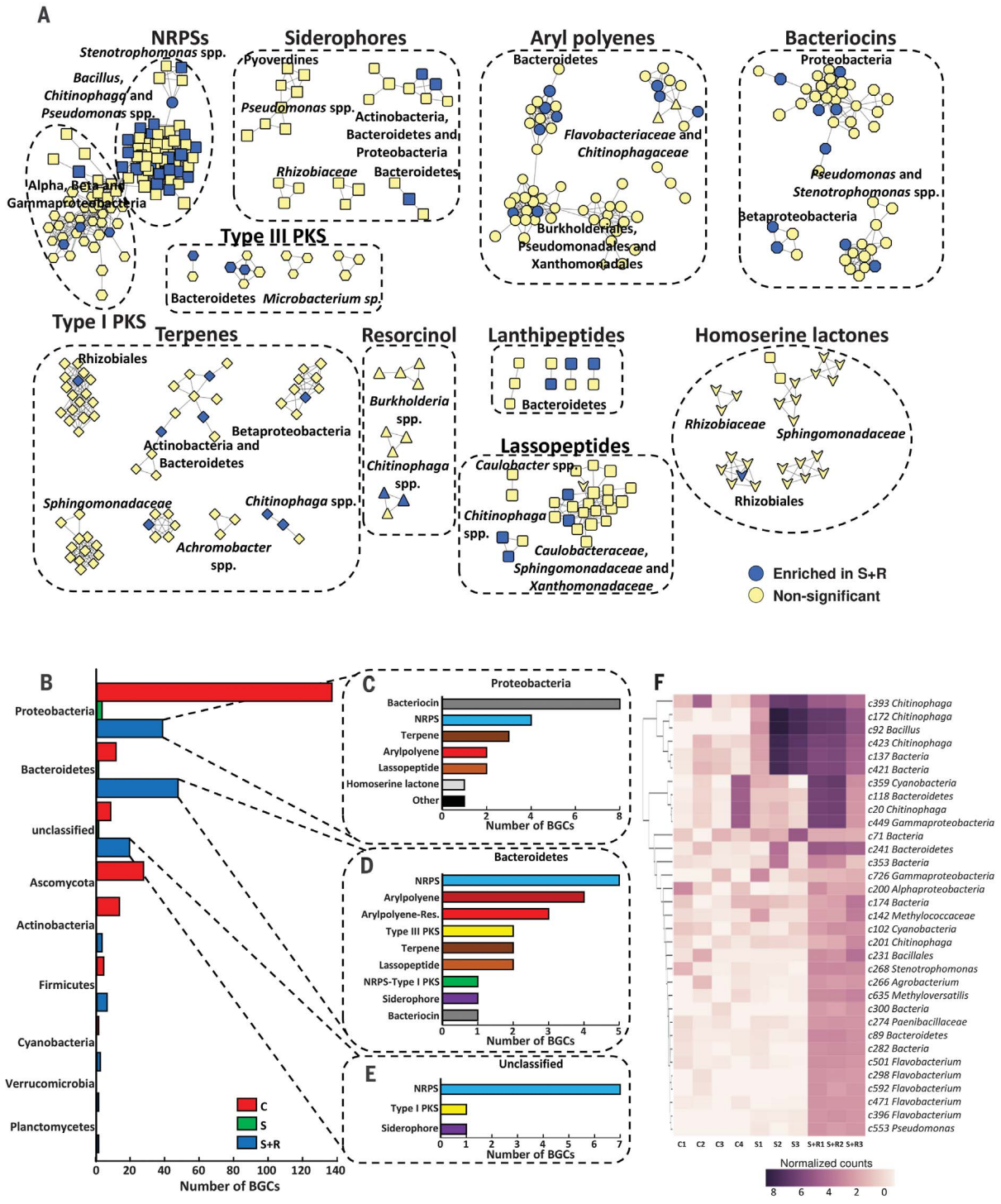


Fig. 3. Diversity and distribution of biosynthetic gene clusters in the endophytic microbiome. (**A**) Sequence similarity network [constructed with BiG-SCAPE (*32*), threshold: 0.8] of the different classes of BGCs detected in the endophytic microbiome. Taxonomic assignment and BGC class annotation of the nodes are shown. Nodes with fewer than three connections were removed; the original network with all nodes can be found in fig. S10. Node colors represent statistical significance based on a Welch's *t* test (FDR < 0.1): Yellow nodes are nonsignificant, and blue nodes are significantly overrepresented in the S+R condition. (**B**) Number of overrepresented BGCs (two-tailed Welch's *t* test, $P < 0.1$) detected by the antiSMASH and Clusterfinder algorithms for the different bacterial phyla in the endophytic root microbiome of plants grown in C, S, and S+R soils. (**C** to **E**) Number and type of BGCs assigned to Proteobacteria (C), Bacteroidetes (D), and unclassified (E) bacterial phyla that were significantly (two-tailed Welch's *t* test, $P < 0.1$) more enriched in S+R BGCs that could not be classified are not included in the (C) to (E) barplots. (**F**) Clustered heat map of relative abundances [cumulative sum scaling (CSS)–normalized RPKM (reads per kilobase per million reads) values] of the 33 NRPS gene clusters that were significantly overrepresented in the different replicate samples of S or S+R versus C. The NRPS cluster number and the corresponding taxonomic assignment are shown on the right side of the panel.

and correlated with disease suppression (Fig. 2A and fig. S9, B and C). Three endophyte families (Chitinophagaceae, Burkholderiaceae, and Xanthomonadaceae) showed statistically significant differences in CAZyme composition between S+R and S (FDR < 0.1; Fig. 2A and fig. S9, A and B). Furthermore, we found that Chitinophagaceae harbored several enzymes with domains associated with fungal cell-wall degradation, such as chitinases, β-glucanases, and endoglucanases (Fig. 2A), and also possessed debranching enzymes, including α-1,6-mannanase and α-L-rhamnosidase. Burkholderiaceae and Xanthomonadaceae families (fig. S9, B and C) also contributed two chitinase domains and three other enzymes involved in chitin degradation, including chitin deacetylase and chitosanase. Only five domains were shared between Chitinophagaceae, Burkholderiaceae, and Xanthomonadaceae (Fig. 2B), indicating limited functional redundancy among these endophytes for this trait. The enrichment of genes encoding chitin-degrading enzymes points to a role in disease suppression for these endophytes (*25*).

Bacterial genomes contain a large diversity of BGCs, the vast majority of which have not yet been linked to specific molecules or functions (*5*, *26*–*28*). Our antiSMASH analysis for secondary metabolites revealed a total of 730 BGCs associated with the biosynthesis of nonribosomal peptides, polyketides, terpenes, aryl polyenes, ribosomally synthesized and post-translationally modified peptides (RiPPs),

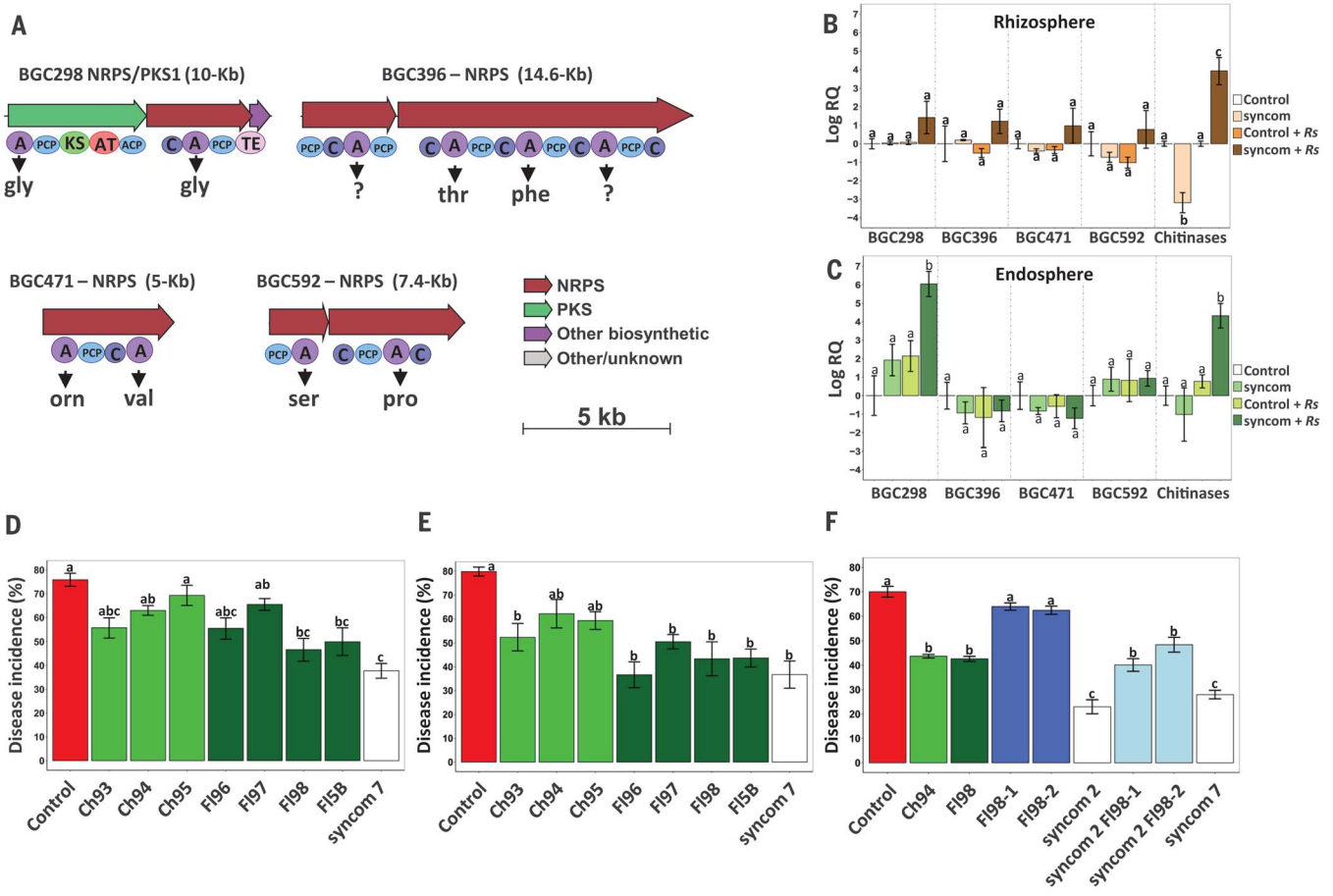


Fig. 4. Transcriptional and functional analyses of disease-suppressive consortia. (**A**) Genetic organization of BGC298, BGC396, BGC471, and BGC592 identified in both the *Flavobacterium* MAG nbed44b64 and in the genome sequences of the four endophytic *Flavobacterium* isolates. Shown below the NRPS and PKS genes are the module and domain organizations of the encoded proteins. The domains are labeled as follows: C, condensation; A, adenylation; KS, ketosynthase; AT, acyltransferase; PCP, peptide carrier protein; and TE, thioesterase. Predicted substrates of the NRPS and PKS modules in BGC298 are glycine, malonyl-CoA, and, again, glycine. (**B** and **C**) Quantitative polymerase chain reaction (qPCR)–based analysis of the expression of BGC298, BGC396, BGC471, BGC592, and chitinase genes (GH18) in the rhizosphere and endosphere of sugar beet seedlings treated with the synthetic endophytic consortium of *Chitinophaga* and *Flavobacterium* isolates (syncom). LogRQ represents the gene expression levels by relative quantification scores: Values below 0 indicate lower expression of the BGC relative to that of the housekeeping gene (*glyA*) used for data normalization. Bars represent the average of three to five biological replicates per treatment, and error bars indicate the standard error of the mean. Different letters indicate statistically significant differences between treatments as determined by one-way ANOVA with post hoc Tukey honestly significant different (HSD) test ($P < 0.05$). *Rs*, *R. solani*. (**D** to **F**) Results of three independent bioassays showing *Rhizoctonia* damping-off disease incidence of sugar beet seedlings treated with single *Chitinophaga* (Ch93, Ch94, and Ch95) and *Flavobacterium* (FI96, FI97, FI98, and FI5B) isolates and with a consortium of all seven endophytic isolates (synthetic community, syncom 7) [(D) and (E)] or treated with single *Chitinophaga* (Ch94) and *Flavobacterium* (FI98) isolates, two independent FI98 mutants (FI98-1 and FI98-2) with a deletion in BGC298, the consortium of Ch94 and FI98 (syncom 2), and syncom 7 (F). For (D) to (F), single isolates and the two syncoms were applied at an initial density of 10^7 colony forming units/g of *Rhizoctonia*-conducive field soil. Bars represent the average of four to eight biological replicates per treatment, and error bars represent the standard error of the mean. Disease incidence was scored 21 to 28 days after *R. solani* inoculation. Different letters indicate statistically significant differences between treatments as determined by one-way ANOVA with post hoc Tukey HSD test ($P < 0.05$). For (B) to (F), box plots with the individual data of each replicate are provided in figs. S20 and S21.

phosphonates, phenazines, and siderophores (Fig. 3A and figs. S10 to S12). Of these 730 BGCs, only 12 have previously been described and the chemical structure of their products elucidated (fig. S11 and table S5). Among these were the BGCs for thanamycin and brabantamide, which are two nonribosomal peptide synthetase (NRPS)–derived products previously detected in the rhizosphere microbiome of plants grown in *Rhizoctonia*-suppressive soil (*5*, *26*, *29*). For the other 718 BGCs, no near or exact matches were found for their genetic architecture and predicted products in the MIBiG repository (*27*). Of the BGCs detected, several proteobacterial RiPPs and NRPSs were noted (Fig. 3C), as well as NRPS and aryl polyene clusters originating from Bacteroidetes [mainly *Flavobacterium* and *Chitinophaga* (Fig. 3D)] and a larger proportion of NRPS clusters from contigs that could not be taxonomically assigned with confidence (Fig. 3E). Altogether, 117 BGCs were significantly overrepresented (two-tailed Welch's t test, $P < 0.1$) in the endosphere under the S+R conditions, with 34 BGCs belonging to Bacteroidetes (Fig. 3, A to F, and figs. S10 to S12). Notably, these did not include the thanamycin and brabantamide BGCs identified previously for the disease-suppressive *Pseudomonas* species from the rhizosphere (*5*, *29*). For the Bacteroidetes species, 10 NRPS gene clusters out of the 117 were overrepresented under S+R conditions, and none of these had a match in antiSMASH with gene clusters from MIBiG.

De novo assembly of endophytic bacterial genomes

From the 730 BGCs identified in the metagenome by antiSMASH, 157 were found in a set of 25 metagenome-assembled genomes (MAGs) that we reconstructed (figs. S13 and S14 and table S6). The MAGs, housekeeping genes, and identified BGCs were subsequently used to generate specific primer sets for transcriptome analyses and to associate the BGCs to isolates in the bacterial endophyte collection.

The initial collection of 935 bacterial endophyte isolates (fig. S1) was taxonomically characterized by 16*S* rRNA sequencing (fig. S15, A and B, and table S7), revealing eight different genera, mostly represented by Bacteroidetes and Gammaproteobacteria. Although no BGCs associated with *Chitinophaga* or *Pseudomonas* species (table S8) were detected by polymerase chain reaction (PCR) screening, four BGCs (BGC298, BGC396, BGC471, and BGC592) were found in the endophytic *Flavobacterium* isolates obtained from the S+R condition. Three of these encoded an NRPS (BGC396, BGC471, and BGC592) and the fourth a hybrid NRPS–polyketide synthase (PKS) gene cluster (BGC298, Fig. 4A). A similar approach confirmed the presence of glycosyl hydrolase (GH18) genes in three endophytic *Chitinophaga* isolates obtained from the S+R condition (Fig. 2A). Subsequent in vitro assays with the bacterial isolate collection showed that the three *Chitinophaga* isolates also had extracellular chitinolytic activity.

Subsequent genome sequencing of the three *Chitinophaga* and four *Flavobacterium* isolates showed >99% similarity among the isolates within each genus (figs. S15C and S16A and table S9). The isolate genomes also clustered with MAGs assigned to each of these genera (fig. S15, B and C), confirming that they correspond to taxa abundant in the microbiome. For the key BGCs, no signs of metagenome misassemblies were identified on the basis of comparisons with the complete genome sequences of the Bacteroidetes isolates (figs. S16, B and C, and S17, A to C).

Reconstruction and functional analysis of disease-suppressive consortia

We selected the seven sequenced Bacteroidetes isolates for root colonization assays and BGC-transcript analysis. All isolates colonized the rhizosphere and the root endosphere of sugar beet seedlings (figs. S18 and S19). Transcriptional analysis showed that chitinase expression was significantly ($P < 0.05$) higher in the consortium colonizing the rhizosphere and endosphere compartments inoculated with the fungal pathogen (Fig. 4, B and C, and fig. S20). Of the four *Flavobacterium* gene clusters, BGC298 was expressed at significantly ($P < 0.05$) higher levels in the endosphere than in the rhizosphere when the plant roots were challenged with the fungal pathogen *R. solani* (Fig. 4C). This BGC was consistently assembled in all four *Flavobacterium* genomes and in a MAG (fig. S16B) and showed no match with known BGCs in MIBiG (fig. S17).

The central place of *Flavobacterium* and *Chitinophaga* in the functional network of plants grown in the disease suppressive soil, their ability to colonize the endosphere, and the fact that expression of BGC298 and chitinase genes in the synthetic consortium are induced by the fungal pathogen suggest a role in *R. solani*-disease suppression. To test this hypothesis, three independent bioassays showed that the consortium of *Chitinophaga* and *Flavobacterium* conferred significant and more consistent protection against fungal root infection than the individual consortium members (Fig. 4, D to F, and fig. S21, A to C). Even when single isolates showed little benefit against disease, consortia always showed a greater degree of protection (Fig. 4, D to F, and fig. S21, A to C). The apparent "minimal" consortium to reconstitute the plant phenotype consisted of one *Chitinophaga* isolate and one *Flavobacterium* isolate (syncom-2), because this consortium showed the same level of disease control observed for the seven-member consortium (syncom-7; Fig. 4F).

To confirm the role of the *Flavobacterium* BGC298 in the disease-suppressive activity, we developed a SpyCas9-mediated system for introduction of double-stranded DNA breaks in *Flavobacterium* sp. 98. We obtained two independent BGC298 mutants (fig. S22, A to D, and tables S10 to S12), for which the PKS gene deletion was verified by Sanger sequencing with specific primers (fig. S22D). The two mutants colonized the rhizosphere and endosphere to the same extent as wild-type *Flavobacterium* sp. 98 when introduced alone or with *Chitinophaga* sp. 94 (table S13). When the two independent BGC298 mutants were tested in the disease bioassay, the mutation reduced disease-suppressive activity of *Flavobacterium* sp. 98 alone and when paired with the *Chitinophaga* isolate (Fig. 4F).

Conclusions

In our previous studies on soils suppressive to fungal root diseases, we showed that rhizosphere bacteria act as first line of defense (*5*–*7*, *10*). If the pathogen breaks through this first line of defense, it will encounter the basal and induced defense mechanisms of the plant (*30*). Here, we show that in this second stage of pathogen invasion of the plant roots, the endophytic microbiome can provide an additional layer of protection. Our experiments showed that on pathogen invasion, members of the Chitinophagaceae and Flavobacteriaceae became enriched within the plant endosphere and showed enhanced enzymatic activities associated with fungal cell-wall degradation, as well as secondary metabolite biosynthesis encoded by NRPSs and PKSs. After de novo assembly of 25 bacterial genomes from metagenome sequences, we were able to reconstruct a synthetic community (syncom) of *Flavobacterium* and *Chitinophaga* that provided disease protection. Site-directed mutagenesis further confirmed the contribution of BGC298 in *Flavobacterium* to this phenotype. Where these two bacterial genera are localized inside the root tissue and how they interact at the molecular level in the endosphere is not yet known. Possibly, chitinase-generated chitooligosaccharides induce expression of the *Flavobacterium* BGC298. Whether BGC298 encodes a metabolite that exerts direct antifungal activity or acts as a regulator of other protective traits is not yet known. Another consideration is that the consortium may have indirect effects through induction of local or systemic resistance in the roots. The results of this study highlight the wealth of as yet unknown microbial genera and functional traits in the endophytic root microbiome. Adopting metagenome-guided analyses and network inference was successful in pinpointing taxa and functions for targeted design of microbial consortia to attain a specific microbiome-associated plant phenotype.

REFERENCES AND NOTES

1. J. A. Vorholt, C. Vogel, C. I. Carlström, D. B. Müller, *Cell Host Microbe* **22**, 142–155 (2017).
2. V. Cordovez, F. Dini-Andreote, V. J. Carrión, J. M. Raaijmakers, *Annu. Rev. Microbiol.* **73**, 69–88 (2019).
3. M.-J. Kwak *et al*., *Nat. Biotechnol.* **36**, 1117 (2018).
4. S. Hacquard *et al*., *Cell Host Microbe* **17**, 603–616 (2015).
5. R. Mendes *et al*., *Science* **332**, 1097–1100 (2011).
6. K. Panke-Buisse, A. C. Poole, J. K. Goodrich, R. E. Ley, J. Kao-Kniffin, *ISME J.* **9**, 980–989 (2015).
7. N. Vannier, M. Agler, S. Hacquard, *PLOS Pathog.* **15**, e1007740 (2019).
8. B. O. Oyserman, M. H. Medema, J. M. Raaijmakers, *Curr. Opin. Microbiol.* **43**, 46–54 (2018).
9. P. Durán *et al*., *Cell* **175**, 973–983.e14 (2018).
10. D. M. Weller, J. M. Raaijmakers, B. B. M. Gardener, L. S. Thomashow, *Annu. Rev. Phytopathol.* **40**, 309–348 (2002).
11. E. Chapelle, R. Mendes, P. A. H. M. Bakker, J. M. Raaijmakers, *ISME J.* **10**, 265–268 (2016).
12. R. L. Berendsen, C. M. J. Pieterse, P. A. H. M. Bakker, *Trends Plant Sci.* **17**, 478–486 (2012).
13. M. Mazzola, *J. Nematol.* **39**, 213–220 (2007).
14. R. Mendes, P. Garbeva, J. M. Raaijmakers, *FEMS Microbiol. Rev.* **37**, 634–663 (2013).
15. J.-Y. Cha *et al*., *ISME J.* **10**, 119–129 (2016).
16. M. van der Voort, M. Kempenaar, M. van Driel, J. M. Raaijmakers, R. Mendes, *Ecol. Lett.* **19**, 375–382 (2016).
17. J. M. Raaijmakers, M. Mazzola, *Science* **352**, 1392–1393 (2016).
18. V. J. Carrión *et al*., *ISME J.* **12**, 2307–2321 (2018).
19. V. Cordovez *et al*., *Front. Microbiol.* **6**, 1081 (2015).
20. K. Faust, J. Raes, *Nat. Rev. Microbiol.* **10**, 538–550 (2012).
21. Y. Yin *et al*., *Nucleic Acids Res.* **40**, W445–W451 (2012).
22. V. Lombard, H. Golaconda Ramulu, E. Drula, P. M. Coutinho, B. Henrissat, *Nucleic Acids Res.* **42**, D490–D495 (2014).
23. T. Weber *et al*., *Nucleic Acids Res.* **43**, W237–W243 (2015).
24. M. Remmert, A. Biegert, A. Hauser, J. Söding, *Nat. Methods* **9**, 173–175 (2011).
25. S. M. Bowman, S. J. Free, *BioEssays* **28**, 799–808 (2006).
26. J. Watrous *et al*., *Proc. Natl. Acad. Sci. U.S.A.* **109**, E1743–E1752 (2012).
27. M. H. Medema *et al*., *Nat. Chem. Biol.* **11**, 625–631 (2015).
28. P. Cimermancic *et al*., *Cell* **158**, 412–421 (2014).
29. Y. Schmidt *et al*., *ChemBioChem* **15**, 259–266 (2014).
30. J. D. G. Jones, J. L. Dangl, *Nature* **444**, 323–329 (2006).
31. V. J. Carrión, M. de Hollander, V. Tracanna, Pathogen-induced activation of disease suppressive functions in the endophytic root microbiome. Zenodo (2019); http://doi.org/10.5281/zenodo.3405564.
32. J. Navarro-Muñoz *et al*., A computational framework for systematic exploration of biosynthetic diversity from large-scale genomic data. bioRxiv 445270 [Preprint] (17 October 2018); https://doi.org/10.1101/445270.

ACKNOWLEDGMENTS

We thank I. de Bruijn, S. P. Vega-Hernández, V. de Jager, and R. Keijzer for their valuable advice on genomic and metagenomic DNA extractions. We would also like to thank the BSc and MSc students C. Rotoni, R. Hijkoop, H. McDermott, A. Nurfikari, J. Spooren, and R. Peters for their valuable help with the *Flavobacterium* and *Chitinophaga* isolation and phenotyping. We thank M. J. McBride at the University of Wisconsin for providing the plasmids for *Flavobacterium* transformation. This is publication number 6824 of the NIOO-KNAW. **Funding:** J.M.R. and V.J.C. were supported by grants from the Netherlands BE-Basic Foundation and the Dutch TTW-Perspective program Back to the Roots. V.J.C. was also supported by a fellowship from the Junta de Andalucía (Proyecto de Excelencia, P07-AGR-02471) and Plan Propio of the University of Málaga. V.C. and S.S.E. were supported by the Dutch STW-program Back to the Roots. J.P.-J. was financially supported by the Department of Science, Technology, and Innovation of Colombia–COLCIENCIAS through doctoral grant 568-2012-15517825. **Author contributions:** V.J.C., V.C., D.R.-B., S.S.E., and J.P.-J. designed and conducted the experiments. R.G.-E. contributed to the soil sample collection. V.J.C. and W.F.J.v.I. generated the metagenome data. P.M., A.A., and J.v.d.O. made the *Flavobacterium* mutants. Data were analyzed by V.J.C., J.P.-J., V.T., L.W.M., M.H.M., J.N.P., and M.d.H. Funding acquisition and project management was provided by J.M.R. The manuscript was written by V.J.C., R.M., G.P.v.W., M.H.M., and J.M.R. All authors read and approved the final manuscript. **Competing interests:** M.H.M. is a member of the Scientific Advisory Board of Hexagon Bio and co-founder of Design Pharmaceuticals. All other authors declare that they have no competing interests. **Data and materials availability:** All data needed to evaluate the conclusions in the paper are present in the paper and/or the supplementary materials. The sequencing data are available under European Bioinformatics Institute (EBI) submission number PRJEB8920. Data, scripts, and code used for statistical and bioinformatic analyses are available at (*31*).

SUPPLEMENTARY MATERIALS

science.sciencemag.org/content/366/6465/606/suppl/DC1
Materials and Methods
Figs. S1 to S22
Tables S1 to S14
References (*33*–*95*)

View/request a protocol for this paper from *Bio-protocol*.

7 February 2019; resubmitted 21 July 2019
Accepted 17 September 2019
10.1126/science.aaw9285

ISOTOPIC SEPARATION

Barely porous organic cages for hydrogen isotope separation

Ming Liu[1], Linda Zhang[2], Marc A. Little[1], Venkat Kapil[3], Michele Ceriotti[3], Siyuan Yang[4], Lifeng Ding[4], Daniel L. Holden[1], Rafael Balderas-Xicohténcatl[2], Donglin He[1], Rob Clowes[1], Samantha Y. Chong[1], Gisela Schütz[2], Linjiang Chen[1,5], Michael Hirscher[2]*, Andrew I. Cooper[1,5]*

The separation of hydrogen isotopes for applications such as nuclear fusion is a major challenge. Current technologies are energy intensive and inefficient. Nanoporous materials have the potential to separate hydrogen isotopes by kinetic quantum sieving, but high separation selectivity tends to correlate with low adsorption capacity, which can prohibit process scale-up. In this study, we use organic synthesis to modify the internal cavities of cage molecules to produce hybrid materials that are excellent quantum sieves. By combining small-pore and large-pore cages together in a single solid, we produce a material with optimal separation performance that combines an excellent deuterium/hydrogen selectivity (8.0) with a high deuterium uptake (4.7 millimoles per gram).

Deuterium (D) is used as a neutron moderator, as a nonradioactive isotopic tracer, and in neutron scattering experiments. These applications need high-purity deuterium, which is expensive because of its low natural abundance (0.0156 mol %). Typically, D_2 is produced by electrolysis of heavy water and extracted through the Girdler-sulfide process (*1*) or by cryogenic distillation at 24 K (*2*). Both processes are costly and energy intensive because of the multiple enrichment steps required (*3*).

An attractive alternative to purify D_2 from H_2/D_2 gas mixtures is to adsorb D_2 selectively on a microporous bed (*4*). Kinetic quantum sieving (KQS) with nanoporous solids was first proposed by Beenakker *et al.* (*5*). The KQS effect becomes pronounced when the difference in size between a hydrogen molecule and the confining space is comparable to the thermal de Broglie wavelength of molecular hydrogen, $\lambda_T = h/(2\pi m k_B T)^{1/2}$ (h, Planck's constant; m, mass; k_B, Boltzmann constant; T, temperature). Quantum sieving has been exploited for the separation of gaseous isotope mixtures such as D_2/H_2 (*6*), but it is challenging to identify suitable porous solids. This is because KQS requires ultrafine pore apertures (~3 Å) (*7*, *8*), and this typically leads to materials with low pore volumes and, hence, low D_2 adsorption capacities, making such processes difficult to scale. An analogous selectivity-capacity trade-off—or, for membranes, a selectivity-permeance trade-off—is observed for a wide range of other gas separations that do not involve KQS (*9*–*12*).

Various porous materials have been studied for hydrogen isotope separation, including carbons (*13*, *14*), carbon nanotubes (*15*), zeolites (*16*, *17*), metal-organic frameworks (MOFs) (*6*, *18*, *19*), covalent organic frameworks (COFs) (*20*), and 2D crystals (*21*). MOFs and COFs have received much attention because of their crystalline nature and synthetically tunable pore size and functionality (*22*). However, even with MOFs or COFs, it is challenging to tune pore sizes at the exceptionally fine level required for KQS. For example, in MOFs, a common strategy for tuning the pore apertures is through systematic expansion or reduction of the number of the phenylene rings in the organic linker, with an increment or a decrement of ~2.8 Å (*23*); that is, too coarse for fine-tuning the aperture for optimum KQS.

Porous organic cages (POCs) (*24*, *25*) are discrete molecules that have been used previously for the separation of xylene isomers (*26*), noble gases (*27*), and chiral molecules (*27*). POCs might also be promising candidates for H_2/D_2 separation but, unlike MOFs and COFs, it is difficult to tune the pore size in POCs simply by changing the constituent linkers. Because POCs are discrete molecules, small changes in their molecular structure can have profound effects on the solid-state packing of the cages and, hence, the pore structure (*24*). Modifying only the interior of the cage molecule, rather than the cage structure itself, could allow us to avoid altering the crystal packing. Internal functionalization is possible. For example, Mastalerz and co-workers described the postsynthetic modification of the interior of organic cages by using a sixfold Williamson etherification (*28*), but this interior modification affected the cage shape, which in turn altered the crystal packing mode.

[1]Materials Innovation Factory and Department of Chemistry, University of Liverpool, 51 Oxford Street, Liverpool, L7 3NY, UK. [2]Max Planck Institute for Intelligent Systems, Heisenbergstr. 3, 70569 Stuttgart, Germany. [3]Laboratory of Computational Science and Modeling, Institute of Materials, École Polytechnique Fédérale de Lausanne, 1015 Lausanne, Switzerland. [4]Department of Chemistry, Xi'an JiaoTong-Liverpool University, 111 Ren'ai Road, Suzhou Dushu Lake Higher Education Town, Jiangsu Province, 215123, China. [5]Leverhulme Research Centre for Functional Materials Design, Materials Innovation Factory and Department of Chemistry, University of Liverpool, 51 Oxford Street, Liverpool, L7 3NY, UK.
*Corresponding author. Email: aicooper@liverpool.ac.uk (A.I.C.); hirscher@is.mpg.de (M.H.)

Systematically tuning the pore size of organic cages by postsynthetic modification

We synthesized a series of internally post-functionalized porous organic cages that crystallized in an isostructural way. Specifically, we used a protection-deprotection strategy to produce cages where five out of the six internal reaction sites in the cage cavity were functionalized by means of a formaldehyde "tying" method we reported previously (*29*) (Fig. 1, A and B). After deprotection, the single unreacted diamine group can be reacted with a range of aldehyde or ketone precursors to achieve ultrafine control over the cage cavity size and, hence, the pore envelope (Fig. 1C). This method allowed us to tune the size and shape of the cage pore systematically at the atomic level without affecting the external cage shape and size or its crystal packing. Using this strategy, we tuned the pore size for the series of POCs in the range 1.95 to 3.5 Å, which is a useful cut-off range for the separation of gas pairs such as H_2/N_2, H_2/CO, CH_4/N_2, and Xe/Kr (*7*).

Previously, we reported that an organic cage with six diamine groups, **RCC3**, reacts with six formaldehyde molecules to form **6FT-RCC3** through the formation of cyclic aminal rings (*29*). **RCC3** was reacted with six equivalents of acetaldehyde to form a new cage, **6ET-RCC3** (reaction *a*, Fig. 1B), where bulkier ethylidene bridges replaced the six methylene bridges in **6FT-RCC3**. By contrast, **RCC3** reacted with just a single acetone molecule to form **1AT-RCC3** (*29*) (reaction *b*, Fig. 1B); steric hindrance prevented further reaction in the cage cavity.

On the basis of this result, we developed a protection-deprotection strategy in which we reacted the five unfunctionalized diamine groups in **1AT-RCC3** with gaseous formaldehyde in the solid state, through a single-crystal–to–single-crystal reaction, to form a new dual "tied" cage molecule, **1AT-5FT-RCC3** (reaction *d*, Fig. 1B and fig. S1). Solid-state synthesis was essential, in that when **1AT-RCC3** was mixed with formaldehyde in solution ($CHCl_3$ or MeOH), the single acetone protecting group was displaced to afford **6FT-RCC3** (reaction *c* in Fig. 1B and fig. S2). By exploiting the different chemical labilities of imidazolidine rings in **1AT-5FT-RCC3**, we could selectively hydrolyze the single propyl "tie" by stirring in $CHCl_3$:MeOH (1:1, v/v), thus synthesizing a new deprotected cage, **5FT-RCC3** (reaction *e* in Fig. 1B and fig. S3). After deprotection, we reacted the now vacant diamine group in **5FT-RCC3** with acetaldehyde and propionaldehyde to synthesize two new cages, **1ET-5FT-RCC3** and **1PT-5FT-RCC3** (reaction *f*, Fig. 1B). All reactions proceeded with nearly 100% conversion with no additional purification steps.

The parent cage for this study, **RCC3**, is derived from the shape-persistent imine precursor, **CC3**, which crystallized from most organic solvents to form a microporous solid

with a diamondoid pore network (*24*, *26*, *27*). For guest molecules to diffuse through this pore network, they must pass through the intrinsic cage cavities that act as the tetrahedral nodes (*25*). Hence, internal functionalization of the cage cavities provided a route to systematically fine-tune pore size without altering the underlying shape and crystallization habit of the cage molecule (*30*). All cages were isostructural with **CC3**, as determined by powder x-ray diffraction (fig. S4) and single-crystal x-ray diffraction (fig. S5 and table S1). The high crystallographic symmetry of the structures (cubic $F4_132$) did not allow us to determine whether the different tied groups were ordered in the microporous pore structures, but all cages had the same diamondoid pore structure.

To allow for the effect of molecular flexibility on the diffusivity of small gas molecules through these structures, we used molecular dynamics (MD) simulations to calculate a time-averaged pore-limiting envelope (PLE) (*27*) rather than measuring a single, static pore diameter. These calculations showed that post-synthetic modification allowed the PLE to range from 1.95 Å (**6ET-RCC3**) to 3.50 Å (**6FT-RCC3**), resulting in a tunability window of 1.55 Å (Fig. 1C). For context, this tunability window equates to the van der Waals (vdW) radius of a single nitrogen atom across the whole series of isostructural cages.

We studied the gas adsorption properties of these cages for four different gases (Fig. 1D). As expected, there is a positive correlation between the cage cavity volume and the overall gas uptake, especially under conditions in which gases are close to saturation (e.g., N_2 at 77 K; orange bars in Fig. 1D). For example, **5FT-RCC3**, with the largest cage cavity in this series, showed the highest uptakes for all four of the gases studied. By contrast, **1AT-5FT-RCC3** showed much lower gas uptakes, and **6ET-RCC3** size-excluded krypton (Kr) and xenon (Xe) altogether.

This synthetic strategy was also used to tune gas selectivity for hard-to-separate gas pairs, such as Xe and Kr (*31*, *32*). Xenon is heavier and more polarizable than Kr, and it tends to form stronger vdW interactions with most sorbents unless the pores are specifically attuned for Kr adsorption. Preferential Kr adsorption is very rare. For example, just one MOF, **FMOFCu**, adsorbs Kr selectively over Xe at temperatures below 0°C (*32*).

Most of these organic cages also exhibit higher uptakes for Xe than for Kr, but **1AT-5FT-RCC3** exhibited reverse uptake for these two gases. As shown in fig. S6, the estimated ideal Kr/Xe molar selectivity could be switched below 0°C. We ascribe this effect to **1AT-5FT-RCC3** having a cavity ideally suited to accommodate Kr but too small for Xe. Inserting one additional methyl group to form **6ET-RCC3** rendered the cavity too small to allow adsorption of either gas.

Hydrogen isotope separation using an ultrafine aperture cage

Efficient KQS requires porous solids in which the difference between aperture size and gas diameter is comparable to the de Broglie wavelength. The kinetic diameter of hydrogen is

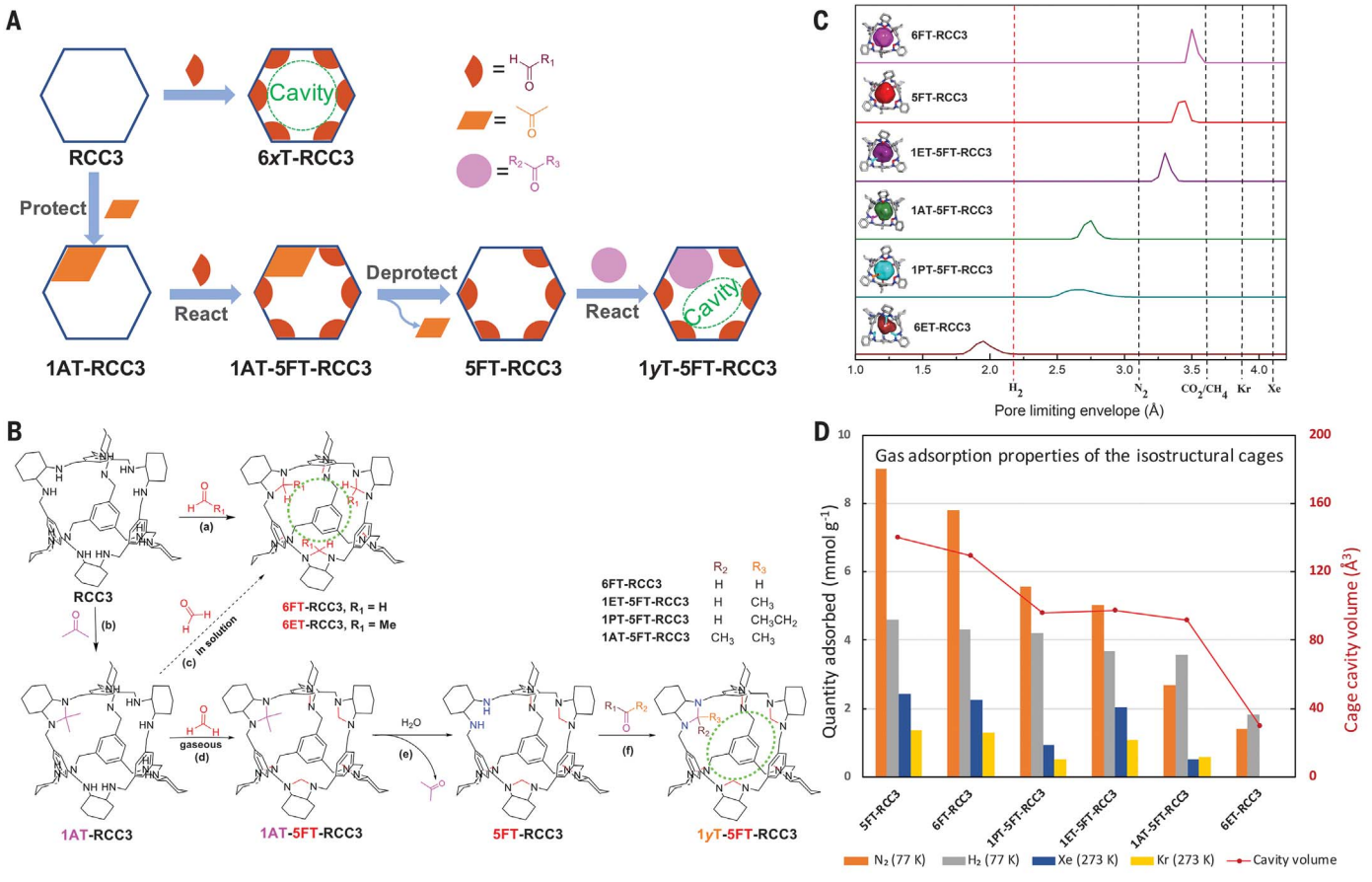


Fig. 1. Fine-tuning pore size by molecular organic synthesis. (**A**) Scheme showing the protect-functionalize-deprotect strategy for internal cage cavity modification. (**B**) Full synthesis route for the modified cages, corresponding to the scheme in (A). **FT**, **AT**, **ET**, and **PT** represent products in which the diamine group(s) were tied with formaldehyde, acetone, ethanal (acetaldehyde), and propionaldehyde, respectively; *x* and *y* represent different possible tying groups (*x* = **E**, **F**; *y* = **A**, **E**, **P**). (**C**) Representative single-crystal structures of the modified cages showing accessible cavities (colored), along with calculated PLEs for each system. (**D**) Summary of gas adsorption properties for a range of gases (histogram; left axis) and cage cavity volumes (right axis) of a single modified cage, as calculated by the VOIDOO program on the basis of their crystal structures (probe radius = 2.0 Å) (*43*).

2.89 Å, and previous studies suggest that the optimum aperture size to achieve KQS with rigid frameworks lies below 3.40 Å (*20*). It is difficult to obtain porous materials with pore apertures in this range, and so far, only one material with pore size <3.00 Å has been reported to separate D_2 and H_2 (*6*).

MD simulations suggested that **6ET-RCC3** has a PLE centered at 1.95 Å but with a relatively broad time-averaged size distribution, with a value near the minimum molecular dimension of H_2 (2.2 Å; Fig. 1C) (*27*). Hydrogen adsorption isotherms obtained from **6ET-RCC3** exhibited hysteresis between 30 and 60 K (Fig. 2B). The H_2 uptake reached a maximum at 50 K (4.8 mmol/g at 1 bar). We observed the same phenomena for D_2 adsorption (figs. S7 and S8). The hysteresis was largest at 30 K and decreased with increasing temperature, suggesting greater equilibration.

We also compared the H_2 adsorption behavior for two other organic cages, **CC3** (*24*) and **6FT-RCC3**, with calculated pore envelopes of around 4.5 and 3.4 Å, respectively. Both **CC3** and **6FT-RCC3** exhibited reversible type I adsorption isotherms (fig. S9), typical of nanoporous materials without kinetic diffusion barriers. The two cages showed an increased H_2 uptake with decreasing temperature, with maximum uptakes at 30 K of 8.0 and 8.2 mmol/g at 1 bar. Unlike **6ET-RCC3**, no hysteresis was observed for **CC3** or **6FT-RCC3**. This difference suggests that the methyl groups in the **6ET-RCC3** cavities were responsible for its temperature-dependent flexibility, as this is the only structural difference between **6FT-RCC3** and **6ET-RCC3**.

Cryogenic thermal desorption spectroscopy (TDS) measurements verified the hydrogen isotope separation performance of **6ET-RCC3**. H_2 and D_2 desorption rates of **6ET-RCC3** (Fig. 2C) were collected during heating under vacuum with a rate of 0.1 K/s, after prior exposure to a 1:1 H_2/D_2 mixture (10 mbar) at various exposure temperatures (T_{exp}) between 30 and 77 K for 10 min of exposure time (t_{exp}). The area under the desorption peak is proportional to the amount of the desorbing gas; hence, the selectivity for D_2 over H_2 could be obtained from the ratio of the peak areas (*6*).

TDS measurements showed that the uptake in **6ET-RCC3** increased with increasing temperature until a maximum for H_2 and D_2 was reached at T_{exp} of 60 K before decreasing again at 77 K. The selectivity, $S_{D2/H2}$, decreased with increasing T_{exp} and exhibited a maximum of 3.9 at 30 K, which is a fairly good separation performance compared with previous reports of KQS (*6*, *33*). The onset temperature of gas desorption is nearly identical to the exposure temperature, because after exposure the chamber is evacuated at T_{exp} before cooling to 20 K. No desorption peak was observed above 60 K for T_{exp} = 30 K, implying no deep penetration into the structure at this temperature. For higher T_{exp}, the desorption spectra were unusually shifted to higher temperatures, which we attributed to an increased penetration depth of gas molecules into the cage structure. In agreement with observations from pure gas isotherms, the properties of **6ET-RCC3** can be attributed to the temperature-dependent opening of the pore aperture. This behavior is similar to that observed in MFU-4 reported previously (*6*), which exhibited different effective aperture sizes at different T_{exp}.

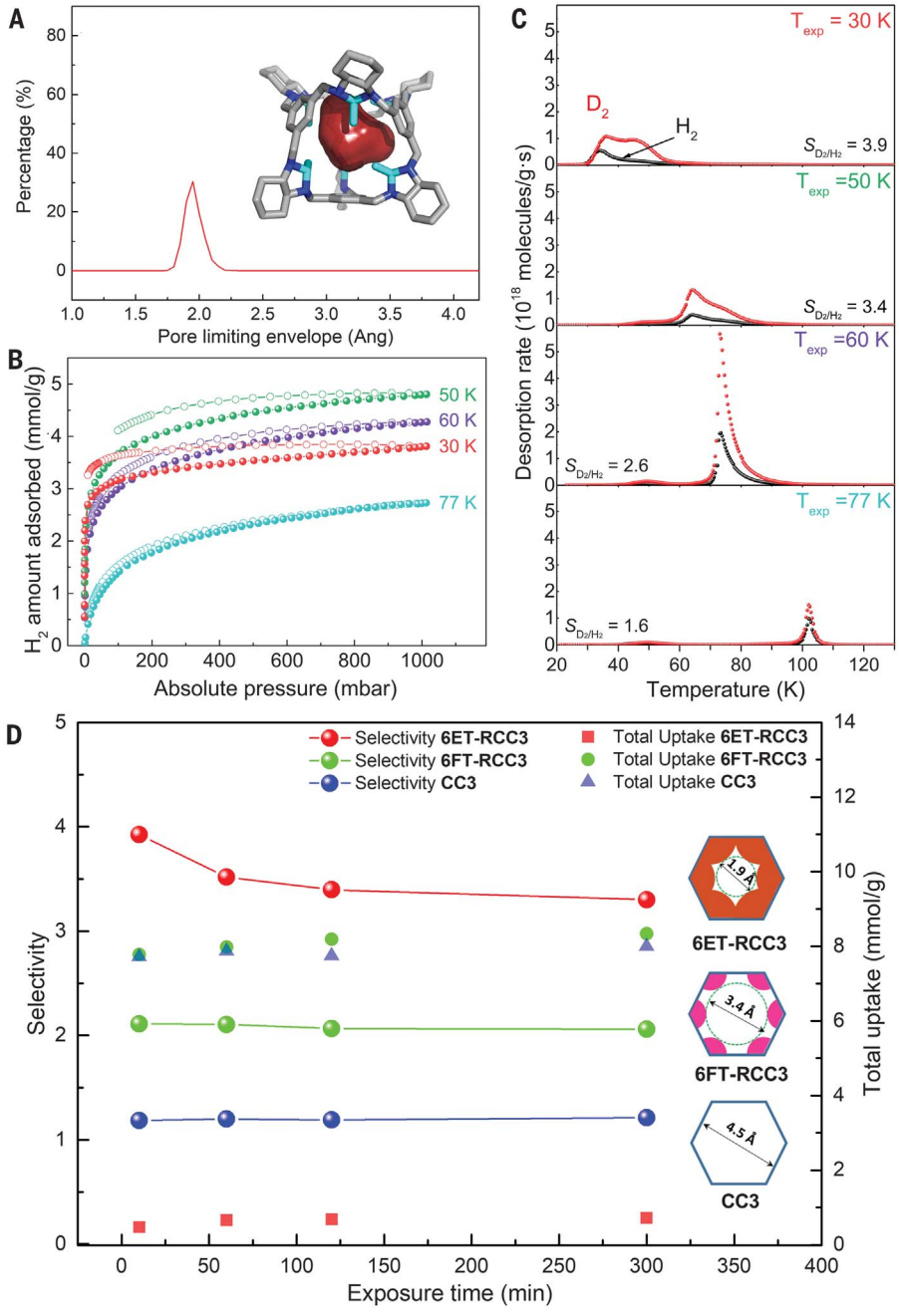


Fig. 2. Kinetic quantum sieving with ultrasmall-pore organic cages. (**A**) PLE for **6ET-RCC3**. The inset image shows the single-crystal structure of **6ET-RCC3** with its accessible cage cavity (colored). Ang, angstroms. (**B**) Hydrogen adsorption (solid symbols) and desorption (open symbols) isotherms of **6ET-RCC3** at different temperatures. (**C**) TDS spectra of **6ET-RCC3** obtained after exposure to a 10-mbar 1:1 D_2/H_2 isotope mixture at different exposure temperatures for a fixed exposure time (t_{exp}) of 10 min. The desorption spectra after evacuation at exposure temperature were measured for a heating rate of 0.1 K/s. (**D**) D_2/H_2 selectivities and gas uptakes as a function of exposure time at 30 K for **CC3**, **6FT-RCC3**, and **6ET-RCC3**; see supplementary materials for additional comparison (figs. S10 and S11).

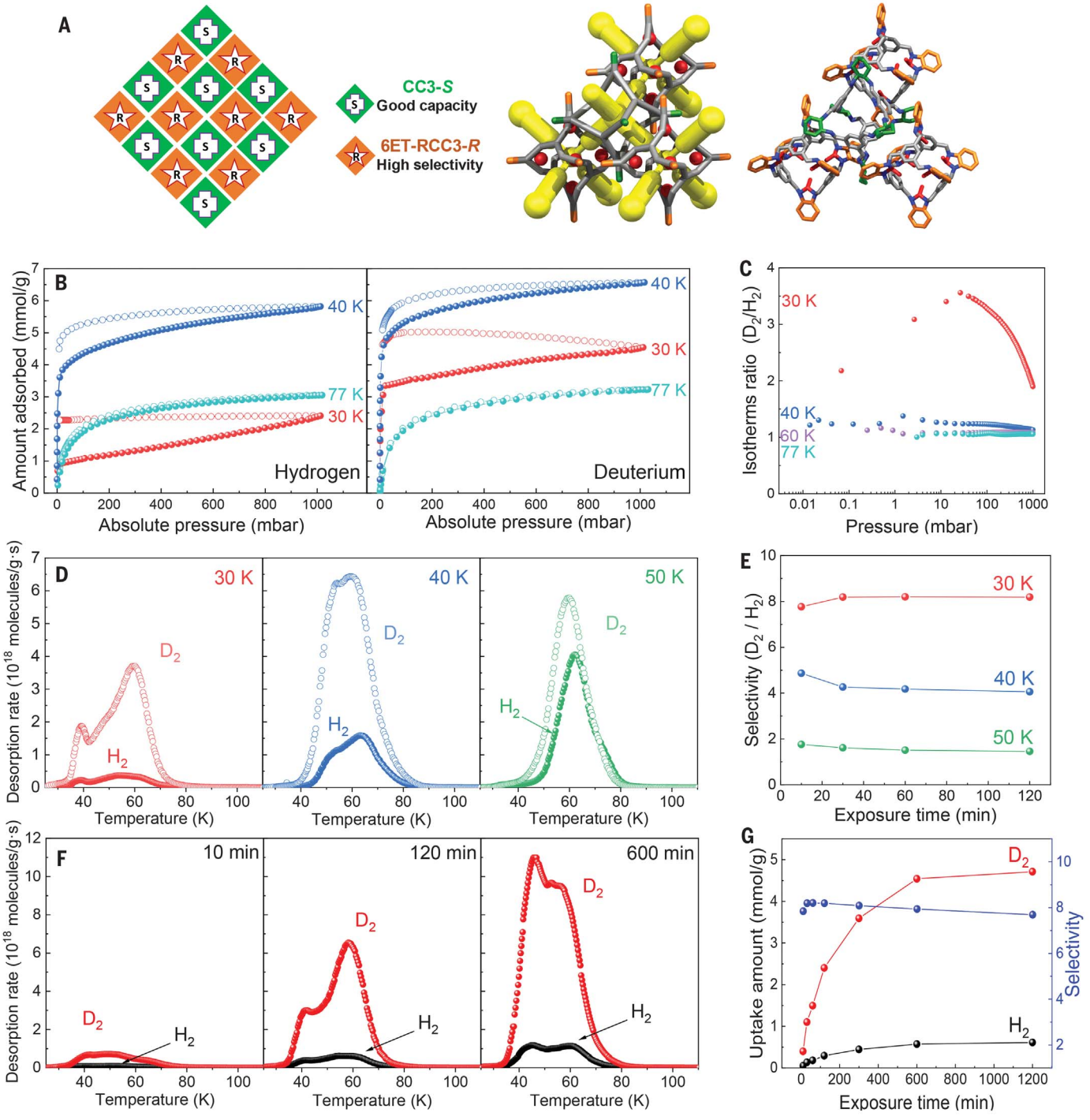


Fig. 3. Formation of a cocrystal enhances the D_2/H_2 separation performance. (**A**) (Left) Scheme showing the cocrystal, **Cocryst1**, formed by chiral recognition between two cages to integrate capacity and selectivity in a single material. (Middle) Simplified representation of the crystal structure of **Cocryst1**, with pore channels shown in yellow. (Right) Single-crystal structure of **Cocryst1**. (**B**) H_2 and D_2 adsorption (closed symbols) and desorption (open symbols) isotherms of **Cocryst1** at different temperatures. (**C**) D_2/H_2 isotherm ratio as a function of pressure for different temperatures. (**D**) TDS spectra for **Cocryst1**, obtained after exposure to a 10-mbar 1:1 H_2/D_2 isotope mixture for different exposure temperatures (T_{exp}) and a fixed exposure time (t_{exp}) of 30 min. (**E**) D_2/H_2 selectivity as a function of t_{exp} at 30 K (red), 40 K (blue), and 50 K (green). (**F**) TDS spectra for **Cocryst1**, obtained after exposure to a 10-mbar 1:1 H_2/D_2 isotope mixture for different exposure times at 30 K. (**G**) The corresponding amount of adsorbed H_2 (black) and D_2 (red) and selectivity (blue) as functions of t_{exp} at 30 K.

This flexibility enhanced the access of the isotope molecules to the pores at higher exposure temperatures.

Figure 2D shows $S_{D2/H2}$ and the total quantity of gas adsorbed for **6ET-RCC3**, **6FT-RCC3**, and **CC3** as a function of t_{exp} at T_{exp} = 30 K (for detailed TDS spectra, see table S2). **6ET-RCC3** showed an increase in uptake for longer t_{exp}, revealing that diffusion was hindered. At 30 K, $S_{D2/H2}$ decreased with longer t_{exp}, from 3.9 to 3.3 between 10 and 300 min of exposure, which is a typical KQS response. The KQS effect is based on the diffusion limitation of the lighter isotope; equilibrium is approached for both isotopes for longer exposure times. The total uptake for **6ET-RCC3** at 30 K was only 0.8 mmol/g at t_{exp} of 300 min, which is related to the hysteresis observed in the isotherm experiment at 30 K. The total gas uptake obtained at 30 K for **CC3** and **6FT-RCC3** was much higher (8.0 mmol/g), consistent with the adsorption results (fig. S8). For the larger-pore materials, **CC3** and **6FT-RCC3**, $S_{D2/H2}$ was lower and remained constant at 1.2 and 2.1, respectively, for different t_{exp}, in keeping with rapid, barrier-free diffusion of H_2 and D_2.

Enhanced quantum sieving performance in a two-component cage cocrystal

These single-component cage crystals exhibited either good selectivity but poor gas capacity (**6ET-RCC3**) or good gas capacity but poor selectivity (**CC3** and **6FT-RCC3**). For the optimal separation of isotopes, the ideal KQS material should combine large cavities to store more D_2 along with a narrow pore aperture to increase the kinetic separation. Taking advantage of the chiral recognition assembly of discrete cage molecules (*34*), we designed a cocrystal structure that combined two different cages: **6ET-RCC3** was chosen as the diffusion barrier, blocking H_2 diffusion and providing the KQS effect, and **CC3** was chosen as the partner cage to provide enough pore space for high gas adsorption (Fig. 3A).

The structure of the cocrystal, **Cocryst1** (**6ET-RCC3**-*R*/**CC3**-*S*, 1:1), is shown in Fig. 3A (at right; see fig. S12 for structural details). Because the cage cavities formed the nodes of the diamondoid pore network, four selective **6ET-RCC3** cages surrounded each **CC3** storage. Gas molecules diffusing through the cocrystal were forced to traverse the small pores in **6ET-RCC3**.

Cocryst1 was studied using D_2 and H_2 high-resolution adsorption experiments collected between 20 and 77 K (Fig. 3B; additional isotherms are in fig. S13). The amount of gas absorbed at 1 bar showed a maximum at 40 K for both gases. As for **6ET-RCC3**, the hysteresis in **Cocryst1** was high at lower temperatures because of the large diffusion barrier, particularly at 30 K; at higher temperatures, a temperature-dependent opening of the aperture allowed both H_2 and D_2 molecules to diffuse faster.

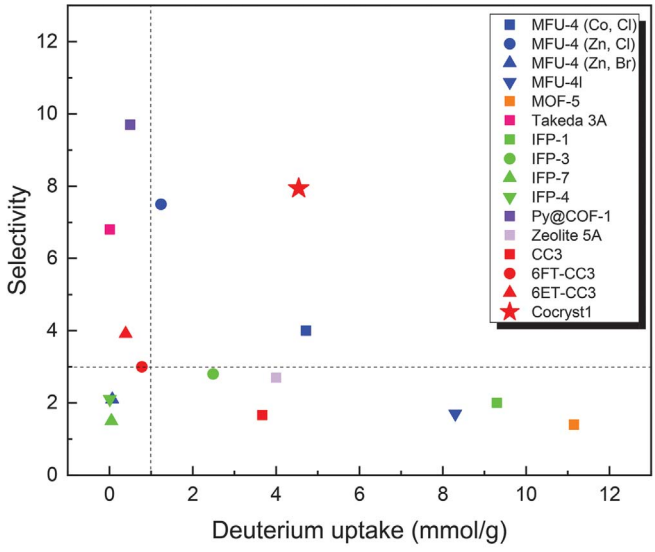


Fig. 4. Summary of hydrogen isotope KQS selectivities and adsorption capacities for various porous materials (directly measured by TDS). The list includes carbon [Takeda 3A (*44*)], MOFs [MFU-4 (*6*, *22*, *44*), MOF-5 (*44*), and IFP (*45*)], COFs [Py@COF-1 (*46*)], zeolite 5A (*16*), and porous organic cages (**CC3**, **6FT-CC3**, **6ET-CC3**, and **Cocryst1**). The practical performance of a KQS adsorbent will be a combination of its selectivity and its capacity; on this basis, the cage cocrystal shows the most promising performance.

The ratio of D_2/H_2 calculated for each point on the isotherms as a function of the pressure is presented in Fig. 3C. **Cocryst1** exhibited a maximum D_2/H_2 uptake ratio of 3.5 at 30 K and 25 mbar, which is consistent with the lack of equilibrium at 30 K, implying that the cocrystal possessed good separation capabilities. To our knowledge, the D_2/H_2 uptake ratio of **Cocryst1** is one of the largest values calculated from pure-gas adsorption isotherms (*6*, *20*, *33*, *35*, *36*).

We investigated actual gas separation by TDS. **Cocryst1** was exposed to 10 mbar of a 1:1 H_2/D_2 mixture for 30 min at various exposure temperatures. The resulting TDS spectra for T_{exp} = 30, 40, and 50 K are shown in Fig. 3D; additional TDS spectra for **Cocryst1** are presented in fig. S14. The uptake after exposure to the gas mixture rose with increasing exposure temperature until a maximum for the combined gas uptake was reached at 40 K. In contrast to **6ET-RCC3**, **Cocryst1** shows desorption up to 80 K for T_{exp} = 30 K, indicating gas penetration of the cages at a lower exposure temperature. The uptake then decreased until no desorption peak is observed at 77 K. $S_{D2/H2}$ reached a maximum of 7.7 at 30 K and dropped to lower values at 40 and 50 K (Fig. 3E). For a constant exposure temperature of 30 K, thermally activated flexibility was again observed. As exposure time increased from 10 to 600 min, $S_{D2/H2}$ remained near 8.0 (7.7 to 8.2), but the D_2 uptake was enhanced from 0.4 to 4.7 mmol/g (Fig. 3, F and G), indicating hindered diffusion. X-ray diffraction data indicate that **Cocryst1** remained highly crystalline and did not change its structure during the TDS measurements (fig. S18).

The kinetics of pure H_2 and D_2 gas uptake was studied by TDS after exposure at 30 K for exposure times varying from 10 to 1200 min (fig. S14). For both gases, **Cocryst1** showed a pronounced increase in uptake for longer exposure time. Whereas the D_2 uptake was almost identical for exposure times between 600 and 1200 min, the H_2 amount still increased at longer exposure times. Because D_2 reached saturation faster, it likely had a much different diffusion rate than H_2.

The H_2/D_2 separation properties of **Cocryst1** were excellent: $S_{D2/H2}$ ~ 8.0, combined with a greatly enhanced D_2 uptake with respect to **6ET-RCC3** (4.7 mmol/g). The experimental $S_{D2/H2}$ values for various reported porous KQS adsorbents are compared in Fig. 4 and table S3. Of these materials, only two other porous solids have combined a selectivity greater than 3 with a gas uptake larger than 1.0 mmol/g (dashed lines in Fig. 4). The cage cocrystal displays the best combination of selectivity and D_2 uptake reported to date.

Molecular simulations of the hydrogen isotope separation in organic cages

To further probe the separation mechanism, we simulated equilibrium adsorption isotherms for both single-component adsorption (Fig. 5, D to F) and an equimolar mixture of H_2 and D_2 (Fig. 5, G to I) in **CC3**, **6ET-RCC3**, and **Cocryst1** by combining grand canonical Monte Carlo (GCMC) simulations with the Feynman-Hibbs effective potential (*37*). We also used a hybrid GCMC-MD scheme, allowing for direct sampling of host motions in adsorption simulations, which was previously shown to be important for gas adsorption in porous organic cages (*27*, *38*). The simulated adsorption isotherms (Fig. 5, D to I) are in good agreement with

experiment, corroborating both the experimental adsorption data and the TDS results. All three cage crystals were predicted to be selective toward D_2 over H_2, with increased selectivity as the temperature decreases. Moreover, computation suggests, in agreement with experiment, that **Cocryst1** exhibits the high D_2 selectivity of **6ET-RCC3** and achieves the higher gas uptake capacities associated with the ***CC3*** partner cage.

Diffusion of the hydrogen isotopes in **CC3**, **6ET-RCC3**, and **Cocryst1** was investigated and interpreted by comparison of the free-energy barriers for H_2 and D_2 in a given crystal structure at infinite dilution (see section 2.10.3,

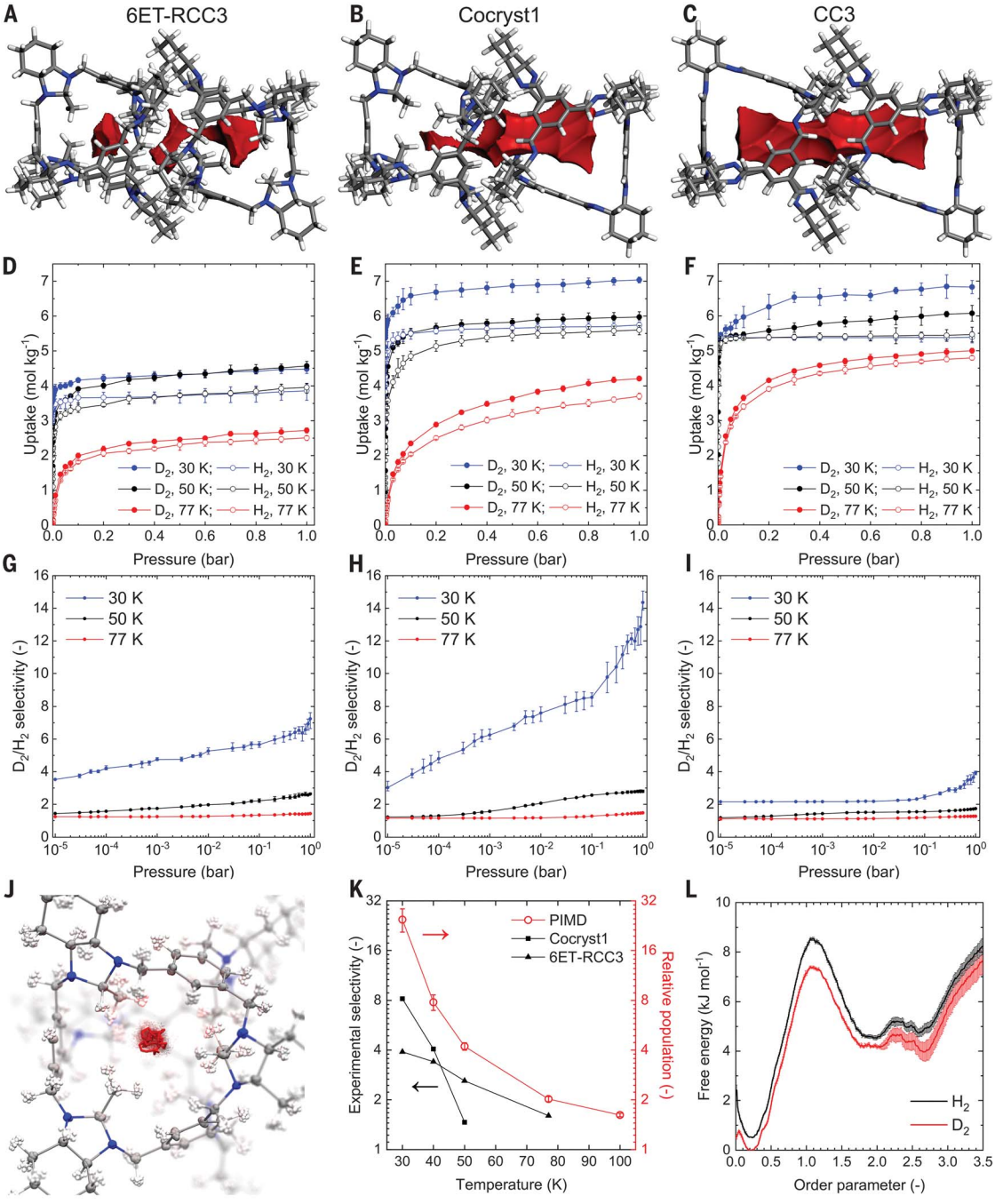


Fig. 5. Simulations provide insights into the mechanism for hydrogen isotope separation by the porous organic cages. (**A** to **C**) A pair of neighboring cage molecules in **6ET-RCC3** (A), **Cocryst1** (B), or **CC3** (C). Gray, white, and blue atoms represent carbon, hydrogen, and nitrogen, respectively; pore spaces inside the cage molecules, defined by a spherical probe with diameter 2.2 Å, are colored in red. In (A), the colored pore space runs through a **6ET-RCC3** cage window with two methyl groups (left cage) and a second **6ET-RCC3** cage window with one methyl group (right cage). In (B), the pore runs through a **6ET-RCC3** cage window with one methyl group (left cage) and a neighboring **CC3** cage window (right cage). (**D** to **F**) Predicted single-component adsorption isotherms of D_2 and H_2 in **6ET-RCC3** (D), **Cocryst1** (E), and **CC3** (F). Five independent simulations were performed to predict the adsorption uptake at each pressure at the respective temperature; the average of the five predicted uptakes was used to plot the isotherm, with error bars showing the maximum and minimum of the five predictions. (**G** to **I**) Predicted D_2/H_2 selectivity, calculated using competitive adsorption simulations of an equimolar D_2/H_2 mixture for **6ET-RCC3** (G), **Cocryst1** (H), and **CC3** (I). Similarly, five independent simulations were performed to predict the average uptake and to determine the error bars. (**J** to **L**) PIMD simulations predict D_2/H_2 selectivity and gas diffusion for a single, isolated **6ET-RCC3** cage (see supplementary text section 2.13 for simulation details). (J) Transition state for the translocation of a quantum H_2 molecule. A single snapshot is shown, with an overlay of all 32 replicas in the PIMD simulation, illustrating the nuclear quantum fluctuations. Additional translucent red dots depict the fluctuations of the translocating H_2 molecule, taken from 100 transition-state configurations. (K) Relative population of D_2 over H_2 inside the cage versus in the gas phase, as a function of temperature, compared with the observed experimental D_2/H_2 selectivities. (L) Free-energy profiles for a single molecule of quantum H_2 (black) or quantum D_2 (red) diffusing through a window of an isolated **6ET-RCC3** molecule at 50 K. Definitions of errors in (K) and (L) are given in section 2.13 of the supplementary text.

supplementary text). In the transition-state theory approximation, molecular diffusivity can be derived from a rate constant for the molecule hopping over the free-energy barrier. Figure S31 (supplementary text) shows the free-energy profile for a diffusion pathway between the center of mass of a cage molecule and the center of mass of a neighboring cage, travelling across two cage windows. In **CC3** (fig. S31C), both H_2 and D_2 moved easily between the two cage molecules in a nearly barrier-free manner. By contrast, the congested cage cavities and narrowed window apertures in **6ET-RCC3** resulted in sharply peaked free-energy barriers (fig. S31A), strongly decreasing the molecular diffusivity compared with **CC3**.

When two methyl groups were located in a single **6ET-RCC3** cage window, the pore space became disconnected and the diffusion barrier became too large to observe any crossing (off-scale in fig. S31A; cage on the left). For windows with only one methyl group (fig. S31A, cage on the right), the pore space ran continuously between the cages, and the free-energy barriers for H_2 and D_2 were lowered substantially. Crucially, **6ET-RCC3** cage windows containing one methyl group provided diffusion barriers that were different for D_2 and H_2 and acted as a kinetic sieve. This feature was also carried over into **Cocryst1** (fig. S31B). In **Cocryst1**, the large **CC3** cavities also provided good dynamical relaxation, resulting in improved D_2 kinetics and higher D_2 uptakes.

We further combined path integral molecular dynamics (PIMD) simulations with quantum mechanical interaction evaluations to probe the adsorption and diffusion behaviors of H_2 and D_2 in the **6ET-RCC3** cage molecule, explicitly accounting for the quantum mechanical nature of both the electrons and the nuclei (Fig. 5, J to L). PIMD simulations predicted the binding free energy of D_2 to be ~0.50 kJ mol^{-1}, lower than for H_2 across the temperature range 30 to 77 K. This difference in binding free energy translates into a relative population of D_2 over H_2 inside the cage of 4.21 at 50 K (Fig. 5H), rising to 24.65 at 30 K (see section 2.13, supplementary text). There is qualitative agreement between these simulated relative populations and the measured D_2/H_2 selectivity in the temperature range 30 to 77 K (Fig. 5K). We also estimated the free-energy barriers for a single molecule of quantum H_2 and quantum D_2 diffusing out of the **6ET-RCC3** cage molecule (Fig. 5L). These simulations show that nuclear quantum effects both destabilize H_2 relative to D_2 inside the cage and also provide a higher free-energy barrier for diffusion of H_2 through the cage windows. The different barrier heights can be understood as the different degrees of zero-point fluctuations that increase the effective size of H_2 more than D_2, thereby making it more difficult for H_2 to pass through the window aperture.

Analysis of the various pore structures and the simulated adsorption and diffusion results (Fig. 5 and fig. S30) may explain why the selectivity for **Cocryst1** was double that of **6ET-RCC3** ($S_{D2/H2}$ = 8.2 versus 3.9). The small channels in **6ET-RCC3** led to single-file diffusion. Once a molecule penetrated the pore, no passing between the isotopes in the channels is possible. Hence, the desorption after exposure to a 1:1 mixture exhibited identical maximum temperatures for both isotopes (Fig. 2C)—the gas molecules left in the same order in which they entered—whereas the maximum for pure gas desorption appeared lower for D_2 than for H_2 (Fig. 2B and fig. S7).

By contrast, **Cocryst1** consisted of a combination of large storage pores (**CC3**, also selective toward D_2 over H_2 at 30 K) and small separation pores, separated by a differential diffusional barrier (fig. S30B and Fig. 5L). Penetration through the small apertures into the adjacent larger cavity yielded an additional sieving effect, whereby D_2 molecules could pass neighboring H_2 molecules, unlike in the single-file pores of **6ET-RCC3**. As a result, **Cocryst1** had an enhanced D_2/H_2 selectivity, although there were half as many small windows as in **6ET-RCC3**.

Outlook

When researchers began to study POCs, there was a strong emphasis on producing materials with large pore volumes and high surface areas to rival solids such as MOFs (*24*, *39*–*41*). Our study suggests that there are benefits in designing solids that are "barely porous" (*40*). By itself, this approach led to materials such as **6ET-RCC3** with low gas capacities, but by pairing small- and large-pore cages in a single cocrystal, we accessed a material with optimal gas separation properties. This strategy might be extended to produce even better performance—for example, by introducing storage cages with larger capacities than that of **CC3**, provided that the differential diffusional barrier between cages is preserved.

Our approach allows extremely delicate tuning of pore size—the entire tunability window for this series of cages spans the diameter a single nitrogen atom—and ideally suits applications such as KQS. Although the synthetic method involves multistep organic synthesis (Fig. 1B), including protection and deprotection steps, each step proceeded in nearly 100% yield. Because there was no need to purify intermediates, there is good potential to scale up the amount of materials made for practical separations.

Computational studies (Fig. 5) helped to explain the enhanced H_2/D_2 separation performance of the cocrystal. Although these calculations served to rationalize the experimental observations, the good agreement between theory and experiment suggests that the a priori design of new systems might be possible, perhaps through methods such as crystal structure prediction to identify suitable hypothetical systems (*34*, *42*).

REFERENCES AND NOTES

1. H. K. Rae, in *Separation of Hydrogen Isotopes* (Symposium Series, ACS, 1978), vol. 68, chap. 1, pp. 1–26.
2. G. M. Keyser, D. B. McConnell, N. Anyas-Weiss, P. Kirkby, in *Separation of Hydrogen Isotopes* (ACS, 1978), vol. 68, pp. 126–133.
3. H. Tanaka *et al*., *J. Low Temp. Phys.* **157**, 352–373 (2009).
4. H. Oh, M. Hirscher, *Eur. J. Inorg. Chem.* **2016**, 4278–4289 (2016).
5. J. J. Beenakker, V. D. Borman, S. Yu. Krylov, *Chem. Phys. Lett.* **232**, 379–382 (1995).
6. J. Teufel *et al*., *Adv. Mater.* **25**, 635–639 (2013).
7. K. Adil *et al*., *Chem. Soc. Rev.* **46**, 3402–3430 (2017).
8. J.-Y. Kim, H. Oh, H.-R. Moon, *Adv. Mater.* **31**, e1805293 (2019).
9. L. M. Robeson, *J. Membr. Sci.* **320**, 390–400 (2008).
10. Z. R. Herm *et al*., *Science* **340**, 960–964 (2013).
11. A. Cadiau, K. Adil, P. M. Bhatt, Y. Belmabkhout, M. Eddaoudi, *Science* **353**, 137–140 (2016).
12. N. B. McKeown, P. M. Budd, *Chem. Soc. Rev.* **35**, 675–683 (2006).
13. P. Kowalczyk *et al*., *J. Phys. Chem. Lett.* **6**, 3367–3372 (2015).
14. G. Garberoglio, M. M. DeKlavon, J. K. Johnson, *J. Phys. Chem. B* **110**, 1733–1741 (2006).
15. Q. Wang, S. R. Challa, D. S. Sholl, J. K. Johnson, *Phys. Rev. Lett.* **82**, 956–959 (1999).
16. R. Xiong *et al*., *Microporous Mesoporous Mater.* **264**, 22–27 (2018).
17. M. Giraudet *et al*., *Microporous Mesoporous Mater.* **270**, 211–219 (2018).
18. H. Oh, I. Savchenko, A. Mavrandonakis, T. Heine, M. Hirscher, *ACS Nano* **8**, 761–770 (2014).
19. B. Chen *et al*., *J. Am. Chem. Soc.* **130**, 6411–6423 (2008).
20. H. Oh, K.-S. Park, S. B. Kalidindi, R. A. Fischer, M. Hirscher, *J. Mater. Chem. A* **1**, 3244–3248 (2013).
21. M. Lozada-Hidalgo *et al*., *Science* **351**, 68–70 (2016).
22. I. Savchenko *et al*., *Microporous Mesoporous Mater.* **216**, 133–137 (2015).
23. H. Deng *et al*., *Science* **336**, 1018–1023 (2012).
24. T. Tozawa *et al*., *Nat. Mater.* **8**, 973–978 (2009).
25. T. Hasell, A. I. Cooper, *Nat. Rev. Mater.* **1**, 16053 (2016).
26. T. Mitra *et al*., *Nat. Chem.* **5**, 276–281 (2013).
27. L. Chen *et al*., *Nat. Mater.* **13**, 954–960 (2014).
28. M. W. Schneider, I. M. Oppel, A. Griffin, M. Mastalerz, *Angew. Chem. Int. Ed.* **52**, 3611–3615 (2013).
29. M. Liu *et al*., *J. Am. Chem. Soc.* **136**, 7583–7586 (2014).
30. T. Hasell *et al*., *J. Am. Chem. Soc.* **136**, 1438–1448 (2014).
31. D. Banerjee *et al*., *Acc. Chem. Res.* **48**, 211–219 (2015).
32. C. A. Fernandez, J. Liu, P. K. Thallapally, D. M. Strachan, *J. Am. Chem. Soc.* **134**, 9046–9049 (2012).
33. D. Noguchi *et al*., *J. Am. Chem. Soc.* **130**, 6367–6372 (2008).
34. J. T. A. Jones *et al*., *Nature* **474**, 367–371 (2011).
35. S. A. FitzGerald, C. J. Pierce, J. L. C. Rowsell, E. D. Bloch, J. A. Mason, *J. Am. Chem. Soc.* **135**, 9458–9464 (2013).
36. B. Xiao *et al*., *J. Am. Chem. Soc.* **129**, 1203–1209 (2007).
37. L. M. Sesé, *Mol. Phys.* **85**, 931–947 (1995).
38. S. Yang *et al*., *Kristallogr. Cryst. Mater.* **234**, 547–555 (2019).
39. M. Mastalerz, M. W. Schneider, I. M. Oppel, O. Presly, *Angew. Chem. Int. Ed.* **50**, 1046–1051 (2011).
40. A. I. Cooper, *Angew. Chem. Int. Ed.* **51**, 7892–7894 (2012).
41. G. Zhang, O. Presly, F. White, I. M. Oppel, M. Mastalerz, *Angew. Chem. Int. Ed.* **53**, 1516–1520 (2014).
42. A. Pulido *et al*., *Nature* **543**, 657–664 (2017).
43. G. J. Kleywegt, T. A. Jones, *Acta Crystallogr. D* **50**, 178–185 (1994).
44. J. Teufel, "Experimental investigation of H_2/D_2 isotope separation by cryoadsorption in metal-organic frameworks," thesis, Universität Stuttgart (2013).
45. S. S. Mondal *et al*., *ChemPhysChem* **20**, 1311–1315 (2019).
46. H. Oh *et al*., *Angew. Chem. Int. Ed.* **52**, 13219–13222 (2013).

ACKNOWLEDGMENTS

We thank Diamond Light Source for access to beamlines I19 (CY21726) and I11 (EE17193). We thank the Advanced Light Source, supported by the Director, Office of Science, Office of Basic Energy Sciences, of the U.S. Department of Energy under contract no. DE-AC02-05CH11231 and also thank S. J. Teat for his assistance during this experiment. We thank M. Wang (University of Liverpool) for computing facilities support and A. Hill (Department of

Chemical Engineering, University of Bath) for discussions on the practicability of using cage materials for hydrogen isotope separation. **Funding:** We gratefully acknowledge the Engineering and Physical Sciences Research Council (EP/N004884/1), the European Research Council under the European Union's Seventh Framework Programme (FP/2007-2013)/ERC through grant agreement no. 321156 (ERC-AG-PE5-ROBOT), and the Leverhulme Trust via the Leverhulme Research Centre for Functional Materials Design for funding. S.Y. and L.D. acknowledge financial support from the Chinese Young Scholar National Science Foundation Grant (21403171), the Xi'an JiaoTong-Liverpool University (XJTLU) Research Development Fund (PGRS-13-03-08), and the Key Program Special Fund in XJTLU (KSF-E-03). D.H. thanks the Oversea Study Program of Guangzhou Elite Project from Guangzhou City, China, for financial support. V.K. and M.C. acknowledge funding from the Swiss National Science Foundation (project ID 200021-159896) and the European Research Council under the European Union's Horizon 2020 research and innovation program (grant agreement no. 677013-HBMAP). **Author contributions:** M.L., L.C., and A.I.C. conceived the project. M.L. and D.H. synthesized and characterized the materials. L.C. conceived the modeling strategy and supervised the computational work, with input from L.D. and M.C. L.C., S.Y., and D.L.H. performed the classical simulations. V.K., L.C., and M.C. performed the electronic-structure, PIMD, and free-energy simulations. M.A.L. supervised the structural part of this study and refined all diffraction data. M.L. and M.A.L. cultured single crystals and performed solid-state crystal synthesis. M.A.L. and S.Y.C. carried out powder x-ray diffraction analyses. R.C. collected gas sorption data. M.H. and G.S. conceived the hydrogen isotope separation measurements. L.Z. and R.B.-X. collected the H_2 and D_2 isotherms. L.Z. performed TDS experiments. L.Z. and M.H. interpreted the TDS data. All authors contributed to the writing of the paper. **Competing interests:** The authors declare no competing interests. **Data and materials availability:** The crystallographic data reported in this paper are listed in the supplementary materials and archived at the Cambridge Crystallographic Data Centre under reference numbers CCDC 1910113 to 1910120. All other data needed to evaluate the conclusions in the paper are present in the paper or the supplementary materials.

SUPPLEMENTARY MATERIALS

science.sciencemag.org/content/366/6465/613/suppl/DC1
Materials and Methods
Supplementary Text
Figs. S1 to S44
Tables S1 to S8
References (*47*–*95*)

18 April 2019; accepted 10 October 2019
10.1126/science.aax7427

REPORT

NEONICOTINOIDS

Neonicotinoids disrupt aquatic food webs and decrease fishery yields

Masumi Yamamuro[1,2]*, Takashi Komuro[2], Hiroshi Kamiya[3], Toshikuni Kato[3], Hitomi Hasegawa[4], Yutaka Kameda[5]

Invertebrate declines are widespread in terrestrial ecosystems, and pesticide use is often cited as a causal factor. Here, we report that aquatic systems are threatened by the high toxicity and persistence of neonicotinoid insecticides. These effects cascade to higher trophic levels by altering food web structure and dynamics, affecting higher-level consumers. Using data on zooplankton, water quality, and annual fishery yields of eel and smelt, we show that neonicotinoid application to watersheds since 1993 coincided with an 83% decrease in average zooplankton biomass in spring, causing the smelt harvest to collapse from 240 to 22 tons in Lake Shinji, Shimane Prefecture, Japan. This disruption likely also occurs elsewhere, as neonicotinoids are currently the most widely used class of insecticides globally.

Lacustrine ecosystems worldwide yield hundreds of tons of fish annually (*1*); however, in Japan, these ecosystems are being severely degraded by human activities (*2*). The introduction of exotic freshwater piscivorous fishes is reported as a primary cause for reduced fish yields (*2*); however, this impact is negligible because invasive freshwater fishes are scarce in half of the 23 brackish lakes in Japan experiencing declining fish yields. Adverse effects of pesticides are also a likely driver of the reduction in fish yields in Japan, but evidence for this has been lacking until now.

Neonicotinoids are used heavily in rice agriculture (*3*) and were first registered in Japan in 1992. Since then, their use has increased exponentially (Fig. 1). Currently, even rivers in metropolitan areas are contaminated with neonicotinoids from the effluent of rice paddies (*4*). Neonicotinoid concentrations in Japanese water bodies frequently exceed chronic limits—and sometimes lethal limits—for aquatic invertebrates measured in laboratory studies. The highest concentrations of two neonicotinoids (thiamethoxam and imidacloprid), sampled weekly for 1 year in the Sagami River of the Tokyo metropolitan area, were 0.202 and 0.104 μg L^{-1}, respectively (*4*). Neonicotinoid exposure of 48 aquatic invertebrate species belonging to 12 orders revealed that chronic neonicotinoid concentrations >0.035 μg L^{-1} or acute concentrations >0.200 μg L^{-1} negatively influence highly sensitive aquatic invertebrate species (*5*). The neonicotinoid concentration in the Sagami River exceeds the acute concentration for highly sensitive organisms.

Sensitive organisms include multiple aquatic invertebrates that represent a substantial dietary component of many fish species. Studies using rice paddy mesocosms showed that the pesticide imidacloprid has pronounced effects on aquatic insects (*6*). However, the effects of neonicotinoids on aquatic ecosystems receiving water from rice paddies have not been investigated; this is in part because even taxonomically and functionally similar species differ greatly in their sensitivity to neonicotinoids. Consequently, species within the same genus or family might exhibit a compensatory increase in abundance after the reduction or elimination of a sensitive species. Such functional redundancy, however, is unlikely in ecosystems with few species. Brackish water systems have low species diversity because of the challenges of osmoregulation. Species diversity in oligohaline waters such as Lake Shinji, Japan (fig. S1), our study site, is the lowest among all brackish water systems (*7*).

Benthic invertebrate species in Lake Shinji either disappeared or noticeably declined in abundance between 1982 (before the use of neonicotinoids in the watershed) and 2016, 23 years after continuous application of neonicotinoids began (Table 1). Among the severely affected taxa, the midge *Chironomus plumosus*, an important diet item for smelt (*8*), was absent from all 39 sampling locations in 2016 despite being abundant on the west coast of Lake Shinji in 1982 (fig. S2). *C. plumosus* inhabited Lake Shinji until October 1992, including August, when oxygen depletion often occurs (fig. S3, A and B). However, this species has been collected only infrequently at four long-term sampling points since 1993: in 1998 to 2000 and 2004 to 2005 (fig. S3C and table S1). The possibility that *C. plumosus* abundance was anomalously high in the 1980s and that the drop in 1993 represents a return to baseline conditions is not plausible because *C. plumosus* declined in other lakes at about the same time that neonicotinoids were introduced (e.g., Lake Suwa) (*9*).

In addition to *C. plumosus*, the isopod *Cyathura muromiensis* (fig. S4), the oligohaline polychaete *Notomastus* sp., and oligochaetes (figs. S5 and S6) had all declined in abundance by 2016 ($p < 0.05$, paired t tests). In contrast, mesohaline polychaetes increased (fig. S7, *Laonome albicingillum*, $p < 0.05$; paired t test) or remained unchanged (fig. S8, *Prionospio japonica*, $p = 0.19$; paired t test), probably because their planktonic larva disperse annually to coastal areas after the concentration of neonicotinoids in these areas has declined.

Pelagic invertebrate species in Lake Shinji also declined as neonicotinoids were introduced into its watershed. The biomass of the pelagic copepod *Sinocalanus tenellus*, an abundant zooplankton species in Lake Shinji and an important fish food for smelt, declined after the introduction of imidacloprid to rice paddies in May 1993. The abundance of this species fell from a mean of 108 μg C L^{-1} ($n = 137$, SD = 119) during the period of May 1981 to April 1993 to 18.2 μg C L^{-1} ($n = 143$, SD = 22) during the period of May 1993 to April 2005 (Fig. 2; $p < 0.0001$, unpaired t test).

Reduced abundance of numerous benthic and pelagic invertebrates in Lake Shinji between 1982 and 2016 cannot be explained by oligotrophication or other confounding factors, including particulate chemical oxygen demand, surface water chlorinity (an indicator of saline water intrusion), bottom water dissolved oxygen concentrations, sediment organic matter content, or the invasion of new fish species. Multiple water-quality characteristics were measured monthly in Lake Shinji and showed no clear changes before and after the introduction of imidacloprid in May 1993 (fig. S9). For example, average particulate chemical oxygen demand values in the period May 1984 to April 1993 versus May 1993 to April 2005 were 1.73 mg L^{-1} ($n = 103$, SD = 1.02) and 1.53 mg L^{-1} ($n = 144$, SD = 0.61) ($p > 0.05$, unpaired t test), respectively. Chlorinity was 1.82 g L^{-1} ($n = 105$, SD = 1.02) and 1.99 g L^{-1} ($n = 144$, SD = 1.06), respectively, for these two periods ($p > 0.05$, unpaired t test). There was also no increasing trend in average salinity at the center of the lake between 1982 and 2016 (data not shown). Thus, increased salinity did not cause decreases in annelid density. Dissolved oxygen was 7.45 mg L^{-1} ($n = 103$, SD = 4.38) and 7.77 mg L^{-1} ($n = 140$, SD = 3.60), respectively

[1]Institute of Geology and Geoinformation, Geological Survey of Japan (GSJ), AIST, Central 7, Higashi 1-1-1, Tsukuba, Ibaraki 305-8567, Japan. [2]Graduate School of Frontier Science, The University of Tokyo, 5-1-5 Kashiwanoha, Kashiwa, Chiba 277-8563, Japan. [3]Shimane Prefectural Institute of Public Health and Environmental Science, Nishihamasadacho, Matsue 690-0012, Japan. [4]Nagoya City Institute for Environmental Sciences, 5-16-8 Toyota, Minami-ku, Nagoya, Aichi 457-0841, Japan. [5]Creative Engineering Department of Civil and Environment Engineering, Chiba Institute of Technology, 2-17-1 Tsudanuma, Narashino, Chiba 275-0016, Japan.
*Corresponding author. Email: limnologyandoceanography@yahoo.co.jp

($p > 0.05$, unpaired t test), and sediment organic matter content sampled from 15 locations in Lake Shinji did not change significantly between 1982 and 2016 (*10*).

Total neonicotinoid concentration at our sampling site, station ST, near the mouth of a small stream from the rice paddies that are within the watershed of Lake Shinji (fig. S1), was 0.072 μg L^{-1} in June 2018 (fig. S10). This is sufficiently high to induce negative chronic effects on sensitive aquatic invertebrates (*5*). Neonicotinoid concentrations in water samples at station S7, near the mouth of the Hii River, were lower because sampling was done when rainfall inflow was minimal. When neonicotinoid concentrations peaked after rainfall, concentrations at station S7 were potentially as high as those at station ST. Furthermore, at least three types of neonicotinoids (imidacloprid, clothianidin, and thiamethoxam) were detected in the surface water of the west lake basin (station S7) after rice planting in May 2018. Toxicity of multiple neonicotinoids seems to be synergistic in aquatic systems. Using experimental in situ enclosures, chronic toxicity of imidacloprid, clothianidin, and thiamethoxam (and their mixtures) to natural aquatic insect communities showed that the cumulative emergence of insects after the mixture treatments was 42%, 20%, and 44% lower, respectively, than when the three neonicotinoids were applied separately (*11*). No reports are available on the synergistic toxicity of neonicotinoids on *C. plumosus*, but mixtures of neonicotinoids have probably negatively influenced *C. plumosus*, other macrobenthos, and zooplankton such as *S. tenellus*.

Reductions in the abundance of invertebrates, particularly zooplankton, were associated with significantly lower landings of smelt (*Hypomesus nipponensis*) and eel (*Anguilla japonica*) in Lake Shinji after the introduction of neonicotinoid use in 1993 (Figs. 1 and 3). Average annual yields of smelt dropped from 240 tons (n = 12, SD = 57) to 22 tons (n = 12, SD = 53) between the periods 1981 to 1992 and 1993 to 2004 ($p < 0.001$, unpaired t test). For eel, mean annual yield declined from 42 tons (n = 12, SD = 9.7) to 10.8 tons (n = 12, SD = 4.8) between the same periods ($p < 0.001$, unpaired t test). By contrast, ice fish (*Salangichthys microdon*) yield remained unchanged before and after the introduction of neonicotinoids; average annual yield in 1981 to 1992 was 40.9 tons (n = 12, SD = 18) and from 1993 to 2004, it was 53.3 tons (n = 12, SD = 50) ($p = 0.43$, unpaired t test).

Under the Fishery Act [http://faolex.fao.org/docs/pdf/jap1710JAP.pdf (in Japanese)], the Lake Shinji Fisheries Cooperative Association has the fishing rights for these species and is obliged to increase their abundance. To increase smelt and eel yield, the Lake Shinji Fisheries Cooperative Association releases eyed eggs of smelt and juvenile eels every year. This stocking occurred throughout the 1990s (fig. S11), yet the same fishing gear (net sets) caught 908 tons of smelt in the 1960s and just 27 tons during 1995 to 1996 (*12*).

Young smelt consume crustacean zooplankton, and they feed proportionately more on epiphytic crustaceans and midges as they grow (*8*, *13*). The decrease in zooplankton biomass (Fig. 2) and *C. plumosus* density by 83% and 100%, respectively, with the introduction of neonicotinoids indicates that decreased smelt abundance at Lake Shinji was indirectly driven by the introduction of neonicotinoids. The same is true for eel, which feed on zoobenthos including polychaetes, oligochaetes, and insects (Chironimidae) (*14*). Eel declines were not caused by a reduction in the number of juvenile eels released into Lake Shinji, as this number did not change before and after the introduction of neonicotinoids (fig. S11). Nor was the decrease of eels caused by lower recruitment of postlarval eels (i.e., glass eels) from the ocean. Larval eel recruitment from the ocean to freshwater bodies in Japan remained relatively constant between 1981 and 2004 (Fisheries Agency: www.jfa.maff.go.jp/j/saibai/attach/xls/unagi-8.xlsx); average annual catches of glass eel in Japan decreased by only 32%, from 25.7 tons (n = 12, SD = 7.5) during 1981 to 1992 to 17.6 tons (n = 12, SD = 5.1) during 1993 to 2004 ($p < 0.05$, unpaired t test).

Ice fish landings were unaffected by the food web changes associated with the introduction of neonicotinoids. Small ice fish (<20 mm total length) in Lake Shinji feed more heavily than smelt or eel on primary producers—diatoms occupy 40% of ice fish gut contents and zoo-

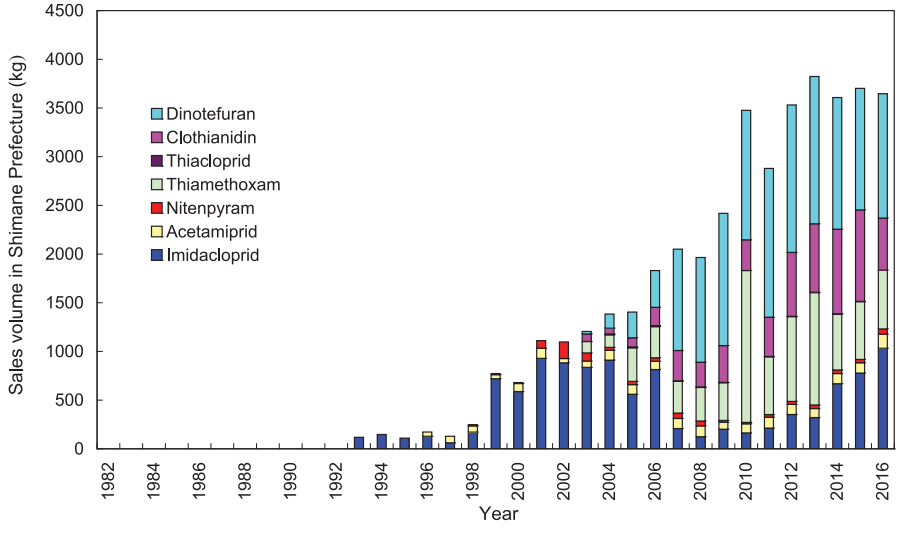


Fig. 1. Quantity of seven kinds of neonicotinoids (kg) sold in Shimane Prefecture, Japan. Data were derived from the "Webkis-Plus: Database of chemicals" (https://www.nies.go.jp/kisplus/).

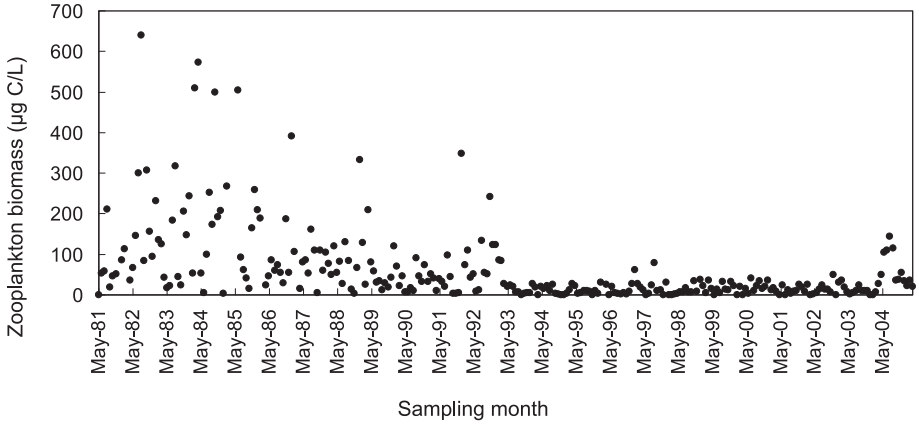


Fig. 2. Zooplankton biomass (μg C L^{-1}) collected monthly at the center of Lake Shinji from May 1981 to April 2005 (data were supplied by the Izumo River Office). Neonicotinoid application began in 1993.

Table 1. Mean (SD) density (individuals m^{-2}) of dominant macrobenthos at 39 locations in Lake Shinji, Japan, sampled in both 1982 and 2016. p values are the result of paired *t* tests. A list of all species collected in 2016 is provided in table S2.

Taxa	1982	2016	p
Arthropods			
Chironomus plumosus	121 (268)	0.0	0.008
Tanypodinae spp.	125 (169)	19 (25)	0.001
Cyathura muromiensis	30 (75)	0.2 (1.1)	0.017
Annelids			
Prionospio japonica	88 (150)	131 (131)	0.192
Notomastus sp.	101 (243)	0.4 (0.8)	0.014
Laonome albicingillum	4.2 (15)	12 (13)	0.026
Oligochaeta spp.	188 (387)	14 (39)	0.007

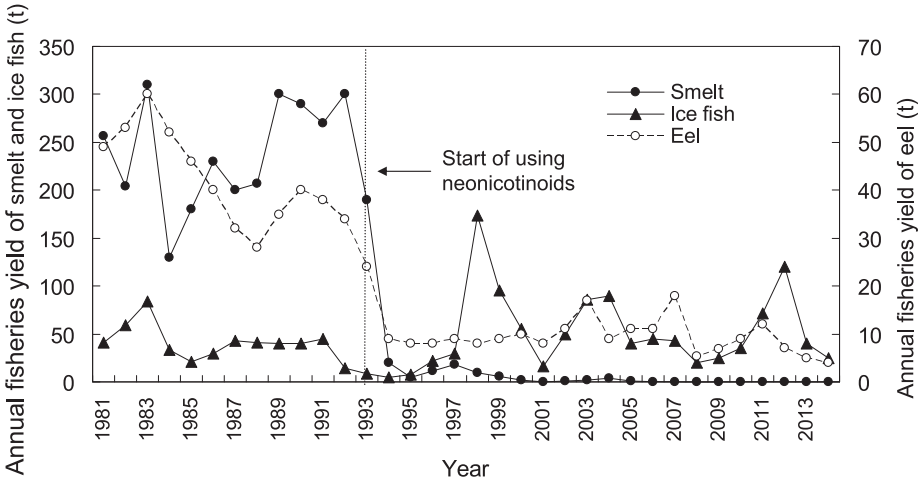


Fig. 3. Annual yield (tons) of smelt, ice fish, and eel in Lake Shinji from 1981 to 2014. The vertical dashed line indicates when neonicotinoid use began in the watershed of the lake.

plankton 60% (*15*). Although larger size classes of ice fish (>21 mm total length) feed mainly on zooplankton, the ability of young ice fish to utilize diatoms may sustain recruitment.

In Lake Shinji, neonicotinoids indirectly reduced fishery yields by decreasing the abundance of invertebrates that serve as food for smelt and eels. Nationwide decreases in fishery yields in the lakes of Japan were also probably caused by food web disruption from neonicotinoids after the widespread use of these pesticides. Neonicotinoids can also affect fish directly. Sublethal effects on fish have been observed from exposure to environmentally relevant concentrations of fipronil, imidacloprid, and thiacloprid (*16*).

Neonicotinoids are the most widely used class of insecticides, representing more than 25% of the global pesticide market, and were valued at more than $3 billion U.S. in 2014 (*17*). Decreased survival, growth, and reproduction of freshwater organisms, particularly aquatic insects and crustaceans, by widespread use of neonicotinoids could alter ecosystem functions related to nutrient transfer from primary producers to secondary consumers, including fish (*16*). Decreased farmland bird populations in the Netherlands was associated with the use of neonicotinoids, which reduced the abundance of insect prey (*18*). In 1962, Rachel Carson wrote in *Silent Spring* (*19*), "These sprays, dusts, and aerosols are now applied almost universally to farms, gardens, forests, and homes—nonselective chemicals that have the power to kill every insect, the 'good' and the 'bad', to still the song of birds and the leaping of fish in the streams…" The ecological and economic impact of neonicotinoids on the inland waters of Japan confirms Carson's prophecy.

REFERENCES AND NOTES

1. A. M. Deines *et al*., *Front. Ecol. Environ.* **15**, 293–298 (2017).
2. S. S. Matsuzaki, T. Kadoya, *Ecol. Appl.* **25**, 1420–1432 (2015).
3. K. Nakanishi, H. Yokomizo, T. I. Hayashi, *Environ. Sci. Pollut. Res. Int.* **25**, 35352–35364 (2018).
4. M. Sato, H. Uemura, K. Kosaka, M. Asami, M. Kamata, *Mizu Kankyo Gakkaishi* **39**, 153–162 (2016) (in Japanese).
5. C. A. Morrissey *et al*., *Environ. Int.* **74**, 291–303 (2015).
6. K. Kobashi *et al*., *Ecotoxicol. Environ. Saf.* **138**, 122–129 (2017).
7. A. Remane, C. Schlieper, "Poverty of species" in *Biology of Brackish Water* (Wiley, 1972), pp. 16–25.
8. T. Yoshioka, E. Wada, H. Hayashi, *Ecology* **75**, 835–846 (1994).
9. K. Hirabayashi, T. Hanazato, N. Nakamoto, *Hydrobiologia* **506**, 381–388 (2003).
10. T. Komuro *et al*., *Jap. J. Limnol.* **79**, 161–168 (2018) (in Japanese).
11. E. M. Maloney, K. Liber, J. V. Headley, K. M. Peru, C. A. Morrissey, *Environ. Pollut.* **243** (Pt B), 1727–1739 (2018).
12. Y. Ishitobi, J. Hiratsuka, H. Kuwabara, M. Yamamuro, *J. Mar. Syst.* **26**, 171–181 (2000).
13. S. Kaneko, K. Kanou, M. Sano, *Fish. Sci.* **82**, 631–637 (2016).
14. H. Itakura, T. Kaino, Y. Miyake, T. Kitagawa, S. Kimura, *Environ. Biol. Fishes* **98**, 1871–1888 (2015).
15. M. Horinouchi, G. Kume, A. Yamaguchi, K. Toda, K. Kurata, *Ichthyol. Res.* **55**, 207–217 (2008).
16. M. Chagnon *et al*., *Environ. Sci. Pollut. Res. Int.* **22**, 119–134 (2015).
17. H. A. Craddock, D. Huang, P. C. Turner, L. Quirós-Alcalá, D. C. Payne-Sturges, *Environ. Health* **18**, 7 (2019).
18. C. A. Hallmann, R. P. B. Foppen, C. A. M. van Turnhout, H. de Kroon, E. Jongejans, *Nature* **511**, 341–343 (2014).
19. R. Carson, *Silent Spring* (Houghton Mifflin, 1962).

ACKNOWLEDGMENTS

We thank the Izumo River Office, Ministry of Land, Infrastructure, and Transport, for allowing the use of their monitoring data. M. V. Moore and N. L. Rodenhouse gave insightful comments and suggestions. **Funding:** This study was supported by the River Works Technology Research and Development Program, Japanese Ministry of Land, Infrastructure, Transport, and Tourism. **Author contributions:** M.Y. designed the research, received funding, and wrote the draft; T.Ko. drew the figures; H.K. and T.Ka. monitored water quality and sampled water for neonicotinoid analysis; H.H. and Y.K. analyzed neonicotinoids. **Competing interests:** The authors declare no competing interests. **Data and materials availability:** Water-quality data are available at the home page of Shimane Prefecture (https://www.pref.shimane.lg.jp/admin/pref/chosa/hokanken/index.data/shinjikonakaumi1984_.xlsx). Macrobenthos data obtained in 1982 and 2016 are summarized in figs. S2 to S8, and long-term monitoring data of the midges *C. plumosus* are provided in table S1.

SUPPLEMENTARY MATERIALS

science.sciencemag.org/content/366/6465/620/suppl/DC1
Materials and Methods
Figs. S1 to S11
Tables S1 and S2
References (*20*–*24*)

15 March 2019; accepted 17 September 2019
10.1126/science.aax3442

SURFACE MAGNETISM

Atomic-scale spin sensing with a single molecule at the apex of a scanning tunneling microscope

B. Verlhac[1], N. Bachellier[1], L. Garnier[1], M. Ormaza[1], P. Abufager[2], R. Robles[3], M.-L. Bocquet[4], M. Ternes[5,6]*, N. Lorente[3,7]*, L. Limot[1]*

Recent advances in scanning probe techniques rely on the chemical functionalization of the probe-tip termination by a single molecule. The success of this approach opens the prospect of introducing spin sensitivity through functionalization by a magnetic molecule. We used a nickelocene-terminated tip (Nc-tip), which offered the possibility of producing spin excitations on the tip apex of a scanning tunneling microscope (STM). When the Nc-tip was 100 picometers away from point contact with a surface-supported object, magnetic effects could be probed through changes in the spin excitation spectrum of nickelocene. We used this detection scheme to simultaneously determine the exchange field and the spin polarization of iron atoms and cobalt films on a copper surface with atomic-scale resolution.

In conventional scanning tunneling microscopy (STM), the magnetic ground state of an isolated atom or molecule is inferred by collecting spin-related fingerprints in the conductance measured with a metallic tip. Isolated atoms or molecules can also serve as spin detectors when controllably moved on the surface with the help of the tip within their local magnetic environment. The magnetic ground state can change in the presence of a magnetic coupling. Exchange- and surface-mediated Ruderman–Kittel–Kasuya–Yosida interactions have been spatially mapped in this way by monitoring the zero-bias peak in the differential conductance (dI/dV) associated with the Kondo effect (*1*–*4*), tunneling magnetoresistance (*5*–*7*), and spin excitation spectra and spin relaxation times (*8*–*12*). Recently, dipolar and hyperfine interactions have also been observed through electrically driven spin resonances (*13*, *14*).

A well-calibrated sensor attached to the tip apex would allow the tip to be freely positioned above a surface target. This detection scheme eliminates surface-mediated interactions and benefits from the vertical-displacement sensitivity of the STM as the sensor-target distance is no longer imposed by the surface corrugation. Probing a magnetic exchange interaction across a vacuum gap is experimentally demanding (*15*–*21*) because scanning probe techniques suffer from poor structural and magnetic characterization of the tip apex. To overcome these limitations, we introduced spin sensitivity by functionalizing the tip apex with a single magnetic molecule. Such a strategy has proven successful for collecting chemical and structural information on surface-supported atoms and molecules otherwise inaccessible with a metallic tip (*22*–*27*). We used a tip decorated by a spin $S = 1$ nickelocene molecule (Fig. 1A) (*28*, *29*), which comprises an Ni atom sandwiched between two C_5H_5 cyclopentadienyl (Cp) rings and we accurately capture the junction geometry by comparison with first-principles calculations.

We prepared the nickelocene-terminated tip (Nc-tip) with atomic control. We first performed soft tip–surface indentations into our pristine working surfaces, either Cu(100) or Cu(111) (*30*), to ensure a monoatomically sharp Cu apex. Nickelocene was then imaged as a ring (inset in Fig. 1B); the molecule adsorbed on copper with one Cp bound to the surface and the other exposed to vacuum (*31*). After transferring the Nc molecule from the surface to the tip [details of the molecule transfer to the tip can be found in (*29*)], the Nc-tip was characterized by spectral features found in the second derivative, d^2I/dV^2, of the current I with respect to the bias V measured at a set of constant distances z between tip and the pristine Cu(100) surface (Fig. 1B). We calibrated z by performing controlled tip contacts to the surface tracking the current I and defining $z = 0$ as the distance where the transition from the tunneling to contact regime occurs [see fig. S1 and accompanying discussion in the supplementary materials (*30*)].

The spectra varied with z only in amplitude and were dominated by a peak at positive V and a dip at negative V at energies symmetric to zero. These peaks and dips correspond to inelastic tunneling events in which tunneling electrons excite the Nc from its magnetic ground state $M = 0$, with M as the magnetic quantum number projected onto the axis perpendicular to the rings of the molecule, to one of the two degenerate excited states $M = \pm 1$. These states are at a higher energy $D = 3.5 \pm 0.1$ meV relative to the ground state (*28*), where D is the axial magnetic anisotropy (Eq. 2). The inelastic conductance was nearly one order of magnitude greater than the elastic conductance [see fig. S2 and accompanying discussion in the supplementary materials (*30*)], highlighting that the spin of Nc was well preserved from scattering events with itinerant electrons of the metal (*28*, *32*). This response is notable, differentiating Nc from other single atoms or molecules, which instead require a thin, insulating spacer between them and the metal surface (*8*, *33*, *34*) or a superconductor (*35*) to preserve their quantum nature.

We used the Nc-tip to probe surface magnetism through changes in the spin excitation spectrum. We initially probed a single magnetic Fe atom adsorbed on Cu(100) (Fig. 1A). Iron atoms on the surface (*30*) protruded by 115 pm and were imaged with the Nc-tip as rings with an asymmetric apparent height (Fig. 1C). The structure observed in the image reflected the presence of Nc on the tip apex and resulted from the tilted adsorption geometry of the molecule. Indeed, density functional theory (DFT) calculations showed that Nc bonded to the tip-apex atom through two C atoms of the Cp ring (*29*). The tilt angle was estimated through the line profile of the Fe atom (inset of Fig. 1C), which revealed that the tips used were typically at angles ~<15° relative to the surface normal.

A set of d^2I/dV^2 spectra recorded at different z heights above the Fe atom (Fig. 1D) showed that, at $z = 133$ pm, the spectrum was indistinguishable from the one acquired above the bare Cu(100) (Fig. 1B). In this low-energy range, Fe was spectroscopically dark, i.e., its contribution to the spin excitation spectrum was negligible, due to the strong screening and broadening effects (*7*). However, for smaller z heights, we observed a splitting of the peak and the dip that became increasingly stronger as z decreased (Fig. 1E). The average position of the spin-split peaks and dips varied at most by 0.2 meV with distance (dashed line in Fig. 1E).

We tested several Nc-tips with tilt angles ranging from 5° to 15°, and all showed similar behavior—the distances for a given splitting changed only by ±10 pm. Apart from the splitting, we also observed a marked intensity asymmetry of the split spectral features. Although the amplitudes of the positive peak and negative dip were identical for the Nc-tip probed against the bare surface (Fig. 1B), at positive bias, the energetically lower excitation had higher peak amplitude than the energetically higher excitation, whereas at negative bias, the dips showed opposite behavior compared with the peaks.

[1]Université de Strasbourg, CNRS, IPCMS, UMR 7504, F-67000 Strasbourg, France. [2]Instituto de Física de Rosario, CONICET and Universidad Nacional de Rosario, Av. Pellegrini 250 (2000) Rosario, Argentina. [3]Centro de Física de Materiales CFM/MPC (CSIC-UPV/EHU), 20018 Donostia-San Sebastián, Spain. [4]PASTEUR, Département de Chimie, Ecole Normale Supérieure, PSL Research University, Sorbonne Universités, UPMC Univ. Paris 06, CNRS, 75005 Paris, France. [5]Institute of Physics II B, RWTH Aachen University, 52074 Aachen, Germany. [6]Peter Grünberg Institut (PGI-3), Forschungszentrum Jülich, 52425 Jülich, Germany. [7]Donostia International Physics Center (DIPC), 20018 Donostia-San Sebastián, Spain.
*Corresponding author. Email: ternes@physik.rwth-aachen.de (M.T.); nicolas.lorente@ehu.eus (N.L.); limot@ipcms.unistra.fr (L.L.)

The splitting and asymmetry of the line shape observed above Fe have a magnetic origin. To rationalize these observations, we assigned the z-axis as the out-of-surface direction neglecting the small tilt of the molecule and used a spin Hamiltonian that includes the magnetic anisotropy of the Nc molecule and of the Fe atom on copper (D_{Fe}) (*7*, *36*):

$$H = D\hat{S}_z^2 + D_{Fe}\hat{S}_{z,Fe}^2 - J\hat{S}_z \cdot \hat{S}_{z,Fe} \quad (1)$$

where J is an Ising-like exchange coupling restraining the Nc-Fe magnetic interaction along the z-axis [see fig. S3 and accompanying discussion in the supplementary materials (*30*)]. Within this framework, the ground state of the combined system is a doublet $G = 0,\Uparrow$ and $0,\Downarrow$, where the energetically lowest states of the Fe spin are noted as $\Uparrow$ and $\Downarrow$. The exchange interaction lifts the degeneracy between the two excited doublets AP (antiparallel) and P (parallel) of the coupled spin system and causes the line shape to split apart. As the exchange interaction is antiferromagnetic ($J < 0$, see below) and the Fe is spectroscopically dark, the lowest excited-state doublet is AP = $-1,\Uparrow$ and $+1,\Downarrow$ and corresponds to an antiferromagnetic configuration where the Fe spin is anti-aligned with the Nc spin. The higher excited-state doublet corresponds to the ferromagnetic configuration, $P = +1,\Uparrow$ and $-1,\Downarrow$. Note that for this derivation, neither the spin magnitude of the Fe atom nor the sign of D_{Fe} has to be explicitly set so long as the ground state is a doublet.

To simplify the discussion, it is preferable to express the spin Hamiltonian of Eq. 1 with an effective Zeeman term consisting of the gyromagnetic factor (g), the Bohr magnetron (μ_B), and the exchange field (B) produced by the Fe atom and acting along the z-axis of the Nc molecule:

$$\hat{H} = D\hat{S}_z^2 - g\mu_B B\hat{S}_z \quad (2)$$

This expression has the advantage of providing a common framework for describing the spin systems investigated in the present study. Within mean-field theory, $B = J\langle S_{Fe}\rangle/g\mu_B$, where $\langle S_{Fe}\rangle$ is the effective spin of Fe on the Cu(100) surface. In the following, for clarity, we restrain the analysis to a $\Downarrow$ Fe spin without loss of generality [see fig. S4 and accompanying discussion in the supplementary materials (*30*)]. Within this viewpoint, the exchange field causes a Zeeman splitting of the line shape into the two excited states +1 and −1 of Nc that are located at low and high energy, respectively. The bias asymmetry in the peaks and dips reflects instead a spin imbalance in the tunneling current (*10*, *21*, *37*–*39*). This mechanism is illustrated in Fig. 2, A and B, and is qualitatively similar to conventional spin-polarized STM (*5*) and, more generally, to spin valves or to Kondo systems coupled to magnetic electrodes (*4*, *19*, *40*, *41*).

As illustrated in Fig. 2A, the excitation of Nc from the ground state to its first excited state +1 requires a change in spin angular momentum of $\delta M = +1$. Because the total angular momentum must be conserved, it can only be induced by electrons that compensated for this moment by flipping their spin direction during the tunneling process from ↑ to ↓. At negative bias, the tunneling process may be viewed as a ↑ electron hopping from the substrate into the molecular orbital with transmission $\mathcal{T}_\uparrow$, whereas a ↓ electron is emitted from the molecular orbital toward the tip. At positive bias, the tunneling direction reverses and the transmission from tip to sample is $\mathcal{T}_\downarrow$. The relative height of the dip at low negative voltage (h_-) compared with the peak at low positive voltage (h_+) yields a quantitative measure of the spin asymmetry $\eta = (h_+ - h_-)/(h_+ + h_-)$, with $h_- \propto \mathcal{T}_\uparrow$ and $h_+ \propto \mathcal{T}_\downarrow$. The excitation of Nc from the ground state to its second excited state −1 requires instead electrons starting

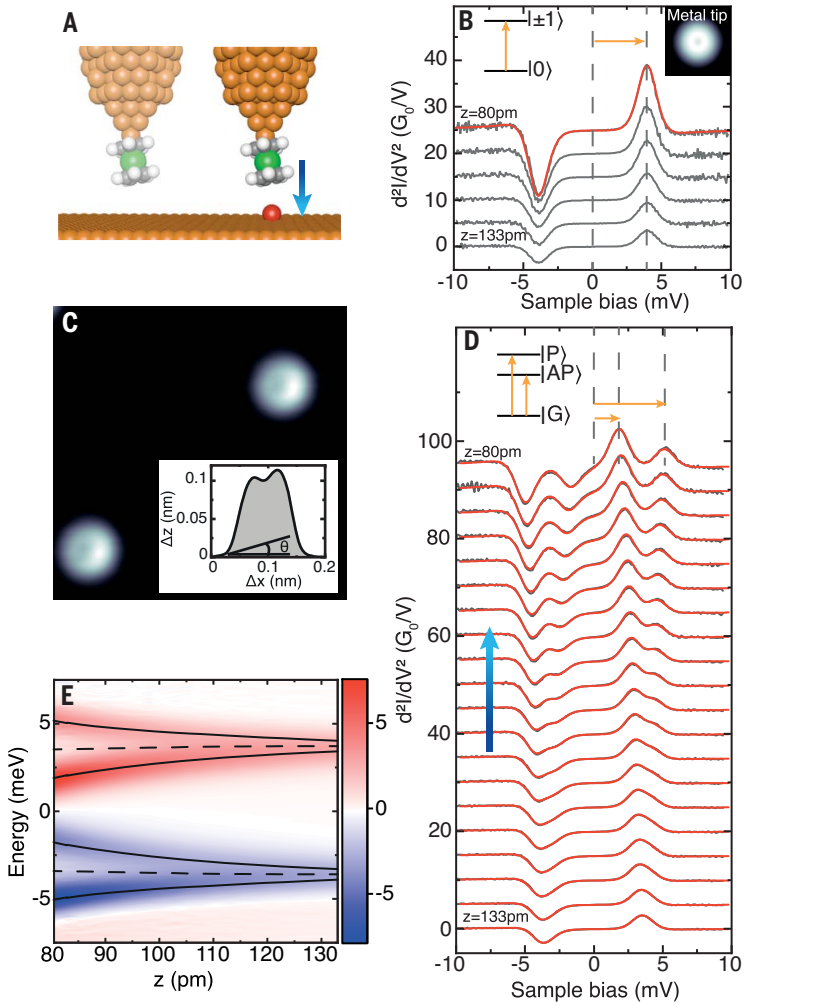


Fig. 1. Spin excitation spectra above the Cu surface and a single Fe atom. (**A**) Schematic view of the tunnel junction. Atom colors: Cu, orange; C, gray; H, white; Ni, green; Fe, red. (**B**) d^2I/dV^2 spectra acquired above a surface atom of Cu(100) at a distance between z = 133 and z = 80 pm. The solid red line is a fit based on a dynamical scattering model (*12*) and yielded an axial magnetic anisotropy of D = 3.5 meV, a coupling between the localized Nc spin and the tip electrons of $J_0\rho_0 = -0.08$, and a spin-conserving potential scattering of U = 0.02. Inset: Image of Nc on Cu(100) acquired with a copper-coated tip apex (V = 20 mV, I = 100 pA, size: 2 nm by 22 nm). (**C**) Image of Fe atoms on Cu(100) (V = −15 mV, I = 30 pA, size: 5 nm by 5 nm) and corresponding line profile of one atom (inset) revealing the presence of a tilted Nc at the tip apex. The tilt angle θ was estimated through the height difference between the left and right protrusion of the line profile. (**D**) d^2I/dV^2 spectra acquired with the tip positioned above the high-intensity side of the ring-shaped Fe atom. Tip distances z < 80 pm resulted in the transfer of Nc atop the Fe atom (figs. S1B and S1C). (**E**) Peak and dip energy positions extracted from the spectra of (D). The color scale flanking the panel corresponds to the d^2I/dV^2 amplitudes and is given in units of G_0/V. For clarity, the spectra in (B) and (D) were shifted vertically from one another by 5 × G_0/V, where $G_0 = 2e^2/h$, the quantum of conductance.

in a ↓ state and ending in a ↑ state (Fig. 2B), resulting in a spin asymmetry of −η.

The spin-polarized nature of the transmission reflects a delicate balance between the spin dependence of the Nc-Fe hybridization and of the density of states (DOS) of both tip and substrate. Neglecting the small tilt angle of Nc relative to the quantization axis z, the Nc-tip DOS is instead unpolarized as the $M = 0$ ground state of Nc leads to a projected moment $\langle m_z \rangle = 0$. As a consequence, the spin polarization of the transmission reflects the polarization of the DOS of the substrate weighted by the spin-dependent Fe hybridization with the π orbitals of Nc [see fig. S6 and accompanying discussion in the supplementary materials (*30*)].

The fit to the line shape using Eq. 2 and a dynamical scattering model (solid red lines in Fig. 1D) (*10*, *12*) was highly satisfactory and provided quantitative values of the spin-asymmetry η and the exchange-field B exerted by the Fe atom onto the Nc molecule assuming a gyromagnetic factor of $g = 1.89$ (*42*). The exchange field was an exponential function of z (Fig. 2C), allowing us to exclude a magnetic dipolar interaction. Assuming an exponential decay of the form $\exp - z/\lambda$, we found a decay length $\lambda = 34 \pm 2$ pm, consistent with other tip-induced exchange interactions (*17*, *18*, *21*, *42*). Different Nc-tips showed similar decay constants [see fig. S5 in the supplementary materials (*30*)]. Using our DFT-computed effective spin of $\langle S_{Fe} \rangle \approx 1.7$, the exchange coupling was $|J| \approx 0.9$ meV at the shortest probed Fe-Nc distances, typical for a tip-adsorbate exchange interaction across a vacuum gap (*19*, *20*). Details regarding the DFT calculations can be found in the supplementary materials (*30*). The magnetic anisotropy D, which corresponds to the average position of the spin-split peaks and dips, remained constant with z (Fig. 1E). This result indicated that the intramolecular structure of Nc was preserved on the tip apex (*28*, *43*).

For the data presented in Fig. 1D, we found a spin asymmetry of η = 32% at the highest fields measured (Fig. 2D). The data collected on an ensemble of different Nc-tips on different Fe atoms yielded a lower average value of η = 23% [see fig. S5 in the supplementary materials (*30*)]. The observed spin asymmetry is in agreement with the spin polarization found for electrons inelastically tunneling between an Fe-terminated tip and the quantized states of single adsorbates (*18*, *21*).

The sign of the exchange interaction between a magnetic atom and a magnetic tip apex is determined by the competition of direct and indirect interactions and may vary with tip-to-atom distance (*44*). To gain insight into the exchange coupling between the Nc-tip and Fe atom, we computed with DFT the exchange energy defined as $E_{ex} = E_P - E_{AP}$ at various Nc-Fe distances by fully relaxing the junction geometry; E_P (E_{AP}) is the total energy of the junction with the spin directions of Nc and Fe in parallel (antiparallel) alignment. To facilitate the comparison with the experimental findings, we took $z = 0$ as the center-to-center distance between the closest carbon atom of Nc and the Fe atom, which is ~250 pm. The exchange interaction favored an antiparallel alignment of the two spins (Fig. 2E)—the junction geometry remained constant up to 50 pm, at which distance a chemical bond started to form between Fe and Nc [see fig. S1 in the supplementary materials (*30*)]. The energy difference between antiparallel and parallel alignment is 13 meV at 120 pm, whereas no difference could be evidenced above 300 pm. The antiferromagnetic coupling was short ranged and attributed to the direct hybridization of the Fe orbitals with the frontier molecular orbitals of Nc.

We extended the proof of concept for the Nc-tip to a collection of atoms by investigating a prototypical ferromagnetic surface consisting of a nanoscale Co island grown on Cu(111) (Fig. 3A) (*45*–*48*). The islands are triangular-like and two layers high with typical lateral extensions ≥10 nm for the Co coverage used (*30*). They possess at low temperature an out-of-plane magnetization perpendicular to the Cu surface (inset of Fig. 3A) (*46*, *49*, *50*). Unlike the Fe atom, the Co spin is fixed and we assume it to be ⇑ without loss of generality. We found that Nc adsorbed preferentially on Co, either on top of the nanoislands or on the bottom edge of the island as described for other molecules (*51*). Nc-tips were routinely prepared by transferring a molecule from the edge of the island to the Cu-tip apex. Given the low molecular coverage, large pristine areas of Co could be found on the sample.

In Fig. 3B, we present a typical constant-height image acquired in a small area located in the center of a Co island (white square in Fig. 3A) at a bias $V = -1$ mV, which is very close to the Fermi energy. The Co atoms of the island can be readily visualized with the Nc-tip, whereas this resolution is lost above nonmagnetic Cu(111) [see fig. S7A in the supplementary materials (*30*)]. This difference points to the magnetic origin of the contrast. At $z = 150$ pm above the Co surface, the spin excitation spectrum (Fig. 3C) was similar to the spectra of

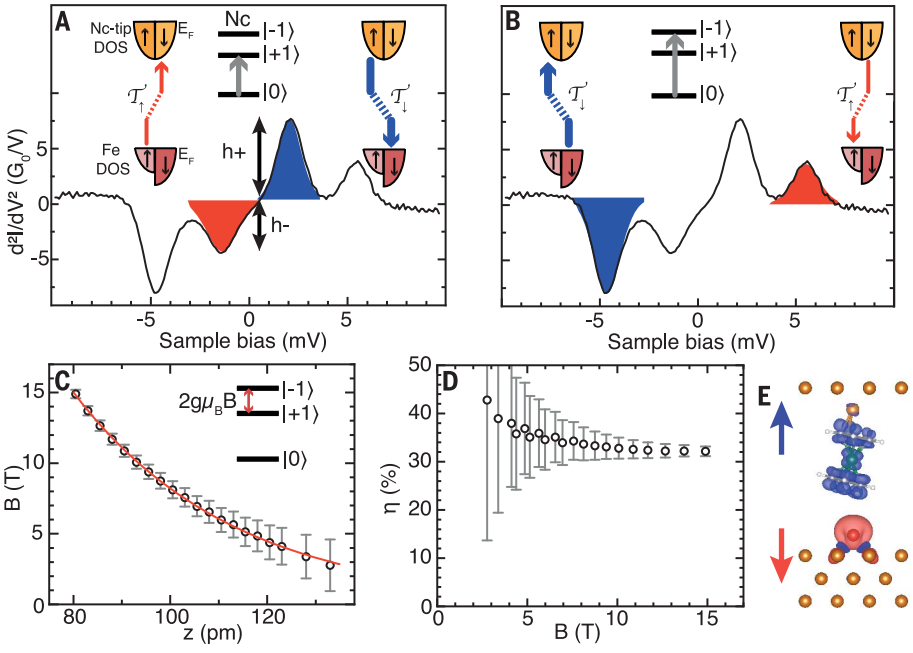


Fig. 2. Inelastic tunneling and magnetic coupling measured above an Fe atom. (**A**) and (**B**) show the mechanism leading to the bias asymmetry in the d^2I/dV^2 spectra acquired above Fe. (A) At negative bias, inelastic electrons tunneled from the spin-up states of the Fe atom to the spin-down states of the Nc-tip with transmission proportional to $\mathcal{T}_\uparrow$, leading to a dip in the d^2I/dV^2 spectrum. At positive bias, the junction polarity was reversed and inelastic electrons tunneled from the spin-up states of the Nc-tip to the spin-down states of the Fe atom with transmission proportional to $\mathcal{T}_\downarrow$, leading to a peak in the d^2I/dV^2 spectrum. During the tunneling process, the electrons excited Nc from its ground to its first excited state. The weaker amplitude for the dip compared with the peak reflects the difference in the transmission ($\mathcal{T}_\uparrow \neq \mathcal{T}_\downarrow$). (B) Same mechanism as (A) but for inelastic tunnel electrons exciting Nc from its ground state to its second excited state. (**C**) Exchange field B and (**D**) spin-asymmetry η extracted from the spectra of Fig. 1D using Eq. 2. (**E**) DFT-calculated configuration of the tunnel junction for a distance of 100 pm with isosurface of the spin density (antiferromagnetic coupling).

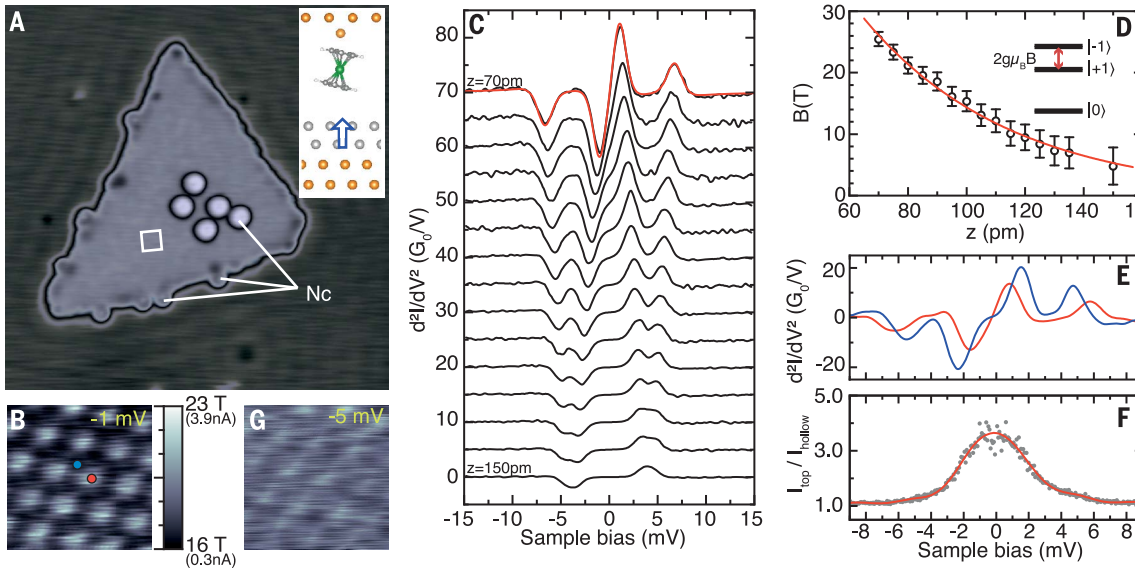


Fig. 3. Spin excitation spectra above a cobalt surface. (**A**) Cobalt island on Cu(111) decorated with Nc molecules (V = −50 mV, I = 20 pA, size: 25 nm by 25 nm). The white lines highlight the presence of Nc. The white square corresponds to the area investigated in (B) and (F). Inset: Schematic view of an Nc-tip above a cobalt island. The arrow indicates the out-of-plane magnetization of the island. Atom colors: Co, gray; Cu, orange. (**B**) Constant-height image acquired in the center of the island at z = 80 pm with V = −1 mV (size: 1 nm by 1 nm). The color scale indicates the value of the tunnel current and the corresponding B, which is estimated using the exchange coupling of the two spectra in (E). (**C**) d^2I/dV^2 spectra acquired with the tip positioned above a Co atom of the island. The tip was moved from z = 150 pm to z = 70 pm. For clarity, the spectra are displaced vertically from one another by 5 × 10^{-3} G_0/mV. The solid red line is a fit based on a dynamical scattering model. Unlike the fits of Fig. 1D, to correctly capture the line shape, we allowed the tunneling electrons to produce out-of-equilibrium state populations (*10*) in Nc by solving the dynamical rate equations of the tunneling process (*12*). (**D**) Exchange field B extracted from the spectra of (C) using Eq. 2. (**E**) d^2I/dV^2 spectra acquired at z = 80 pm above a top site [red dot in (B)] and above a hollow site [blue dot in (B)]. (**F**) Ratio between the tunnel current above a top site and the tunnel current above a hollow site. (**G**) Constant-height image of the same area in (B) also acquired at z = 80 pm, but with lower tunnel bias (−5 mV).

Fig. 1B, which indicated that the island was spectroscopically dark. However, upon vertically approaching a Co atom in the cobalt island, the peak and dip in the d^2I/dV^2 spectrum progressively split apart. Using the spin Hamiltonian of Eq. 2 and g = 1.89, we found that the exchange field varied exponentially and reached values as high as 26 T at the shortest distances explored (z = 70 pm; Fig. 3D). The decay length was λ = 50 ± 5 pm. Consistent with the exponential decay of the exchange field, we found that the image corrugation increased when decreasing z [see fig. S7B in the supplementary materials (*30*)].

The exchange field originates mostly by direct orbital overlap and corresponds to an exchange coupling of $|J| \approx 3.2$ meV taking our DFT-computed value of $\langle S_{Co} \rangle \approx 0.9$ for the effective spin of a Co atom. The spectra showed weak spin asymmetry (η = 5 to 15%) and changed in sign at the island rim [see fig. S8 in the supplementary materials (*30*)], in agreement with spin-polarized STM measurements (*46*, *47*, *50*–*52*). The spin polarization found is lower compared with STM measurements carried out with a superconducting tip (*53*), suggesting a π-orbital influence on the transmission $\mathcal{T}$, as evidenced in other molecular tips (*54*, *55*).

To clarify the observed atomic resolution in the constant-height images taken at bias voltages near the Fermi energy, we compare in Fig. 3E two spectra, one with the Nc-tip positioned above a Co atom (designated hereafter as a top site of the surface; red dot in Fig. 3B) and the other with the Nc-tip above a hollow site of the surface (blue dot in Fig. 3B). As shown in the figure, the exchange field varied among the two sites and with it the position of the low-energy excitation peak and dip. These moved toward zero bias when the exchange field increased, shifting instead toward $e|V| = D$ when the exchange field decreased.

The shift of the low-energy peak (dip) translated into a variation of the tunneling current I by working at biases sufficiently low. In particular, at $|V|$ = 1 mV and z = 80 pm, inelastic excitation to the first excited state was possible

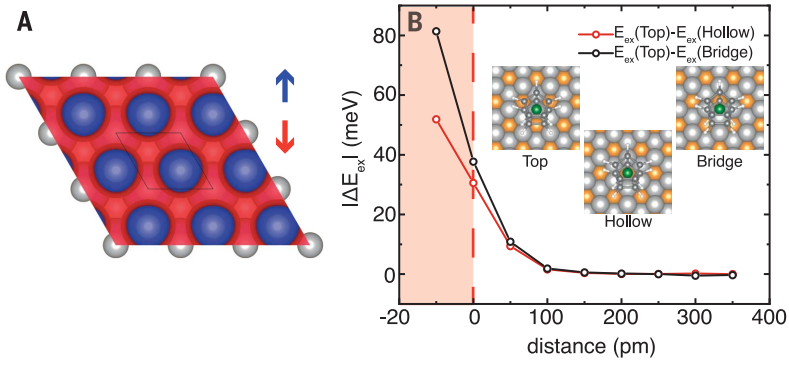


Fig. 4. Computed exchange interaction between Nc and Co. (**A**) Isosurface of the spin density for a Co bilayer. Spin-down (↓) and spin-up (↑) densities are plotted in red (−0.003 Å^{-3}) and blue (+0.003 Å^{-3}), respectively. The unit cell is indicated by a black line and Co atoms are in gray. Spin-up d electrons are mainly located on the Co atoms, whereas spin-down sp electrons are dispersive in nature (*45*, *47*, *50*). The Co atoms had a magnetic moment of 1.76 μ_B, which was mainly carried by the d orbitals (d: 1.81 μ_B, p: −0.04 μ_B, s: −0.01 μ_B). The spatial confinement of sp electrons within the island (*45*, *47*, *50*) was not accounted for. (**B**) Difference in exchange energy ($|\Delta E_{ex}|$) between the top and the hollow positions (red) and between the top and bridge positions (black). The energy difference was computed as a function of tip distance to the Co surface. The filled red area indicates the contact regime where the Nc molecule is covalently bond to the surface. Inset: Junction geometry used in the DFT calculations defining the top, hollow, and bridge site. Atom colors: Co, gray; Cu, orange. Experimentally, the difference in exchange energy between the top and hollow sites is 2 meV when z = 80 pm (see peak/dip splittings in Fig. 3E).

only when the Nc-tip was placed above the top site; above the hollow site, this channel was closed. The ratio of $I_{top}/I_{hollow} \approx 3$ (Fig. 3F) produced a contrast in the constant-height image. At increased absolute bias ($|V| > 5$ mV), I_{top}/I_{hollow} was reduced to 1.25, which led to a loss of contrast in the constant-height image (Fig. 3G). At first approximation, the low-bias image shown in Fig. 3B reflected the spatial dependence of the exchange field at the atomic scale [for completeness, fig. S7, C and D, in the supplementary materials (*30*) presents a low-bias constant-current image]. Alternatively, it could also be possible to plot the exchange field from the spectra as a function of position at the expense of considerably increasing the acquisition time of the image.

To confirm the magnetic origin of the contrast, we computed with DFT the exchange energy $E_{ex} = E_P - E_{AP}$ by varying the distance between the Nc-tip and the Co surface (surface spin density is presented in Fig. 4A). Three locations were investigated, corresponding to an Nc-tip laterally positioned above the surface with its Ni atom centered above a top, hollow, or bridge site of the surface (inset of Fig. 4B). Just before the contact formation between Nc and the surface, which is the distance interval explored in the experiment, the exchange energy was markedly different between these sites (Fig. 4B) because the local character of the *d* electrons starts imprinting a lateral corrugation to the interaction. The exchange field can then be expected to change when moving the Nc-tip above the surface, in qualitative agreement with our experimental findings of Fig. 3B. We stress that for a quantitative comparison, which is beyond the scope of the present study, the noncollinearity among magnetic moments of Co and Nc should be taken into account.

The spin excitation spectrum of an Nc molecule attached to the apex of an STM tip can be used to probe the magnetism of an adsorbate and of a surface with atomic-scale resolution. Magnetic information is gathered through the simultaneous measurement of the exchange field across the vacuum gap, as in pioneering magnetic exchange-force microscopy experiments (*15*, *56*), and of the sample spin polarization at the Fermi level. Unlike conventional spin-polarized STM, the sample spin polarization is determined with minimal influence of the probe on the system owing to the well-characterized Nc-tip apex. A large variety of magnetic systems can be investigated, ranging from systems having resolvable magnetic quantum states (*28*, *42*) to systems having a magnetic moment but nonresolvable quantum states (as shown here). The latter could include single atoms and organometallic molecules on magnetic surfaces or surfaces with complex magnetic structures. The visualization of complex spin textures should benefit from an external magnetic field, making it possible to experimentally determine the sign of the magnetic exchange interaction (*20*, *42*). Minor drawbacks of the technique are the tip-related patterns in the images, which can be corrected given tip-status knowledge, and the possible back action by the Nc-tip on the sample.

REFERENCES AND NOTES

1. A. F. Otte *et al.*, *Phys. Rev. Lett.* **103**, 107203 (2009).
2. N. Tsukahara *et al.*, *Phys. Rev. Lett.* **106**, 187201 (2011).
3. N. Néel *et al.*, *Phys. Rev. Lett.* **107**, 106804 (2011).
4. Y.-S. Fu, Q.-K. Xue, R. Wiesendanger, *Phys. Rev. Lett.* **108**, 087203 (2012).
5. F. Meier, L. Zhou, J. Wiebe, R. Wiesendanger, *Science* **320**, 82–86 (2008).
6. A. A. Khajetoorians, J. Wiebe, B. Chilian, R. Wiesendanger, *Science* **332**, 1062–1064 (2011).
7. A. A. Khajetoorians *et al.*, *Phys. Rev. Lett.* **106**, 037205 (2011).
8. C. F. Hirjibehedin, C. P. Lutz, A. J. Heinrich, *Science* **312**, 1021–1024 (2006).
9. X. Chen *et al.*, *Phys. Rev. Lett.* **101**, 197208 (2008).
10. S. Loth *et al.*, *Nat. Phys.* **6**, 340–344 (2010).
11. S. Yan *et al.*, *Sci. Adv.* **3**, e1603137 (2017).
12. M. Ternes, *New J. Phys.* **17**, 063016 (2015).
13. F. D. Natterer *et al.*, *Nature* **543**, 226–228 (2017).
14. P. Willke *et al.*, *Science* **362**, 336–339 (2018).
15. U. Kaiser, A. Schwarz, R. Wiesendanger, *Nature* **446**, 522–525 (2007).
16. J. Bork *et al.*, *Nat. Phys.* **7**, 901–906 (2011).
17. R. Schmidt *et al.*, *Phys. Rev. Lett.* **106**, 257202 (2011).
18. S. Yan, D.-J. Choi, J. A. J. Burgess, S. Rolf-Pissarczyk, S. Loth, *Nat. Nanotechnol.* **10**, 40–45 (2015).
19. D.-J. Choi *et al.*, *Nano Lett.* **16**, 6298–6302 (2016).
20. M. Muenks, P. Jacobson, M. Ternes, K. Kern, *Nat. Commun.* **8**, 14119 (2017).
21. K. Yang *et al.*, *Phys. Rev. Lett.* **122**, 227203 (2019).
22. L. Gross, F. Mohn, N. Moll, P. Liljeroth, G. Meyer, *Science* **325**, 1110–1114 (2009).
23. C. Weiss *et al.*, *Phys. Rev. Lett.* **105**, 086103 (2010).
24. C. L. Chiang, C. Xu, Z. Han, W. Ho, *Science* **344**, 885–888 (2014).
25. C. Wagner *et al.*, *Phys. Rev. Lett.* **115**, 026101 (2015).
26. J. Guo *et al.*, *Science* **352**, 321–325 (2016).
27. H. Mönig *et al.*, *Nat. Nanotechnol.* **13**, 371–375 (2018).
28. M. Ormaza *et al.*, *Nano Lett.* **17**, 1877–1882 (2017).
29. M. Ormaza *et al.*, *Nat. Commun.* **8**, 1974 (2017).
30. See supplementary materials for more details.
31. N. Bachellier *et al.*, *Phys. Rev. B* **93**, 195403 (2016).
32. C. Rubio-Verdú *et al.*, *Commun. Phys.* **1**, 15 (2018).
33. A. J. Heinrich, J. A. Gupta, C. P. Lutz, D. M. Eigler, *Science* **306**, 466–469 (2004).
34. I. G. Rau *et al.*, *Science* **344**, 988–992 (2014).
35. B. W. Heinrich, L. Braun, J. I. Pascual, K. J. Franke, *Nat. Phys.* **9**, 765–768 (2013).
36. G. E. Pacchioni *et al.*, *Phys. Rev. B Condens. Matter Mater. Phys.* **91**, 235426 (2015).
37. T. Balashov, A. F. Takács, W. Wulfhekel, J. Kirschner, *Phys. Rev. Lett.* **97**, 187201 (2006).
38. F. Delgado, J. J. Palacios, J. Fernández-Rossier, *Phys. Rev. Lett.* **104**, 026601 (2010).
39. F. D. Novaes, N. Lorente, J.-P. Gauyacq, *Phys. Rev. B Condens. Matter Mater. Phys.* **82**, 155401 (2010).
40. A. N. Pasupathy *et al.*, *Science* **306**, 86–89 (2004).
41. K. von Bergmann, M. Ternes, S. Loth, C. P. Lutz, A. J. Heinrich, *Phys. Rev. Lett.* **114**, 076601 (2015).
42. G. Czap *et al.*, *Science* **364**, 670–673 (2019).
43. B. W. Heinrich, L. Braun, J. I. Pascual, K. J. Franke, *Nano Lett.* **15**, 4024–4028 (2015).
44. K. Tao *et al.*, *Phys. Rev. Lett.* **103**, 057202 (2009).
45. L. Diekhöner *et al.*, *Phys. Rev. Lett.* **90**, 236801 (2003).
46. O. Pietzsch, A. Kubetzka, M. Bode, R. Wiesendanger, *Phys. Rev. Lett.* **92**, 057202 (2004).
47. O. Pietzsch *et al.*, *Phys. Rev. Lett.* **96**, 237203 (2006).
48. M. V. Rastei *et al.*, *Phys. Rev. Lett.* **99**, 246102 (2007).
49. F. Huang, M. T. Kief, G. J. Mankey, R. F. Willis, *Phys. Rev. B Condens. Matter* **49**, 3962–3971 (1994).
50. H. Oka *et al.*, *Science* **327**, 843–846 (2010).
51. C. Iacovita *et al.*, *Phys. Rev. Lett.* **101**, 116602 (2008).
52. S. Schmaus *et al.*, *Nat. Nanotechnol.* **6**, 185–189 (2011).
53. M. Eltschka *et al.*, *Nano Lett.* **14**, 7171–7174 (2014).
54. L. Gross *et al.*, *Phys. Rev. Lett.* **107**, 086101 (2011).
55. B. W. Heinrich, M. V. Rastei, D.-J. Choi, T. Frederiksen, L. Limot, *Phys. Rev. Lett.* **107**, 246801 (2011).
56. J. Grenz, A. Köhler, A. Schwarz, R. Wiesendanger, *Phys. Rev. Lett.* **119**, 047205 (2017).

ACKNOWLEDGMENTS

Funding: L.L. acknowledges support by the Agence Nationale de la Recherche (grant nos. ANR-13-BS10-0016, ANR-15-CE09-0017, ANR-11-LABX-0058 NIE, and ANR-10-LABX-0026 CSC). M.T. acknowledges support by the Heisenberg Program (grant no. TE 833/2-1) of the German Research Foundation. N.L. acknowledges support by the Spanish MICINN (grant no. RTI2018-097895-B-C44). N.L. and R.R. acknowledge support by the EU H2020 FET open project MeMo (grant no. 766864). L.L. acknowledges F. Scheurer and V. Speisser for technical assistance. We have used VESTA to plot geometrical structures and isosurfaces (https://jp-minerals.org/vesta/en/download.html). **Author contributions:** Experiments were performed by B.V., N.B., L.G., M.O., and L.L. and calculations were performed by P.A., R.R., M.-L.B., M.T., and N.L. **Competing interests:** The authors declare no competing financial interests. **Data and materials availability:** All data are available in the main text or the supplementary materials.

SUPPLEMENTARY MATERIALS

science.sciencemag.org/content/366/6465/623/suppl/DC1
Materials and Methods
Supplementary Text
Figs. S1 to S8
References (*57*–*67*)

26 April 2019; accepted 8 October 2019
10.1126/science.aax8222

NEUROSCIENCE

Coupled electrophysiological, hemodynamic, and cerebrospinal fluid oscillations in human sleep

Nina E. Fultz[1,2], Giorgio Bonmassar[2,3], Kawin Setsompop[2,3], Robert A. Stickgold[4,5], Bruce R. Rosen[2,3], Jonathan R. Polimeni[2,3], Laura D. Lewis[1,2]*

Sleep is essential for both cognition and maintenance of healthy brain function. Slow waves in neural activity contribute to memory consolidation, whereas cerebrospinal fluid (CSF) clears metabolic waste products from the brain. Whether these two processes are related is not known. We used accelerated neuroimaging to measure physiological and neural dynamics in the human brain. We discovered a coherent pattern of oscillating electrophysiological, hemodynamic, and CSF dynamics that appears during non–rapid eye movement sleep. Neural slow waves are followed by hemodynamic oscillations, which in turn are coupled to CSF flow. These results demonstrate that the sleeping brain exhibits waves of CSF flow on a macroscopic scale, and these CSF dynamics are interlinked with neural and hemodynamic rhythms.

Sleep is crucial for both high-level cognitive processing and also basic maintenance and restoration of physiological function. During human non–rapid eye movement (NREM) sleep, the electroencephalogram (EEG) exhibits low-frequency (<4 Hz) oscillatory dynamics that support memory and neural computation (*1*–*8*). In addition, functional magnetic resonance imaging (fMRI) studies measuring blood oxygen level–dependent (BOLD) signals have demonstrated widespread hemodynamic alterations during NREM sleep (*9*–*15*). Sleep is also associated with increased interstitial fluid volume and clearance of metabolic waste products into the CSF (*16*), and clearance is stronger in sleep with more low-frequency EEG oscillations (*17*). Why these diverse physiological processes co-occur in this state of low arousal is not known. In particular, it remains unclear how CSF dynamics change during sleep and how they relate to the major changes in neural activity and hemodynamics.

We simultaneously measured BOLD fMRI dynamics, EEG, and CSF flow during human sleep. To achieve high–temporal-resolution imaging, we acquired fMRI data at fast rates [repetition time (TR) < 400 ms]. While fMRI is often used to detect local oxygenation changes, fast acquisition paradigms also enable detection of fluid inflow: Fresh fluid arriving at the edge of the imaging volume has high signal intensity because it has not yet experienced radiofrequency pulses (fig. S1). By placing the boundary edge of the imaging volume at the fourth ventricle (Fig. 1A), CSF flow into the brain was detected as increased signal in the lower slices (Fig. 1B), allowing us to measure dynamics of CSF flow simultaneously with BOLD fMRI. We combined this imaging with simultaneous EEG (n = 13 participants) and identified continuous segments of clear stable wake or NREM sleep with low motion (fig. S2 and materials and methods) to enable analysis of continuous low-frequency dynamics.

We first investigated whether sleep was associated with distinct CSF flow dynamics (Fig. 1, C to E). During wakefulness, the CSF signal exhibited a small-amplitude rhythm synchronized to the respiratory signal at ~0.25 Hz (Fig. 1, E and G), consistent with previous studies (*18*, *19*). By contrast, during NREM sleep, we observed a large oscillation in the CSF signal at 0.05 Hz (Fig. 1, E and G). We analyzed this CSF signal across all sleep segments, confirming that identified sleep segments exhibited low-frequency EEG signatures of NREM sleep (Fig. 1F). We found a 5.52-dB increase in the CSF signal peaking at 0.05 Hz during sleep (Fig. 1, G and H, and fig. S2) [95% confidence interval (CI) = (2.33, 7.67); P = 0.003, signed-rank test], suggesting that large waves of CSF inflow occur approximately every 20 s. We additionally analyzed nearby non-CSF regions of interest (ROIs) with matched slice positioning and saw no such effect [change = −0.03 dB, CI = (−2.7, 1.3); P = 0.003 for difference, signed-rank test], suggesting that this sleep-associated pattern was specifically driven by physiological signals in the ventricle (Fig. 1I).

Because inflow signals are caused by fluid flowing into the acquisition volume, CSF flow signals should be brightest in edge slices and decay as fluid passes into central slices (Fig. 2, A and B, and fig. S1). We indeed observed a gradient of signal amplitudes across the slices (Fig. 2, C and D). Some large inflow events exhibited equally bright amplitudes across the lower slices (Fig. 2D), suggesting the CSF flow velocity had exceeded the imaging critical velocity (11.4 mm/s for slice 2). Together, these results identified a large-amplitude pulsatile flow of CSF at 0.05 Hz that appears during NREM sleep.

We next examined whether these slow macroscopic CSF oscillations were linked to hemodynamic signals. Previous studies have proposed microscopic arterial pulsation, corresponding to the ~1-Hz cardiac cycle, as a mechanism for driving interstitial fluid flow (*20*–*23*). To test what might generate the much slower macroscopic CSF rhythm we observed, we analyzed the changes in BOLD signal during sleep. We observed an increase in BOLD signal amplitude in the cortical gray-matter fMRI signal during sleep, as compared with wakefulness (Fig. 3A versus B and C) [mean = 3.28 dB; CI = (0.09, 6.54); P = 0.032, signed-rank test], consistent with previous reports of low-frequency BOLD fluctuations during sleep (*9*, *10*, *24*). Furthermore, the CSF signal was tightly temporally coupled to the cortical gray-matter BOLD oscillation during sleep (Fig. 3, A and B), exhibiting a strong anticorrelation (fig. S3) (maximal r = −0.48 at lag 2 s, P < 0.001, shuffling).

This anticorrelation suggested a possible alternation of blood flow and CSF flow during sleep. We hypothesized that the BOLD oscillations corresponded to an oscillation in cerebral blood volume and that, because of constant intracranial volume, more CSF flows into the head when less volume is occupied by the blood (*25*, *26*). This hypothesis predicts that the CSF signal should approximately match the negative derivative of the BOLD oscillation, after setting negative values to zero (materials and methods). Consistent with this hypothesis, the CSF time series and the thresholded derivative BOLD signals were strongly correlated (Fig. 3, D and E) (maximal r = 0.59 at lag −1.8 s; P < 0.001, shuffling).

We next examined whether neural activity was linked to these coupled hemodynamic and CSF oscillations during sleep. In conventional fMRI, the BOLD response is elicited by neural activity, which drives flow of oxygen-rich blood (*27*, *28*), and EEG oscillations are associated with hemodynamic signals (*29*–*32*). We therefore hypothesized that the large, slow-delta (0.2 to 4 Hz) electrophysiologic oscillations characteristic of NREM sleep could be coupled to oscillations in blood volume and, in turn, displacement effects on CSF flow. We analyzed the instantaneous amplitude of slow-delta EEG relative to the peak of the CSF waves and found that neural, BOLD, and CSF waves were coupled (Fig. 4, A to C, and fig. S4). The neural waves preceded the CSF waves, with a peak in slow-delta EEG occurring 6.4 s before the CSF peak (peak amplitude = 21%, P < 0.001, shuffling). We calculated the best-fit impulse response between the EEG and CSF (Fig. 4D)

[1]Department of Biomedical Engineering, Boston University, Boston, MA 02215, USA. [2]Athinoula A. Martinos Center for Biomedical Imaging, Massachusetts General Hospital, Boston, MA 02129, USA. [3]Department of Radiology, Harvard Medical School, Boston, MA 02115, USA. [4]Department of Psychiatry, Beth Israel Deaconess Medical Center, Boston, MA 02215, USA. [5]Department of Psychiatry, Harvard Medical School, Boston, MA 02115, USA.
*Corresponding author. Email: ldlewis@bu.edu

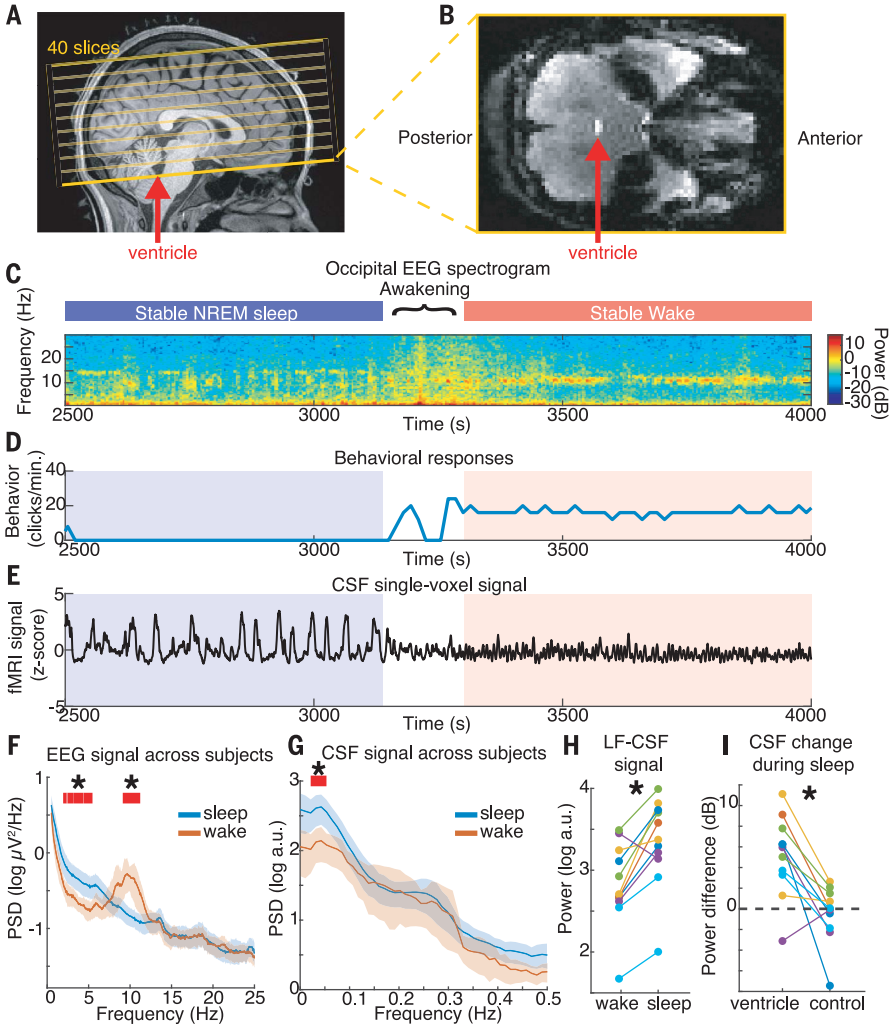


Fig. 1. Large oscillations in CSF signals appear in the fourth ventricle during sleep. (**A**) Example scan positioning. Thick yellow line: position of the functional image relative to the anatomy. The bottom edge intersects with the fourth ventricle (red arrow), allowing CSF inflow to be measured. A subset of the 40 acquired slices are displayed. (**B**) Example functional image from the bottom slice. Inflow through the ventricle is detected as a bright signal (red arrow). (**C**) EEG spectrogram from this individual shows long periods of NREM sleep and wake (~10 Hz occipital alpha). (**D**) Behavioral responses from this individual. (**E**) Time series of a single CSF voxel (smoothed with 10-TR kernel) shows large, slow dynamics in sleep that subside during wakefulness. (**F**) Mean power spectral density (PSD) of occipital EEG confirms slow-delta power in sleep, as opposed to high alpha power in wake (n = 13 participants sleep; 11 participants wake). (**G**) PSD of CSF signal shows increased 0.05 Hz power during sleep (n = 13 participants sleep; 11 participants wake). Shaded regions denote 95% CIs; red lines and asterisks mark non-overlapping CIs. (**H**) Low-frequency (LF, 0 to 0.1 Hz) CSF power increased during sleep (n = 11 participants for pairwise comparison). a.u., arbitrary units. (**I**) This sleep-selective power increase was specific to the ventricle ROI and not observed in a neighboring size-matched control ROI (n = 11 participants).

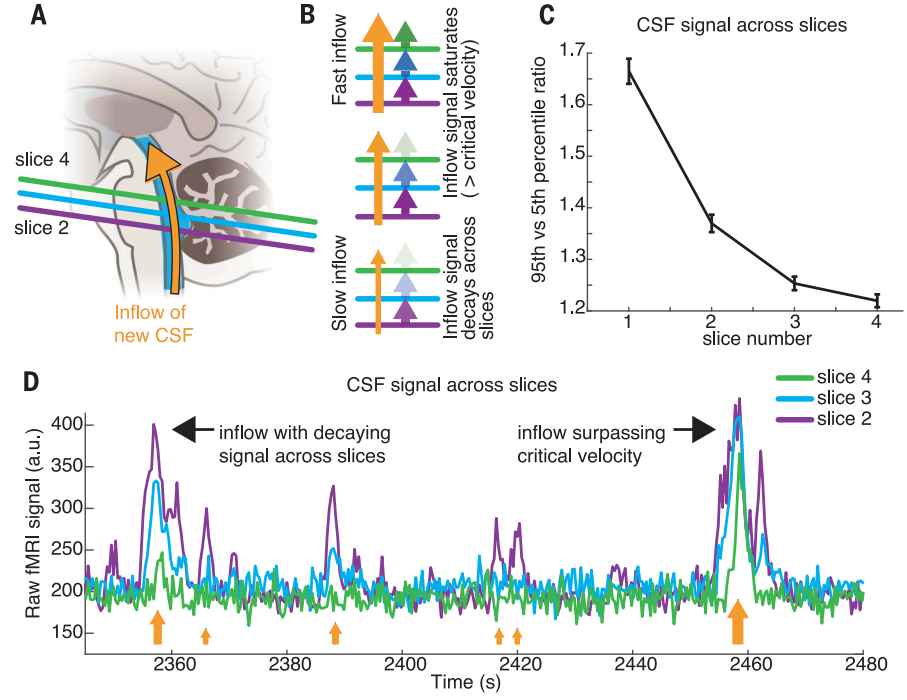


Fig. 2. Ventricle signals correspond to a ~0.05-Hz pulsatile inflow of CSF. (**A**) Schematic of acquisition. New CSF flowing into the imaging volume will generate bright signals. (**B**) Inflow signals will be largest in the bottom slice and decrease in amplitude inwards. If flow exceeds the critical velocity, then CSF in the bottom slice is completely replaced, and signal amplitudes are large in inner slices as well. (**C**) Mean amplitude across slices decays in ascending slices. Error bars are standard error across all sleep segments, with the ROI present in four contiguous slices (n = 129 segments, 11 participants). (**D**) Example time series from the bottom slices of the imaging volume in the fourth ventricle demonstrates the largest signal in the lower slices (e.g., second) and smaller signals in higher slices (e.g., fourth). Orange arrows schematically illustrate flow velocity (larger arrows denote higher velocity), and black arrows point out individual events.

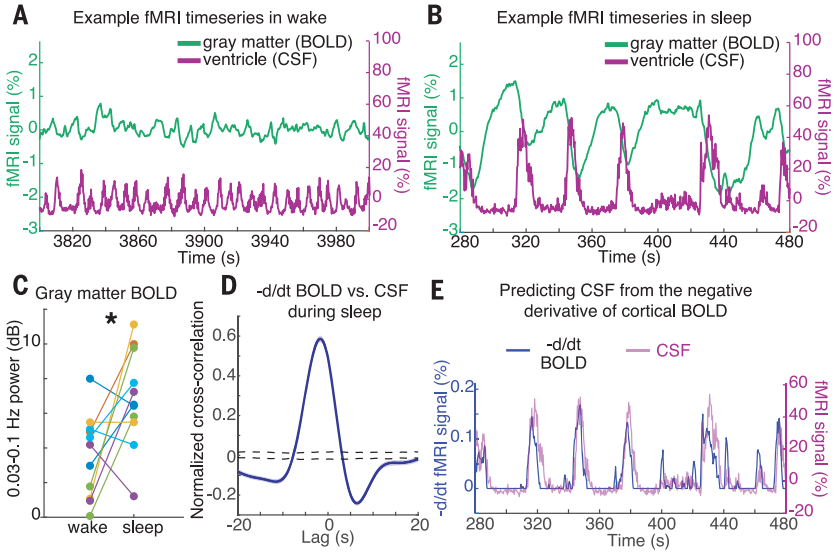


Fig. 3. CSF flow oscillations are anticorrelated to a hemodynamic oscillation in the cortical gray matter that appears during sleep, with CSF flow increasing when blood volume decreases. (**A**) Example time series of the cortical gray-matter BOLD signal and the mean CSF signal from one participant. During wake, signals are low-amplitude and synchronized to respiration (0.25 Hz). (**B**) During sleep, a large-amplitude BOLD oscillation appears, and its time course is coupled to the ventricle CSF signal (~0.05 Hz). (**C**) Mean cortical gray-matter BOLD signal power increases during sleep (n = 11 participants for pairwise test). (**D**) Mean cross-correlation between the zero-thresholded negative derivative of BOLD and CSF signals shows strong correlation (n = 176 segments, 13 participants). The shaded blue region indicates the standard error across segments; the black dashed line denotes the 95% interval of shuffled distribution. (**E**) Example time series showing the correlation, suggesting that CSF flows up the fourth ventricle when cerebral blood volume decreases.

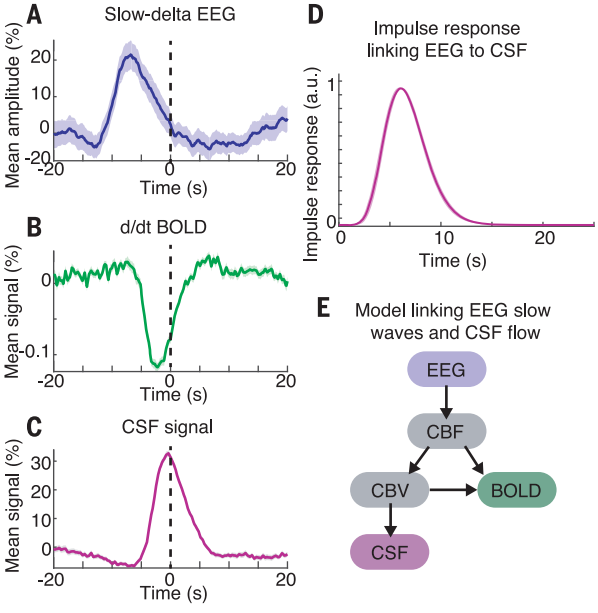


Fig. 4. EEG slow-delta waves are coupled to and precede BOLD and CSF oscillations. (**A**) Mean amplitude envelope of slow-delta EEG, (**B**) mean derivative of BOLD signals, and (**C**) mean CSF signal, all locked to the peaks of CSF waves during sleep. The shaded region represents the standard error across peak-locked trials (n = 123 peaks). (**D**) Calculated impulse response of the CSF signal to the EEG envelope shows a time course similar to that of previously established hemodynamic models. Shading indicates standard deviation across model folds. (**E**) Diagram of model linking the time course of neural activity to CSF flow. Variables include CBF and cerebral blood volume (CBV).

and found that convolving the EEG with this impulse response yielded a significant prediction of CSF dynamics (fig. S5A) (zero-lag r = 0.23, cross-validated r = 0.22 ± 0.07). To examine whether this EEG-CSF coupling was specifically linked to the appearance of CSF waves during sleep, we tested how well the EEG predicted CSF dynamics in the segments with the largest CSF waves. Performance was higher in segments with larger CSF waves (fig. S5, B and C) (zero-lag r = 0.54, P < 0.001, shuffling), suggesting that the EEG was more strongly linked to CSF in the sleep segments richest in CSF waves.

The coherent dynamics of the EEG, BOLD, and CSF signals thus exhibited a specific timing sequence, with neural rhythms preceding subsequent BOLD and CSF waves. To test whether these observed correlations and delay patterns could arise from biophysical mechanisms, we constructed a computational model using established models of hemodynamic coupling (Fig. 4E and fig. S6). We extracted the envelope of slow-delta EEG, expected to correlate with decreases in cerebral blood flow (CBF) signal because of its associated suppression of neural activity (*2*). The neural oscillation was then used to predict the time courses of blood flow, blood volume, and CSF (*33*, *34*). The model first used previously reported physiological parameters (*35*), with no additional parameter fitting, to test whether our observations were consistent with established biophysical coupling between these signals. This model performed as well as the best-fit impulse response [zero-lag R = 0.22; CI across segments = (0.16, 0.27); P < 0.001, shuffling] (fig. S6 and S7). The model prediction was significantly larger than the maximal correlation between the original EEG envelope and CSF across all lags (maximal r = 0.15, P < 0.05), demonstrating that our data were consistent with biophysical coupling between neural activity, hemodynamics, and CSF.

We conclude that human sleep is associated with large coupled low-frequency oscillations in neuronal activity, blood oxygenation, and CSF flow. Although electrophysiological slow waves are known to play important roles in cognition (*1*), our results suggest that they may also be linked to the physiologically restorative effects of sleep, as slow neural activity is followed by brain-wide pulsations in blood volume and CSF flow.

These results address a key missing link in the neurophysiology of sleep. The macroscopic changes in CSF flow that we identified are expected to alter waste clearance, as pulsatile fluid dynamics can increase mixing and diffusion (*20*, *21*, *36*). Neurovascular coupling has been proposed to contribute to clearance (*37*), but why it would cause higher clearance rates during sleep was not known. Our study suggests slow neural and hemodynamic oscillations

as a possible contributor to this process, in concert with other physiological factors. Studies in animals could next test for causal relationships between these neural and physiological rhythms.

Our identification of sleep-associated CSF fluid dynamics also suggests a potential biomarker to be explored in clinical conditions associated with sleep disturbance. Memory impairment in aging is associated with suppressed slow waves (*38*); our model suggests that this slow-wave loss would, in turn, be associated with decreased CSF flow. Furthermore, our results hint at a potential bridge between recent findings that tau CSF levels and amyloid beta depend on sleep and neural activity (*39*–*41*) and that oscillatory neural activity leads to reduced tau (*42*)—coherent neural activity might signal higher protein aggregate clearance. Taken together, our results identify waves of CSF flow that appear during sleep and show that slow rhythms in neural activity are interlinked with these CSF waves, with hemodynamic oscillations as an intermediate mechanism through which these processes are coupled.

REFERENCES AND NOTES

1. S. Diekelmann, J. Born, *Nat. Rev. Neurosci.* **11**, 114–126 (2010).
2. M. Steriade, A. Nuñez, F. Amzica, *J. Neurosci.* **13**, 3252–3265 (1993).
3. M. Massimini, R. Huber, F. Ferrarelli, S. Hill, G. Tononi, *J. Neurosci.* **24**, 6862–6870 (2004).
4. L. Marshall, H. Helgadóttir, M. Mölle, J. Born, *Nature* **444**, 610–613 (2006).
5. A. Destexhe, D. Contreras, in *Sleep and Anesthesia*, A. Hutt, Ed. (Springer, 2011), p. 258.
6. E. J. W. Van Someren, Y. D. Van Der Werf, P. R. Roelfsema, H. D. Mansvelder, F. H. L. da Silva, *Prog. Brain Res.* **193**, 3–15 (2011).
7. V. V. Vyazovskiy, K. D. Harris, *Nat. Rev. Neurosci.* **14**, 443–451 (2013).
8. B. O. Watson, D. Levenstein, J. P. Greene, J. N. Gelinas, G. Buzsáki, *Neuron* **90**, 839–852 (2016).
9. M. Fukunaga *et al.*, *Magn. Reson. Imaging* **24**, 979–992 (2006).
10. S. G. Horovitz *et al.*, *Hum. Brain Mapp.* **29**, 671–682 (2008).
11. A. Mitra, A. Z. Snyder, E. Tagliazucchi, H. Laufs, M. E. Raichle, *eLife* **4**, e10781 (2015).
12. M. Boly *et al.*, *Proc. Natl. Acad. Sci. U.S.A.* **109**, 5856–5861 (2012).
13. T. T. Dang-Vu *et al.*, *Proc. Natl. Acad. Sci. U.S.A.* **105**, 15160–15165 (2008).
14. C. Kaufmann *et al.*, *Brain* **129**, 655–667 (2006).
15. L. J. Larson-Prior *et al.*, *Proc. Natl. Acad. Sci. U.S.A.* **106**, 4489–4494 (2009).
16. L. Xie *et al.*, *Science* **342**, 373–377 (2013).
17. L. M. Hablitz *et al.*, *Sci. Adv.* **5**, eaav5447 (2019).
18. S. Dreha-Kulaczewski *et al.*, *J. Neurosci.* **35**, 2485–2491 (2015).
19. V. Kiviniemi *et al.*, *J. Cereb. Blood Flow Metab.* **36**, 1033–1045 (2016).
20. D. Schley, R. Carare-Nnadi, C. P. Please, V. H. Perry, R. O. Weller, *J. Theor. Biol.* **238**, 962–974 (2006).
21. J. J. Iliff *et al.*, *J. Neurosci.* **33**, 18190–18199 (2013).
22. H. Mestre *et al.*, *Nat. Commun.* **9**, 4878 (2018).
23. I. F. Harrison *et al.*, *eLife* **7**, e34028 (2018).
24. P. S. Özbay *et al.*, *Neuroimage* **176**, 541–549 (2018).
25. A. Scouten, R. T. Constable, *Magn. Reson. Med.* **59**, 308–315 (2008).
26. S. K. Piechnik, J. Evans, L. H. Bary, R. G. Wise, P. Jezzard, *Magn. Reson. Med.* **61**, 579–586 (2009).
27. S. Ogawa, T. M. Lee, A. R. Kay, D. W. Tank, *Proc. Natl. Acad. Sci. U.S.A.* **87**, 9868–9872 (1990).
28. K. K. Kwong *et al.*, *Proc. Natl. Acad. Sci. U.S.A.* **89**, 5675–5679 (1992).
29. N. K. Logothetis, J. Pauls, M. Augath, T. Trinath, A. Oeltermann, *Nature* **412**, 150–157 (2001).
30. B. J. He, M. E. Raichle, *Trends Cogn. Sci.* **13**, 302–309 (2009).
31. C. Mateo, P. M. Knutsen, P. S. Tsai, A. Y. Shih, D. Kleinfeld, *Neuron* **96**, 936–948.e3 (2017).
32. M. L. Schölvinck, A. Maier, F. Q. Ye, J. H. Duyn, D. A. Leopold, *Proc. Natl. Acad. Sci. U.S.A.* **107**, 10238–10243 (2010).
33. R. B. Buxton, K. Uludağ, D. J. Dubowitz, T. T. Liu, *Neuroimage* **23** (suppl. 1), S220–S233 (2004).
34. K. J. Friston, A. Mechelli, R. Turner, C. J. Price, *Neuroimage* **12**, 466–477 (2000).
35. A. B. Simon, R. B. Buxton, *Neuroimage* **116**, 158–167 (2015).
36. M. Asgari, D. de Zélicourt, V. Kurtcuoglu, *Sci. Rep.* **6**, 38635 (2016).
37. A. K. Diem, R. O. Carare, R. O. Weller, N. W. Bressloff, *PLOS ONE* **13**, e0205276 (2018).
38. B. A. Mander *et al.*, *Nat. Neurosci.* **16**, 357–364 (2013).
39. J. K. Holth *et al.*, *Science* **363**, 880–884 (2019).
40. E. Shokri-Kojori *et al.*, *Proc. Natl. Acad. Sci. U.S.A.* **115**, 4483–4488 (2018).
41. J.-E. Kang *et al.*, *Science* **326**, 1005–1007 (2009).
42. H. F. Iaccarino *et al.*, *Nature* **540**, 230–235 (2016).
43. N. E Fultz *et al.*, Sleep-wake imaging ROI time series. Figshare (2019); doi: 10.6084/m9.figshare.9992054.

ACKNOWLEDGMENTS

We thank T. Witzel for contributing to the imaging, J. Voigts and C. Robertson for comments, and S. Williams, K. Gupta, and M. Albrecht for assistance. **Funding:** This work was supported by the National Institutes of Health (R00-MH111748, R01-EB019437, P41-EB015896, R01-MH111419, R01-MH048832, R01-EB024343, R01-MH111438, R21-NS106706, S10-RR023043, and S10-OD010759) and the Martinos Center for Biomedical Imaging. **Author contributions:** All authors contributed to experiment design; L.D.L. and N.E.F. collected and analyzed data; L.D.L. wrote the manuscript; and all authors edited the manuscript. **Competing interests:** L.D.L., B.R.R., and J.R.P. are inventors on a provisional patent coversheet. **Data availability:** The ROI and EEG time series reported here are available at Figshare (*43*).

SUPPLEMENTARY MATERIALS

science.sciencemag.org/content/366/6465/628/suppl/DC1
Materials and Methods
Supplementary Text
Figs. S1 to S10
References (*44*–*57*)

View/request a protocol for this paper from *Bio-protocol*.

15 April 2019; accepted 18 September 2019
10.1126/science.aax5440

CELL BIOLOGY

Spontaneous emergence of cell-like organization in *Xenopus* egg extracts

Xianrui Cheng[1]* and James E. Ferrell Jr.[1,2]*

Every daughter cell inherits two things from its mother: genetic information and a spatially organized complement of macromolecular complexes and organelles. The extent to which de novo self-organization, as opposed to inheritance of an already organized state, can suffice to yield functional cells is uncertain. We used *Xenopus laevis* egg extracts to show that homogenized interphase egg cytoplasm self-organizes over the course of ~30 minutes into compartments 300 to 400 micrometers in length that resemble cells. Formation of these cell-like compartments required adenosine triphosphate and microtubule polymerization but did not require added demembranated sperm nuclei with their accompanying centrosomes or actin polymerization. In cycling extracts with added sperm, the compartments underwent multiple cycles of division and reorganization, with mother compartments giving rise to two daughters at the end of each mitotic cycle. These results indicate that the cytoplasm can generate much of the spatial organization and cell cycle function of the early embryo.

If an organism were homogenized, most of us would predict that it would not spontaneously reform its original structure and return to life (*1*). Indeed, organismal development unfolds the body plan in a specific sequence that is not likely to be reproduced by simply mixing its underlying chemical ingredients. However, it is not immediately clear whether the same is to be expected for the cytoplasm of a cell. If a cell is mechanically homogenized, will the resulting cytoplasm remain in the homogenized state?

We used *Xenopus laevis* egg extracts (Fig. 1A) to address this question, in part because *Xenopus* extracts can be prepared without substantial dilution and in part because they have been shown to be remarkably functional (*2*–*9*). Interphase-arrested *Xenopus* extracts were prepared by standard methods (*10*) and supplemented with demembranated *Xenopus* sperm nuclei plus one or more of the following probes to allow visualization of the nucleus, microtubules, endoplasmic reticulum (ER), and mitochondria: green fluorescent protein or mCherry with a nuclear localization signal (GFP-NLS or mCherry-NLS), fluorescently labeled tubulin or SiR-tubulin, ER-Tracker dye, and MitoTracker dye. The resulting extracts were mixed thoroughly and imaged over time in a fluorinated ethylene propylene (FEP)–clad chamber by bright-field and fluorescence microscopy (Fig. 1B).

Over the course of ~30 min, the homogenized extract self-organized into a sheet of 300- to 400-μm compartments that resembled cells (Fig. 1C and movies S1 and S2). The added sperm nuclei migrated during compartment formation, and their initial localization did not entirely determine the final pattern (movie S2). Pattern formation did not appear to be coordinated by a propagating spatial signal, because the emergence of compartments across a large 2.6-mm field was approximately synchronous (movie S1). Because interphase-arrested extracts contain cycloheximide, which inhibits protein translation, the pattern formation appeared to be independent of genomic input from the added nuclei or translation of preexisting maternal mRNA.

The localization of the nuclei, microtubules, mitochondria, and ER was reminiscent of that in a typical interphase cell (*11*) (Fig. 1D). The dark gray regions observed in bright-field images contained microtubules, ER, and mitochondria (Fig. 1D). The center of the compartment was populated by a single nucleus or a cluster of nuclei, as indicated by the GFP-NLS or mCherry-NLS signal. Typically, the microtubules were denser around the periphery of the compartments and were organized in a wreath-like structure (Figs. 1, D and E; 2, A to D; 3A; and 4A; and movie S2) that closely resembled the microtubule structures seen in intact *Xenopus* embryos (*4*). The ER and mitochondria were denser near the centers of the compartments (Figs. 1, D to F, 3A, and 4A; fig. S3; and movie S2). Higher-magnification confocal microscopy corroborated these findings and allowed the evolving texture of the microtubules and ER to be better appreciated (Fig. 1E and fig. S2).

The border zones between the cell-like compartments were largely free of microtubules and organelles (Fig. 1D and movies S2 and S3). Typically, the borders were ~40 μm wide, as measured by the distance between neighboring microtubule structures (Fig. 1G). Overall, the borders constituted 25 ± 3% (mean ± SD, from six independent experiments) of the total cross-sectional area. Organelles initially extended to near the tips of the microtubules but, upon extended incubation, moved toward the center, so that the distance between adjacent organelle compartments became greater than the distance between the outermost parts of the microtubule structures (quantified in Fig. 1G for microtubules versus ER). There was no apparent correlation between the size of a compartment and the size of the border surrounding it (Fig. 1G, right). The simplest hypothesis is that the border regions consist of cytosol—cytoplasm largely depleted of organelles and microtubules—although it is possible that they are enriched or depleted in particular cytosolic components. Sometimes a dark boundary line in the middle of the border regions could be seen in the bright-field images (Fig. 1D and fig. S1). This boundary line weakly stained with ER-Tracker, MitoTracker, and a plasma membrane stain (fig. S1). In addition, bright foci of microtubules could often be seen at the junctions between the cell-like units (Fig. 1E and fig. S2). Similar junctional complexes have been reported for extracts with intact actin filaments (*5*, *6*), but in the experiments shown here, actin polymerization was suppressed by addition of cytochalasin B (vide infra).

The self-organization of the extract raised the question of which cytoplasmic constituents mediate the process. Sperm possess centrosomes, and the earliest step in the self-organization appeared to be the formation of large microtubule asters from the centrosomes of the added sperm (Fig. 1E, fig. S2, and movie S2). The asters were always detectable by the first frame of the video, 5 to 10 min after the extracts were taken off ice. We therefore tested whether the added sperm, with their accompanying centrosomes, were required for pattern formation. To our surprise, grossly normal cell-like compartments still formed in the absence of sperm (Fig. 2, A and B; fig. S3; and movie S4). Even though some maternal nuclear DNA might be expected to be present in the no-sperm extracts, in the vast majority of the self-organizing fields, no DNA was detected by Hoechst staining (fig. S4). Compared with sperm-supplemented extracts, extracts without sperm took longer to form cell-like compartments, and the initial dynamics of pattern formation were distinctly different—the ultimate wreath-like microtubule structures did not emerge from asters. Nevertheless, the final patterns and compartment appearances in these two types of extract were almost the same (Fig. 2, A and B, and movie S4). Therefore, the self-organization phenomenon does not require the presence of a centrosome or chromatin and does not need to begin from a large microtubule aster.

In the absence of added sperm, the first step in pattern formation appeared to be a local depletion of microtubules (Fig. 2C, fig. S5, and

[1]Department of Chemical and Systems Biology, Stanford University School of Medicine, Stanford, CA 94305-5174, USA. [2]Department of Biochemistry, Stanford University School of Medicine, Stanford, CA 94305-5307, USA.
*Corresponding author. Email: xianrui.cheng@gmail.com (X.C.); james.ferrell@stanford.edu (J.E.F.)

movie S5). The depleted zones began as circular, tubulin-depleted regions with a small bright focus of microtubules at their centers (Fig. 2C and fig. S5), and the depleted zones ultimately extended and fused to produce the final border region, with the small foci of microtubules persisting at junctions between the compartments. As mentioned above, similar junctional microtubule complexes could also be seen in extracts with added sperm (Fig. 1E and fig. S2), and they appeared at approximately the same time as they did in the no-sperm extracts (movie S5). They were detected by both labeled tubulin and SiR-tubulin, indicating that they are not an artifact

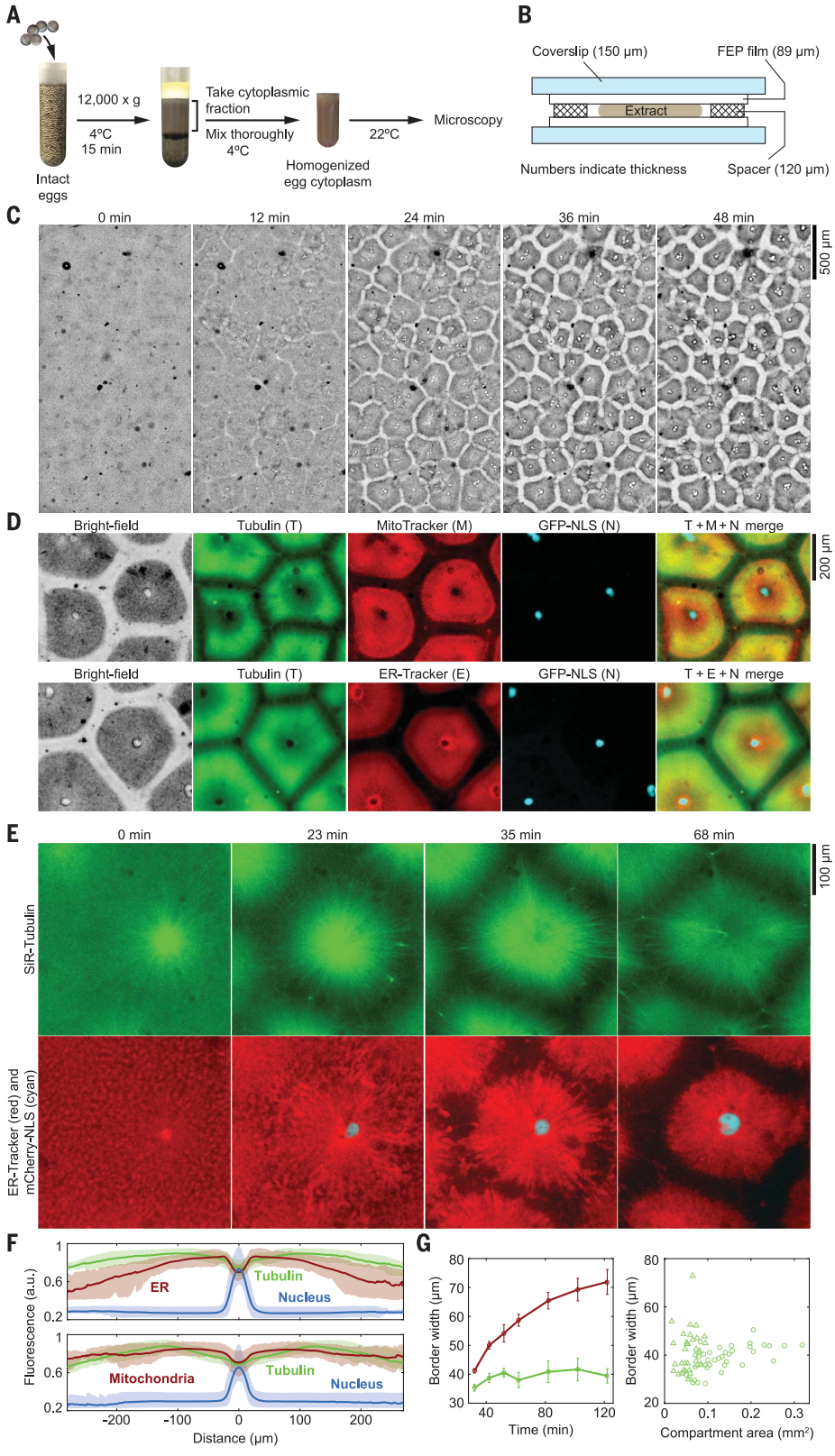


Fig. 1. Homogenized *X. laevis* egg extracts self-organize into cell-like compartments. (**A**) Schematic diagram of the experimental procedure. (**B**) The design of the chamber used to image extracts. (**C**) Bright-field microscopy images showing that homogenized *X. laevis* egg cytoplasmic extracts spontaneously organized into cell-like compartments in a multimillimeter-scale field. Pattern formation dynamics in bright-field images as well as tubulin and ER channels are presented in movies S1 and S2. (**D**) Spatial organization of microtubules, ER, nuclei, and mitochondria in the cell-like compartments, visualized with added HiLyte 647–labeled porcine tubulin (T), ER-Tracker Red (E), GFP-NLS (N), and MitoTracker Red CMXRos (M). Pattern formation dynamics are presented in movie S3. The still images shown in (D) are from the last frame of movie S3, at 60.6 min after imaging began. (**E**) Confocal images of tubulin (top) and a merge of the ER and nuclear channels (bottom) during pattern formation. SiR-tubulin, a docetaxel derivative, was used to monitor microtubules because of its superior signal-to-background ratio. Control experiments verified that the same basic features revealed by SiR-tubulin, including asters and junctional complexes, were also seen with labeled tubulin (for example, fig. S5). Images are maximum intensity projections from five confocal z-slices 10 µm apart. A more detailed time course with channels for all probes is presented in fig. S2. (**F**) Quantification of the spatial distributions of labeled tubulin, ER-Tracker, MitoTracker, and GFP-NLS or mCherry-NLS signal across the compartments. For the top plot, data are from five separate experiments with 15 compartments quantified from each experiment. For the bottom plot, data are from two separate experiments, with 30 compartments quantified from one and 45 from the other. Shaded regions are the interdecile range. a.u., arbitrary units. (**G**) Quantification of the width of the border region. The left plot shows how border width changes with time. The green line shows the average border width between neighboring microtubule compartments and the red line the average border width between ER compartments. The error bars indicate standard errors (n = 9). The right plot shows the relationship between compartment size and the surrounding border width. Circles correspond to compartments containing at least one nucleus, and triangles correspond to compartments with no nuclei. Data are from a single representative experiment.

of possible SiR-tubulin–induced microtubule stabilization (fig. S5).

At a high sperm concentration (800 nuclei/μl), some patterning still occurred, but discrete cell-like compartments failed to form (Fig. 2D and movie S6). At an intermediate concentration of sperm (160 nuclei/μl), almost all of the compartments contained nuclei and appeared relatively uniform in size, with an average cross-sectional area of 0.129 ± 0.044 mm^2 (mean ± SD). However, at lower sperm concentrations (16 to 40 nuclei/μl), the global patterns were a mix of nucleated and non-nucleated cell-like compartments of different sizes. For each sperm concentration in this range, the nucleated compartments were larger than the non-nucleated ones, possibly because they formed earlier and thus had more time to grow (Fig. 2, D and E, and movie S6). In the complete absence of nuclei, the compartments were fairly uniform in size and were smaller than those seen in the presence of nuclei, with an average area of 0.060 ± 0.025 mm^2 (Fig. 2E and movie S6). These findings suggest that competition may be at play in determining the final length scale of the compartments.

We tested various inhibitors for their effects on pattern formation (Table 1). Two treatments abolished pattern formation: the microtubule depolymerizer nocodazole (Fig. 3A and movie S7) and the adenosine triphosphate (ATP)–depleting enzyme apyrase (Table 1). Several other inhibitors changed the character of pattern formation without completely abolishing it. Ciliobrevin D, an inhibitor of cytoplasmic dynein, which is the main minus-end–directed microtubule motor protein, had several effects. It largely abolished the formation of normal nuclei from added sperm (Fig. 3B and movie S8), and the nuclei that formed did not become properly centered within the compartments (fig. S6). Ciliobrevin D also largely abolished the formation of discrete ER compartments (Fig. 3B). Moreover, microtubules in treated samples moved from within the compartments to the borders and became mixed with microtubules from neighboring

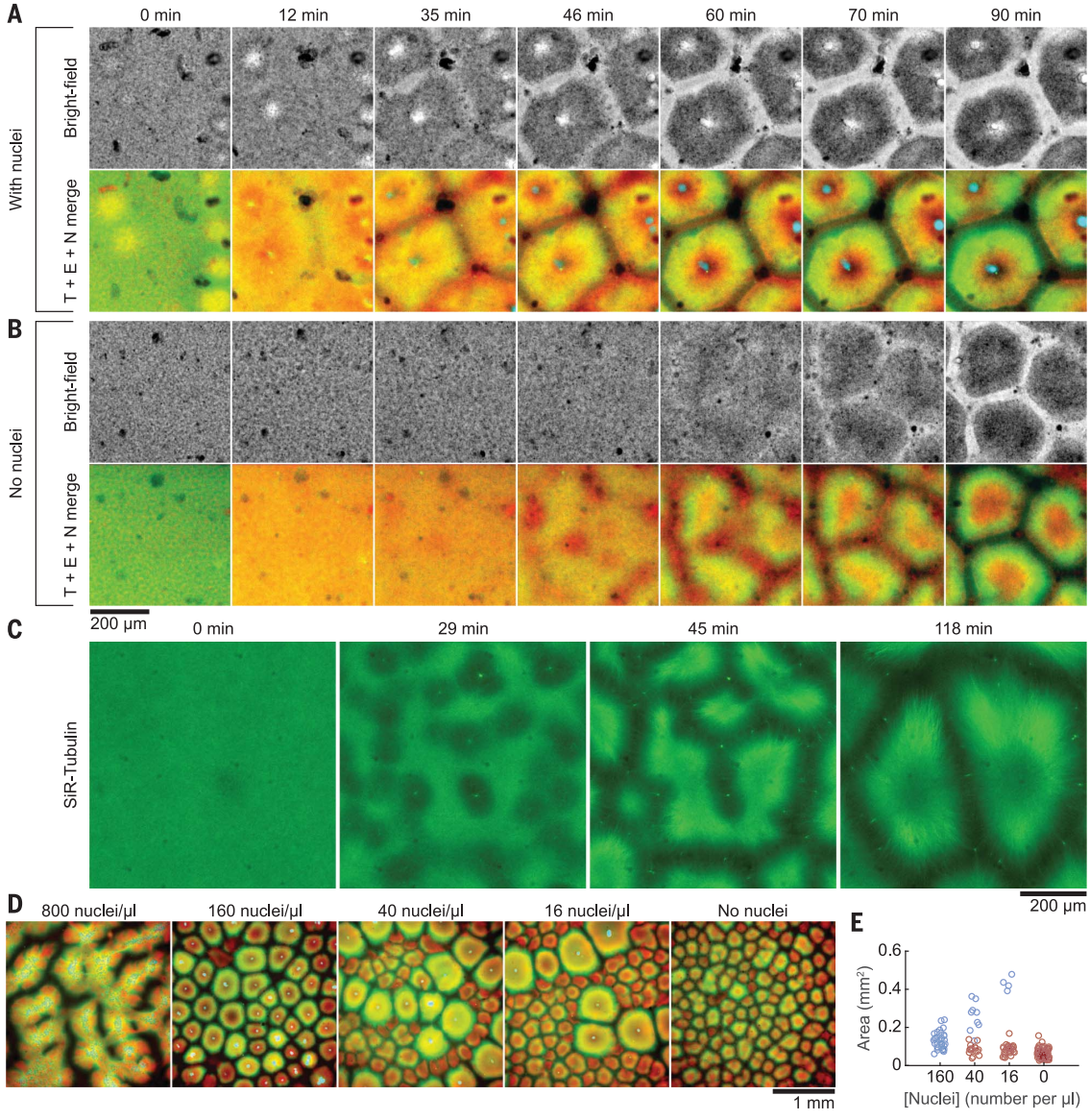


Fig. 2. The formation of cell-like compartments in egg extracts does not require added demembranated sperm nuclei. (**A**) Time-lapse montage of cell-like compartment formation in an interphase egg extract with approximately 160 demembranated *X. laevis* sperm nuclei added per microliter of extract. (**B**) Time-lapse montage of compartment formation in an extract from the same experiment as (A) but with no sperm nuclei added. Dynamics of pattern formation in (A) and (B) are presented in movie S4. (A) and (B) share the scale bar located at the bottom of (B). "T + E + N" denotes a merge of the fluorescent tubulin (T), ER-Tracker (E), and mCherry-NLS (N) images. The individual fluorescent images are shown in fig. S3. (**C**) Confocal microscopy time-lapse images of microtubule dynamics during compartment formation in an interphase extract without added sperm nuclei. Images are maximum intensity projections from five confocal z-slices 10 μm apart. More-detailed time-lapse images comparing SiR-tubulin to labeled tubulin are presented in fig. S5. The time courses of extracts with and without added sperm are compared in movie S5. (**D**) Interphase egg extracts supplemented with different concentrations of sperm nuclei. Microtubules are shown in green, ER in red, and nuclei in cyan. The dynamics of pattern formation are presented in movie S6. (**E**) Size measurements of cell-like compartments from the same experiment as (D). Blue symbols indicate measured areas of individual nucleated compartments and red symbols non-nucleated ones. Areas are taken as the area of the tubulin compartment plus half of the associated border zone.

compartments (Fig. 3B and movie S8). Despite these overall abnormalities, the length scale of the patterning remained close to normal. Thus, ATP and microtubule polymerization are essential for pattern formation, and the minus-end–directed motor dynein is required for partitioning the ER and for properly localizing the microtubules.

Two inhibitors of the polo-like kinase Plk1 also affected pattern formation (Table 1 and fig. S7). At maximal concentrations, they abolished microtubule aster formation and resulted in a grossly abnormal pattern of ER localization (fig. S7). Inhibitors of aurora kinase A, Eg5, kinesin spindle protein, centromere-associated protein-E (CENP-E), and myosin II had little or no effect on pattern formation.

In standard *Xenopus* extracts, including the interphase extracts used here, the actin-polymerization inhibitor cytochalasin B is present (*10*, *12*), and, therefore, actin polymerization is expected to be minimal. To further test for a possible dependence of pattern formation on actin polymerization, we prepared extracts in the absence of cytochalasin B. As assessed by the F-actin probe SiR-actin, actin filaments were present throughout the compartments and were concentrated around the nuclei and in junctional complexes (Fig. 3, C to E, and fig. S8). After extended incubation, F-actin became more concentrated at the periphery of the compartments, and the compartments contracted, with the intercompartment border zones expanding correspondingly (Fig. 3D). One example was found where a contracted compartment appeared to roll, revealing a cage-like structure of its actin (Fig. 3E and fig. S9). Treatment of actin-intact extracts with the actin-polymerization inhibitor latrunculin A abolished the F-actin staining and the late-stage contraction of the compartments but otherwise did not affect pattern formation (Fig. 3C and fig. S10). Thus, microfilaments are not required for the formation of cell-like compartments.

A special feature of *Xenopus* extracts is that they can be prepared with essentially no dilution. We tested how much dilution could be tolerated by the self-organizing cytoplasm. We mixed undiluted interphase extracts with various amounts of egg lysis buffer and monitored pattern formation in the diluted extracts. Nearly normal compartments still formed in extracts diluted to 70% of the original concentration (fig. S11). When cytoplasmic concentration was 50%, the pattern was noticeably abnormal, and when reduced to 30%, the compartments failed to form. Therefore, cell-like compartment formation requires a threshold concentration of the cytoplasm.

We wondered whether the cell-like compartments can carry out biological functions expected of an embryo. One of the hallmarks of the early embryo is its rapid reductive divisions, which allow the large egg to quickly develop into a 4000-cell embryo whose total volume is no greater than that of the original egg. We therefore tested whether the cell-like compartments could divide and reorganize if the extracts were allowed to progress through the cell cycle. We prepared a cycling egg extract (*12*) in the absence of cycloheximide, which permits cyclin synthesis and allows Cdk1 to be periodically activated and inactivated. The extract was supplemented with demembranated sperm nuclei (to provide centrosomes and DNA), plus ER-Tracker and fluorescently

Table 1. The effect of perturbations on compartment formation. ADP, adenosine diphosphate; AMP, adenosine monophosphate.

Perturbant	Function	Concentration	Description and number of independent experiments (*n*)
Nocodazole	Tubulin polymerization inhibitor	33 μM	Compartment formation abolished (*n* = 3)
Apyrase	Hydrolyzes ATP to ADP and ADP to AMP	0.0125 units/μl	Compartment formation abolished (*n* = 1)
		0.005 units/μl	Compartment formation abolished (*n* = 1)
Ciliobrevin D	Cytoplasmic dynein inhibitor	50 μM	Compartment formation severely impaired; nuclear import of mCherry-NLS and GFP-NLS severely impaired and nuclei mispositioned; microtubules accumulated in border zones (*n* = 5)
BI 2536	Polo-like kinase 1 inhibitor	50 μM	Compartment formation severely impaired and web-like patterns formed; asters abolished; mislocalized nuclei (*n* = 4)
		5 μM	Compartment formation impaired; relatively small asters; mislocalized nuclei (*n* = 2)
		0.5 μM	Mislocalized nuclei (*n* = 2)
Volasertib (BI 6727)	Polo-like kinase 1 inhibitor	50 μM	Compartment formation severely impaired and web-like patterns formed; asters abolished; mislocalized nuclei (*n* = 5)
		5 μM	Compartment formation impaired; relatively small asters; mislocalized nuclei (*n* = 2)
		0.5 μM	Mislocalized nuclei (*n* = 2)
TC-S 7010	Aurora kinase A inhibitor	50 μM	Compartments formed with a delay (6/7) or failed to completely separate (1/7) (*n* = 7)
		5 μM	Normal compartment formation (*n* = 4)
		0.5 μM	Normal compartment formation (*n* = 4)
(+)-*S*-Trityl-L-cysteine	Kinesin Eg5 inhibitor	100 μM	Normal compartment formation (*n* = 3)
SB743921 HCl	Kinesin spindle protein inhibitor	100 μM	Normal compartment formation (*n* = 3)
		50 μM	Normal compartment formation (*n* = 1)
Ispinesib (SB-715992)	Kinesin spindle protein inhibitor	100 μM	Normal compartment formation (*n* = 1)
GSK923295	CENP-E kinesin inhibitor	100 μM	Normal compartment formation (*n* = 3)
(−)-Blebbistatin	Nonmuscle myosin II inhibitor	100 μM	Normal compartment formation (*n* = 2)
Cytochalasin B	Actin polymerization inhibitor	10 μM	Normal compartment formation (*n* > 40)
Latrunculin A	Actin polymerization inhibitor	10 μM	Normal compartment formation (*n* = 3)

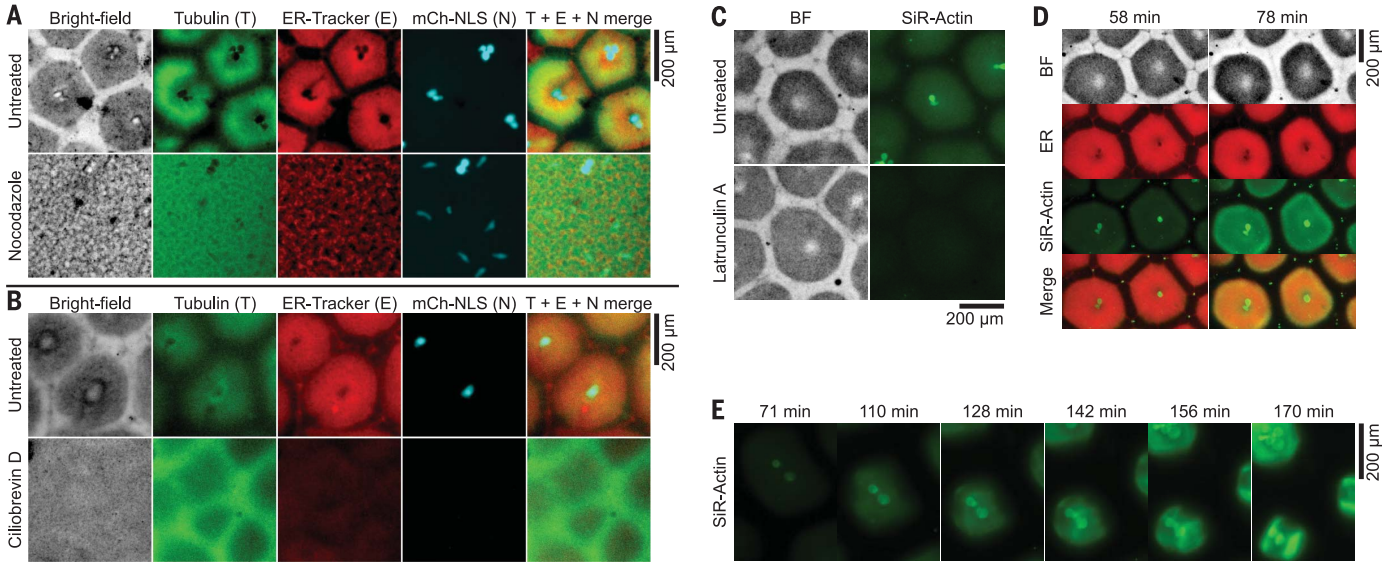


Fig. 3. Perturbing microtubule polymerization and cytoplasmic dynein activity disrupts pattern formation, whereas changes in actin polymerization have little effect. (**A**) Nocodazole, a microtubule polymerization inhibitor, abolished the formation of cell-like compartments. Dynamics of the process are shown in movie S7. (**B**) Ciliobrevin D, an inhibitor of the minus-end–directed microtubule motor cytoplasmic dynein, led to a pattern with microtubules at the compartment boundaries and disorganized ER. mCh-NLS in (A) and (B) denotes mCherry-NLS. (**C** to **E**) Compartment formation in extracts for which actin polymerization was permitted (actin-intact) or inhibited. (C) Latrunculin A treatment abolished F-actin but had no effect on compartment formation. Images shown are at 54 min. BF, bright field. (D) F-actin became enriched at the compartment cortex upon extended incubation in an actin-intact extract. (E) After cortical enrichment of F-actin, a compartment further contracted and rolled on its side, revealing a cage-like actin cortex that contained an actin-rich nuclear cluster at its center. Data for (C) to (E) are from a single representative experiment. More details are presented in fig. S9.

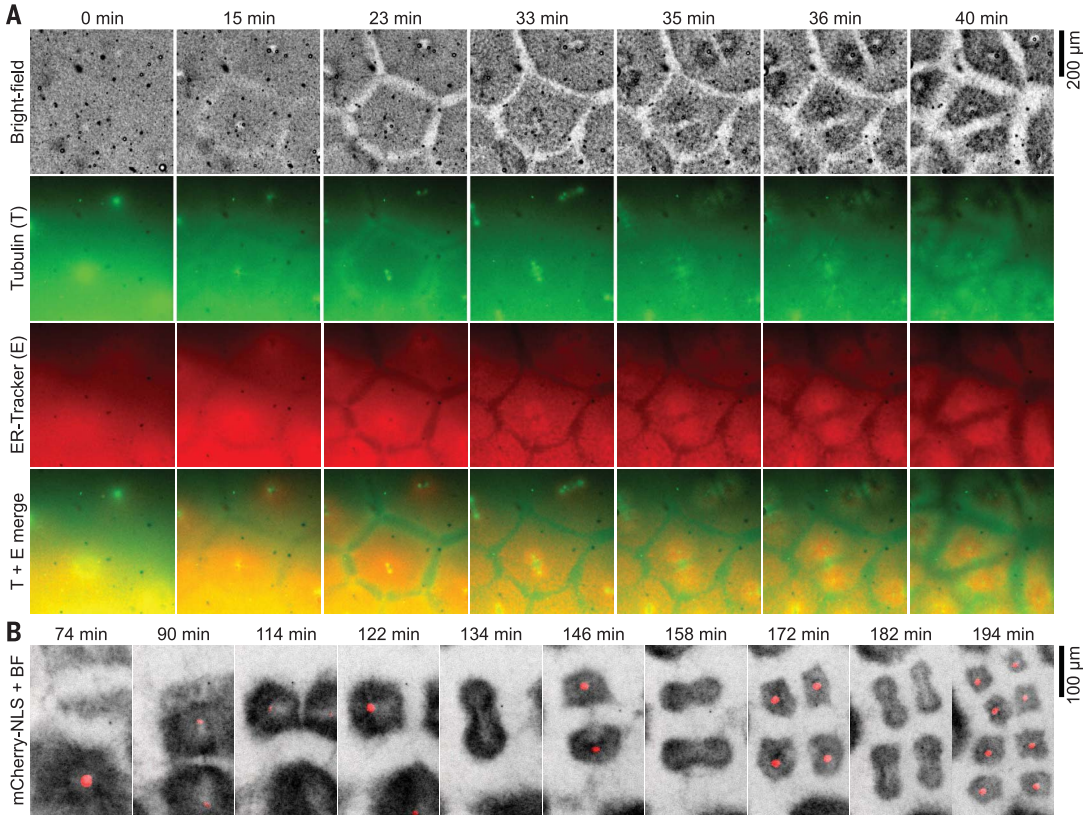


Fig. 4. Cell-like compartments are capable of mitotic division. (**A**) Time-lapse images of cell-like compartments performing a mitotic cell cycle in a sperm-supplemented cycling *X. laevis* egg extract. Formation of the mother compartments became apparent at 15 min and was completed by 23 min, when duplicated centrosomes could also be seen. A mitotic spindle subsequently formed at 33 min. The mother compartments completed their divisions at 40 min, each giving rise to two daughter compartments. Detailed dynamics of the process are shown in movie S9. (**B**) Time-lapse images of cell-like compartments undergoing five consecutive cell division cycles in a sperm-supplemented cycling extract. In this experiment, the daughter compartments formed after every division contained a single nucleus each. Bright-field images are shown in gray, and mCherry-NLS signal, which visualizes interphase nuclei, is shown in red. The corresponding time-lapse video is presented as movie S10.

labeled tubulin, and the dynamics were tracked by bright-field and fluorescence microscopy (Fig. 4A and movie S9).

Initially, the cycling extract was in the first interphase after meiotic exit, and it appeared relatively homogeneous. By 15 min, cell-like compartments had begun to form, and by 23 min, they were indistinguishable from those seen in interphase-arrested extracts. The centrosomes separated at about this time, and, shortly thereafter, the texture of the ER changed, becoming coarser in appearance. At 33 min, well-defined mitotic spindles were visible. At this time, the ER-Tracker signal concentrated around the spindle poles, and a corresponding darker gray region was visible in the bright-field image. At 35 min, the division of the cell-like compartments began. Large microtubule asters emanated from the two daughter centrosomes, now pulled further away from each other, and a microtubule-enriched zone emerged near the bisecting point. ER appeared to be depleted from the same zone. By 40 min, the mother compartment had completely divided into two daughter compartments, each with the same pattern of microtubules and ER as had been present in the mother compartment before mitosis. Often the compartments underwent multiple consecutive cycles of such reductive divisions, yielding a population of much smaller offspring compartments (Fig. 4B and movie S10). These results demonstrate that the cell-like compartments are not only morphologically similar to cells but can also perform one of the most important functions of a living cell.

These experiments show that homogenized *X. laevis* egg cytoplasm can self-organize into spatially distinct compartments that resemble cells. The formation of these cell-like compartments does not require the presence of nuclei or centrosomes but requires energy, microtubule polymerization, cytoplasmic dynein function, and a threshold concentration of the cytoplasm. When supplemented with sperm, the cell-like compartments are capable of multiple rounds of division and reorganization. These results suggest that the cytoplasm can robustly generate the basic spatial organization of the cell and retains some of its distinctive functions.

Cytoplasmic ingredients self-organize on many different scales. Minimal sets of purified cytoplasmic macromolecules can self-organize into molecular assemblies such as the apoptosome (*13*) and the ribosome (*14*) and subcellular structures such as the centrosome (*15*) and ER (*16*). Cell-free extracts can autonomously assemble larger subcellular structures like the bipolar meiotic spindle (*3*) and the machinery of cytokinesis (*4*). The phenomena described here show that self-organization of the cytoplasm can occur on the cellular level in terms of both scale and complexity, underscoring the importance of nongenetic information inherent in the components of the cytoplasm.

REFERENCES AND NOTES

1. P. Weiss, in *Dynamics of Development: Experiments and Inferences*, P. A. Weiss, Ed. (Academic Press, 1968), pp. 24–95.
2. A. W. Murray, M. W. Kirschner, *Nature* **339**, 275–280 (1989).
3. R. Heald *et al.*, *Nature* **382**, 420–425 (1996).
4. P. A. Nguyen *et al.*, *Science* **346**, 244–247 (2014).
5. C. M. Field, J. F. Pelletier, T. J. Mitchison, *Curr. Biol.* **29**, 1999–2008.e4 (2019).
6. P. A. Nguyen, C. M. Field, T. J. Mitchison, *Mol. Biol. Cell* **29**, 304–316 (2018).
7. T. J. Mitchison, P. Nguyen, M. Coughlin, A. C. Groen, *Mol. Biol. Cell* **24**, 1559–1573 (2013).
8. A. C. Groen, M. Coughlin, T. J. Mitchison, *Mol. Biol. Cell* **22**, 3139–3151 (2011).
9. K. Ishihara, P. A. Nguyen, A. C. Groen, C. M. Field, T. J. Mitchison, *Proc. Natl. Acad. Sci. U.S.A.* **111**, 17715–17722 (2014).
10. P. Deming, S. Kornbluth, *Methods Mol. Biol.* **322**, 379–393 (2006).
11. B. Alberts *et al.*, *Molecular Biology of the Cell* (Garland Science, New York, ed. 6, 2015), p. 24.
12. A. W. Murray, *Methods Cell Biol.* **36**, 581–605 (1991).
13. H. E. Kim, F. Du, M. Fang, X. Wang, *Proc. Natl. Acad. Sci. U.S.A.* **102**, 17545–17550 (2005).
14. G. Mangiarotti, S. Chiaberge, *J. Biol. Chem.* **272**, 19682–19687 (1997).
15. J. B. Woodruff *et al.*, *Cell* **169**, 1066–1077.e10 (2017).
16. R. E. Powers, S. Wang, T. Y. Liu, T. A. Rapoport, *Nature* **543**, 257–260 (2017).

ACKNOWLEDGMENTS

We thank H. Funabiki and M. Dasso for providing the GST-GFP-NLS construct; T. Meyer, S. Pfeffer, T. Stearns, and J. Theriot for helpful discussions; O. Afanzar, Y. Chen, W. Huang, J. Kamenz, S. Liu, and C. Phong for comments on the manuscript; and the Stanford Cell Sciences Imaging Facility for use of their spinning disc confocal microscope. **Funding:** This work was supported by grants from the National Institutes of Health (R01 GM110564 and P50 GM107615). **Author contributions:** X.C. and J.E.F. jointly designed the studies, made the figures, and wrote the paper. X.C. carried out the experiments. **Competing interests:** None declared. **Data and materials availability:** All data needed to evaluate the conclusions in the paper are present in the paper or the supplementary materials.

SUPPLEMENTARY MATERIALS

science.sciencemag.org/content/366/6465/631/suppl/DC1
Materials and Methods
Figs. S1 to S11
References (*17–19*)
Movies S1 to S10

View/request a protocol for this paper from *Bio-protocol*.

18 October 2018; accepted 17 September 2019
10.1126/science.aav7793

BLACK HOLES

A noninteracting low-mass black hole–giant star binary system

Todd A. Thompson[1,2,3]*, Christopher S. Kochanek[1,2], Krzysztof Z. Stanek[1,2], Carles Badenes[4,5], Richard S. Post[6], Tharindu Jayasinghe[1,2], David W. Latham[7], Allyson Bieryla[7], Gilbert A. Esquerdo[7], Perry Berlind[7], Michael L. Calkins[7], Jamie Tayar[1,8], Lennart Lindegren[9], Jennifer A. Johnson[1,2], Thomas W.-S. Holoien[10], Katie Auchettl[2,11,12], Kevin Covey[13]

Black hole binary systems with companion stars are typically found via their x-ray emission, generated by interaction and accretion. Noninteracting binaries are expected to be plentiful in the Galaxy but must be observed using other methods. We combine radial velocity and photometric variability data to show that the bright, rapidly rotating giant star 2MASS J05215658+4359220 is in a binary system with a massive unseen companion. The system has an orbital period of ~83 days and near-zero eccentricity. The photometric variability period of the giant is consistent with the orbital period, indicating star spots and tidal synchronization. Constraints on the giant's mass and radius imply that the unseen companion is $3.3^{+2.8}_{-0.7}$ solar masses, indicating that it is a noninteracting low-mass black hole or an unexpectedly massive neutron star.

The observed distributions of neutron star and stellar black hole masses are connected to the mechanism of core-collapse supernovae, its rate as the Universe evolves, and the physics of binary stars (*1*, *2*). An unbiased census of neutron star and black hole masses is required to understand these interconnected areas. However, our knowledge of neutron star and black hole demography is limited because mass measurements are obtained almost exclusively for pulsar and accreting binary systems selected from radio, x-ray, and gamma-ray surveys (*3*–*5*). While gravitational microlensing has the potential to reveal compact object mass distributions (*6*), individual systems are difficult to characterize. The detections of merging black hole and neutron star binaries by gravitational wave experiments (*7*, *8*) provide compact object masses, but these merging systems are an intrinsically biased subset of the parent population.

[1]Department of Astronomy, The Ohio State University, 140 W. 18th Ave., Columbus, OH 43210, USA. [2]Center for Cosmology and AstroParticle Physics, The Ohio State University, 191 W. Woodruff Ave., Columbus, OH 43210, USA. [3]Institute for Advanced Study, 1 Einstein Dr., Princeton, NJ 08540, USA. [4]Department of Physics and Astronomy and Pittsburgh Particle Physics, Astrophysics and Cosmology Center, University of Pittsburgh, 3941 O'Hara St., Pittsburgh, PA 15260, USA. [5]Institut de Ciències del Cosmos, Universitat de Barcelona, Martí Franqués 1, E08028 Barcelona, Spain. [6]Post Observatory, Lexington, MA 02421, USA. [7]Harvard-Smithsonian Center for Astrophysics, 60 Garden St., Cambridge, MA 02138, USA. [8]Institute for Astronomy, University of Hawaii, 2680 Woodlawn Dr., Honolulu, Hawaii 96822, USA. [9]Lund Observatory, Department of Astronomy and Theoretical Physics, Lund University, Box 43, 22100 Lund, Sweden. [10]The Observatories of the Carnegie Institution for Science, 813 Santa Barbara St., Pasadena, CA 91101, USA. [11]Department of Physics, The Ohio State University, 191 W. Woodruff Ave., Columbus, OH 43210, USA. [12]Dark Cosmology Centre, Niels Bohr Institute, University of Copenhagen, Lyngbyvej 2, 2100 Copenhagen, Denmark. [13]Department of Physics and Astronomy, Western Washington University, Mail Stop 9164, Bellingham, WA, 98225, USA.
*Corresponding author. Email: thompson.1847@osu.edu

Studies of compact object populations are complemented by those of massive star binary systems (*9*), whose more massive "primary" components ultimately produce neutron stars and black holes [for stars $>10\ M_\odot$ (solar masses)]. These studies reveal a broad distribution of secondary masses and orbital periods, implying that many massive stars have low-mass, long-lived companions. Quiescent noninteracting black hole stellar binaries have not been found in radial velocity searches, although the existence of such systems has been discussed for decades (*10*, *11*). The only known candidate formed by dynamical scattering processes in a dense globular cluster (*12*), so it did not form as an isolated binary in the more typical Galactic field environment. Although subject to their own selection biases, a sample of Galactic binary star systems with black hole or neutron star companions would inform binary evolution models, which are currently limited by comparison to pulsar binaries and interacting or merging systems.

We searched for stellar binaries with massive unseen companions in data from the Apache Point Observatory Galactic Evolution Experiment (APOGEE) (*13*). APOGEE provides multi-epoch near-infrared spectroscopy for $>10^5$ stars in the Milky Way. These observations provide stellar elemental abundances and can also reveal radial velocity variations indicative of binary orbital motion (*14*). We searched for systems with large apparent accelerations—the difference in radial velocity divided by the difference in time between two epochs. Systems were ranked by an estimate of the binary mass function given the irregular timing of the APOGEE observation epochs.

Although the radial velocity measurements from APOGEE can immediately indicate the presence of a binary, the mass of the companion is not determined, because the orbital period, inclination, and eccentricity are unknown. To constrain the orbital periods of the ~200 APOGEE sources with the highest accelerations, we searched for periodic variations in photometric data from the All-Sky Automated Survey for Supernovae (ASAS-SN) (*15*, *16*) for evidence of transits, ellipsoidal variations, or star spots. This process identified the giant star 2MASS J05215658+4359220 (hereafter J05215658), which exhibits an acceleration of $\simeq$2.9 km s^{-1} day^{-1} and periodic photometric variability with a period of ~82.2 ± 2.5 days (Fig. 1 and table S2). This system lies in the constellation Auriga, near the outer Galactic plane, with Galactic coordinates (l, b) = (164.774°, 4.184°).

Previous analysis of J05215658 determined an effective stellar temperature $T_{\rm eff} \simeq 4480 \pm 62$ K, a surface gravitational acceleration $\log[g/({\rm cm\ s^{-2}})] \simeq 2.59 \pm 0.06$, and a near-Solar value for the carbon-to-nitrogen abundance ratio (*17*). Our analysis of the APOGEE spectrum yields a projected rotational velocity of $v{\cdot}\sin i_{\rm rot} \simeq 14.1 \pm 0.6$ km s^{-1} (*18*), where $i_{\rm rot}$ is the inclination angle of the rotation axis projected onto the plane of the sky. We obtained additional optical spectra with the Tillinghast Reflector Echelle Spectrograph (TRES), which indicate a consistent effective temperature but lower $\log g \simeq 2.35 \pm 0.14$, and higher $v{\cdot}\sin i_{\rm rot} \simeq 16.8 \pm 0.6$ km s^{-1}. We adopt the TRES $\log g$ and the APOGEE $v{\cdot}\sin i_{\rm rot}$ in our analysis (*18*).

We further constrained the system using radial velocity and multiband photometric follow-up (Fig. 2). The photometric variability amplitude increases from the redder to bluer bands. The shape, character, and phasing of the light curve are inconsistent with stellar pulsations or ellipsoidal variations but are typical of the class of spotted K-type giants such as HD 1833, V1192 Orionis, and KU Pegasi (*19*, *20*). Binary systems with periods less than ~150 days often have low eccentricities, implying rapid tidal circularization (*21*, *22*). The change in the shape of the light curve over time (Fig. 1) is likely due to star spot evolution.

Figure 2B shows the TRES radial velocity measurements. The APOGEE and TRES spectra exhibit only a single set of absorption lines, i.e., a single-lined spectroscopic binary. The system has a nearly circular orbit with orbital period $P_{\rm orb} \simeq 83.2 \pm 0.06$ days, radial velocity semi-amplitude $K \simeq 44.6 \pm 0.1$ km s^{-1}, and eccentricity $e \simeq 0.0048 \pm 0.0026$. The mass function is

$$f(M) \equiv \frac{M_{\rm CO}^3 \sin^3 i_{\rm orb}}{(M_{\rm giant} + M_{\rm CO})^2} = \frac{K^3 P_{\rm orb}}{2\pi G}(1-e^2)^{3/2} \simeq 0.766 \pm 0.006\, M_\odot \quad (1)$$

where G is the gravitational constant, $M_{\rm CO}$ is the compact object companion mass, $i_{\rm orb}$ is the orbital inclination, and $M_\odot$ is the mass of the Sun. Figure 3 shows allowed values of $M_{\rm CO}$ as a function of the mass of the giant star $M_{\rm giant}$

for several values of sin i_{orb}. For $M_{giant} \geq 1\,M_\odot$ and sin i_{orb} = 1.0, the minimum possible companion mass is $M_{CO} \geq 1.8\,M_\odot$. The observed spectral energy distribution (SED) is inconsistent with a stellar companion of such high mass (*18*) (fig. S8). We conclude that the unseen companion is either a massive neutron star or a black hole. Follow-up x-ray observations yield a tight upper limit on emission from the system (*18*).

To determine the nature of the compact object companion we must constrain the mass of the giant and the orbital inclination. We can estimate minimum values of the giant radius and bolometric luminosity using the star's projected rotation velocity. The low orbital eccentricity and the correspondence between the orbital and photometric periods imply that the system is tidally circularized and synchronized. We therefore adopt the hypothesis that the giant's rotational period is equal to the binary orbital period and that they have the same inclination ($i_{rot} = i_{orb} = i$). This yields a minimum radius of $R \simeq 23 \pm 1\,R_\odot/\sin i$, a minimum luminosity $L = 4\pi R^2 \sigma_{SB} T_{eff}^4 \simeq 210 \pm 20\,L_\odot/\sin^2 i$ for $T_{eff} \simeq 4500$ K, and a minimum distance $D \simeq [L/(4\pi F)]^{1/2} \simeq 2.45 \pm 0.1$ kpc/sin i, where $R_\odot$ is the radius of the Sun, $L_\odot$ is the luminosity of the Sun, σ_{SB} is the Stefan-Boltzmann constant, and F is the bolometric (all-wavelength) flux measured from the SED (*18*). Combining the minimum giant radius with the TRES log $g \simeq 2.35 \pm 0.14$ gives an estimate for the giant mass of $M_{giant}^{\log g} = gR^2/G \simeq 4.4^{+2.2}_{-1.5}\,M_\odot/\sin^2 i$, implying a minimum companion mass of $M_{CO} \gtrsim 2.9\,M_\odot$.

Alternatively, R and L can be determined directly from the measured distance and flux. The parallax of this system measured by the Gaia satellite is 0.272 ± 0.049 milliarcseconds (mas) (*23*), corresponding to a nominal distance of 3.7 kpc, but there are systematic offsets in the Gaia parallaxes that are a function of both sky position and brightness (*23*). Additionally, the companion will induce astrometric binary motion of the giant that is not accounted for in Gaia's parallax measurement (*23*). Given $f(M)$ and P, the ratio of the binary angular motion to the parallax is 0.34/sin i, which could bias the measured parallax. Applying a zero-point offset and an additional systematic uncertainty, and accounting for the phased binary motion with the geometry and timing of the observations by Gaia for J05215658 using Monte Carlo simulations for an arbitrary orbital sky projection (*18*), we find a parallax of $\pi \simeq 0.322^{+0.086}_{-0.074}$ mas (1σ confidence interval) for all sin $i > 0$, corresponding to a distance $D \simeq 3.11^{+0.93}_{-0.66}$ kpc. The observed flux then gives $L \simeq 331^{+231}_{-127}\,L_\odot$ and $R \simeq 30^{+9}_{-6}\,R_\odot$, consistent with the estimates from v·sin i. Combining the Gaia lower bound of $R \simeq 24\,R_\odot$ with the TRES log g gives $M_{giant}^{\log g} \gtrsim 4.8\,M_\odot$ and a value of M_{CO} in the black hole regime (Fig. 3).

Direct comparison between $R \simeq 30^{+9}_{-6}$ derived from the parallax and $R \simeq 23 \pm 1\,R_\odot/\sin i$ derived from v·sin i suggests that sin $i \simeq 0.8 \pm 0.2$. The 2σ upper limit on the Gaia parallax of 0.486 mas for sin $i > 0.6$, gives lower limits of $L \gtrsim 150\,L_\odot$ and $R \gtrsim 20\,R_\odot$ (*18*). The TRES log $g = 2.35 \pm 0.14$ then gives $M_{giant}^{\log g} \gtrsim 3.2^{+1.2}_{-0.9}\,M_\odot$, implying a lower limit on the companion mass of $M_{CO} \gtrsim 2.5\,M_\odot$.

The giant mass can also be estimated by comparing its properties to single-star evolutionary models, with the caveats that (i) strong binary interaction likely occurred in the history of the system, and (ii) rapidly rotating, spotted

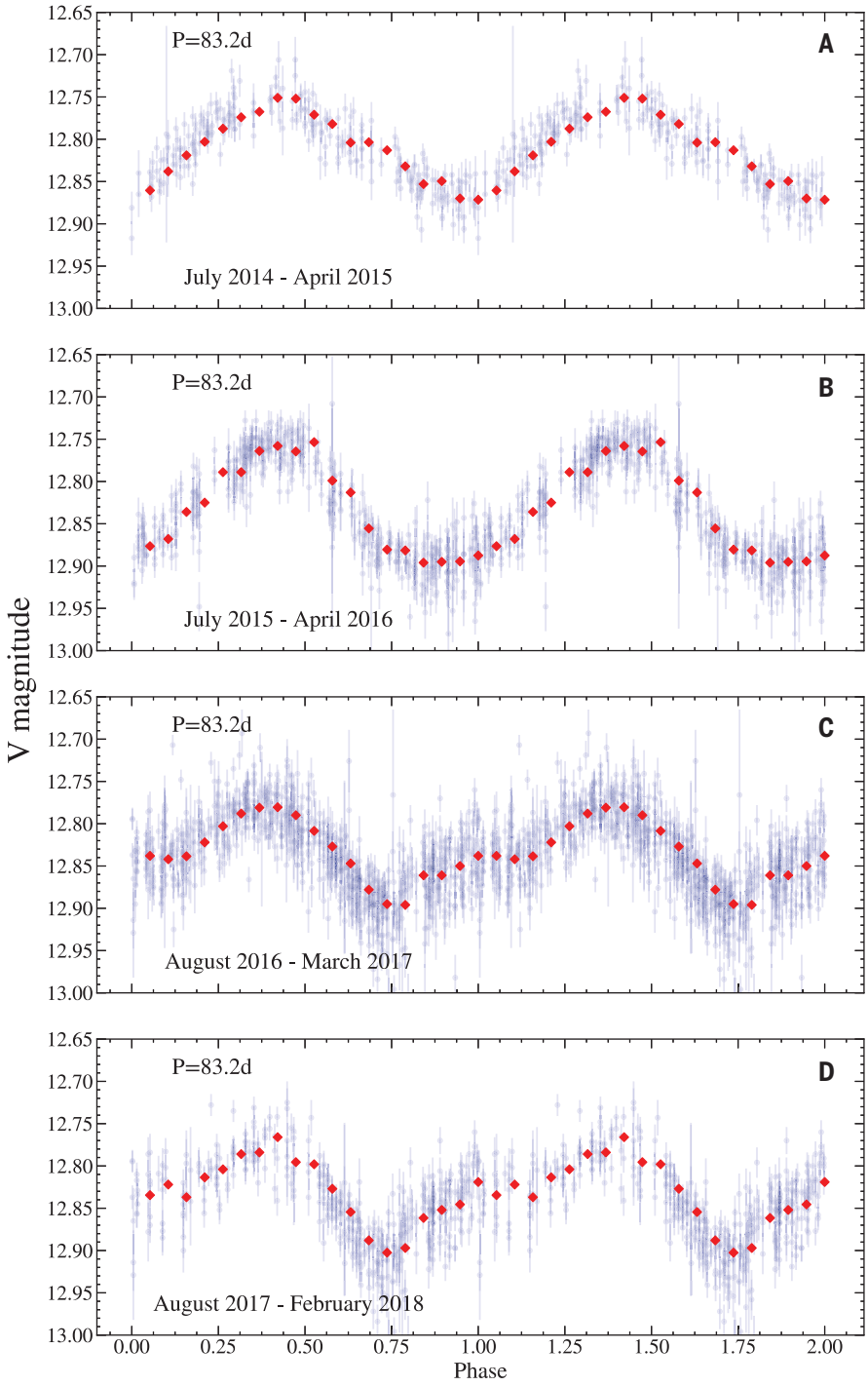


Fig. 1. Multi-epoch ASAS-SN light curves. *V*-band ASAS-SN light curves for J05215658 over four observing seasons (**A** to **D**), phased to the orbital period of 83.2 days and duplicated over two periods. Blue points are the observed data with 1σ error bars. Red points are the running median of 20 data points. The same data before phasing are shown in fig. S1.

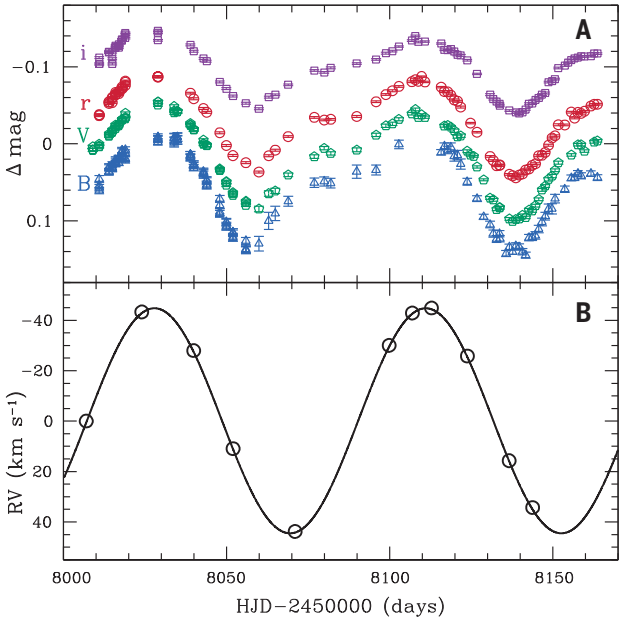


Fig. 2. Multicolor light curves and TRES radial velocities. (**A**) The *B*-band (lowest, triangles), *V*-band (pentagons), *r*-band (circles), and *i*-band (highest, squares) light curves with arbitrary zero-point offsets applied for display. (**B**) The TRES radial velocity (RV) measurements as a function of heliocentric Julian date (HJD). Maximum blueshift (negative RV) occurs near the photometric maximum in all bands, and maximum redshift occurs after photometric minimum, near the shoulder or plateau in the light curve at HJD − 2,450,000 ≃ 8080. Figure 1 shows the evolution of the phased multi-epoch *V*-band ASAS-SN light curve for comparison.

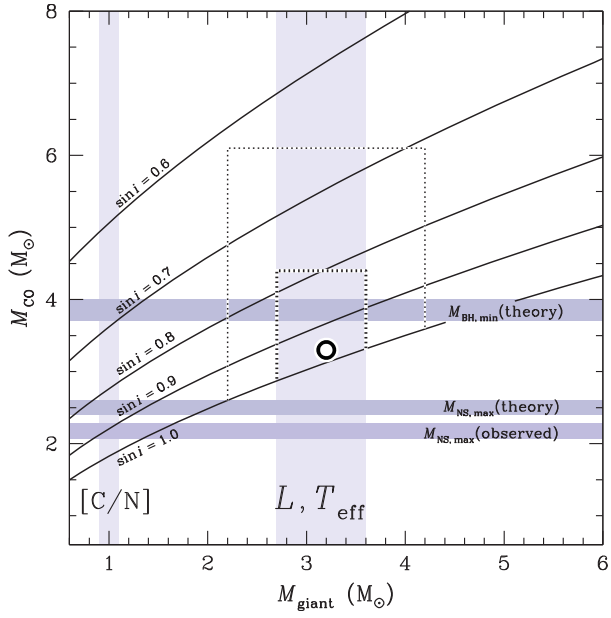


Fig. 3. Compact object mass constraints. Solutions to the mass function (solid black lines) for the compact object's mass M_{CO} as a function of the giant's mass M_{giant} at five values of the orbital inclination from sin i = 1.0 to 0.6. The vertical band labeled L,T_{eff} denotes the best-fitting range of M_{giant} when the giant's measured L,T_{eff}, and log g are matched to theoretical single-star evolutionary models. The regions enclosed by the thick and thin dashed lines show the resulting 1σ and 2σ mass ranges, respectively. The best-fitting value is denoted with the empty circle. The vertical band labeled [*C*/*N*] denotes the range of M_{giant} implied by the observed carbon to nitrogen ratio and the mean locus of the observed [*C*/*N*] – M_{giant} correlation for giant stars (*18*), although we regard this solution as unlikely (see text). The horizontal bands denote the largest observed neutron star mass (lowest), a theoretical maximum neutron star mass (middle), and a theoretical minimum black hole mass (top).

giants like J05215658 are observed to be redder than expected for a given luminosity, underestimating the true dynamical mass (*24*). Nevertheless, we searched for the best-fitting model over a range of stellar metallicity and with the constraint log g = 2.35 ± 0.14, and the other parameters (L, R, and T_{eff}) inferred from the parallax and SED. We found it difficult to simultaneously match the temperature and surface gravity, which is a known systematic problem for models of giant stars (*25*). The best matches were for solar metallicity models. Combining all models, the joint best-fitting mass is $M_{giant} \simeq 3.2^{+1.0}_{-1.0}\,M_\odot$ (2σ), shown in Fig. 3. The model fitting is driven to a giant mass of 2 to 4 $M_\odot$ primarily by the L and R inferred from the parallax and SED. Given the APOGEE measurement of v·sin i, the best-fitting mass implies $\sin i \simeq 0.97^{+0.03}_{-0.12}$. Solving the mass function $f(M)$ for this range of M_{giant} and sin i yields $M_{CO} \simeq 3.3^{+2.8}_{-0.7}\,M_\odot$ (2σ; also shown in Fig. 3). While a lower assumed value of v·sin i allows for a lower mass giant, it also leads to a smaller sin i that drives M_{CO} upwards. Similarly, if we assume a lower log g, or impose no constraint on log g, we obtain best-fitting giant masses at the low end of the range denoted in Fig. 3 ($M_{giant} \simeq 2.2 - 2.5\,M_\odot$), but with compact object companion masses of ≃ 2.9 to 4.0 $M_\odot$.

All of our determinations consistently require $M_{giant} \sim 2$ to 4 $M_\odot$. Stars in this mass range are rare in APOGEE (*18*). However, J05215658 would be unusual even among APOGEE's massive giants because it has a near-solar carbon-to-nitrogen abundance ratio. Giants exhibit a strong correlation between this abundance ratio and mass that would imply a low value of $M_{giant} \simeq 1.0\,M_\odot$ for J05215658. We also show this "low-mass giant" possibility in Fig. 3 but consider it highly unlikely, because it is inconsistent with the mass determination from all other methods, and because some higher-mass giants with solar carbon-to-nitrogen abundance ratios do exist in the APOGEE sample (*18*).

We conclude that J05215658 likely consists of a $\simeq 3.2^{+1.0}_{-1.0}\,M_\odot$ giant star and a noninteracting low-mass black hole companion with $M_{CO} \simeq 3.3^{+2.8}_{-0.7}\,M_\odot$ (the 2σ range in Fig. 3). This range of compact object mass falls in the so-called mass gap between neutron stars and black holes (*5*). It is above the highest neutron star masses thus far observed [$2.01 \pm 0.04\,M_\odot$ (*26*) and $2.14^{+0.10}_{-0.09}\,M_\odot$ (*27*)], and the uncertainty range nearly spans from the predicted theoretical maximum neutron star mass [$\simeq 2.5\,M_\odot$ (*28*)] to the lowest well-measured black hole masses [5 to 6 $M_\odot$ (*4*, *5*)]. Whereas some models of black hole formation indicate a lower mass limit of ~4 $M_\odot$ (*1*, *29*), others predict a wide range of masses throughout the mass gap (*30*, *31*). J05215658 joins a handful of other known binaries that may host compact objects in this mass range, including the x-ray binaries GX 339-4 [2.3 to 9.5 $M_\odot$ (*32*)] and 4U 1543-47 [2.7 to 7.5 $M_\odot$ (*33*)].

REFERENCES AND NOTES

1. O. Pejcha, T. A. Thompson, *Astrophys. J.* **801**, 90 (2015).
2. K. Belczynski, V. Kalogera, T. Bulik, *Astrophys. J.* **572**, 407–431 (2002).
3. F. Özel, D. Psaltis, R. Narayan, A. Santos Villarreal, *Astrophys. J.* **757**, 55 (2012).
4. F. Özel, D. Psaltis, R. Narayan, J. E. McClintock, *Astrophys. J.* **725**, 1918–1927 (2010).
5. W. M. Farr *et al.*, *Astrophys. J.* **741**, 103 (2011).
6. B. Paczynski, *Astrophys. J.* **304**, 1 (1986).
7. LIGO Scientific Collaboration and Virgo Collaboration, *Phys. Rev. Lett.* **116**, 061102 (2016).
8. LIGO Scientific Collaboration and Virgo Collaboration, *Phys. Rev. Lett.* **119**, 161101 (2017).
9. H. A. Kobulnicky *et al.*, *Astrophys. J.* **213** (suppl.), 34 (2014).
10. O. K. Guseinov, Y. B. Zel'dovich, *Sov. Astron.* **10**, 251 (1966).
11. V. L. Trimble, K. S. Thorne, *Astrophys. J.* **156**, 1013 (1969).
12. B. Giesers *et al.*, *Mon. Not. R. Astron. Soc.* **475**, L15–L19 (2018).
13. S. R. Majewski *et al.*, *Astrophys. J.* **154**, 94 (2017).
14. C. Badenes *et al.*, *Astrophys. J.* **854**, 147 (2018).
15. B. J. Shappee *et al.*, *Astrophys. J.* **788**, 48 (2014).
16. C. S. Kochanek *et al.*, *Publ. Astron. Soc. Pac.* **129**, 104502 (2017).

17. B. Abolfathi *et al*., *Astrophys. J.* **235** (suppl.), 42 (2018).
18. Additional data, materials, and methods are provided as supplementary materials.
19. K. G. Strassmeier, L. Kratzwald, M. Weber, *Astron. Astrophys.* **408**, 1103–1113 (2003).
20. M. Weber, K. G. Strassmeier, *Astron. Astrophys.* **373**, 974–986 (2001).
21. M. Mayor, J. C. Mermilliod, in *Observational Tests of the Stellar Evolution Theory*, A. Maeder, A. Renzini, Eds., vol. 105 of *International Astronomical Union Symposia* (Springer, 1984), p. 411.
22. F. Verbunt, E. S. Phinney, *Astron. Astrophys.* **296**, 709 (1995).
23. L. Lindegren *et al*., *Astron. Astrophys.* **616**, A2 (2018).
24. K. Oláh *et al*., *Astron. Astrophys.* **620**, A189 (2018).
25. J. Tayar *et al*., *Astrophys. J.* **807**, 82 (2015).
26. J. Antoniadis *et al*., *Science* **340**, 1233232 (2013).
27. H. T. Cromartie *et al*., *Nat. Astron.* 10.1038/s41550-019-0880-2 (2019).
28. J. M. Lattimer, *Annu. Rev. Nucl. Part. Sci.* **62**, 485–515 (2012).
29. C. S. Kochanek, *Astrophys. J.* **785**, 28 (2014).
30. S. E. Woosley, T. A. Weaver, *Astrophys. J.* **101** (suppl.), 181 (1995).
31. D. Kushnir, Thermonuclear explosion of rotating massive stars could explain core-collapse supernovae. arXiv:1502.03111 [astro-ph.HE] (10 February 2015).
32. M. Heida, P. G. Jonker, M. A. P. Torres, A. Chiavassa, *Astrophys. J.* **846**, 132 (2017).
33. J. A. Orosz, R. K. Jain, C. D. Bailyn, J. E. McClintock, R. A. Remillard, *Astrophys. J.* **499**, 375–384 (1998).

ACKNOWLEDGMENTS

We thank J. Choi for making MIST models available and C. Jordi and C. Fabricius for discussions. We thank the Ohio State University College of Arts and Sciences Technology Services for setting up the ASAS-SN Sky Patrol light curve server, which was critically useful during this work. T.A.T. thanks J. Zinn, T. Sukhbold, S. Gaudi, O. Pejcha, K. Stassun, M. Pinsonneault, A. Brown, C. Gammie, E. Rossi, J. Fuller, S. Phinney, A.-C. Eilers, D. Hogg, K. Cunha, and R. Poleski for discussions, and K. A. Byram for encouragement and support. Full facility acknowledgments are provided in the supplementary materials. **Funding:** T.A.T. acknowledges support from Scialog Scholar grant 24216 from the Research Corporation; a Simons Foundation Fellowship; and an IBM Einstein Fellowship from the Institute for Advanced Study, Princeton. C.B. acknowledges support from PHY 14-30152: Physics Frontier Center/JINA Center for the Evolution of the Elements (JINA-CEE), awarded by the National Science Foundation. C.S.K. and K.Z.S. are supported in part by NSF grants AST-1515927 and AST-1515876. J.T. acknowledges support from NASA Hubble Fellowship grant 51424 awarded by the Space Telescope Science Institute, which is operated by the Association of Universities for Research in Astronomy, Inc., for NASA, under contract NAS5-26555. **Author contributions:** T.A.T. led the project, conceived of the search strategy, led the analysis, and led the writing of the text. C.S.K. analyzed the SED and the ASAS-SN photometry and fitted the observational data with evolutionary models. K.Z.S. analyzed the Post and ASAS-SN photometry and interpreted the system. R.S.P. provided the Post photometry. C.B. provided APOGEE RV analysis and interpretation of the system. T.J. carried out the time-series analysis of the ASAS-SN photometry. D.W.L., A.B., G.A.E., P.B., and M.L.C. obtained the TRES data and carried out the RV analysis. J.T. provided the rotation measurement from the APOGEE spectrum. L.L. provided the Gaia parallax bias analysis. J.A.J. consulted on the APOGEE spectra. T.W.-S.H. and K.A. obtained and analyzed the Swift data. K.C. participated in preparing the text and discussions of the APOGEE RV data. **Competing interests:** There are no competing interests to declare. **Data and materials availability:** The ASAS-SN light curve data are available at https://asas-sn.osu.edu/photometry/166c0f1c-2502-5e10-b5aa-38d31dddb398. The APOGEE observations, including all individual spectra, the combined spectrum, and analysis results are available at https://dr14.sdss.org/infrared/spectrum/view/stars?id=68401. Photometry for J05215658 is listed in table S8. X-ray and ultraviolet observations from the Neil Gehrels Swift Observatory (*18*) are available at https://heasarc.gsfc.nasa.gov/cgi-bin/W3Browse/swift.pl under target id 10442. The code used to calculate the parallax bias in the Gaia observations is available at https://github.com/chargedcurrent/Gaia_parallax_J05215658.

SUPPLEMENTARY MATERIALS

science.sciencemag.org/content/366/6465/637/suppl/DC1
Materials and Methods
Figs. S1 to S9
Tables S1 to S8
References (*34*–*89*)

7 June 2018; accepted 10 October 2019
10.1126/science.aau4005

STRUCTURAL VIROLOGY

Architecture of African swine fever virus and implications for viral assembly

Nan Wang[1,2]*, Dongming Zhao[3]*, Jialing Wang[1,2]*, Yangling Zhang[1,2]*, Ming Wang[3], Yan Gao[4,5], Fang Li[3], Jingfei Wang[3], Zhigao Bu[3]†, Zihe Rao[1,4,5,6]†, Xiangxi Wang[1,2]†

African swine fever virus (ASFV) is a giant and complex DNA virus that causes a highly contagious and often lethal swine disease for which no vaccine is available. Using an optimized image reconstruction strategy, we solved the ASFV capsid structure up to 4.1 angstroms, which is built from 17,280 proteins, including one major (p72) and four minor (M1249L, p17, p49, and H240R) capsid proteins organized into pentasymmetrons and trisymmetrons. The atomic structure of the p72 protein informs putative conformational epitopes, distinguishing ASFV from other nucleocytoplasmic large DNA viruses. The minor capsid proteins form a complicated network below the outer capsid shell, stabilizing the capsid by holding adjacent capsomers together. Acting as core organizers, 100-nanometer-long M1249L proteins run along each edge of the trisymmetrons that bridge two neighboring pentasymmetrons and form extensive intermolecular networks with other capsid proteins, driving the formation of the capsid framework. These structural details unveil the basis of capsid stability and assembly, opening up new avenues for African swine fever vaccine development.

African swine fever (ASF), first described in Kenya in 1921 (*1*), is a highly contagious viral disease of swine with mortality rates approaching 100% as measured by virulent isolates. Over the past decade, ASF has spread through many countries of the Caucasus, the Russian Federation, and Eastern Europe, posing a serious risk of further expansion (*2*). During the period from January to September 2019, the World Organisation for Animal Health (OIE, www.oie.int/en/animal-health-in-the-world/animal-diseases/african-swine-fever/) was notified by 26 countries of new or ongoing outbreaks: 13 in Europe, 10 in Asia, and 3 in Africa. With no vaccine or treatment available, culling pigs is the most effective way to contain the outbreaks, and more than 30 million pigs have been culled from 2018 to 2019. The ASF pandemics have caused estimated economic losses of $2 billion for swine production worldwide. The African swine fever virus (ASFV) is stable in the environment and transmits rapidly and efficiently among pigs.

ASFV is the only member of the Asfarviridae family and the only known DNA arbovirus (a term used to refer to any viruses that are transmitted by arthropods). Despite sharing structural, genomic, and replicative characteristics with other nucleocytoplasmic large DNA viruses (NCLDVs) (*3*), ASFV differs by possessing a multilayered structure and overall icosahedral morphology. Intracellular ASFV has a genome-containing nucleoid (the first layer) surrounded by a thick protein layer referred to as the core shell (the second layer), which is wrapped by an inner lipid envelope (the third layer) and an icosahedral protein capsid (the fourth layer); these four layers comprise more than 50 proteins (*4*, *5*). Extracellular ASFV gains an external envelope (the fifth layer) as it buds through the plasma membrane (*6*). Large gaps in knowledge concerning the composition and structure of the infectious virion and the identification of viral proteins responsible for inducing protective immune responses in pigs hinder vaccine development.

ASFV targets macrophages, which are monocytes that are mainly present in the blood and bone marrow (*7*). Here we isolated porcine bone marrow (PBM) cells from 30- to 40-day-old specific pathogen-free pigs, propagated ASFV [HLJ-2018 strain, isolated from a pig spleen sample collected from an ASF outbreak farm in China (*8*)] in primary PBM cells, purified extracellular ASFV particles from the cell supernatants, and then inactivated the viral particles with formaldehyde. The purified virions were examined by cryo–electron microscopy (cryo-EM) (fig. S1). The extracellular ASFV particle is, on average, 260 to 300 nm in diameter (fig. S1), which is considerably larger than previous observations (~200 nm) (*9*) likely owing to the incompleteness of the viral particle or the dehydration treatment of the specimen before EM observation.

Like most NCLDVs (*10*–*13*), the size (250 to 500 nm in diameter) and potential flexibility of the ASFV particle have restricted its structure determination to no better than 10 Å. We obtained an 8.8-Å resolution, icosahedrally imposed reconstruction of ASFV by averaging 43,811 particles (fig. S2). The three-dimensional reconstruction clearly shows the structure of all five layers, of which the capsid (the fourth layer) has a maximum diameter of 250 nm and the third layer is a 70-Å-thick lipid bilayer membrane that envelopes a 180-nm-diameter core shell (the second layer). The three layers adopt an overall icosahedral morphology that roughly follows the contour defined by the capsid (Fig. 1A). However, the outermost envelope and innermost nucleoid present weak density owing to the loss of some structural features resulting from icosahedral averaging.

By using an optimized "block-based" reconstruction approach combined with gradient defocus correction, the resolution of the capsid reconstruction was improved to 4.8 Å (Fig. 1 and figs. S2 and S3). The capsid is constructed of 2760 pseudo-hexameric capsomers and 12 pentameric capsomers arranged in a triangulation number (T) = 277 icosahedral lattice (h = 7 and k = 12) (Fig. 1B). In this lattice, there are 12 pentasymmetrons (containing 30 pseudo-hexameric capsomers and a pentameric capsomer) and 20 trisymmetrons (containing 120 pseudo-hexameric capsomers); a similar organization has been observed in other NCLDVs (*10*–*12*). Notably, capsomers within a trisymmetron all pack in essentially the same orientation, rotated by ~60° from the capsomers in neighboring trisymmetrons, creating 30 zippers (cleavage lines) on the capsid. Additionally, the core shell separately reconstructed to 9 Å shows 180 six-blade propeller-like capsomers with a central channel (30 Å in diameter) and 12 starfish-like pentons surrounded by 10 antennae, yielding a T = 19 icosahedral lattice (Fig. 1B).

The cryo-EM maps for the pseudo-hexameric capsomer of the capsid were improved further by local averaging of equivalent copies present in the trisymmetron to achieve a resolution of 4.1 Å (Fig. 2A and fig. S3). The backbone of the polypeptide and many side chains were clearly defined (Fig. 2A), allowing us to build an atomic model of the ASFV major capsid protein, p72 (table S1). Each pseudo-hexameric capsomer is composed of three p72 molecules, and five copies of penton protein (a protein that is not p72) constitute a pentameric capsomer. Many of the remaining uninterpreted densities decorating the inner capsid surface represent minor capsid proteins (Fig. 1C), presumably facilitating capsid assembly and maintaining the stability of the capsid shell. To determine potential identities for the minor capsid proteins, we analyzed the protein composition of PBM cell–produced extracellular ASFV particles by mass spectrometry and identified 63 viral proteins and 25 host cellular proteins (tables S2 and S3), including 13 additional viral

[1]CAS Key Laboratory of Infection and Immunity, National Laboratory of Macromolecules, Institute of Biophysics, Chinese Academy of Sciences, Beijing 100101, China. [2]University of Chinese Academy of Sciences, Beijing 100049, China. [3]State Key Laboratory of Veterinary Biotechnology and National High Containment Laboratory for Animal Diseases Control and Prevention, Harbin Veterinary Research Institute, Chinese Academy of Agricultural Sciences, Harbin 150069, China. [4]Shanghai Institute for Advanced Immunochemical Studies and School of Life Science and Technology, ShanghaiTech University, Shanghai 201210, China. [5]Laboratory of Structural Biology, School of Medicine, Tsinghua University, Beijing 100084, China. [6]State Key Laboratory of Medicinal Chemical Biology, Nankai University, Tianjin 300353, China.
*These authors contributed equally to this work.
†Corresponding author. Email: xiangxi@ibp.ac.cn (X.W.); buzhigao@caas.cn (Z.B.); raozh@tsinghua.edu.cn (Z.R.)

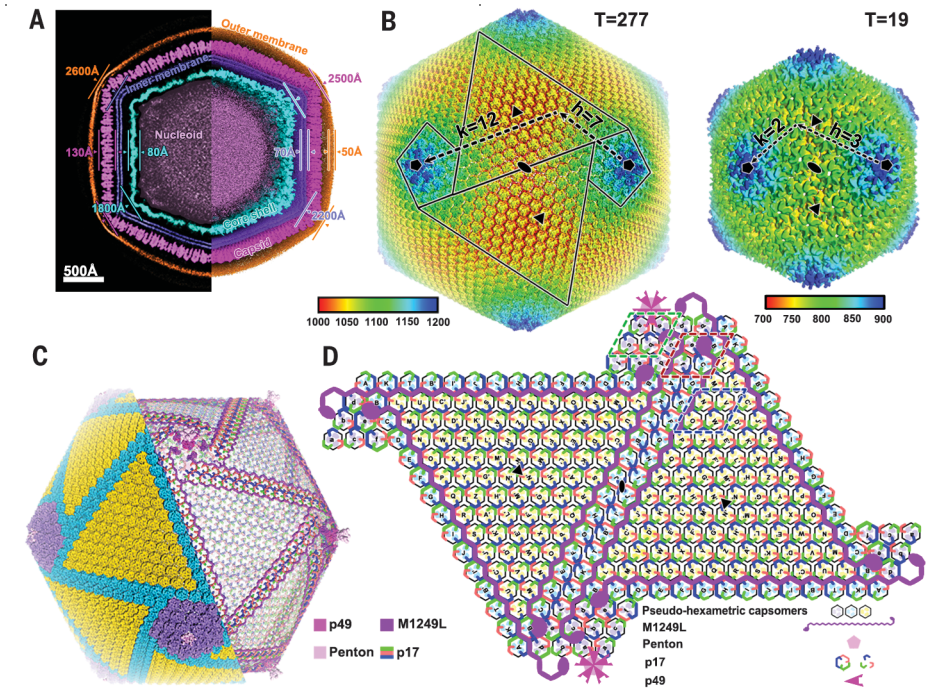


Fig. 1. Architecture of the ASFV virion. (**A**) The central slice (left) and cross section (right) of the icosahedral ASFV virion structure. The outer membrane, capsid, inner membrane, core shell, and nucleoid are colored in orange, magenta, deep blue, cyan, and gray, respectively. The radius and thickness of each layer are labeled. (**B**) Radially colored representations of the ASFV capsid and core shell. The *T* number, including the *h* and *k* vectors, is indicated. The color scale represents radial distance in angstroms. (**C**) Cryo-EM reconstruction of the ASFV capsid. The left half shows the trisymmetron and pentasymmetry organization, and the trisymmetrons, pentasymmetrons, and zippers (the boundaries of two neighboring trisymmetrons) are colored in yellow, light purple, and cyan, respectively. The right half shows the density of the minor capsid proteins, including the penton proteins after removing the outer capsid shell; each minor capsid protein is shown in a different color, as indicated at the bottom right. Boxes in green, red, and blue show the locations with the representative capsomer assembly patterns that will be discussed in Fig. 2D. (**D**) Diagrammatic organization of the minor capsid proteins and capsomers as viewed from inside the capsid. The pseudo-hexameric capsomers are outlined. The icosahedral threefold and twofold axes are shown as solid black triangles and ovals, respectively. Different minor capsid proteins, including the penton proteins, are shown as different shapes with different colors, as indicated at the bottom right. The pseudo-hexameric capsomers are labeled A, B, C, ... in the trisymmetrons and a, b, c, ... in the pentasymmetrons.

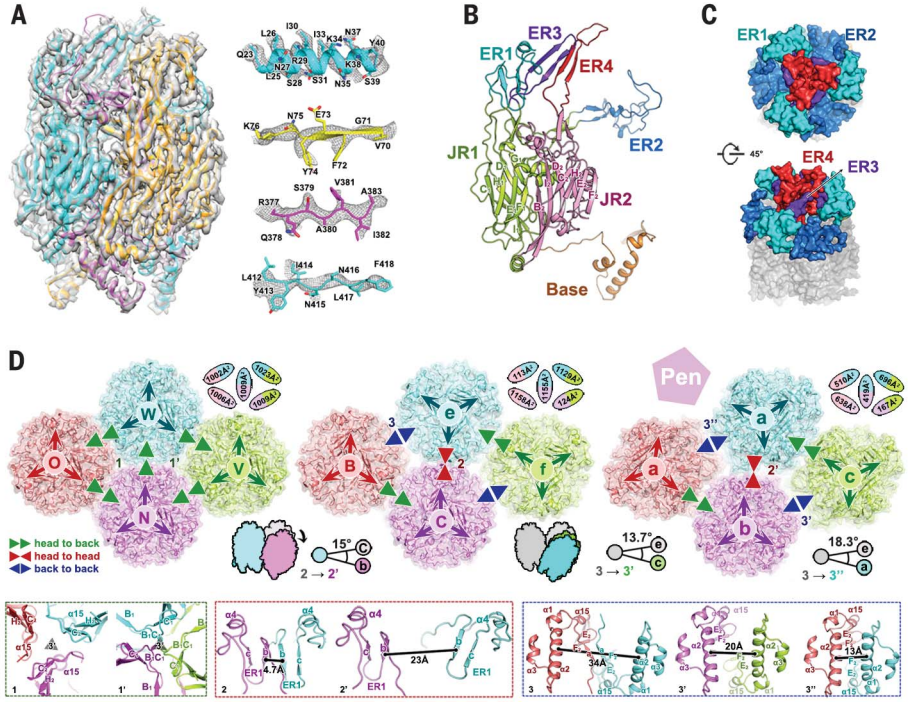


Fig. 2. Structure and organization of p72. (**A**) Density maps and atomic model of the p72 trimer. Each subunit is depicted in a different color. Side-chain features are illustrated on the right. Residues with side chains are labeled. Single-letter abbreviations for the amino acid residues are as follows: E, Glu; F, Phe; G, Gly; I, Ile; K, Lys; L, Leu; N, Asn; Q, Gln; R, Arg; S, Ser; V, Val; W, Trp; and Y, Tyr. (**B**) Ribbon diagram of the p72 monomer. The domains base, JR1 (jelly roll 1), JR2 (jelly roll 2), and ER1 to ER4 are presented in different colors. (**C**) Surface presentation of the p72 trimer. ER1 to ER4 domains are depicted in the same colors as in (B); other parts are colored in gray. (**D**) Detailed depictions of three distinct assembly patterns according to their locations: in the trisymmetron (left), zipper (middle), and pentasymmetron (right). The identities of p72 capsomers are labeled according to the location, as in Fig. 1D. Three types of interaction mode—head to back, head to head, and back to back—are indicated by green, red, and blue triangles, respectively. Interaction areas between two capsomers are measured and marked. Notably, the capsomer interactions in the same interaction mode vary under different microenvironments. These are labeled as 1, 1′; 2, 2′; or 3, 3′, 3″. The cartoon models depict the changed microenvironments. The diagrams in the dashed boxes show the detailed structural organization in the different microenvironments.

proteins when compared with a recent proteomic analysis of Vero cell culture–adapted ASFV strain BA71 (*5*). The minor capsid proteins should be among these. The combination of proteomic analysis, protein abundance level in the ASFV particle, and similarity of the cryo-EM map with predicted structural features of target proteins—including protein sequence, protein secondary structure, and protein topology—led to the identification of the penton protein (H240R) and three minor capsid proteins (p17, p49, and M1249L) (Fig. 1C). Each icosahedral asymmetric unit of the outer capsid shell contains 46 pseudo-hexameric capsomers, with six of these in the pentasymmetron (a, b, c, d, e,

and f) and 40 in the trisymmetron (A, B, C, D, E, F, G, H, I, J, K, L, M, N, O, P, Q, R, S, T, U, V, W, X, Y, Z, A′, B′, C′, D′, E′, F′, G′, H′, I′, J′, K′, L′, M′, and N′) (Fig. 1D). The penton and minor capsid proteins (p17, p49, and M1249L) form a complicated network immediately below the outer capsid shell, stabilizing the whole capsid (Fig. 1, C and D).

Given that both intracellular and extracellular ASFV forms are infectious (*6*), a combination of antibodies that block these two types of infection by targeting both outer membrane proteins and capsid proteins are required to confer efficient protection against ASFV. p72 acts as one of the key protective antigens, and its monoclonal antibodies were shown to neutralize virulent ASFV isolates (*14*, *15*). On the viral capsid, p72 forms a homotrimer, with each monomer adopting a double jelly-roll structure that makes up pseudo-hexameric capsomers (also called p72 capsomers). A similar double jelly-roll fold is found in many other viral capsid proteins (Fig. 2B and figs. S4 and S5), including adenovirus (*16*), the phage PRD1 (*17*), and vaccinia virus (*18*). A single jelly-roll structure consisting of eight antiparallel β strands (from B to I) exists in many more viral capsid proteins, indicative of common ancestry (*19*). As is the case for other double jelly roll capsid proteins, four insertions within the D_1E_1, D_2E_2, F_1G_1, and H_1I_1 loops form exposed regions (ERs). The ERs, together with the N-terminal base domain, determine the specific differences between the virus types (Fig. 2, B and C, and fig. S6). Sterically, the crown of the p72 capsomer is formed by ER1 and its neighboring ER2 and orients toward the outside of the capsid, which may contribute to a conformational epitope (Fig. 2, B and C). β strands from ER3 and ER4 within the same subunit constitute a four-stranded β sheet that shapes the head of the p72 capsomer and might represent another conformational epitope (Fig. 2, B and C). ER3 surrounded by ER1, ER2, and ER4 may link these two conformational epitopes. These four ERs probably define the neutralizing epitopes and could be used to guide ASF vaccine design (Fig. 2, B and C).

Besides surrounding the penton to fill the pentasymmetron, p72 capsomers also pack together to form the trisymmetron and zipper (Fig. 1, C and D). p72 capsomers adopt different arrangements to allow three distinct assembly patterns: "head to back," "head to head," and "back to back" (Fig. 2D). Within the trisymmetron, all p72 capsomers are arranged head to back to create two types of trimers of p72 capsomers (labeled 1 and 1′ in Fig. 2D; 1 has less interaction at the quasi-equivalent threefold axis, whereas 1′ has tight associations at the quasi-equivalent threefold axis). In the zipper and pentasymmetron, p72 capsomers possess all three contact modes, of which head-to-head associations exist in two forms (labeled 2 and 2′ in Fig. 2D) and back-to-back interactions occur in three different microenvironments (labeled 3, 3′, and 3″ in Fig. 2D). The head-to-head interactions in the zipper are straight and tight with a four-stranded β sheet contributed from two adjacent ER1s, whereas the corresponding interactions in the pentasymmetron are considerably decreased owing to the relative rotation of the p72 capsomer caused by higher curvature in the pentasymmetron (Fig. 2D). By contrast, back-to-back contacts in the zipper are the weakest when compared with their counterparts in the pentasymmetron, where a four-helix bundle is formed in the microenvironment of 3″ (Fig. 2D). Overall, the back-to-back contacts in the zipper and all three modes of contacts in the pentasymmetron seem insufficient to facilitate the assembly of higher-order structures, which suggests that minor capsid proteins are needed to build the networks that trigger the assembly of the whole capsid.

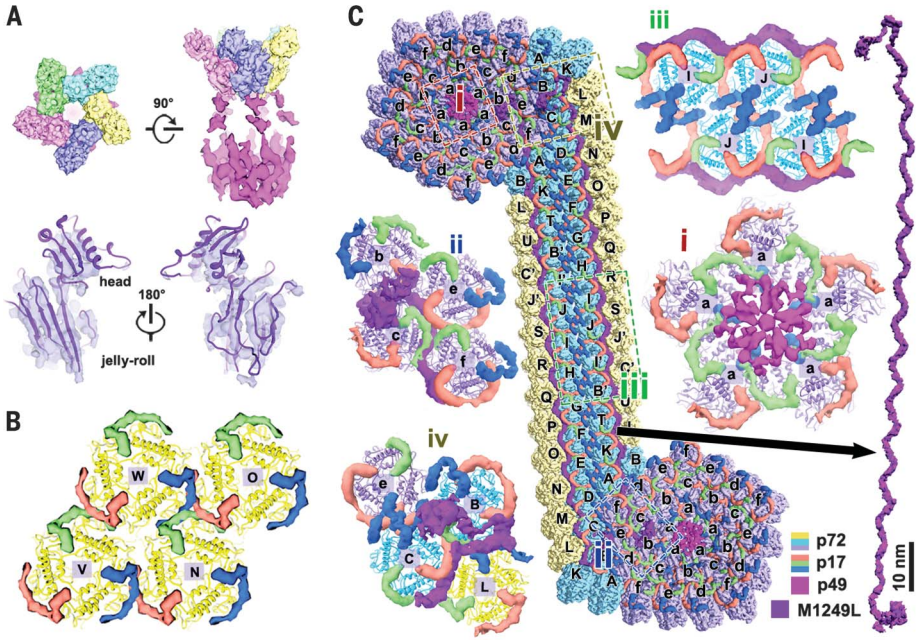


Fig. 3. Extensive intermolecular networks from minor capsid proteins underpin capsid stability. (**A**) Cryo-EM map of the penton complex (top). Each subunit of the penton is depicted in a different color, and the pentameric p49 is colored in magenta. The putative homologous structure of the mavirus penton protein is fitted into the ASFV penton cryo-EM map (bottom). (**B**) Structures of the p17 minor capsid proteins that glue together capsomers within each trisymmetron. Three copies of p17 molecules from one p72 capsomer are depicted in three colors (red, green, and blue), and p72 capsomers are shown as cartoons. (**C**) Overview of the intermolecular contacts at the inner capsid. One zipper and two neighboring pentasymmetrons are shown with the p72 capsomers labeled. The view is from the inside of the capsid, and the color scheme is the same as that in Fig. 1D. The diagrams labeled (i) to (iv) show enlarged views of the interactions indicated by the dashed boxes.

Correlated with fewer contacts among capsomers, interactions in the pentasymmetron are strengthened by all three minor capsid proteins and the penton (Fig. 3). The penton at the fivefold vertices of the outer capsid exhibits a single jelly roll and a globular cap (Fig. 3A), suggesting that the penton protein is different from, yet homologous to, p72, consistent with structural observations in some known large double-stranded DNA viruses (e.g., PBCV-1, mavirus, PRD1, and others). Flexible fitting of the mavirus penton protein structure into our map was straightforward, with the jelly-roll fold well aligned (Fig. 3A). A protein BLAST search with the mavirus penton sequence against all ASFV open reading frames identified a homolog with 37.7% sequence similarity, H240R, an uncharacterized but essential virion protein (*5*) (fig. S7 and table S2). H240R is 240 residues in length, enriched with β strands, and predicted to possess a single jelly-roll fold and a ~70–amino acid N-terminal extension (fig. S8), which further supports the identity of the penton in ASFV. Underneath the pentons, weak lantern-like densities (~9 Å) are observed connecting the penton and inner membrane and associating five neighboring capsomers, presumably playing roles in the assembly of the vertices (Fig. 3, A and C). Previous studies reported that the putative capsid protein p49 (B438L) is required for the formation of the capsid vertices (*20*) and is located in close proximity to the capsid vertices (*5*). Additionally,

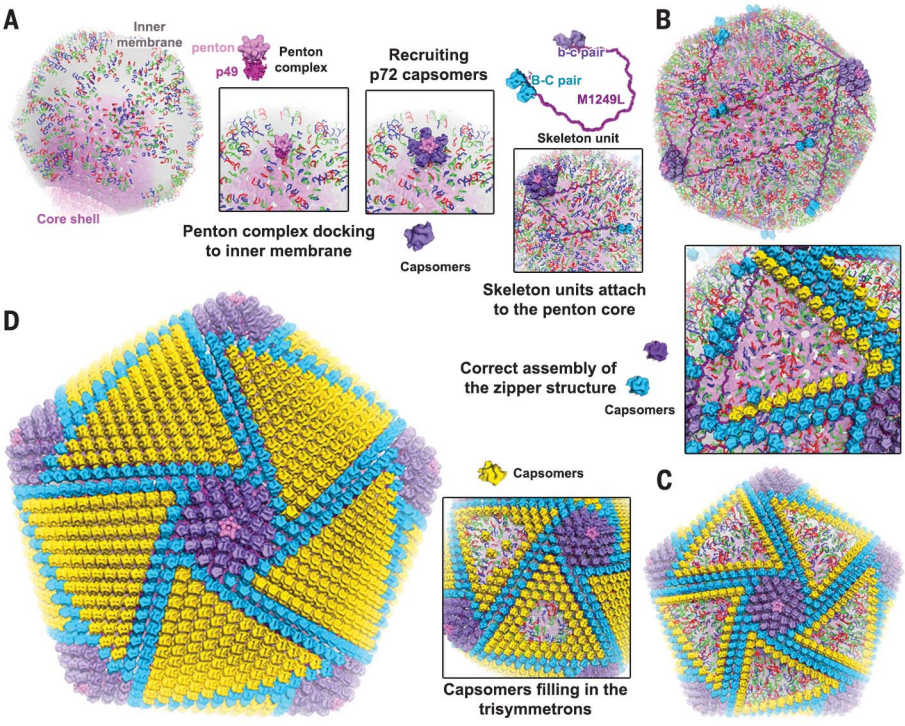


Fig. 4. The proposed assembly pathway for the ASFV capsid. (**A**) Formation of the penton cores on the inner membrane. The ASFV capsid assembly begins with appearance of viral inner membrane precursors that envelop the core shell and nucleoid progressively. During the early stage, the inner membranes exhibit generally open structures, with various inner membrane proteins, for example, p17, floating on them. The penton complexes associate with the inner membrane and then recruit p72 capsomers to form the penton cores, initiating the assembly. (**B**) Correct assembly of the zipper structures mediated by skeleton protein M1249L and p17 and p72 capsomers. (**C**) Construction of the polyhedral cage by 12 pentasymmetrons and 30 zippers. (**D**) Accompanying the formation of the polyhedral framework, p72 capsomers fill in the trisymmetrons to complete the capsid assembly.

p49, which behaves as an integral membrane protein, is not involved in particle transportation from the virus assembly sites to the plasma membrane (*20*), suggesting that it might be positioned at the inner shell of the capsid. Based on these observations, we propose that the lantern-like densities are five copies of p49 (Fig. 3, A and C).

Inner membrane protein p17 (D117L) is an essential and highly abundant protein required for the assembly of the capsid and icosahedral morphogenesis (*21*). Our reconstructions show repeated densities underneath the p72 capsomers. The snake-shaped structure consisting of three continuous α helices matches well with the secondary structure prediction of the ectodomain of p17 (Fig. 3B and fig. S9) and supports the protein abundance level analysis, suggesting that the density is p17 (table S2). p17 closely associates with the base domain of p72, and three copies of p17 encircle each p72 capsomer in the inner capsid shell, firmly anchoring p72 capsomers on the inner membrane (Fig. 3B). Interestingly, tight interdigitations of three p17s from three adjacent p72 capsomers mediate interactions among three capsomers under the type 1 microenvironment (Figs. 2D and 3B). These, together with interactions among three capsomers under the type 1′ microenvironment, guide an ordered packing of the capsomers in the trisymmetron, which comprises most of the capsid.

The microenvironments within pentasymmetrons and zippers are, however, more complicated. Here, the skeleton protein M1249L holds 34 capsomers together, not only fixing one pentasymmetron but also linking two neighboring pentasymmetrons (Figs. 1D and 3C). The essential 1249–amino acid–long M1249L is predicted to be full of coils (fig. S10) and exhibits a fiber-like configuration with two terminal lobes (~150 residues per lobe). The fiber part is about 100 nm in length and possesses 30 extended helices (~30 residues per helix) (Figs. 1D and 3C). M1249L starts from capsomers b and c (contacting a) within one pentasymmetron, extends along the outer edge of the zipper (capsomers c-e, d-f, B-A…N-E, M-D, and L-C), and ends with the capsomers B and C, interacting with the capsomer e from a neighboring pentasymmetron (Fig. 3C). The capsomer pairs (b-c and B-C), which normally show the weakest interactions (~150 Å^2) in the mode of back to back (types 3′ and 3), are now held together by the two lobes of M1249L (Figs. 2D and 3C). Additionally, M1249L extensively interacts with p17 and p72 capsomers to form the rigid zipper structure, where capsomers tightly contact each other in the head-to-head mode (type 2) to generate 17 geminate capsomers (d:B, e:C, f:D, A:E, K:F, T:G, B′:H, I′:I, and J:J) and 30 zippers construct the capsid framework. Surprisingly, p17 in the zipper adopts a distinct conformation compared with the one in the trisymmetron (Fig. 3, B and C). Double lasso structures formed by two sets of p17 pairs (Fig. 3C, red and blue) at quasi-equivalent twofold axes and tight intertwinements of p17s (Fig. 3C, red and green) and M1249L at the edge largely facilitate associations of capsomers along the fiber of M1249L, ensuring correct assembly of the zipper.

ASFV assembly begins with the appearance of viral inner membrane precursors, which presumably derive from the endoplasmic reticulum, and then proceeds into icosahedral intermediates and icosahedral particles by the progressive assembly of the capsid layer (*21*, *22*). During the early stage of viral assembly, the inner membranes are flexible and bear various morphologies, even open structures, with various mobile inner membrane proteins—for example, p17—floating on them. The capsid appears to be assembled under the guidance of the inner membrane proteins and minor capsid proteins, but no preassembled arrays or symmetrons have been observed in the infected cells. By combining previous experimental observations and our structural analysis, we can propose a detailed hypothesis for a further stage in understanding ASFV capsid assembly. First, the ability of p49 to associate with the membrane mediates the docking of the penton complex to the inner membrane, where it recruits capsomers (capsomer a) to form the penton core (Fig. 4), initiating the assembly. This is consistent with the in vivo assembly of the mimivirus capsid, which starts from the fivefold vertex and proceeds gradually to complete the capsid shell (*23*, *24*). Second, the skeleton unit M1249L with two capsomer pairs (b-c and B-C) attaches to the penton core; meanwhile, skeleton units, penton cores, and p17 can move around on the inner membranes, increasing their chance to form higher-order assemblies (Fig. 4). Under the guidance of p17 capsomers, skeleton protein M1249L and p17 contribute to the formation of the zippers, which connect neighboring penton cores and gradually construct a polyhedral framework (Fig. 4). Accompanying the formation of the polyhedral framework, capsomers fill in the trisymmetrons to complete the capsid assembly (Fig. 4). In our model, skeleton protein M1249L serves as the backbone for the

construction of the capsid framework and determines the size of the capsid. In line with this, fiber-like proteins with similar functions have also been observed in PRD-1 (*17*), PBCV-1 (*25*), and Bam35 (*26*), suggesting a similar assembly pathway.

The ASFV architecture at near-atomic resolution reported here allows us to take the first steps toward understanding what drives the assembly of the capsid and the basis for its stability. In addition, the structural details, and the p72 atomic structure in particular, can guide the rational design of an epitope-focused immunogen, which will affect the development of new strategies for vaccine intervention against ASFV infections.

REFERENCES AND NOTES

1. R. E. Montgomery, *J. Comp. Pathol. Ther.* **34**, 159 (1921).
2. P. J. Sánchez-Cordón, M. Montoya, A. L. Reis, L. K. Dixon, *Vet. J.* **233**, 41–48 (2018).
3. L. M. Iyer, L. Aravind, E. V. Koonin, *J. Virol.* **75**, 11720–11734 (2001).
4. M. L. Salas, G. Andrés, *Virus Res.* **173**, 29–41 (2013).
5. A. Alejo, T. Matamoros, M. Guerra, G. Andrés, *J. Virol.* **92**, e01293-18 (2018).
6. G. Andrés, R. García-Escudero, E. Viñuela, M. L. Salas, J. M. Rodríguez, *J. Virol.* **75**, 6758–6768 (2001).
7. R. Muñoz-Moreno, I. Galindo, M. A. Cuesta-Geijo, L. Barrado-Gil, C. Alonso, *Virus Res.* **209**, 118–127 (2015).
8. D. Zhao *et al*., *Emerg. Microbes Infect.* **8**, 438–447 (2019).
9. J. L. Carrascosa *et al*., *Virology* **132**, 160–172 (1984).
10. X. Zhang *et al*., *Proc. Natl. Acad. Sci. U.S.A.* **108**, 14837–14842 (2011).
11. C. Xiao *et al*., *Sci. Rep.* **7**, 5484 (2017).
12. T. Klose *et al*., *Proc. Natl. Acad. Sci. U.S.A.* **113**, 6206–6211 (2016).
13. C. Xiao *et al*., *PLOS Biol.* **7**, e1000092 (2009).
14. L. Zsak, D. V. Onisk, C. L. Afonso, D. L. Rock, *Virology* **196**, 596–602 (1993).
15. P. Gómez-Puertas *et al*., *J. Virol.* **70**, 5689–5694 (1996).
16. V. S. Reddy, G. R. Nemerow, *Proc. Natl. Acad. Sci. U.S.A.* **111**, 11715–11720 (2014).
17. N. G. A. Abrescia *et al*., *Nature* **432**, 68–74 (2004).
18. M. W. Bahar, S. C. Graham, D. I. Stuart, J. M. Grimes, *Structure* **19**, 1011–1020 (2011).
19. X. Yan *et al*., *J. Mol. Biol.* **385**, 1287–1299 (2009).
20. C. Epifano, J. Krijnse-Locker, M. L. Salas, J. Salas, J. M. Rodríguez, *J. Virol.* **80**, 11456–11466 (2006).
21. C. Suárez, J. Gutiérrez-Berzal, G. Andrés, M. L. Salas, J. M. Rodríguez, *J. Virol.* **84**, 7484–7499 (2010).
22. C. Epifano, J. Krijnse-Locker, M. L. Salas, J. M. Rodríguez, J. Salas, *J. Virol.* **80**, 12260–12270 (2006).
23. N. Zauberman *et al*., *PLOS Biol.* **6**, e114 (2008).
24. Y. Mutsafi, E. Shimoni, A. Shimon, A. Minsky, *PLOS Pathog.* **9**, e1003367 (2013).
25. Q. Fang *et al*., *Nat. Commun.* **10**, 388 (2019).
26. P. A. Laurinmäki, J. T. Huiskonen, D. H. Bamford, S. J. Butcher, *Structure* **13**, 1819–1828 (2005).

ACKNOWLEDGMENTS

We thank Z. Liu, G. Jiang, Q. Sun, S. Cao, X. Huang, B. Zhu, and G. Ji for cryo-EM data collection and the Electron Microscopy Facility of ShanghaiTech University and the Center for Biological imaging (CBI) in the Institute of Biophysics for EM work. Work was supported by the African Swine Fever Research Emergency Program of the Chinese Academy of Sciences (KJZD-SW-L06), the Strategic Priority Research Program (XDB29010000 and XDB08020200), the National Key Research and Development Program (2017YFC0840300, 2018YFC1200600, and 2018YFA0900801), Center for Biosafety Mega-Science, CAS, and Applied Technology Research and Development Project of Heilongjiang Province (GA19B301). X.W. was supported by the Ten Thousand Talent Program and the NSFS Innovative Research Group (no. 81921005). **Author contributions:** N.W., D.Z., Jia.W., Y.Z., Y.G., F.L., M.W., Jin.W., and X.W. performed experiments; X.W., Z.B., and Z.R. designed the study; all authors analyzed data; and X.W., Z.B., and Z.R. wrote the manuscript. **Competing interests:** All authors have no competing interests. **Data and materials availability:** Cryo-EM density maps of ASFV; the vertex, facet, and edge blocks; the asymmetric unit; and averaged map of the p72 capsomer have been deposited in the electron microscopy data bank under accession codes EMD-0815, EMD-0813, EMD-0812, EMD-0811, EMD-0810, and EMD-0814, respectively, and the atomic coordinate of p72 has been deposited in the Protein Data Bank under accession code 6L2T. Live ASFV is restricted to BSL3+ laboratories and may be subject to import controls.

SUPPLEMENTARY MATERIALS

science.sciencemag.org/content/366/6465/640/suppl/DC1
Materials and Methods
Figs. S1 to S10
Tables S1 to S3
References (*27*–*42*)

View/request a protocol for this paper from *Bio-protocol*.

16 August 2019; accepted 9 October 2019
Published online 17 October 2019
10.1126/science.aaz1439

BATTERIES

Reversible epitaxial electrodeposition of metals in battery anodes

Jingxu Zheng[1]*, Qing Zhao[2]*, Tian Tang[1], Jiefu Yin[2], Calvin D. Quilty[3], Genesis D. Renderos[3], Xiaotun Liu[2], Yue Deng[1], Lei Wang[4], David C. Bock[4], Cherno Jaye[5], Duhan Zhang[6], Esther S. Takeuchi[3,4,7], Kenneth J. Takeuchi[3,4], Amy C. Marschilok[3,4,7], Lynden A. Archer[1,2]†

The propensity of metals to form irregular and nonplanar electrodeposits at liquid-solid interfaces has emerged as a fundamental barrier to high-energy, rechargeable batteries that use metal anodes. We report an epitaxial mechanism to regulate nucleation, growth, and reversibility of metal anodes. The crystallographic, surface texturing, and electrochemical criteria for reversible epitaxial electrodeposition of metals are defined and their effectiveness demonstrated by using zinc (Zn), a safe, low-cost, and energy-dense battery anode material. Graphene, with a low lattice mismatch for Zn, is shown to be effective in driving deposition of Zn with a locked crystallographic orientation relation. The resultant epitaxial Zn anodes achieve exceptional reversibility over thousands of cycles at moderate and high rates. Reversible electrochemical epitaxy of metals provides a general pathway toward energy-dense batteries with high reversibility.

Electrodeposition is a two-century-old electrochemical method for creating thin, conformal coatings of metals on electrically conducting substrates. The method has in recent years reemerged as an area of scientific and technological interest owing to the role electrodeposition plays in the reversibility of energy storage in secondary/rechargeable batteries that use active metals—including lithium (Li), sodium (Na), potassium (K), magnesium (Mg), calcium (Ca), zinc (Zn), and aluminum (Al)—as anodes (*1*–*4*). The propensity of metals to form rough, nonuniform electrodeposits is a barrier to practical batteries because it leads to active material loss through multiple mechanisms (*5*–*11*). It is also dangerous because short circuits created when the nonuniform or dendritic metal electrodeposits proliferate in the interelectrode space to bridge the electrodes (Fig. 1A, left) can lead to fire or explosion.

In an epitaxial electrodeposition process, a thin-film electrodeposit forms a coherent or semicoherent lattice interface with the substrate. The single crystalline new phase (epilayer) exhibits a correlated orientation in relation to the substrate and low residual stresses. The strongest orientation correlations are achieved through directed nucleation and growth of the epilayer on a substrate that imposes minimal lattice strain. The process can be used to deposit metals, such as copper (Cu) (*12*, *13*) and platinum (Pt) (*14*)—on substrates of different chemistries. Textured interphases that add negligibly to the mass of a battery electrode and form low-lattice-mismatch interfaces are of specific interest in the present study. Furthermore, because the epilayer and substrate can be composed of the same (homo-) or different (hetero-) materials, either homoepitaxy or heteroepitaxy could be used in the process.

During battery charging, an electrochemically inactive interphase with selected crystal symmetry and lattice parameters would ideally facilitate heteroepitaxial nucleation and growth of a metal anode in a strain-free state. Once the nucleates cover the substrate, the as-deposited metal layer would enable homoepitaxial deposition (Fig. 1A) to create uniform metal coatings. Upon discharging, the metal is stripped away, while the substrate remains intact and, therefore, available for a subsequent cycle of charge and discharge. Thus, the critical steps in implementing the concept are (i) identifying electrically conductive substrate materials that have crystallographic facets with low lattice mismatch with the metal anode of interest and (ii) fabrication of a macroscopic, textured substrate that preferentially exposes these facets.

We studied the morphology and reversibility of a zinc metal anode in a 2 mol/liter-$ZnSO_4$ aqueous electrolyte. This system is of interest because rechargeable batteries based on Zn anodes have remerged as an area of scientific and technological interest (*15*–*17*). The most important considerations in choosing Zn include (i) it has low reactivity and relatively low cost; (ii) the divalent Zn can be electrochemically coupled with low-cost cathode chemistries [for example, MnO_2 (*18*, *19*)] in nonflammable aqueous electrolytes; and (iii) Zn anodes do not suffer from continuous parasitic reaction with electrolytes, which has plagued other metal anode batteries. The last of these attributes is the most important here because it allows us to focus on the atomic-scale processes that control the onset of morphological instability in the metal anode. Furthermore, Zn has a much higher Young's modulus (E) than that of alkali metals of contemporary interest as battery anodes ($E_{Zn} \approx 108$ GPa; $E_{Li} \approx 5$ GPa; $E_{Na} \approx 10$ GPa); once formed, Zn dendrites can more easily proliferate to cause

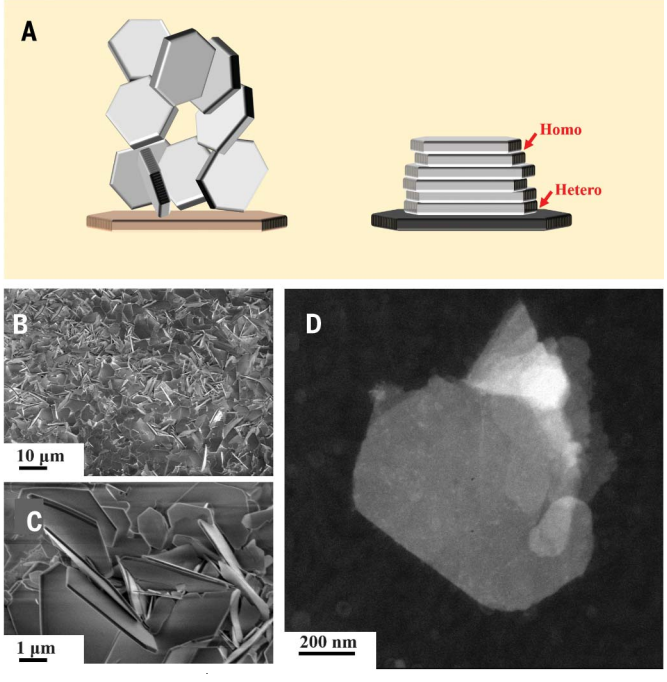


Fig. 1. Electrochemical growth pattern of Zn. (**A**) Scheme illustrating the design principle of epitaxial metal electrodeposition. (**B** and **C**) Scanning electron microscopy (SEM) images and (**D**) HAADF-STEM image of Zn electrodeposits on bare stainless steel from aqueous electrolyte current density $J = 4$ mA/cm^2.

[1]Department of Materials Science and Engineering, Cornell University, Ithaca, NY 14853, USA. [2]Robert Frederick Smith School of Chemical and Biomolecular Engineering, Cornell University, Ithaca, NY 14853, USA. [3]Department of Chemistry, Stony Brook University, Stony Brook, NY 11794, USA. [4]Energy Sciences Directorate, Brookhaven National Laboratory, Interdisciplinary Sciences Building, Building 734, Upton, NY 11973, USA. [5]Material Measurement Laboratory, National Institute of Standards and Technology, Gaithersburg, MD 20899, USA. [6]Sibley School of Mechanical and Aerospace Engineering, Cornell University, Ithaca, NY 14853, USA. [7]Department of Materials Science and Chemical Engineering, Stony Brook, NY 11794, USA.
*These authors contributed equally to this work.
†Corresponding author. Email: laa25@cornell.edu

battery failure by metal orphaning (*20*) or short-circuiting (*21*) mechanisms.

The intrinsic growth mode of electrodeposited Zn is shown in Fig. 1, B to D. Zn exhibits a strong tendency to deposit as platelets, implying that a lower thermodynamic free energy is associated with the exposed closest packed plane—(0002) in hexagonal close-packed (hcp) metal (*22*). High-angle annular dark field scanning transmission electron microscopy (HAADF-STEM) (Fig. 1D, and fig. S1, energy-dispersive x-ray spectroscopy mapping) confirmed the plate-like morphology. The electron diffraction pattern (fig. S2) shows that the plane normal of the Zn plate is $[0001]_{Zn}$. Therefore, a candidate substrate for epitaxial electrodeposition of Zn should show similar atomic arrangement to the $(0002)_{Zn}$ plane (fig. S3).

A preliminary screening based on crystal structure was performed. Criteria included (i) does the crystal plane exhibit a small lattice misfit with $(0002)_{Zn}$. Numerically, the lattice misfit should be no larger than 25% as an empirical value to form a coherent or semicoherent interface (*23*). (ii) Does the crystal plane of interest have a low lattice index? A low lattice index is preferred because it indicates higher atomic packing density and therefore higher surface stability (*24*). And (iii) the substrate should remain intact and therefore electrochemically inactive during cycling. Within this screening framework, graphene stands out as a candidate material that meets all the specified criteria (fig. S3).

Creating a macroscopic material in which the basal plane of graphene is parallel to an electrode surface is not straightforward. We designed a fluid-based route for creating aligned graphene coatings. The method takes advantage of the ease with which high-aspect-ratio graphene flakes in a slurry are aligned by shear flow (*25*). The rheological properties of the graphene suspensions are shown in Fig. 2A. The initially elastic slurry ($G' > 10*G''$) yields at a low shear strain ($\gamma \approx 0.05$) and transitions to a liquid-like state at high strain in which $G'' > G'$. Correlations between graphene sheets are evidently broken in a modest shear flow. In continuous shear, the suspensions are shear-thinning at low rates $\dot{\gamma}(\sim 10^{-2}\ s^{-1})$ (fig. S4), and relaxation after cessation of shear is a two-step process (fig. S5), with the slower step lasting several hundreds of seconds. Subjecting a graphene suspension to a moderate shear rate for even a short period of time could therefore produce relatively long-lived orientation parallel to the shear plane.

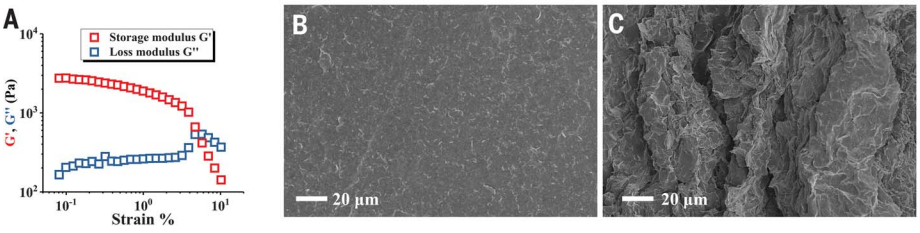


Fig. 2. Preparation of the epitaxial substrate in which graphene sheets are parallel to the substrate. (**A**) Strain sweep of the 4% graphene in NMP slurry. (**B** and **C**) SEM images of graphene membranes prepared (B) with and (C) without the shearing.

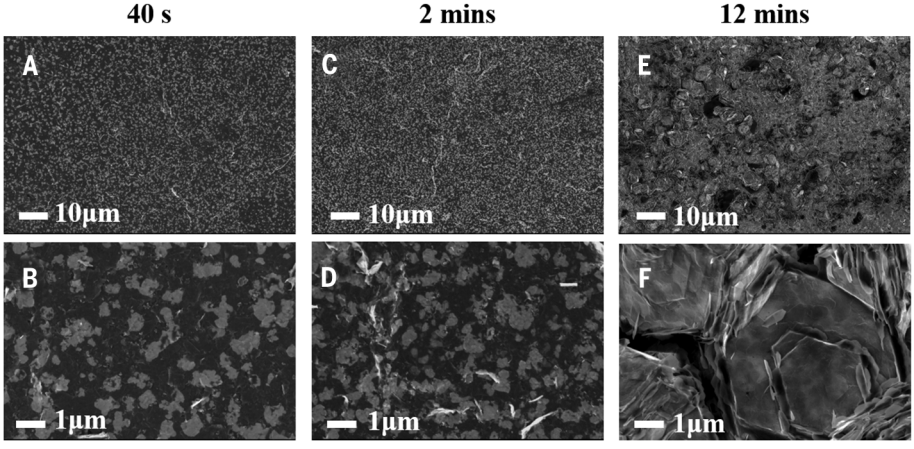


Fig. 3. SEM of Zn deposits on graphene-coated stainless steel. SEM deposition times, (**A** and **B**) 40 s, (**C** and **D**) 2 min, and (**E** and **F**) 12 min. Current density, J = 4 mA/cm^2.

We designed a doctor-blade–type apparatus to implement this process using suspensions composed of graphene flakes in *N*-methyl-2-pyrrolidone (NMP). To lock in the alignment, the sheared coatings were immediately transferred to a vacuum chamber, where the NMP solvent was removed. The effectiveness of the method can be seen by comparing morphologies and polarized near-edge x-ray absorption fine structure (NEXAFS) spectra of the graphene coating prepared with (Fig. 2B) and without (Fig. 2C) shearing (fig. S6 to S9). It is evident that our approach provides a simple, scalable route toward planar interphases composed of well-aligned graphene sheets with $[0001]_{graphene}$ facets perpendicular to the substrate.

In contrast to the deposition morphology on stainless steel (Fig. 1, B and C), in which Zn platelets are randomly oriented, Zn deposits formed on graphene are well directed, showing a locked orientation relation with the graphene substrate (Fig. 3 and fig. S10). Further analysis reveals that there are two stages in the epitaxial electrodeposition: stage I, heteroepitaxy between Zn and graphene (Fig. 3, A to D), and stage II, homoepitaxy of Zn after the graphene surface has been fully occupied (Fig. 3, E and F). Small newly deposited Zn layers are attached to the surface of the Zn formed in stage I (Fig. 3F and fig. S11). The Zn deposition rate on graphene appears lower than that on a bare stainless-steel substrate because the epitaxial regulation produces thin plates that are parallel to the substrate, more uniform, and compact, as schematically illustrated in Fig. 1A. This highly ordered growth is sustained at the high current density of 40 mA/cm^2 (fig. S12). Atomic force microscopy (fig. S13) and x-ray diffraction (figs. S14 to S16) results confirmed the epitaxial regulation of Zn deposition. As a comparison, no epitaxial growth was observed on Ketjen black–coated (an isotropic carbon) stainless steel (fig. S17). The plating and stripping of Zn was studied by means of cyclic voltammetry (CV) (fig. S18), and the results show no obvious impact of the deposition process on the electrochemical reaction mechanism.

When used as a battery anode, a successful metal electrode must be reversibly plated and stripped over hundreds or thousands of charge-discharge cycles. The coulombic efficiency (CE) is a measure of this reversibility. We quantified the CE for epitaxially and nonepitaxially deposited Zn using a procedure in which a certain amount of metal is plated on the substrate and then stripped away; the ratio of charge passed in each segment of the cycle determines the CE. Zn plating and stripping on an electrochemically inert substrate, such as stainless steel, shows CE values around 80% (fig. S19). These cells quickly fail, however, after only 20 plate-strip cycles. The observed voltage fluctuations are consistent with failure either as a result of

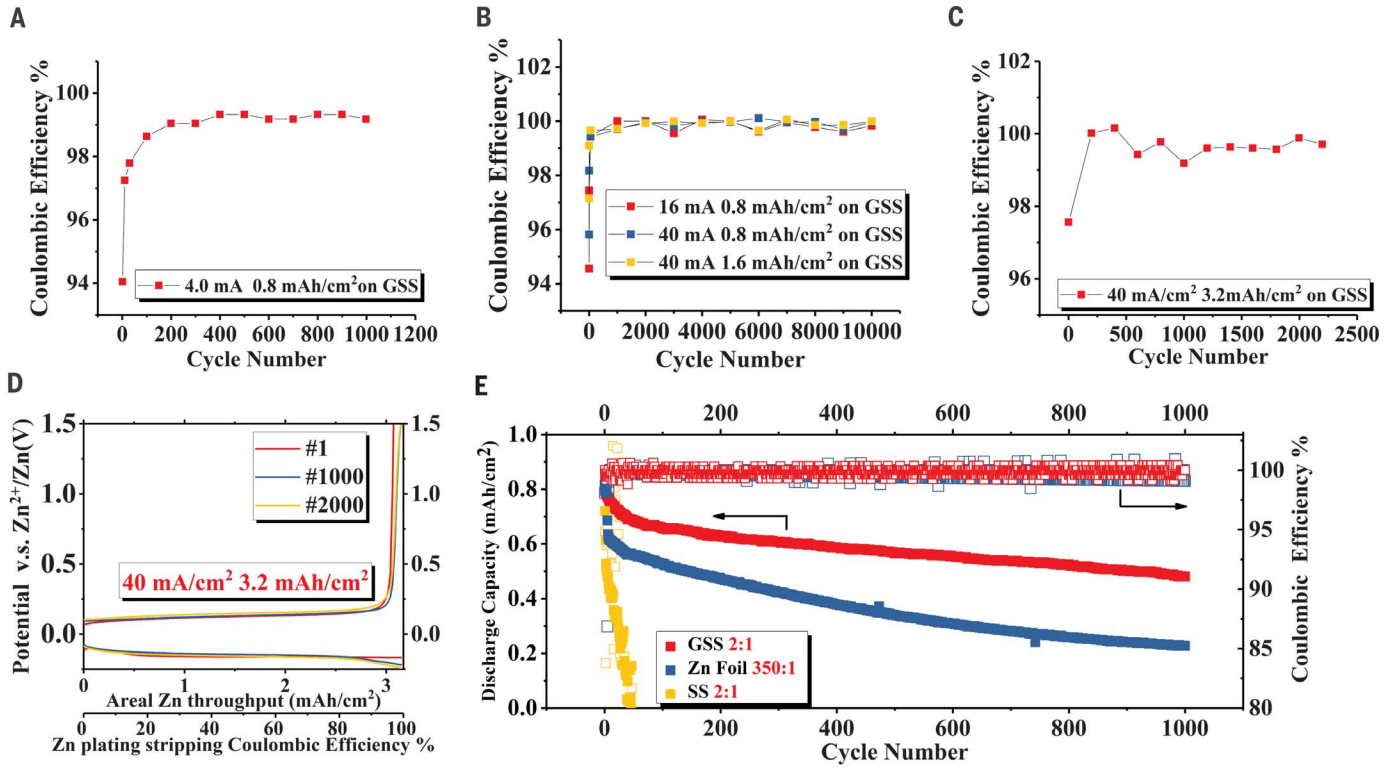


Fig. 4. Electrochemical performance of epitaxial Zn metal anodes. (**A**) CE at moderate current density on graphene coated stainless steel (GSS) substrate. (**B**) CE at high current densities on GSS. (**C**) CE under high current and high areal capacity condition on GSS. (**D**) The corresponding voltage profile. (**E**) Cycling performance of Zn||α-MnO_2 full cells with and without graphene, with controlled N:P electrode capacity ratios.

Table 1. Potential epitaxial substrates for anode metals.

Anode metal	Potential epitaxial substrate	Lattice misfit δ %
Al	Au/Ag	0.7/0.7
Ca	Sr/Pb	8/11
Zn	Co/Ti	6/9
Mg	Zr/Ti	0.9/8
Li	Ta	6
Na	Eu	8
K	Ba	4

localized short circuiting or by reconnection of fragmentary Zn deposits that broke away from the electrode ("orphaned" Zn) (figs. S20 and S21) (*21*). By contrast, epitaxial deposition of Zn yields quite noticeable improvements in reversibility (CE > 99% over 1000 cycles) (Fig. 4A).

We measured the CE at higher current densities of 16 and 40 mA/cm^2 (table S1) (*17*, *26*, *27*). As reported in Fig. 4B, high CE values (CE = 99.9% over 10,000 cycles) were observed. By contrast, electrodes without the graphene coating fail after just eight cycles (fig. S22). We also evaluated the performance of unaligned graphene substrates, created without the shearing procedure. With erratic voltage behavior, the measured average CE was 94%, and the cells failed by 125 cycles, which is attributable to the uneven Zn deposition morphology (fig. S23).

We increased the areal Zn throughput to 3.2 mAh/cm^2 to assess the stability of the homoepitaxy component of the deposition. High electrode reversibility (CE ≈ 99.7% over 2000 cycles), stable voltage profiles, and homoepitaxial regulation of deposition morphology are reported in Fig. 4, C to D (fig. S24). By contrast, the unmodified electrode fails after the first cycle.

The high reversibility of the epitaxial anode allowed us to study rechargeable batteries with low negative-to-positive electrode capacity (N:P) ratio (*28*, *29*). A low N:P ratio is required for high overall energy density of a battery (fig. S25). We created electrochemical cells in which the epitaxial Zn anode is paired with a conventional α-MnO_2 cathode with a N:P ratio of 2:1. The cell with the epitaxial Zn anode maintains excellent capacity retention over 1000 cycles at 8 mA/cm^2 (Fig. 4E and fig. S26). Analogous Zn||MnO_2 cell cycling results at the same current density, but using anodes composed, respectively, of a Zn coating on stainless steel (N:P = 2:1) and a 620-μm-thick Zn foil (N:P ~ 350:1) are provided in Fig. 4E.

In addition to aqueous electrolytes, the results in fig. S27 to S29 reveal that the epitaxial approach can be readily extended to other electrolytes of interest, such as 0.2 mol/liter Zn $(CF_3SO_3)_2$ in dimethylether. In this nonaqueous electrolyte, a 99.97% CE was achieved. The improvement could stem from the suppression of hydrogen evolution and other side reactions.

Epitaxial electrodeposition as a strategy for creating highly reversible metal anodes is relevant for other electrode chemistries of contemporary interest. For face-centered cubic (FCC) metals (Al and Ca), body-centered cubic (BCC) metals (Li, Na, and K), and HCP metals (Mg), the screening for potential substrates can be performed on the basis of the atomic arrangements of their closely packed planes. Previously, epitaxial electrodeposition of various metals has been demonstrated (*30*, *31*). Although none of these efforts have considered

reversibility of the process, they indicate that the concept is broadly useful. In line with the criteria used to screen epitaxial substrates for Zn, we performed a screening for potential substrates for FCC, HCP, and BCC metals (Table 1 and tables S2 to S4). As a demonstration, we studied the morphology of Al on (111)–textured gold (Au) nanosheets (*32*). This pairing stands out for the small lattice misfit $\delta_{Au\text{-}Al}$ = 0.7% and chemical inertness of Au. We also performed electrodeposition in a Lewis-acidic electrolyte that can dissolve surface oxide layer (*33*, *34*), which may prevent direct contact between the metals and the substrate. The results reported in figs. S30 and S31 show that the Au sheets facilitate formation of evenly distributed, nanosized Al electrodeposits, in contrast to the uneven, coarse particulate Al morphologies formed in the absence of epitaxial regulation.

We report that reversible epitaxial electrodeposition at a metal electrode can be achieved by using textured electrically conducting electrode coatings with low lattice mismatch with the metal of interest. An epitaxial aqueous-Zn anode is reported to achieve high reversibility (CE > 99.7%) at moderate and high current densities. The epitaxy regulation concept can be extended to achieve reversible cycling in nonaqueous-Zn electrochemical cells as well as in other rechargeable batteries that use metals as anode.

REFERENCES AND NOTES

1. J. F. Parker *et al*., *Science* **356**, 415–418 (2017).
2. D. Lin, Y. Liu, Y. Cui, *Nat. Nanotechnol.* **12**, 194–206 (2017).
3. M. S. Whittingham, *Science* **192**, 1126–1127 (1976).
4. M.-C. Lin *et al*., *Nature* **520**, 325–328 (2015).
5. M. D. Tikekar, S. Choudhury, Z. Tu, L. A. Archer, *Nat. Energy* **1**, 16114 (2016).
6. Y. Li *et al*., *Science* **358**, 506–510 (2017).
7. M. J. Zachman, Z. Tu, S. Choudhury, L. A. Archer, L. F. Kourkoutis, *Nature* **560**, 345–349 (2018).
8. P. Bai, J. Li, F. R. Brushett, M. Z. Bazant, *Energy Environ. Sci.* **9**, 3221–3229 (2016).
9. K. E. K. Sun *et al*., *ACS Appl. Mater. Interfaces* **9**, 9681–9687 (2017).
10. A. Pei, G. Zheng, F. Shi, Y. Li, Y. Cui, *Nano Lett.* **17**, 1132–1139 (2017).
11. R. F. Voss, M. Tomkiewicz, *J. Electrochem. Soc.* **132**, 371–375 (1985).
12. C. M. Hull, J. A. Switzer, *ACS Appl. Mater. Interfaces* **10**, 38596–38602 (2018).
13. S. Hwang, I. Oh, J. Kwak, *J. Am. Chem. Soc.* **123**, 7176–7177 (2001).
14. K. Uosaki *et al*., *J. Phys. Chem. B* **101**, 7566–7572 (1997).
15. A. R. Mainar *et al*., *J. Energ. Stor.* **15**, 304–328 (2018).
16. D. Kundu, B. D. Adams, V. Duffort, S. H. Vajargah, L. F. Nazar, *Nat. Energy* **1**, 16119 (2016).
17. F. Wang *et al*., *Nat. Mater.* **17**, 543–549 (2018).
18. N. Zhang *et al*., *Nat. Commun.* **8**, 405 (2017).
19. G. G. Yadav *et al*., *Nat. Commun.* **8**, 14424 (2017).
20. J. Zheng *et al*., *ACS Energy Lett.* **4**, 1349–1355 (2019).
21. S. Higashi, S. W. Lee, J. S. Lee, K. Takechi, Y. Cui, *Nat. Commun.* **7**, 11801 (2016).
22. R. Sato, *J. Electrochem. Soc.* **106**, 206–211 (1959).
23. D. A. Porter, K. E. Easterling, M. Sherif, *Phase Transformations in Metals and Alloys (Revised Reprint)* (CRC, 2009).
24. C. Klein, B. Dutrow, J. D. Dana, *Manual of Mineral Science* (Wiley, ed. 23, 2007).
25. G. Natale, N. K. Reddy, R. K. Prud'homme, J. Vermant, *Phys. Rev. Fluids* **3**, 063303 (2018).
26. A. Naveed, H. Yang, J. Yang, Y. Nuli, J. Wang, *Angew. Chem.* **131**, 2786–2790 (2019).
27. S.-D. Han *et al*., *ACS Appl. Mater. Interfaces* **8**, 3021–3031 (2016).
28. P. Albertus, S. Babinec, S. Litzelman, A. Newman, *Nat. Energy* **3**, 16–21 (2018).
29. J. Zheng *et al*., *ACS Energy Lett.* **4**, 271–275 (2018).
30. J. Petermann, G. Broza, *J. Mater. Sci.* **22**, 1108–1112 (1987).
31. P. Allongue, F. Maroun, *Curr. Opin. Solid State Mater. Sci.* **10**, 173–181 (2006).
32. C. C. Li *et al*., *Adv. Funct. Mater.* **16**, 83–90 (2006).
33. Q. Zhao *et al*., *Sci. Adv.* **4**, eaau8131 (2018).
34. N. Jayaprakash, S. K. Das, L. A. Archer, *Chem. Commun.* **47**, 12610–12612 (2011).

ACKNOWLEDGMENTS

The authors express their gratitude to X. Zheng, L. Li, L. Luo, R. Luo, M. Pfeifer, and X. Ren for valuable discussions. **Funding:** This work was supported as part of the Center for Mesoscale Transport Properties, an Energy Frontier Research Center supported by the U.S. Department of Energy, Office of Science, Basic Energy Sciences, under award DE-SC0012673. NEXAFS experiments were carried out at the 7-ID SST-1 beamline in the National Synchrotron Light Source II at Brookhaven National Laboratory, which is supported by the U.S. Department of Energy under contracts DE-AC02-98CH10886 and DE-SC-00112704. G.D.R. acknowledges the Graduate Assistance in Areas of National Need Fellowship (GAANN). L.A.A. acknowledges the James A. Friend Family Distinguished Professorship in Engineering. E.S.T. acknowledges the William and Jane Knapp Chair in Energy and the Environment. This work made use of the Cornell Center for Materials Research Shared Facilities, which are supported through the NSF Materials Research Science and Engineering Center program (DMR-1719875). The work also used CESI Shared Facilities partly sponsored by the NSF MRI DMR-1338010 and Kavli Institute at Cornell University (KIC). Certain commercial names are mentioned in this manuscript and the supplementary materials for the purpose of example and do not constitute an endorsement by the National Institute of Standards and Technology. This research used Beamline 7-ID-1 of the National Synchrotron Light Source, a U.S. Department of Energy (DOE) Office of Science User Facility operated for the DOE Office of Science by Brookhaven National Laboratory under contract DE-SC0012704. **Author contributions:** L.A.A. directed the research. J.Z., Q.Z., T.T., and L.A.A. conceived and designed this work. J.Z., Q.Z., and T.T. performed the electrodeposition, electrochemical measurements, and structure characterizations. J.Y. carried out the AFM investigation. L.A.A., J.Z., X.L., Q.Z., Y.D., and D.Z. conducted rheology measurements. C.D.Q., G.D.R., J.Z., E.S.T., K.J.T. and A.C.M. performed the XRD characterization. L.W., D.C.B., C.J., E.S.T., K.J.T., and A.C.M. performed the NEXAFS characterizations. J.Z., L.A.A., Q.Z., and T.T. wrote the article with edits and approval from all the authors. **Competing interests:** L.A.A. is a founder and member of the board of directors of NOHMs Technologies. This company develops and commercializes electrolytes for Li-ion and Li-sulfur battery technology. The authors declare no other competing interests. **Data and materials availability:** All data needed to evaluate the conclusions in the paper are present in the paper or the supplementary materials.

SUPPLEMENTARY MATERIALS

science.sciencemag.org/content/366/6465/645/suppl/DC1
Materials and Methods
Figs. S1 to S31
Tables S1 to S4
References (*35*–*38*)

13 April 2019; accepted 8 October 2019
10.1126/science.aax6873



Broad-Range RNA Quantitation Kits

AccuBlue boasts the widest linear range (5 ng–1000 ng RNA) of available RNA quantitation kits, while providing exceptional accuracy, sensitivity, and high RNA selectivity. The kit is compatible with fluorescent microplate readers, Qubit fluorometers, or other small fluorometers, and is ideal for applications like next-generation sequencing and real-time PCR. Unlike absorbance-based measurements, the RNA dye is highly selective for RNA over double-stranded DNA (dsDNA) and can tolerate an equimolar amount of dsDNA without any significant effects on RNA quantitation. A mammalian RNA standard is included for accurate quantitation of mammalian cell RNA.

Biotium
For info: 800-304-5357
www.biotium.com

Wheat Exome Panel

The new myBaits Expert Wheat Exome panel was developed in collaboration with the International Wheat Genome Sequencing Consortium (IWGSC) using the most up-to-date and comprehensive genome-wide annotations for the Chinese spring wheat cultivar. The panel enriches the complete set of high-confidence exon annotations in hexaploid wheat, retrieving over 250 megabase pairs of the greater-than-15-gigabase-pair *Triticum aestivum* genome. This kit saves the exome-focused researcher orders of magnitude in sequencing and analysis costs when compared to whole-genome sequencing, and pairs seamlessly with virtually all library preparation chemistries and sequencing platforms. The Wheat Exome v1 panel is provided as a complete in-solution target capture kit, including buffers, blockers, and baits, along with an easy-to-use protocol.

Arbor Biosciences
For info: 734-998-0751
arborbiosci.com/products/mybaits-expert-wheat-exome-panel

Automated Cell Counter

CellDrop incorporates DeNovix' patented DirectPipette Technology, removing the need for expensive, environmentally damaging plastic slides. CellDrop brings the simple load, measure, and wipe-clean functionality of nanovolume spectrophotometers to cell counting. The unique, variable-volume counting chamber can be automatically adjusted to the optimum height for each sample, delivering greater accuracy and allowing measurements across the widest range of cell densities ($7x10^2$ and $4x10^7$ cells) without the need for dilution or concentration. Combining dual fluorescence and brightfield optics with powerful onboard EasyApps software enables a range of cell counting, viability, and transfection efficiency assays. Instruments come preinstalled with apps for acridine orange/propidium iodide (AO/PI), brightfield, trypan blue, and green fluorescent protein, and allow the user to easily customize methods. CellDrop is a stand-alone instrument, with high-definition, 7-in. touchscreen ideal for reviewing live images, data, and reports. All instruments contain Wi-Fi, USB, and Ethernet connectivity, allowing users to easily export data via email, network drives, network printers, or USB drive. CellDrop is available in dual fluorescence and brightfield or brightfield-only models.

DeNovix
For info: 302-442-6911
www.denovix.com

Exosome Isolation and Detection Kits

AMS Biotechnology introduces exosome isolation and detection kits designed for investigating targeted cancer therapy. Exosomes expressing specific surface markers (e.g., CD81, CD63, and CD9) have been found to play roles in cancer progression and tumorigenesis as transporters of microRNA. As a delivery system, they can therefore potentially be used as a specific carrier of immunotherapy/chemotherapy and cancer vaccines, as is shown by the growing number of biotech companies developing exosome-based therapies. Our new column-based exosome isolation kit works to isolate intact exosomes from both serum and cell-conditioned media. Exosome detection ELISA kits quantify exosome levels in the fractions as well as in samples such as culture media and sera. In addition, we also provide monoclonal antibodies against common exosome markers and immune checkpoint ligands for immunostaining, ELISA, or flow cytometry.

AMS Biotechnology
For info: 617-945-5033
www.amsbio.com/exosomes.aspx

25-mL Conical Tubes

Eppendorf has developed the Eppendorf Conical Tube 25 mL—available with either the new, patented SnapTec cap or with a screw cap. These conical tubes have the same diameter as conventional 50-mL conical tubes but a ~20% lower height. This allows space-saving storage, for example in freezers. The wide opening, combined with the lower height, offers easy sample access. Premium raw materials, manufactured without the use of plasticizers and biocides, ensure the highest sample integrity and optimal sample and pellet visibility. The most innovative feature is the SnapTec cap, which is firmly connected to the tube. No need to put the cap on the bench, running the risk that caps from different tubes may become mixed up or contaminated. The cap allows single-handed opening and closing for quick liquid extraction or addition of sample. This feature is particularly advantageous in multistep lab protocols.

Eppendorf
For info: 800-645-3050
www.eppendorf.com/25mL

Microfluidic 3D Cell Culture Plate

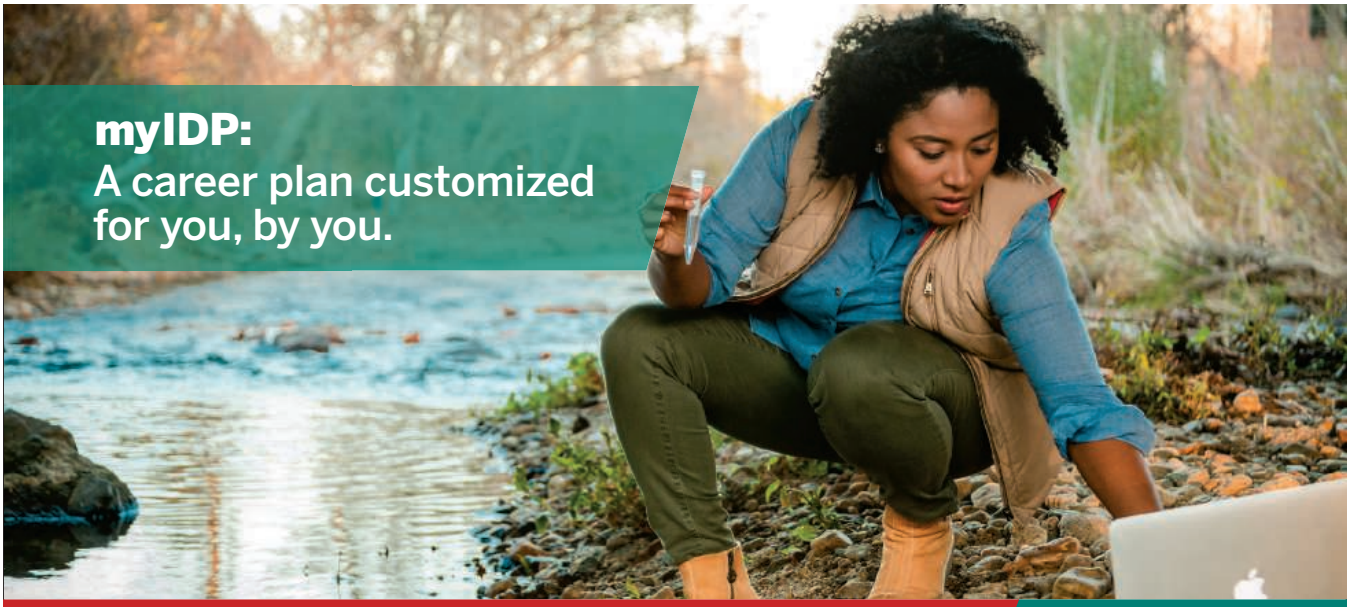
The OrganoPlate is a microfluidic 3D cell culture plate, supporting up to 96 tissue models on a single plate. Our PhaseGuide technology enables precise, barrier-free definition of culture matrices and cells in 3D, supporting cell–cell interactions and unprecedented imaging and quantification. Continuous perfusion of media through the microfluidic networks in the OrganoPlate mimics blood flow and allows exchange of nutrients, oxygen, and metabolites. Our unique, gravity-driven leveling technology maintains flow without the use of pumps and tubing, making this culture plate suitable for any throughput. The Perfusion Rocker Mini provides continuous medium flow, with minimal settings required. The PhaseGuide platform is arguably the most cost-effective microfluidic liquid-handling platform available. Being a passive technology, it requires no moving parts, and plate functionality is fully programmed by its geometry. The OrganoPlate is versatile, supporting chemical gradients of chemical compounds, proteins, and coculture conditions, and makes organ-on-a-chip technology affordable and available to nonspecialized end-users.

Mimetas
For info: +31-(0)-85-888-31-61
mimetas.com/page/technology

Electronically submit your new product description or product literature information! Go to www.sciencemag.org/about/new-products-section for more information.

Newly offered instrumentation, apparatus, and laboratory materials of interest to researchers in all disciplines in academic, industrial, and governmental organizations are featured in this space. Emphasis is given to purpose, chief characteristics, and availability of products and materials. Endorsement by *Science* or AAAS of any products or materials mentioned is not implied. Additional information may be obtained from the manufacturer or supplier.

ScienceCareers online @sciencecareers.org



For your career in science, there's only one Science

Features in myIDP include:

- Exercises to help you examine your skills, interests, and values.
- A list of 20 scientific career paths with a prediction of which ones best fit your skills and interests.
- A tool for setting strategic goals for the coming year, with optional reminders to keep you on track.
- Articles and resources to guide you through the process.
- Options to save materials online and print them for further review and discussion.
- Ability to select which portion of your IDP you wish to share with advisors, mentors, or others.
- A certificate of completion for users that finish myIDP.

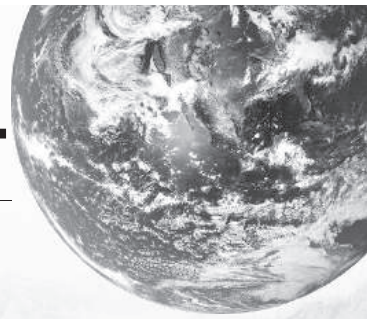
myIDP

Visit the website and start planning today!
myIDP.sciencecareers.org

ScienceCareers In partnership with:

FASEB Federation of American Societies for Experimental Biology
UMASS University of Massachusetts Medical School
UCSF University of California San Francisco
UIC
BURROUGHS WELLCOME FUND

HIGH-END GLOBAL TALENTS RECRUITMENT



Welcome back to hometown.
Thousands of academic job vacancies are in fast-developing China.

On-the-spot Recruitment in America
Oct. 30, 2019 12:00-14:00
University of Chicago

Oct. 30, 2019 16:30-19:00
Northwestern University

Oct. 31, 2019 16:30-19:00
Illinois Institute of Technology

Scan the QR code to apply for Canada&America Job Fair

Scan the QR code to apply for UK&France Job Fair

On-the-spot Recruitment in UK
Dec. 10, 2019 Imperial College London
Dec. 11, 2019 Queen Mary University of London
On-the-spot Recruitment in France
Dec. 14, 2019 Pierre and Marie Curie University
Dec. 15, 2019 Université Paris-Sud
Online Job Fair
Dec. 21, 2019(GTM+8) www.edu.cn/cv
Qualification for Applicants
Overseas scholars, Doctor and Post-doctor
Participating Approach
Please send your CV to consultant@acabridge.edu.cn for on-the-spot Recruitment in Canada, America, UK and France and Online Job Fair.

Job Vacancies in China's Universities and Institutes
Please visit https://www.acabridge.edu.cn/
Contact consultant@acabridge.edu.cn



Overseas Chinese Scholars' Visit to Top Chinese Universities

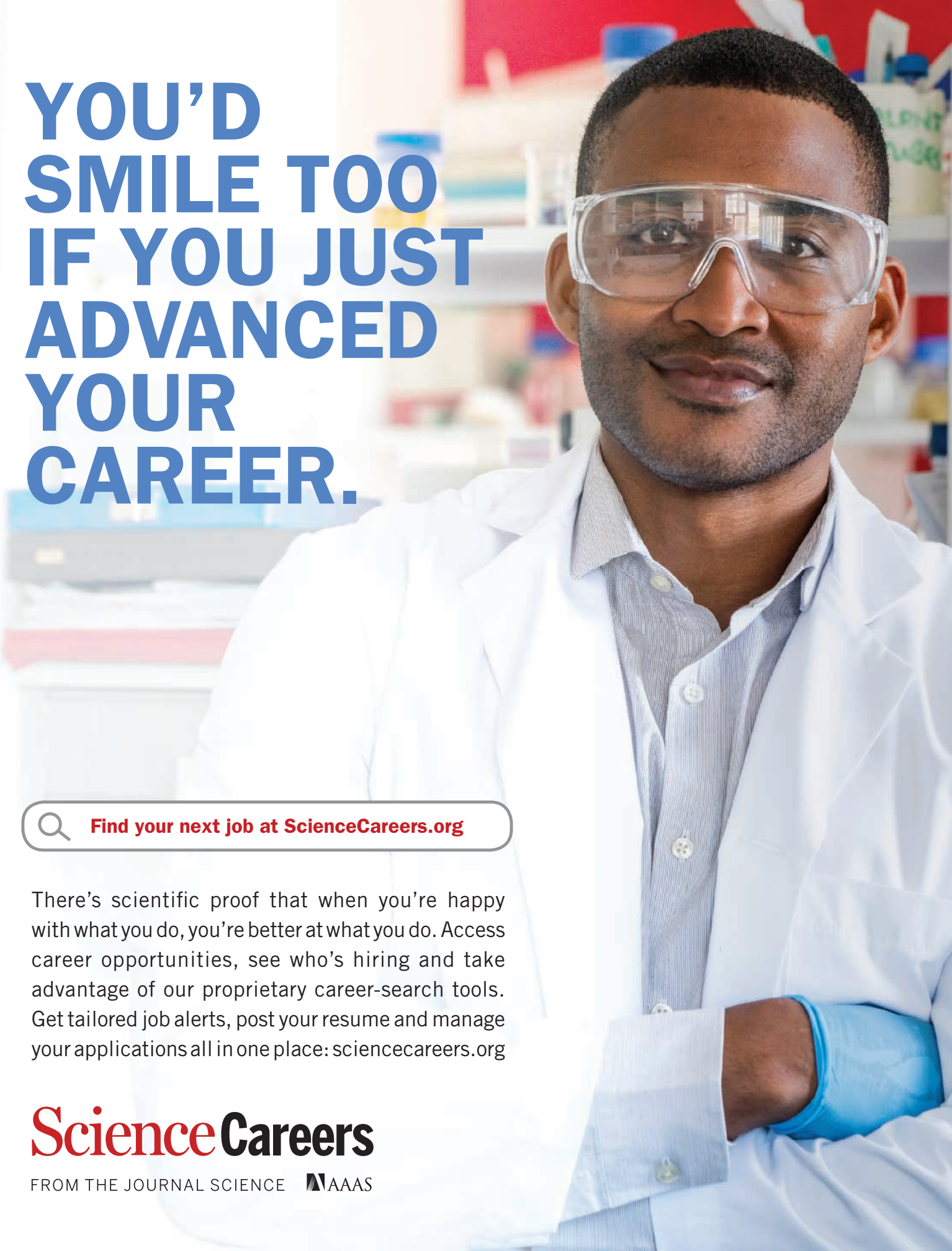
Check the Details from www.edu.cn/zgx

- **10,000+ academic job vacancies in China**
- **Free one-to-one consultation service**

Send your CV to
consultant@acabridge.edu.cn

上海外国语大学　贵州医科大学
江西理工大学　南京工业大学

YOU'D SMILE TOO IF YOU JUST ADVANCED YOUR CAREER.



Find your next job at ScienceCareers.org

There's scientific proof that when you're happy with what you do, you're better at what you do. Access career opportunities, see who's hiring and take advantage of our proprietary career-search tools. Get tailored job alerts, post your resume and manage your applications all in one place: sciencecareers.org

ScienceCareers

FROM THE JOURNAL SCIENCE AAAS

ScienceCareers
FROM THE JOURNAL SCIENCE AAAS

Confused about your next career move?

Download Free Career Advice Booklets!

ScienceCareers.org/booklets







ASSISTANT PROFESSOR

The Department of Biochemistry and Molecular Biology at The Pennsylvania State University College of Medicine invites applications from outstanding scientists for a full-time tenure-track position. We seek candidates at the Assistant Professor level who have an active highly competitive independent research program or who show a strong potential to develop such a program, particularly in the area of bioinformatics and genomics. Qualifications include a PhD or equivalent degree in the area of bioinformatics, especially with respect to high-throughput data extraction, analysis and modeling, and computational biology, with expertise in development of tools and algorithms for interrogating and exploiting large datasets. For additional information, please visit the following websites: https://med.psu.edu/biochemistry and https://research.med.psu.edu/departments/personalized-medicine/. Applicants should submit a curriculum vitae and a brief statement of research plans, and arrange for three letters of reference to be sent to Faculty Search Committee, mailto:biochem_apply@psu.edu or to Department of Biochemistry and Molecular Biology H171, The Pennsylvania State University College of Medicine, Hershey PA 17033.

Apply online at **https://apptrkr.com/1628872**

CAMPUS SECURITY CRIME STATISTICS: For more about safety at Penn State, and to review the Annual Security Report which contains information about crime statistics and other safety and security matters, please go to http://www.police.psu.edu/clery/, which will also provide you with detail on how to request a hard copy of the Annual Security Report.

Penn State is an equal opportunity, affirmative action employer, and is committed to providing employment opportunities to all qualified applicants without regard to race, color, religion, age, sex, sexual orientation, gender identity, national origin, disability or protected veteran status.

UNIVERSITY OF ARKANSAS

TENURE-TRACK ASSISTANT PROFESSOR in GENOMICS AND BIOINFORMATICS

The Department of Biological Sciences at the University of Arkansas invites applications for a **tenure-track Assistant Professor faculty position** in Genomics and Bioinformatics (Posting # 37386). We seek candidates who creatively apply genomics and bioinformatics to address significant questions in biology. Requirements include: a Ph.D. in biological sciences or a related field with postdoctoral experience, extensive experience in genomics and bioinformatics, and a strong research record. Expectations: establish an externally funded research program, contribute to undergraduate/graduate education, and service.

All applicants must submit a cover letter, a curriculum vitae, a research statement, a teaching statement, a diversity and inclusion statement, and three letters of reference. For a complete position announcement and information regarding how to apply, visit **http://jobs.uark.edu/postings/37386**. For information about the department see: http:/biology.uark.edu. Completed applications received by **December 13, 2019** will be assured full consideration. Late applications will be reviewed as necessary to fill the position. Inquiries should be addressed to the committee chair Dr. Dan Lessner. (dlessner@uark.edu).

The University of Arkansas is an Equal Opportunity Institution committed to achieving diversity in its faculty. Therefore, the university is especially interested in applications from qualified candidates who would contribute to the diversity of our academic departments. The university welcomes applications without regard to race/color, sex, gender, pregnancy, age, national origin, disability, religion, marital or parental status, protected veteran or military status, genetic information, sexual orientation, gender identity or any other characteristic protected under applicable federal or state law. Persons must have proof of legal authority to work in the United States on the first day of employment. All applicant information is subject to public disclosure under the Arkansas Freedom of Information Act.

OMEROS

Senior Scientist, Medicinal Chemistry

Omeros is seeking a **Senior Scientist** to join our Medicinal Chemistry team. The primary responsibilities will include the design, synthesis, and characterization of organic molecules to be used in our drug discovery programs.

Who is Omeros?

Omeros is a commercial-stage biopharmaceutical company committed to discovering, developing and commercializing small-molecule and protein therapeutics for large-market as well as orphan indications targeting inflammation, complement-mediated diseases, disorders of the central nervous system and cancer.

What are your job responsibilities?

- Designing and synthesizing potential drug candidate molecules
- Working effectively with project teams to identify preclinical candidate compounds
- Conducting complex air- and moisture-sensitive organic reactions
- Analytically characterizing organic compounds using routine methods (NMR, HPLC/MS, etc.)
- Understanding and applying DMPK and biological principals toward the design of small molecules; determining structure activity relationships of compounds
- May supervise or manage Associate Scientists

What experience and education do you need?

You'll need to have a Ph.D. in Organic Chemistry with 5+ years industry experience. We are seeking individuals with:

- Experience in organic synthesis and proven ability to design and synthesize novel compounds through multi-step synthetic routes is required
- The ability to work effectively under pressure, handling multiple priorities simultaneously
- Excellent communication and interpersonal skills.

Please apply through our careers site at **Omeros.com/careers**

ScienceCareers online @sciencecareers.org

By **Vivienne Tam**

Finding community during coffee breaks

I had always heard the stereotype: North Americans value independence, and Europeans value togetherness. But I never fully understood it until 2 months ago, when I left my Ph.D. lab in Canada for a 4-month stint in a lab in France. On my first day, Pierre—a Ph.D. student whose desk is across from mine—tapped me on my shoulder and asked: "Coffee?" I nodded and followed him down the hallway to the common room, where other grad students were filing in. One student brewed an espresso for me that was five times stronger than my normal Americano. Milk and sugar were nowhere to be found. So I sat there, gingerly sipping the bitter liquid and trying hard not to reveal my uncultured tastes, while lab chatter filled the air.

I had traveled to France to work on a project with Pierre. We'd cooked up an idea for a collaboration when he was visiting my university, and we were excited to get started. I had no idea going in, though, that I'd also get a lesson in lab culture.

Coffee breaks are a ritualistic part of work life here. The chatter sometimes turns to serious scientific topics. But mostly, the meetups offer a chance to unwind—to share stories about life inside and outside the lab and to commiserate with people who understand what you're going through.

The lighthearted atmosphere and sense of community is a welcome contrast to my life in Canada, where I spent the bulk of my workdays in isolation. I went into the lab each morning with set goals for my day. At lunch, I'd keep my eyes glued to my computer while I shoveled forkfuls of salad into my mouth, trying to power through my to-do list.

Our lab held weekly meetings where we'd take turns presenting our latest work and getting feedback from colleagues. But we didn't take daily coffee breaks—or any other kind of communal break. My labmates and I were too busy collecting data and publishing papers.

Looking back now, I realize how much we were missing. Researchers need community because good ideas don't just come from reading literature and thinking deep thoughts; it's helpful to bounce ideas off others, particularly in a nonthreatening environment. It's also helpful to have a venue to share the day-to-day ups and downs of life as a grad student. How else are you supposed to know that you're not the only one suffering from challenges such as anxiety and impostor syndrome?

I could've used that kind of camaraderie 2 years ago. For 9 months, I struggled to figure out why I couldn't replicate the results of another study. I worried that something was wrong with my protocols, so I stayed up late at night reading papers, combing over their methods. My adviser was supportive, but I didn't want to pester her too much. I was also hesitant to ask my labmates for help because they had their own projects to worry about.



"It's ... helpful to have a venue to share the day-to-day ups and downs of life as a grad student."

Eventually, my supervisor and I decided to switch our focus. At that point, though, I'd spent months feeling that I was failing in some way—that I wasn't smart enough to figure out what was going on, or that I was making novice mistakes that I wasn't even conscious of.

Would coffee breaks have solved all my problems? Probably not. But I think sharing my feelings and frustrations with my peers would have helped. They might have had ideas about steps I could take to solve my research dilemma. They might have also opened up about how they, too, suffer from setbacks and feelings of failure.

My time in France has taught me that it's important to create space for organic conversations about lab life—failures, incomprehensible data, and personal struggles. In places where that's not the norm, I think grad students should make a point of reaching out to peers, asking them to take coffee breaks or to meet up for lunch—something that I plan to do when I'm back in Canada. The life of a scientist can feel isolating, but it's much less isolating when you're connected to a supportive community. ■

Vivienne Tam is a Ph.D. student at McGill University in Montreal, Canada, who is currently working at the University of Strasbourg in France. Send your career story to SciCareerEditor@aaas.org.

ILLUSTRATION: ROBERT NEUBECKER

Published by AAAS